Open Research Online

The Open University's repository of research publications
and other research outputs

Coring Planetary Ices; Their Thermomechanical Behaviour

Thesis

How to cite:

Garry, James Robert Creighton (2002). Coring Planetary Ices; Their Thermomechanical Behaviour. PhD thesis The Open University.

For guidance on citations see FAQs.

© 2002 The Author

https://creativecommons.org/licenses/by-nc-nd/4.0/

Version: Version of Record

Link(s) to article on publisher's website:
http://dx.doi.org/doi:10.21954/ou.ro.0000e7ec

Copyright and Moral Rights for the articles on this site are retained by the individual authors and/or other copyright owners. For more information on Open Research Online's data policy on reuse of materials please consult the policies page.

oro.open.ac.uk

31 0263637 7

UNRESTRICTED

Coring Planetary Ices;
Their Thermomechanical Behaviour

A thesis submitted for the degree of Doctor of Philosophy

by James Robert Creighton Garry, BSc (Hons), MSc.

March 2002

Planetary and Space Sciences Research Institute

The Open University

Milton Keynes

AUTHOR NO: R7832866
DATE OF SUBMISSION: 29 MARCH 2002
DATE OF AWARD: 16 SEPTEMBER 2002

Abstract

Spacecraft missions are underway that will mechanically probe the material found at the surface of cometary nuclei. Little is known about the physical properties of these bodies and how their surface material will respond to a probe's sampling mechanisms. Tools such as rotating drills or hammering bits can cause the otherwise pristine material to be damaged and heated. This work addresses the phenomenon of tool-induced heating and examines the properties of ices in three planetary environments in which such coring processes may occur.

A unique drilling system has been built to provide data on the thermal response of ices under space-like conditions. Cold (~150 K) samples of water ice and carbon dioxide ice have been formed from the vapour phase and cored with an instrumented cutting head under low pressures. The effort used to core these ices has been measured as a function of temperature, coring speed, and depth rate. Three broad conclusions can be drawn from these experiments.

1) Carbon dioxide ice grown from its vapour at 150 K requires approximately one third of the mechanical effort needed to core or drill the same volume of water ice at a given rate at the same temperature.

2) The power needed to drive a coring tool through water ice at a fixed rotation speed and a given vertical rate trebles as the ice's temperature falls from 240 to 140 K. Specific cutting energies greater than 55 J m^{-3} have been recorded for ice at 140 K, and dense carbon dioxide at the same temperature has been shown to have one half of that strength displayed by water ice.

3) Mechanical effort is mostly converted into heat in a coring process. Temperature rises of at least 10 K have been measured in dense samples of cryogenic (~140 K) carbon dioxide ice around a coring tool that operated with power levels of no more than 2 W. For the same applied power, water ices are expected to display one third of this temperature rise seen when coring void-free carbon dioxide ice at the same temperature.

The magnitude of this heating effect is assessed for a comet sampling tool on the *Rosetta* comet lander. It is expected that temperature rises of a few degrees will occur in water-ice rich material retrieved by the tool if the comet, at depths of several tens of centimetres, shows little porosity. It is also suggested that higher temperatures will be developed by extracting material from greater depths, where carbon dioxide may be present as a void-free ice.

Acknowledgements

Firstly, I thank the Particle Physics and Astronomy Research Council (PPARC) for their help in supporting me during the last three years, and in enabling me to attend workshops and conferences in several countries. As I have found myself engaged in work that differs somewhat from the original predicted area of research, I give thanks also for the flexibility of PPARC and for the adaptable attitude of the PSSRI and the Open University.

Dr Ian Wright, my front-line supervisor deserves particular mention for not abandoning hope during the long months that I spent chasing air-leaks and blind alleys of thought from this work. The calm tolerance he displayed when told of the creation of yet another gadget from unlikely parts was a blessing and allowed work to progress rapidly. Thanks must also go to Dr Martin Miller and Dr Ian Franchi for their patience in tolerating *my* lack of patience when dealing with Excel which, despite its many 'special features', never succeeded in making me beat my Macintosh with a crowbar. I also wish to thank Prof. Colin Pillinger FRS, for giving me the opportunity to work in such an active department.

Outside the Open University I wish to thank Dr Norbert Kömle and Dr Günter Kargl of the Institut für Weltraumforschung in Graz, Austria, for their hospitality and kindness during our meetings there and other countries. On a less serious note, Dr Axel Hagermann is also thanked for his unstinting research on Japanese beer and groceries, messages emailed from the other side of the world are always entertaining – usually because they tend to arrive late at night when spirits are low.

I also thank my family for once again being supportive of my decision to return to academia. Looking back at over these years, the analogy of a roller-coaster ride comes to mind, as they too are often handmade from wood and polished metal and deliver an equal number of unpredictable ups and downs at high speed. But no matter how engrossing the work, the last three years would have been much less enjoyable if it hadn't been for a very dear friend, and so I thank Cindy Lo – for her Beeps and wise words in equal measure.

Publications

REFEREED

Garry J. R. C., 2001. Experiments on drilling cold water ices for planetary sampling, in Proceedings of 1st International Workshop on Penetrometry in the Solar System, held in Graz, published by ÖAW Verlag.

Lorenz R. D., B. Hathi, M. R. Leese, J. C. Zarencki, and J. R. C. Garry, 2001. The Huygens SSP penetrometer, in Proceedings of 1st International Workshop on Penetrometry in the Solar System, held in Graz, published by ÖAW Verlag.

Zarnecki J. C., M. R. Leese, J. R. C. Garry, N. Ghafoor, and B. Hathi, 2002. Huygens' surface science package, Space Science Review, in press

Garry J. R. C., M. C. Towner, A. J. Ball, J. C. Zarnecki, and G. Marcou, 1999. The effect of ambient pressure and impactor geometry on low speed penetration of unconsolidated materials, *Adv. Space Res.* **23** (7), 1229-1234.

POSTERS, ARTICLES, ADDRESSES

Garry J. R. C. and I. P. Wright, 2002. In-situ temperature rises caused by coring vapour-grown CO_2 ice, LPSC XXXIII abstract #1797

Garry J. R. C., 2001.The measured permittivity of CO_2 ice grown under Martian polar conditions, 1st conference on the Geophysical detection of subsurface water on Mars, held in Houston, abstract 7045

Garry J. R. C. and M. C. Towner, 2001. Sonar behaviour in non-terrestrial ocean exploration, LPSC XXXII abstract #1726

Garry J. R. C., 2000. Generalised cutting tool temperatures for a spacecraft payload, Near-Earth Sample Return workshop held in Houston December 2000

Garry J. R. C. and I. P. Wright, 2000. The cutting strength of cryogenic water ice, LPSC XXXI abstract #1982

Garry J. R. C., V. K. Pearson, M. C. Towner, and M. A. Sephton, 2000. Attempted UV photolysis of naphthalene in the presence of martian regolith simulant, LPSC XXXI abstract #1979

Garry J. R. C., I. P. Wright, and C. T. Pillinger, Recreating a cometary coma - applications for martian surface processes, EGS 24 (The Hague), April 1999

Garry J. R. C., I. P. Wright, and C. T. Pillinger, 1999. Isotopic fractionation of cometary volatiles by drilling operations, LPSC XXX abstract #1602

Contents

Symbols and abbreviations used

AU Astronomical Unit (m) ~1.495 x 10^{11}

A A measure of area (m^2)

a Albedo, also a general coefficient

b A general coefficient

c Specific heat of a material (J kg^{-1} K^{-1})

c_{sub} Latent heat of sublimation (J kg^{-1})

D Plate spacing of a capacitor (m)

d A vertical speed (m s^{-1})

E_S Specific cutting energy (Pa)

f Frequency of rotation (rev s^{-1})

g Local acceleration by gravity (m s^{-2})

G Const. of univ. gravitation (N m^2 kg^{-2}) ~ 6.67 x 10^{-11}

I A heat flux (W m^{-2})

k Boltzmann's constant (J K^{-1}) ~ 1.381 x 10^{-23}

l, L Generic lengths (m)

m A generic mass (kg)

n A generic number (dimensionless)

p Local pressure (Pa)

P Power (W)

Pe Péclet number (dimensionless)

Q Power (W)

q A heat flux (W m^{-2})

r A generic radius (m)

r_{out} The outer radius of a coring tool (m)

r_{eff} The effective radius of a coring tool (m)

R Electrical resistance (Ω)

t_1 Undeformed chip thickness (m)

t_2 Removed chip thickness (m)

T A generic temperature (K)

$u_{S,F}$ Volume specific cutting energy (J m^{-3})

V Speed (m s^{-1})

v Volume (m^3)

w Width of a tool or tooth (m)

α A tool's rake angle (degree)

β A friction angle (degree)

δ Dielectric loss tangent (degree)

$\Delta T_{1,2}$ Temperature shifts (K)

ε Strain within a material (dimensionless)

$\varepsilon_{b,c,p}$ Emissivity relative to a blackbody (dimensionless)

ε_r Relative permittivity (dimensionless)

θ An azimuthal angle (degree)

κ Thermal diffusivity (m^2 s^{-1})

λ Thermal conductivity (W m^{-1} K^{-1})

μ Coefficient of sliding friction (dimensionless)

ρ Density (kg m^{-3})

σ A limiting stress (Pa)

σ_{SB} Stefan's constant (W m^{-2} K^{-4}) ~ 5.670 x 10^{-8}

τ Torque (N m)

ϕ Shear angle, also elevation (degree)

ω Rotation speed (rev s^{-1})

The matrix represention of stress

When discussing stress or failure strength, the matrix notation should be used to represent the stress in a material at a given point. The overall distribution of stresses within an object may also be referred to as a stress-field. In an arbitrary co-ordinate system, the stress at a given point in this field is fully characterised by nine[1] components.

$$[\sigma_{ij}] = \begin{bmatrix} \sigma_{11} & \sigma_{12} & \sigma_{13} \\ \sigma_{21} & \sigma_{22} & \sigma_{23} \\ \sigma_{31} & \sigma_{32} & \sigma_{33} \end{bmatrix} \qquad \text{Eq i}$$

A co-ordinate system can always be found that makes the non-diagonal components of this matrix zero. The diagonal components of the stress matrix are then parallel to the axes of this new co-ordinate system and are called the components of principal stress.

$$[\sigma'_{ij}] = \begin{bmatrix} \sigma'_{11} & 0 & 0 \\ 0 & \sigma'_{22} & 0 \\ 0 & 0 & \sigma'_{33} \end{bmatrix} \qquad \text{Eq ii}$$

In the following chapters various stresses will be referred to with particular emphasis on uniaxial stresses, such as tension or compression, which are written as scalars and correspond to the appropriate components in the matrix above. Confining or hydrostatic pressures can be written as $(\sigma'_{11} + \sigma'_{22} + \sigma'_{33}) / 3$, and shear stresses would be the arithmetic difference along two directions such as $(\sigma'_{22} - \sigma'_{33})$. Very brief mention will be made of deviatoric stress, and this is found by subtracting the components of the principal stress from the original stress matrix components. The original stress matrix may be thought of as being the sum of an isotropic stress (given by the mean of the principal stress components) and the deviatoric stress field which is not isotropic and which seeks to distort the material, rather than uniformly squeeze or stretch it. The stresses discussed in this work are primarily uniaxial in nature and so stresses of confinement, compression, and tension that cause failure will be described by appropriately named scalars.

---

[1] Although by symmetry $\sigma_{ij} = \sigma_{ji}$, and only six components of the matrix are needed.

List of figures and tables

* The text in parentheses is the file name for the data sets and is used here only as a guide - the name itself has no significant meaning.

1 Introduction

"There are worlds infinite in number and different in size.
The distance between the worlds are unequal, in some directions there are more of them...
Their destruction comes about through collision with one another."

Democritus of Abdera (450 - ? BCE)

Questions about the past are intrinsically hard to answer. Information is progressively degraded in physical systems and knowledge about the past must be reconstructed from fragmentary clues that have been scattered and faded by time. Yet information is hardy stuff, clues about the origin of the Solar System and the changes it has experienced are partially encoded in the chemistry and make-up of matter in and around the Sun and may be understood through measurements and physically testable models. This goal of building a consistent record about events in the distant past is not a purely academic exercise that lacks practical utility. Through understanding the past and current state of a system from recorded events, predictions can be made about how it may behave in the future, a critical consideration for our planet and its inhabitants.

Ideas about the origin of the Solar System and its subsequent evolution have been shaped and advanced first by the use of ground-based telescopic and spectroscopic observations, and then by finer remote and *in-situ* measurements from planetary probes. The mass and power limitations placed on a probe's payload by current launch technology generally result in space-going experiments using simpler and less capable instruments than their laboratory counterparts. However, some technologies employed by spacecraft cannot be realistically improved upon, and this work examines such a process in a particular setting; the acquisition of a cometary surface sample by drilling. This task will be performed by the spacecraft of the *Rosetta* project operated by the European Space Agency (ESA). In this mission, the spacecraft will be studying an object about which there will be relatively little prior information. While this lack of knowledge underpins the rationale of the mission it is also a hindrance to the design of efficient measuring systems. In general a compromise is struck between the precision and range over which a quantity is measured and a wholly novel environment is best explored with tools that rely on only a few broad assumptions.

In its operation on the comet the *Rosetta* lander spacecraft will mechanically excavate samples from the surface and scrutinize them with a variety of analytical sensors to reveal their structural and chemical composition. To accomplish this goal the material passes through many separate devices and processes before it reaches the analytical instruments. Along the way as few undesirable changes should be made to the sample as possible. It is equally beneficial to have reliable proof from similar laboratory-based systems, that the sample will be gathered and handled with a well-described level of isolation. Change in a quantity that results from unwanted phenomena is rarely problematic if the amount of alteration can be predicted in advance and accounted for. It is that type of calibration which is considered in this work.

One of the earliest processes in the chain of analysis endured by a sample extracted from a comet's surface is the least well understood. Specifically, the degree to which the excavated material is warmed by the sampling device is appreciated only in a very broad manner. By applying work, and thus heat, to the extracted sample, changes may be made in the structural, chemical, or isotopic make-up of the substance. When compared with terrestrial ice coring rigs, the power requirements of proposed spacecraft-carried tools are many orders of magnitude smaller, yet temperature rises may still occur at power levels of only a few watts. The contact area between a material and a drill head having a diameter of a few centimetres might be only a few square millimetres, through which several watts of mechanical power are transmitted and converted into heat. For comparison, the filament in a light-bulb with a similarly small power rating has a surface area broadly comparable to the contact region of such a drilling tool. The significant temperature rise seen in the light-bulb filament is a result of its thermal isolation in the evacuated bulb and this naïve example shows that cutting temperature shifts cannot be dismissed out-of-hand for media with unknown thermal conductivities. This argument can also be applied to the removal from other planetary bodies of materials that are neither thermally nor physically robust and which may be unintentionally altered by heat.

Quantifying this type of phenomenon requires an analogue of the relevant spacecraft part and the intended sample material; most space missions use a suitable environmental system to separately test either the instruments or the processes that are used in the mission. The *Rosetta* mission faces particular difficulties in the task of producing environments that have the likely properties of a comet's surface. The lack of information about the target comet

(and comets in general) means that any test material for the surface will differ from the actual surface to an unknowable extent.

A reasonable strategy is then to calibrate the spacecraft sensors against materials which have properties that span the possible range of values for the mission's target. In other words, rather than trying to emulate a particular multi-component substance or environment to a high degree of fidelity, a more useful approach is to expose the lander's payload to a variety of simple materials that can be reliably produced and which have property values that cover the range likely to be found at the target. A second difficulty occurs in trying to calibrate a complex sensor or sub-system. The chosen test method can lie between two extremes in which either the component parts have their individual behaviour thoroughly recorded in response to various situations, or the whole sub-system can be tested in its flight-ready configuration. Ideally, some combination of all-up calibration and component-level testing should be performed; but choosing either approach alone can lead to costly delays when wringing out bugs from a final and essentially frozen design, or chasing problems that have arisen from the interaction between two otherwise well-behaved components. Examples of the perils associated with either approach in the field of aerospace engineering are given in the chastening study of Pinkus *et al.* (1997) on the design and test procedures of the Space Shuttle Main Engines.

This thesis therefore examines a small and clearly-bounded subject centred on the operation of rotary drills or coring tools carried by spacecraft to investigate ice-rich material. By limiting the study to the interaction of a tool with a target material and the extent to which unwanted heating can occur in the drilling process, secondary problems of processing and analysing the material are left for further study. To assess the extent to which material may be heated during its acquisition it was necessary to examine the resistance of realistic planetary surface ices to deformation by sharp cutting tools. Knowledge of this property, which is related to various measures of a substance's strength, is important because mechanical work expended by a cutting tool is transformed into heat, and excavation of a harder material therefore requires more effort and produces more waste heat than deformation of a softer substance. It should be noted that the ices used in this work are all either formed or studied at low temperatures (~140 K). While success was had in finding values in the literature for thermal properties of the ices examined here, few reports could be found describing their response to

the rapid mechanical shearing generated by a cutting operation, and no detailed analyses could be found for this process at cryogenic temperatures, let alone under reduced pressures.

A dedicated vacuum drilling system was therefore designed and built to measure the effort required to cut cryogenic ice at various rotation rates and loads. This apparatus, which was built over a period of some 18 months, would be unusual if coring ice under vacuum had been its sole function. It can be further described as a wholly unique system because it could not only form its ice samples from the vapour phase, but was equipped with miniature *in-situ* thermometers to report the temperatures at the interface of the ice and the cutting tool. No similar capability exists in the three other known vacuum systems that investigate the mechanical alteration of ices under conditions present in cometary nuclei. From the dynamics of the system's cutting tool, as recorded by load sensors, the temperature rises generated by a coring process could be estimated using models taken from industrial machining studies. Those predictions were then compared with data gained from the *in-situ* thermometers embedded in the ices, and with these comparisons the actual operation of spacecraft-borne sampling tools could be considered.

1.1 Thesis structure

Having introduced the general nature of the problem, the specific environments that may be considered for an ice-sampling spacecraft will be introduced in the following sections of this chapter. Three particular planetary regions will be described with a view to their ice make-up: the nuclei of active comets, the polar areas of Mars, and the surfaces of certain satellites.

The next chapter will describe the physical processes at work in the application of the simplest of geotechnical tools, the penetrometer. A model based on a general penetration algorithm will be applied in the chapter's first section to a specialized version of this tool, the blade penetrometer. The remaining parts of that chapter summarize models of cutting dynamics and the resulting temperature rises produced by cutting tools. Consideration is then given to the spacecraft lander of the *Rosetta* project, and its sampling sub-system.

Chapter three describes an early attempt to grow and drill cryogenic samples of water ice. The method used to grow bubble-free ice samples is described, and a method outlined in chapter four is applied to gain novel data on the strength exhibited by cryogenic water ice when cut by a coring tool.

Following this crude work, a more elaborate and capable vacuum drilling system is detailed in chapter four. This apparatus allows materials to be cooled to low temperatures and to be probed with an electrically powered tool under vacuum conditions. The system's calibration, its electrical, mechanical, and sensing sub-systems are also described.

Chapter five presents the work accomplished with this coring rig which consists of;

1 The formation of carbon dioxide snows and the subsequent probing of the material with a blade penetrometer head under reduced pressures and at low temperatures. Comparisons with another porous material are made, and the failure strength of this CO_2 snow found.

2 The growth of dense forms of CO_2 from vapour under conditions similar to those that exist at the martian poles in winter. This material is shown to have a very low porosity and its dielectric properties were measured. Slabs of this ice were then cored with an instrumented tool to calculate the cutting resistance of this material at high strain rates.

3 The slow freezing of purified water into bubble-free ice blocks that were cooled to various cryogenic temperatures in a vacuum and then cored, giving data for the failure of water ice at the high strain rates and low temperatures that may be encountered in surface missions to outer Solar System satellites.

4 A brief and unfortunately inconclusive attempt at growing and coring water ice from the vapour phase.

5 The *in-situ* measurement of temperature within a slab of carbon dioxide ice at a point in the path of a coring tool with the aid of miniature semiconductor thermometers.

Charts are drawn up that summarize the experiment results. The trends visible are discussed and compared to the predictions made for the mechanical resistance and cutting temperatures experienced by the cutting head. A number of improvements are also suggested that may be made to the experimental apparatus in ices order to refine and extend this work.

Finally, chapter six summarizes the experimental findings and considers the thermo-mechanical properties of brine and dust-loaded ices. The performance of a named spacecraft sampling tool in a cometary environment is also broadly discussed.

1.2 To aim for a comet

Before discussing the make-up of comets it is useful to describe their behaviour and origins. While planets have been the obvious target for many spacecraft studies they have, as a result of their mass, been differentiated and chemically evolved as can be readily seen from their appearance. Conversely, indications of the chemical and thermal environment of the early Solar System should be found only in those objects which are both too small to have warmed appreciably through accretion and which have experienced little solar heating. Traditionally, those requirements would have been thought of as being applicable only to comets but the detection of minor bodies in relatively stable trans-Neptunian orbits has broadened the scope for the telescopic study of early planetary materials. At present none of these more distant, and presumably more primitive, objects are practical targets for reconnaissance; spacecraft studies are limited to those bodies which either make relatively close passes to the Earth, or which permit modest energy trajectories to intersect their path.

The sizes of many known cometary nuclei (typically 10^2 to 10^4 m) make them poor targets for the naked eye. Their sometimes spectacular appearance is caused by the presence of a great number of small sunlight-scattering grains that are lifted from the nucleus by the expansion of gas which is in turn produced by the sublimation of material within the comet. As well as illuminating the dust from the comet, the Sun's particulate and electromagnetic radiation interacts with the nucleus' liberated gas in a complex manner that results in a partially ionized cloud of atoms and molecules, the details of which will not be discussed as there are many standard texts that deal with cometary physics in general (e.g. Huebner, 1990; and Newburn *et al.*, 1991). Comets that were visible in the dark pre-industrial skies of antiquity led to them being noted in chronicles of celestial phenomena dating back over two and a half millennia (Kronk, 1999). Yet, it wasn't until the 1580s that the first attempts at measuring their distance from the Earth were published. Using the parallax method, Tycho Brahe observed comets over a span of almost twenty years, and deduced that they were not only located beyond the Moon, but that they also moved along paths that came no closer than Venus to the Sun (Haubold, 1997). With the development of accurate gravitational models, and the formulation of the laws of planetary motion, comets with their near-clockwork periodicity became a glowing example of the predictive power of mathematical physics. The prime

example of which was the prediction by Edmund Halley that the sightings scattered throughout history of a comet could be assigned to a single object with an average orbital period of around 76 years.

Over the next three hundred years new comets were observed and catalogued and yet from time to time comets, such as Brookes 2 were seen to fragment (Spencer-Jones, 1947) with no diminution in the rate at which new comets were seen. Perhaps the lack of curiosity about the origins of comets in the face of their observed destruction is understandable in the absence of accurate dating methods for the Earth. With no time scale to compare the orbital lifetime of comets with, there could be no means of assessing the relative number of objects that had yet to be discovered based on their rate of destruction. Although the Earth was hypothesized to be considerably older than the 35,000 to 50,000 year-old figure derived from experiments by among others, Kelvin (Thompson, 1863) and the Comte de Buffon[1], no accurate upper limit had been set by the start of the twentieth century. The development of radiometric dating by Bertram Boltwood in 1907 (Badash, 1968) led ultimately to an appreciation of the period ($> 4.5 \times 10^9$ years) in which the Earth had been a separate entity, and similar ages could be ascribed reasonably to the other bodies of the Solar System.

Firm data for the hypothesis that some comets also had to have very long histories could be found by examining the distributions of orbital parameters among the known comets. Figure 1 shows orbital data for 296 comets. If that set is not heavily influenced by selection effects that make particular types of object difficult to detect, then it is clear that the majority of comets seen in the last few hundred years have orbital planes that lie within 30° of the ecliptic, and occupy orbits that show a wide range of eccentricity values (0.8 to 0.2). Aside from these bodies, there is a relatively small number of comets that have near-unity values for their orbital eccentricity and which show no preferred orbital inclination. It is an observable and perhaps surprising fact that these two populations have markedly different average orbital periods. This is shown by the different marker styles which discriminate between comets with orbital periods either longer or shorter than 200 years. This distinction is sufficiently useful for it to be used to classify comets and they may be described as either having short period (SP) or long period (LP) orbits.

---

[1] George-Louis Leclerc (1707-1788), who published estimates of 75 kyr based on the cooling rates of heated spheres but who later privately advocated the exceptional age of 3 Myr for the Earth (Steel, 1997).

Comets with periods of less than 20 years tend to have orbital aphelia[2] commensurate with the radius of Jupiter's orbit and are thus named Jupiter family comets.

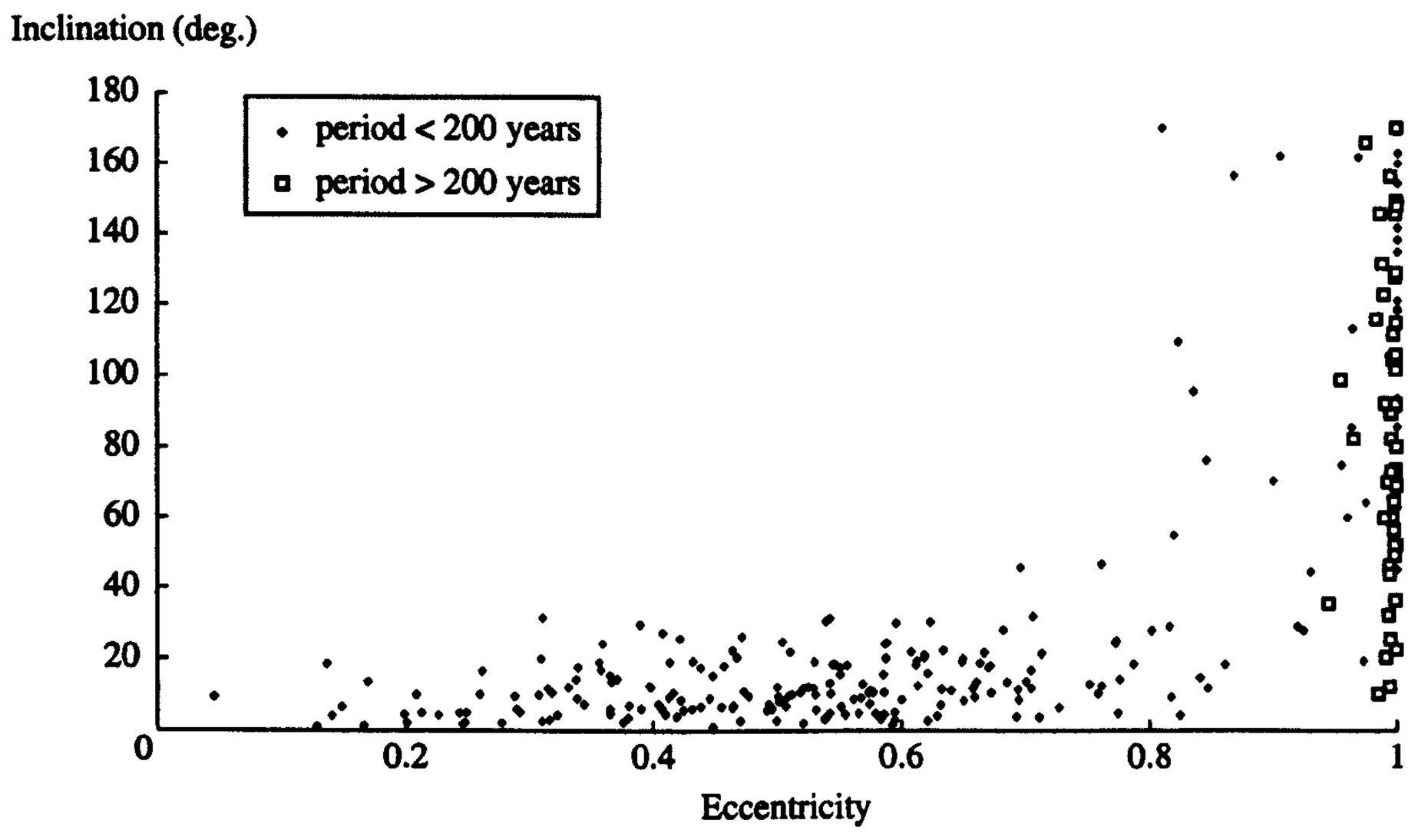

Figure 1 – Orbital inclination and eccentricity data for some 300 comets, data taken from the IAU Minor Planet Center & Central Bureau for Astronomical Telegrams.

The Dutch astronomer Jan Oort suggested that those comets with very long orbital periods and near-unity orbital eccentricities will have necessarily made few earlier passages through the Solar System (Oort, 1950). To be weakly bound to the Sun in this way Oort calculated that a long-period comet would spend a considerable length of time at distances of around 10^5 astronomical units (1 AU being the average Earth-Sun distance). At such distances comets travel in non-Keplerian paths and drift at low speed (~50 m s^{-1}) with the Sun as one of several gravitational influences. Although the notion of a distant source for LP comets was first proposed by Ernest Öpik in 1932, the name 'Oort Cloud' has been generally adopted as referring to the population of comet-like bodies bound loosely to the Sun and extending mid-way between the Sun and its nearest stellar neighbours. Despite its name, the average density of objects in this proposed source is very low and un-cloud like. If the figures suggested by Weissman (1998) are taken as guide values, then the postulated 10^{12} objects form a very tenuous Oort 'haze' with a spatial density of a little less than 1 per AU^3. In this model the presence and re-supply of long-period comets is explained by having the cometary nuclei

---

2 For a Sun-orbiting body, the point on its orbit which has the maximum separation from the Sun.

formed in the early Solar System, subsequently ejected by planetary encounters to large solar distances, and then nudged back toward the Sun by various gravitational disturbances, with the galactic gravitational tide playing a significant role (Torbett, 1986, and Matese and Whitmire, 1996). The following cartoon of the process is taken from Weissman (1998).

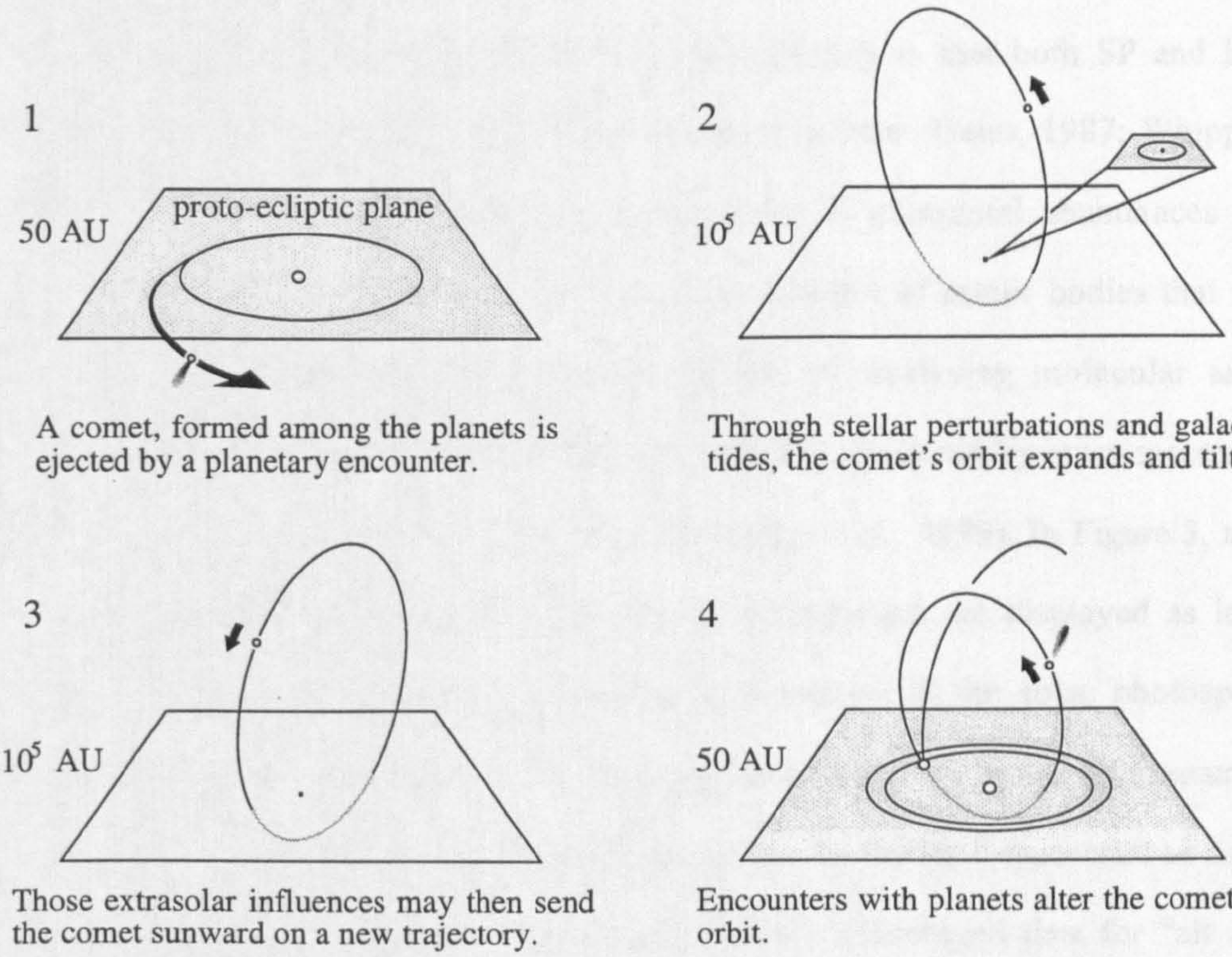

Figure 2 – The hypothesized orbital evolution of a long-period comet.

The above model does not explain the known abundance of short-period comets. The efficiency with which LP comets may be 'transformed' into SP objects by capture encounters with the large planets has been calculated as being four orders of magnitude too low (Joss, 1973) for LP objects alone to account for the SP population. A second reservoir of objects was suggested to address this shortfall, with Kenneth Edgeworth's work being one of the first to postulate the existence of such a source in the form of a trans-Neptunian comet belt (Edgeworth, 1949). In the course of modelling the early Solar System as a two-dimensional ensemble of planetesimals he found it "unreasonable to suppose that the original… material came to an abrupt end outside the orbit of Neptune" and concluded that there may be a "vast reservoir of potential comets" in this outer region. More modern numerical models (Joss, 1973; Fernández 1980; Duncan *et al.*, 1988) illustrate that a low-inclination population

beyond Neptune could indeed be a plausible reservoir of bodies capable of being perturbed into shorter orbits similar to those of SP comets. The first member of this trans-Neptunian reservoir (1992 QB_1) was found in 1992 (Jewitt and Luu, 1992), and since then over four hundred objects[3] have been found in similarly distant orbits - the topic is reviewed comprehensively by Weissman (1995) and Jewitt (1999).

A common feature of many cometary formation models is that both SP and LP comets are thought to have been formed within the early Solar System (Geiss, 1987; Whipple, 1987). Testing this hypothesis would require the measurement of elemental abundances in comets alongside those of other Solar System bodies. Of the handful of minor bodies that have been encountered by spacecraft carrying payloads capable of analysing molecular and atomic abundances, only 1P/Halley[4] has had its coma gas and dust measured by mass-spectrometers on several spacecraft over a period of several days (Altwegg *et al.*, 1999). In Figure 3, taken from table 7 of Anders and Grevesse (1989), the atomic abundances are displayed as logarithmic ratios with respect to the abundance of elements measured in the solar photosphere. The cometary values, plotted with open circles and large error bars, are from the measurements of 1P/Halley's coma by the PUMA-1 mass spectrometer on the *VeGa* 1 spacecraft as analysed by Jessberger *et al.* (1988). Closed circles are used to plot the averaged data for "all acceptable analyses" of meteorite chemistry (Anders and Grevesse, 1989). That there are no significant deviations between the elemental abundance of the cometary and meteoritic data when compared to the solar values for elements other than hydrogen, suggests that all three objects, or classes of object, have indeed been made from essentially the same material. However, different formation temperatures will have led to varied chemistries and the formation of differing molecular abundances.

---

[3] Referred to variously as Kuiper Belt objects, trans-Neptunian objects, and Edgeworth-Kuiper objects.
[4] For brevity, the pre-1995 IAU comet nomenclature is used to introduce objects in this thesis. The code shows that 1P/Halley was the first recorded comet, and that it makes or is calculated to have made, periodic appearances.

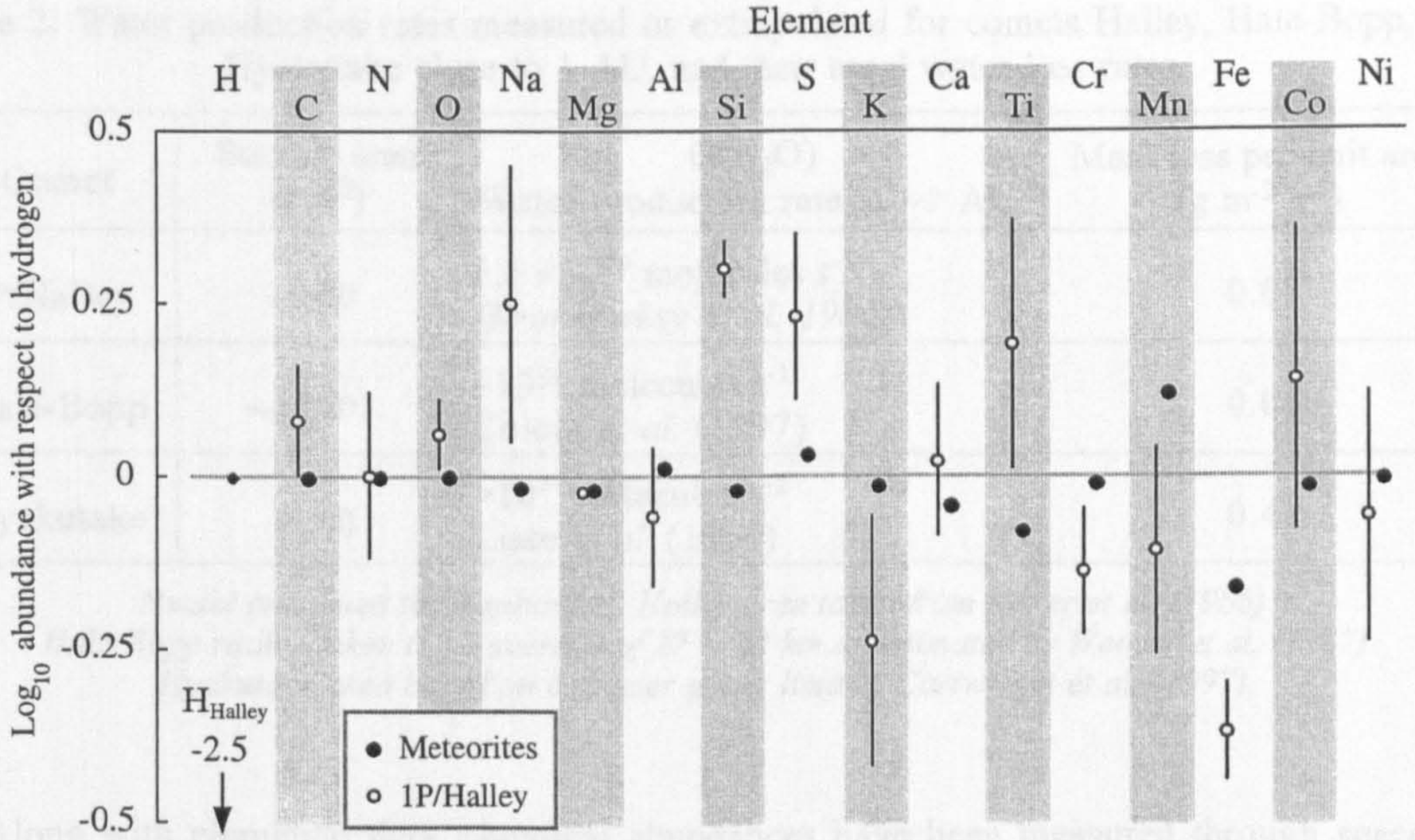

Figure 3 – The elemental abundances in some Solar System objects as ratios of the solar photospheric abundance.

The dominant molecule found in known cometary comæ is water or its photo-dissociated ions, with the next most abundant species being carbon monoxide which can have a mixing ratio relative to water of between 1% to 30% for different comets (A'Hearn and Festou, 1990). Ground-based measurements of spectral emission features have revealed the presence of other less abundant molecules in comæ spectra. For two recent bright comets P/1996 Hyakutake and P/1995 Hale-Bopp, Table 1 lists the major coma species detected and their abundances, with data taken from Crovisier and Bockelée-Morvan (1999).

Table 1: Significant molecules in the comæ of comets Hale-Bopp and Hyakutake.

Molecule	Hyakutake abundance	Hale-Bopp abundance	Detection method
H_2O, water	100	100	IR
CO, carbon monoxide	6 – 30	20	radio, UV, IR
CO_2, carbon dioxide	-	20 (at 2.9 AU)	IR
CH_4, methane	0.7	0.6	IR
CH_3OH, methanol	2	2	radio, IR
H_2CO, methanal	0.2 - 1	1	radio
H_2S, hydrogen sulphide	0.8	1.5	radio
NH_3, ammonia	0.5	0.7	radio, IR

The similar make-up of the comæ for these two comets should be considered in the light of their different sizes and activities which are shown in Table 2.

Table 2: Water production rates measured or extrapolated for comets Halley, Hale-Bopp, and Hyakutake close to 1 AU, and their areal water loss rates.

Comet	Surface area (km^2)	$Q(H_2O)$ Water production rate at ~1 AU	Mass loss per unit area ($g\ m^{-2}\ s^{-1}$)
1P/Halley	~300	5.5×10^{29} molecules s^{-1} *(Krankowksy et al. 1986)*	0.05
Hale-Bopp	~4000	$\sim 10^{31}$ molecules s^{-1} Colom *et al.* (1997)	0.08
Hyakutake	< 80	$>10^{30}$ molecules s^{-1} Lisse *et al.* (1999)	0.4

Nuclei presumed to be spherical. Halley area taken from Keller et al. (1986)
Hale-Bopp radius taken to be average of 27 to 42 km as estimated by Weaver et al. (1997)
Hyakutake area based on diameter upper limit of Cartwright et al. (1997)

Along with elemental data, chemical abundances have been measured through spacecraft encounters with comets and their comæ. Measurements by mass-spectrometers onboard the *Giotto* spacecraft of the composition of 1P/Halley's coma found over one hundred species, and their abundances are reviewed in Geiss *et al.* (1991) and Huebner *et al.* (1991) among others. Despite the success with which the chemical composition of comæ can be recorded, many of the observed molecules do not have unique formation routes and it is therefore not possible in general to relate detected molecular abundances to unambiguous mixing fractions of their solid phase in the nucleus.

Warming of a comet's nucleus by the Sun leads to the observable outgassing of vapour to form the coma. It is widely believed that the loss of condensed ices from the near-surface also leads to the formation and slow growth of an ice-free crust of cohered grains that, to some degree, chokes the sublimation of gas from underlying ices. This model, developed by Brin and Mendis (1979) has been elaborated upon by many researchers; Prialnik and Bar-Nun (1988) through their consideration of the exothermic conversion of water ice phases, modelling of the dynamic evolution of the grain-grain geometry within the crust (Rickman *et al.*, 1990), calculation of the variation of local vapour pressure and gas flow direction as a function of depth (Mekler *et al.*, 1990), and the consideration of cohesion between grains of the desiccated crust (Kührt and Keller, 1994). Although accurate physical analogues of such nuclear crusts probably cannot be formed on Earth[5], their formation is widely accepted as being a common feature of cometary nuclei that experience regular solar heating.

---

[5] The tenuous forces present at a comet's surface arising from electrostatic, Van der Waals, and drag forces are all much smaller than terrestrial gravity (Ball and Kömle, in press)

The formation of these crusts is accompanied by the gradual desiccation of the comet nucleus but this is not the only fate that a comet can face; comets may also be catastrophically disrupted by tidal interactions. A self-gravitating and cohesionless body of density ρ_m is likely to be sundered if it passes a larger object, of radius R and density ρ_M, within the Roche[6] limit of the larger body. At this point the force of gravity holding the smaller body together becomes smaller than the tidal force developed by the gravity gradient of the larger mass and for a notional object with zero tensile strength this limiting distance of approach can be written as

$$R_{roche} = R\left(\frac{2\rho_M}{\rho_m}\right)^{\frac{1}{3}} \qquad \text{Eq. 1}$$

By observing comets as they pass large bodies such as the Sun, it is possible to place limits on their combined strength and density by simply watching whether they fragment or not. Breakup events are common and do not necessarily spell the end of the comet as a visible object. The fragmentation often leaves large discrete 'boulders' rather than a swarm of dust grains, as witnessed recently by the multiple splitting events seen in comet LINEAR. This comet fragmented twice in the course of one year, with the last break-up occurring just a week before its passage through perihelion (ESO press release, 18a-b/01, 2001). Encounters with massive planets such as Jupiter can also destroy comets, purely through tidal effects without the presumed aid of thermally driven internal pressures generated by the Sun. In 1889 16P/Brooks 2 was seen to split during an approach of Jupiter (Spencer-Jones, 1947), and from that event its bulk density has been estimated in the work of Sekanina and Yeomans (1985) as being 250 ± 80 kg m^{-3}, comparable to that of loosely compacted snow. A much more closely observed cometary breakup occurred in 1992 and led to the destruction two years later of comet Shoemaker-Levy 9 (SL9). In its apparition of 1992, SL9 is believed to have passed Jupiter sufficiently closely for its orbit to be perturbed such that it would impact the planet two years later[7]. Not only was its orbit altered, but in that encounter of 1992 it is thought that the comet passed within the Roche limit of Jupiter (R_{roche} = 91 000 km), and was tidally disrupted into around twenty major fragments which subsequently struck the planet in July 1994. Unfortunately the break-up event itself was not observed, and because the distance at which

---

6 Derived by Édouard A. Roche (1820-1883), in 1849. The smaller body is not assumed to have an equipotential shape for simplicity.

7 Details on this comet's orbital evolution are given in the review paper of Chodas and Yeomans (1996).

fragmentation occurred is not known, the density of SL9 could not be calculated using the Roche limit model. However, for plausible 'miss distances' with the planet it is thought that tidal stresses no greater than 1 kPa could have been involved (Weaver and Jewitt, 1995). In addition, the bulk density of the original nucleus could be predicted by modelling how the fragments should have clumped under their self-gravitation in the two years until their impact with Jupiter. Through this type of modelling Asphaug and Benz (1994) gave a bulk density range for the nucleus of 300 to 700 $kg\,m^{-3}$. Uncertainties in the perijove of the comet's penultimate encounter with Jupiter caused some variation in the maximum permissible bulk density, and similar work by Boss (1994) found a higher upper limit for SL9's bulk density of 2000 $kg\ m^{-3}$. Some of the pre-impact fragments are shown in the left-most part of Figure 4 taken with the Hubble Space Telescope, the image shows an elongated train of pieces, the largest of which are believed to have been up to a few kilometres in diameter.

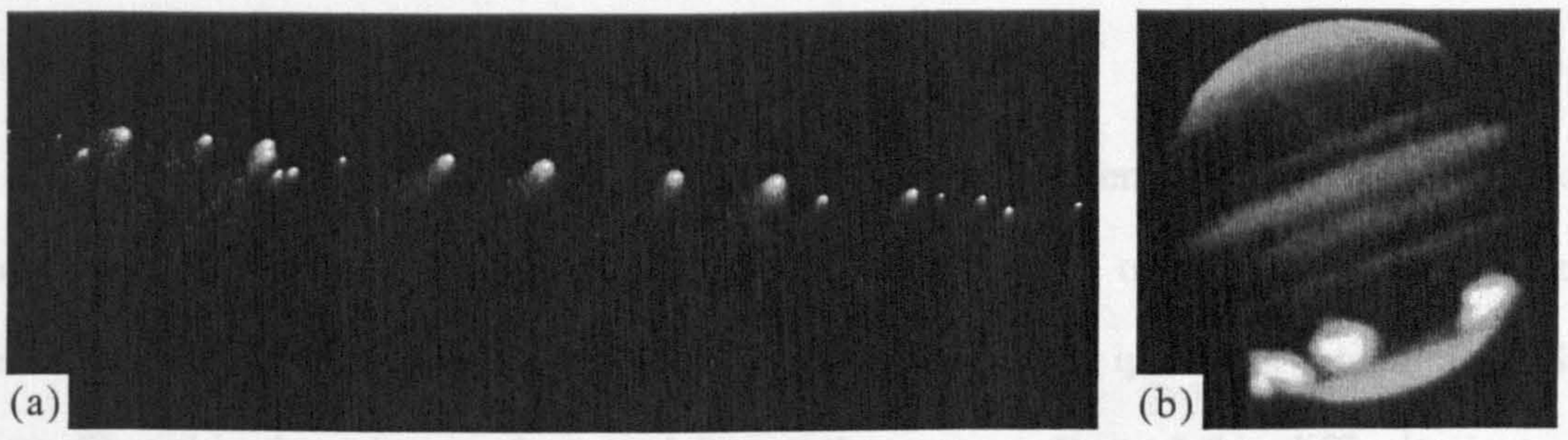

Figures 4a/b – False colour images of the larger pre-impact fragments of comet SL9 (a) and the resulting infra-red impact marks in the jovian atmosphere (b).

In Figure 4 the image of Jupiter was taken at a wavelength of 2.5 μm by the 3.5 m Calar Alto observatory on the 20th of July and shows the thermal traces left by the impact of the comet fragments on the lower left limb of the planet which were carried into view by the planet's rotation. It is notable that some of the fragments formed from the original disruption were seen to break into smaller pieces in their terminal approach to Jupiter, suggesting that if SL9 had had an inner structure made up from discrete 'boulders', then they too cannot have a cohesive strength radically greater than the whole comet (Weaver and Jewitt, 1995, pp49). Close encounters with massive bodies such as the Sun or Jupiter are not the only means by which comets can be made to fragment. Comet LINEAR (C/1999 S4) broke apart at a distance of 115 million kilometres (0.77 AU) from the Sun, implying that another process, such as internal gas 'pressurization' was probably responsible for its destruction, and such a mechanism

is suggested by Ruzmaikina (1999) as an aid to tidal disruption by fluidizing the particles within a marginally compacted body.

Estimation of a comet's bulk properties can be made without waiting for it to have a catastrophic meeting with a planet. A common technique used to infer a comet's mass uses observations of the orbital perturbations caused by the reaction force exerted on the nucleus by erupting gas jets. Uncertainties in the density and speed distribution of material in such jets compromise the accuracy of this method, and when applied to comet 1P/Halley, for example, Peale (1989) constructed a worst-case range for its bulk density with this method of 30 kg m^{-3} to 4900 kg m^{-3} through a pessimistic combination of errors, and derived a probable upper bound of 1480 kg m^{-3}. Along with these remote and indirect methods, the mass and thus bulk density of a comet can be measured by monitoring the perturbation that a spacecraft's trajectory experiences in its vicinity. The craft may perform range-rate measurements to reveal the orbital changes, or ground-based monitoring of the Doppler shift in the spacecraft's radio transmissions can be used to infer the mass of the body.

Despite the hazards faced by comets there is general agreement that among all known Solar System bodies their nuclei are believed to contain some of the least altered material (Weidenschilling, 1997) associated with the Solar System. Yet questions remain about how comets fit within the scheme of an evolving stellar system. Part of this difficulty is one of taxonomy. With continued development in the capabilities of observational instrumentation it is unsurprising that bodies are found which blur the distinction between comets and other objects of the solar neighbourhood. A number of bodies have been identified through reflection spectra and orbital measurements which fall outside the traditional classification schemes. Objects displaying comæ have been observed on trajectories that are associated with deep-system asteroids (Kerr, 1988). Some of these remote objects display the spectral signatures of surface water ice, as demonstrated through observations by Foster *et al.* (1999) of minor body 2060 Chiron. Similar spectral techniques can be used to identify not only chemical species, but also to measure the extent to which isotopic relationships are shared among various bodies. Isotope ratios are characteristic of particular formation conditions and temperatures. It is possible to show whether two dissimilar bodies share a common origin by measuring specific ratios of their constituent isotopes. Through such observations of the isotopic composition of

coma gases, and by inference, a comet nucleus' ices, it has been possible to constrain the contributions that comets may have made in transferring chemicals through the Solar System. Data from spectroscopic comet observations and from the fly-by sampling and analysis of 1P/Halley's coma in 1986 have been used by Laufer *et al.* (1999), and Eberhardt *et al.* (1995) among many others, to suggest that a significant fraction of the terrestrial water was delivered by cometary impacts: a current review is made by Robert (2001). This hypothesis is supported by the observed large difference between the deuterium to hydrogen ratio of water in the Earth's oceans (D:H = 1.49×10^{-4}) and the mixing ratios for those same isotopes observed in the protosolar neighbourhood (D:H ~ 8×10^{-5}). The comets listed in tables 1 and 2 have broadly similar and small HD:H_2O ratios (Eberhardt *et al.*, 1995; Meier *et al.*, 1998) that are used to infer D:H ratios of around 3×10^{-4}. The enrichment in deuterium seen in cometary water suggests that a fraction of the Earth's water did not form in the protosolar nebula but shares a common origin with cometary water. Moreover, the D:H ratio seen in cometary water cannot arise simply through ice condensation at low temperatures because no enrichment is seen in the ratio of HDO to H_2O in ice frozen from a mixture of these waters' vapours at low temperatures (Laufer *et al.*, 1999). A postulated source for such deuterium-enriched water is that of interstellar molecular clouds. These objects can support ion-molecule reactions capable enriching water ice with deuterium and yield D:H ratios of ~3×10^{-4} (Gensheimer *et al.*, 1996), broadly similar to cometary D:H ratios. Comets formed with water ice arising in these regions may deliver volatiles to the Solar System at any point in its history. Orbital calculations by Fernández and Ip (1983) suggest that the outer planets can gravitationally scatter comet-like objects sufficiently well for the make-up of terrestrial water to have been modified[8] from its original protosolar state by the delivery ice-rich objects condensed far from the early Sun.

The broad concept of cometary volatile transport is reviewed by Delsemme (1995) and details of the final stage of the process are discussed by Chyba *et al.* (1990) with emphasis on the impact survivability of complex organic molecules. While beneficial to the early terrestrial biosphere, cometary impacts can be calamitous to the present Earth and this hazard will be addressed after the following discussion of cometary exploration.

---

[8] The amount of comet-borne water delivered to the Earth over its history is suggested as being around 10^{22} kg (Delsemme, 1995).

1.2.1 Cometary spacecraft missions

The ESA cornerstone mission, *Rosetta*, will attempt to rendezvous a two-part spacecraft made of an orbiter and lander, with a comet. This will be the first cometary spacecraft programme to perform long-term reconnaissance of its target, and the first to deliver a lander to a comet's surface. All previous missions to comets having been fly-pasts, the encounter details for which are given in Table 3.

Table 3: Spacecraft that have been launched successfully to comets.

Flyby Date	Comet	Spacecraft	Fly-by mass (kg)	Fly-by speed (km s^{-1})	Miss distance (km)
11 / 09 / 85	21P/Giacobini-Zinner	ICE[9]	478	21	7 800
06 / 03 / 86	1P/Halley	VeGa 1	3400	79	8 890
08 / 03 / 86	1P/Halley	Suisei	138	28	150 000
09 / 03 / 86	1P/Halley	VeGa 2	3400	77	8 030
11 / 03 / 86	1P/Halley	Sakigake	140	29	7 000 000
14 / 03 / 86	1P/Halley	Giotto	550	68	600
10 / 07 / 92	26P/Grigg-Skjellerup	Giotto	< 550	14	~150
22 / 09 / 01	19P/Borrelly	Deep Space 1	415	16	2 200

Data from Huntress (1999), Keller (1990), Reinhard (1986), and mission specific Internet sites such as the National Space Science Data Center (`http://nssdc.gsfc.nasa.gov/`)

The target comet of the *Rosetta* mission, 46P/Wirtanen, will be reconnoitred by the orbiter spacecraft prior to the deployment of the 90 kg lander which will attempt to make a soft-landing on the nucleus. Limitations in launch vehicle capability, and the related restrictions on a spacecraft's manoeuvring ability mean that the paired *Rosetta* craft will not be launched to their target along a direct (Hohmann) trajectory. Its complicated early tour includes three gravitational assist manoeuvres: one at Mars and two at Earth. These encounters are designed to increase the craft's orbital energy so that it meets 46P/Wirtanen on the sunward leg of its 2011 apparition with relatively little difference in speed. Figure 5 shows the likely trajectory of the *Rosetta* spacecraft as of mid-2000. The diagram also shows partial tracks for two minor bodies that are designated as flyby targets for the spacecraft. Of the two, 140 Siwa is the larger object, a C-type asteroid being around 110 km in diameter (Barucci *et al.*, 1998; Le Mouélic *et al.*, 2001). C-type asteroids have a dark (0.04 to 0.06 albedo) neutral-

[9] The International Comet Explorer, formerly known as International Sun-Earth Explorer 3, ISEE-3.

coloured surface with a spectrum suggestive of hydrated silicates and carbon (Lodders and Fegley, 1998). The other flyby candidate, asteroid 4979 Otawara, was observed between 1998 and 1999 (Doressoundiram *et al.*, 1999) and found to have a circular equivalent radius of between 2 km and 1.3 km - the uncertainty arising from insufficient data which also prevented it from being identified with any particular spectral class.

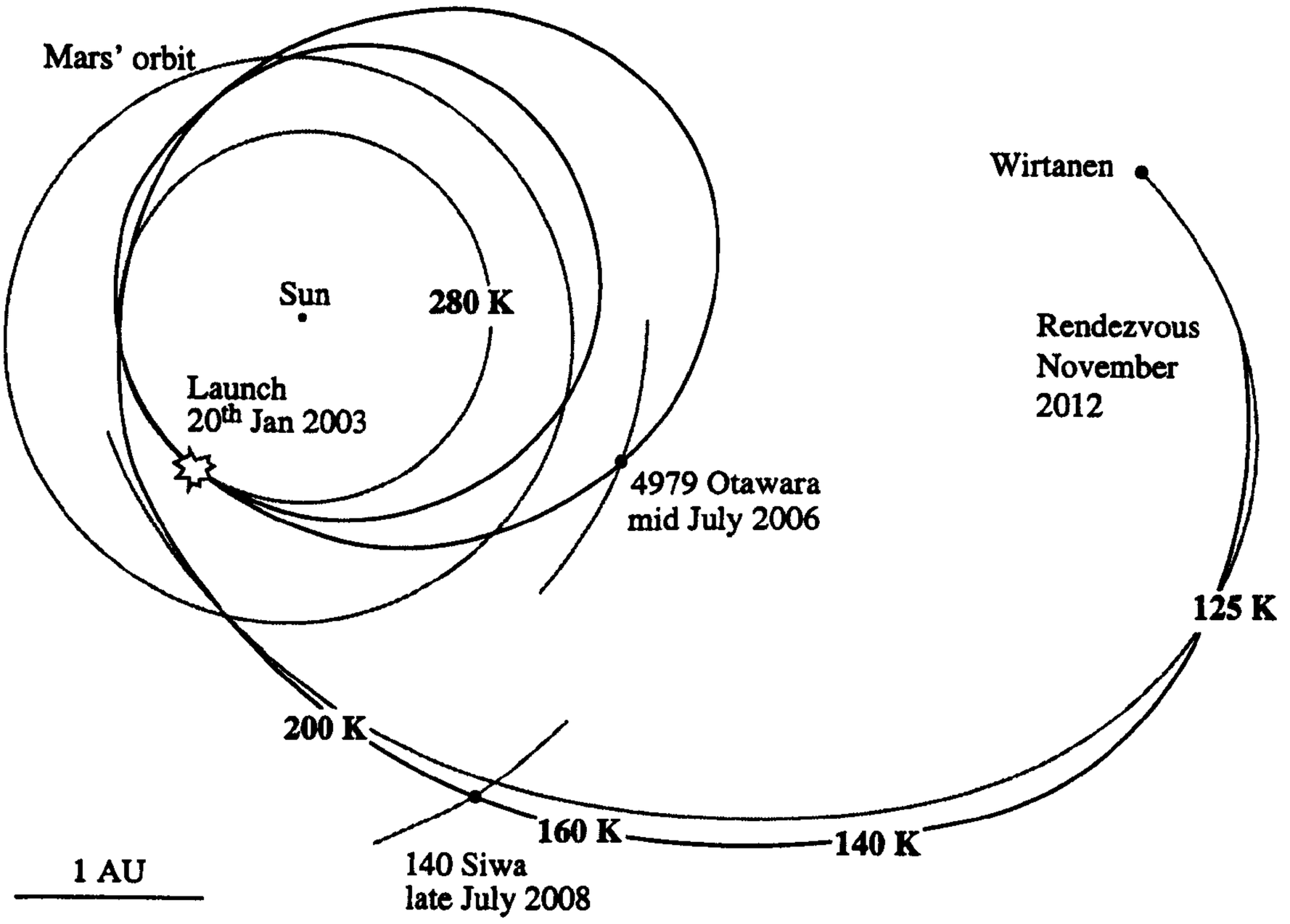

Figure 5 – Current planned trajectory of the *Rosetta* spacecraft. Numbers in bold type show the temperature of a black test body at various points along the spacecraft's path to indicate the changing thermal environment of the spacecraft.

The numbers in bold type in Figure 5 show the temperature of a black body in radiative thermal equilibrium with the local solar heating flux, and were calculated using;

$$T_{fast} = T_{sun}\sqrt{\frac{r_{sun}}{2R}} \qquad \text{Eq. 2}$$

where r_{sun} and T_{sun}, are the average radius of the Sun (7×10^8 m) and its effective surface temperature (5800 K) respectively. Further details about this model are given in appendix D, but it is sufficient to note that while the *Rosetta* spacecraft are built so that their interiors are well insulated from thermal extremes, 46P/Wirtanen has no such advantage. Spacecraft are

designed to reject solar heat so as not to add to the difficulty of cooling the craft's interior and so the spacecraft's exterior is commonly shrouded in reflective multi-layer insulation. By contrast, comets and minor bodies have low albedo values, although only 1P/Halley and comet 19P/Borrelly have had their nucleus directly imaged at close-quarters and their geometric albedo accurately measured. Comet Halley's geometric albedo of 0.04 (+0.02, -0.01) was calculated by Sagdeev *et al.* (1986) with data from the *VeGa* imaging system, and similar figures were found from the *Giotto* cameras. More recently, the encounter between the *Deep Space 1* spacecraft and comet Borrelly has shown that this minor body also has a dark surface with a geometric albedo of between 0.042 and 0.031 (Buratti *et al.*, 2001)

Within two years of the 1986 1P/Halley encounter, similarly dark surfaces had been detected by terrestrial telescopes on the surfaces of comets P/Arend-Rigaux and P/Neujmin 1 (A'Hearn, 1988) and it is not expected that similar comets will have surface properties that differ radically in this regard. By acting as near-ideal absorbers the surfaces of comets may be expected to display large temperature changes between sunlit and shadowed regions. The nucleus of 1P/Halley was measured to have temperatures of between 350 and 400 K on its sunlit face (Emerich *et al.*, 1987) and it is possible that shading by local topography will lead to sharp variations in temperature across the surface of similar bodies such as 46P/Wirtanen.

Following the thorough mapping of the comet's surface the orbiter will eject the smaller lander along a trajectory that is designed to intercept Wirtanen's surface at a speed no greater than 1.5 m s^{-1} (Schwehm and Schulz, 1999). Once on the surface, *RoLand* (the ROsetta LANDer[10]) is designed to acquire and analyse samples of the surface and subsurface material. Bulk properties of 46P/Wirtanen's nucleus will continue to be examined by the *Rosetta* orbiter spacecraft with optical, spectroscopic, and radio science instruments. The payloads of the two craft are summarized in Table 4 which is an updated version of that given by Schwehm and Schultz (1999) and an earlier summary may be found in the paper of Ulamec *et al.* (1997).

---

10 An apt name. Roland, nephew to the 8th century french king Charlemagne, is mythologized in the 11th century poem 'Chanson de Roland', and in Robert Browning's 'Childe Roland to the Dark Tower Came' (1852). Both works describe Roland facing a dire fate in a remote place.

Table 4: Payload of the *Rosetta* orbiter and lander spacecraft.

Orbiter

Instrument	Description	Principal Investigator
OSIRIS	Multi-colour narrow & wide angle camera	H. Keller, Max-Planck Inst (MPI). Katlenburg-Lindau, DE
ALICE	UV spectrometer	A. Stern, SRI Boulder, US
VIRTIS	Visible and IR mapping spectrometer	A. Coradini IAS-CNR, Rome, IT
MIRO	Microwave spectrometer	S. Gulkis JPL, California, US
ROSINA	Neutral gas and ion mass spectrometer	H. Balsiger, University of Bern, CH
COSIMA	Dust mass spectrometer	J. Kissel, Max-Planck Inst. Für Extraterrestrische Physik, Garching, DE
MIDAS	Coma grain atomic force 'microscope'	W. Riedler, Inst. für Weltraumforschung (IWF) Graz, AT
CONSERT	Nucleus radio 'sounding' apparatus	W. Kofman, LPG-CNRS, Grenoble, FR
GIADA	Dust velocity and impact sensor.	L. Colangeli, Obs. di Capodimonte, IT
RPC	Langmuir probe Ion and electron sensor Magnetometer Ion analyzer Impedance probe	R. Boström, Sw. Inst. Space Phys. Uppsala J. Burch, SRI, Texas, US K.-H. Glassmeier, TU Braunschweig, DE R. Lundin, Sw. Inst. Sp. Phys. Kiruna, SE J. Trotignon, LPCE/CNRS, Orleans, FR
RSI	Radio science	M. Pätzold, University of Köln, DE

Lander

APX	Alpha-proton X-ray spectrometer	R. Reider. MPI für Chem. Mainz, DE
COSAC	Evolved gas elemental and molecular analyser	H. Rossenbauer, MPI für Aeronomie, Katlenburg-Lindau, DE
MODULUS Ptolemy	Evolved gas analyser and mass spectrometer	I. Wright, Open University, GB
CIVA	Panoramic camera and IR microscope	J.-P. Bibring, IAS, Orsay, FR
ROLIS	Descent imaging camera	S. Mottola, DLR Berlin, DE
SESAME	Nucleus acoustic sounding experiment Dust monitor Permittivity probe	D. Möhlmann, DLR Köln, DE I. Apathy KFKI, Budapest, HU H. Laakso, FMI, Helsinki, FI
MUPUS	Nucleus thermal and geophysics suite	T. Spohn, Univ. Münster, DE
ROMAP	Magnetometer and plasma monitor	U. Auster, TU Braunschweig, DE I. Apathy KFKI, Budapest, HU
CONSERT	Nucleus radio 'sounding' apparatus	W. Kofman, LPG-CNRS, Grenoble, FR
SD2	Sample excavation equipment	ASI, Matera, IT

Before a spacecraft such as the *Rosetta* lander can be designed in detail it is useful to have a range of models for the environment that it will encounter at its target. The unusual thermal environment found on the dark rotating nuclei of comets is perhaps one of their most accurately modelled properties, with other aspects of the comet nucleus being known less well.

Table 5 lists a number of surface properties pertinent to the *Rosetta* project and their estimated or measured values as of September 1998. The three main columns show the expected range of values that 46P/Wirtanen may exhibit for specific physical parameters. The mechanical attributes of the surface are the least well constrained, as might be expected in the absence of any prior contact of spacecraft with cometary nuclei. Some of these parameters, particularly those relating to the surface, may be reassessed following the delivery of the *Deep Impact* probe to comet 9P/Tempel 1 in 2005. This unusual craft, described by Belton and A'Hearn (1999), should provide a unique view of the sub-surface of an active comet by using a 350 kg hypervelocity impactor to excavate a crater in the comet's nucleus.

Table 5: Model nucleus properties of 46P/Wirtanen.

Parameter	Minimum	Typical	Maximum
Outgassing rate (kg s^{-1} m^{-2})	~2 x 10^{14}	~10^{19}	2 x 10^{20}
Effective radius (m)	500	800	1500
Axes ratio a:b	1.09	1.74	2.6
Mass (kg)	10^{11}	1.1 x 10^{12}	1.8 x 10^{13}
Subcrust density (kg m^{-3})	200	500	1000
Albedo	0.02	0.04	0.1
Surface temperature (K)			
Ice-snow cover	150 (*a*)	180 (3 AU)	210 (*p*)
Dust grain cover	150 (*a*)	< 230 (3 AU)	< 390 (*p*)
Surface properties			
Crust density (kg m^{-3})	100	200	500
Subcrust density (kg m^{-3})	200	500	1000
Albedo	0.02	0.04	0.1
Fracture strength (Pa)	1.4 x 10^{3} to 3 x 10^{4}	6 x 10^{5} to 2 x 10^{7}	>1 x 10^{8}
Near surface environment			
Gas speed (m s^{-1})	10	300	400
Mean free path (m)	2 x 10^{5} (5 AU)	10 (3 AU)	0.05 (1.1 AU)
Mean pressure (Pa)	10^{-7} (5 AU)	0.002 (3 AU)	0.5 (1 AU)

Note: a and p stand for the aphelion and perihelion of the comet's orbit.
Data from preliminary reference model for 46P/Wirtanen prepared at Deutschen Zentrum für Luft-und Raumfahrt (DLR) in October 1998.

1.2.2 Hopes and fears

The scientific rationale for taking a suite of analytical instruments to a comet centres on the belief that these bodies preserve chemical and isotopic signatures that have been little changed since their formation. By gathering samples of these bodies it is hoped that the conditions and processes associated with their formation will be better understood - these goals are laudable for the intellectual rewards that they will yield. As well as helping to constrain models of the early Solar System, the mapping of a comet's internal structure and surface properties will improve the understanding we have of comets not just as fossils of the deep past, but as potential agents of change in the future of the Solar System.

No object in space is immune to the risk of impact from meteoroids. Predicting the size range of objects that can strike the Earth is possible by fitting population models to the observed crater distribution seen on the Moon's surface, which acts as a witness surface for the impactor population at 1 AU. Computation of the rate at which perturbations modify meteoroid and minor body orbits such that they pass close to that of the Earth can then be made to give an impact probability for the larger population of undetected objects. Alongside such assessments of the general risk posed by asteroids and similar objects, observational programmes can identify and catalogue *specific* bodies, as shown by the ever-rising number of asteroidal discoveries by programmes[11] such as Spacewatch, LINEAR, and NEAT. Similar prediction techniques can be applied to comets but with three major differences.

(1) The rate at which comets are ejected from the Oort cloud is poorly known. With such long orbital periods, much longer than the span of time over which accurate astronomical observations have been made, LP comets can arrive with little warning. A comet with a highly eccentric orbit and a small perihelion distance takes only 300 days to reach Earth's orbit if it is first detected at Jupiter's orbital radius.

(2) Highly active nuclei display random orbital perturbations arising from the reaction force of jets of gas being released from their surface. Although the average influence of this effect can be calculated as a stochastic process, it is generally not possible to predict accurately the path of a periodic comet from apparition to apparition. The most dramatic example of such changes in a comet's orbit occurs when the nucleus splits or fragments. Whether the

---

[11] Individual Internet sites are listed at: `http://cfa-www.harvard.edu/iau/NEO/TheNEOPage.html`

disruption is caused by gravitational tides as mentioned earlier, or through internal gas pressure, comets can split into smaller pieces. These fragments retain almost all of the orbital characteristics of the parent object, and for the 21 disrupted comets reviewed by Sekanina (1982) the debris dispersal speed was between 0.3 and 2 m s^{-1}. Such a slow dispersal in comparison to the original orbital speed leaves an expanding cloud of material along the track of the disrupted body. The Earth encounters such meteoroid streams regularly, but the irregular distribution of bodies within such streams does not allow the extent and severity of the encounter to be assessed accurately, and modern encounters with meteor streams have not included fragments large enough or strong enough to impact the ground.

(3) Comets can have highly eccentric orbits and may cross the Earth's orbit at speeds close to the local Solar System escape speed. The closing speed of a comet and the Earth can therefore be many times higher than that for a near-Earth asteroid. At such high speeds the energy delivered by a comet can be up to two orders of magnitude larger than the energy released by the same mass of explosive[12] material.

Only in the last few decades has the probability of the terrestrial impact hazard been rigorously assessed (Chapman and Morrison, 1994). Whatever the probability, a body will eventually be found moving on an impact trajectory with the Earth. Some means of removing the risk will therefore be needed and schemes that use kinetic impactors (Solem, 1993) require knowledge of the approaching body's density and strength (Huebner and Greenberg, 2000) if the hazard is to be accurately diverted. However, among the potential assailants, comets may also pose an unusual threat because of their presumed *low* tensile strength. Whether shattered by design or chance, if a sufficiently large comet were to break up, the impact risk from this cloud of debris slowly spreading along the original orbit could be greater than the background risk from asteroids that cross the Earth's orbit (Clube and Napier, 1984). Indeed, the break-up of large comets into such swarms has been suggested as a cause for mass-extinctions in the geological record (Hut *et al.*, 1987). The rarity of this hazard, and the lack of unambiguous evidence for these events (LaViolette, 1987 vs. Clube and Napier, 1987) does not remove the need to understand the strengths of materials likely to be found in asteroids and cometary nuclei.

---

[12] 1 tonne of TNT yields ~ 4 GJ (Brown, 1998). A near-Earth asteroid strikes the Earth no slower than 11.2 km s^{-1}, and a 1 tonne mass moving at this speed has a kinetic energy of ~62 GJ.

1.3 Volatiles in the Solar System

Our experience of fires and everyday objects points to the eventual cooling of hot objects and many current models for the formation of the Solar System posit a hot and gas-rich environment for the proto-Sun and its protoplanets – modern reviews of the many intricacies of formation models are given by Taylor (1992) and the summaries of Ruzmaikina (1997) and Stevenson *et al.* (1986). In brief, the Sun and planets are widely believed to have condensed jointly from a cloud of gas and solid grains. Heating by the emerging star at the centre of this cloud, and the dense collisional nature of the dense gas in the accretion disc around it, gave rise to a non-uniform temperature distribution. Crudely, the temperature field would have varied with solar radius as R^{-1} (Stevenson, 1986). Despite its attractive simplicity, such a temperature distribution ignores many of the physical processes, such as multi-species condensation and the development of shock fronts, that would occur in a planetary disc. However, this general rule of condensation temperatures varying inversely with the solar radius, supports the gross observation that ice-rich bodies occupy more distant solar orbits than volatile-poor objects.

The temperature of a region in the early Solar System is important in characterizing the processes that distribute and transform the elements and chemical compounds. Chemical reactions are often accompanied by phase changes which may also be brought about by the more general processes of sublimation and condensation. When held in a perfect vacuum at a fixed temperature all solids loose matter through sublimation. If the gas is not allowed to escape, and if the solid and its gas are held at a fixed temperature, then an equilibrium pressure will arise at which point material is condensing at a rate which equals its loss through sublimation. If the equilibrium pressure is sufficiently low then a liquid phase may never be produced. The exact dependence of this equilibrium pressure with temperature for different ices will be discussed with more detail in chapter 5, here it is adequate to describe water ice as being more stable at a given temperature than carbon dioxide ice, which is in turn more stable than solid carbon monoxide.

In turning to examine the presence of ice in the Solar System three specific planetary environments will be considered next. These all allow landed spacecraft platforms to make contact with ice-rich surfaces and some of the scientific goals sought through their exploration will be described briefly.

1.3.1 Comets and minor bodies

The period and eccentricity of a comet's orbit determines the frequency and severity of the solar heating it experiences during its perihelion. By definition, SP comets will, on average, have experienced many perihelion events in their lifetime. With each heating event some gas is lost to space and forms the coma, and some fraction of the liberated vapour diffuses into the colder interior where it may re-condense. With each orbit the surface and near-surface layers become progressively depleted of ice and with a few exceptions, such as 1P/Halley, the activity of short period comets is weak. Their smaller rate of gas emission is believed to be associated with the recession of ice-rich zones within the comet and the formation of a widespread brittle and marginally porous ice-free surface crust. A thermally insulating yet mechanically weak layer of refractory material would lower the heat flux to the interior, generate higher surface temperatures, and act as a diffusive barrier to gas released from within. Where the crust can be broken, by gas pressure for example, localized regions of gas sublimation may re-occur from the underlying ice, resulting in the loss of material from that area, and its (eventual) closure by a newly formed ice-free crust. This layered model is not contradicted with observations of cometary nuclei. Of the 15 comets surveyed by Sekanina (1991) the outgassing rate was found to be consistent with predicted surface temperatures only if a fraction (between 1% and 30%) of the surface was assumed to be an active source of gas, although some exceptionally active comets appear to have surfaces that are entirely active (e.g. Hyakutake, see Lisse *et al.*, 1999). Thermal models of comets also support this general view of cometary nuclei. Studies by Capria *et al.* (1996) and Podolak and Prialnik (1996) have been made of the thermal evolution of an icy body analogous to 46P/Wirtanen. The results, which may be extended to similar comets, are that, when heated repeatedly by solar radiation a porous mantle free of all volatiles is formed at the surface. Beneath this crust of poorly constrained thickness, lies a dust-rich layer of water ice which in turn covers strata of water ice intermingled with CO_2 ice, with the CO_2 ice found no closer than several metres to the surface (Podolak and Prialnik, 1996)

The most tangible support for a partial crust-like surface on some active comets came from imaging of 1P/Halley's nucleus by the *Giotto* probe (Keller *et al.*, 1986) which revealed the nucleus to be a predominantly dark inactive body at the surface of which a number of gas jets were seen. Attempts to model crust formation, (Kührt and Keller, 1994), tend to produce mantles that are sufficiently strong for cometary activity to be largely suffocated. The activity

that comets show from apparition to apparition suggests that the macroscopic properties of a comet's mantle are still not well understood. At smaller scales, the growth of ice-free crusts has been seen in the laboratory experiments of many groups over the past decades (Ibadinov and Kaimakov, 1970; Saunders *et al.*, 1986; Kochan *et al.*, 1989; Ibadinov, 1989; Grün *et al.*, 1991; Kossacki *et al.*, 1997) and a good summary is presented in Sears *et al.* (1999). A common thread among these experiments is that heating silicate-ice-organic mixtures *in vacuo* removes the ice by sublimation and yields a brittle porous layer of ice-free silicate grains (Figure 6). The sublimated water vapour is simultaneously lost from the surface to free space, and recondensed at depth into more solid partially porous layers of ice (Kömle *et al.*, 1996).

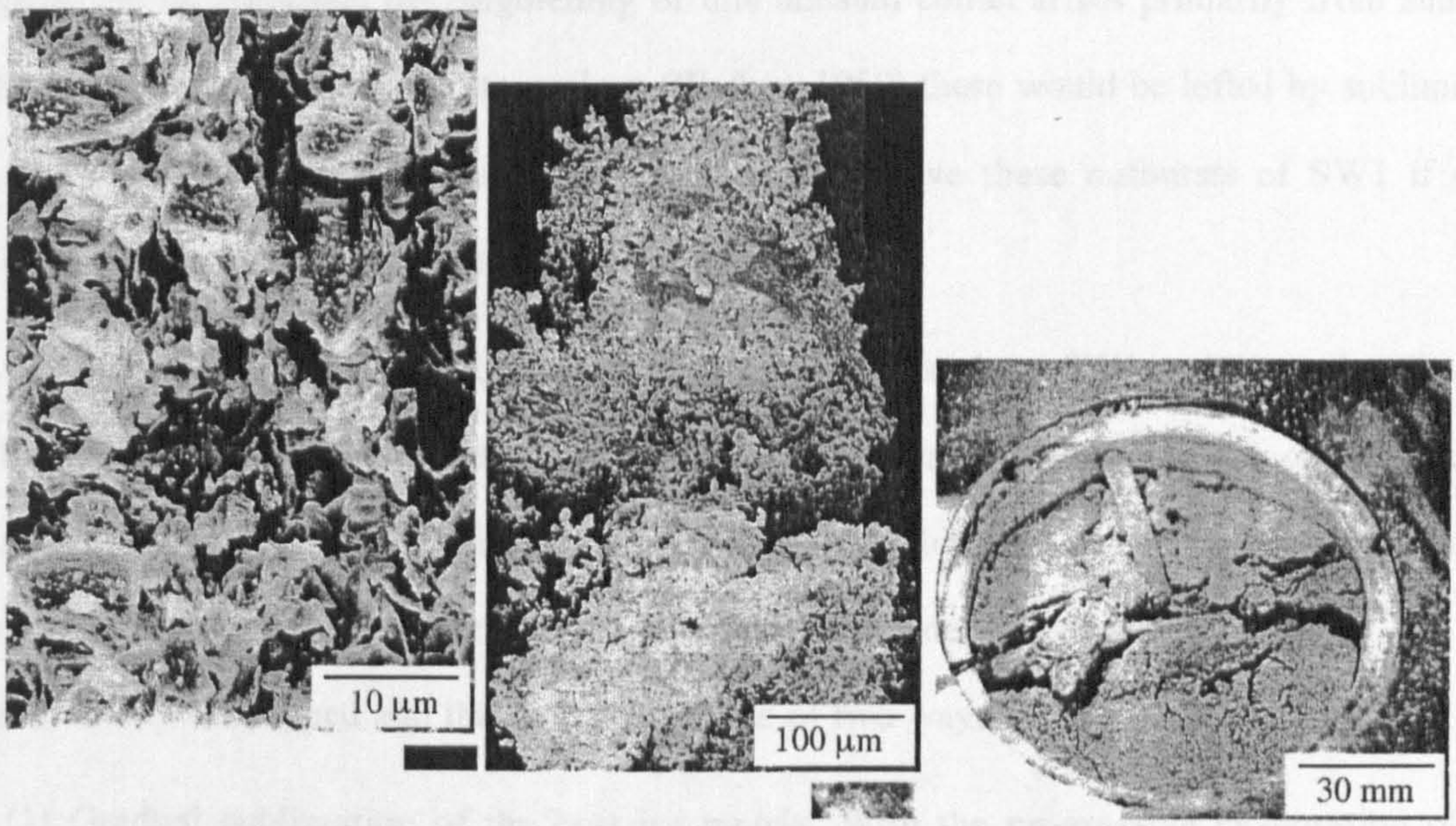

Figure 6 – Structures formed by the vacuum desiccation and radiant heating of a Cometary Analogue Material (CAM) based on water, dust, and organic compounds (paraffins).

These three images are taken from Kömle *et al.* (1996) and show a mixture made from ground ice, a powdered mineral (Dunite[13]), and a finely divided 'hard' paraffin (melting point 363 K). Similar structures have been seen by Saunders *et al.* (1986) in experiments using flash-frozen suspensions of mineral grains and water without an organic component.

Despite the complex relationship between the composition of a comet's nucleus and its coma make-up, the sublimation of water ice and the transfer of heat into the cometary interior are thought to be the dominant processes in the evolution of a comet's nucleus. Even the seemingly orderly process of progressive sublimation, by which an ice-rich object loses mass with each passage through perihelion, is an oversimplified model of reality. Roughly 3 % of

---

13 An igneous rock formed almost wholly from the mineral olivine ($MgFeSiO_4$)

known comets display rapid unpredictable rises in brightness, often brightening by two or three magnitudes, and more rarely, by up to five magnitudes[14] with little correlation between the comet's type or its inferred surface temperature at the time of the outburst (Hughes, 1991). An example of such a comet is P/Schwassmann-Wachmann 1 (SW1) which has a moderately low eccentricity orbit (e=0.22) with a semi-major axis of 6.044 AU. If it is treated as a black body then its surface temperature should never exceed 130 K which is too cold for water ice to be a significant source of gas. Yet, SW1 brightens rapidly at a rate approaching two events per year, and has been seen to do so on a semi-regular basis since 1927 (Whitney, 1955). These are not trivial events either, SW1 can liberate between 10^8 kg to 10^9 kg of matter in a few days (Hughes, 1991). Although the brightening of this unusual comet arises primarily from sunlight scattered by grains ejected from its nucleus (Walker, 1959) these would be lofted by sublimating gas and an ice more volatile than water is needed to drive these outbursts of SW1 if solar heating is the main cause of its activity.

Aspects of the out-gassing behaviour seen in comets such as SW1 at large solar distance can be understood through the micro-physics of ice sublimation. Water ice can occur either as an amorphous or crystalline solid. In its amorphous phase, ice shows no long-range order and a network of voids can exist within the material that render it porous. In such an ice, gas molecules may be trapped and then released in one of two ways.

(1) Gradual sublimation of the host ice matrix. With the progressive evaporation of the caging material the gases held in the ice's structure are liberated.

(2) Liberation of the 'guest' vapour in temperature windows that correspond to the thermally-induced breakdown of specific capture processes such as absorption, or the destruction of clathrate structures.

An example of point 2 is shown in Figure 7 which plots the abundance of gaseous argon evolved during the warming of gas-doped amorphous water ice (Bar-Nun *et al.*, 1987). Each peak in the argon release curve is associated with the break-down of a trapping mechanism when it becomes thermodynamically unstable. The dashed line marked 'Ar' is the sublimation curve of pure argon, showing that the role of the water ice matrix is to delay and complicate the release of the dopant gas.

---

14 Corresponding to a 100 fold increase in the light received.

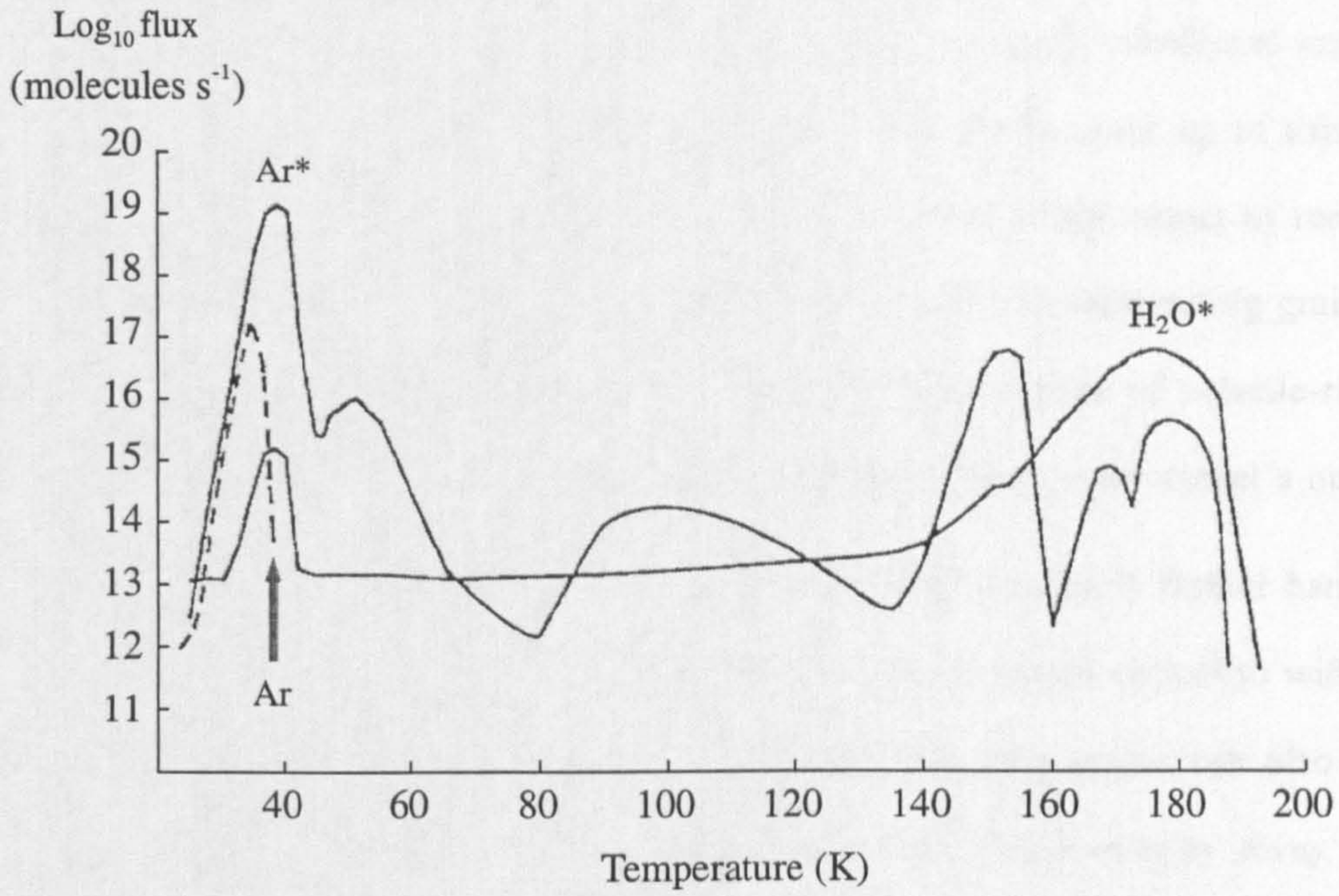

Figure 7 – The thermally-driven release of gas from argon-doped amorphous water ice (after Bar-Nun *et al.*, 1987).

Similar behaviour is seen in the work of Hudson and Donn (1991) for other gases, such as carbon monoxide; the release of gases from amorphous and crystalline water ices is reviewed by Klinger (1989). From such experiments it can be appreciated that in general the make-up of a comet's coma will not track the molecular mixing fractions of the gases' solid phases in a simple way. Without samples of cometary nuclear material it is not possible to state how ices are stored within an active nucleus and so the extent to which ices are mixed on the molecular scale is not clear. Intimate mixtures of different ices will allow complex sublimation processes to occur, such as those outlined above for argon and water ice. If the ices form separate zones of predominantly single-component material, then the outgassing behaviour is simpler, but even then, without information about a comet's internal thermal profile the extent and sublimation activity of these single-component ice reservoirs cannot be known. The situation is further complicated because molecular species detected in a comet's coma may also arise from sources other than the ices' condensed phases within the comet's nucleus. Measurements of emission spectra associated with specific compounds in the coma of comet Hale-Bopp suggested the presence of an extended source of sublimating water ice (Blake *et al.*, 1999) - believed to consist of small icy grains lofted by aerodynamic forces. Not only would this distributed extra-nuclear source yield a radial gas density function that differs from a simple

inverse-square law[15], but localized variations in density of isotopically substituted molecules in the coma of Hale-Bopp (Blake *et al.* 1999) suggest that the volatile make-up of this halo-like reservoir differs from that of the nucleus as a whole. One other bright comet of recent years, P/1996 Hyakutake, also has been shown to have an extended halo of sublimating grains (Harris *et al.*, 1997) and it is likely that other active comets produce a haze of volatile-rich grains which may have ice inventories that differ in some respect to those of the comet's nucleus.

Reconstructing the content of the nucleus from coma observations is further hampered by the dust emitted from a comet. It not only serves to brighten a comet optically, with micron-size grains being the dominate light scatterers, but these refractory grains can also carry icy material from the nucleus, flattening the radial distribution of gas density away from the nucleus in the same manner as lofted ice grains; the role of dust in coma dynamics is reviewed by Festou (1999). In the microgravity of a cometary surface such μm-sized dust or ice grains are not the largest items that may be lifted by gas drag; the ejection of larger objects from comet nuclei has been established by radar observations. Measurements of comet IRAS-Araki-Alcock (IAA) by Harmon *et al.*, (1989) gave a radar cross-section consistent with a nuclear diameter between 5 km and 16 km along with a diffuse echo stretching ~10^3 km around the nucleus. This extended return was interpreted as being made by a halo of objects with sizes no smaller than the illuminating radar wavelength (126 mm). The rate at which these bodies are ejected can be modelled to give a flux rate and at the time of observation, particles roughly one centimetre in size were being ejected from each square metre every few hours or so with an ejection speed of ~3 $m\,s^{-1}$. This corresponds to a number density of one particle per cube of space ~20 m on a side. Such lofted material poses an obstacle to the safe prolonged operation of orbiting spacecraft and landers alike through the obscuration of sensors and perhaps by smothering portions of the craft with larger particles. Work by Fulle *et al.* (1997) discusses the potential for radiation pressure to modify the asymmetric emission of dust from an active comet. Their calculations suggest that a Wirtanen-like nucleus can deliver mass fluxes of several grams per m^2 each orbit to a craft circling the nucleus at a 100 km altitude[16].

---

[15] Spacecraft in orbit around, or tethered to, a comet nucleus may be subjected to considerable aerodynamic forces from the gas-drag of the *coma* (Kömle *et al.*, 1997; Scheeres *et al.*, 1998) and can lead to modified mission and operation strategies.

[16] Giving the craft an orbital period of a few tens of days.

1.3.2 Polar regions of Mars

The notion that ice can be a relatively long-lived feature in cold regions of a planetary surface predates this century's development of planetology as a comparative science. Reportedly observed first by Huygens and Cassini in 1666 and 1672 respectively (Slipher, 1962), the bright material at the poles of Mars was tacitly assumed to be mostly water ice. Other candidate materials were roundly dismissed by Lowell (1908) on the grounds that no other likely solid could melt to give the colour changes he saw around the retreating polar caps. By the 1950s Mars had been shown to have an atmosphere dominated by CO_2 (Kuiper, 1955) although the surface atmospheric pressure was not accurately measured until the arrival of the *Viking* landers in 1976. Spectroscopic observations from the fly-by of *Mariner 7* in 1969, were interpreted as indicating the presence of solid CO_2 in the icy mass at Mars' southern pole (Herr and Pimental, 1969) and further spectroscopic ground-based observations identified CO_2 as the major ice component (Larson and Fink, 1972) at that pole. Despite its arid appearance, water vapour *is* present on Mars, but at a very low mixing ratio. The average column abundance of water is equivalent to a global coating of ice only 10 μm thick (Jakosky 1985) and this sparse fraction manifests itself as thin frosts at latitudes above 44° north (Hart and Jakosky, 1986). In contrast to these thin ice coatings the arrival of winter in each hemisphere causes almost a sixth of the atmospheric carbon dioxide (Tillman *et al.*, 1993) to freeze out to form seasonal layers many hundreds of kilometres in diameter and with an average thickness which can be approximated by:

$$\frac{\Delta P}{\rho_{ice}\, g}\left(\frac{A_{pole}}{A_{Mars}}\right) \qquad \text{Eq. 3}$$

Here g is the acceleration due to gravity at Mars' surface (3.71 m s^{-2}), ρ_{ice} is the density of the polar CO_2 ice, ΔP is the average annual atmospheric pressure change (~240 Pa) and the areas A_{pole} and A_{Mars} represent the areas of the visible polar seasonal cap (~10^5 m^2) and the surface of Mars respectively. If the seasonal ice forms as a non-porous solid (density~1500 kg m^{-3}) then seasonal layers with an *average* depth of order 1m can form, with thicker deposits occurring perhaps on pole-facing slopes or in shaded hollows. Recent topographic surveys made with the laser altimeter on the Mars Global Surveyor orbiter show that winter layers of CO_2 ice up to 1.5 m thick appear at each pole (Smith *et al.*, 2001).

Every summer this coating of carbon dioxide sublimates to reveal a more permanent polar deposit. In the present epoch this residual material at the north pole is water ice (Farmer *et al.*, 1976) with some admixture of dust (Kieffer *et al.*, 1976). At the south pole a smaller cap with a surface of carbon dioxide ice (Kieffer, 1979; Paige *et al.*, 1990) is uncovered each summer although there are suggestions that in some years an underlying mass of water ice is revealed at the south pole (Jakosky and Barker, 1984). Views of the northern and southern polar caps in their respective summers are shown in Figures 8a and b.

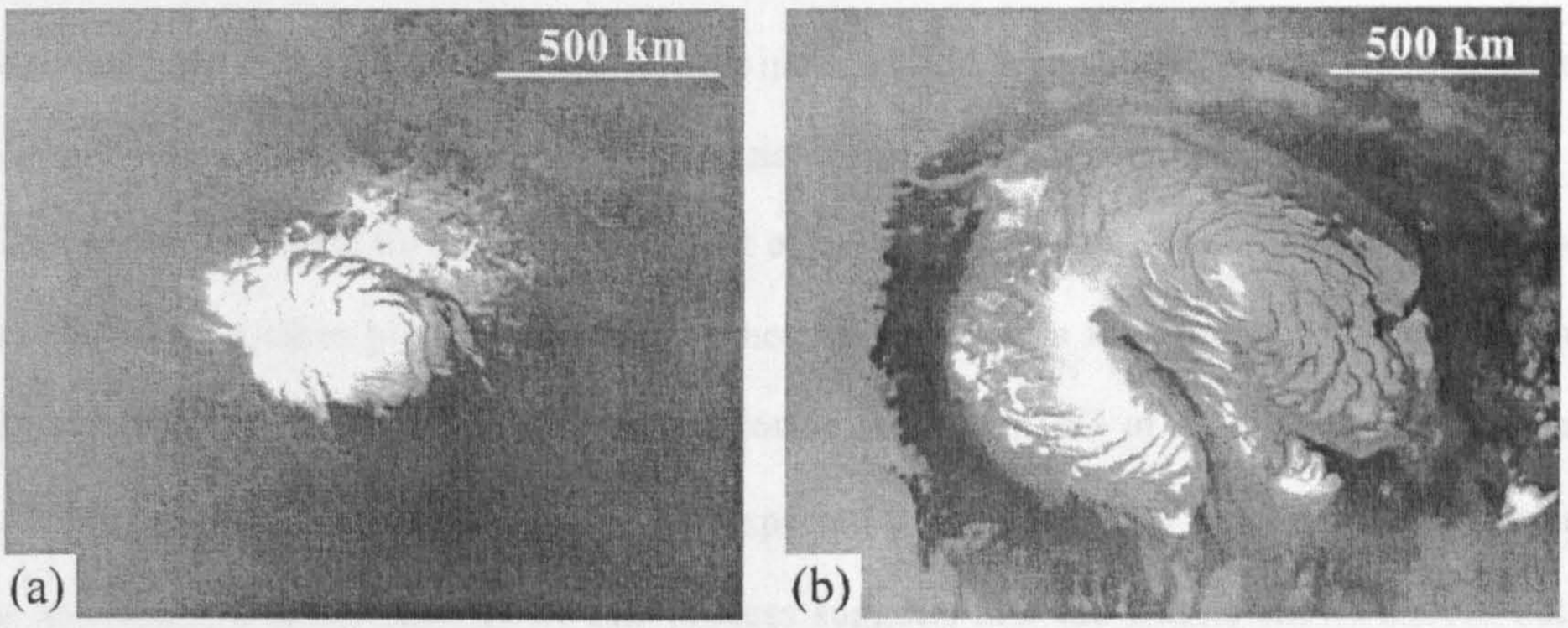

Figures 8a/b – Images of the southern (a) and northern (b) residual martian polar caps made from Mars Orbiter Camera images taken in March (1999) and February (2000). Images are M12-00291 & FHA-00455, from the Malin Space Science Systems web site. (http://www.msss.com)

The condensation and sublimation of the polar carbon dioxide occurs in near-equilibrium with the atmospheric vapour pressure and so the surfaces of the polar ice are broadly isothermal, but anomalies exist in this model. The infra-red mapping instrument of the two *Viking* orbiters observed regions that persisted for days and weeks at both poles that had brightness temperatures > 20 K lower than the surrounding areas, as inferred from the recorded strength of particular infra-red emission bands (Keiffer *et al.*, 1976). Interpreting these large ($10^{10}\,m^2$ in extent for the northern cap) regions as being physically colder than their surroundings requires that air around the cold spot is somehow prevented from diffusing or convecting to the cold region. A fairly specialized model is needed to justify this, based on the sublimation point of CO_2 which is lowered by the local depletion of condensable gas (Weiss and Ingersoll, 2000). Instead, Forget *et al.* (1995) hypothesized that these were not actually cold regions but instead were regions with surfaces that were able to scatter infra-red radiation more efficiently than a compacted solid. This model is tenable because carbon dioxide ice has an

absorption coefficient at near-IR wavelengths that is very much smaller than that for water ice and thus it scatters light more efficiently than a water snow[17] would (Ditteon and Kieffer, 1979). The review of Warren *et al.* (1990) uses this property to argue that changes in the grain size and dust load of a CO_2 ice can lead to large variations in the scattering properties of a realistic frost; more so than occurs for water ice, which is a better absorber. Thus, the patches of depressed brightness temperatures seen at Mars' southern CO_2 cap may be caused by minor changes in ice morphology. These remotely viewed changes in scattering behaviour suggest that CO_2 frosts do not have durable structures on the surface of Mars. The dominance[18] of CO_2 in the atmosphere (mixing ratio ~ 95 % with nitrogen and argon < 3% and < 2% respectively) ensures that a snow pack cannot trap substantial quantities of non-condensable martian air. By modelling the evolution by diffusive transport of porous CO_2 snows Eluszkiewicz (1993) found that densification takes place most rapidly when the material is fine-grained, with a CO_2 snow formed from 10 μm grains compacting and losing more than 2/3 of its porosity in ~ 10 days. Snows formed from micron-size grains are expected to lose the same fraction of their porosity in a few hours, and the rapidity of this process suggests that old fragile snows should not be present at the surface of either pole during their winter seasons. It is therefore possible for a freshly formed CO_2 snow to transform into a solid in a matter of days resulting in an equally significant change in the ice's IR scattering properties.

Both of Mars' surface ice caps sit atop broader expanses of a complicated layered terrain believed to consist of fine strata of dust and water ice-rich material (Kieffer *et al.*, 1976; Edgett and Malin, 1999). How the porosity and the mixing ratios of carbon dioxide and water ice change in this layered material with depth is not known. Nor is the relationship understood between the dust-load in the atmosphere and its presence in these layered regions (Cutts and Lewis, 1982). It is supposed that these layered terrains hold chemical or structural clues to Mars' climatic history stretching back at least ~10^5 to 10^8 years (e.g. see the review of Clifford *et al.*, 2000). The extraction and analysis of material from these polar archives is an important step in understanding the development of Mars as a planet and, perhaps, as a biome in its past. Having to breach the thin seasonal carbon dioxide caps is simply avoided by

---

17 In contrast, water snow is essentially a blackbody emitter of heat under almost all conditions.
18 Carbon dioxide was detected first by Gerard Kuiper in 1947 (Sheehan, 1996) at abundances twice those of Earth, the *dominance* of CO_2 was observed by Mariner 4's remote-sensing measurements (Kliore 1972) and confirmed by data from the Viking landers.

appropriate scheduling of the drilling process but deep excavation of the underlying water ice/dust mixture will benefit from an understanding of its mechanical properties. Vapour diffusion models for the densification rates in the layered terrains suggest that Mars currently does not accumulate enough water snow to prevent polar water ices from sintering into a pore-free ice (Arthern *et al.*, 2000). Systems designed to extract cores from the martian polar terrain may therefore be faced with dense materials close to the surface, unlike the deep snow layers seen in terrestrial polar settings[19].

1.3.3 Surfaces of outer planet satellites

Volatile materials become progressively more stable against loss through sublimation as the temperature of the substance falls. For a planetary body, lower temperatures are synonymous with ever-larger orbital radii. Numerical modelling of the sublimation caused by solar heating (Lebofsky, 1975) showed that beyond the orbit of Jupiter water ice is cold enough for it to be stable for lengths of time comparable to the age of the Solar System. To illustrate this, Figure 9 shows the orbits of four objects having the same orbital semi-major axis (5 AU) but different orbital eccentricities. The net result is that although body **d** experiences the highest temperature, it does so over a small fraction of its orbit and the average temperature of the bodies falls in going from body **a** to **d**.

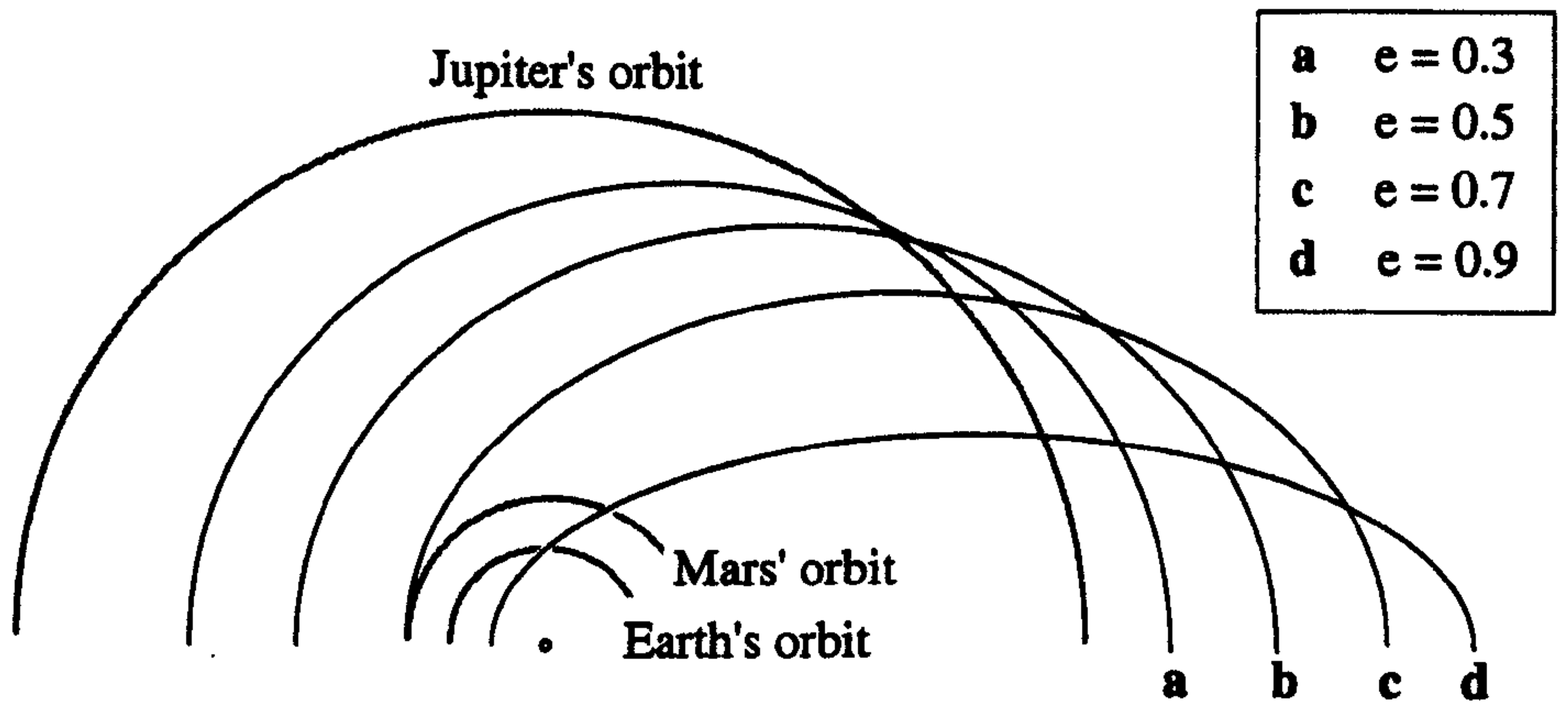

Figure 9 – Four objects and their half-orbits drawn to scale in the inner Solar System.

Table 6 lists the mass loss rates given by Lebofsky (1975) for spheres of dark water ice (albedo = 0.5) moving in the orbits drawn in Figure 9. The bodies are assumed to be sufficiently

---

19 Snow on Earth can retain a network of interconnected pores up to depths of 100 m or so till overburden closes the voids.

small and conductive that they warm and cool rapidly enough for them to be considered isothermal. The example orbits used were taken from Lebofsky (1975), along with the mass loss rates, and the peak and minimum temperatures were calculated using equation E3 in appendix E.

Table 6: Thermal conditions and mass loss rates for four hypothetical solar objects

Object	Temperature (K) Minimum	Maximum	Perihelion (AU)	Aphelion (AU)	Erosion rate ($\mu m\ yr^{-1}$)
a	93	126	3.5	6.5	< 0.1
b	86	149	2.5	7.5	25
c	81	192	1.5	8.5	6000
d	77	333	0.5	9.5	80 000

The Galilean satellites (excluding Io) are perhaps the best-known examples of ice-rich bodies in the Solar System and excellent reviews of the post-Voyager state of knowledge of these moons can be found in the University of Arizona text edited by Morrison (1982). The presence of water ice on these moons is suggested by their bright optical appearance. Ganymede and Europa have geometric albedoes of 0.43 and 0.64 respectively (Lodders and Fegley, 1998), much greater than the albedo of ice-free bodies such as the Moon (average geometric albedo ~ 0.1). The existence of optically bright surfaces, along with particular spectroscopic features (Pilcher *et al.*, 1972) indicate that water ice is a persistent and common constituent of these moons' surfaces (Calvin *et al.*, 1995). Information about their sub-surface composition can be gained from radar backscatter experiments which allow the presence of ice at depth to be inferred. Ganymede, Callisto, and Europa were seen to have exceptionally high radar reflectivities and similar polarization signatures in their backscattered decimetre radar echoes (Campbell *et al.*, 1978). These 'bright' echoes were enhanced in the same-sense of circular polarization as the transmitted signal, in contrast to the opposite-sense of polarization seen in reflections from common dielectric materials. This behaviour was modelled by, among others, Hapke (1990) as indicating the presence within the ice of discrete bodies[20] which allow multiple scattering paths to produce a depolarized echo. Other mechanisms may be at work on the Galilean moons to cause these unusual echoes and these are reviewed in Ostro and Shoemaker (1990) and Black *et al.* (2001). That the Galilean satellites contain large fractions

[20] At frequencies below 2 GHz and higher than 200GHz cold water ice is a poor absorber of radio energy and is therefore relatively transparent to radar.

of ice and are not simply frosted balls of rock was deduced from measurements of the moons' bulk densities. These were inferred from orbital perturbations of the Voyager craft and led to Europa and Ganymede, for example, being known to have ice mixing fractions of at least 5% and 45% respectively (Schubert *et al.* 1986). These moons are massive enough for such mixtures of ice and rock to become differentiated. Callisto, despite its large ice fraction of 50% by mass (Schenk and McKinnon, 1997), is thought to experience little tidal heating and may be undifferentiated. Its low geometric albedo of less than 0.2 (Roush *et al.*, 1990) also suggests the presence of substantial amounts of rock-like material spread over its surface, and presumably, distributed at depth.

In the absence of ground-truth, the consensus is that thick layers of water ice are expected to be commonplace at the surface of the Galilean satellites, and by extension on other distant small bodies. It is reasonable then to ask what form the water ice takes on the surfaces of such icy satellites. Through their lack of a shielding atmosphere, Europa and the other jovian moons will be hit by impactors having a broad range of sizes and impact rates. However, the surface of Europa currently has only a dozen or so craters larger than 20 km (Zahnle *et al.*, 1998) and by using models for the impactor population at Jupiter's orbit the age of Europa's surface has been estimated to be around 50 Myr (Zahnle, 2001). By contrast, Ganymede and Callisto are much more heavily cratered and for the europan surface to show such a relatively sparse cratering history the destruction wrought by impacts must be held in check by resurfacing phenomena of some form. The extensive fracturing and localized plate-like structures seen on Europa have been interpreted as indications that the surface is mobile to some degree. Modelling the fractures as the result of tectonic stresses (Greenberg *et al.*, 2001) has led to the hypothesis that the surface overlies a body of liquid water at some depth. Evidence for this notion is reviewed by Carr *et al.* (1998) and later measurements by the *Galileo* spacecraft of the magnetic field induced by Jupiter in the body of Europa have been interpreted by Khurana *et al.* (1998) as pointing to a highly conductive layer under its surface. An ocean-like body of water lying kilometres beneath the surface is not the only possible solution to the question of what causes Europa's surface features. Alternative models (Moore *et al.*, 1998; and Pappalardo *et al.*, 1998) invoke convection in a liquid-free ice mass as a cause for the surface's disrupted geometry.

Whatever the nature of Europa's resurfacing process, the mechanism has affected much of the satellite at global scales. Observations by the Near Infra-red Mapping Spectrometer (NIMS) on the *Galileo* orbiter have allowed the distribution of water ice to be mapped over this, and other, jovian satellites by recording their optical and IR spectra and comparing them to those of hydrated minerals. From such comparisons McCord *et al.* (1998) and McCord *et al.* (1999) have shown that the spectra can be well fitted by mixtures of hydrated salts and brines. The strongest salt features are seen in regions close to areas where freshly excavated material may be exposed (e.g. around lineaments that cross the plains). The correlation between visible and spectral features of Europa is shown well in the two images of Figure 10.

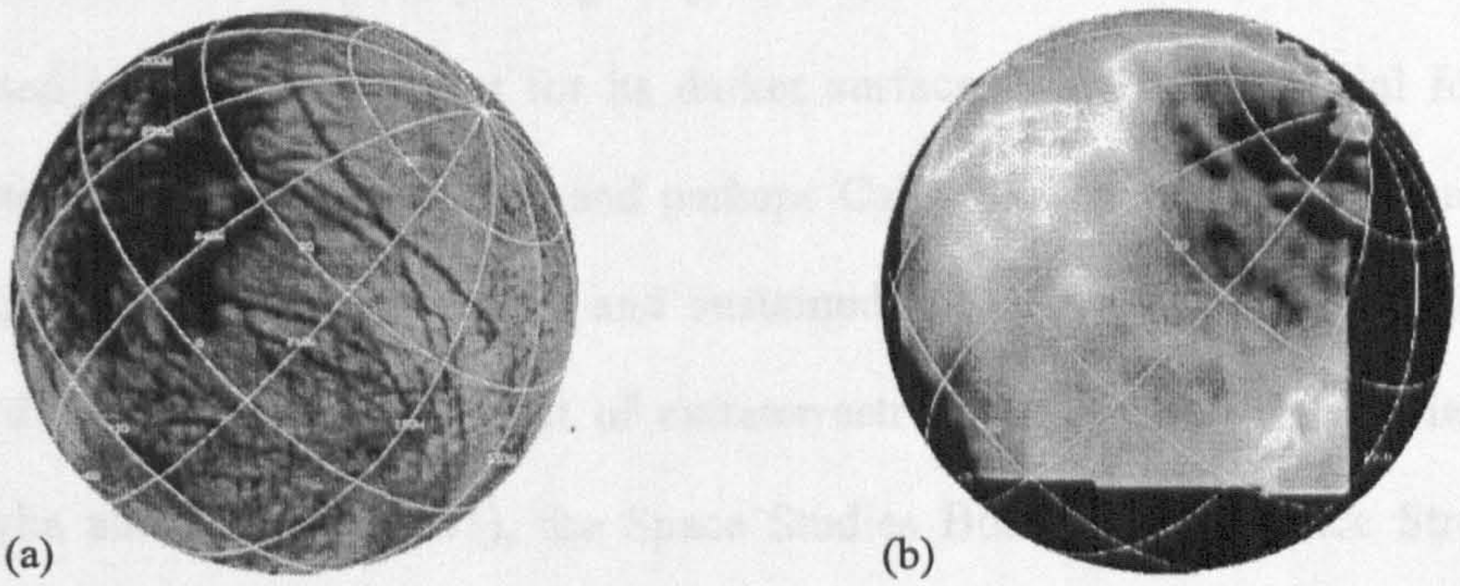

Figures 10a/b – Optical (a) and 1.5 μm spectral images (b) of Europa taken by the *Galileo* spacecraft taken from the public domain NIMS data set. Note the correlation between optically dark and spectrally bright (and brine rich) regions.

At smaller scales, commensurate with the size of a typical spacecraft lander, the surface of Europa will be microscopically fractured and tilled by micrometeorite impacts. The model of Divine (1993) suggests an areal flux of around 10^{-14} m^{-2} s^{-1} for gram-mass objects at a distance commensurate with Jupiter's orbit. If the gravitational enhancement of neither Europa nor Jupiter is considered, then an average of around 10^2 gram-mass hypervelocity impactors will have struck each square metre of Europa's face in the space of 50 Myr. In the absence of resurfacing flows, this is likely to yield a very disturbed and porous ice regolith at the scale of potential spacecraft sampling tools. Along with the state of the ice, knowledge of the chemistry of the material is of importance for prospective sampling missions as the thermo-mechanical properties of an ice can change significantly with the addition of relatively small amounts of other compounds as will be shown in chapter five.

In trying to understand the chemistry seen on Europa's surface, Zolotov and Shock (2000) have calculated how a salt and brine solution may freeze when ejected on to a cold

surface. Their models indicate that particular solid salt deposits are preferentially formed; the K/Na and Ca/Mg ratios are calculated to be higher in the surface deposits compared to an underlying ocean. This process of concentration means that the chemistry of the surface will not reflect that of the underlying ocean in a simple way, and when the micro-fracturing of the surface is also considered, it is unlikely that a europan sampling mechanism will encounter a surface that is mechanically or chemically simple.

Other satellites of Jupiter are believed to be differentiated and so share Europa's ice-over-rock structure. Ganymede's ice composition is similar to that of Europa in some respects, in that NIMS measurements of this moon also point to a salt / brine component at locations on its surface (McCord *et al.*, 2001) although a greater fraction of silicate material is presumed to be incorporated in order to account for its darker surface. With the potential for harbouring submerged 'seas', Europa, Ganymede, and perhaps Callsito, may provide sub-surface habitats that are congenial to the development and sustained activity of indigenous life-forms. The most recent discussions on the subject of extraterrestrial biology in these buried oceans are those of Chyba and Phillips (2001), the Space Studies Board's "A Science Strategy for the Exploration of Europa" (1999), and the thorough summary of Kargel *et al.* (2000). In considering the techniques available to reach and analyse these hypothetical oceans the exploration of an analogous terrestrial locale may allow novel programmatic methods and technologies to be tested. Such earthly settings may be found within the Antarctic ice sheet. Of specific interest are those regions where buried lakes of water may be found, and although lake Vostok (Kapitsa *et al.*, 1996) is one of the most well-known examples, there are at least 75 bodies of water known to exist beneath permanent covers of ice in the Antarctic ice sheet (Siegert *et al.*, 1996). The water in lake Vostok is believed to have been isolated from the surface for around one million years (Kapitsa *et al.*, 1996). By being disconnected from the rest of the terrestrial biosphere, any exploration of this unusually large lake may result in the dispersal of modern organisms such as bacteria or micro-flora into this environment. To minimize the disturbance of such habitats' biospheres, exploration technologies will have to be developed that can be sterilized and have their biological integrity monitored to a high degree of certainty (Abyzov *et al.*, 1999). The development of sterilization techniques and sampling technologies to explore these unique polar habitats has been suggested (Wynn-Williams and Edwards, 2000) as a useful spring-board to the development of sensors and protocols for

spacecraft platforms. Examples of such cross-over technologies are examined by Di Pippo *et al.* (1999) and Horvath *et al.* (1997) in their proposed Europan sub-surface missions. These use both mechanical and thermal boring methods, such as the eponymous Philberth[21] probe which has been employed in terrestrial ice sheets since its development in the 1960s.

1.3.4 Dark polar regions of Mercury and the Moon

Despite the preceding emphasis on surface ice deposits it is worth mentioning that ice may also be found beneath the surfaces of otherwise desiccated bodies. This notion is not particularly new; the possibility that the Moon may have such frozen polar sub-surface deposits was discussed well before remote-sensing technologies were capable of deciding the matter (Lœwy and Puiseux, 1897). For ice to persist it must be shaded from sunlight, and this situation arises in crater floors at the poles of bodies with small axial tilts such as Mercury and the Moon. Mercury's current axial tilt of ~7° allows regions within polar craters to be in permanent shadow, and temperatures in such locations might never rise above 110 K (Vasavada *et al.* 1999). The argument that these cooler regions may be host to water ice has been supported from radar studies of Mercury's polar regions. Radar imaging of high latitude regions performed by Slade *et al.* (1992), revealed strong echoes with polarization signatures that were suggestive of water ice. The polarization data associated with the reflective areas were similar to those seen in radar studies of the icy Galilean moons, which are generally interpreted as being indicative of water ice[22]. Later, repeated measurements made with higher levels of spatial resolution (>1.5 km) and sensitivity by Harmon *et. al.* (1994; 2001) showed that the radar-bright regions were geographically stable and many coincided with craters in those areas that had been photographed during the fly-bys of Mariner 10 in 1974-1975.

Similar radar backscatter measurements have been made of the Moon's poles by ground-based telescopes, and the high radar reflectivities and polarization changes detected in regions of the south polar region have been interpreted by some (Nozette *et al.*, 1996) as being caused by near-surface water ice deposits. Stacy *et al.* (1997) have argued that because particularly rough terrestrial surfaces can yield comparably high radar albedoes and polarization signatures

---

21 An electrically heated probe developed by Karl Philberth and subsequently used in the Greenland polar ice sheet (Aamot, 1967).

22 *Pure* water ice has a permittivity, (e=3.15) similar to that of lunar rocks (Carrier *et al.* 1995, pp553) but only 10% of the loss factor of lunar material.

there is at present no unique interpretation of the radar data. However, the lunar poles have also been examined from orbit with instruments sensitive to water ice, rather than particular forms of backscattering. The neutron emission spectra of the Moon's poles have been measured by the *Lunar Prospector* spacecraft with a spatial resolution of some tens of kilometres (Feldman *et al.*, 1998). From those data, which reveal the presence of hydrogen nuclei, 0.1×10^8 to 3×10^8 tonnes of ice are inferred to be present. Feldman *et al.* (1998) argue that if the ice is only found beneath in permanently shadowed craters, then deposits up to 2 m deep may be present. However, solar wind protons implanted in the regolith can seemingly duplicate the neutron emission signature of ice (Starukhina and Shkuratov, 2000).

1.3.5 Alteration phenomena

Processes at work in the Solar System such as gravitational perturbation, micrometeorite bombardment, and thermal processing can readily disguise the original state of an object's trajectory, surface, and sub-surface composition, leaving few obvious clues to its origin and history. Successful recovery of information about the past conditions experienced by a body requires the action of processes that leave an unambiguous trace or feature in some observable property. For an ice-rich body the most obvious transformation that it may suffer is the depletion of its ice through sublimation, with chemical species sublimating at rates determined by both the local temperature and their vapour pressures. Complications arise immediately if more than one compound is present as was shown for argon/ice mixtures (see 1.3.1). Ices, when mixed cannot generally be treated as being non-interacting; the sublimation behaviour must be found empirically. If the sublimation history can be established by experimentation for a given ice mixture, then measurements of the species lost from an object with an unknown composition can constrain the make-up of that object's ices.

In practice such deductive reasoning, when taken outside the laboratory and applied to a celestial body such as comet, is hampered by the lack of information about the distribution of material within the object. Barriers such as surface crusts or significantly porous interiors will impede the flow of gas and heat. A thermal gradient, for example, results in the condensation of different gases at physically separate layers, leading to a differentiated ice content. The gas that does escape from the comet nucleus may have undergone an unknown degree of chemical

and isotopic fractionation in diffusing from its source to the surface of the nucleus. In all likelihood the weak and marginally fractionated flow permitted through the evolved crust of an active comet may be swamped by the vigorous sublimation from freshly exposed ices that are thought to be the source of gas jets seen in many comets.

The rate at which an alteration phenomenon, such as diffusion, proceeds is dependent on the temperature, T, of the material. Models for the rate at which many phenomena proceed often include a term such as $exp(-E/kT)$ where E represents a energy barrier to the process and k is Boltzmann's constant. One process with a similar temperature dependence is the sublimation rate of a solid. The temperatures at which this and other phenomena are active are shown in Figure 11 which has been collated from the work of Gooding (1990), Neal (2000), Hudson and Donn (1991), and Ocampo *et al.* (1986). Of particular interest are the reference works by Gooding and Neal who independently examined the criteria needed to preserve samples returned from Mars. For each identified process in Figure 11 the temperature region in which it occurs at a significant rate is shown by a grey stripe. Thus the transformation of amorphous water ice to the crystalline cubic form of ice (denoted by Ic) occurs at temperatures around 130 K; these forms of water ice will be discussed in greater detail in section 1.4.1.

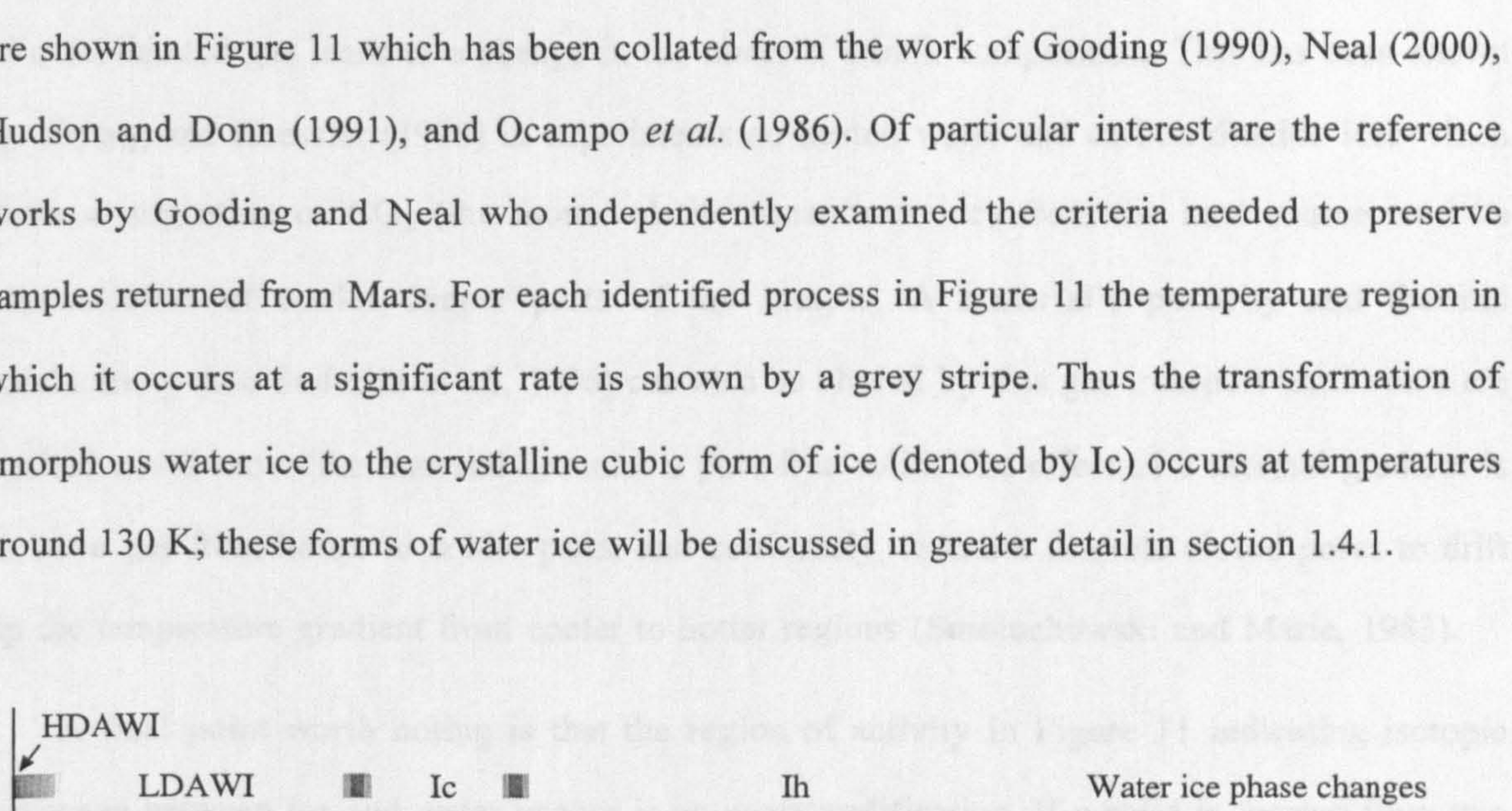

Figure 11 - A list of alteration processes active in ice-rich materials at various temperatures. Along with two crystalline forms (Ic, Ih), water ice can be frozen into at least two disordered solid forms; Low Density Amorphous Water Ice (LDAWI) and High Density AWI (HDAWI). VL1 and VL2 refer to the temperature ranges experienced by the *Viking* Mars landers.

There is little conceptual difference between martian or cometary ices and this chart can be read as a simplified subset of the potential changes that may occur in any cryogenic ice-rich material. Three of the traces in Figure 11 merit further explanation. Water ice, when condensed to its amorphous phase from a vapour in the presence of a second gas, was described in the previous section as being able to trap other gases. This trapping behaviour can occur whether the water is co-deposited with the vapour of the second compound, or is formed first and then exposed to the non-condensing gas. The subsequent release of material by sublimation, gives the vapour a chance to re-condense, and material can then be transferred[23] from hotter to colder regions. The preferential re-condensation of the more volatile fraction of a sublimated gas leads to a change in the material's bulk composition. This has been shown by Hsiung and Roessler (1990) in experiments on heated water and carbon dioxide ices which show a migration of CO_2 (the more volatile constituent ice) from the heat source, and its accumulation at cooler deeper parts of the sample. A material's porosity and thermal conductivity (see Seiferlin *et al.*, 1996) can also be altered by this gas transport until voids are infilled and a snow-like material becomes a pore-free solid. The effect of a thermal gradient is to drive gas from hotter to colder parts, and conversely, to cause discrete closed pores to drift up the temperature gradient from cooler to hotter regions (Smoluchowski and Marie, 1983).

A final point worth noting is that the region of activity in Figure 11 indicating isotopic exchange between ice and water vapour is an oversimplification. If a solid is formed from two different substances (C_1 and C_2), then the pressure of each component's vapour $p(C_i)$ above that solid is a function of the concentration of that substance in the solid mixture;

$$p(C_i) = f(n(C_1, C_2), T) \qquad \text{Eq. 4}$$

The form of $f(n(C_i...), T)$ may not be simple if the two materials can coexist in different physical phases or structures, but these details will be ignored as will the exact form of the temperature dependence. It is sufficient to describe the vapour pressure of gas in equilibrium with a solid component C_i as varying like

$$p(C_i) \propto \exp\left[-\frac{a_i}{T}\right] \qquad \text{Eq. 5}$$

---

23 Strictly the process is distinct from sintering which affects only the contact area between grains and does not cover the net transfer of material to or from grains.

Each compound in an ice mixture can be treated as having different values for the term a_i, which characterizes the volatility of that component. For a compound or condensed element which shows isotopic variation, the two isotopically different materials will show small variations in a_i; much smaller than may be found among different members of a group of similar chemicals, such as the family of alkanes. If we consider an ice that is made from two isotopically substituted forms (e.g. water, HDO and H_2O) , then at high temperatures each of the two components of the ice sublimate with equal rapidity and produce identical vapour pressures in equilibrium[24]. In contrast, at low temperatures this icy mixture will sublimate weakly and yield a small equilibrium pressure. A few simple calculations show that while the pressure of gases with slightly different values of a_i have low values at low temperatures, the *ratio* between the relative pressure of each component becomes greater as the temperature falls. This isotopic fractionation becomes more pronounced as the difference in the molecular weights of the two isotopically substituted compounds increases; the fractionation occurs as a result of the mass-*difference* and not the absolute molecular masses. It is useful to assess the magnitude of this effect for water ice with regard to hydrogen or oxygen isotope composition. In Figure 12, adapted from Kaye (1987), the vapour pressures arising from two ice mixtures are considered: one ice made of $H_2{}^{16}O$ and $H_2{}^{18}O$, and one made from $H_2{}^{16}O$ and $HD^{16}O$.

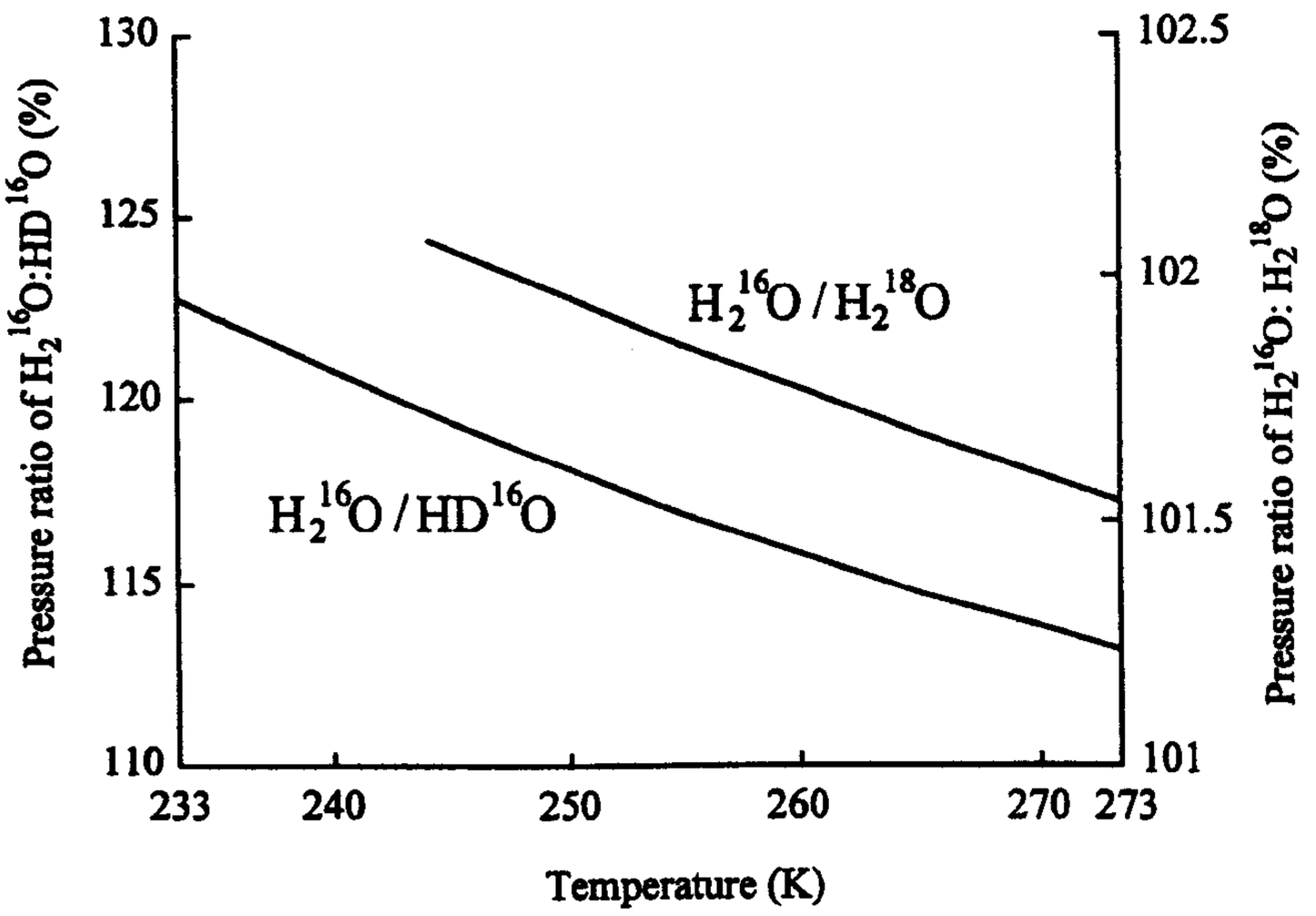

Figure 12 – Fractionation in two isotopically substituted water ice / vapour systems in thermal equilibrium. Note that the make-up of the gas above the solid ice is *not* dependent on the mixing fraction of the isotopically distinct water ices, but varies only with the temperature.

---

24 The speed of the sublimating molecules will differ, this being an example of non-equilibrium isotope fractionation.

If the ice mixture can be regarded as an infinite resource of the isotopically substituted waters then, in the H_2O and HDO system for example, the released vapour can have an composition ratio for H_2O:HDO that varies from 120:100 at 233 K to 113:100 at 250 K - irrespective of the ratio of HDO contained in the solid phase. Conversely, in the $H_2{}^{16}O$ and $H_2{}^{18}O$ system, the $H_2{}^{16}O$:$H_2{}^{18}O$ ratio of the vapour above this ice mixture varies little over the same temperature range and is broadly constant at ~102:100.

Sampling the sublimated vapour from an ice containing two separate compounds, such as isotopically substituted water in this case, therefore may reveal little about the composition of the solid. However, it is important to recognize that this ambiguity occurs only when the gas is in thermal equilibrium with its solid phase. This generally requires that the sublimated gas molecules experience enough collisions for a significant fraction of the gas to strike the surface of the sublimating solid again. No fractionation through this method can occur if the solid is able to sublimate into a void. In this case, which is a specialised form of Rayleigh fractionation, the make-up of the sublimated gas depends on the relative rates of sublimation of the two individual compounds. For the case of an isotopically substituted ice mixture made of a molecule A and its isotopically substituted counterpart B, the gas that is released from this ice in a non-equilibrium setting has a make-up of A_g and B_g given by

$$\frac{B/A}{B_g/A_g} = f^{\alpha'-1} \qquad \text{Eq. 6}$$

where f is the fraction of ice remaining after the sublimation has ceased and α' is the measure of the relative rates at which the two components A and B sublimate, namely;

$$\alpha' = \frac{k_A}{k_B} \qquad \text{Eq. 7}$$

where

$$\frac{\partial A_g}{\partial t} \propto k_A A \quad \text{and} \quad \frac{\partial B_g}{\partial t} \propto k_A B \qquad \text{Eqs 8a,b}$$

In the unusual situation that the reservoir of solid material is large in comparison to the amount of gas that sublimates from it, then f, the amount of material left after the sublimation has finished, is unity and the evolved gas has an isotopic make-up indistinguishable from that of the solid ice. The criterion for whether the reservoir is 'large' will depend on the brevity

and magnitude of the sublimation event and will be re-examined later.

The evolution of ices can be studied independently through laboratory experiments although the complexity of the processes is daunting. These include assessing the non-linear sublimation of multi-component ices and the extent to which a porous refractory matrix will fractionate a suffusing gas. Other alteration processes such as radiation-induced radical chemistry are also likely to be active in cometary materials and are also enabled at raised temperatures (Roessler and Nebeling, 1986). With these, and other temperature-dependent processes at work, reconstruction of the make-up of an extracted cometary sample can be simplified by minimizing the heat load that it experiences. Without knowledge about the mechanical or structural properties of *any* comet's surface, the temperature gradient through the surface cannot be known in advance. Thus, the depth at which condensed volatiles may be found for a given comet is very poorly constrained. Such uncertainties suggest that the appropriate thermal and mechanical properties of ices that make up a cometary nucleus should be well understood and these will be discussed next.

1.4 Properties of Water Ice

The ubiquity of water on Earth, and in the wider Solar System, makes it an obvious candidate for study as a planetary material. Such work has revealed a complex formation behaviour and anomalous properties when considered with similar compounds.

1.4.1 Water ices on cometary and planetary surfaces

Along with two amorphous states, water ice can form at least eleven crystalline phases (Lobban *et al.*, 1998). At pressures below 200 MPa only one of these crystalline phases is stable. This ice is named ice 'one' (I) and its relationship to the other phases of ice is shown in Figure 13.

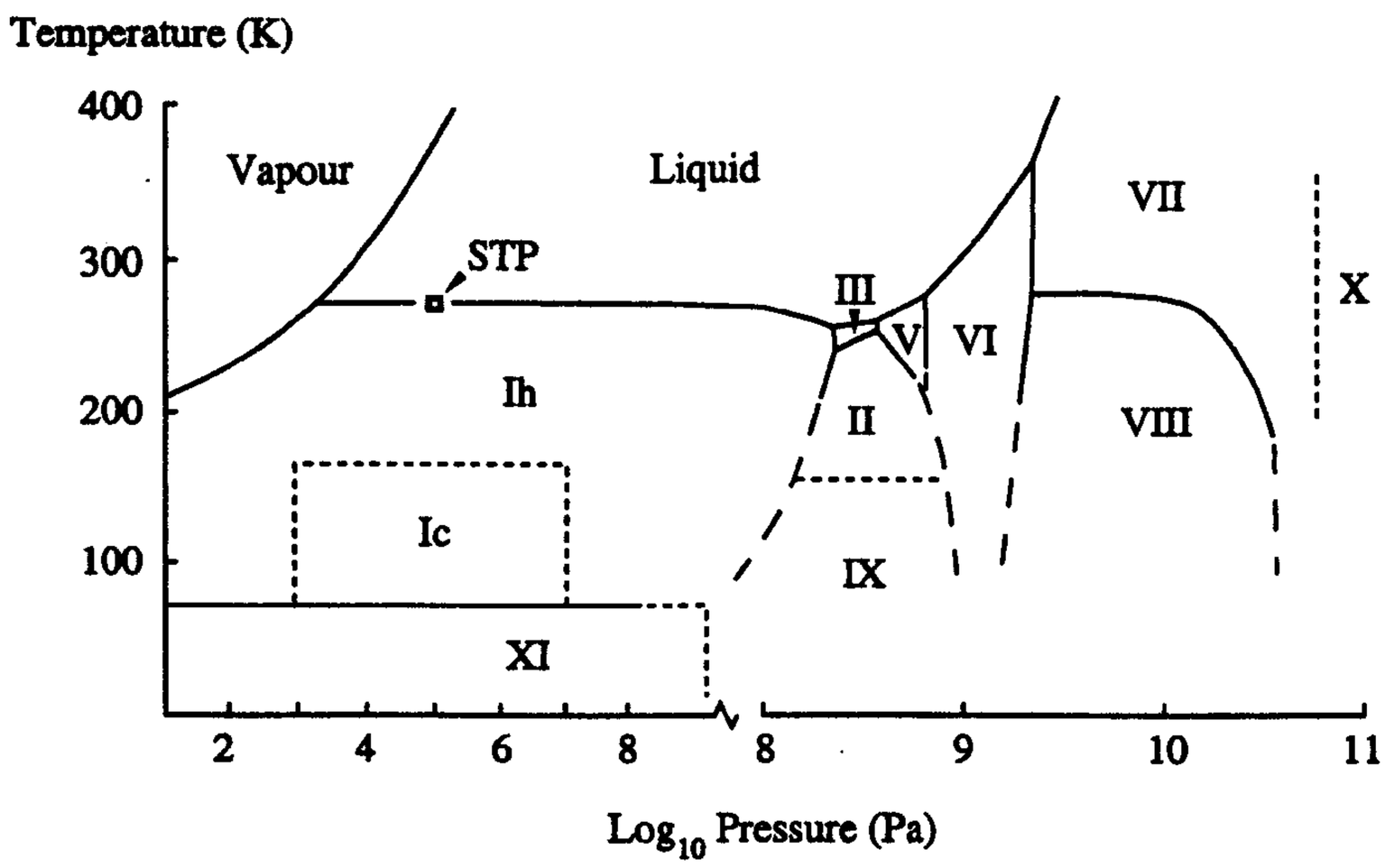

Figure 13 – The current known phases of water, excluding amorphous ices, after Lobban *et al.* (1998)

The classification of water ice I can be further divided into two types; hexagonal, and cubic ice. Hexagonal ice, Ih, forms by cooling liquid water and is the most familiar type of ice in everyday experience. The cubic form of ice I, Ic, is made by condensing water vapour onto surfaces that have been cooled to temperatures between roughly 110K and 150 K, and may occur in terrestrial clouds (Whalley, 1983). This vapour-grown form of ice I can be turned irreversibly into Ih by warming the ice to around 200 K (Klinger, 1989) with the onset of the change starting at ~160 K (Roessler and Nebeling, 1986). Water can also form a number of amorphous ices by condensing the vapour at even lower temperatures. Two of these disordered

ices are distinguished on the basis of their density, with partial evidence for a third form shown by Jenniskens and Blake (1994). Both the 'low' and 'high' density forms of amorphous ice (0.94 g cm^{-3} and 1.1 g cm^{-3}, Narten *et al.*, 1976) are made at temperatures much lower than 135 K and typically lower than 77 K (Sack and Baragiola, 1993).

Although these amorphous ices do have differing thermal properties and may play an important role in the formation and evolution of cometary nuclei, they will not be studied in this work. Their exclusion is partly due to the difficulty in performing experiments with large quantities of these ices as a result of their metastable nature.

1.4.2 Thermophysics of water ice

Although only ice Ih will be examined in this section, the discussion that follows is also applicable to the data sets for carbon dioxide ice's thermal properties. Before describing some of water ice's properties it should be stated that wherever practical, original data sets from experiments with water ice and carbon dioxide ice have been located, and those data are listed in Appendix A. In several cases inaccuracies can be found in the literature as a result of fitting model equations for properties over wide temperature ranges. To avoid this problem models for the thermophysical properties of interest have been made only for the temperature range employed in this work (~100 K to ~250 K).

From the experimenter's point of view, water in both its liquid and solid forms has a number of properties, such as its large heat of vaporization and heat capacity[25], that make it an exceptional compound. Among the members of the XH_n series of compounds (such as NH_3) its liquid form has the highest heat of vaporization, and Needham (1965) expansively describes water as having a heat of vaporization "greater than that of any other known substance". Of particular interest to this work are the specific heat[26], c, the thermal conductivity, λ, and heat of sublimation, c_{sub} of ice. A commonly quoted work for the specific heat capacity of water ice is that of Giauque and Stout (1936), which is often referred to by quoting the following model:

$$c = 7.49T + 90 \qquad \text{Eq. 9}$$

---

25 These and other properties of water are given in Needham (1965) and Franks (1972).
26 Assumed to be measured at constant pressure throughout this work.

The original work of Giauque and Stout gives no such model and instead simply tabulates their experimental data. At temperatures below 80 K the curve of c against T is poorly fitted with a linear model and at 80 K the tabulated values of heat capacity differ by more than 7% from the above model, and by even greater amounts at lower temperatures (see Appendix A1). Such deviation illustrates the general problem of assuming that model equations provide a uniformly good fit over their range of applicability. For water ice, a better fit can be written for its specific heat capacity in the temperature range of 100 K to 270 K with an R^2 figure of merit > 0.999 as

$$c = 6.96T + 185 \qquad \text{Eq. 10}$$

Phenomenological models for the thermal conductivity, λ (W m^{-1} K^{-1}), of ice can also be made and at temperatures higher than 25 K; an empirical model for λ in pure Ih ice at constant pressure is often cited in the literature, (e.g. Squyres *et al.*, 1985; Steiner and Kömle, 1991) as

$$\lambda = \frac{567}{T} \qquad \text{Eq. 11}$$

Despite the useful simplicity of the above model, it too overestimates the best estimate of the earlier experimental data collated from a number of sources by Slack (1980). The discrepancy in λ is around 10% at some temperatures and in the temperature range of 100 K to 150 K the difference amounts to over 5%. The data tabulated by Slack has been fitted here by a polynomial in T that differs from the data by an error of half of one percent in the temperature range of 80 K to 270 K.

$$\lambda = \frac{656.3}{T} - 0.077T \qquad \text{Eq. 12}$$

The thermal conductivity and heat capacity of ice will often appear in later equations as a product and it is useful to plot the value of λc (which has units of J^2 kg^{-1} K^{-2} m^{-1} s^{-1}) as a function of temperature. The value of this product is plotted against temperature in the next chart, and gives a measure of the rate at which heat is exchanged from a heat source in contact with an object at some different temperature.

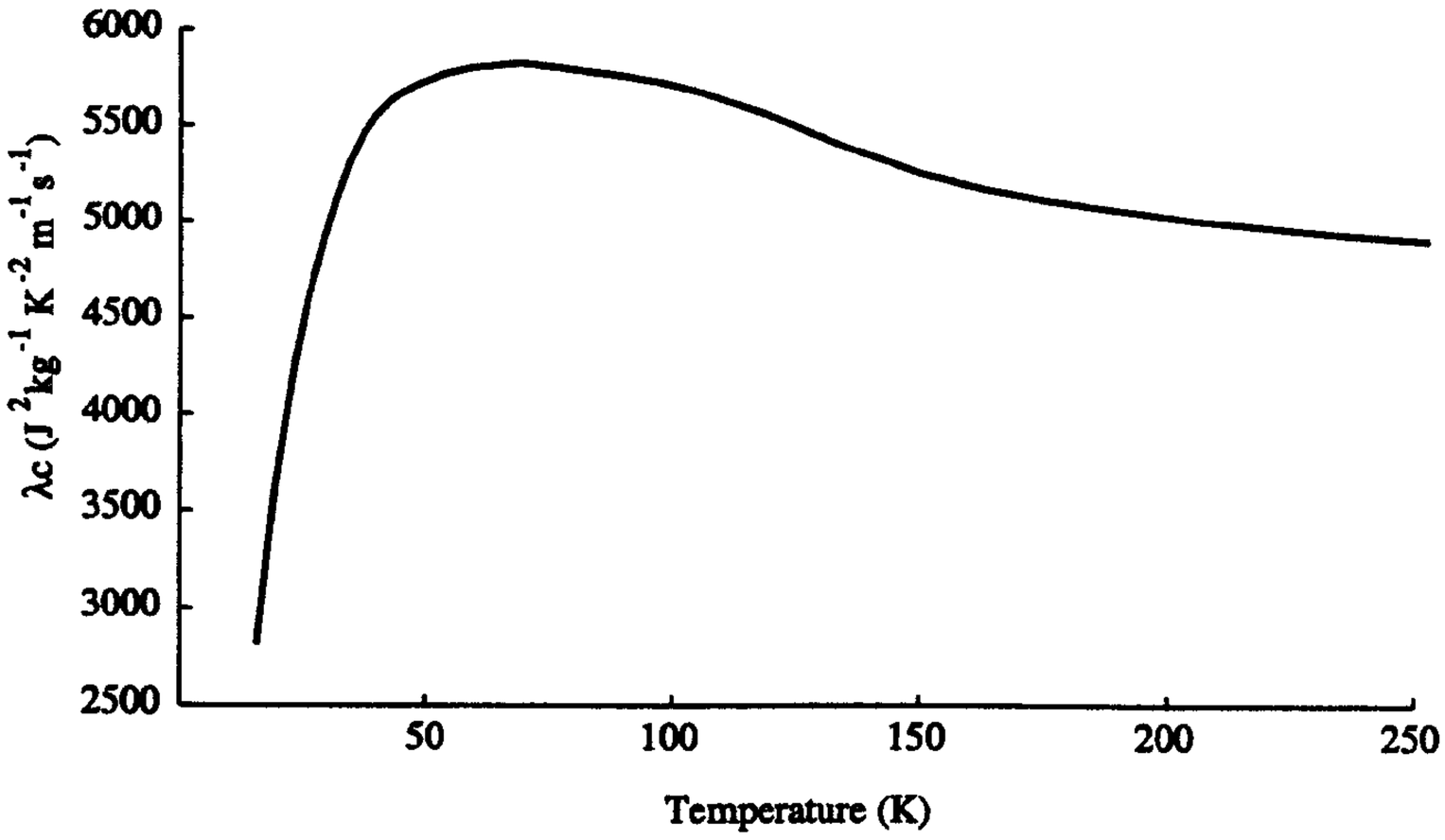

Figure 14 – The temperature variation of the best-fit models of λc for ice Ih.

A similar chart (Figure 15) may be drawn up for solid carbon dioxide ice with the use of the thermal properties described in Appendix A (A4 to A6). The impact of these properties on the temperature gradient set up by a heating source will be examined in section 2.4

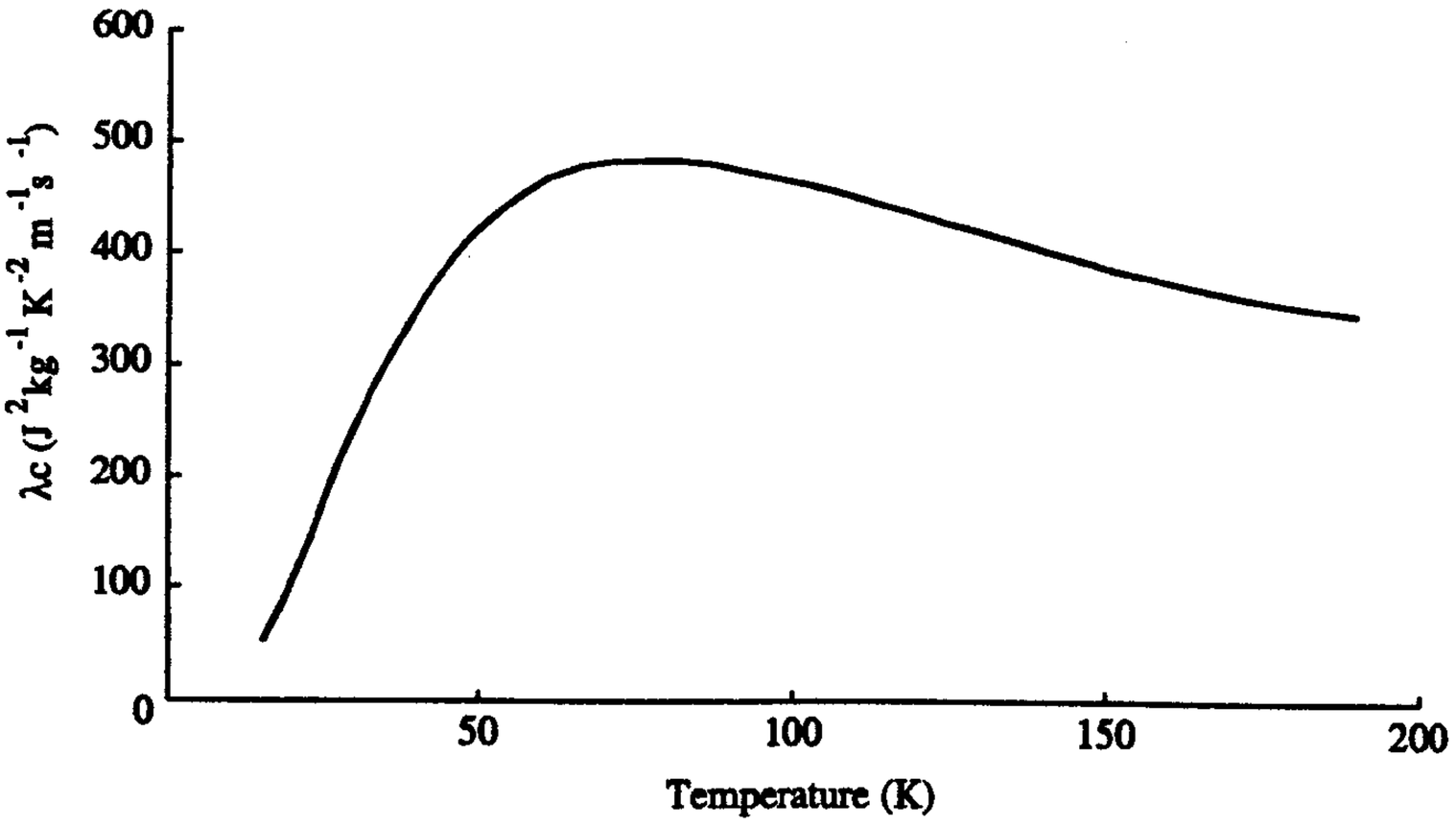

Figure 15 – The temperature variation of the best-fit models of λc for solid CO_2.

The third quantity of interest is an ice's latent heat of sublimation and this too has a chequered history in terms of which models ought to be relied upon. An oft-quoted work that examines the specific heat of sublimation for water ice is that of Delsemme and Miller (1971) which summarizes the then-extant data for the latent heat of sublimation, c_{sub} (J kg^{-1}), of various ices. A 'least-squares' fit against temperature for their collated data yields;

$$c_{sub} = 2888000 - 1124T \qquad \text{Eq. 13}$$

Other models have been suggested for this property and some works, such as that of Gombosi *et al.* (1985) treat the heat of sublimation as being independent of temperature in the range of interest (100 K to 200 K) and equal to 5×10^{11} ergs mol^{-1} (=2.6669×10^{6} J kg^{-1}). The practical difference between such formulations for c_{sub} is smaller than the discrepancies between the models of c and K. At temperatures above 100 K the models for c_{sub} give values that differ by less than 4% and this property is also tabulated in the appendices (A6) for the other solid ice considered in this thesis, carbon dioxide.

Of the preceding parameter models only the thermal conductivity of an ice varies with the material's porosity. Heat may be transported by three processes in such an ice; radiative transfer in the voids between particles, conduction through the solid matrix, and the mass movement of gas which may also remove or deposit heat by a change of phase. Even without the addition of other ice components the general problem is further complicated by the ability of a gas to re-condense and alter the geometry of the matrix through which it is flowing. These complexities add to the difficulties of making and using porous ice samples in experiments and for this reason only void-free ices have had their thermomechanical properties measured in this thesis. Detailed models for porous ice's thermal conductivity are reviewed and compared with experiments in Steiner and Kömle (1991), Seiferlin *et al.* (1995), and Kossacki *et al.* (1994). If these studies are summarized crudely, at temperatures lower than 190 K, heat transport by sublimated vapour within the pores is not significant. The ice then has an overall thermal conductivity that is proportional to the contact area of the grains in the ice. At higher temperatures the pressure within the pores rises and the latent heat carried by this gas becomes a significant carrier of heat, and for particular void-fractions a porous ice may have a thermal conductivity higher than that of solid ice (Steiner and Kömle, 1991).

1.4.3 Mechanical behaviour of water ice

Although the aesthetic geometrical properties of water ice in the form of snowflakes were appreciated by Chinese scholars as long ago as 135 BCE (Mason, 1992), it was not until the last century that interest blossomed in ice's bulk properties (Schulson, 1999). Much of this research was driven by military needs, which variously saw ice as an obstacle, a hazard, and as a building material. In the wider Solar System the presence of ice on other worlds and their

satellites prompted the study of ice under conditions of high pressure and low temperature. However, some regions in the space of temperature and strain rate have not been well examined and the boundaries of this area of knowledge will be described.

The strain-rate experiments of Durham *et al.* (1983) represent some of the first comprehensive studies of the failure process involving compression of water ice samples at low rates of strain. At temperatures much lower than 140 K, Durham *et al.* (1983) showed that unconfined samples of polycrystalline water ice fail in a brittle manner for strain rates in the range of 10^{-6} to 10^{-4} s^{-1}. At higher temperatures, in the same strain rate regime, the ice displays ductile deformation until at temperatures above 195 K no brittle failure is seen. Conversely, at elevated temperatures, brittle failure behaviour is seen at all strain rates under low confining pressures. A point worth noting is that in the brittle failure regime, imposing a confining pressure of 100 MPa on the ice sample triples its compressive strength. In contrast, the plastic (warmer than 140 K) ice samples, when confined, display only a slight strength variation with pressure. Figures 16a-c are taken from Durham *et al.* (1983) at three particular temperatures and the filled symbols indicate brittle failure.

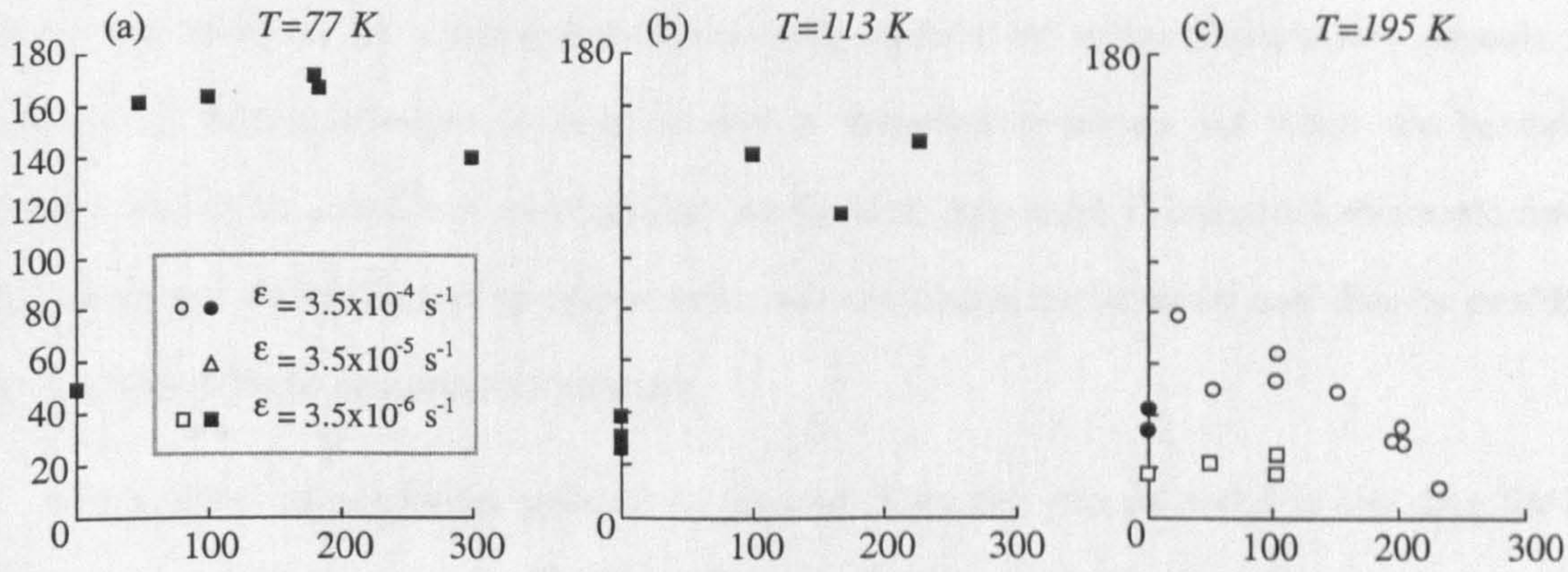

Figures 16a/b/c – Charts from Durham *et al.* (1983) showing the compressive strength (MPa) *vs* horizontally plotted confining pressure (MPa) for water ice at three temperatures: (a) 77K, (b) 113 K, and (c) 195 K.

If confining pressure is important in determining ice's compressive strength then it may be useful to calculate the peak confining pressures of comet-like objects. For a non-compressible material the peak pressure, p, inside a porous body can be calculated as

$$p_{\text{int}} = \frac{2\pi}{3} G\rho^2 R^2 \qquad \text{Eq. 14}$$

For an isothermal sphere with a radius of around one kilometre and a bulk density of 2000 kg m^{-3} (appropriate for a dirty snowball having a 1:1 rock to ice ratio), the central pressure caused by self-gravitation cannot be higher than 560 Pa. This example presumes that the material has no tensile strength, and it may be useful to think of this object not as a solid but as an aggregate of grains having vanishingly small points of contact with each other. Yet this moderate pressure may be at least one magnitude larger than that which exists within many comets as a result of their postulated porosity (Hughes, 1996) which may be as high as 50%. Support for these high void-fractions has come from predictions by Rickman (1986) who used the non-gravitational effect of gas plumes to deduce that the bulk nucleus density of 1P/Halley lies between 100 and 200 kg m^{-3}. The method used to derive these figures relied on observing the comet's motion in response to the reaction force exerted by gas jets emanating from the nucleus. Unsurprisingly, this method has a high uncertainty, given the difficulty in modelling the density and speed of gas jets, and hence the total impulse they deliver. Nevertheless, as inferred by the same method, only P/Temple 2 has a higher bulk density (540 kg m^{-3}) than 1P/Halley, with other comets such as P/Encke and P/Grigg-Skjellerup having modelled densities well under 200 kg m^{-3}. If a nominal average density of 250 kg m^{-3} is used in equation 14, then the central pressure of a kilometre-radius body cannot be larger than a few pascals. No variation of failure strength in compression is therefore expected for water ice beneath a comet's surface as a result of gravitational overburden. Appendix C examines this topic further and results are shown from a computer code that calculates the pressure and density profile of objects with a finite compressive strength.

If the effect of confining pressure is ignored, then the general trend in the data for low strain rates of Durham *et al.* (1983) is that the failure strength rises with strain rate. The plastic deformation data shown in Figure 16c show this most clearly. A similar trend is also visible in the work of Jones (1997) who summarized compressive strength data taken at higher strain rates for unconfined water ice at -10°C. His results are plotted in Figure 17 which shows that as the strain rate rises, the compressive strength data cease to show a clear trend. The chart shows a composite data set of tests on polycrystalline ice (marked with a 'o') and ice with an oriented column-like grain structure (plotted with a '+'). The slight dip in the data is not significant according to Jones (1997) and the important feature is that at high strain rates the brittle failure strength varies less strongly with strain than at low strain rates.

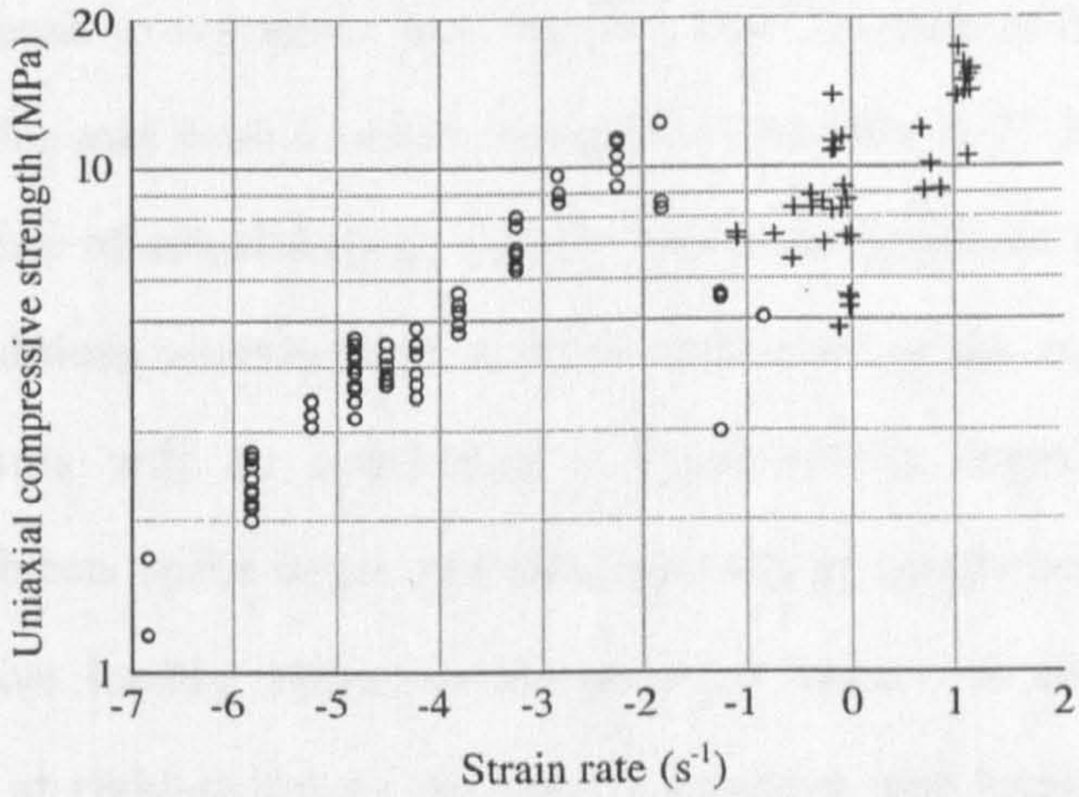

Figure 17 – Collected values of ice's compressive strength at modest strain rates, after Jones (1997). The different symbols represent separate studies undertaken at different strain rates and under otherwise similar conditions.

Those studies that have been conducted on the tensile properties of Ih water ice at high rates of strain (Lange and Ahrens, 1981; Currier and Schulson, 1982; Lange and Ahrens, 1983) indicate that at temperatures of between 230 and 250 K polycrystalline ice has a tensile strength of 17 MPa. Although these works do not examine the temperature dependence of this strength, this value is similar to the average of the points shown in Figure 17 at high rates of strain for compressive failure.

The absence of data sets showing specifically the failure under drilling of cryogenic water ice means that some relationship between this process and the more traditional laboratory tests is needed. Discussions with researchers of the Colorado School of Mines about experimental drilling studies of rocks revealed that drilling efficiency is generally inversely proportional to the *tensile* strength of the material[27]. In the complex two-dimensional stress field around a cutting edge it is not reasonable to rely purely on uniaxial tensile strength data. Models, such as those of Mohr[28] can be used to find failure strengths in more complicated stress-fields and without adding unnecessary detail, these models can be paraphrased to suggest that a brittle material displays a near-constant value for the ratio of its compressive to tensile strengths in uniaxial stress. For example, uniaxial compressive and tensile tests on concrete (Raphael, 1984; Griffin, 1995) show that this ratio is around 10; for water ice this ratio appears to be lower, and close to unity.

If the close similarity between compressive and tensile strengths of water ice at high

---

27 Personal communications with Mr B. Blair, studying at the Colorado School of Mines.
28 Which are described in many undergraduate texts on strain and fracture such as Feltham (1966).

temperatures are germane to cryogenic ices, the data from Durham *et al.* (1983) may be used to suggest that water ice may have a tensile strength of ~50 MPa at 77 K and perhaps half that at 113 K. In the absence of actual drilling data for ices at temperatures much lower than those met under arctic conditions another field of work that involves the rapid loading of ices at cryogenic temperatures will be considered - hypervelocity impact research. In such experiments, where objects strike target materials typically at speeds between 1 and 5 km s^{-1}, very rapid compressive loading occurs at the point of impact. A shear wave is launched through the material at right-angles to the impact direction and away from the impact site large tensile stresses are produced at the target's surface and this tensile load causes spallation of material from the face of the target. From detailed shock-loading experiments of ice from moderate speed impacts (0.14 to 1 km s^{-1}) Lange and Ahrens (1981) were able to infer the threshold energies needed to generate particular impact phenomena, with 81 K ice samples requiring energies almost an order of magnitude higher than 257 K samples to achieve the same degree of destruction. The presumption that the colder targets were inherently stronger is tempting but untestable as the method used by Lange and Ahrens (1981) for forming the coldest samples resulted in a great number of small bubbles and flaws in the ice which, in their colder ices, could have disposed them to fracturing more readily than comparatively bubble-free ice targets. With these doubts in mind a final study will be described; the hypervelocity impact studies of ice targets by Kato *et al.* (1992). Their work on cryogenic ices (77 K) not only demonstrated similar failure strengths of around 5 MPa at higher temperatures (255 K), but also displayed a ten-fold increase in the peak stress needed to achieve the same degree of fragmentation in cryogenic ice.

The diversity of results and methods can be broadly summarized by saying that water ice's compressive and tensile strengths increase at least by one order of magnitude as the temperature of the ice falls from room temperature to that of 77 K. Expected values for either of these strengths would be somewhat higher than 5×10^7 Pa at temperatures close to 100 K. The resistance which a water ice sample would display when drilled may also be expected to rise as the ice's temperature falls.

2 Sampling Planetary Surfaces

"The speculation... is interesting, but the impossibility of ever doing it is so certain that it is not practically useful."

The editor of Popular Astronomy, rejecting a letter written by R. Goddard "On the possibility of navigating interplanetary space" (1907)

In the past three decades samples have been gathered and analysed *in-situ* on three Solar System bodies, with varying degrees of finesse and overall success. Dedicated mechanisms first made in-situ measurements of another world, the Moon, with the impact penetrometry tests of the *Surveyor* 1 craft in June 1966, and followed in the same year by the density measurements of *Luna* 13 in its Christmas Eve landing. The first Soviet and American payloads concentrated on resolving the most immediate questions about the lunar regolith, notably the bulk properties such as the load-bearing strength, and the degree of compaction it displayed with depth. In estimating the bearing capacity of the lunar surface, cone-tipped penetrometers were used extensively in both the Soviet and American missions and a variant of this device will be examined in the next section.

2.1 Penetrometry

As the word suggests, the act of penetrating a material with a pointed or shaped tool is classed as penetrometry only if some aspect of the process is recorded. Thus, the emplacement of legs into a planetary body with no associated measure of the process is simply an anchoring method, and can reveal only the crudest properties of a material. From the viewpoint of spacecraft exploration the body of the penetrating tool may even be considered as a separate delivery system for other sensors such as thermal, radionuclear, and seismic devices (e.g. Ball *et al.*, 1996; Boynton and Reinert, 1995). Table 7 shows the current history of extraterrestrial penetrometry. Those spacecraft missions that have used a dedicated penetrometer, instead of making opportunistic measurements, are shaded in grey.

Table 7: Mechanical tools deployed in lunar (L), martian (M), and venusian (V) missions.

Craft & target		Launch date	Landing date	Geotechnical instruments deployed
Surveyor 1	L	30-05-1966	02-06-1966	Foot pad strain gauges
Luna 13	L	21-12-1966	24-12-1966	Rocket driven 35 mm conical penetrometer
Surveyor 3	L	07-04-1967	20-04-1967	Soil scoop arm and foot dynamics
Surveyor 5	L	08-09-1967	11-09-1967	Foot pad strain gauges
Surveyor 6	L	07-11-1967	10-11-1967	Foot pad strain gauges
Surveyor 7	L	07-01-1968	10-01-1968	Soil scoop arm and foot pad data
Apollo 11	L	16-07-1969	20-07-1969	Hammered core tube 19.7mm ID
Apollo 12	L	14-11-1969	19-11-1969	Hammered core tube 19.7mm ID
Luna 16	L	12-09-1970	20-09-1970	Rotating regolith excavator
Luna 17	L	10-11-1970	17-11-1970	Shear vane cone penetrometer on Lunokhod 1
Apollo 14	L	31-01-1971	05-02-1971	Hammered core tube 20 mm ID
Apollo 15	L	26-07-1971	30-07-1971	Recording penetrometer, hammered corer (41 mm ID), and rotary-percussive corer
Luna 20	L	14-02-1972	21-02-1972	Improved rotary-percussive sampling corer
Apollo 16	L	16-04-1972	21-04-1972	Recording penetrometer, hammered corer (41 mm ID), and rotary-percussive corer
Apollo 17	L	07-12-1972	11-12-1972	Hammered core tube (41 mm ID), and rotary-percussive corer
Luna 21	L	08-01-1973	15-01-1973	Shear vane cone penetrometer on Lunokhod 2
Luna 23	L	28-10-1974	06-11-1974	Rotating drill regolith excavator
Viking 1	M	20-08-1975	20-07-1976	Soil scoop and foot pad dynamics
Viking 2	M	08-09-1975	03-09-1976	Soil scoop and foot pad dynamics
Luna 24	L	09-08-1976	18-08-1976	Rotating drill regolith excavator
Venera 11	V	09-09-1978	25-12-1978	Shear vane penetrometer*
Venera 12	V	14-09-1978	21-12-1978	Shear vane penetrometer*
Venera 13	V	30-10-1981	27-02-1982	Surface rotary coring tool and shear vane penetrometer
Venera 14	V	04-11-1981	05-03-1982	Surface rotary coring tool and shear vane penetrometer
VeGa 1	V	15-12-1984	11-06-1985	Surface rotary coring tool and shear vane penetrometer*
VeGa 2	V	21-12-1984	15-06-1985	Surface rotary coring tool and shear vane penetrometer
Mars Pathfinder	M	04-12-1996	04-07-1997	Soil mechanics from rover traction

Launch dates from Thompson (1997), Apollo details from Carrier et al. (1995), Luna data abstracted from Cherkasov et al. (1967), and information about the VeGa and Venera missions from Johnson (1979) and Barmin and Shevchenko (1983).
** = device operated in all likelihood, but without data being received at Earth.*

The subject of penetrometry measurements from spacecraft landers is comprehensively described in the summary paper of Ball and Lorenz (2001). Furthermore, penetrometry, continues to be proposed as a technique in lander payloads, with the papers of Gromov *et al.* (1997) and Haas and Shinn (2000) describing only a few of the many varied designs. For a historical overview of the wider field of geophysical penetrometry, and for a discussion of current practice, the review by Lunne *et al.* (1997) is a detailed and well-illustrated resource.

At its simplest, penetrometry consists of driving a probe through a medium at a given rate while measuring the force needed to generate that motion. The magnitude of this resistance will depend on a number of other factors, not least of which is the strength of the material and the speed at which the penetrometer is being pushed. While concentrating on the simplest forms of penetrometry, this chapter will mention in passing, developments that have some degree of applicability to spacecraft-deployed instrumentation.

The most common form of penetrometer used in civil engineering is the cone penetrometer, which typically takes the form of a cylindrical rod tipped with a conical head. The half-angle of the head varies among the many types of penetrometer that are available, with the majority having half-angles (θ, see Figure 18) that lie between 15° and 45°. Two important design changes have raised the usefulness of this object above the level of a sharp stick. The 'piezocone' head incorporates a load cell, usually a piezoelectric or piezoresistive element, between the head and the probe's body, and it allows the reaction force against the head alone to be measured. A second critical development was the addition, in the late 1950s, of a strain gauge element mounted on a tubular sleeve positioned midway along the cylindrical shaft of the penetrometer (detailed in Barone and Faugno, 1996). When the device is driven into the ground the load cell under the conical head measures a force which has at least two components. One of these arises from the compression and deformation of the soil, and a second force appears from a component of the friction exerted by the soil grains as they move over the surface of the conical head. By using the strain measured by the sleeve on the flat body of the probe to calculate the friction of the soil moving against a plane surface, the purely compressive fraction of the composite force measured by the head-mounted load cell can be found. A penetrometer is commonly driven at a constant rate by an above-surface motor, allowing measurements to be correlated with depth. Where this cannot be managed,

devices that record their own depth have been devised with the most famous example being that of the self-recording lunar penetrometer of the Apollo missions (Costes *et al.*, 1971).

The simplicity of the portable cone-penetrometer has led to the development of many empirical relationships between the resistance encountered by the penetrometer and various material properties of interest to engineers and geologists. Its major disadvantage is that interpretation of the data relies on the application of an identical penetrometer to materials studied with other techniques. A database of calibration force histories from standard conical shapes driven at particular speeds into standard soils is therefore a critical key to using penetrometry effectively and an example of such a parametric study in sand is that of Houlsby and Hitchman (1988). From such calibration work a commonly sought parameter is the failure strength of a material at depth but in progressing through a material, a penetrometer can compact and deform the surrounding medium. Obviously, the material through which the penetrometer is passing may then bear little resemblance to the undisturbed medium and once again a calibration table must be sought in which a second measurement method is used as a comparative guide.

The compaction of particularly fragile media can be avoided with the use of specialized penetrometer designs and one such non-conical tool is the blade penetrometer. This device has the appearance of a knife-edged plate of constant cross-section and was refined in the snow strength studies of Dr. Masaharu Fukue of Tokai University in Japan. The development of this tool is briefly described by Shapiro *et al.* (1997) in their summary of the various techniques that have been devised for measuring the mechanical properties of fallen snow. A penetrating blade, such as that shown in Figure 18, minimally compacts and deforms the material ahead of it. In a fragile material, such as snow, its motion is then impeded only by the friction of material sliding over its vertical faces, and the effort needed to break the inter-granular bonds in the snow at the inclined facets of the blade edge. When driven at a given rate through water snow, the reaction force experienced by such a blade penetrometer has been shown to correlate well with the axial compressive strength (Shapiro *et al.* 1997) for snows with bulk densities between 350 and 480 kg m^{-3}. A relatively simple model can be devised to recover the strength of the snow as a function of depth from the indentation force of such a penetrometer and the following analysis is adapted from the model developed first by Anderson *et al.* (1996) to

model the high speed (< 1 km s^{-1}) impact of rocky materials by sampling penetrators. The model of Anderson *et al.* (1996) has been applied successfully at lower speeds by Kömle *et al.* (1997) to characterize the progress of a spear-like penetrator at 20 m s^{-1}. With appropriate changes to the modelled geometry of the penetrator the same model was used at yet lower speeds *in-vacuo* by Garry *et al.* (1999) to investigate granular media. A cross-section of the geometry is shown below and the material being probed is assigned two simple properties; a strength-like parameter, σ, and a coefficient of sliding friction, μ, for the material in contact with the penetrator's surface. Strictly, σ is the component of the failed material's deviatoric stress measured normal to the penetrator's surface. Furthermore, the material is assumed to have a homogeneous make-up and a well-defined boundary at z=0.

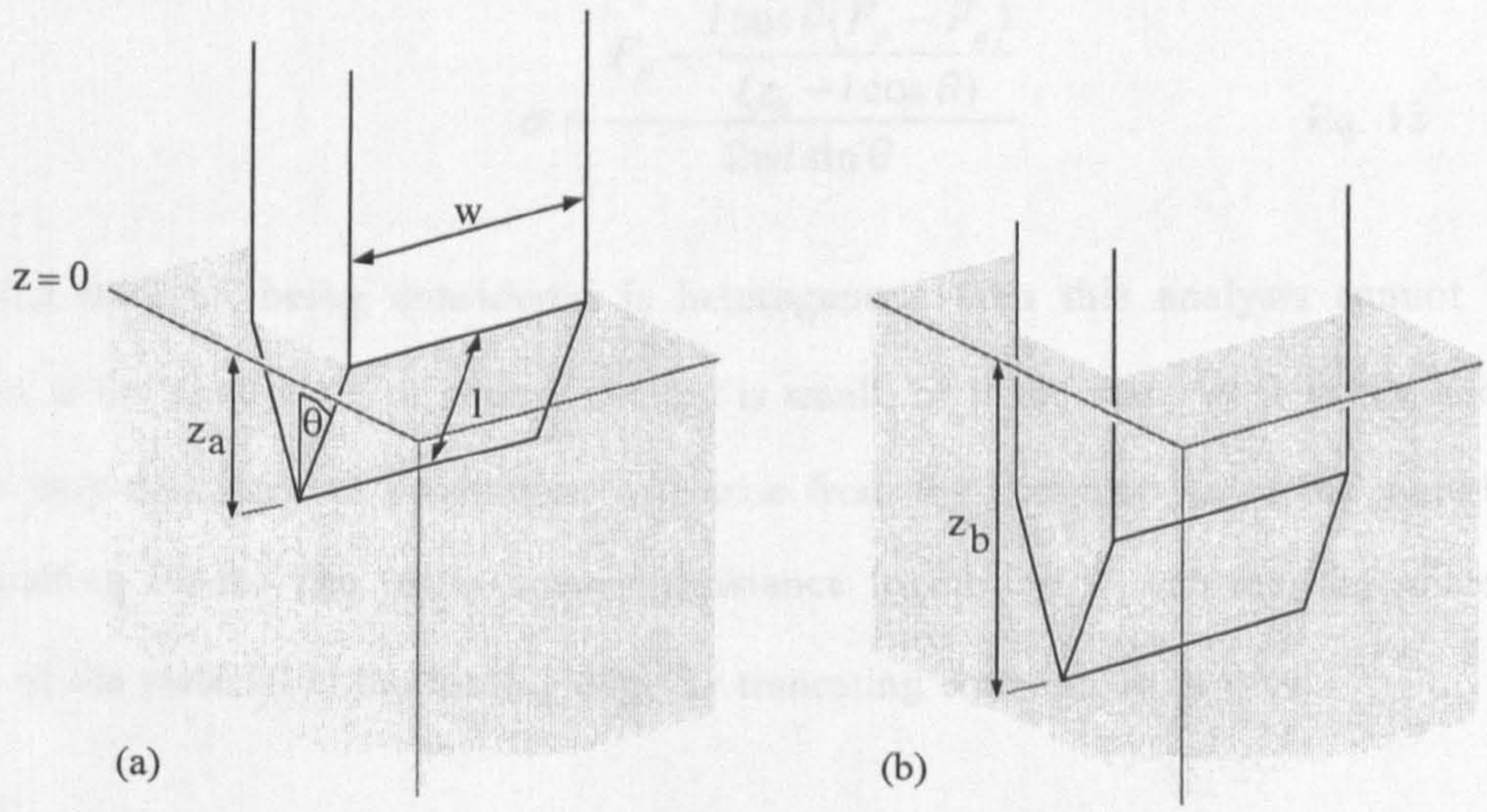

Figure 18 – Two penetration regimes described for a knife blade penetrometer. (a) for partial penetration of the leading edge, and (b) full edge burial.

For a blade being inserted slowly into the material then at a depth $z_a=l\cos\theta$, the resistance F_A can be written as:

$$F_a = 2\sigma(\sin\theta + \mu\cos\theta)wl \qquad \text{Eq. 15}$$

The condition of slow insertion allows hydrodynamic terms ($\propto$ penetration speed^2) to be neglected from the original formulation given by Anderson *et al.* (1996). Once the blade's tapered leading edge has been fully embedded an extra term must be added to account for the friction experienced by the plane faces of the penetrometer of width w. When, as in Figure 18b, the blade's plane surface has penetrated the material further ($z_b>>l\cos\theta$), the resistance

encountered may then be written as;

$$F_b = F_a + 2\sigma\mu w(z_b - l\cos\theta) \qquad \text{Eq. 16}$$

By measuring the resistance to motion experienced when only the leading edge of the blade is embedded (F_a), and the force at some later point when a known portion of the blade's plane surface has penetrated (F_b), the above two equations can be rearranged to find unique values for σ and μ.

$$\sigma\mu = \frac{(F_b - F_a)}{2w(z_b - l\cos\theta)} \qquad \text{Eq. 17}$$

where

$$\sigma = \frac{F_a - \dfrac{l\cos\theta(F_b - F_a)}{(z_b - l\cos\theta)}}{2wl\sin\theta} \qquad \text{Eq. 18}$$

If the material being considered is heterogenous then this analysis cannot be used. However, if the coefficient of sliding friction is small, or if the material is brittle and porous, then the only resistance to penetration will arise from the compression of the material ahead of the cutting blade. The instantaneous resistance to motion F_i can then be related to the strength of the material at the leading edge by truncating equation 16 to give

$$F_i \approx 2\sigma wl\sin\theta \qquad \text{Eq. 19}$$

Samples with varying degrees of homogeneity will be examined with this method in chapter five which will also describe the results obtained by other methods of deformation that are discussed in the next sub-section.

2.2 Cutting and coring

There are four basic mechanisms that may be used to remove material from a worked medium: the application of mechanically-induced stress, thermally induced stress, fusion then vaporization, and chemical attack. Although only mechanical sources of work will be considered in this work, it is worth briefly introducing some of the more exotic techniques (see Table 8). At least one of the methods, in the guise of an ultrasonic reciprocating edged tool, is

being studied currently by NASA with a view to its use as a rugged low-power device for asteroid-sampling spacecraft (Dr. Y. Bar-Cohen[1], personal communications). Unfortunately, most of the non-mechanical methods are inappropriate for sample recovery because of the high temperatures involved. Despite their exotic nature, these exothermic drilling processes all rely on overcoming a strength of some kind, in common with the purely mechanical cutting methods. In the case of a sharp blade piercing a material then shear and tensile strengths are being overcome, similarly, modern rock drills rely on the application of tough load-bearing surfaces to the rock face, to load and fracture the rock by compression.

Table 8: Working efficiencies of various excavation methods, after Maurer (1968)

Drilling method	Removal mechanism	Specific energy (J / cm^3)	Maximum potential drilling rate (cm / min)
Rotary	Mechanical	200-500	14 - 85
Erosion	Mechanical	2000-4000	35 - 140
Ultrasonic	Mechanical	20 000	0.04 - 0.07
Laser	Spallation by thermal stress	1500	1-2
Electron beam	Spallation by thermal stress	1500	1-2

Whatever the chosen drilling process, it is often desirable to expend as little energy as possible in removing material from a workpiece with a given tool. This is roughly equivalent to asking that each unit mass of excavated material be deformed as little as possible, and ideally this would correspond to removing the debris with cuts that are as deep and coarse as possible. Energy wasted on pulverizing debris trapped around the tool into powder is energy that could have been otherwise spent on excavating fresh material. However, energetic efficiency is not the only measure of a tool's worth. Deep cuts generate large reaction forces and power loads, both of which are lacking from the payload of a landed spacecraft platform. Before discussing one excavation process in detail, that of rotary coring, it should be noted that sample acquisition is not synonymous with excavation. Several techniques have been proposed for the recovery of material from planetary surfaces that have no counterpart in terrestrial prospecting. Some of these unusual approaches, such as the use of scoops that accumulate gas-jet driven surface debris, and trawl nets, are described in Clark *et al.* (1986) and in Sears and

[1] Who leads JPL's Nondestructive Evaluation and Advanced Actuator Technologies unit.

Clark (2000). The latter reference enlarges upon the speculative designs of Clark *et al.* (1986) and describes the recent development of inertia-driven augers and counter-rotating cutters, among other sampling mechanisms. Despite the variety of other devices available for remote sample acquisition, the drill and the hollow coring tool have been successfully deployed on three planetary bodies and it is likely that they will continue to be used for spacecraft sampling missions. Their success has been due in part to the robust nature of the cutting process. As a technique it can be applied over many size and power scales and this section will address one of the simplest examples of this procedure; the application of a sharp edge to a material. This section is not intended to be a comprehensive study of the cutting process, but will instead focus on the use of this method in cutting ice at low temperatures with relatively low power loads. Background information on the principles at work has been gathered from the broader field of industrial machining with edged tools, with particular reference to the works of Shaw (1984) and Trent (1977). No mention will be made of the physics of surface wear under reduced pressures. Phenomena, such as the loss of lubricating oxide-films on metal tools and other metallurgical effects of vacuum exposure are well-described in the aerospace literature (Dunn, 1997).

By concentrating only on the removal of material by the shearing action of a sharp edge, a relatively simple geometry can be constructed that captures the salient forces. In the following diagram a sharp-edged tool of width w is made to move over a flat and homogeneous material in such a way that the blade penetrates the worked substance to a depth t_1.

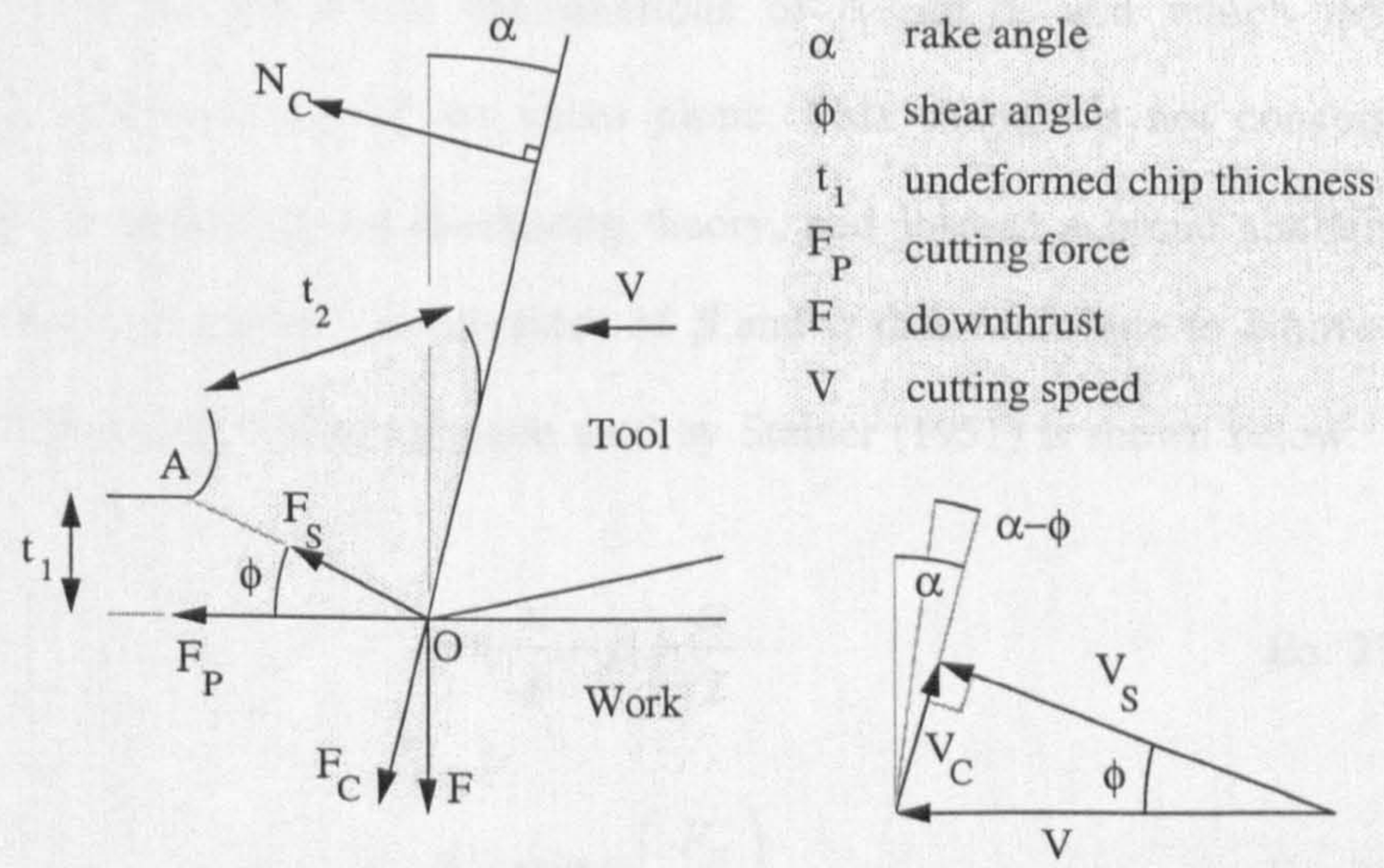

Figure 19 – Illustrating the general arrangement of an edged tool and a worked material.

Establishing the strength displayed by materials in the cutting process is a natural first step in the design of a drilling system. The following analysis is adapted from that of the physicist Väinö Piispanen as elucidated by Shaw (1984). Firstly, the material is presumed to be plastic, and so the tool can remove material continuously from the workpiece. This debris may take the form of small chips or a continuous ribbon of material. The cut material initially piles-up ahead of the tool, and if its bulk density is not changed then conservation of mass dictates that $V_C \leq V$. From the two applied forces F and F_P a number of other forces can now be constructed.

$$F_C = F_P \sin\alpha + F\cos\alpha \qquad \text{Eq. 20}$$

$$F_S = F_P \cos\alpha - F\sin\phi \qquad \text{Eq. 21}$$

$$N_C = F_P \cos\alpha - F\sin\alpha \qquad \text{Eq. 22}$$

Unfortunately, even if a pair of orthogonal forces is measured, such as the cutting force, F_P, and the downthrust, F, the energy needed to overcome the failure strength through cutting is still undefined, as the shear plane angle, ϕ, is not known. It is this quantity that dictates the length of the shear plane (OA) and hence determines the amount of material that is made to fail by the applied forces. However, dimensional analysis dictates that this unknown quantity must be some function of the other angular measures in the system namely the rake angle α and the parameter β, which is often referred to as the friction angle. While the rake angle is a very visible quantity, β is best thought of as a measure of how well the chip attaches to the tool's upper face. Many formulations for ϕ have been developed, Shaw describes a handful of variants, all of which are linear combinations of α and β, and which make different assumptions about the nature of the shear plane. This chapter is not concerned with the smallest details of metallurgy or machining theory, and instead a broad similarity is sought among the models. In general the functions of β and α that contribute to ϕ have multiplying coefficients of order unity and an example used by Stabler (1951) is shown below.

$$\phi = \frac{\pi}{4} - \beta + \frac{\alpha}{2} \qquad \text{Eq. 23}$$

where

$$\beta = \arctan\left(\frac{F_C}{N_C}\right) \qquad \text{Eq. 24}$$

The angle β is a measure of the sliding friction that the deformed chip experiences as it passes over the cutting head; a value of zero for β would represent frictionless sliding of the chipped material. If the rake angle is small then the above model reduces to $\phi = 45°$, which is expected from classical uniaxial compression tests of brittle materials.

Note that the speed, V_C, at which the material crosses the tool head is never greater than V, and can be calculated by considering the ratio of the chip thickness, t_2, to the depth of the undeformed material, t_1. By assuming that the substance's density does not change in the cutting process, the ratio $t_2 : t_1$ must be identical to $V : V_C$ for mass to be conserved.

$$\frac{V_C}{V} = \frac{\sin\phi}{\cos(\phi - \alpha)} \qquad \text{Eq. 25}$$

Equation 25 fully describes the motion of the chip relative to the tool. It is also necessary to calculate the speed of the chip with respect to the shear zone from which it is produced.

$$\frac{V_S}{V} = \frac{\cos\alpha}{\cos(\phi - \alpha)} \qquad \text{Eq. 26}$$

With the dynamics of the process fully identified it is now possible to list the two energy sinks present. There is the energy dissipated per unit volume of cut material by the friction of the chip pressing against the tool (u_F), and the energy needed to remove a unit volume of material (u_s). These quantities, which have identical dimensions of pressure or, identically, energies per unit volume, can now be calculated.

$$u_F = \frac{F_C V_C}{V w t_1} \qquad \text{Eq. 27}$$

$$u_S = \frac{F_S V_S}{V w t_1} \qquad \text{Eq. 28}$$

These two strength-like terms are not the only routes by which work is dissipated. Other sinks of energy are present such as the energy required to form a new face (between the chip lower surface and the work material), and the energy used in accelerating the chip upwards from the bulk of the cut substance. These last two paths for the expended energy are negligible in comparison to the energy used to overcome the shearing and friction forces (Trent, 1977)

and the majority of the work expended is dissipated as heat through the routes described by equations 27 and 28. A further simplification can arise if, at the imposed rate of strain, the material does not fail through plastic deformation. Brittle failure will lead to the chipped debris being ejected from the cutting site and away from intimate contact with the tool's upper face. In this situation there may be negligible contact between the tooth and the machined waste and little work will be expended through frictional losses. Although the cutting debris will have been shattered rather than stretched in its passage through the region of maximum shear, work will still be dissipated ahead of the tool and equation 28 alone may be used to model the specific cutting energy of the worked material.

All of these specific cutting energies referred to are dimensionally equivalent to a strength and u may be equivalently described as the cutting strength (or specific volumetric energy) for the materials discussed and experimented upon in later chapters. This quantity is often referred to in machining theory by the symbols σ_d, but for clarity the letter u will be used so that the term will not be confused with another common geophysical quantity, the deviatoric stress.

The above model for a cutting process applies to a single tooth of arbitrary width. One may then use such a model for an annular coring tool if the width of its teeth is small compared to the overall radius of the tool to meet the condition of uniform motion of the cutting edges. In practice, the downforce F is known by measuring the load applied by the tool normal to the surface, and F_P is found by recording the total torque τ needed to rotate the tool. If a coring head has an annular leading face composed of n teeth, then during the cutting process each tooth contributes a fraction, $1/n$, of the total torque needed to rotate the head. Equally, each of the teeth is loaded vertically with a force of F/n. To a first approximation there should be no variation in the cutting *rate* through increasing or reducing the number of cutting edges. An annular tool with a small number of teeth will result in large forces and deep cuts, but conversely, if the tool has many cutting teeth then each revolution results in many more commensurately shallower cuts. While a larger number of teeth will give some back-up cutting ability if any teeth break, a disadvantage in having multiple cutting faces from the point of view of the energy consumed is that for the same overall vertical force each tooth is loaded by a proportionately smaller force. This results in a shallower cut and a thinner chip. In the extreme case of a very large number of teeth, the tool slices away molecule-thick slivers of

material and although the tool may be made to progress at the same vertical rate, the energy needed to remove a unit volume of material will be essentially that substance's sublimation energy.

In the following sections attention will be given to a specific tool which takes the form of an annular array of cutting teeth that is rotated such that each tooth engages with the workpiece. The torque required to rotate the device should arise purely from the product of F_P and the effective radius r_{eff} of the tool which, for a sufficiently broad tool, can be approximated by the mean of the outer and inner tool radii. Other projects such as that reported by Marchesi *et al.* (2001) on the action of an annular ice coring tool have used the following analytical model. If a tool is driven at a vertical rate, d (m s^{-1}), then the torque, τ (Nm), needed to rotate the tool at a speed of ω (rev. s^{-1}) is given by

$$\tau = \frac{r_{eff}^2 \, du}{8\omega} \qquad \text{Eq. 29}$$

From a record of the vertical motion of the tool the undeformed feed thickness t_1 faced by each tooth of a coring head may be known since

$$t_1 = \frac{d}{n\omega} \qquad \text{Eq. 30}$$

All of the parameters needed to calculate the specific cutting energy u for a coring process can therefore be found by monitoring the four parameters of the coring process; the rotation and depth rates, and the applied downforce and torque values.

2.3 Dynamics of cutting ice-rich materials

Existing practical technologies for forming holes in thick ice layers rarely seek to minimize the energy consumed per unit depth of progress. Within reasonable limits, human effort and diesel fuel can be supplied without end even in polar conditions, and this has allowed energy intensive techniques such as the eponymous 'Philberth' probe to be developed. This device, designed by Karl Philberth for exploring polar ice caps, is an electrically heated probe which melts its way through the ice beneath it. It is worth stating that ice's heat of fusion of 334 kJ kg^{-1} is comfortably higher than that of several metals and only the easy availability of

electrical power has made this drilling method practicable. Related to the Philberth probe are those drilling systems that use heated working fluids such as pressurized steam, as detailed by Heucke (1999), and even antifreeze liquids, as examined by Zagorodnov *et al.* (1998).

A common goal of these terrestrial systems has been the recovery of near-continuous unfractured ice cores. From these cores, air trapped within the ice can be extracted and examined, with the air being held either in the form of a gas hydrate or as discrete bubbles. The poor thermal conductivity and high specific heat of solid water ice allows these records of Earth's atmospheric history to be largely unaffected by the often vigorous chemical and thermal attack that the core's exterior can face. When the cores are not made of an impervious material, a connected network of voids can exist which allows the transport of gases and liquids. Therefore, devices such as slow-moving augers and 'dry' (unlubricated) mechanical cutting heads tend to be used in coring studies of moderately packed snows and soils. This last method, mechanical coring, is of particular interest for landed spacecraft platforms although Philberth-like probes have been considered for missions to ice-rich satellites in which craft are presumed to use the fixed power but effectively unlimited energy available from radiothermal generators (Di Pippo *et al.*, 1999).

2.3.1 Previous experiments

To uncover the rules-of-thumb used by other polar investigators, and to discuss the statement[2] that, "There is no practical theory for design of ice drill cutters." the author visited the British Antarctic Survey (BAS) of Cambridge (England) to meet with Prof. R. Mulvaney. For recent expeditions mounted by the BAS, Prof. Mulvaney has been responsible for estimating the power usage of drill systems designed to bore polar ice and heavily compacted snow. The types of drill heads commonly used by the BAS and many other teams consist of unheated mechanical drill heads that carry an annular array of chisel-like cutting teeth. The general arrangement of this type of tool is shown in Figure 20 which is of a cutting head from the Norwegian Geotechnical Institute.

---

2 Vasiliev and Talalay (1994)

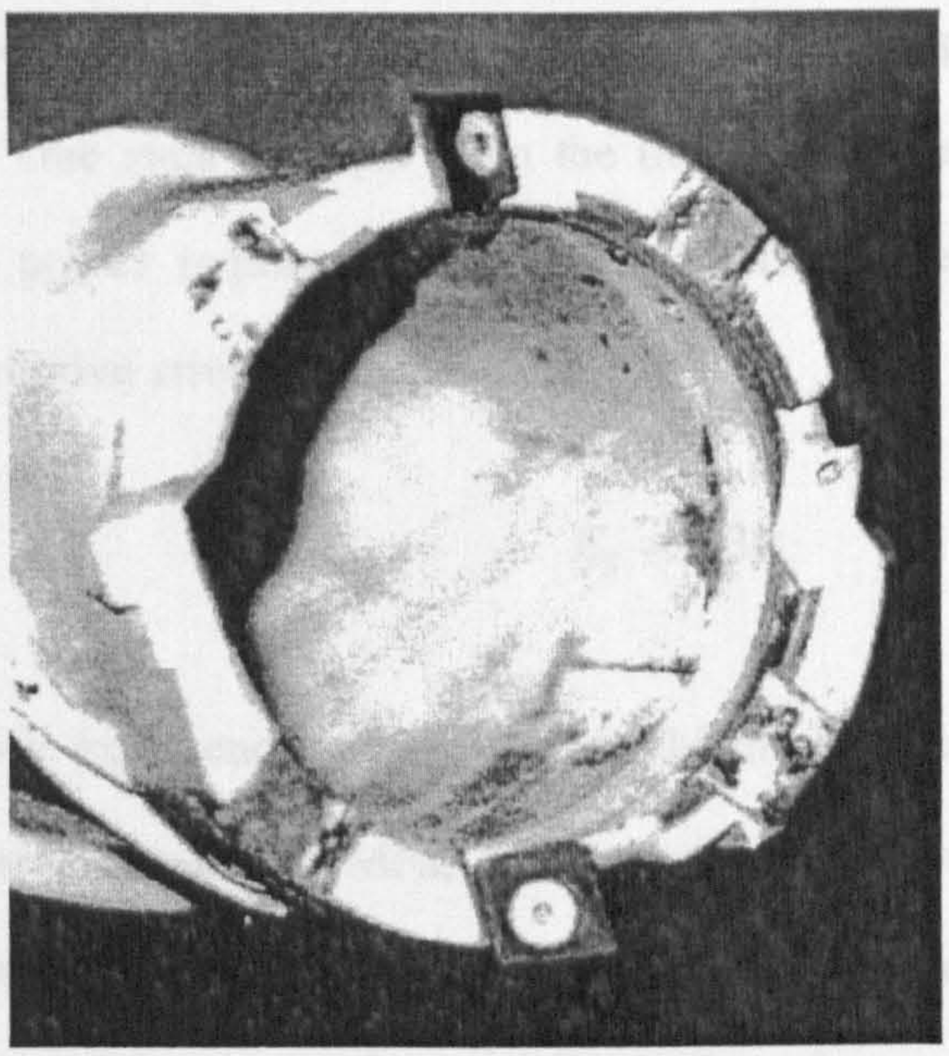

Figure 20 – An ice coring head with two removable chisel-bit cutters (the black angular inserts at 11 o'clock and 5 o'clock on the tool face in this picture)

The tool head shown in Figure 20 is generally supported inside a cylindrical casing and powered at depth by attaching lengths of drive shaft to the rear of the tool head. Debris is lifted from the work face by a narrow helical ledge, called the flight, fixed to the outside of the coring head's rotating stem. The tools commonly used by the BAS and other teams have outer diameters of between 10 cm and 15 cm. Power requirements for these coring systems are routinely estimated by a relationship that was originally provided by Suzuki and Shiraishi (1982) to analyse the progress of the Japanese Antarctic Research expeditions' coring tools. This model relates the power requirement Q, for a coring tool of cross-sectional area A, cutting at a vertical speed d, as simply;

$$Q = AE_s d \qquad \text{Eq. 31}$$

The parameter E_s is described as being related to the drilling 'efficiency' rather than as an intrinsic measure of the ice's resistance to deformation, although it has dimensions of energy per unit volume and as such is dimensionally equivalent to the specific cutting energy u_s considered a little earlier. Such an unsophisticated model assumes that the work expended by deformation per unit time is independent of the parameters associated with the act of drilling, such as the rotation speed, the vertical load, or the depth of cut t_1. Numerical relationships between the energy expended in cutting water ice and some more objective measure of a

material's strength are not common and will similarly depend in some way on the method of drilling used. One such example from the literature is that of Walsh (1999) which is used to calculate the power requirement for an Antarctic tunnelling machine from the compacted snow's compressive strength as

$$E_S = 0.3\sigma_c \qquad \text{Eq. 32}$$

From their experience in the field Suzuki and Shiraishi (1982) suggest that E_S may range in value between 1 and 10 MPa, and vary with the density of the material being cut; for compacted snow having a density of 850 to 870 kg m^{-3} a value of around 5 MPa is reported for E_S. Fully solid ice, having a 10% higher density, might be expected to display a proportionately higher resistance to coring at similar temperatures[3]. These simple models for the variation in the specific cutting energy, E_S, should be considered with the data from Figure 17 for the compressive strength of warm water ice which, at high rates of strain, is generally a little larger than 10 MPa.

There are few published examples of the models used by polar drilling teams to calculate the energy requirements of drilling through ice, and little information about the optimal design of tool heads. It is not obvious from the preceding section on machining models that ice, which is weaker and more brittle than any metal, also needs specific tool shapes for it to be cut rapidly. This was seen by Vasiliev and Talalay (1994) who measured the forces involved in coring ice at temperatures of –20°C in the Vavilov glacier (79°N 95°E) with various cutting head shapes. A cutting head having teeth with a rake angle, α, of 15° appeared to be an optimum geometry – giving the lowest torque for a given penetration rate, and the smallest power usage over almost the whole vertical speed range (of 1 to 4 m $hour^{-1}$) in their tests. Larger rake angles were progressively worse in their performance, as were tools with $\alpha \rightarrow 0°$. Figure 21, from Vasiliev and Talaly (1994) shows these changes.

---

[3] Which are not reported by Suzuki and Shiraishi, but the ice is unlikely to have been colder than -40°C.

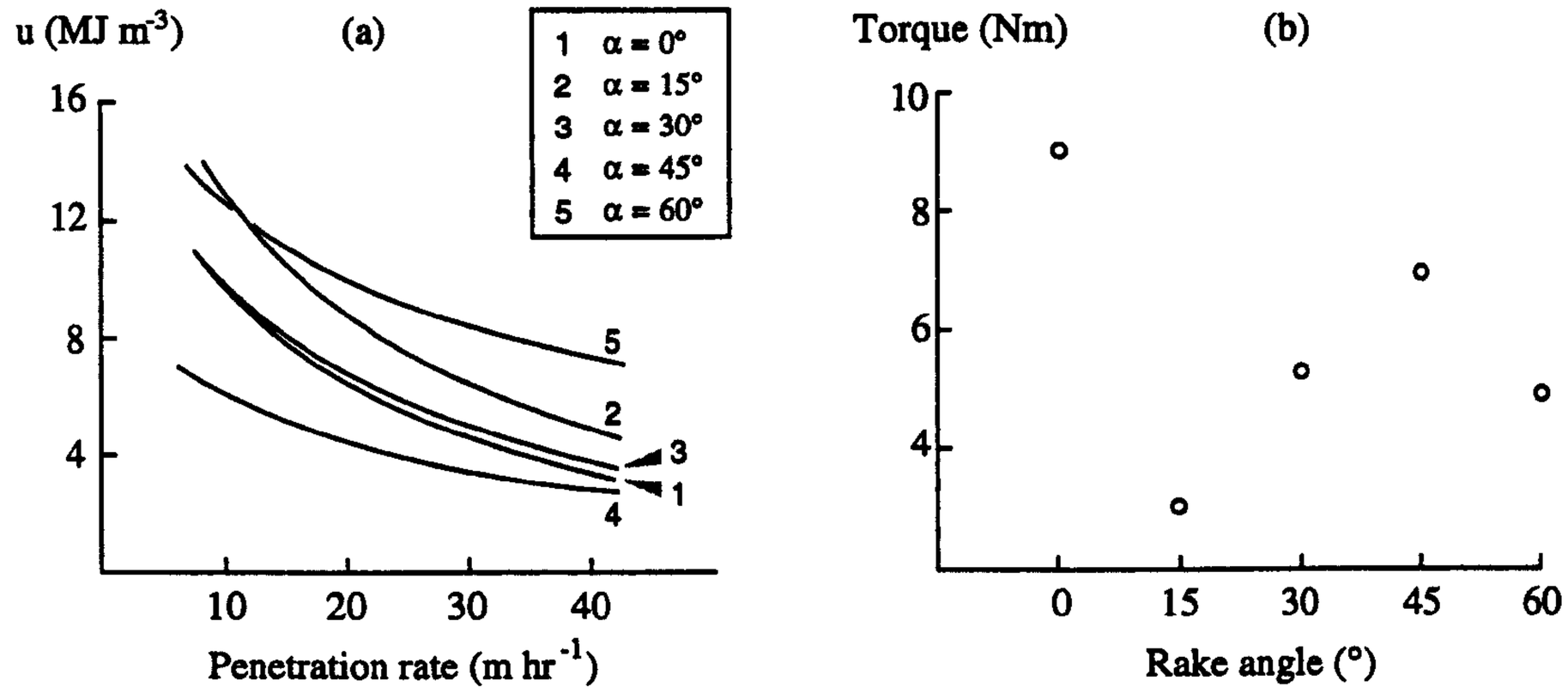

Figures 21a/b – Results from Vasiliev and Talalay (1994) which suggests that the optimal rake angle for coring heads cutting water ice is small, and close to 15°.

In Figure 21a the specific cutting energy clearly varies with the vertical penetration rate, as was expected earlier. Tools with smaller rake angles appear to penetrate the material more rapidly. However, it is difficult to state whether there is a trend in the data shown in Figure 21b - if the data are accurate, and no mention in the source paper is made of the precision with which the coring parameters are known, then a tooth rake angle of 15° is noteworthy.

To complement this sparse data set a similar set of experiments was conducted by Narita *et al.* (1994) using a laboratory-based coring head that could be driven at a specified rate into deliberately cooled ice samples in the presence of a pressurized confining silicone liquid. Their work also showed that smaller rake angles lead to higher penetration rates, with the large rake angle of 50° leading to a situation in which "the drill could not penetrate" (Narita *et al.* 1994). The smallest rake angle tested by Narita *et al.* (1994) was 17°, and so it is not possible to comment on whether smaller rake angles would show a fall in the cutting efficiency. Along with changes in rake angle, the work of Narita *et al.* (1994) examined the effect of the ice's temperature on the drilling rate. In Figure 22 the downforce is presented as a loading mass per unit length of the cutting edge, a value of 100 kg m^{-1} would for example correspond to a force of ~0.98 N for a cutter of width 1 mm.

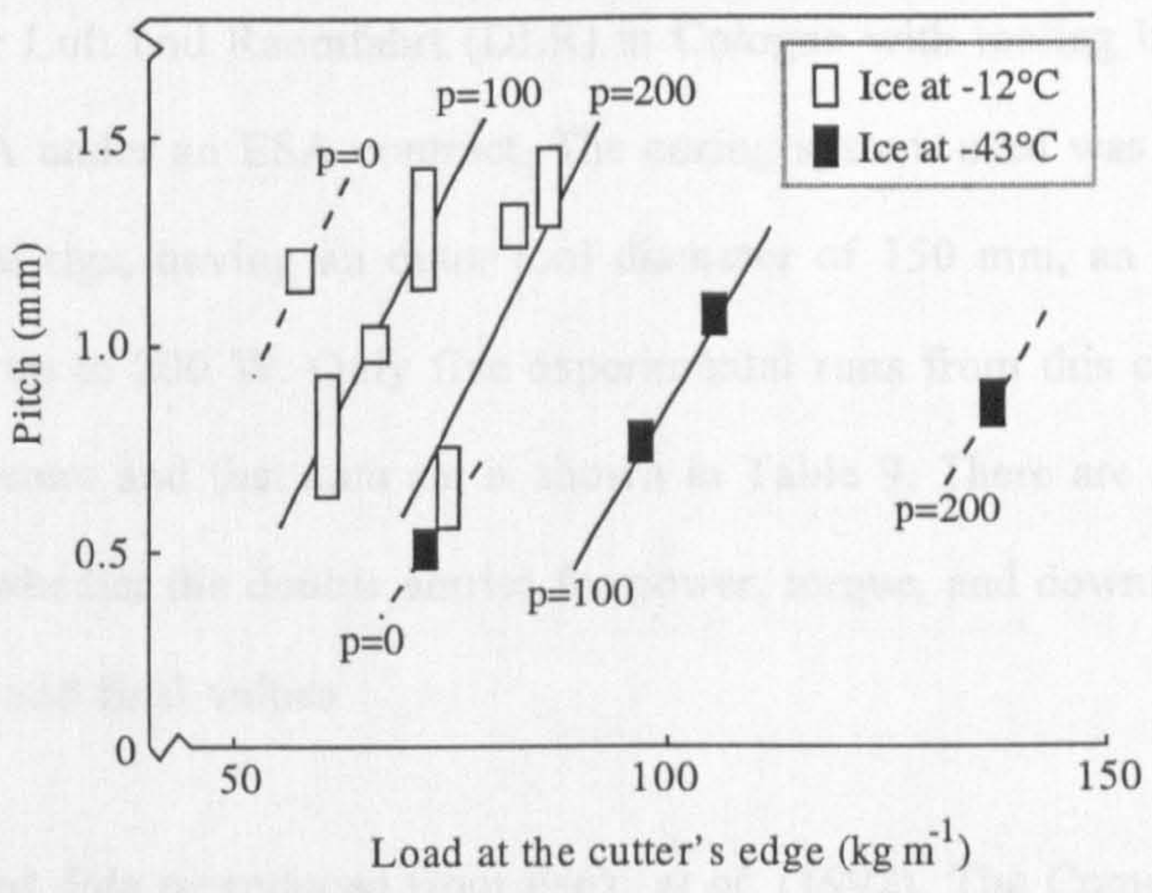

Figure 22 – The data of Narita *et al.* (1994) for coring ice at various pressures and temperatures. The two temperatures examined are distinguished by the use of empty or solid boxes and the pressure of the confining fluid in units of MPa is marked at the end of each trend. The pitch is the vertical distance between successive passes of a rotary cutting tool.

Two conclusions can be drawn from Figure 22, that drilling either under lower temperatures or at higher confining pressures requires a larger applied vertical load. The dependence on pressure will not be remarked upon further as all of the experiments conducted in the later chapters of this thesis are performed with a vanishingly small confining pressure in comparison to those used in the above work. What is relevant is that irrespective of the confining pressure, for a given penetration rate a tool coring though ice needs almost twice the downforce at -43°C than is needed at -12°C. This trend is consistent with the variation of ice's compressive strength with temperature shown in Figure 16.

A conclusion that can be drawn from both of these independent studies, one from a laboratory and one from the field, is that coring tools with small rake angles for their teeth are more efficient at cutting brittle materials such as ice than tools with large rake angles. Curiously, this demonstrably efficient tooth geometry is not commonly used, and bits having rake angles of 35° and higher are reported in the literature (Suzuki and Shiraishi, 1982) and have been seen by the author at the BAS.

All of these reported experiments have been performed under ambient atmospheric pressures and are not wholly appropriate for understanding the behaviour of a cutting tool exposed to cryogenic materials at a very low ambient pressure. Only one study in this area has, to the knowledge of the author, been carried out prior to the work described in this thesis. To support the *Rosetta* project a set of experiments were performed in the early 1990s at the

Deutschen Zentrum für Luft und Raumfahrt (DLR) in Cologne with tooling built by the Italian firm Tecnospazio S.p.A under an ESA contract. The coring system used was similar in its size and power to terrestrial rigs, having an outer tool diameter of 150 mm, an inner diameter of 100 mm, and drawing up to 200 W. Only five experimental runs from this contract have been found in the open literature and that data set is shown in Table 9. There are ambiguities in the table as it is not clear whether the double entries for power, torque, and downthrust describe the data range or its initial and final values.

Table 9: The reported data reproduced from Fenzi *et al.* (1992). The Cometary Analogue Material (CAM) samples used were all identically formed from an aqueous suspension of olivine dust sprayed into liquid nitrogen. The 'tuff' sample being a compacted volcanic ash.

Sample material	CAM#1	CAM#2	CAM#3	Ice	Tuff
Sample temperature (°C)	-190	-190	-190	-170	-180
Depth traversed (mm)	380	417	420	501	490
Penetration rate (mm s^{-1})	6.33	6.95	2.23	0.5	0.026
Downthrust (N)	50	50	20	60 / 100	60 / 350
Torque (Nm)	4	5	1.5	5 / 10	3 / 26
Rotation rate (rpm)	150	100	100	150	130 / 150
Average power (W)	63	52	17	80	100 / 400
Average specific energy (MPa)	1	1	1	40	1250

These results are of interest primarily because of what they do *not* show. No indication is given that a range of temperatures were used, and only the rate at which the tool head is driven vertically is shown to vary significantly among the experiments. Without a record of the density of the CAM samples it is impossible to try and recreate the results shown for this substance, and the single reported test of water ice (of unknown constitution, presumably bubble-free and formed from the degassed liquid) does not allow any information about drilling efficiency with temperature, or drilling speed, or rotation rate to be gathered.

This section has emphasized the effort that must be applied to remove material from a material with a tool, without concern for the heating of the tool, the surrounding material, or the cutting debris. The next sub-section addresses the conversion of the applied work to heat, and the subsequent temperature rise around the cutting tool.

2.4 Thermodynamics of cutting

The development of consistent and accurate models for the heat evolved during cutting and drilling has been a long-held goal in mechanical engineering. From Benjamin Thompson's studies in the 1790s of the thermodynamics of boring cannon barrels, as described by Angrist and Hepler (1973), to the use of computerized finite-element analysis, attempts have been made to describe the temperature rise around a moving cutting edge. The need to model the heating process has been driven by the need to understand and avoid the unwanted metallurgical changes to tool and workpiece metals at raised temperatures, such as oxidation and hardening. In comparison to the well-characterized and often unidirectional stresses commonly used in material testing, the area ahead of a cutting tool experiences compression and shear, frequently in a complicated geometry. As the interest in this work on the cutting process is purely one of establishing approximate figures for the machining strengths of cold substances, only one type of model has been fully explored for its application to drilling planetary and cometary ices.

In common with manufacturing industry's need to minimize the cutting temperature and maximize the quantity of material removed for a given amount of work, a similar goal drives the need for analysis of a non-terrestrial planetary drilling system. Despite the smaller power levels available to current designs for lander-based coring tools, the sources of heat from a cutting tooth are the same as those encountered in industrial machining. There are generally two sources of heating present in the cutting process. The first arises in the shear zone that lies ahead of the tool edge. In this region the material is being heavily deformed and a sliver of material is removed from the bulk of the substance being worked. When a sufficiently competent material is being cut, this debris often takes the form of a chip, the thickness of which plays an important role in the degree of work exerted by the tool. This sliver of material may then be forced up against the cutting tool by its relative motion and heat can be generated by friction in the area of contact between the chip and the tool face. In trying to estimate the heat generated in cutting, the thermal properties of the material must be known along with the amount of work being expended in physically altering the workpiece. A necessary assumption is that most of the mechanical work expended by the cutting tool is converted into heat although some fraction of the applied power is used to accelerate the cutting debris but this can be shown to be a negligible amount by estimating the gain in kinetic

energy of the debris. These and other sinks of applied energy are discussed and dismissed by Sgubini and Buratti (1989) in their treatment of coring which will be used in the experiments in later chapters.

The problem of modelling the temperature shifts in a material during a cutting process is a complex one and has been tackled from a number of directions. The first and simplest approaches used dimensional analysis. The pertinent machining parameters can be combined in a unique way to yield a quantity that has the dimensions of temperature. This approach is over fifty years old and was first examined in detail by Kronenberg (1949), but despite its simplicity it is still a fruitful method as it predicts how a temperature rise varies with the material's properties and the cutting dynamics. In a medium of thermal conductivity λ, and specific heat capacity c, a process that dissipates heat through deformation at some speed V generates a temperature rise, ΔT, that can be expressed in a unique combination of these factors:

$$\Delta T \propto u\sqrt{\frac{Vl}{\lambda \rho c}} \qquad \text{Eq. 33}$$

In this model, l is a length that is characteristic of the distance over which the heat is dissipated and u is the specific cutting energy of the substance; the energy required to remove a unit volume of material from the bulk of the workpiece by some process of deformation. From the earlier definition of u, the above model for the nominal temperature rise can be re-written for the two physically separated regions in which heat can be generated; the shear zone OA in Figure 19, and the portion of the tool face that experiences frictional heating from contact with the cutting chips. For the shear zone heating, the quantity l_S is simply the length of the shear zone, $(t_1 / sin\phi)$ and the characteristic speed for this mode of heat dissipation is V_S.

$$\Delta T_S \propto u_S\sqrt{\frac{V_S l_S}{\lambda \rho c}} \qquad \text{Eq. 34}$$

By considering the speed at which the chip encounters the tool, and the length over which the chip is in contact with the cutting face, a similar prediction can be made for the temperature rise that may occur at the chip / tool boundary. However, it has been argued earlier that debris from a brittle material may not make contact with the moving tool and this form of heating is expected to be negligible. Debris may subsequently jam other parts of a

coring tool, but this problem is too complicated to be addressed as it depends on the ease with which cuttings can be lifted from the workface and this will vary with the local atmospheric density and gravity.

The general form of the above equations allows an estimate to be made for how the temperature rise caused by a heating source changes with different operating characteristics or material properties. The results shown in Figures 14 and 15 show a ten-fold difference between the values of λc for water ice and solid carbon dioxide. If the respective densities[4] of the two ices at cryogenic temperatures are included with the displayed difference in λc then equation 33 can be used to calculate the temperature rises seen in these ices for a *constant* specific cutting energy. In this constant-power condition, a tool bit cutting water ice would cause only ~35 % of the temperature rise that would be seen for the same tool cutting carbon dioxide ice. The difference between the two ice's specific cutting energy and its effect on the peak temperatures seen in cutting will be calculated later.

Instead of this simple dimensional relationship more rigorous models can be used to calculate the temperature field around a cutting tool. Such an analytic model has been developed jointly by Rome University and Space Systems Studies of Rome for the *Rosetta* cometary mission. This model was first developed and applied by Sgubini and Buratti (1989) to the problem of heating during a coring operation, with obvious application to the sampling tool of the *Rosetta* comet lander spacecraft. After the development of this model no reports on heat generation by spacecraft sampling tools appear to have been published in the open literature. Only one paper (Eiden and Coste, 1991) has been found that mentions this process but unfortunately the single figure[5] given for the temperature rise in ice, as measured in some unspecified manner, is not accompanied with a clear description of the drilling speed, downforce, rotation rate, or tool geometry.

The analysis of Sgubini and Buratti (1989), referred to as SB89, modelled a hollow cylindrically symmetric coring tool as an unvarying annular heat source of power Q that is applied to a semi-infinite block having a thermal capacity of c, a density ρ, and a thermal conductivity λ. The physical basis of these models, and code for their implementations are

---

[4] ρ = 1590 kg m^{-3} for CO_2 (Thorpe and Whitely, 1966) and ~950 kg m^{-3} for water ice.
[5] "Temperature rises ... 1.5 °C in ice..." for cutting rates of *perhaps* 0.1 mm s^{-1}, cutter loads of 20 Nm^{-1}, and rotation speeds of no more than 2 rev s^{-1}.

given in Appendix B. For a tool having an outer radius of r_{out}, and a wall thickness w progressing through a target material at a vertical rate of d, the temperature shift experienced ahead of the annular heating region may be described as a function of distance from the central axis. In this general description of the temperature field, $T(r)$, there are two regions of interest that were treated separately by SB89; the temperature rise at the axis (r=0) of the cylindrical heating annulus, and the temperature rise at the edge of the annular cutting head ($r=r_{eff}$).

On the axis;

$$\Delta T(r=0)=\frac{Q}{4\pi r_{out}\lambda\sqrt{a^2+1}}\exp\left(-2a\left[\sqrt{a^2+1}-a\right]\right) \quad \text{Eq. 35}$$

where

$$a=\frac{c\rho d\, r_{out}}{4\lambda} \quad \text{Eq. 36}$$

and

$$\Delta T(r=r_{eff})=\frac{Q}{16\pi\lambda a' r'}\left(1-\exp[-4a']\right) \quad \text{Eq. 37}$$

Primed variables refer to a disc that has the same area A as the annular face of the coring tool. The radius of this equivalent disc is

$$r'=\sqrt{{r_{out}}^2-\left[r_{out}-w\right]^2} \quad \text{Eq. 38}$$

and so

$$a'=\frac{c\rho d\, r'}{4\lambda} \quad \text{Eq. 39}$$

The total heating power Q is found by first recalling that cutting processes convert mechanical energy into heat with near perfect efficiency. Thus, the power applied around the rim of the cutting tool cannot be greater than the sum total of the mechanical work expended by each of the n teeth. As mentioned in section 2.2, the strength encountered in cutting a workpiece is equivalent to an amount of work, or heat, expended per unit volume and so the power dissipated by a tool is the rate at which a volume displaying a given strength can be cut. In the absence of frictional losses the power drawn from the drill motor is wholly converted into heat around the cutting head, and the parameter Q in the earlier equations is given by

$$Q=Aud \quad \text{Eq. 40}$$

The quantity A is the area of the annular cutting region of the tool and no further information is needed to represent the gross temperature field around an annular coring tool. To summarize this intermediate point, the specific cutting energy u is calculated by equation 28 from the measured forces and rates[6] of the coring tool and with that figure the geometry and thermal properties of the worked material then determine the temperature field around the head which is modelled by equations 35 and 37.

So far the rotation speed of the cutting head has not been introduced and the models for temperature rise consider only the work needed to disrupt the annular region ahead of the tool. No further refinement of the model was made by SB89 to represent the tool as a rotating set of discrete heat sources. By neglecting this aspect of coring, the relative speed with which the hypothetical annular non-rotating head encounters the workpiece is simply the vertical depth rate. As was seen from dimensional analysis (equation 33) the relative speed of the cutting tool to the undeformed material plays a role in determining the temperature rise. In assuming that this relative speed is given purely by the slow vertical progression of the tool into the work, the more localized heating developed by the rapid horizontal motion of the rotating teeth is ignored. This topic will now be explored in more detail. In the reference frame of the undisturbed medium, a coring tool can be thought of as a circular arrangement of heat sources which pass through the sample and which generate two different temperature fields at some point in the material. The first temperature field is associated with the long-term delivery of heat from all of the cutting edges. This can be described as the background temperature field generated by the tool as a whole which can be modelled using the equations of SB89. The second temperature field consists of a cyclic temperature variation having the same period as the motion of the heating source and is the local temperature field associated with each tooth. This will be referred to as the 'flash' temperature shift. To calculate this temperature gradient the heat liberated from each tooth must be estimated by considering the tool as being made from n elemental quadrilateral heat sources of dimensions w by $(t_1/\sin\phi)$. The heat liberated, Q_n, from each elemental patch is

$$Q_n = \frac{Q \sin\phi}{n w t_1} \qquad \text{Eq. 41}$$

---

6 The downforce and torque applied for a measured rotation speed and vertical speed.

The rate at which heat is conducted into the material around the sheared region can be treated by considering each patch as moving in a circular path on the surface of an infinite half-space. Whether this localized temperature rise is significant or not depends on the size of the region in which the temperature is affected by the heat load from individual teeth. If the tool is allowed to rotate at an increasing speed then the resulting depth of influence shrinks and the tool becomes increasingly well modelled by a uniform annular source of heat. In such a case the equations of SB89 need no further adjustment. If numerical factors are ignored, then such a 'heating-depth' scale length, δ, can be made from a characteristic time and the thermal diffusivity of a material, the derivation being identical to that outlined in appendix E for the earlier problem of solar heating.

$$\delta = \sqrt{t\kappa} \qquad \text{Eq. 42}$$

Let t be the time between successive passes of the teeth in this notional coring head which rotates every $1/\omega$ seconds. For a head having n teeth, the depth affected by the 'flash' heating of the cutting teeth is then;

$$\delta = \sqrt{\frac{\kappa}{n\omega}} \qquad \text{Eq. 43}$$

To illustrate the spatial extent of this heating, δ is calculated for a few dense materials in Table 10 and it should be remembered that δ is simply a measure of how far the heat from a cutting edge propagates before the following tooth passes through the same region.

Table 10: The depth of the 'flash' heating associated with the cutting edge of a coring tool.

Workpiece material	δ (ω=1 rev s^{-1})	δ (ω=10 rev s^{-1})	δ (ω=100 rev s^{-1})
Water ice at 260 K	0.5 mm	0.2 mm	50 μm
Water ice at 140 K	1 mm	0.3 mm	0.1 mm
Carbon dioxide ice at 140 K	0.2 mm	70 μm	24 μm
Brass (70:30 Cu:Zn) at STP	9 mm	3 mm	0.9 mm

The temperature rise produced in this depth by each tooth can be calculated by applying the method used by Tian and Kennedy (1995). In this model a shift in temperature ΔT_{flash}, is experienced at the surface of a sliding heat source which delivers a heat flux, q (W m^{-2}), to a plane-surfaced infinite half-space.

In such a situation the modelled temperature rise, ΔT_{flash}, which occurs in a region of depth δ may be approximated by

$$\Delta T_{flash} = \frac{ql}{\lambda\sqrt{\pi Pe}} \qquad \text{Eq. 44}$$

The two unfamiliar terms, l, and Pe, are respectively the length of the heat source's contact with the work material, and the Péclet number[7]. This local 'flash' heating temperature rise is superimposed on the general temperature rise produced by the dissipation of mechanical work from the tool head as a whole and with models for all of these temperature fields (equations 35, 37 and 44) this simplistic thermal analysis of a cutting tool is complete. To test these models it is useful to be able to measure the temperature distribution around working machine tools. A variety of techniques have been devised for use in industrial settings and two of these methods will be mentioned for their possible application to the practical drilling of cold ice-rich material.

a) Direct measurements

Where two junctions of dissimilar metals are placed in series with each other, the voltage difference across the circuit will be proportional to the junctions' temperature difference. By embedding a wire inside the material under investigation, and using the tool as the other half of the couple, the interface formed at the tool's cutting edge can act as the hot junction of a thermocouple. This technique has not changed appreciably since its development in the mid-1920s, and a typical experimental arrangement for this form of thermometry is described in Agapiou and Stephenson (1994). An obvious drawback of this method is the practical difficulty of embedding an insulated thermocouple wire in a material such that it causes no change to the machining or thermal properties of the work piece.

Another *in-situ* measurement method could rely on embedding small sacrificial thermometer elements in the worked material. As with the thermocouple method, this technique has the potential of perturbing the work piece's machining properties and has to

---

7 A dimensionless number, it can be defined by (speed x length / thermal diffusivity) and is a measure of the efficiency with which heat is transferred from a moving source.

rely on careful positioning of the sensors within the workpiece. This method has some merits if the workpiece can be formed *around* the thermometer elements, instead of having to drill out and backfill accurate channels in the material to accommodate the sensors.

b) Radiant pyrometry

The heat radiation emitted by a cutting tool may be directly observed with a suitable bolometer or pyrometer. By drilling a narrow viewing hole through the material to be cut, the drill bit under investigation may be fleetingly observed and its temperature measured as it passes the opening. An early description of this method is given by Chao *et al.* (1961) for rotary metal machining. With modern infra-red detectors, such as micro-bolometers or pyroelectric sensors, this method may be successfully applied to those situations where the cutting tool can be directly viewed.

Other, more exotic techniques, have been considered for particular material and tool combinations with varying degrees of utility. Dyes and paints can be synthesized that display an abrupt change in their optical absorption characteristics - giving rise to colour changes at certain temperatures. However, such thermochromic chemicals tend to operate at relatively high temperatures to permit the chemical reactions to occur with a useful speed. The coldest temperature at which commercially available chemicals operate is around 270 K and they can exhibit a hysteresis-like thermal 'memory' that lowers their accuracy in detecting small temperature changes. A further drawback of such chemical reactants is that they generally are sensitive to shifts of a few degrees or so, and are modified with a second agent to move their range of sensitivity to the temperature window of interest. Thus, they generate only one bit of information: that the local material is hotter or colder than a pre-chosen temperature.

The preceding general discussion of temperature rises through coring is broadly applicable to the specific problem of cutting ice and other brittle materials. Those differences which do arise when cutting ice result from the poorly predictable fracture behaviour of flawed water ice - bubbles and existing cracks can act as stress-enhancing *foci* that allow cracks to grow rapidly. Other problems that can arise are peculiar to the coring of water ice, not least of which is the

melting of the worked material around the head, where, to quote from Suzuki and Shiraishi (1982), "There, the chips would become wet from frictional heat and apt to cling to the bits and bit-holder" (p 270). This problem can occur only on Earth, although one other large ice-rich body in the Solar System, Titan, has a high enough atmospheric pressure to allow heated surface ices to melt. Another common terrestrial drilling problem that may not be common in other settings is the clogging of a drill core with debris. The generally minuscule surface gravity found on asteroids and comets may speed the removal of such debris from the tool along the helical flight of the drill tube although the potential for adverse phenomena such as charge separation and subsequent debris adhesion in a hard vacuum has been raised (Mellor, 1989). Other differences will arise through the necessity of providing an anchoring system so that appropriate forces and torques can be applied to the coring head. Similar unquantified problems, such as the problems of autonomous core handling are outlined in Boucher and Dupuis (2000), and will require practical study if large-scale mining operations on extraterrestrial bodies are to run efficiently.

Having described the general problem of driving a coring tool into water ice, the specific coring apparatus of the *Rosetta* lander spacecraft will now be described.

2.5 The mechanisms of RoLand

The *RoLand* spacecraft is designed to perform a wide variety of tests of material at the surface of, and under, the landing site. Broader information about the nucleus' properties will be gained through a radio transmission experiment to assess the internal structure of 46P/Wirtanen, with the coma's behaviour and composition being measured by the orbiter spacecraft that delivers the lander to the surface. In the vicinity of the landing site two physico-mechanical experiment packages will be employed to evaluate a number of properties, the MUPUS (MUlti-PUrpose Sensor for surface and sub-surface science) package, and the Drill, Sample and Distribution tool (SD2) system. The MUPUS suite of instruments has been developed at Münster University (Germany) and it is intended to measure five physical properties of the near-surface material close to the landing site of the *RoLand* spacecraft. The largest part of this package consists of a number of sensors mounted within a thin rod that is driven into the comet's nucleus with an electromagnetic hammering device. This deployment method cannot be readily modelled by a continuous cutting or penetration model, and will not be discussed in this work.

2.5.1 Anchoring devices

To provide the *RoLand* spacecraft with a firm footing on the nucleus of 46P/Wirtanen, two separate types of anchoring devices are carried by the lander. The first of these is employed prior to touchdown and consists of a redundant pair of gas-ejected harpoons. Each harpoon, having a mass of around 100 grams, is equipped with a number of barbs that are designed to prevent the harpoon heads from being easily pulled out from the comet surface. The location of the harpoons, close to the centre of the lander's body, prevents the harpoon cable from exerting any restoring torque if the lander is unexpectedly twisted about its vertical axis. To counter such rotations and also to provide extra holdown force, a second anchoring system is built into the landing feet of the *RoLand*. Each footpad of the lander contains a narrow-diameter auger-style drill bit and drive motor, the design of which are given in Ebert *et al.* (2000).

2.5.2 The SD2

This subsystem, the Drill, Sample, and Distribution (SD2) equipment, is designed to collect material from depths of around 200 mm beneath the comet's surface, and to subsequently distribute portions of that retrieved matter to instruments of the *RoLand* spacecraft. In Figure 23, the lander's various anchoring tools are shown along with the SD2 drill, which is outlined in Camaschella (1998).

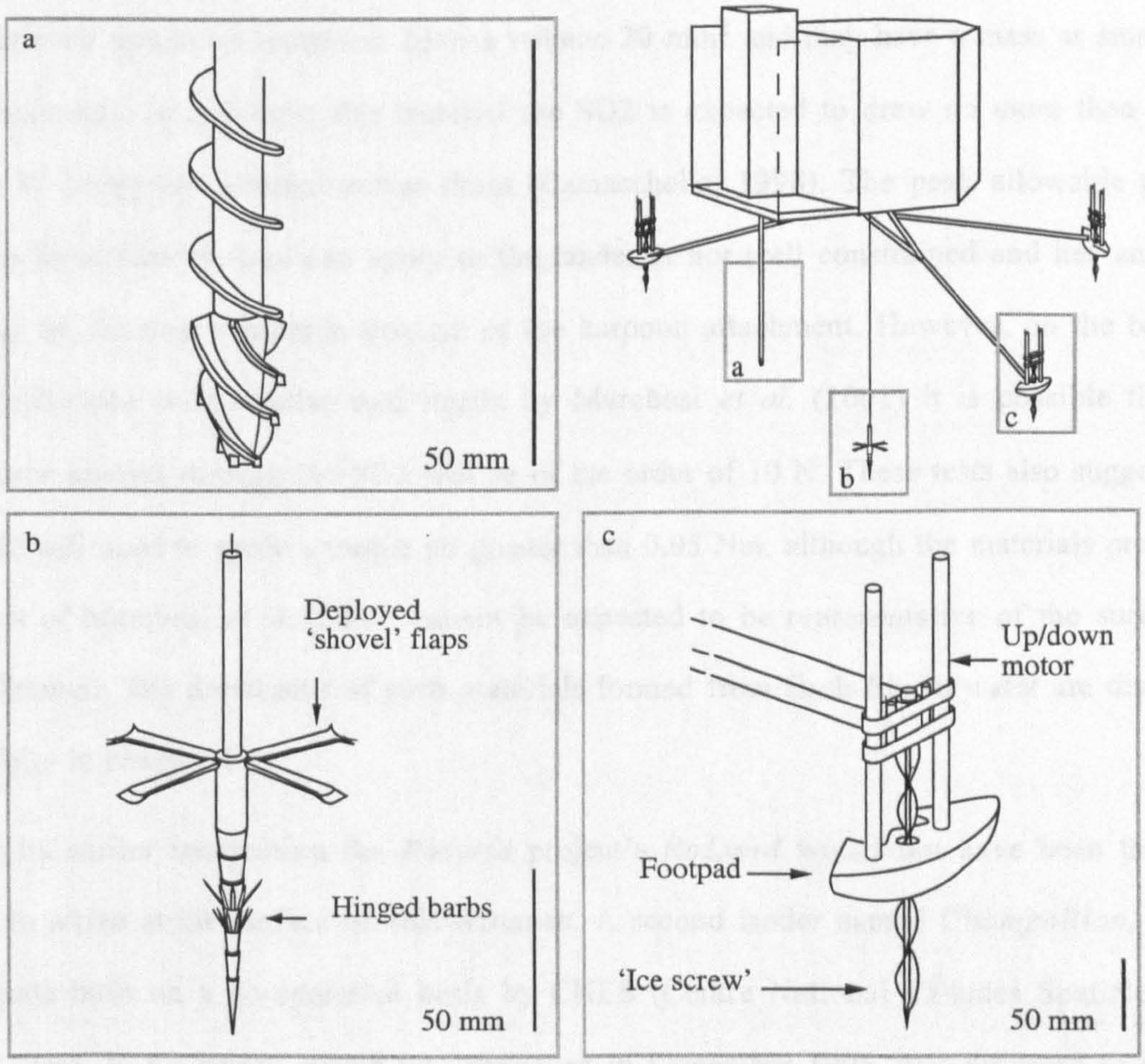

Figure 23 – The SD2 (a) and anchoring tools (b and c) of the *RoLand* spacecraft. The MUPUS experiment has not been drawn so as to show the SD2 more clearly.

The company contracted by ESA (Tecnospazio S.p.A.) to build the SD2 has proposed a number of classes for potential comet nucleus analogues: three uncohesive soil-like materials, a cohesive 'soil' and two brittle substances. Representative practical material examples for these classes are solid tuff, water ice, mixtures of dust and water ice, clathrate material, and 'fluffy stuff' – presumed to be a poorly cohered highly porous aggregate of small grains. Table 11, adapted from the SD2 specification (Camaschella, 1998), lists the absolute range of parameter values for the materials that are expected to be encountered by the SD2.

Table 11: Extreme values for parameters of comet surface analogues.

Characteristic	Minimum	Maximum
Bulk density (kg m^{-3})	200	3300
Compressive strength (Pa)	600	10^8
Porosity % (void fraction)	0	60

The SD2 is designed to first drill a hole roughly 25 cm deep in the cometary surface and to then remove a portion of the cutting debris with a separate sampling tool (Camascehlla, 1998). The retrieved sample is limited to have a volume 20 mm^3 and may have a mass as small as a few milligrams. In gathering this material the SD2 is expected to draw no more than 12 W, with 6 W being the nominal power drain (Camaschella, 1998). The peak allowable normal reaction force that the tool can apply to the lander is not well constrained and has an upper limit set by the unpredicatable strength of the harpoon attachment. However, on the basis of tests performed with similar tool heads by Marchesi *et al.* (2001) it is possible that the downforce applied through the SD2 will be of the order of 10 N. These tests also suggest that the SD2 will need to apply a torque no greater than 0.05 Nm, although the materials probed in the tests of Marchesi *et al.* (2001) cannot be expected to be representative of the surface of 46P/Wirtanen. The drawbacks of such materials formed from flash-frozen water are discussed more fully in chapter 4.

In its earlier incarnation the *Rosetta* project's *RoLand* would not have been the only lander to arrive at the surface of 46P/Wirtanen. A second lander named *Champollion*, was to have been built on a co-operative basis by CNES (Centre National d'Études Spatiales) and NASA. This 76 kg lander, which was cancelled in September 1996, was designed to carry a sampling tool which bore some resemblance to the current SD2 of *RoLand*, however, it would also have included several features that are lacking from the present sampler. The papers of Neugebauer and Bibring (1998) and Weissman (1997) describe the pre-cancellation design of the *Champollion* lander and its payload. It is notable that the SATM, (Sample Acquisition and Transfer Mechanism) apparatus used by *Champollion* to excavate material from the comet's surface was, according to Neugebauer and Bibring (1998), to have been equipped with force and torque sensors. By monitoring these sensors and other load transducers mounted on the footpads the instantaneous power delivered by the drill could be calculated. With these data the lander's onboard computer then could control the drilling process in order to avoid jamming

the drill bit and stalling the motor with potentially irreparable results. An obvious hazard in such a situation is that some part of the drive system or the drill bit may break, but for a spacecraft anchored with low degree of certainty in a microgravity field, there is also a real risk that an unexpectedly large reaction torque from the drill will dislodge the anchoring mechanism and remove the spacecraft from its site. Following the cancellation of *Champollion* as part of the *Rosetta* project in 1996, the programme was 're-badged' to become the *Deep Space 4/Champollion* lander and a new target was selected for it, comet 9P/Tempel 1. By this time (1999) the lander had grown to 120 kg (Muirhead and Kerridge, 1999) and it was being studied under NASA's New Millennium program. Subsequent programme cuts in July of 1999 redirected the mission to become a study for the 4th Science and Technology (ST4) mission, and as of 2001 it is no longer being developed by NASA for flight.

The second lander of the earlier *Rosetta* sample return mission evolved into the *RoLand* spacecraft, and in its earlier guise there were plans to incorporate thermometers into the coring tool of this European lander in order to monitor sample temperature rises. The potential for sample degradation through warming was clearly understood in the early stages of the project as is shown in this quote from the 1991 *Rosetta* mission definition document (ESA SP-1125, p92) "cometary material is highly sensitive to temperature changes... It is therefore very important to measure the temperature of each sample in-situ... during the sampling process". No specific alteration processes are mentioned in that document.

In contrast to the *Champollion* and early *RoLand* systems, the SD2 in its current (mid-2001) design has no provision for monitoring the torque or downthrust applied through the drill stem and so an absolute measure cannot be made of the power applied through the cutting head to the comet's surface. However, by recording the current drawn by the SD2 from its power bus, and by noting the voltage difference across the motor power controller in calibration tests, it may be possible to estimate the power expended by the drill. It is believed that a similar power-monitoring method has been used for preliminary tests that involved coring materials under low pressures and at cryogenic temperatures. However, no detailed information appears to be available in the public domain from these initial tests which used coring tools that were dissimilar in scale and design to the flight version of the *RoLand* sampler.

3 Preliminary Experiments in Ice Coring

> "What are called the mechanical arts carry a social stigma and are rightly dishonoured in our cities"
>
> ***Xenophon (444-357 BCE)***

To obtain some experience in cutting and handling samples of cold water ice, a short study was carried out to establish the ease with which the requisite material could be formed and cored. This chapter describes the apparatus and the method of ice sample growth. Because both force and torque levels were measured along with the cutting rate and rotation speed during the coring process, a value of the failure strength could be obtained by applying the model outlined in chapter 2. This chapter enlarges on the brief and relatively non-technical summary of Garry (2001) and also provides predictions for the temperature field in cryogenic water ice around a manually driven coring tool.

3.1 The Apparatus

Research at the PSSRI had already examined the utility of melting and re-freezing ice cores under reduced pressure in order to remove, and subsequently study, dissolved gases recovered from the water. Freezing of the water was accomplished by cooling it from its base. Any gas dissolved in the liquid would then be exsolved as bubbles at the ice-water interface. If the water is not cooled too rapidly, then the bubbles of gas that form as the water freezes do not get overtaken by the rising ice-water interface and can escape to the surface for collection. This so-called 'zone-freezing' method not only allows dissolved gas to be collected, but also yields a useful side-product: clear and bubble-free water ice. Help in growing large samples of clear ice was obtained from Dr. Gray of the University of Kent at Canterbury (England) following their success in making large (30 cm diameter) slabs of ice for hypervelocity impact experiments. The description that follows is specific to the zone-freezing equipment but may be modified with little difficulty.

A clean *Pyrex®* beaker containing around 75 ml of de-ionized water was boiled within a microwave oven so as to remove as much dissolved air from the liquid as was practicable. Once the water had cooled to around room temperature, it was siphoned into the freezing tank which was then capped and made air-tight. This container was made from a short length of stainless steel tubing capped at both ends with demountable con-flat flanges (DIN40 size). By siphoning water into the tank the air entrainment associated with pouring was avoided. Around 50 ml of water could be held inside the freezing tank which is shown in the top left of Figure 24. This tank was connected to a vacuum line via a short piece of stainless steel pipe fitted with a *Swagelok®* fitting. The water was frozen by cooling the tank with liquid nitrogen. This cryogenic fluid was held in a Dewar vessel and a large (10 cm x 5 cm x 5 cm) aluminium heatsink was suspended from the neck of the Dewar flask in such a way that the fins of the heatsink were in contact with the cryogen. The tank holding the water would then be placed on the heatsink and cooled by conduction. With regular topping-up of the croygen, a billet of ice could be formed in around two hours in which time a thick layer of frost grew over most of the tank, evidence of the low and uniform temperatures within. The closed stainless steel vessel had no window ports in its walls and if this system was to be used frequently then thought may be given to devising some means of detecting whether the water had fully frozen or not.

Once frozen, the tank was disconnected from the pumping system and the tank was opened to reveal the ice, a photograph of which is shown in the middle of Figure 24. Instead of extracting the sample from the tank, the ice was retained in the container. The tank had been chosen partly on the grounds of its volume, and also because of its shape. One side of the cylindrical vessel had been deformed at some earlier time and a slight dent was visible in the chamber's wall. This asymmetry meant that if the tank could be immobilized then torque from a rotating tool would not cause the ice sample to spin within its housing

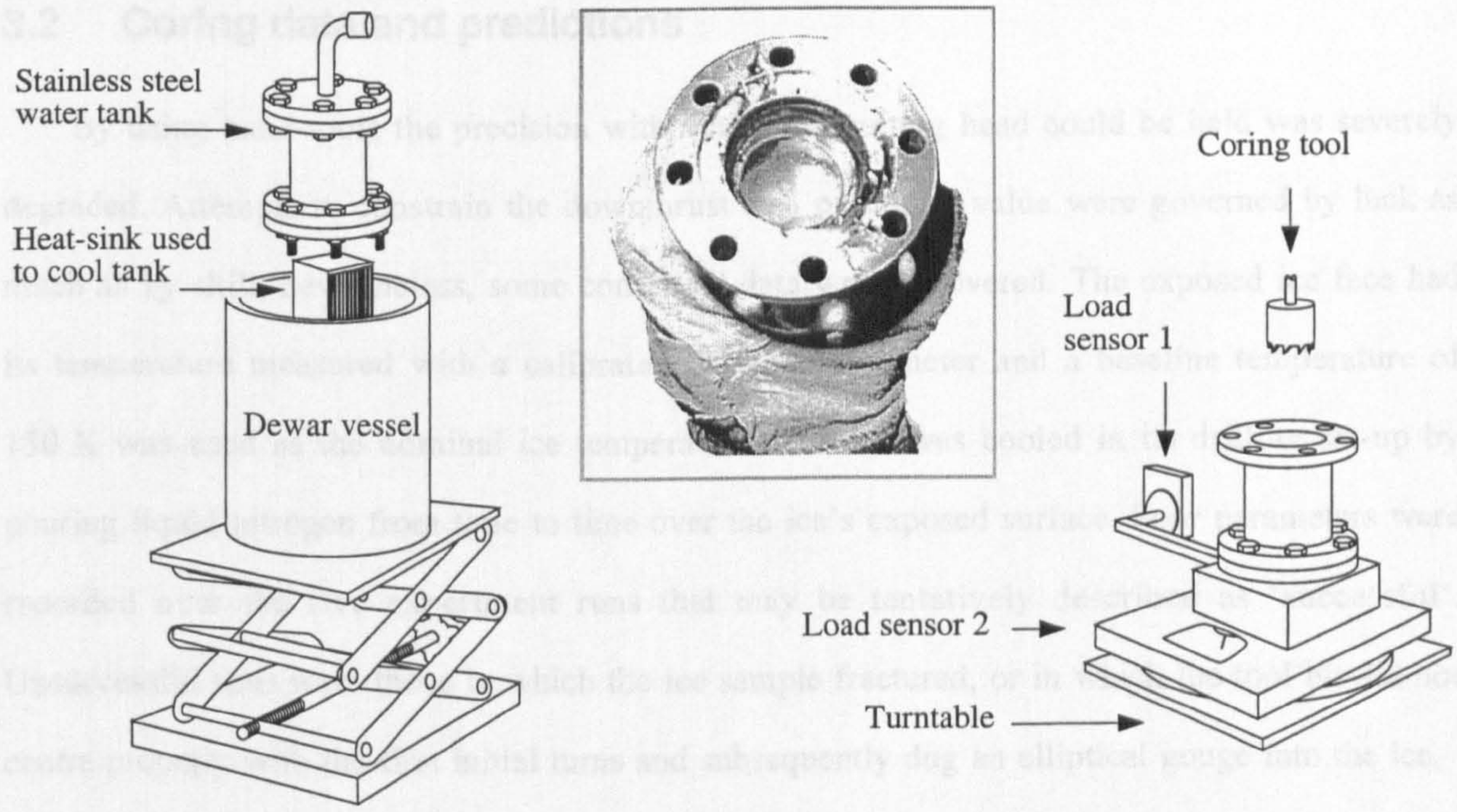

Figure 24 – Showing the ice freezing device, an ice sample, and drilling apparatus.

To hold the tank in this manner a wooden block was made with holes that corresponded to the bolts securing the lower flange of the tank body. This wooden stage was then used to mate the tank to the first load transducer, and the whole apparatus was pivoted so that the applied torque could be monitored by a second force meter, as shown in the above diagram. The fit between this wooden stage and the tank was sufficiently firm for no wobble or looseness to be detected with hand-applied forces. A hand-drill was used to drive the tool bit which was a 1" outer-diameter 'Blu-Mol' coring tool with 18 teeth of width 1.5 mm, made by *Ingersoll-Rand*. Each drilling test, typically of 30 second duration, required that the normal load and torque were held essentially constant, and although the downthrust could be constrained fairly well, the demands of counting total revolutions, watching a clock, and simultaneously registering the mean torque did not permit accurate data collection.

An estimate of the feed thickness, t_1 in Figure 19, was made by measuring the vertical depth that the tool had travelled in a fixed period of time. With a measure of the rotation speed the feed thickness encountered by each tooth could then be calculated using equation 30.

3.2 Coring data and predictions

By using hand-tools the precision with which the cutting head could be held was severely degraded. Attempts to constrain the downthrust to a particular value were governed by luck as much as by skill, nevertheless, some consistent data were recovered. The exposed ice face had its temperature measured with a calibrated Pt100 thermometer and a baseline temperature of 150 K was used as the nominal ice temperature. The ice was cooled in its drilling set-up by pouring liquid nitrogen from time to time over the ice's exposed surface. Four parameters were recorded over the five experiment runs that may be tentatively described as 'successful'. Unsuccessful runs were those in which the ice sample fractured, or in which the tool bit did not centre properly with the first initial turns and subsequently dug an elliptical gouge into the ice.

The specific cutting energy (u) was calculated using the cutting model shown in equation 28 with information on the tool's geometry, the recorded force, torque, rotation speed, and an estimated feed thickness. For each run the *calculated* figure for the specific cutting energy and the estimated depth rate value was fed into the model of SB89 to produce two predictions for the peak temperature rises experienced on the sample axis and at the radial position of the teeth. All of the pertinent figures are shown in Table 12.

Table 12: Cutting data and calculated specific cutting energy, u, for water ice with a poorly constrained temperature cored at ~ 60 rpm. The temperature rise at the centre of the tool, T_1, and the temperature shift at the cutting teeth T_2, are found using the model of SB89 and the calculated value of specific cutting energy.

Downthrust (N)	Torque (Nm)	Depth rate ($m\ s^{-1}$)	u (MPa)	ΔT_1 (K)	ΔT_2 (K)
10	0.14	10^{-4}	71	1.1	2.3
15	0.21	10^{-4}	105	1.7	3.3
55	0.7	0.001	37	3.5	6.4
88	1.0	0.0015	37	4.3	7.3
115	5	0.0015	150	17	30

For the temperature shifts to be given credibility the data fed into the model of SB89 must be equally believable, and the scant and imprecise data set obtained in this preliminary sequence of tests does not inspire a large degree of confidence. No rigorous error analysis will be performed for the gathered data, the dominant sources of error arose from the estimation of the downforce, torque, and final depth of cut. A figure of 20% inaccuracy is probably a reasonable value for these figures but it is obvious that there is still a considerable amount of

disagreement in these sparse figures and it is not profitable to make further estimates of the sources of error. Much more accurate measurements taken with an electrically powered precision coring rig will be described later but for now it is instructive to work with order of magnitude figures for the specific cutting energy and to show the range of temperature rises that might be expected from a representative sample of water ice.

In Figure 25 the on-axis and bit temperatures predicted by the model of SB89 for the coring operation of the particular tool head are shown for two materials that share the thermal properties of water ice at 150 K, but which differ in their toughness. This chart is offered only as a guide to how the computed temperatures change with vertical cutting speed and specific cutting energy. The range of specific cutting energies spans the rather wild scatter of values that is seen in the preceding table at similar depth rates. The darker lines show the predicted temperature rise at the radial position of the cutting teeth, and the lighter curves marks the values of the modelled axial temperature rises.

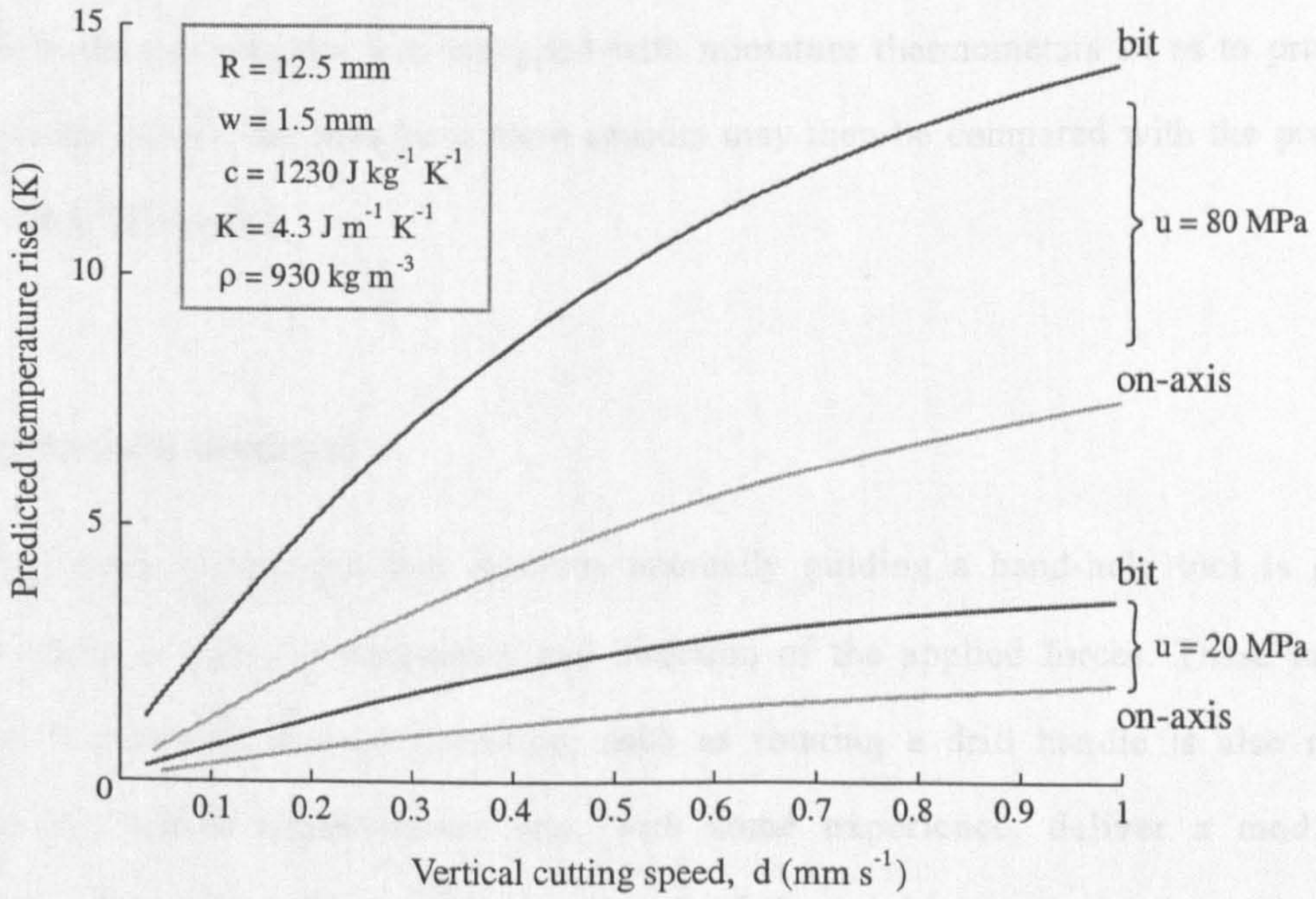

Figure 25 – On-axis and bit temperatures computed using the model of SB89 for two values of the specific cutting energy of water ice at 150 K using particular coring conditions.

For the levels of force and torque employed it appears that temperature rises of a few degrees are possible around the tool head. The difference between the temperature at the axis of the corer and at the edge of the tool is also seen to scale directly with the specific cutting energy over a wide range of vertical cutting rates.

Two caveats have to be identified for these predicted values of ΔT. The chip thickness, t_1, has been inferred by assuming that all of the teeth shave away an identical and constant amount of material as they pass over the freshly exposed ice left by a preceding tooth. The reality is that relatively few teeth may be taking part in any significant excavation and that the transducers are therefore sampling an average work load by the entire tool which may not reflect the actual work performed by a given tooth. Such changes in the cutting geometry will yield inaccuracies in the calculated values of u. If an erroneous value for the specific cutting energy is then used in the models of SB89, or the simpler representation of the 'flash' heating, then the temperature rises predicted in the cored material will also have their accuracy compromised.

The second deficiency lies in the approximations made in the model of SB89, which do not accurately reflect the annular nature of the head, or the motion and localized heating of the cutting teeth. These shortcomings can only be properly assessed with data on the temperature fields present around coring heads. Therefore the vacuum coring system that is described in the next chapter was equipped with miniature thermometers so as to provide *in-situ* temperature data. The data from these sensors may then be compared with the predictions made by the SB89 model.

3.3 Lessons learned

A machining experiment that involves manually guiding a hand-held tool is going to generate errors in both the magnitude and direction of the applied forces. These errors are magnified if a second manual operation, such as rotating a drill handle is also required. Although the typical experimenter can, with some experience, deliver a modicum of repeatability, the order of magnitude 'accuracy' of these initial tests clearly pointed to the need for mechanical sources of motive power and for the minimum of human involvement in similar drilling operations. Following these instructive, if not especially illuminating tests, a three-axis coring system was constructed by which a tool could be brought into contact with a cold workpiece with the minimum of human intervention. This system, its ancillary equipment, and its operation is described in the next chapter.

4 A Vacuum Drilling System

"All parts should go together without forcing.
You must remember that the parts you are reassembling were disassembled by you.
Therefore, if you can't get them together again, there must be a reason.
By all means, do not use a hammer."

IBM maintenance manual, 1925

The presence of a relatively warm and humid atmosphere in a laboratory hinders the testing of spacecraft systems under mission conditions in a number of ways. For mechanisms such as drilling tools the three main problems are that;

1 Cold surfaces can rapidly condense water out from the atmosphere, leading to a growth of frost over surfaces colder than 0°C. Mechanical devices can suffer if ice is permitted to form on them, usually by removing mechanical tolerances between moving parts, and water from the melted ice can be an aid to corrosion and the cause of electrical short-circuits once the apparatus has warmed up.

2 An atmosphere can act as a lubricant at a cutting surface, leading to reduced cutting depths and lower forces. Studies by Kragelsky (1981) of the efficiency of metal tools in cutting ceramics and metal alloys under low pressures suggest that it is the absence of an oxide layer on ferrous tools that leads to raised cutting forces at low speeds *in vacuo*. The use of very hard carbide or nitride based tool pieces such as WC or TiN may avoid this process to some extent, and the liberation of vapour from a cut material might also remove this source of vacuum friction.

3 The material, if sufficiently porous, will contain a portion of the ambient atmosphere, particularly if the pores are well-interconnected with relatively simple adjoining passages. Significantly porous materials can have their thermal properties radically altered by either the convective transfer of gas, by the conduction of heat through the suffusing gas, or even through the condensation and sublimation of the gas.

4.1 Chamber resurrection and modification

Following the decommissioning of an ultra-high vacuum system in the PSSRI, a relatively large vacuum chamber became available for use. The system consisted of an ion sublimation pump and a pair of half-cylindrical chamber sections mounted on rails fixed to a stout trolley. This chamber had been identified some years ago as being of potential use for other experimental vacuum projects and at the start of this work it was moved from its resting place into a more spacious laboratory. A total working volume of 35 litres was available within the chamber, and it boasted over twenty ports in a wide variety of diameters, lengths, and fitting styles. Given the availability of this system, and the speculative nature of the author's intended research, it was clear that there would be great advantage in refurbishing this older chamber rather than building a customized system. Several months were spent in simply bringing the chamber and its associated pumping system back to a vacuum-tight condition, and as might be expected, a number of false-avenues were explored in the course of refining the system. One unwavering goal for the chamber was that it should be able to form, and subsequently mechanically alter, materials analogous to those found on or near to a comet's surface. A closely related hope was that this would allow the more general study of planetary cryogenic ices with sampling gear comparable to those on actual and proposed spacecraft.

Simply studying the formation and evolution of cometary analogues is not a particularly novel ambition in itself. Similar chambers have been used by various teams around the world since the 1960s to partially recreate the conditions of cometary environments. However, relatively few of these experiments have studied interactions between ice-rich materials and spacecraft mechanisms and sensors. The closest present counterparts to the PSSRI vacuum drilling chamber are those operated at the DLR in Cologne, and the comet chamber of the IWF of the Österreichische Akademie der Wissenschaften in Graz (Austria). The first of these two groups has operated three simulation chambers in its work, and they are all generally referred to by the name of the guiding project; KOSI (*KO*metten*SI*mulation). The smallest of these three chambers, named the Small Simulation Chamber (SSC) is capable of handling kilogram-mass samples of decimetre size, and is described in Seidensticker *et al.* (1995). The latest KOSI system uses a heavily instrumented double-walled chamber, and permits objects up to 1.4 m by 1.8 m to be cooled and studied under vacuum. This mid-size vacuum chamber has many of the

features of the SSC such as a cryogenically-cooled radiation shroud, but is almost twice the size of the SSC. The largest chamber, described in Grün *et al.* (1991) is no longer operational. Its original role as a spacecraft test chamber allowed it to house items up to 3.5 m in diameter and 5 m long (Kochan *et al.* 1989).

The majority of the KOSI work concentrated on making complex analogues of cometary material made from carbon dioxide, water ice, and dust in varying proportions. A common theme to the KOSI experiments was the use of a particular form of Comet Analogue Material (CAM) made by spraying water jets into liquid nitrogen. The method was first described by Saunders *et al.* (1986), subsequently elaborated upon by Stöffler *et al.* (1991), and details of the apparatus were provided by Stöffler and Düren (1992). Despite the conceptual difficulty of generating large bodies of water in comets the use of this KOSI type of CAM as a source of granular ice is widespread in the field of cometary simulation (Roessler *et al.*, 1989; Hesselbarth *et al.*, 1991; Lämmerzahl, 1995, among others). There may, however, be some unintended problems with this form of ice production, as it is not clear that purely Ih ice is formed in such a rapid-quenching process. The X-ray diffraction studies of Mayer and Hallbrucker (1987) used samples formed from droplets of water around 3mm in diameter. These droplets were rapidly frozen by being directed against a cryogenically cooled plate and were found to be frozen into the cubic (Ic), rather than hexagonal (Ih) ice. No diffraction studies could be found that described the structure of the KOSI CAM and no mention has been made of the possibility that cubic ice, with its different thermal properties, may have been made instead.

The relatively broad range of experiments undertaken by the KOSI project meant that no systematic exploration was made of the CAM properties. The eleven KOSI experiments for which data have been published are summarized in Table 13 which has been adapted from Sears *et al.* (1999) and Stöffler and Düren (1992).

Table 13: Relevant published details of the KOSI work performed in the 1990s - note the dominant use of water ice in all experiments.

	Experiment number										
Content	1	2	3	4	5	6	7	8	9	10	11
H_2O (%)	90	90	78	77	70	42	83	100	90	90	45
CO_2 (%)	-	-	14	-	15	17	15	-	-	-	5.8
Methanol	-	-	-	-	-	-	-	-	-	-	9.1
Dust*	10	10	8	8	9	43	2	-	10	10	40
Density (g cm^{-3})	0.4	0.6	0.48	0.51	0.56	0.59	0.46	0.4	0.44	0.5	0.54
Duration (hr)	38.4	39.4	47.2	35.5	12.9	30.3	34	40	59	4.75	15.25

**Mixtures of Olivine, Montmorillonite, carbon black, and Kaolinite in varying proportions.*

Some of the KOSI experiments (3, 4, and 8 onwards) attempted to measure the mechanical properties of cryogenic CAM samples and these tests are described in the works of Jessberger and Kotthaus (1989) and Kochan *et al.* (1989). In the first of these two studies well-formed billets of CAM made of finely ground mixtures of H_2O and CO_2 ices were subjected to conventional uniaxial and triaxial material tests. The second paper describing some mechanical properties of KOSI CAM used a form of penetrometry which involved driving a hemispherically-tipped *Teflon®* probe of 5 mm diameter into the CAM while measuring the resistance to the probe's progress. Unfortunately all of the materials tested in these works were multicomponent mixtures of no less than two different mineral dusts and KOSI-style water ice. Up to four mineral types were used in the work of Jessberger and Kotthaus, and carbon dioxide ice was present at a fixed mixing ratio in the penetrometry work. Despite the complexity of the materials and the lack of a systematic study of varied mixtures, two trends can be seen. Firstly, the overall compressive strength of CAM is seen to rise with time, presumably as a result of sintering and void infill by recondensed gas. Secondly, the exposed surface of the CAM becomes preferentially harder upon heating. This is expected as sintering and mass transport will be most active where the thermal gradient is largest, which for a heated sample, is the free surface of the material.

Similar lines of work have been conducted with the chamber at the IWF (Graz). Here the 0.4 m diameter chamber has been primarily used for making thermal profile studies of CAM. Published experiments from this chamber include the work of Kömle *et al.* (1996) on the evolution of paraffin-doped dust and ice mixtures, and the studies by Seiferlin *et al.* (1996) on

the thermal conductivity of CAMs. Inside this smaller chamber, a cylindrical sample holder 8 cm wide has been used to study the properties and evolution of cometary analogues containing, among other components, organic compounds such as paraffins. This last chamber, which is described along with its data collection system in Kargl (1998), has been re-housed in a new laboratory and is likely to become fully operational again by the start of 2002 (Dr. Günter Kargl, personal communications). One other system that the author is aware of is the vacuum chamber system operated by Dr. Jacklyn Green of the Jet Propulsion Laboratory (JPL). This last chamber was built to support the *Champollion* mission and it is now operating as a science tool and technology demonstration system for the study of surface operations on minor bodies (Dr. J. Green of JPL; personal communications). This system is outlined in Green (1998).

From the literature describing these chambers and similar systems it was possible to establish four broad aims for the PSSRI vacuum chamber in its current form.

1 To be able to expose ice-rich materials to vacuum at low temperatures comparable to those experienced by SP cometary nuclei at perihelion. Or, in the absence of such a capability, to at least be able to assess the influence that comparable temperatures and pressure may have on sample growth and alteration.

2 To study the mechanical alteration of such icy materials by mechanisms representative of spacecraft surface-science payloads with the emphasis on rotating cutting tools.

3 To be able to measure the degree to which material has been evolved in some way, either by capturing and extracting some fraction of the sample, or by making *in-situ* measurements.

4 To acquire experience in constructing robust vacuum systems for space and planetary environment simulation.

None of the above aims were immutable. For example, the second point regarding the use of sample mechanisms was raised dramatically in importance by the discovery of an intact five-degree-of-freedom manipulator stage which was added to the system after some minor changes to the chamber's halves. Prior to this a linear actuator was to have been the means of altering the sample, restricting the scope of studies to those of penetrometry. After a number

of similar modifications, the overall design had stabilised by early 2000. Figure 26 illustrates the salient points of the system and colour photographs of the apparatus can be seen in appendix F.

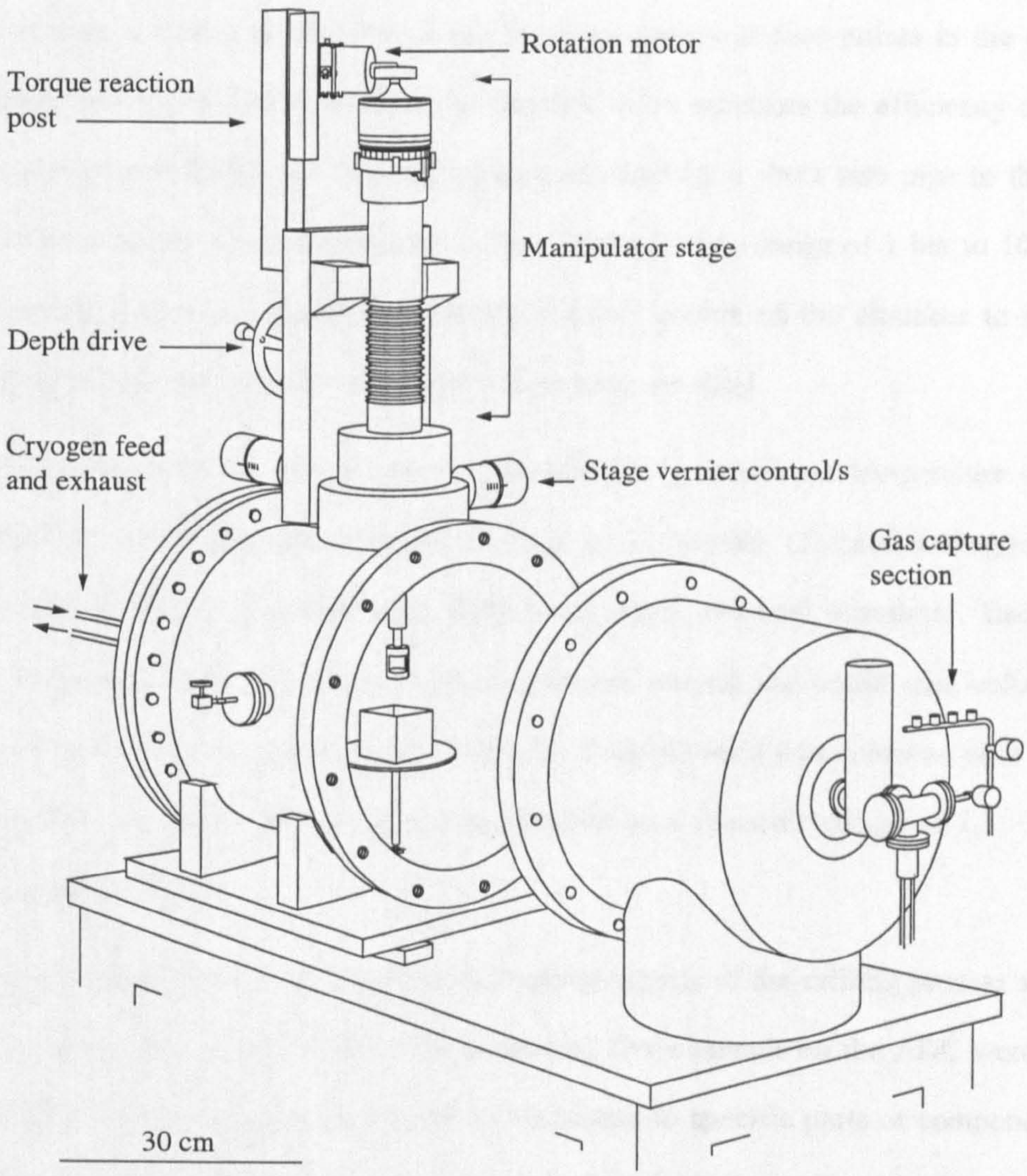

Figure 26 – A sketch of the cryogenic vacuum drilling system opened to show the box-like sample holder and its position within the chamber.

Separate aspects of the chamber will now be discussed in the following sections; the ability to sense and then control the cavity environment, the scope for mechanical interaction with a sample, and the system for capturing material from a sample.

4.2 Chamber environment sensing and control

Before control can be exercised over a system, knowledge of the parameters to be regulated must be gained. Along with the chamber's internal pressure, the temperature of particular items within the chamber are two of the most important measurable quantities. Pressure sensing is achieved with Pirani and Penning gauges at four points in the chamber; a Pirani sensor on the pump-side of the main chamber valve monitors the efficiency of the main pumping system, and Pirani and Penning gauges attached by a short side pipe to the chamber are used to measure the absolute pressure in the chamber over a range of 1 bar to 10^{-6} mbar. A further Penning sensor is connected to the gas capture system of the chamber to ensure that the sampling vessels are correctly evacuated before they are used.

Aspects of the chamber environment measured by its pressure and temperature sensors can be recorded by connecting the sensors' outputs to an eleven channel analogue-to-digital converter (ADC) that is attached to an IBM compatible personal computer. Each channel could be sampled at up to eleven thousand samples per second and could read voltages in the range of 0 V to 2.5 V. Conversion of the voltage to a digital word was achieved with ten bits of precision and so the least significant bit corresponded to a channel voltage of $2.5 \div 2^{10}$ volts, or a little under 2.5 mV.

Six of the channels were dedicated to monitoring aspects of the drilling process and will be described in detail later in this section. The remaining five channels on the ADC were available for general data logging purposes and were not dedicated to specific parts or components of the vacuum system. The wiring layout of the chamber along with its ancillary equipment is shown in Figure 27.

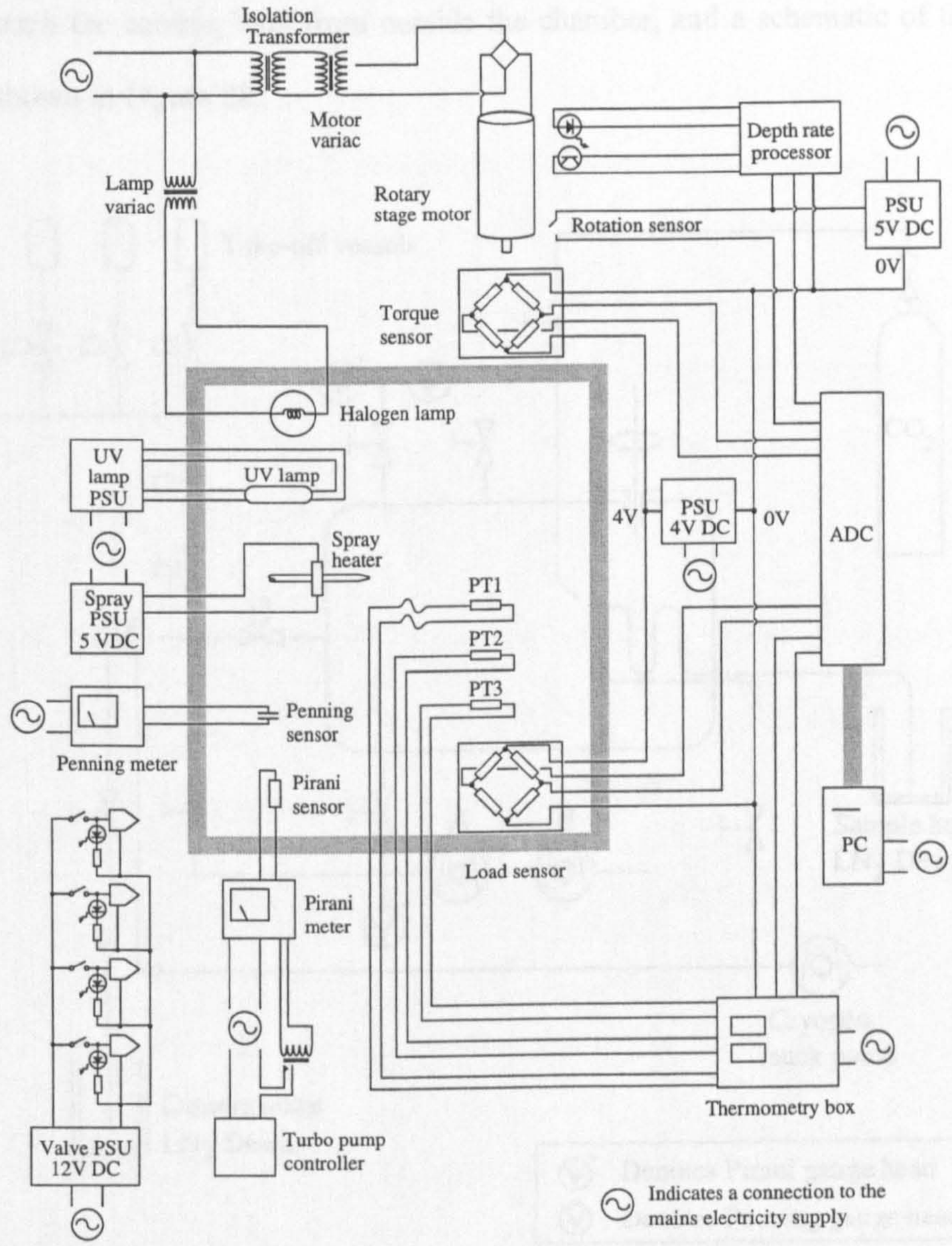

Figure 27 – A schematic of the vacuum chamber's electrical apparatus and layout.

Working with materials under low ambient pressures and temperatures brings about another problem; that of thermal control. Heat could be easily created within the chamber by operating the internal halogen lamp (300 W maximum rating), but heat would also have to be actively extracted in some way. Not only does the substance being investigated have to be cooled to an appropriate temperature, but any device that makes contact with the cooled object should not introduce a heat path that significantly warms the material. The first problem, that of cooling a material, was achieved in the vacuum system by using a stainless steel pipe to carry liquid nitrogen. This cooling pipe was coiled into a spiral, and then soldered to a stout circular copper plate which formed the base of the sample holder. The sample holder is an open box made from thin sheet tinned steel and was soldered to the copper sample plate. A cryogenic feed-through flange equipped with *Swagelok*® connectors allowed cooling fluid to

be piped through the cooling loop from outside the chamber, and a schematic of the chamber's pipework is shown in Figure 28.

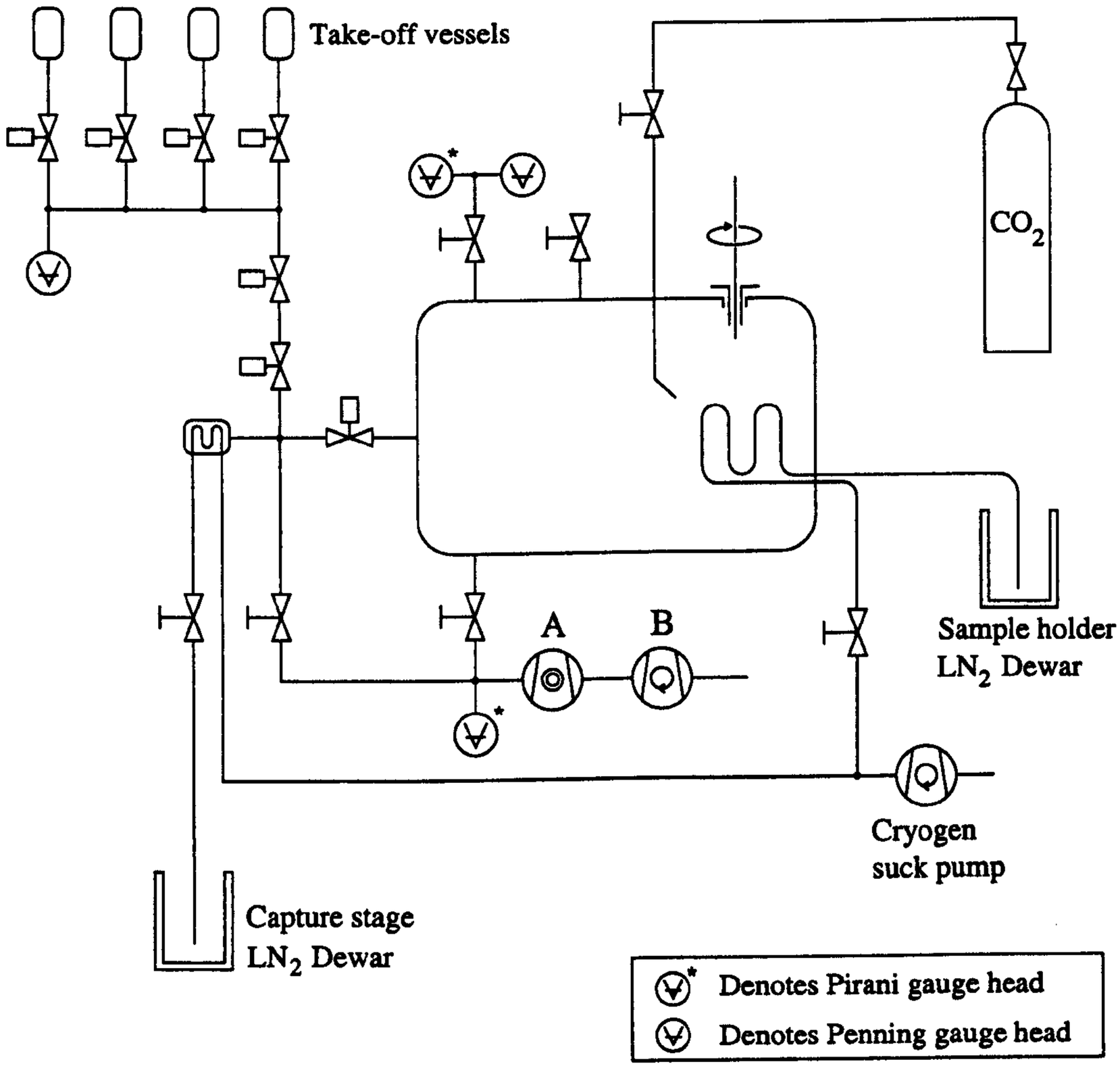

Figure 28 – The vacuum chamber's pipework. Pumping of the chamber cavity and the take-off lines is achieved with a turbomolecular pump (A - Pfeiffer TPH330 model) which is backed by the rotary pump (B - a two-stage Alcatel 2004 model).

By connecting a rotary pump to one pipe of the cryogenic feed-through, and a Dewar vessel of liquid nitrogen to the other, liquid nitrogen could be drawn through the stage's cooling coil. The flow-rate could be controlled by a valve in-line with the rotary pump. In the simulation chambers operated by the DLR and IWF, a further cooling element is included that takes the form of a cylindrical shell that encloses the experimental work area. A liquid nitrogen transfer line is coiled around this shell, or cold shroud, which serves two purposes. From the point of view of a cold sample inside the chamber, such a shield would obscure the walls of the chamber. The steel of the chamber is relatively warm (typically 300 K) and such a shield would prevent poorly conducting materials from being warmed by radiant heating. A second use of such a shield is that it can act as an extremely efficient pump by condensing any

volatile compounds such as water or pump-oil. The chamber in its current form does not have such a cold shroud as it was not expected that ultra-high vacua would be needed in the experimental work and no careful studies of radiatively heated samples were foreseen. However, it is useful to assess the magnitude of the heat leaks present into the chamber, and both the heat load delivered by radiation from the chamber walls and the heat conducted along the drill stem of the chamber will be calculated in the following pages. For such calculations the thermal properties of the constituent materials in the chamber must be known and the following table lists these quantities and their values.

Table 14: Material properties used for estimating thermal processes.

Material	Thermal conductivity λ (W m^{-1} K^{-1})		Heat capacity c (J kg^{-1} K^{-1})		Density (kg m^{-3})	Emissivity
	77 K	200 K	77 K	200 K		
Stainless steel	7.5[c]	13[a]	144[d]	384[d]	~8000	(as steel)[b]
Copper	550[a]	400[a]	170[d]	355[d]	8960	0.05[b]
Mild steel	58[a]	65[a]	144[d]	464 (0°C)	7860	0.08[b]

[a] *Lide (2000),* [b] *Siegel and Howell (1981),* [c] *Rosenberg (1965),* [d] *Ellis et al. (1984),* [d] *Gray (1972)*

Let the chamber be approximated by a sphere of radius r at the centre of which a small flat circular plate of area A_p and albedo a_p is positioned. The chamber wall will radiate an amount of heat at a rate that is governed by the temperature T_c and emissivity ε_c of the chamber's wall material. From the sample plate's point of view an infinitesimal solid angle intercepts an area of the chamber interior dA that scales as the square of its mean distance and from which the received total heat falls off as the inverse-square; the total heat received is obviously independent of the sphere's radius. If the chamber material is assumed to radiate like a greybody then the plate absorbs an amount of heat, dI, radiated from an elemental patch at an angular distance ϕ from the pole of the co-ordinate system, is;

$$dI = \frac{\varepsilon_c \sigma T^4 A_p (1 - a_p) \cos\phi \, dA}{4\pi r^2} \qquad \text{Eq. 45}$$

The rotational symmetry about the plate is trivially accounted for and the patch area dA is simply;

$$dA = r^2 \sin\phi \, d\phi \, d\theta \qquad \text{Eq. 46}$$

Thus;

$$I = \frac{\varepsilon_c \sigma_{SB} T^4}{2r^2} A_p (1 - a_p) \int_0^{\frac{\pi}{2}} r^2 \sin\phi \cos\phi \, d\phi \qquad \text{Eq. 47}$$

$$I = \frac{\varepsilon_c \sigma_{SB} T^4}{4} A_p (1 - a_p) \qquad \text{Eq. 48}$$

So far this model neglects the reflection of heat energy from the chamber, to the sample stage, and back to the sample holder and if this more complicated assumption is considered it can be shown that the amount of power transferred from the chamber to the sample stage can be written as;

$$I_{trans} = \sigma_{SB} \varepsilon_{eff} A_p \left(T_1^4 - T_2^4 \right) \qquad \text{Eq. 49}$$

The radiative properties of the plate and the chamber walls are now replaced by an effective emissivity. For a geometry which is essentially identical to the case of an object surrounded by a spherical shells, the effective emissivity of the inner object can be calculated, and this is treated in Siegel and Howell (1981) as;

$$\varepsilon_{eff} = \left(\frac{1}{\varepsilon_p} + \frac{(1 - \varepsilon_c) A_p}{\varepsilon_c R^2} \right)^{-1} \qquad \text{Eq. 50}$$

In the course of using the chamber, the copper stage was repeatedly exposed to laboratory air, leading to oxidisation and tarnishing. Although the stage was kept visually clean and in a high state of polish, the emissivity of metals can be changed through relatively minor changes to the state of the surface, and so the emissivity values given in Table 14 are not expected to be constant throughout the lifespan of the chamber. Specifically, the emissivity of a metal rises as the surface becomes progressively rougher or more heavily oxidised. To accommodate the potential changes that may occur in surface finishes, a range of values for ε_p and ε_c were considered, based on the values in Table 14. The radiant heating power applied to the sample stage by the chamber's interior can then be calculated. For a chamber temperature T_1 of 300 K, and a sample stage temperature of 120 K, Table 15 lists the heating power in watts (shown in bold text) that is transferred to the sample stage for a range of stage emissivities. The value of the effective emissivity for that heating rate is printed in italics for each case.

Table 15: The radiant power (W) shown in bold type delivered to the chamber sample holder for various effective emissivities which are printed in italics.

		Emissivity of whole sample stage		
		0.1	0.2	0.3
Chamber interior emissivity	0.1	**0.5** *0.08*	**0.9** *0.15*	**1.1** *0.19*
	0.2	**0.5** *0.09*	**1.0** *0.17*	**1.4** *0.24*
	0.3	**0.5** *0.09*	**1.0** *0.18*	**1.5** *0.27*

This heating power should be compared to the heat leak delivered through the manipulator stem, and the steps taken to minimize and measure this quantity will be described next.

A temperature differential between a tool head and the worked material will allow heat to flow between the two and this may lead to a change in the measured properties of the sample. The experimental work of this thesis required that, at some point, rotating tool bits would be brought into contact with cold materials under reduced ambient pressures. Without a method of cooling the tool head, its equilibrium temperature would follow the temperature of the rotating stem, which is in contact with the warm laboratory air through the mounting flange of the stem. There is little point in attempting to investigate a cryogenic material if the tool used to probe the sample is 200 K warmer than the material being examined and allows a significant heat flow when the two items are brought into contact. Two steps were therefore taken to reduce the mismatch in temperature between the tool head and prospective samples. Firstly, the thermal conductivity of the physical link between the tool head and the chamber wall was reduced. A threaded cylinder of steel connected the tool heads to the drill stem of the manipulator. This cylinder, referred to as the tool holder, was modified by first drilling and then filing away more than 95 % of its cross-section over a fraction of its length thus reducing the overall thermal conductivity of the tool holder by a similar amount. Two of the tool head designs and the once-cylindrical tool holder, are shown in Figure 29a, with a photograph of the coring tool shown in Figure 29b.

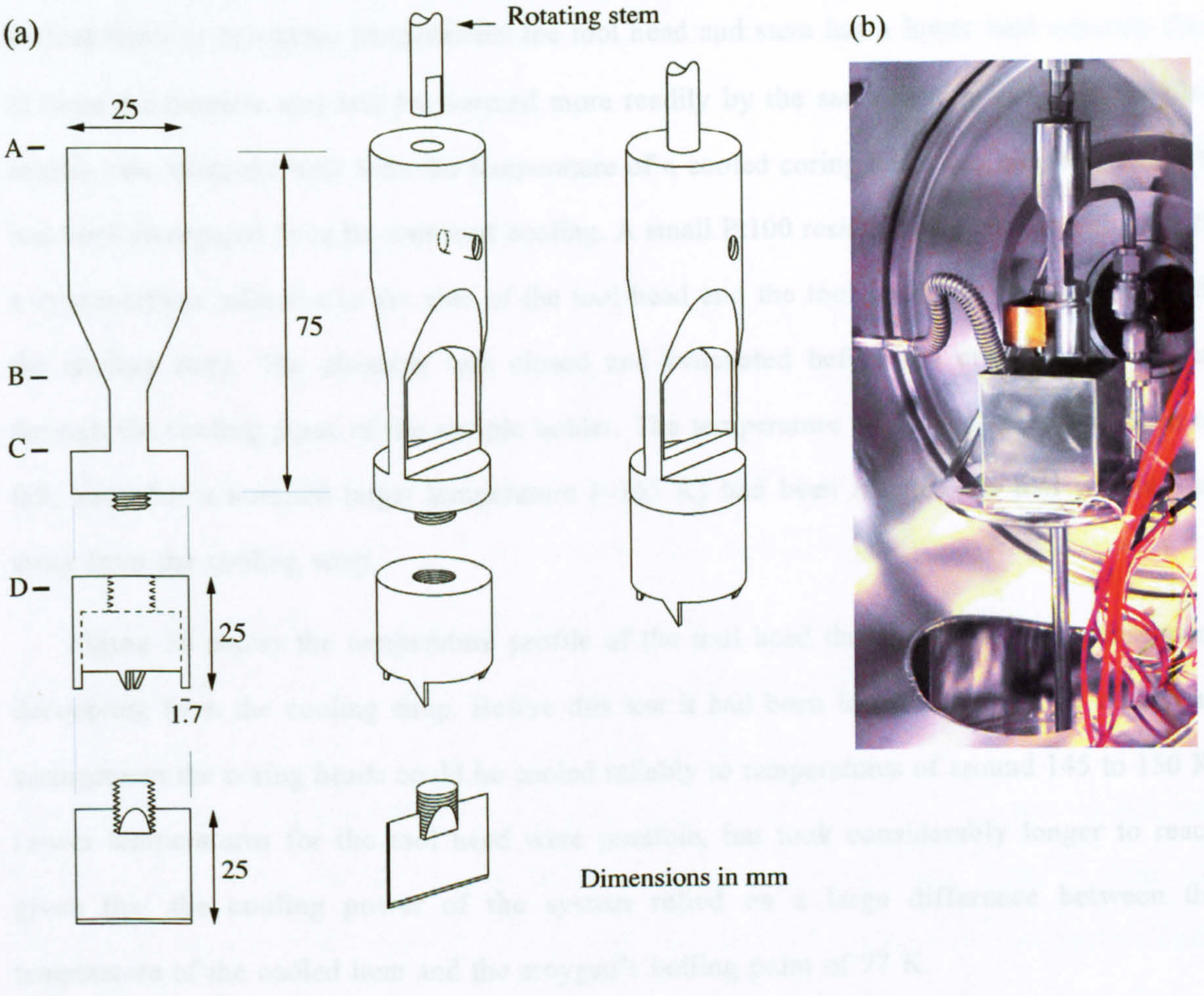

Figure 29a/b — Diagrams (a) and a photograph (b) of the tool holder and the tool heads used to probe icy materials. The markers A,B,C, and D indicate points where the temperature will be estimated using a one-dimensional conduction model.

With this diminished thermal link, or thermal break, established between the tool and the outside of the chamber, a second step was taken by which heat had to be extracted from the tip of the tool. A passive method was eventually devised in which the tool holder was allowed to butt up against a thick copper strap that was soldered to the stainless steel cryogen feed pipe. That part of the copper strap which would make contact with the tool holder was curved so that it snugly cupped the tool head along half of its circumference. A film of lead was then flowed over the side of the copper strap that faced the tool. Repeated rotation of the tool against this ductile metal surface with the addition of a fine grinding paste allowed an intimate contact to be made between the tool holder and the copper cooling strap.

The effectiveness of this method of passive cooling was assessed by calculating the rate at which heat flows along the drill stem. Such a model has to recognize the temperature-dependence of the thermal properties shown by the drill stem's materials shown in Table 14.

For example, at cryogenic temperatures the tool head and stem has a lower heat capacity than at room temperature and will be warmed more readily by the same heating rate. To find this heating rate along the drill stem the temperature of a cooled coring head was monitored after it had been disengaged from its source of cooling. A small Pt100 resistive element was glued with a cyanoacrylate adhesive to the side of the tool head and the tool head was then docked with the cooling strap. The chamber was closed and evacuated before the cryogen was driven through the cooling pipes of the sample holder. The temperature of the tool head was seen to fall, and after a nominal target temperature (~165 K) had been reached the tool was moved away from the cooling strap.

Figure 30 shows the temperature profile of the tool head during cooling and subsequent decoupling from the cooling strap. Before this test it had been found that with the cold-strap arrangement the coring heads could be cooled reliably to temperatures of around 145 to 150 K. Lower temperatures for the tool head were possible, but took considerably longer to reach given that the cooling power of the system relied on a large difference between the temperature of the cooled item and the croygen's boiling point of 77 K.

Figure 30 – The thermal history of a coring head that has been chilled by contact with the chamber's cooling strap and then separated. The dashed line is a straight-line to the first few temperature values that follow the removal of the head from the cooling strap.

In calculating the heating power conducted to the tool head, both it and the portion of the tool holder into which it screws were treated as a single entity. The two coring heads used

throughout this work have masses of 46 grams, and that part of the tool holder below the thermal break had an estimated mass of 26 grams. By lumping together the tool head and the lowermost threaded part of the holder in this way, the rate at which the tool's temperature changes is related to the heating power, Q, by

$$\frac{\partial T}{\partial t} = \frac{Q}{mc} \qquad \text{Eq. 51}$$

Here, m is the mass of the tool and of that section of the tool-holder beneath the thermal break, and c is the heat capacity of the stainless steel tool head and the threaded part of the mild steel tool holder. The platinum sensor's mass is negligible in comparison and the thermometer should yield an objective record of the tip temperature. Using the peak warming rate, the mass of the head, and the heat capacity of the steels[1] at ~160 K, it is possible to calculate the rate at which heat is being conducted down the drill stem. This heating rate was found to be a little over 2.3 W. By knowing the rate at which heat flows in from the manipulator and out of the tool it is then possible to estimate the temperature of various parts that make up the drill stem. Although not of any direct relevance to the experiments described in this work, it may be useful to calculate the effect of the thinned section in the tool holder on the temperature distribution along the drill stem. With the above value for the heating rate by conduction, and for a given tool temperature, the temperature at various points along the drill stem can be found if values for its cross-section and thermal properties are known. The transfer of heat at a rate Q in one dimension by conduction is well described by Fourier's model and across a segment of constant cross-section A_i, length l_i, and thermal conductivity λ_i, the temperature change (T_{i+1} - T_i) is

$$T_{i+1} = T_i + \left(\frac{Q l_i}{\lambda_i A_i} \right) \qquad \text{Eq. 52}$$

Ideally, the segments in the model should be vanishingly small to allow the replacement of the temperature gradient $\partial T/\partial x$ with its algebraic approximation $(T_1-T_2) / (x_1-x_2)$, but here, only rough figures are required and the tool holder and tool were divided into four discrete sections, the junctions of which are labelled A through D in Figure 29a. The temperatures of these points are listed in Table 16.

---

1 ~265 J kg^{-1} K^{-1} for stainless steel and ~305 J kg^{-1} K^{-1} for mild steel.

Table 16: Predicted temperatures along the drill stem for a tip cooled to 165 K.

Point in Figure 29a	A	B	C	D
Temperature at maximum cooling rate (K)	235	226	166	163 – known from thermometry

Clearly, the thinned portion of the tool holder has a significant influence on the temperature distribution because T_B-T_C>>T_A-T_B. It is possible that the rate at which heat leaks through the drill stem can be further reduced by introducing additional breaks into the tool holder or through the use of ceramic fasteners or spacing washers. For the current configuration the overall result of the heat leak is that the temperature of the tool head rises by around 11 K in the first minute after it has been removed from the cooling strap.

This calibration test was not repeated at lower temperatures, which generally take longer to achieve than the modest temperature of 165 K. However, the results of the above calculations can be extrapolated to these conditions because the heating power conducted to the head will vary directly with the temperature difference between the tool head and the laboratory. Thus, if the tool is cooled to, say, 140 K, a temperature 20% lower than 165 K, it should warm up at a correspondingly faster rate (13 deg per minute) when removed from its cooling strap. It should be emphasised that these figures apply to the tool when it is no longer in contact with *any* source of cooling. Once the tool has been driven a short distance into a cold material, it would be reasonable to assume that the slender teeth of the coring head will rapidly take on the temperature of the surrounding material. The slight heat leak of 2 W through the drill stem would warm the material in contact with the sides of the tool head by a very small degree. This may seem at odds with the notion that comparable amounts of mechanical power dissipated at the tool face can cause substantial temperature rises until it is recalled that the cutting teeth dissipate mechanical power through contact with very small amounts of material. For example, the coring head may apply a mechanical power of a watt or so. However, that power is absorbed by the failure of an area no wider than the cutting teeth, and barely deeper than the depth of the un-cut material, which may be measured in tenths of a millimetre. The exterior of the coring tool has an area of 1570 mm^2 and the larger heating rate resulting from conduction through the drill stem should set up a temperature gradient very much smaller than that which arises from the action of the cutting teeth.

4.2.1 Thermometry

Two Pt100 thermometers were attached at the points marked PtA and PtB in Figure 31, by soldering their stainless steel cases to the thin tin-plated steel of the holder and the thicker copper of the plate. A third, much smaller, Pt100 thermometer was connected by two lengths of enamelled wire (26 swg) to the internal points of the chamber's main electrical flange. This small (5 mm x 2 mm x 1 mm) thermometer could be placed on the exposed surface of the sample material, or on the face of the coring tool as the occasion warranted. Its electrical properties were essentially identical to those of the two larger fixed Pt100 thermometers and it could be interrogated with a resistance meter in the same manner as the larger sensors.

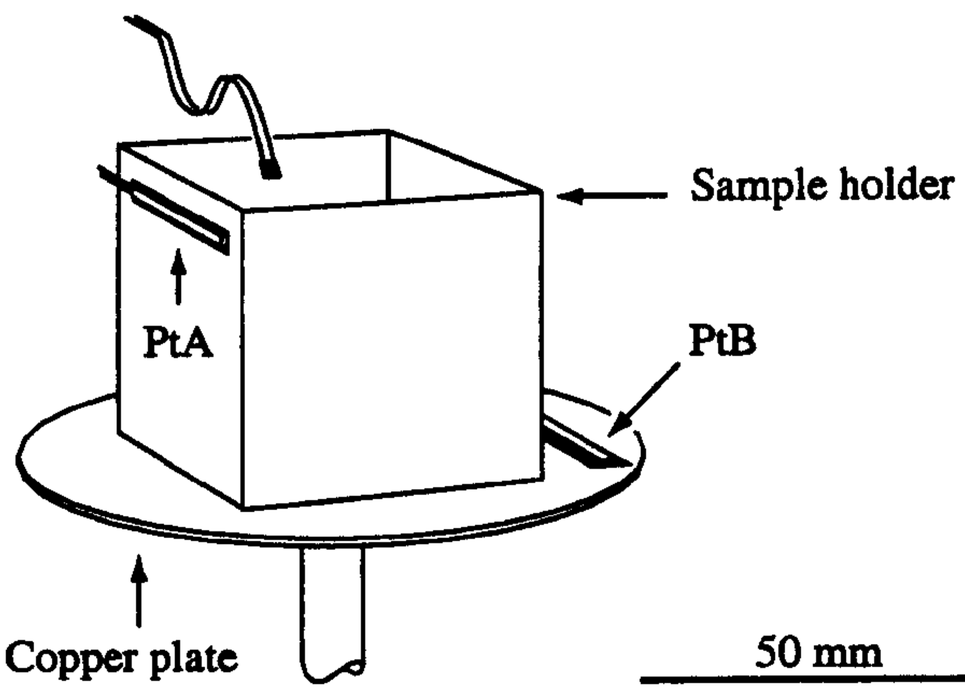

Figure 31 – The location of the fixed and mobile thermometers in the vacuum coring system.

All three of these resistance thermometers use a thin platinum filament deposited onto a ceramic substrate as their sensing elements. Their size and robust construction make them ideal for this application and their correct operation can be verified with a simple resistance meter. For temperatures, measured on the Celsius scale, from –200 °C to 0 °C, the resistance, $R(T)$, of a standard Pt100 element is frequently modelled as being;

$$R(T) = R_0\left(1 + aT + bT^2 + c(T - 100^\circ C)T^3\right) \qquad \text{Eq. 53}$$

The coefficients have the following values: a=0.003908 K^{-1}, b=-5.775 x 10^{-7} K^{-7}, and c=-4.183 x 10^{-12} K^{-12}, these figures being taken from British Standard EN 60751 and are applicable to appropriate commercial calibrated elements. The four orders of magnitude between the coefficients of the quadratic and linear terms of $R(T)$ and the author's experience

of many similar elements suggests that an electrical circuit that yields an output that varies linearly with the resistance of a platinum element will represent the temperature of the element with an accuracy of at least a few degrees K. Two operational amplifier circuits using OP 07 devices were built and made to drive a pair of LCD displays. Thermal baths of boiling liquid nitrogen and melting pure water ice were used to provide set temperature points for the calibration of these amplifier circuits and in the course of two years the amplifiers and their sensors have drifted so that their nominally isothermal readings differ by around 4 K. Re-calibrating the thermometers would require the sensors to be desoldered from their stations and this has been avoided to minimize the heat load on each device over its lifetime. The temperatures reported in the rest of this work should be assumed to have a nominal uncertainty of ±3 K unless indicated otherwise.

4.2.2 Pressure sensing

The chamber has two pressure transducers connected to the internal volume. Each sensor operates over a different pressure regime. The devices, a Pirani, and a Penning sensor, allow pressure measurements to be made over the range of 10^{-3} to 10^{-5} Pa with an accuracy of around 20 %, and provide coarser information over an even broader range of pressures. Both sensors were calibrated against an active Pirani gauge that is used for checking the performance of pumps in the PSSRI and little disagreement was found between the three pressure sensing systems. By being connected via pipework to flanges on the chamber, the two sensors do not have an ideal response to rapid changes in the chamber's internal pressure. The rate at which shifts in pressure can propagate to the sensors is affected by the gas molecules' mean free path in the connecting pipework. For a gas at a temperature T, with an effective molecular diameter d_m, the mean-free path, l, is

$$l = \frac{kT}{\sqrt{2}\pi d_m^2 p} \qquad \text{Eq. 54}$$

For the water molecule, d_m is approximately 0.28 nm (Kossacki *et al.*, 1997), the effective molecular diameter of CO_2 being somewhat larger at around 0.5 nm (Kossacki *et al.*, 1997). The mean free paths of three atmospheric gases are plotted in Figure 32. At its working pressure of a few tens of Pa, the scale of the vacuum system permits only continuum flow

throughout its volume. This type of flow can lead to the formation of pressure and temperature gradients within the chamber, but these topic will not be addressed in detail.

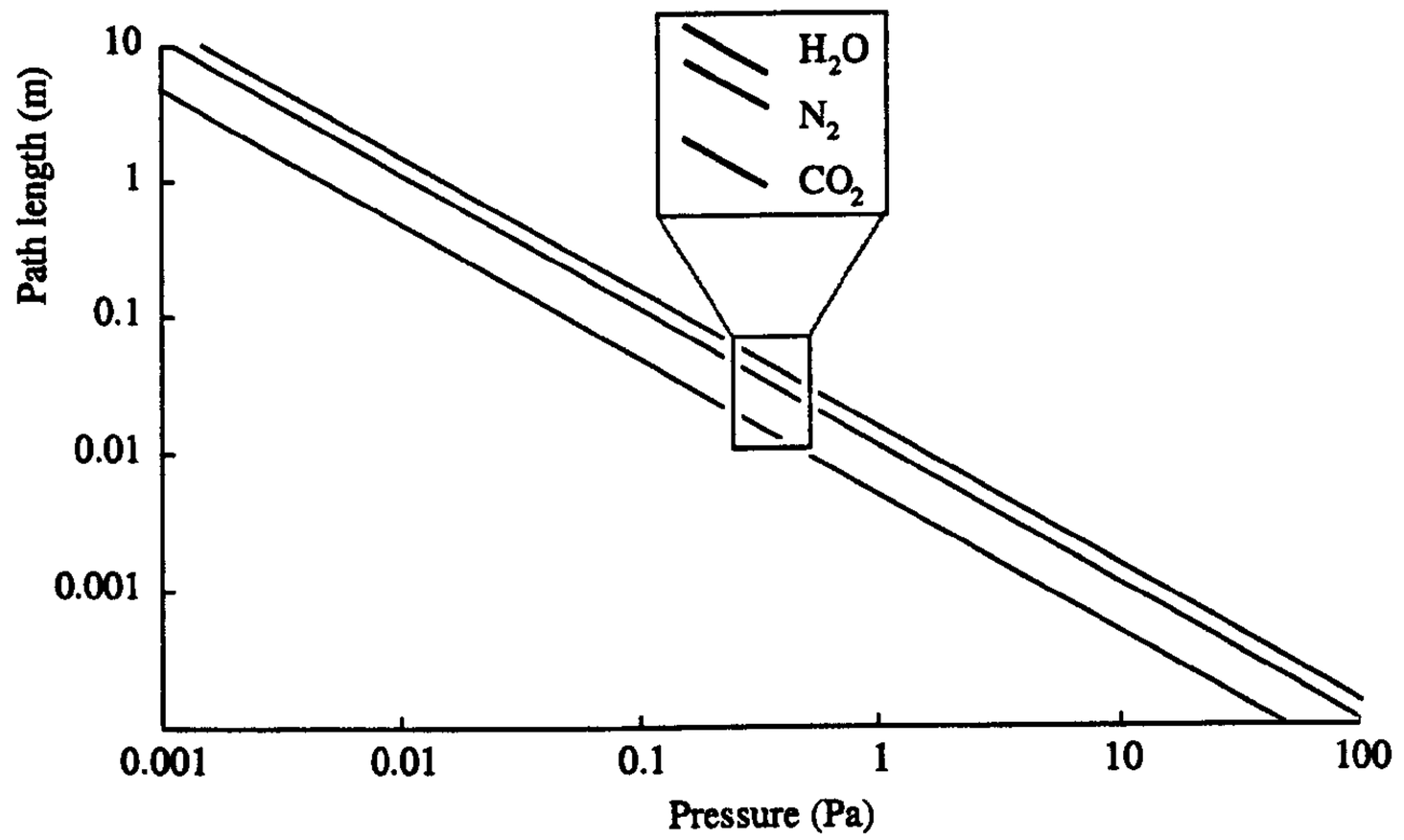

Figure 32 – The mean free path for three atmospheric gases under various pressures at 300 K.

Unlike double-walled chambers that have a gas-tight inner vessel, the vacuum system of this work has a single wall and so the gas temperature T inside the chamber is essentially the same as that of the laboratory air. By being able to predict the mean free path of a gas within the chamber it is possible to determine whether the gas behaves as a fluid (giving rise to continuum, or viscous flow) or as an ensemble of non-interacting molecules. If the physical scale of the system is much smaller than the gas' mean free path then the gas may be modelled as having molecular flow and, at the pressures used in this work (~1 Pa), the chamber interior should instead display continuum flow. The pipework that joins the chamber to the pressure sensors has a diameter comparable to the mean-free path of the ambient gas molecules. The resulting ballistic motion of the gas molecules in the pipework to the pressure sensors should cause a lag in their response to a change in the chamber pressure. This delay can be estimated by calculating the flow rate ($m^3\ s^{-1}$) at which a gas with a mean molecular speed of c can pass through a pipe of length L, and radius a. Such a relationship is given in the reference work of Delchar (1993) as

$$flow \approx \frac{2\bar{c}a^3}{L} \qquad \text{Eq. 55}$$

The pressure sensors share a common section of pipe attached to a 'T' section joint from the chamber with a total volume of approximately 50 cm^3. If this is treated as a separate cavity then it may be evacuated to a given pressure in a time of around (50×10^{-6} m^3 / *flow*) seconds. The gas sensed by the pressure sensors will have undergone at least two collisions with the pipe wall and will therefore be isothermal with the laboratory. The average molecular speed[2] will therefore be no lower than 380 m s^{-1}. The above equation then predicts that a maximum time of 50 milliseconds is needed for the gas in the pressure sensor pipework to be evacuated into the chamber. Conversely, that same delay will occur if the pressure sensor pipework is exposed to a rise in the chamber pressure. At present there is no perceived need for the chamber pressure to be sensed with this rapidity, therefore the pressure sensing equipment is fit for use in the current experiments.

[2] Assuming a Maxwellian speed distribution, the average speed of which is $(8kT/\pi m)^{1/2}$ where m is the molecular mass.

4.3 Mechanical sample alteration

Making deliberate changes to the physical structure of an ice within the vacuum chamber can be achieved by altering the sample's temperature to cause sublimation or condensation, or more finely, by use of a tool attached to the drill stem. This stem consists of a rotatable shaft that is held by a vacuum-tight seal within a frame that allows translation of up to 50 mm along three orthogonal axes. Vernier scales are located on each of the axes and these allow the position of the rotating shaft's tip to be monitored. Information about only the position of the stem's tip is not sufficient by itself - the rate of change of depth is often a more important quantity to measure. To recover this information a depth sensor was attached to the vertical axis of the manipulator stage. This consisted of an optical encoder disc that was connected by an idler wheel to the rotary manual control knob on the vertical axis of the stage. The encoder disc passes between a paired infra-red (IR) emitter and detector, with slots in the disc's circumference periodically blocking the beam when the vertical control knob is rotated. By connecting the detector's amplified output to an input channel on the ADC of the control computer the resulting data stream could be processed to give a very fine record of depth with respect to time. The precision with which the depth rate is recorded depends on the gearing of the vertical axis manual control, and the angular resolution of the optical encoder disc. By counting the number of pulses generated in translating the drill stem through a well-measured distance, it was calculated that one millimetre of vertical displacement produced 298 obscurations[3] of the beam between the IR transmitter-receiver. This gives an overall vertical precision for the position of the tool head of about 1.5 μm.

The downthrust and torque applied through the drill stem were measured by a pair of force-measuring load sensors (Honeywell PK88870) that were mounted as shown in Figure 33. This type of transducer has a small metal piston that, when loaded, causes an imbalance in the arms of a micro-machined silicon Wheatstone bridge. When an appropriate voltage is applied across the bridge the sensor generates a potential difference that is proportional to the force applied. To verify the nominal published sensitivity of 23.5 mV N^{-1} for the sensors, their response to loads up to and beyond their rated range was measured. A regulated 4 V power supply provided the excitation voltage for the sensors.

---

3 Strictly, the software counts the *changes* in the opto-coupler receiver state, thus light to dark and dark to light transitions form the basis of its counting system.

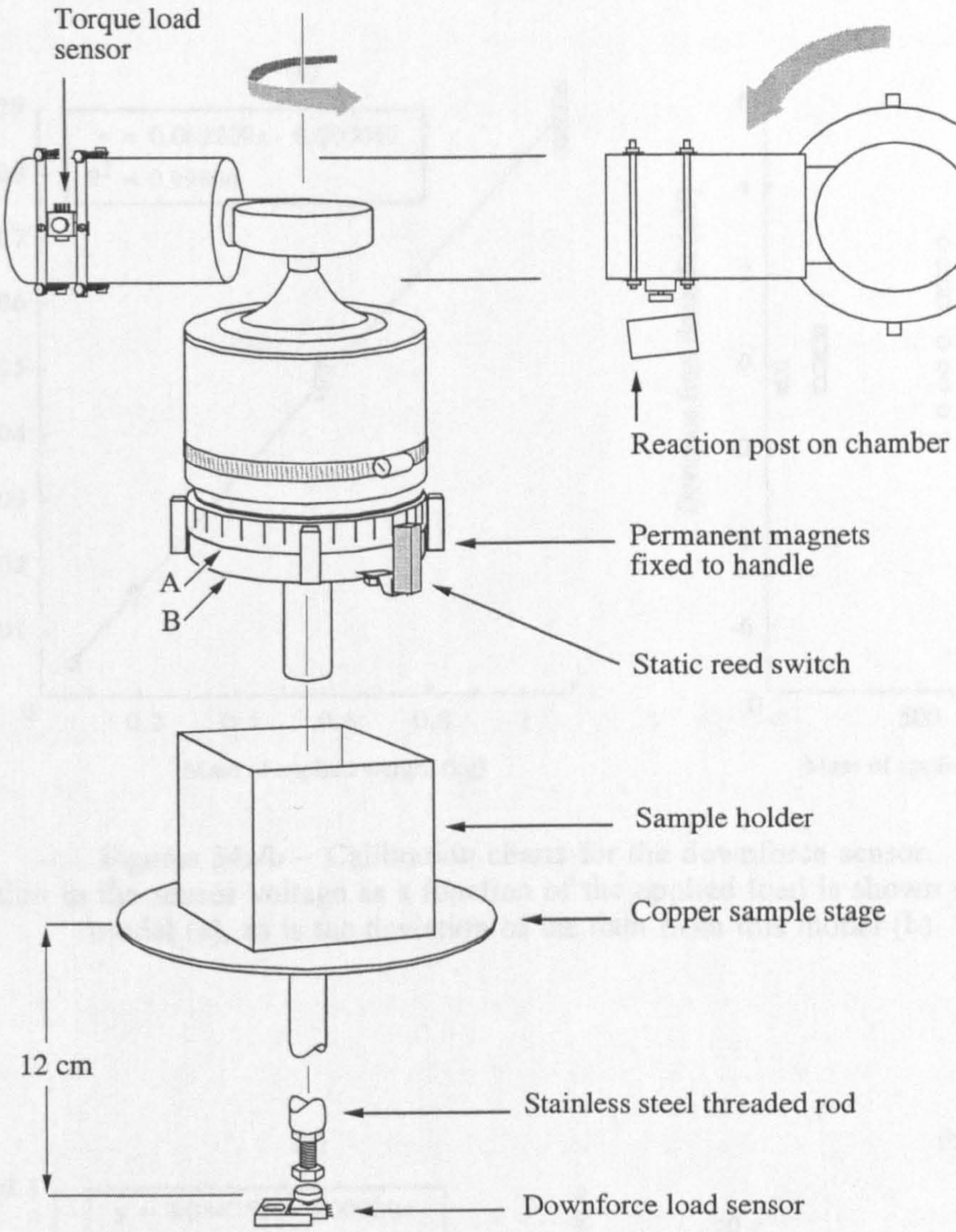

Figure 33 – Showing the arrangement of the load sensors along with the drive system and the magnetic switch used to sense the tool's rotation. The part marked B is fixed and cannot rotate, the part marked A and all parts above it, can rotate.

The arrangement used to support the sample inside the chamber meant that the downforce sensor had to be calibrated *in-situ*, with masses being repeatedly placed in, and then removed from the sample holder. At the start of these calibration tests the leg that joins the downforce transducer to the underside of the sample stage was adjusted so that the sensor was slightly compressed, even when no extra mass had been put in the sample holder. To account for this pre-load force the sensor was calibrated by noting the *change* that an applied load caused to the sensor's output, and not its absolute value. Similarly, when the torque sensor is mounted on the chamber there is a slight load applied by the sensor wiring, and this sensor was also calibrated by noting the *difference* in output caused by a change in its load. The output of the downforce and torque sensors as a function of applied load are shown in Figures 34a/b and 35a/b.

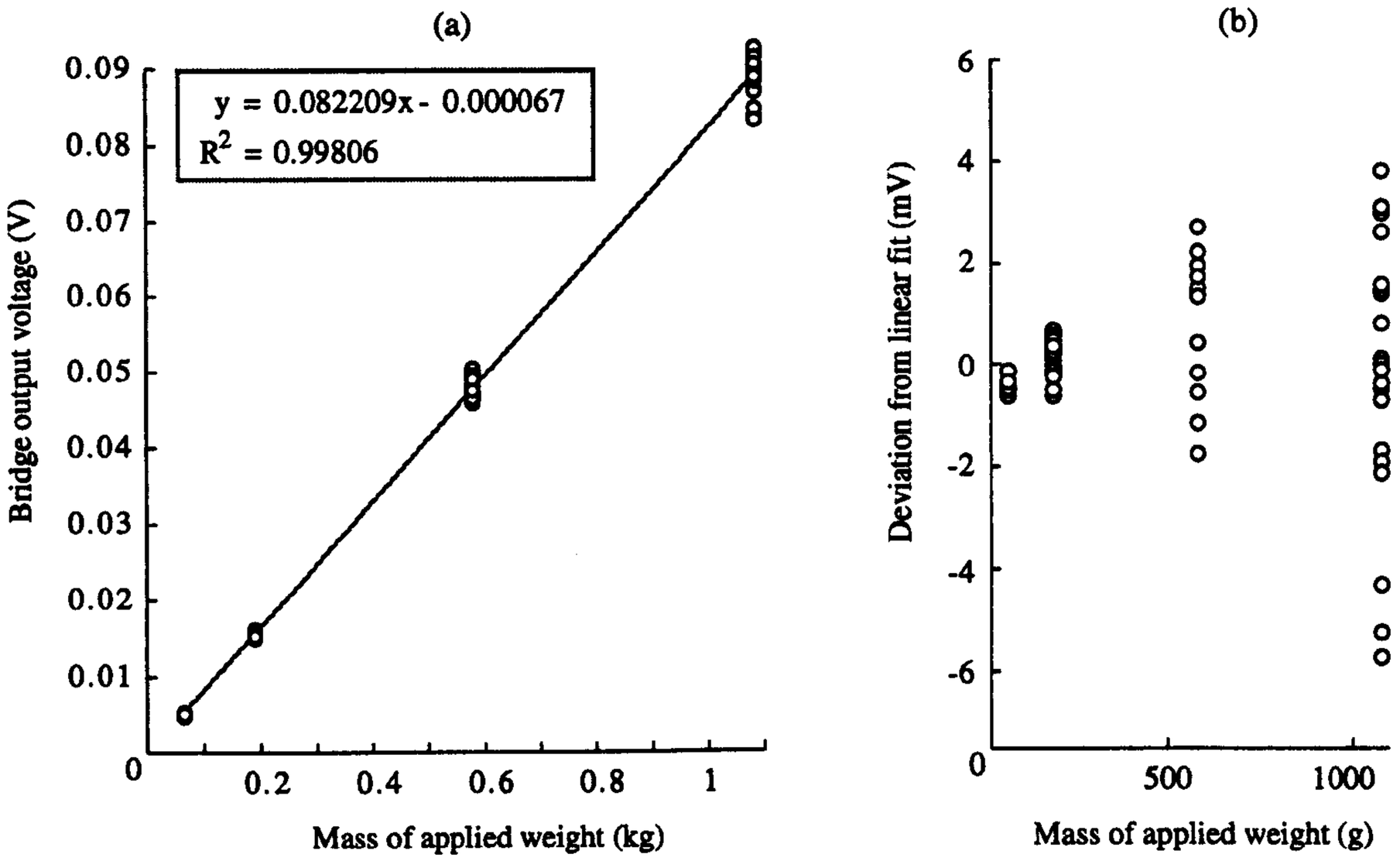

Figures 34a/b – Calibration charts for the downforce sensor.
The variation in the sensor voltage as a function of the applied load is shown with a 'best-fit' model (a), as is the deviation of the data from this model (b).

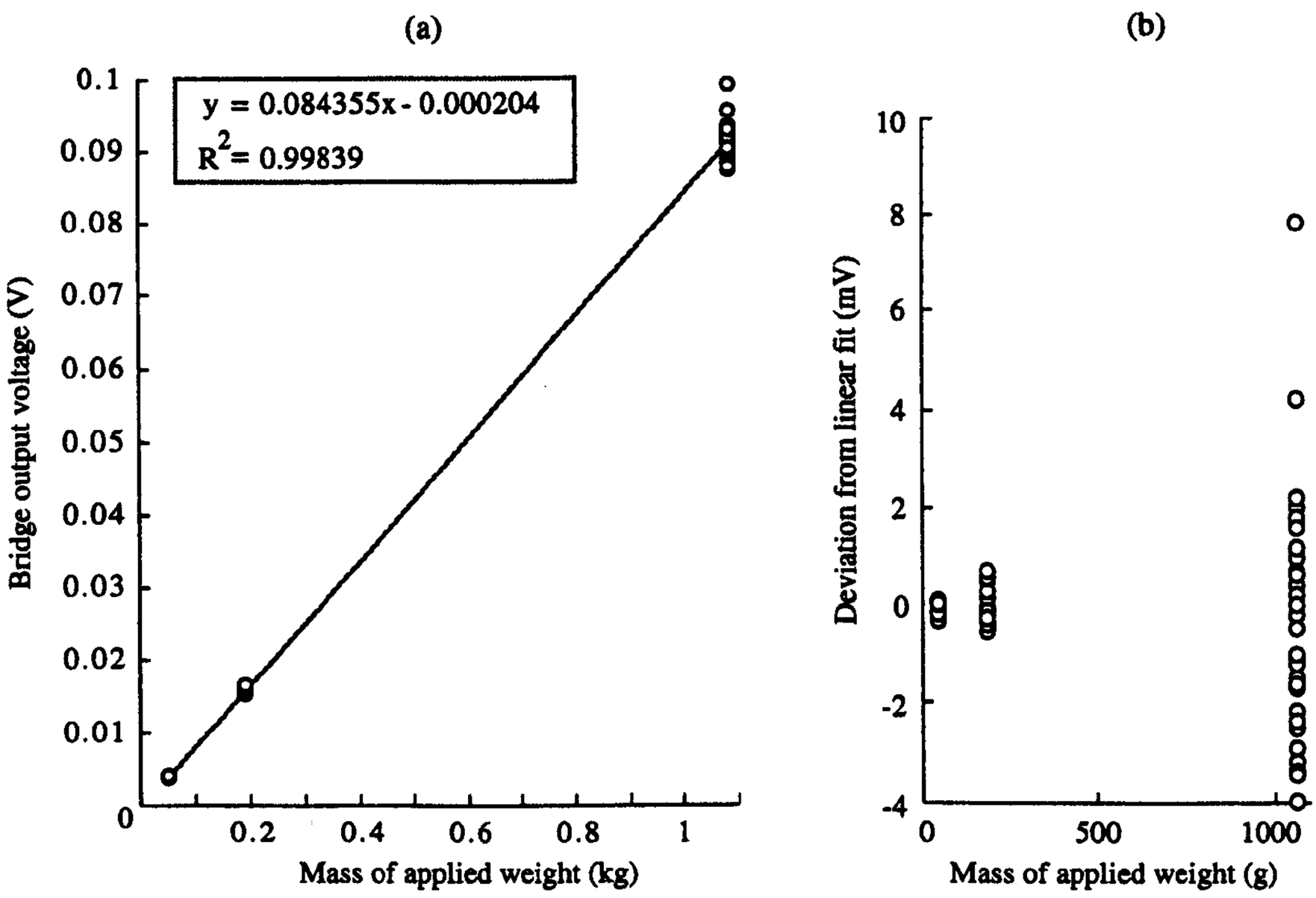

Figures 35a/b – Calibration charts for the torque sensor.
The variation in the sensor voltage as a function of the applied load is shown with a 'best-fit' model (a), as is the deviation of the data from this model (b).

Both of the sensors are essentially linear in their response to the application of a load caused by a mass, m, and for a fixed excitation voltage their output can be described by;

$$V = am + b \qquad \text{Eq. 56}$$

This relationship can be re-written with the local gravitational acceleration g (m s^{-2}) to yield the applied load, F, rather than the loading mass as a function of the sensor output voltage (V).

$$F = \frac{g}{a}(V - b) \qquad \text{Eq. 57}$$

The coefficients of the two transducers (a and b) are derived from the model equations fitted to the data of Figures 34a and 35a For sensor output potential differences measured in volts, and loads measured in newtons, the coefficients for equation 57 for the downthrust transducer are a = 82.2 mV kg^{-1}, and b = -67.4 μV. For the transducer used to measure the torque applied through the manipulator stem the calibration coefficients are a = 84.4 mV kg^{-1}, and b = -204 μV. The scatter in the data may arise from a number of sources, the least controllable of which is the exact position of the sample stage leg on the piston of the sensor. Desk-top tests with a transducer showed that the sensor's specification document was rather generous when it described the 'minimal effect on sensor performance' that off-centre loading caused. A variation comparable to that seen in the sensor calibration charts could be generated by off-centre loads applied to the face of the sensing piston.

4.3.1 Rotation

The manipulator stage can have its central stem rotated by driving a low voltage DC motor which is fixed to the exterior handle of the drill stem. By measuring the force between the motor casing and a fixed part of the chamber, the torque exerted by the motor can be measured and will be essentially equivalent to the torque delivered at the tip of the manipulator stage within the chamber. The particular motor used to rotate the tool uses a worm-drive gear box and its very high stall torque was not measured. In all the experiments no loads were encountered by the motor that led to a significant reduction in its rotation speed and for a given driving voltage it operated as a constant-speed motor.

The torque sensor is mounted such that it has a 100 mm moment arm from the rotation axis of the drill stem, as was shown in Figure 33. A rotation sensing system was devised which consisted of four permanent magnets glued to the outer face of the manipulator handle. A reed switch was mounted to the fixed portion of the manipulator stage at such a distance that rotation of the drill stem handle would cause the reed switch regularly to open and close. By connecting the reed relay to a fixed voltage the rotation speed could be calculated by measuring the frequency of the square-wave signal developed by this magnetically operated switch. This processing was achieved by feeding the digital signal from the reed switch into the computer's ADC which would then save that signal in a file along with other measured variables from a drilling operation. The resulting data file could then be processed in software to recover the required parameters of drilling force, torque, speed, and rotation rate.

The stage and its mechanisms was built by Vacuum Generators of England as a slow-speed multi-axis manipulator (similar to the Omniax model) and it was not designed to support the rapid and sustained rotation of the central stem with an unvarying amount of friction. When the chamber is evacuated the control handle will be brought into contact with the barrel of the stage, shown in Figure 33 as the arrowed items A and B respectively. To account for the resistance to rotation arising from this contact, and the extra torque that would have to be applied to overcome it, each coring experiment started by lowering the cutting head onto the sample material while the tool was rotating at the chosen speed. The torques recorded during the coring experiments were then measured not as an absolute value, but as an offset from the torque level measured before the tool head made contact with the sample.

Along with changes in the drill performance arising from differing chamber pressures, the variation of the torque with an unloaded drill stem was measured and found to be broadly constant for a range of rotation speeds. This finding is shown in the two traces in Figure 36 which were recorded with the drill stem rotating with no axial load at atmospheric pressure. The torque applied by the motor is seen to be essentially constant, if rather 'noisy', for speeds up to 0.72 rev s^{-1}.

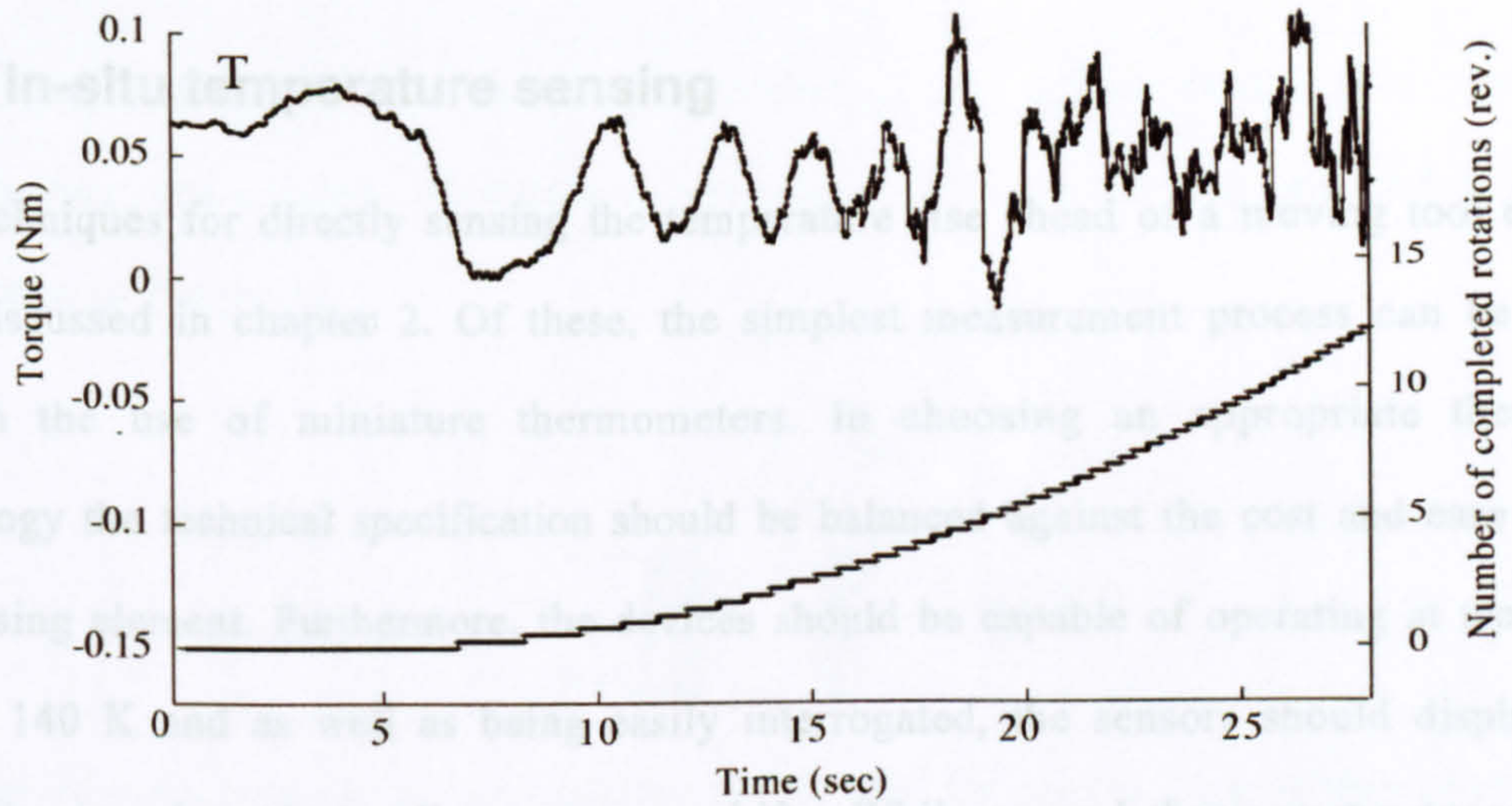

Figure 36 – The torque ('T') needed to rotate the drill stem at an ever-increasing rate (lower trace)

As a demonstration of the accuracy of the manipulator's seals and bearings, Figure 37a shows a coring head that has been driven into a block of water ice to a depth of a few millimetres. Figure 37b shows the sharpness and regularity of the groove cut by the tool.

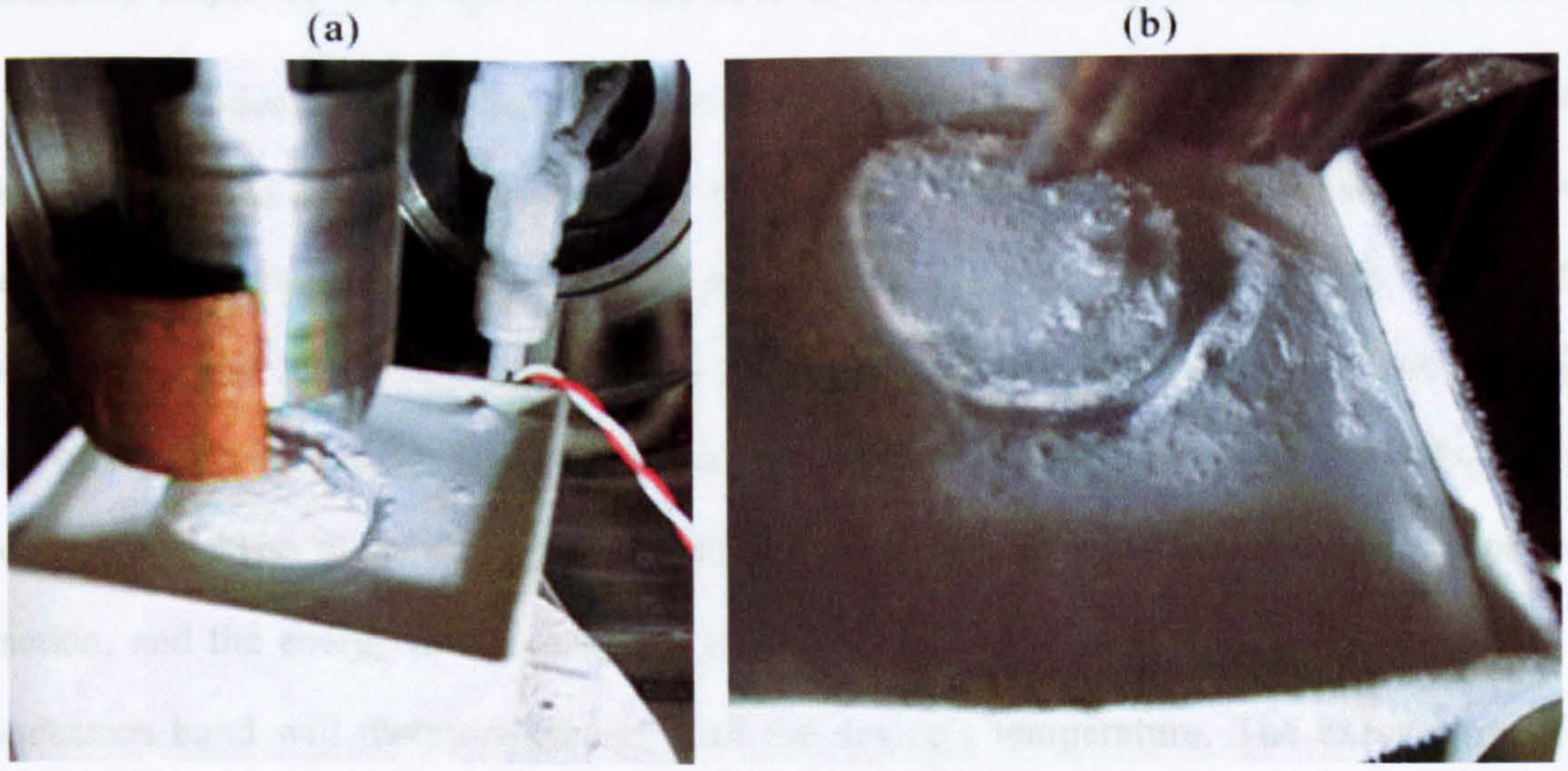

Figures 37a/b – Evidence of the steadiness of the coring head when coring water ice.

Despite the clear-cut appearance of the annular groove there is a very slight degree of eccentricity in the rotation of the tool. Adjustments to the tool holder and the drill stem of the manipulator have not removed this sub-millimetre wobble head although the pipes that support the sample holder can flex and accommodate an amount of off-axis motion. It may be appreciated that the presence of eccentric motion will force the sidewall of the tool, and the vertical edges of the teeth into contact with the cored material. Thus, the torque needed to turn the tool may be expected to vary during each revolution in a cyclical manner.

4.4 In-situ temperature sensing

Techniques for directly sensing the temperature rise ahead of a moving tool edge have been discussed in chapter 2. Of these, the simplest measurement process can be achieved through the use of miniature thermometers. In choosing an appropriate thermometer technology the technical specification should be balanced against the cost and ease of use of the sensing element. Furthermore, the devices should be capable of operating at temperatures around 140 K and as well as being easily interrogated, the sensors should display a high sensitivity to relatively small temperature shifts. While several thermometer types, such as platinum resistance devices, can work at low temperatures and meet the other criteria, miniature versions of these sensors are too expensive to justify their use in the destructive path of a coring head. The ideal device should therefore be technically well-suited, cheap, and easily used. Such thermometer elements do exist in the form of semiconductor diodes which are commonly employed in cryogenic systems as level indicators for liquid nitrogen Dewar vessels.

In the conduction band theory of semiconductor devices, a diode has a conduction band energy that is separated from the valence band of the material by some well-defined amount; the 'band-gap'. If a voltage of appropriate polarity and size is applied across such a device then electrons present in the valence band can be promoted to the conduction band, resulting in a flow of current. For silicon devices the minimum voltage required to cause a flow of current, is around 0.6 V. The diode's temperature affects the energy distribution of the electrons in its junction, and the energy that a particular electron needs to acquire for it to be 'raised' to the conduction band will therefore change with the device's temperature. The exact form of the electrons' energy distribution is not important, but in general the number of electrons with an energy greater than some value E will follow a function similar to

$$N(E) \propto \exp\left[\frac{-E}{kT}\right] \qquad \text{Eq. 58}$$

Thus, at infinite temperatures diodes become perfect conductors because the electrons' energies evenly populate the conduction and valence bands and no forward voltage appears across the diode when current flows through the device. At low temperatures the converse is true and this property can be used to turn commercial electronic components into

thermometers. With this goal in mind, a number of tiny silicon diodes were used to form thermometers; one of these devices is shown with a 'K' type thermocouple and scale bar for comparison in Figure 38.

Figure 38 – An example of the miniature diodes used for *in-situ* thermometry along with a thermocouple junction shown at the same scale

One advantage offered by the miniature diode over the thermocouple is that it is possible to solder very fine wires to the device, much finer than the wires which are generally available for thermocouple junctions. By minimizing the cross-section of the wire the sensor is isolated more effectively from changes in the ice's temperature away from the immediate vicinity and a faster response should be seen to the 'flash' heating of the individual teeth in the coring head. However, this type of thermometer is not without its problems. A voltage source such as a forward-biased diode cannot be used reliably as a thermometer within an electrically conducting material without further modification but it should be noted that pure water ice is an excellent electrical insulator. In principle no unwanted current paths should form around a voltage source, such as a forward-biased diode, when it is embedded in a suitably pure ice sample.

The forward voltage drop across the diode was amplified with a battery-powered instrumentation amplifier, the circuit of which is shown in Figure 39. Values for components in the amplifier's feedback network and in the potential divider at the input were chosen such that the circuit's output spanned as much of the ADC's input range as possible for the temperature region of interest (130 to 150 K). Despite all being taken from the same batch, individual diodes displayed small variations in their electrical behaviour which necessitated each device being calibrated separately. Instead of testing each device in a separate calibration rig, every diode under test was wired to the chamber's harness and monitored using the same cables and logging software that would be employed during the coring procedure.

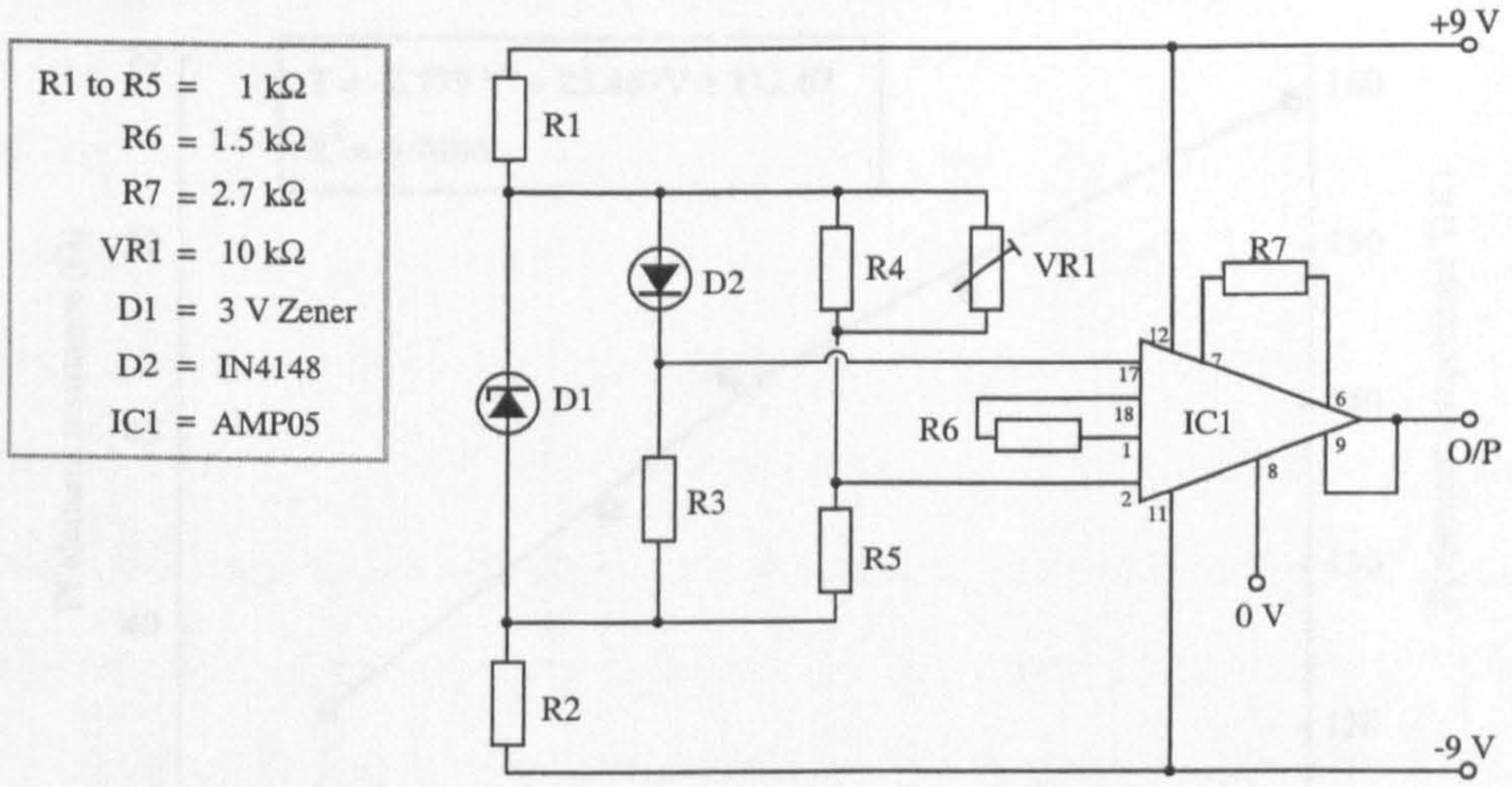

Figure 39 – The amplifier circuit used to amplify the thermometer diode's voltage drop.

Cooling of the diode was achieved by positioning the sensor at various heights above a quantity of liquid nitrogen held in a Dewar vessel. A known Pt100 resistance thermometer was used to measure the temperature of the diode's body and this resistive thermometer was read separately by a high accuracy digital multimeter. The relationship shown in equation 53 was inverted to calculate the platinum thermometer's temperature from its measured resistance. The instrumentation amplifier's output was then fed into the ADC of the computer and the value displayed by the logging software was recorded. To date three experiments have been made with these thermometers; calibration charts for which are shown in Figures 40 to 42.

It is also worth examining the diode's speed of response to changing thermal environments at ambient temperatures of 150 K. If these glass-encapsulated thermometers are presumed to have the bulk thermal properties of silica glass, then the specific heat capacity of the diodes will, at these low temperatures, be around 330 J kg^{-1} K^{-1} (Yang *et al.*, 1992). At 150 K the CO_2 ice surrounding a diode has a specific heat capacity more than three times larger than that of the diode (see appendix A5). By contrast, glass and CO_2 ice at 150 K have near identical thermal conductivities (Yang, *et al.* 1992). From equation 33 one may infer that the temperature rise experienced by the diode ought to vary as $(\lambda\rho c)^{-0.5}$ and therefore for a constant heating power one of the diodes should warm faster than the same volume of ice, by a factor of 140 %. This does not suggest that the diode thermometers will ever be hotter than their surrounding ice, which is the source of the heating power. It simply means that the diode's reported temperature does not lag behind that of the volume of ice that would otherwise occupy its space, thus these diodes are fit for their chosen use.

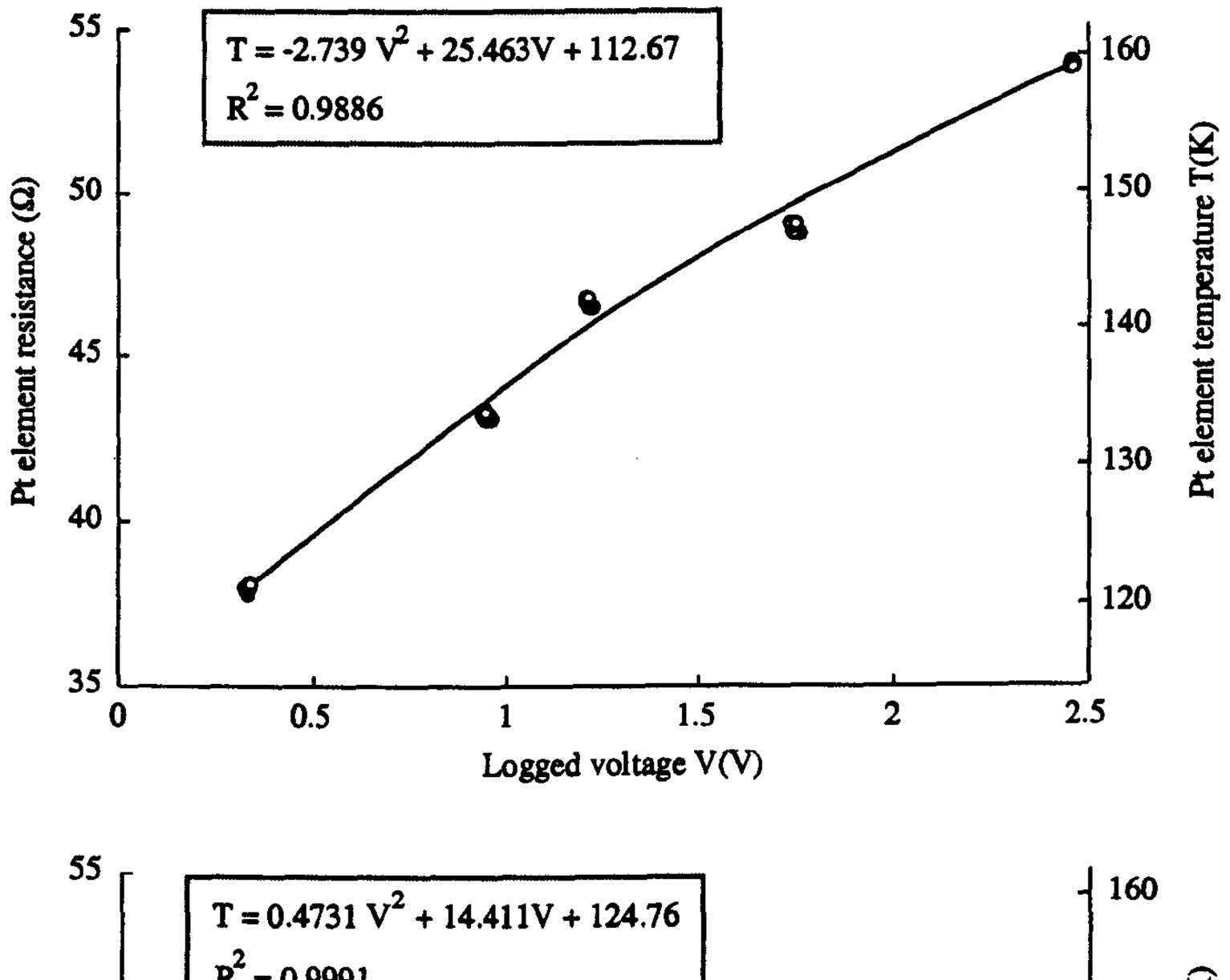

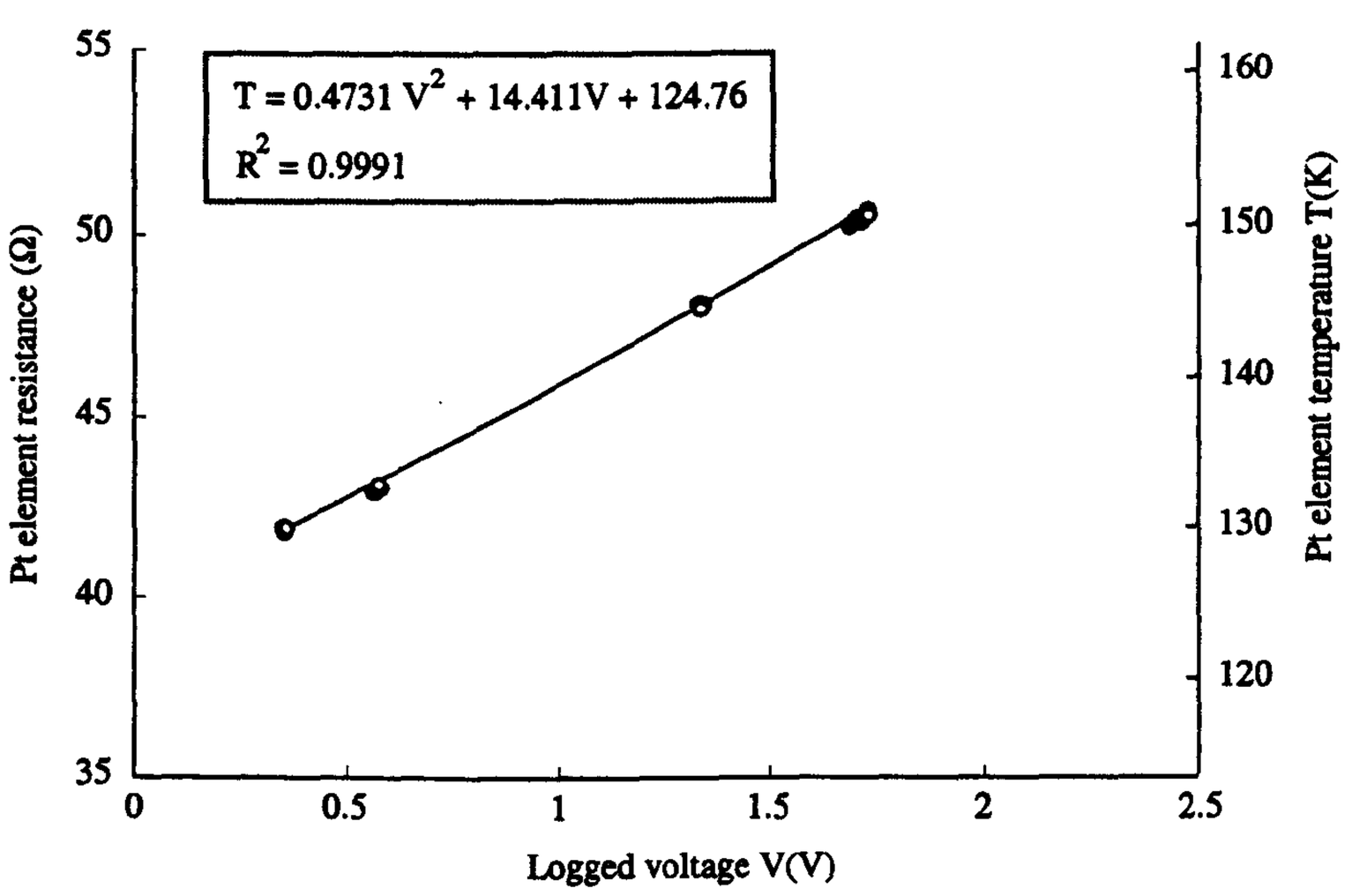

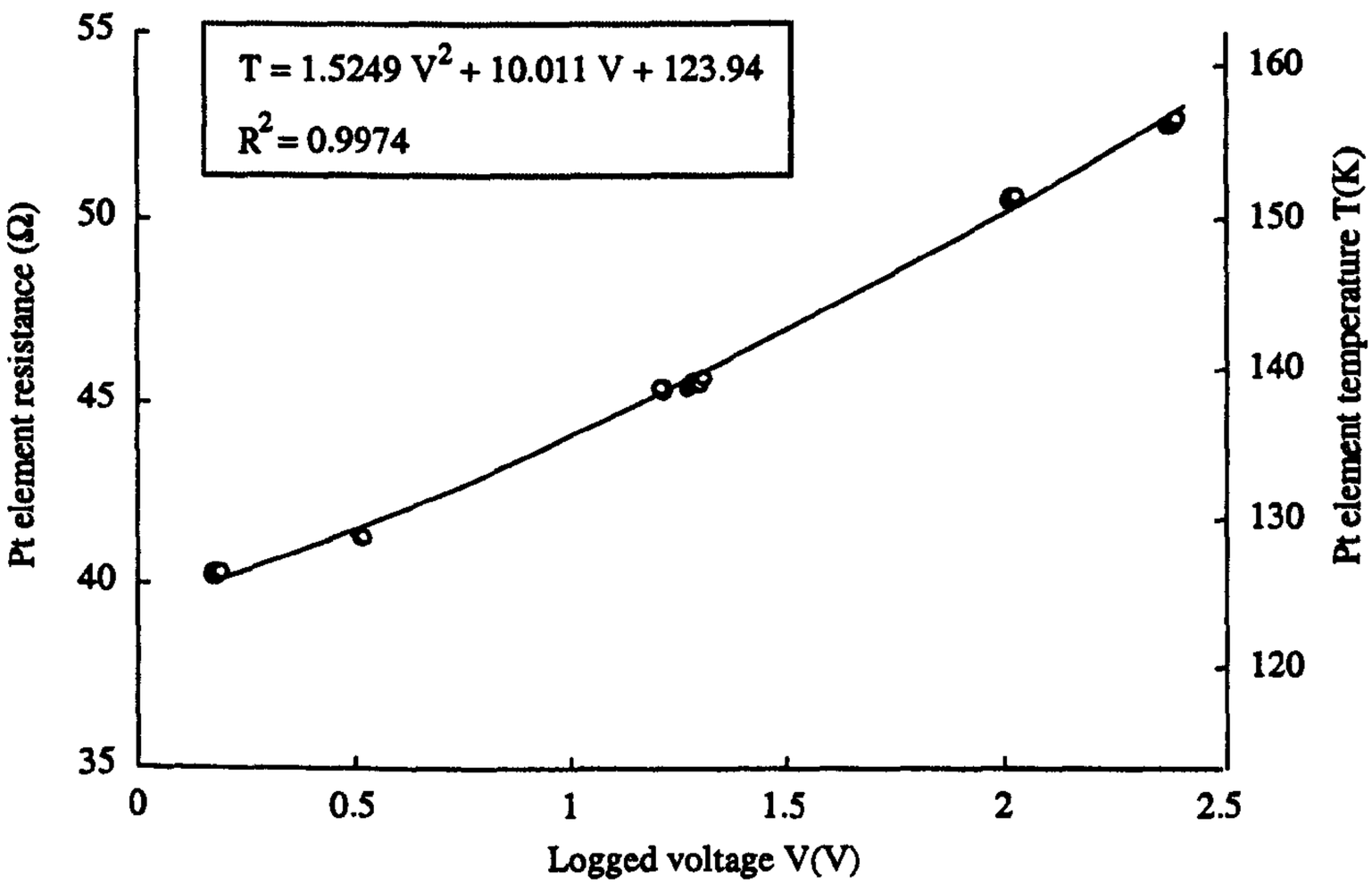

Figures 40, 41, 42 – Calibration charts of output voltage from the thermometer diode amplifier against temperature for diodes #1, #2, #3

With the particular amplifier circuit and the most sensitive of the diodes (#1) a precision of 0.033 K was achieved given the 10 bits of precision with which the signal range of 0 V to 2.5 V is sensed. For the least sensitive thermometer (#3), a change in the lowest bit of the ADC corresponded to a shift of 0.043 K. The diodes were soldered to a pair of thin wires that were in turn attached to a non-conductive frame that could be positioned in the base of the sample holder. By using an inspection mirror the coring head could then be manoeuvred in the horizontal plane until the annular wall of the tool was positioned directly above the diode. This 'coring' position was verified by winding the drill stem downwards so that the head would touch the diode and the 'x' and 'y' vernier scale values on the manipulator stem were noted.

This system was used to measure the temperature rises associated with coring cryogenic ices, and the formation of these materials and the accompanying temperature data will be described in the next chapter.

4.5 Gas capture apparatus

Although not used in conjunction with any of the experiments described in this work, a system was designed which permitted up to four consecutive samples to be taken of the gas inside the chamber and stored in removable vessels. A series of in-line pneumatic valves allowed this gas-capture pipework to be evacuated independently of both the main chamber and the retained samples. This equipment will not be described here but its possible use in further experiments is discussed in chapter 6.

4.6 Data acquisition protocols

Each experiment, using either a rotating coring head, or a blade penetrometer took place over a period of around thirty seconds. During this interval a number of dynamic variables were measured and logged on a computer by a data sampling program[4]. The software on the logging computer performed no processing of the figures during the data capture. Its sole task was to generate a file containing the digital representation of the channel values in the format shown in Table 17.

---

4 "Picolog" produced by Pico Technology Ltd of Cambridge, England.

Table 17: Format of a data file produced by the logging software.

Column	Name	*Format* - brief description
1	Time stamp	*Integer (>0)* Number of microseconds since start
2	Rotation state bit	*Real (0 to 2.5V)* Reed switch open if value > 2 V Reed switch closed if value < 2 V
3	Downthrust channel A	*Real (0 to 2.5V)*
4	Downthrust channel B	*Real (0 to 2.5V)* Force proportional to: (Downthrust_A) - (Downthrust_B)
5	Vertical position marker	*Real (0 to 2.5V)* Reed switch open if value > 1 V Reed switch closed if value < 1 V
6	Torque channel A	*Real (0 to 2.5V)*
7	Torque channel B	*Real (0 to 2.5V)* Torque proportional to: (Torque_A) - (Torque_B)

Two further processing stages were applied to the sampled data. The first consists of winnowing the data file to remove nine out of ten of the entries. This was necessitated because the spreadsheet program used to display the data cannot handle data sets exceeding 32,000 records and the ADC software produces data at a rate of 10,000 samples per second. At this rate data sets could easily be made which could not be manipulated by the charting software (Microsoft Excel 98). Slower sampling rates could be employed by the ADC but the software used an obscure method of setting the sampling period and it was simpler to allow the code to run at full-speed and to discard 90% of the data afterwards. The full-size data files were kept as a safeguard against information being discarded or overlooked and the smaller more tractable files of approximately three to four thousand records were fed into the spreadsheet program. Using the calibration models for the down force and torque sensors the instantaneous loads on the sensors were calculated by that program. The pulses seen in the channels for the rotation and depth rate sensors could also then be summed to give running-totals which gave the tool's angular and vertical displacement at any time during the experiment. Four consecutive high-to-low transitions of the rotation channel data would, for example, correspond to a single rotation of the manipulator stem and 298 consecutive high-to-low changes in the vertical depth channel would be equivalent to 1 mm of vertical motion.

In both the penetrometry and the coring experiments the sampled data are shown as a pair of graphs. The first plots the downforce and torque with respect to the current depth of the tool head, and the second chart shows the running summed values of the digital outputs from the rotation and depth sensors. For the penetrometry tests the torque and rotation traces are not applicable and these traces are omitted. An example of each chart is shown below in Figure 43. The torque and force data are charted in Figure 43a, and the rotation and depth histories are shown in Figure 43b. As has been mentioned earlier, the downforce sensor is always under slight compression and so its output voltage is never zero. Similarly, the trace representing the torque data also may not start at zero because the sensor wiring exerts a small force that holds the sensor gently against its reaction post. Thus, for each run only the changes in the torque and force values during the experiment should be noted.

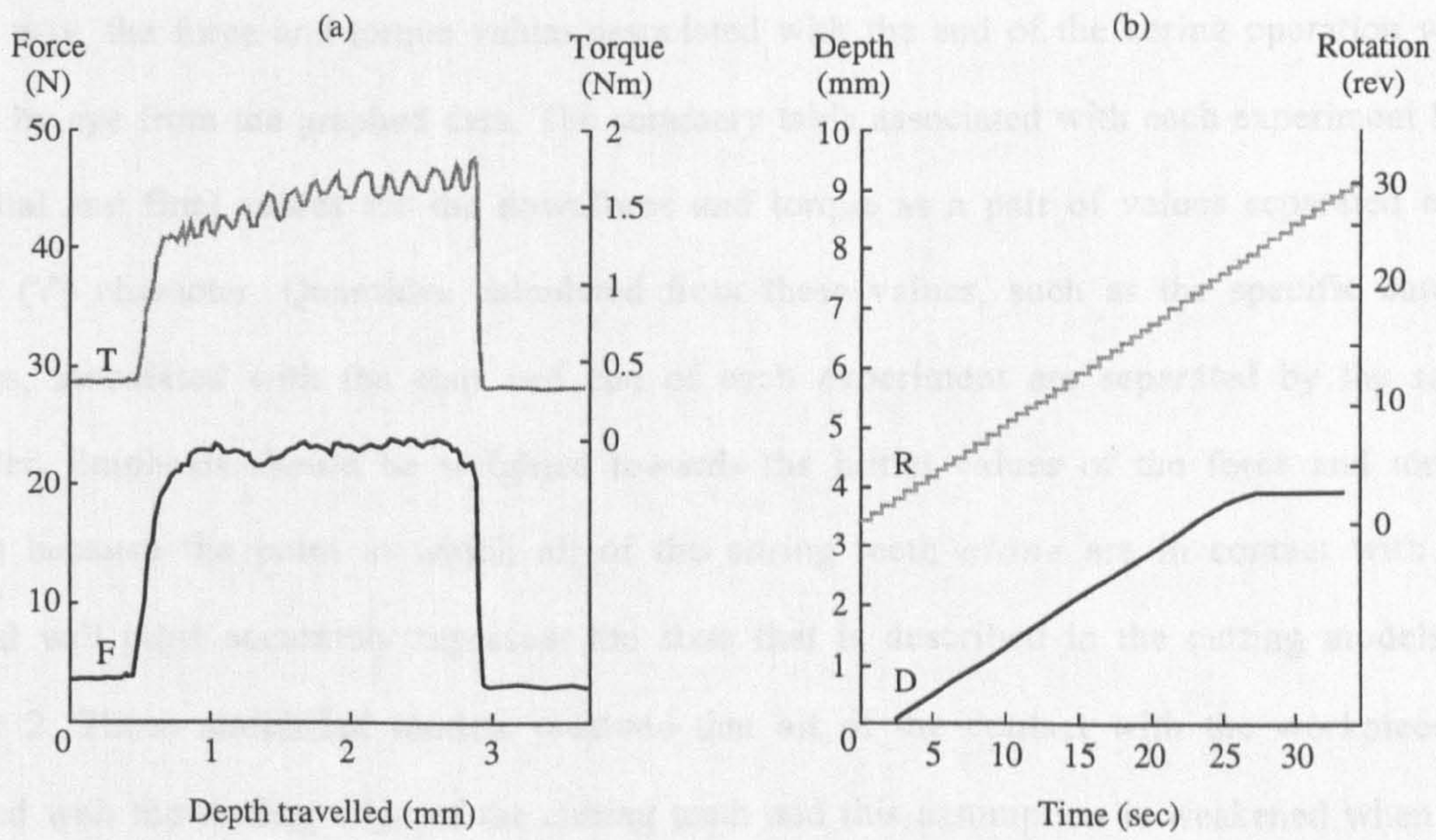

Figure 43a/b - Data sets from a hypothetical coring experiment that illustrate the broad features of the experimental data shown later.

To avoid ambiguity the torque and force traces are labelled 'T' and 'F' respectively and the depth and rotation data are marked with the letters 'D' and 'R'. Each chart that describes a coring or penetration process is also accompanied by a table that summarizes pertinent data from the chart. Except for a single instance in which the drive system jammed, both the rotation speed and depth rate are essentially constant throughout the coring process and only the average value for these variables will be shown in the summary tables.

The force and torque records are harder to summarize neatly. For the coring experiments, it is impossible to guarantee that the tool will meet the material square-on in such a way that it engages all of the cutting edges simultaneously. Therefore all of the teeth on the coring head will be in contact with the material at some short time after the first resistance to motion is recorded. As the head progresses into the material more of the tool's external surface will be forced into sliding contact with the sample, and the vertical outer edges of the cutting teeth will also make regular contact with the workpiece. This extra contact area between the tool and the sample will manifest itself as a rising trend in the torque needed to turn the drill stem. Unlike the torque record, the force value should remain essentially constant during the coring run provided that the cored material has a uniform density and strength. The initial forces and torques shown in the summary tables correspond to the point, judged by eye, at which the appropriate trace has settled from its quiescent value at the beginning of the experiment. In a similar way, the force and torque values associated with the end of the coring operation were gauged by eye from the graphed data. The summary table associated with each experiment lists the initial and final values for the downforce and torque as a pair of values separated by a solidus ('/') character. Quantities calculated from these values, such as the specific cutting energies, associated with the start and end of each experiment are separated by the same character. Emphasis should be weighted towards the initial values of the force and torque records because the point at which all of the coring teeth *alone* are in contact with the material will most accurately represent the state that is described in the cutting models of chapter 2. Those simplified models presume that all of the contact with the workpiece is achieved with the leading edge of the cutting teeth and this assumption is weakened when the tool progresses much deeper into the material.

The summary tables also list the failure stress for the blade penetrometry tests, or the specific cutting energy for the coring experiments. For the coring work the specific cutting energy was calculated with equation 28 from the figures giving the 'initial' point of each coring run described in the last paragraph. Work can then only be dissipated through the cutting of material by the head's teeth. The calculated value of u should accurately reflect only the material's properties and will exclude unwanted 'strengths' that result from overcoming sliding friction or the action of unwanted cutting faces.

5 Vacuum Chamber Experiments

"Don't do nuthin' dumb."

*Akin's 26th law of spacecraft design**

This chapter details the experiments performed with the drill-equipped vacuum system described in chapter 4. The materials studied were chosen to represent the condensed volatiles that are expected to occur in the three regions mentioned in chapter 1, namely a comet nucleus, the polar ices of Mars, and the surfaces of ice-rich Galilean satellites. In forming the samples for the experiments a deliberate choice was made to produce sample targets that had significantly differing bulk densities and strengths. Without firm evidence for the state in which either carbon dioxide or water ices are present at depth in cometary nuclei, or at the surface of Mars' poles, it was prudent to generate materials that would encompass the widest range of bulk strengths and densities. Although the samples formed represent the end-member examples of planetary ices in terms of their porosity, a degree of consideration was also given to the manner in which they would be produced. For bodies with low ambient surface pressures such as Mars and cometary nuclei, the only plausible formation process for an ice is that of condensation from its vapour phase. Furthermore, given the tenuous nature of both cometary comæ and the current martian atmosphere, any condensation will occur without a large temperature gradient and thus with only a modest supersaturation. This ought to lead to the slow formation of a solid from its vapour. In contrast, at the surface of the ice-rich Galilean satellites, ice can also form during the vigorous boiling of water exposed by crustal melting or fracture. In such cases, a layer of ice can rapidly form that insulates the water below from further rapid cooling, and when thick enough, acts as a mechanical brace to prevent boiling in the remainder of the liquid. It is unlikely that pore-free ice would form in such circumstances, but it is useful to study a zero-porosity material to set a limiting case for water ice's behaviour.

The densest samples used in the experiments described later in this chapter took the form of ices that were essentially non-porous and both water ice and carbon dioxide ices were made. All of the carbon dioxide ices were grown from the vapour phase, and the majority of the

* http://spacecraft.ssl.umd.edu/

water targets were made from slowly freezing liquid water. The least dense materials tested in the vacuum system were made from a snow-like form of carbon dioxide and displayed great fragility and significant porosity (~20 %). In using such poorly cohered materials it was hoped that the dependence of failure stress with some bulk property, such as density, could be established. Such a relationship has not been measured empirically for cometary analogue materials, which are frequently formed from porous ice mixtures.

The differences between the ices used in this chapter led to the use of two separate methods for measuring the failure strength. The low density snow-like samples were probed with a broad blade penetrometer and a strength-like parameter was found by measuring the resistance to motion of this penetrometer. Materials, such as the dense ices, with failure strengths several orders of magnitude higher than the snow-like samples could not be indented with the blade penetrometer. Instead, the method described in section 2.2.1 was used to measure the amount of work needed to fail the material through cutting and in doing so the specific cutting energy and the power expended by the tool were calculated.

5.1 Blade penetrometry of weak materials

As was discussed in chapter 2, penetrometry as practised in surveying and geophysical prospecting relies upon a database of empirical data that relate the resistance experienced by a penetrometer to other quantities such as its tensile strength, which would usually be determined through laboratory testing. In the absence of such well-constrained experiments a test material with well-characterized properties was sought that would allow comparative measurements to be made of the cryogenic carbon dioxide snow samples.

5.1.1 Test material properties and results

A low density closed-cell polymer called *Rohacell®* (type 31), made by Röhm GmbH of Darmstadt, was available in a small selection of foamed polymers at the Open University and this material was used to demonstrate the utility of the simple models derived in section 2.1 (equations 16 to 18). The pertinent property values of *Rohacell®* are listed in Table 18 along with the same properties for dry balsa wood as a comparison.

Table 18: Comparative properties of *Rohacell* (a test material), balsa wood, and water ice.

Property	*Rohacell*®	Dry balsa wood	Water ice (0°C)
Compressive strength (Pa)	4×10^5	5×10^6	$\sim 10^7$
Tensile strength (Pa)	1×10^5	9.5×10^6	$\sim 10^7$
Density (kg m^3)	30	96	1090

Figure 44 shows a photograph of the blade penetrometer and a cross-sectional cut through a piece of *Rohacell*®. The scale bars show that the material's cells are not larger than the breadth of the blade and over the 25 mm length of the knife's leading edge the material may be treated as a continuum because the failure of one cell will lead to an imperceptible change in the force opposing the blade's motion.

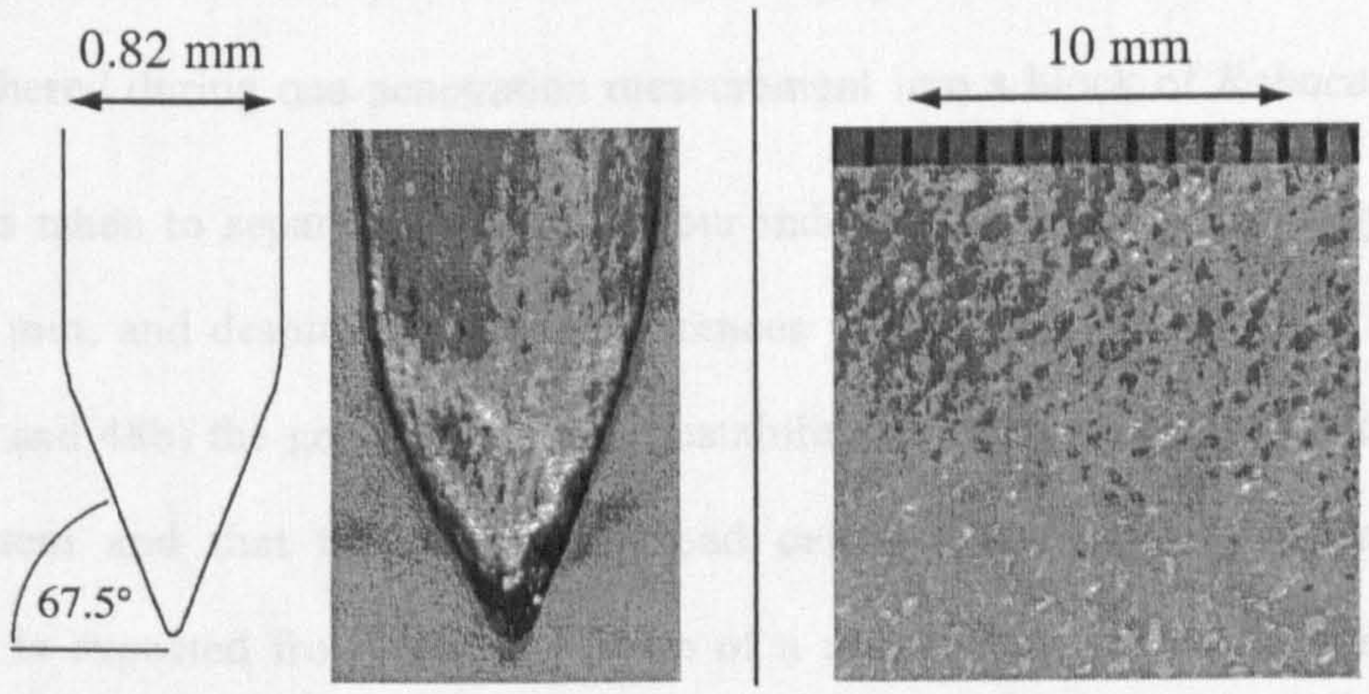

Figure 44 – The blade penetrometer tip and a photograph of a section through the test material.

The blade was fashioned from a section of copper sheet and manually filed to a knife-edge with regular checks made with a microscope to ensure an even and symmetric edge. Copper was chosen for the blade's material so that it could be easily polished to a high sheen to minimize the coefficient of sliding friction. It was hoped that by removing any asperities from the blade's surface, the motion of the penetrometer through both the *Rohacell*® and the cryogenic snows would be impeded only by the act of slicing and failing the material ahead of the blade. In such a case the simplified model of equation 19 might then be applied to establish the failure strength of the cryogenic snows.

The blade shown in Figure 44 was mated to a short piece of stainless steel studding as shown in Figure 29, so that the blade could be fixed to the stem of the manipulator in the

vacuum system. A slab of the *Rohacell®* was then cut so that it would be firmly held within the sample holder and present a flat plane to the knife edge of the penetrometer. The blade was then driven at a constant rate through the plastic foam, with the downforce and vertical depth rate being logged by the computer through its ADC. Each penetration event lasted for only a few seconds and generated approximately 20,000 lines of data which held the four channels of interest; a time-stamp, a vertical displacement counter, and two channels for the downforce sensor. No rotation was applied to the manipulator stem and so the fields in the final output file for rotation and torque were blank. The downforce data were fed into a spreadsheet program that calculated both the vertical depth traversed by the blade, and the applied downforce. The results from that program are shown in Figures 45 to 48, and in Tables 19 and 20. To allow the data to be compared more easily, data from two applications of the penetrometer are shown on each of the following two pages. Each chart and its associated table shows data gathered during one penetration measurement into a block of *Rohacell®*.

Care was taken to separate each of the four indentations into the block by a distance of no less than 8 mm, and despite the slight differences visible in the penetration rates[1] (Figures 45b, 46b, 47b, and 48b) the good degree of repeatability suggests that there is little slack in the manipulator stem and that the downforce load cell has accurately reported the smooth resistance that is expected from the penetration of a uniform material by a normally inclined knife-edge.

Figure 45a (top-left overleaf), 45b (middle-left) and Table 19a represent the data from one experiment, with Figures 46a, 46b, and Table 19b showing the data for a second separate indentation of the test material with the penetrometer.

The trend seen in each record of downforce suggested that there was a measurable coefficient of friction between the test material and the blade penetrometer; the downforce required as a function of depth rises during each penetration. To quantify the sliding friction the full penetrometry model of equation 16 was applied and so the summary tables also list values for the coefficient of sliding friction.

---

1 The charts show how the blade depth changes with time and the slope of that line is therefore equivalent to an instantaneous speed.

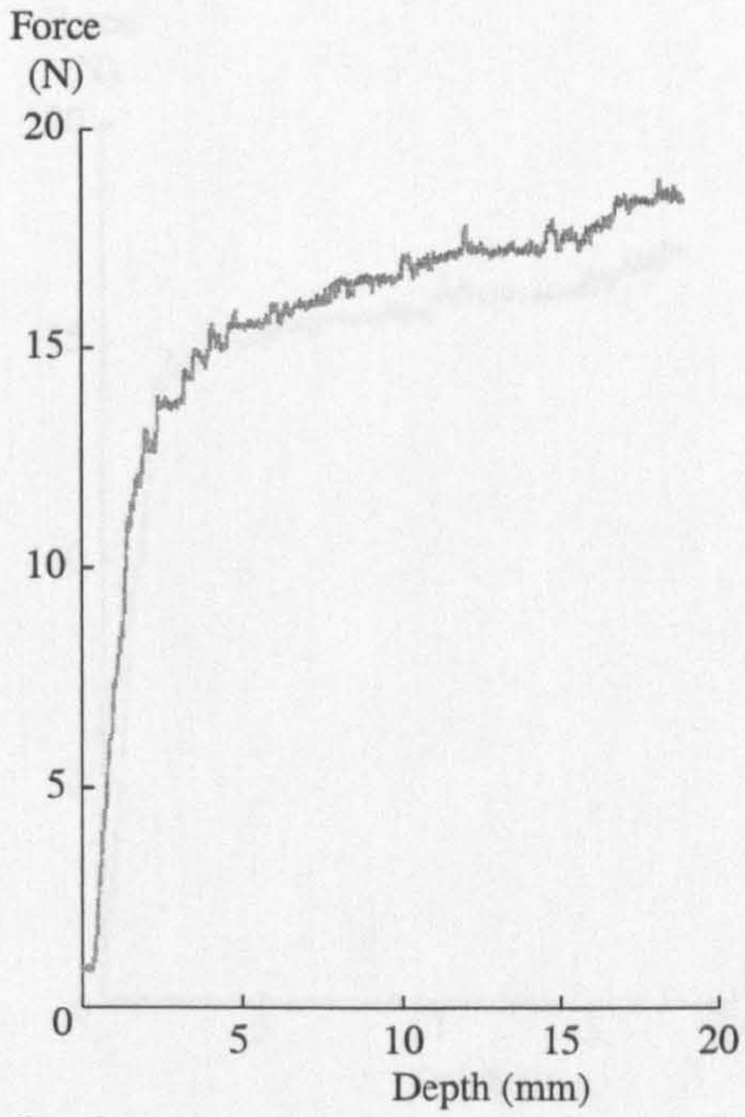

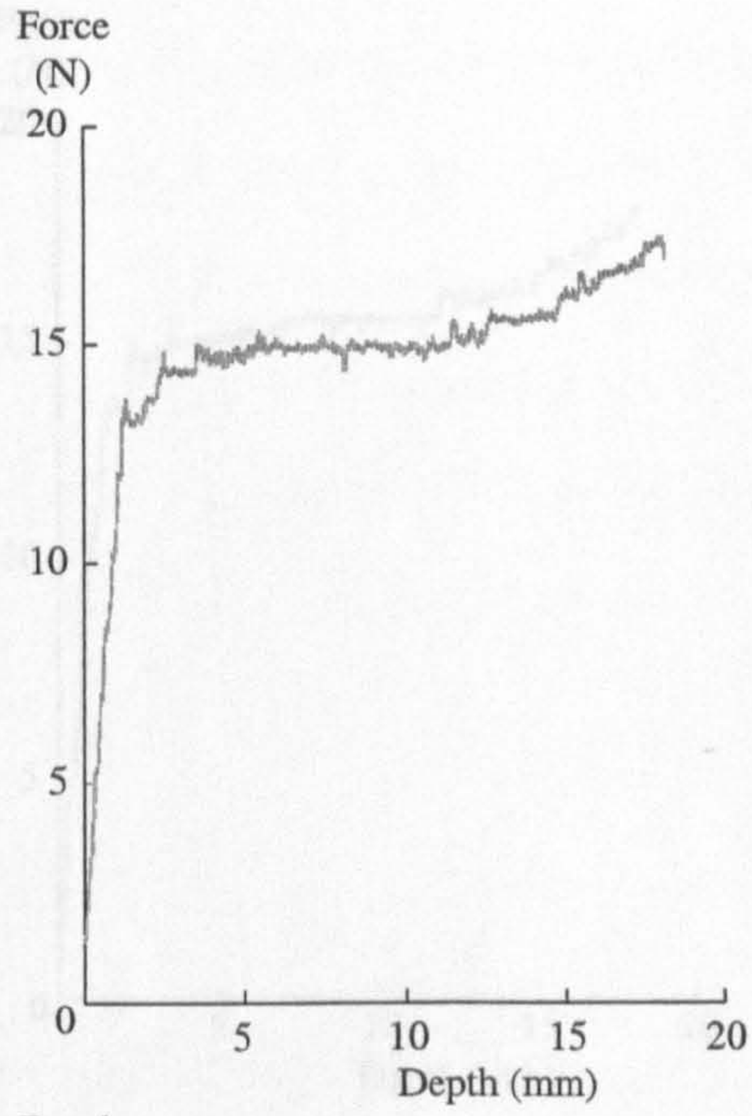

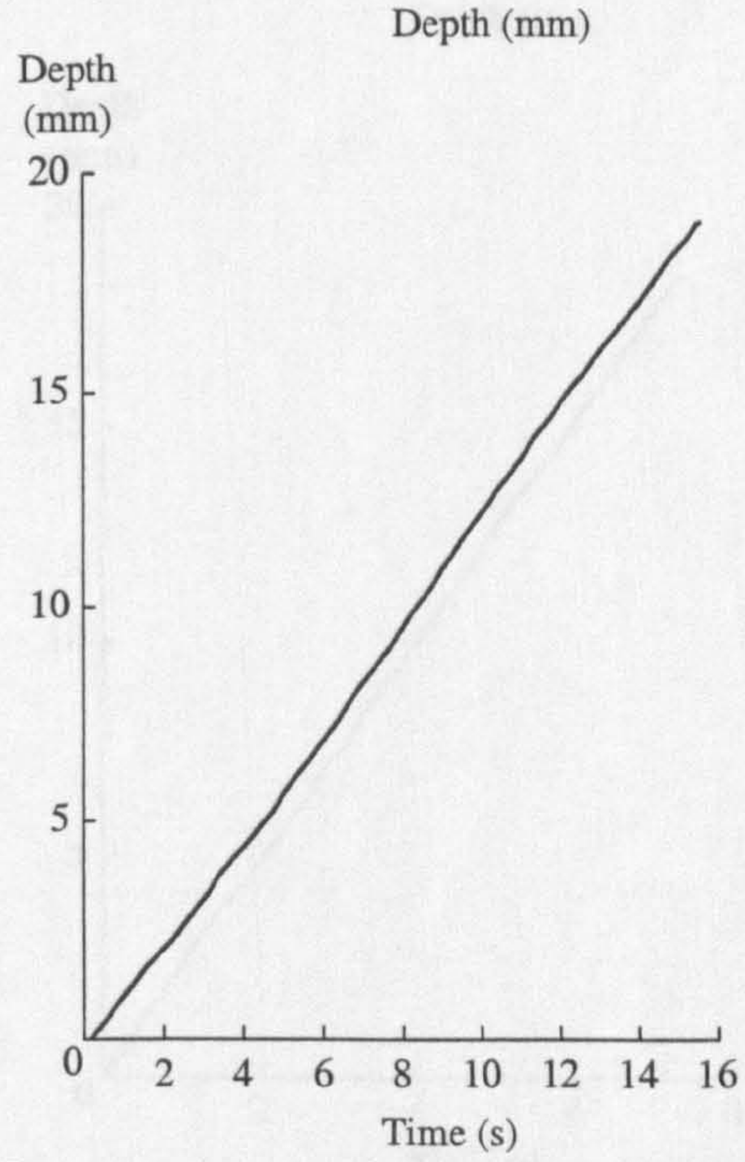

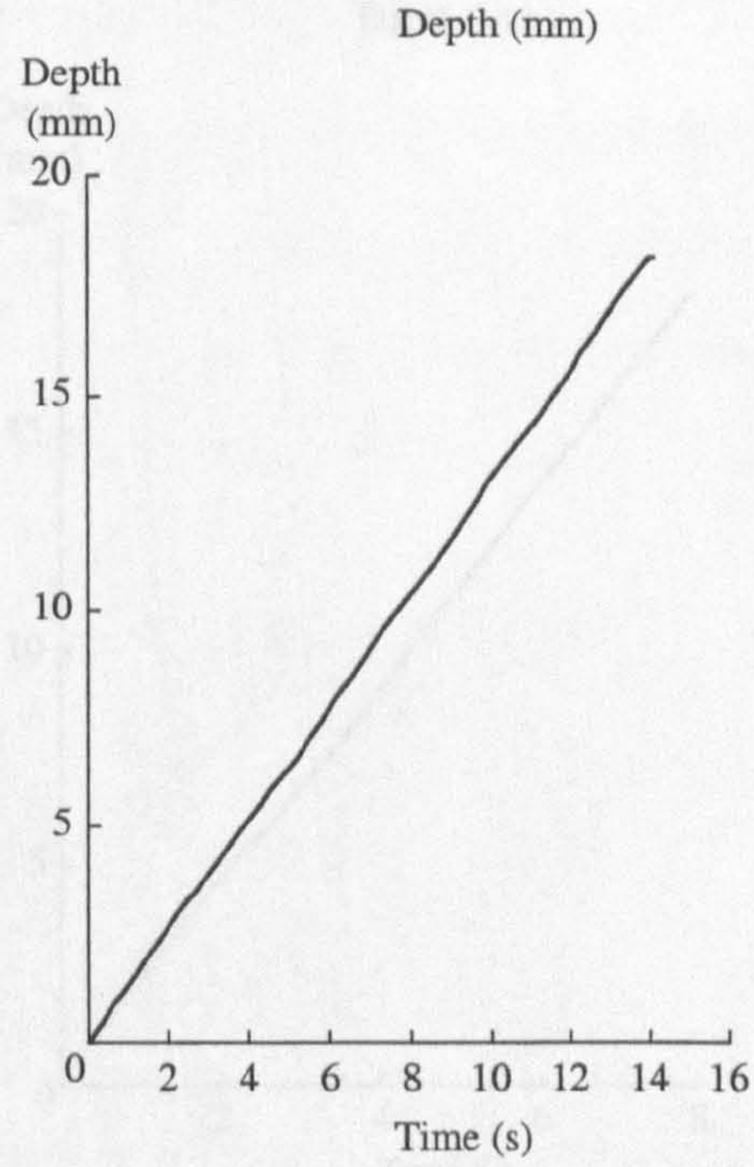

Figures 45a,b and 46a,b - Force and distance data for two separate indentations of a block (called sample A) of Rohacell®. The left-most charts and table show the data from the first experiment, and the right-most charts and table display the data from the second.

Tables 19a and 19b: Summary data for the above charts.

Sample temperature (K)	300
Chamber pressure (Pa)	10^5
Tool depth rate (mm s^{-1})	1.249
Initial / final force (N)	14.7 / 18.5
Coefficient of friction	0.005
Failure stress (kPa)	670

Sample temperature (K)	300
Chamber pressure (Pa)	10^5
Tool depth rate (mm s^{-1})	1.3023
Initial / final force (N)	14.1 / 17
Coefficient of friction	0.004
Failure stress (kPa)	620

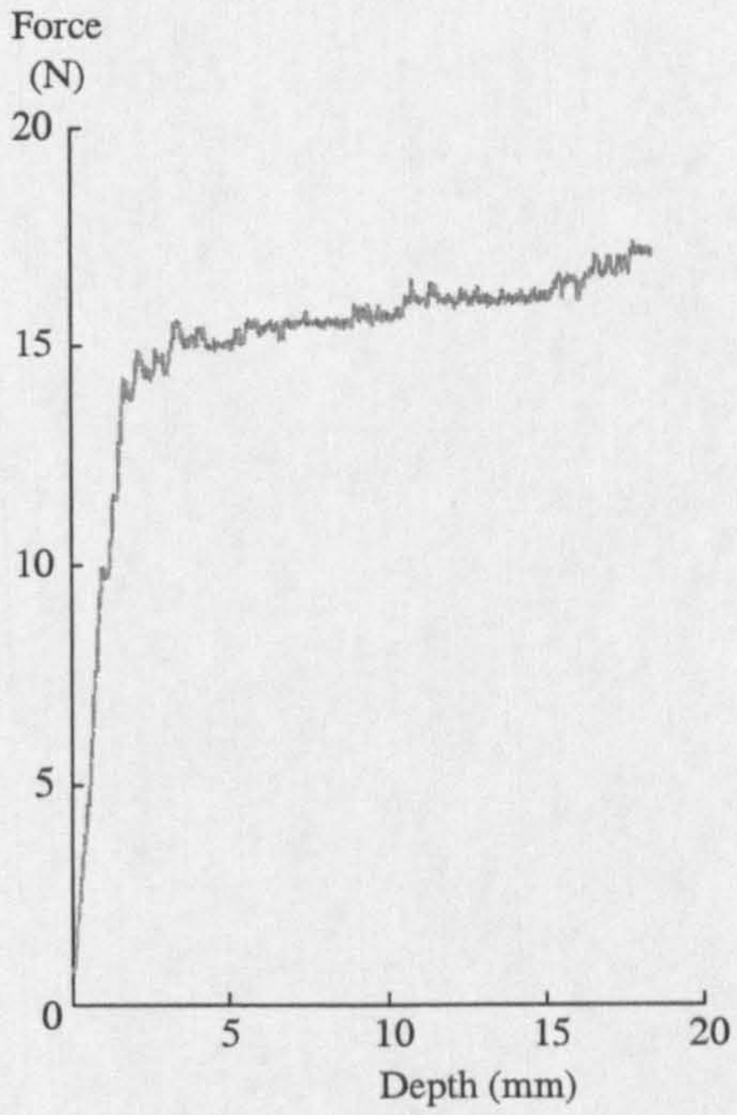

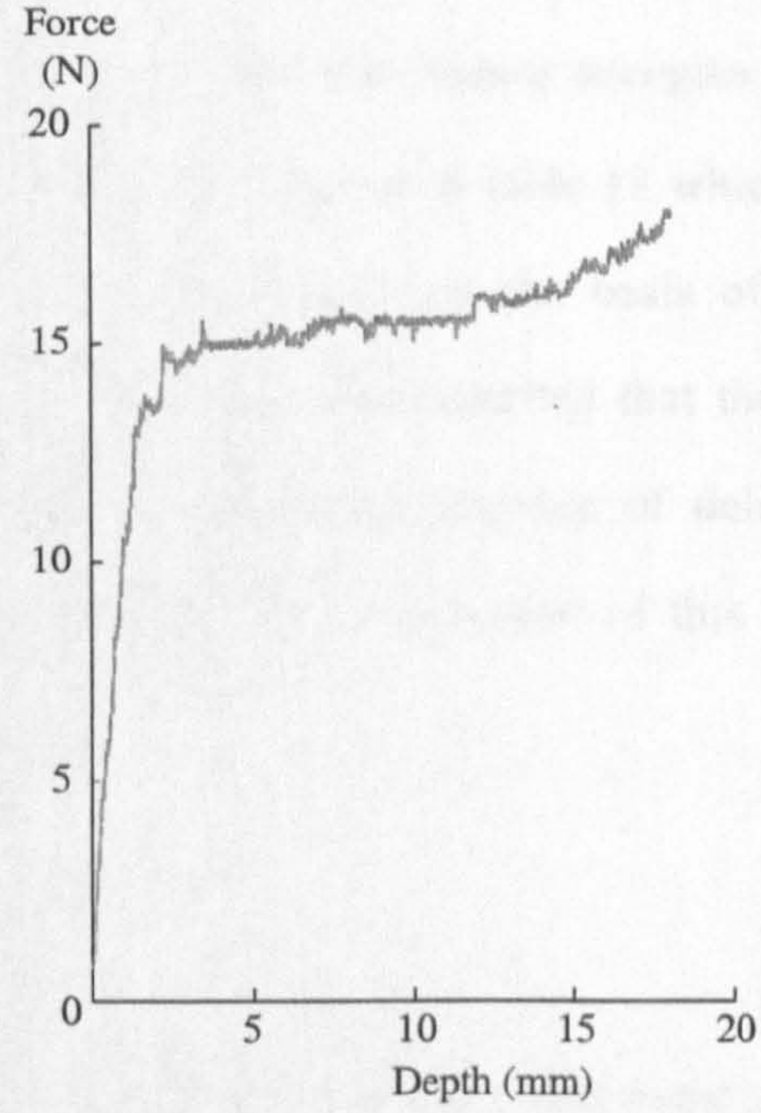

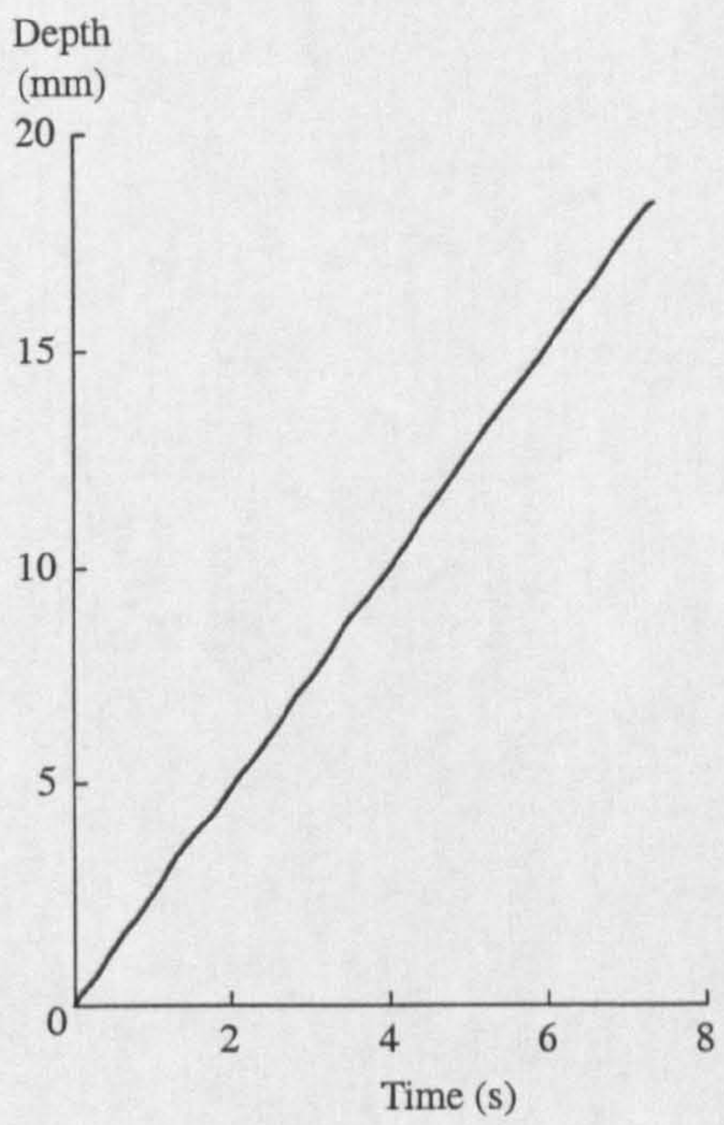

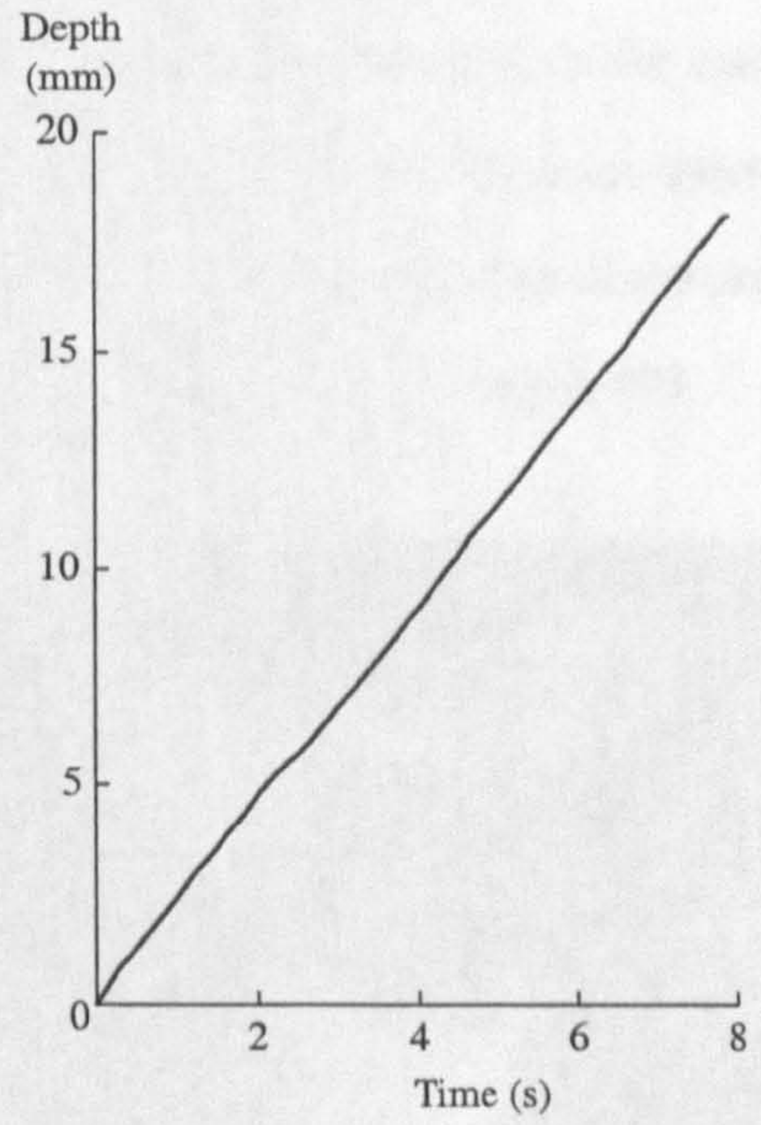

Figures 47a,b and 48a,b - Force and distance data for two separate indentations of a second block (sample B) of Rohacell®. The left-most charts and table show the data from the first experiment, and the right-most charts and table display the data from the second.

Tables 20a and 20b: Summary data for the above charts.

Sample temperature (K)	300
Chamber pressure (Pa)	10^5
Tool depth rate (mm s^{-1})	2.573
Initial / final force (N)	14.7 / 17
Coefficient of friction	0.005
Failure stress (kPa)	620

Sample temperature (K)	300
Chamber pressure (Pa)	10^5
Tool depth rate (mm s^{-1})	2.266
Initial / final force (N)	14.5 / 17.5
Coefficient of friction	0.003
Failure stress (kPa)	640

The *Rohacell*™ test material yielded an average σ_d value of 630 ± 15 kPa and, for the polished copper surface employed, a value for μ_f of 0.004 ± 0.001. The failure strengths of this test material lie between the compressive and tensile strengths reported in table 18 which is in accord with the limiting strength that a brittle material can display on the basis of stress models such as those of Mohr. The use of this penetrometer has demonstrated that the load-sensing apparatus of the chamber and its data logging software are capable of delivering repeatable objective measures of a material's failure strength. The application of this tool to fragile cryogenic snows ice is described next.

5.1.2 CO_2 snow penetrometry

One practical advantage of the blade penetrometer design over the more usual conical head was that by translating the penetrometer sideways to a fresh section of the material a number of experiments could be performed with a single block of snow. Separate indentations could not be made less than 5 mm apart before the snow failed at the wall area of the preceding penetration. An example of an indentation made by the blade is shown in Figure 49b.

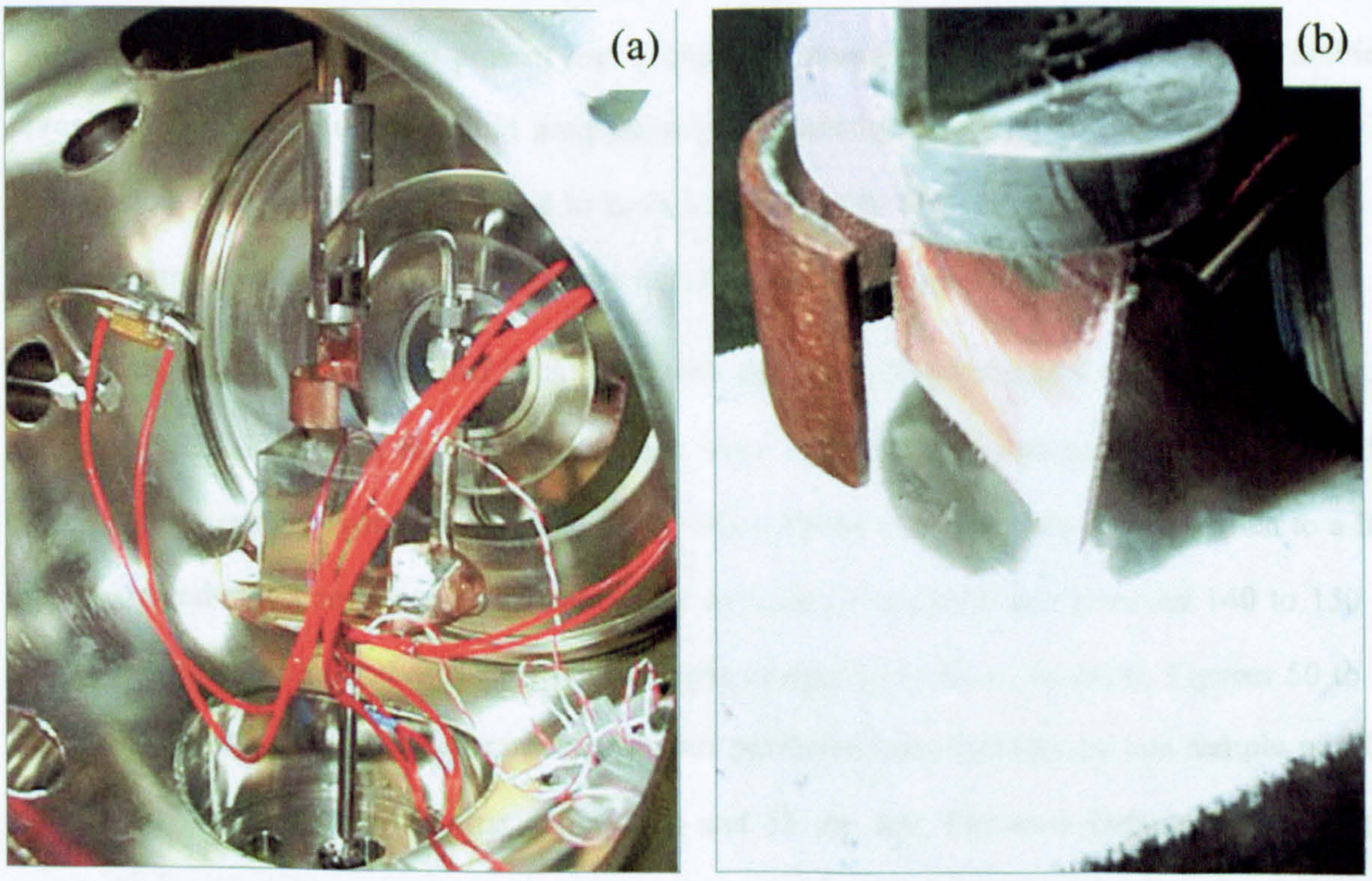

Figures 49a,b — The chamber prior to the addition of the CO_2 / liquid nitrogen emulsion (a) and an example indentation made by the blade penetrometer (b).

The samples were formed away from the chamber with a device made by the Nichi Koeki company (Tokyo). This apparatus, fed by a high-pressure cylinder of liquefied carbon dioxide, forms a fine-grained snow by Joule-Thompson expansion through a narrow orifice. The snow was held in a polystyrene box and then saturated with a few hundred millilitres of liquid nitrogen to form a smooth emulsion. By mixing the snow with nitrogen it was hoped that sublimation and subsequent sintering of the material could be avoided. At this storage temperature of around 77 K the vapour pressure of carbon dioxide gas over its solid is a little more than 0.6 μPa (Brown and Ziegler, 1980) and there should be a negligible amount of mass transfer between the solid and gas phases of the ice.

The sample holder in the vacuum chamber was pre-chilled by running the cryogen feed system at a low level while pouring a small amount of liquid nitrogen into the holder to displace moisture-laden air. Once the sample holder had been cooled to around 200 K the emulsion of CO_2 and liquid nitrogen was ladled into the holder and scraped level with a knife blade. By cooling the CO_2 with liquid nitrogen very little CO_2 gas would be evolved from the ice and safety precautions centred on the use of appropriate gloves and liquid nitrogen handling techniques. Measurement of the material's density was, however, hampered by the liquid nitrogen carrier fluid. When poured into a chilled container of known dimensions at ambient pressure, the CO_2 emulsion would progressively lose nitrogen through boiling. In its minimally compacted state the snow was found to have a bulk density of 1300 ± 50 kg m^{-3}, in contrast to the literature value of 1590 kg m^{-3} for the density of fully compacted carbon dioxide ice.

Once the sample holder had been filled with the CO_2 / liquid nitrogen emulsion the vacuum chamber was closed and the system's pumps were started along with the cryogen pump. The pumping and cooling systems were allowed to run until the chamber pressure had fallen to a few millibars and the sample holder thermometers indicated a temperature of around 140 to 150 K. The blade penetrometer was then driven into the sample at various locations. Figures 50 to 53 show the results from four separate experiments performed sequentially on one sample of CO_2, with Figure 50 showing the first penetration and 53 the last. For each indentation the initial peak force, and the final force measured by the penetrometer is shown with the values separated by a solidus ('/'). From these data the corresponding failure stress is computed by equation 19. All four indentations were made over the course of around two minutes.

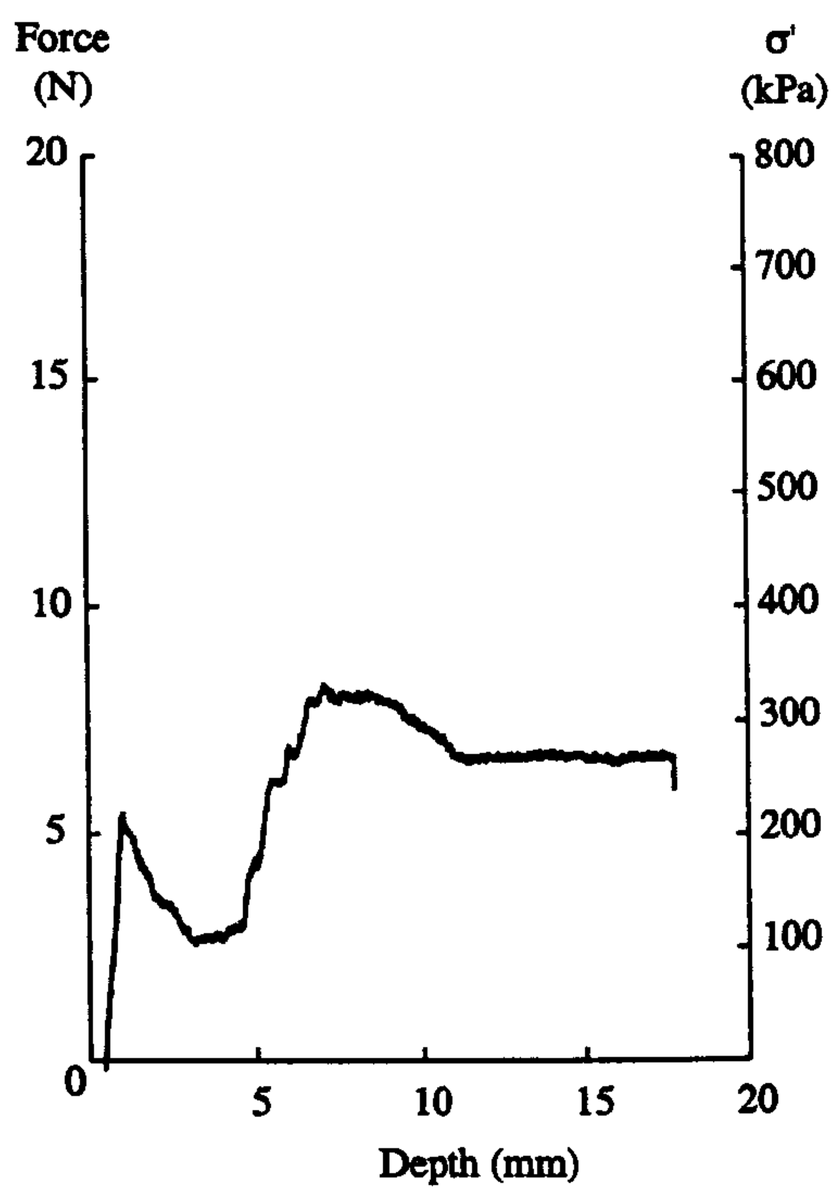

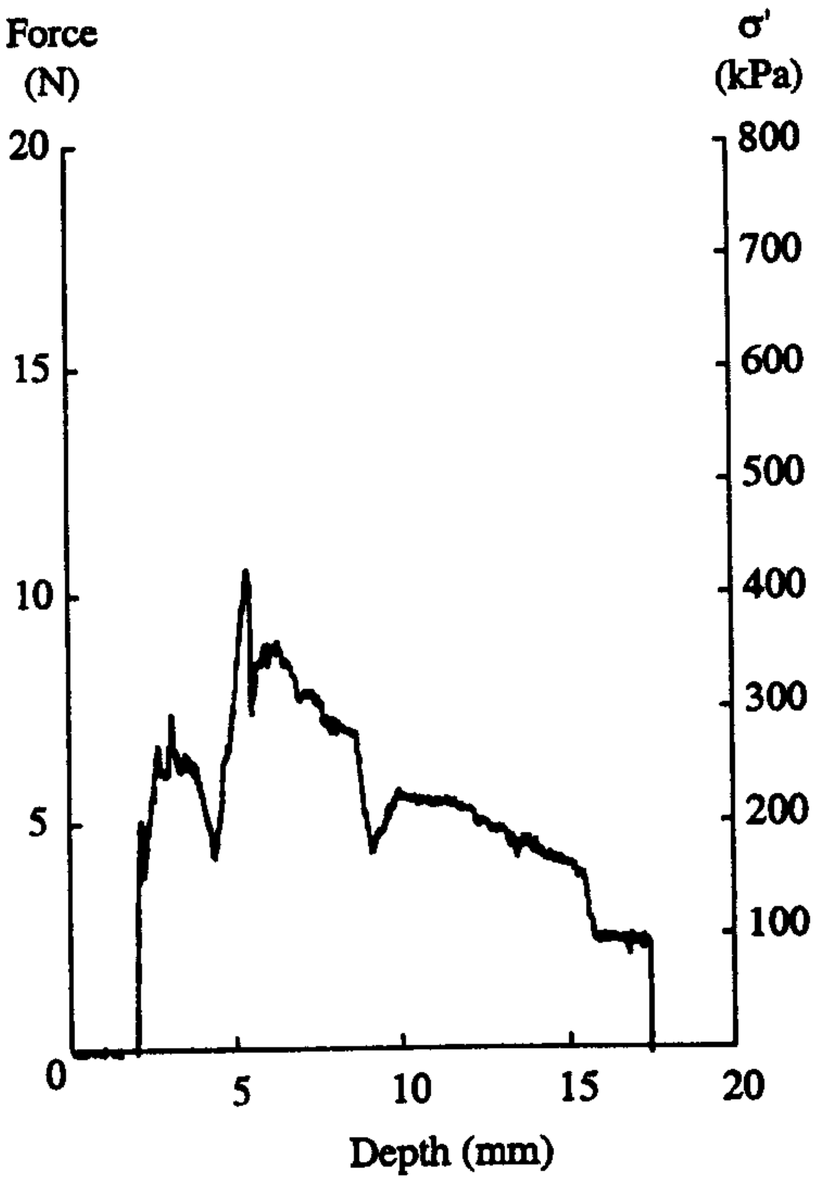

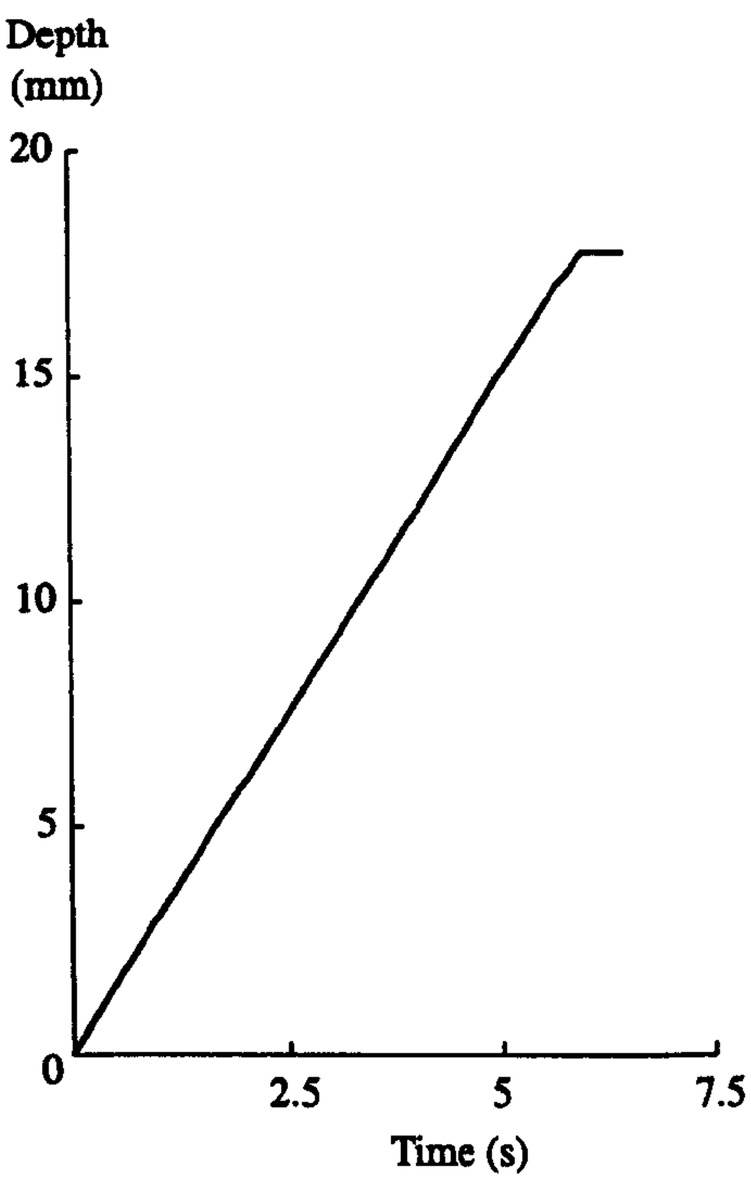

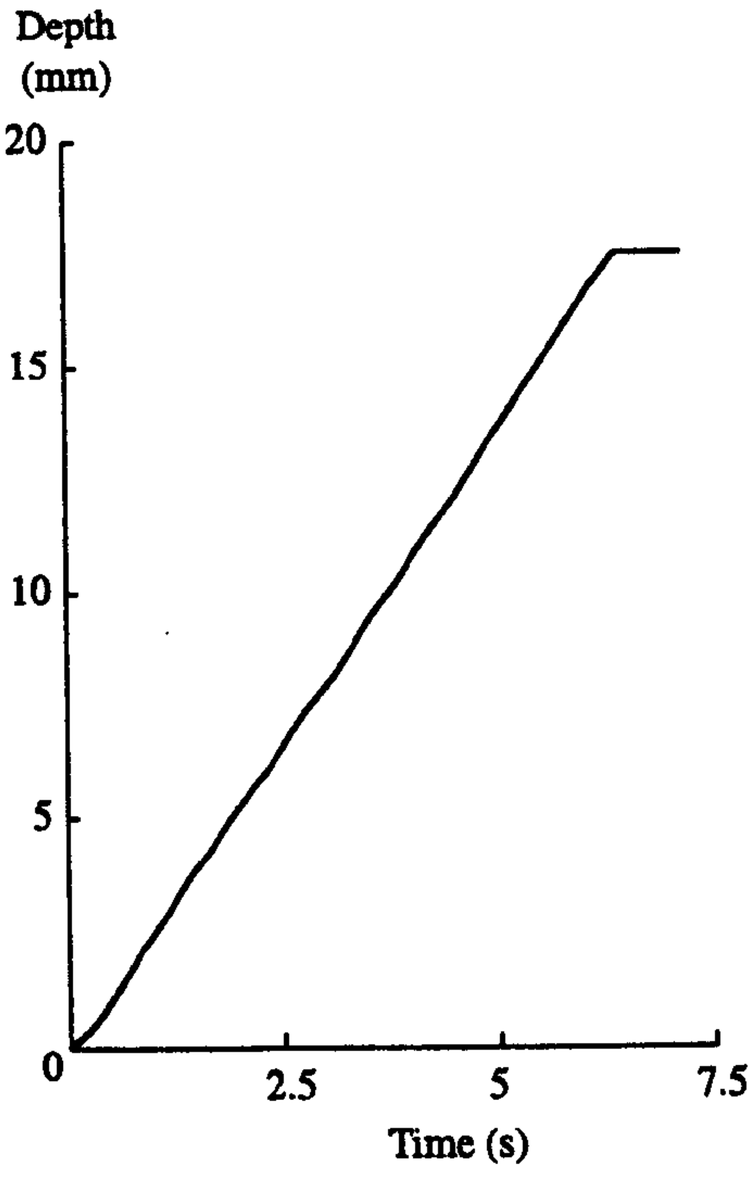

Figures 50a,b & 51a,b - Force and depth charts for the penetration of a CO_2 snow sample

Tables 21a and 21b: Summary data for the penetration of CO_2 snow samples.

Sample temperature (K)	140 ± 10
Chamber pressure (Pa)	10
Tool depth rate (mm s^{-1})	3.04
Initial/final force (N)	5.4 / 6.9
Failure stress (kPa)	220 / 270

Sample temperature (K)	137 ± 8
Chamber pressure (Pa)	7
Tool depth rate (mm s^{-1})	2.83
Initial/final force (N)	7.1 / 2.4
Failure stress (kPa)	300 / 95

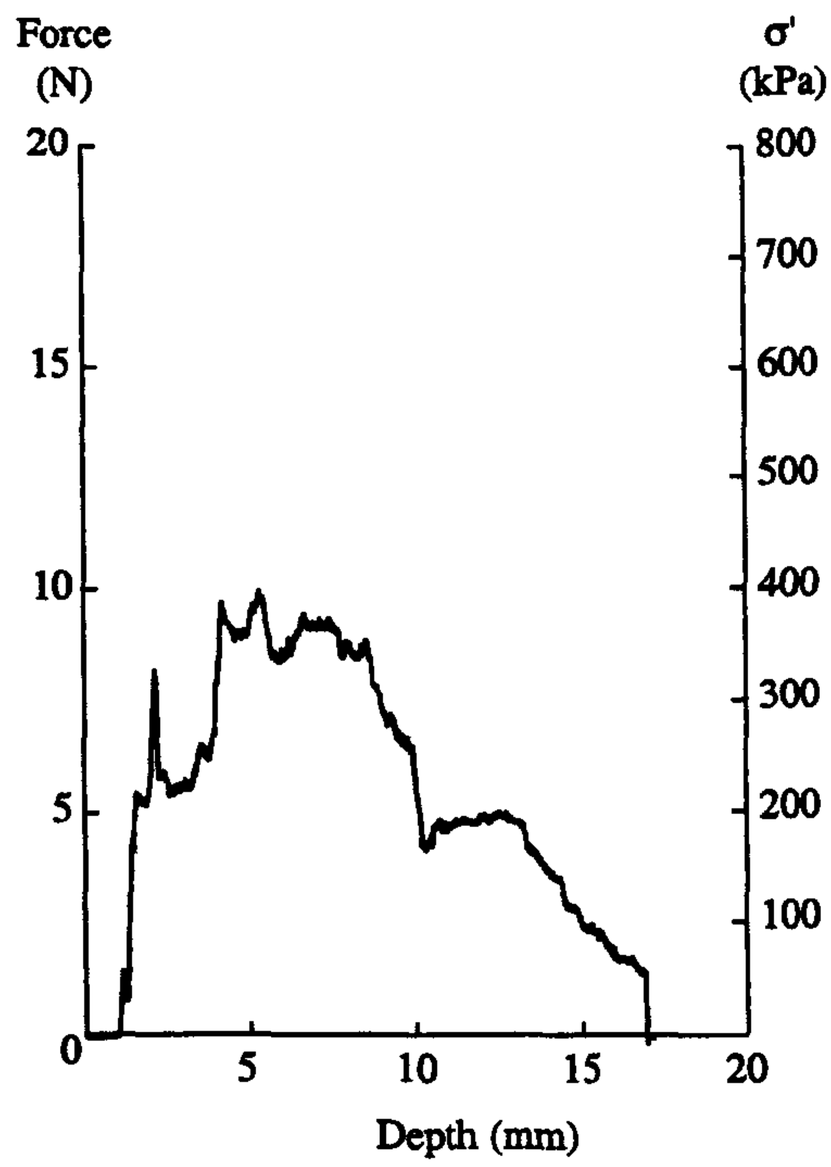

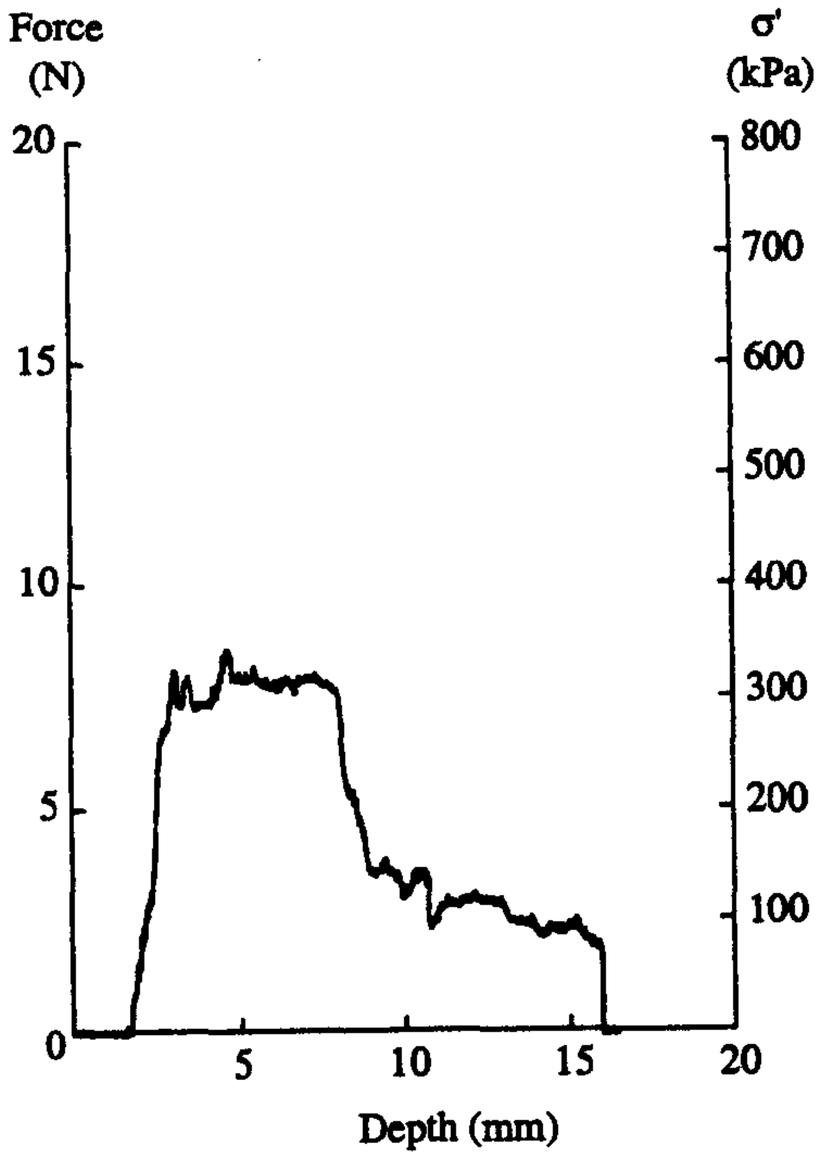

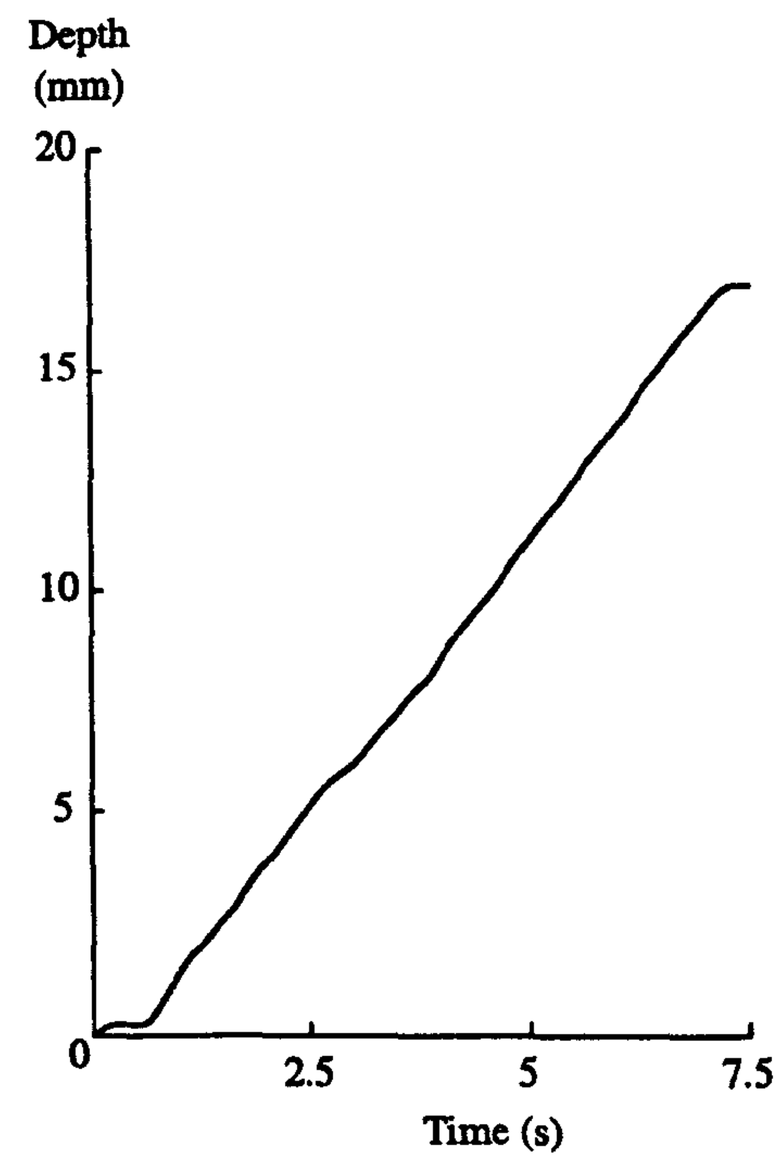

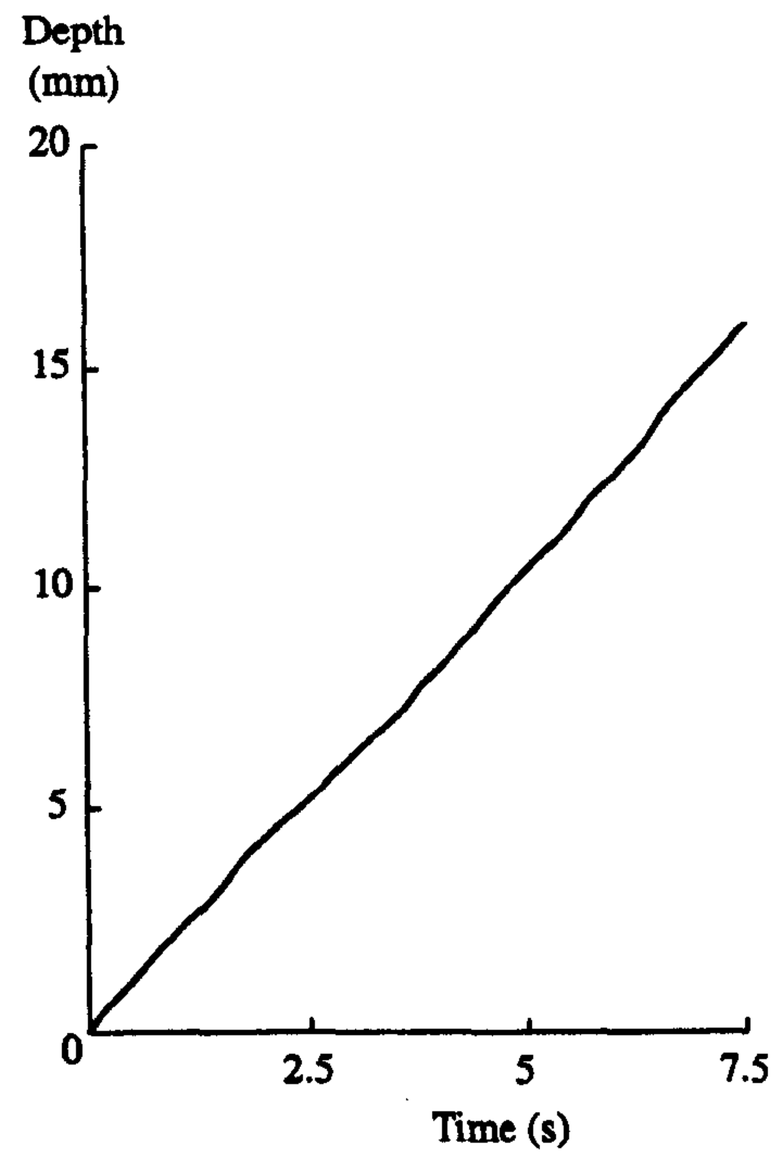

Figures 52a,b & 53a,b - Force and depth charts for the penetration of a CO_2 snow sample

Tables 22a and 22b: Summary data for the penetration of CO_2 snow samples.

Sample temperature (K)	136 ± 10
Chamber pressure (Pa)	7
Tool depth rate (mm s^{-1})	2.44
Initial/final force (N)	8.1 / 1.3
Failure stress (kPa)	330 / 55

Sample temperature (K)	140 ± 10
Chamber pressure (Pa)	7
Tool depth rate (mm s^{-1})	2.14
Initial/final force (N)	8.0 / 1.7
Failure stress (kPa)	320 / 70

5.1.3 Analysis of penetrometry results

No existing work could be found that examined the failure strength of carbon dioxide snows. For comparison representative charts from the work by Kochan *et al.* (1989) on porous samples of mixed water and carbon dioxide ice are shown below. Figure 54a shows the stress record for an unirradiated ice and after being heated[2] by a solar lamp the same penetrometer is reapplied to the ice at a different location, giving rise to the trace in Figure 54b.

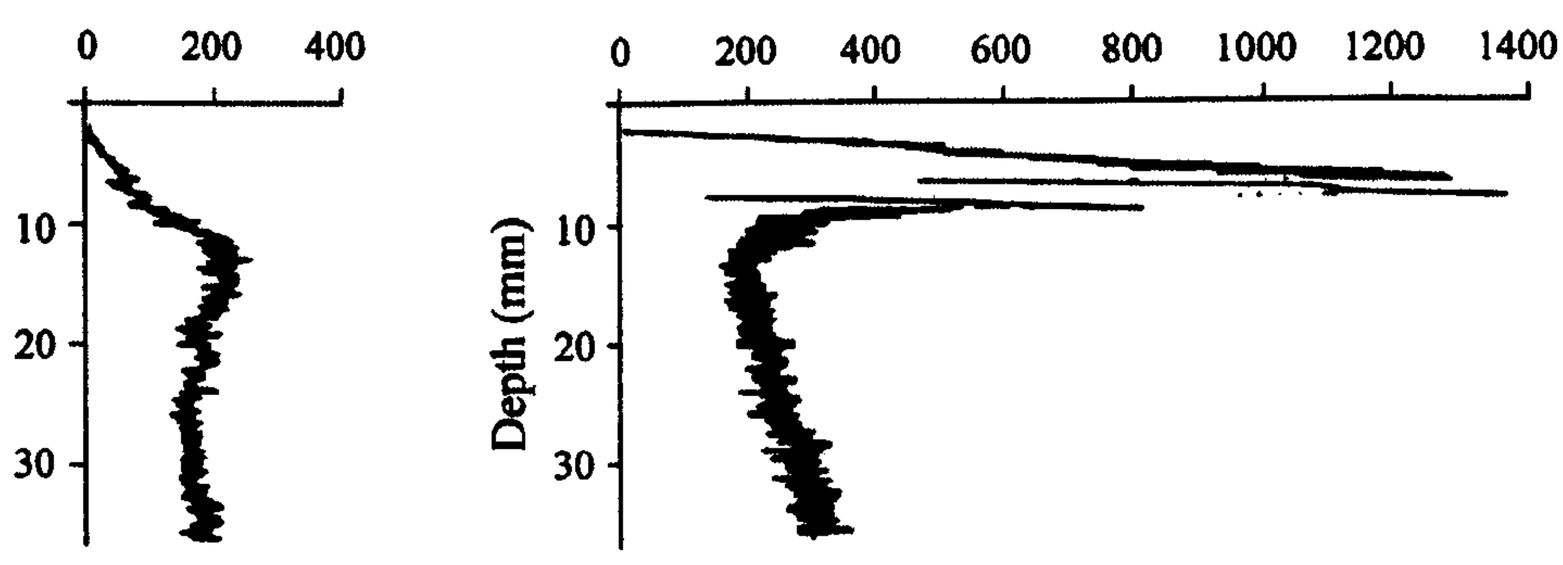

Figure 54a/b - A pair of penetrometry records taken with a cylindrical probe driven into cold (~110 K) dust and CO_2-doped KOSI CAM, charts copied from Kochan *et al.* (1989). The harder material shown in 54b was made by radiatively warming the pristine CAM.

The material used by Kochan *et al.* (1989) is seen to become slightly harder at all depths with time, with the greatest enhancement being found at its surface where the maximum thermal gradient occurs. The strength records in Figure 54 show features that are broadly similar to those of the pure CO_2 snows described in section 5.1.2, with the main difference being that the KOSI (H_2O/CO_2) ices are intrinsically stronger. Following exposure to heat, the CAM has presumably sintered, yielding a harder crust which overlies a relatively unaltered mass of material.

Unfortunately, the penetrometry measurements made on the KOSI samples did not include heads with small cross-sectional areas. The traces in Figure 54 are therefore, unlike the charts of Figures 50 to 53, more indicative of the compressive strength of the material, and not of its resistance to being cut with a sharp blade. Without data on the density and mixing fractions of the ices used by Kochan *et al.* (1989) it is not possible to relate the blade penetrometry data to those of the KOSI project. However, one finding from the blade

---

2 The duration and intensity of this illumination is not known, but is probably comparable to the remainder of the KOSI experiments that used ~1 kW m^{-2} fluxes to heat cryogenic ices for no more than 40 hours.

penetrometry tests can, perhaps, be broadened to include these older measurements. The bulk porosity of the CO_2 snows used in the vacuum system is around 0.18 ± 0.04. Yet, the stress needed to failure the material is still two orders of magnitude smaller than that which is needed to excavate CO_2 ice that is believed to have no significant porosity[3]. This suggests that the bulk density of a material is a poor predictor of its failure stress in a cutting process, and that the dominant factor influencing cutting strength is the degree, and perhaps type, of sintering and grain-grain contact within the material. In the confines of the chamber no method could be devised that allowed the porosity of a snow sample to be measured without disturbing the material. Additionally, without a simple method of controlling the temperature within a porous snow sample, it is not possible to form a material with a desired degree of sintering. These problems led to porous media being discounted from the experiments involving coring tools. However, the arguments made earlier regarding the observed low density of cometary nuclear material are still valid, and porous ices are still an area of interest for proposed spacecraft sampling technologies.

[3] Described later in detail in section 5.2

5.2 Coring experiments with dense ices

Published material from the four comet chambers of the DLR and IWF describes only the use of samples that have been manufactured *outside* their respective vacuum chambers. The material most frequently used is formed by rapidly freezing sprays of water with liquid nitrogen and this substance has been used extensively as the KOSI project's chosen type of CAM formation (Stöffler *et al.*, 1991). It has already been pointed out that this formation process is not only unlikely to occur in nature, but it is also difficult to standardize procedures such that ices made in one laboratory can be compared meaningfully with that made by another. An alternative approach is to form the sample inside the vacuum chamber, and with the exception of the penetrometry work mentioned in the preceding section, all of the work presented here has used samples that were produced inside the chamber, either from the liquid or vapour phase.

Historically, understanding the growth of icy materials from their vapour phase has concentrated on the formation of water ice, with an understandable emphasis on the conditions that may be encountered on Earth. All solids, when held in a closed system below their melting point sublimate to some degree. The pressure of this vapour is a function of the material itself and of the system's temperature. Several representations may be used to calculate the gas pressure, p, when in equilibrium with its solid phase, such as;

$$\log(p) = a - \frac{b}{T + c} \qquad \text{Eq. 59}$$

Derived from the Clausius-Clapeyron gas law, this so-called Antoine model uses a three-parameter fit to empirical data, with the work of Fanale and Salvail (1984) being that most frequently quoted in the literature. More accurate polynomial fits to the experimental data, such as those found in the International Critical Tables, have been made for the saturated vapour pressure of water and carbon dioxide in contact with their respective ices. Examples taken from Lebofsky (1975) and the more comprehensive multi-species study of Brown and Ziegler (1980) are shown along with simpler Antoine models in Figure 55 as a function of temperature. The higher precision of the polynomial models should not be confused with their accuracy. The CO_2 data in particular are 65 years old and there is some recent experimental evidence by Nelson *et al.* (1999) that they may be in error by a factor of two at temperatures lower than 90 K. Therefore these results should be treated with caution.

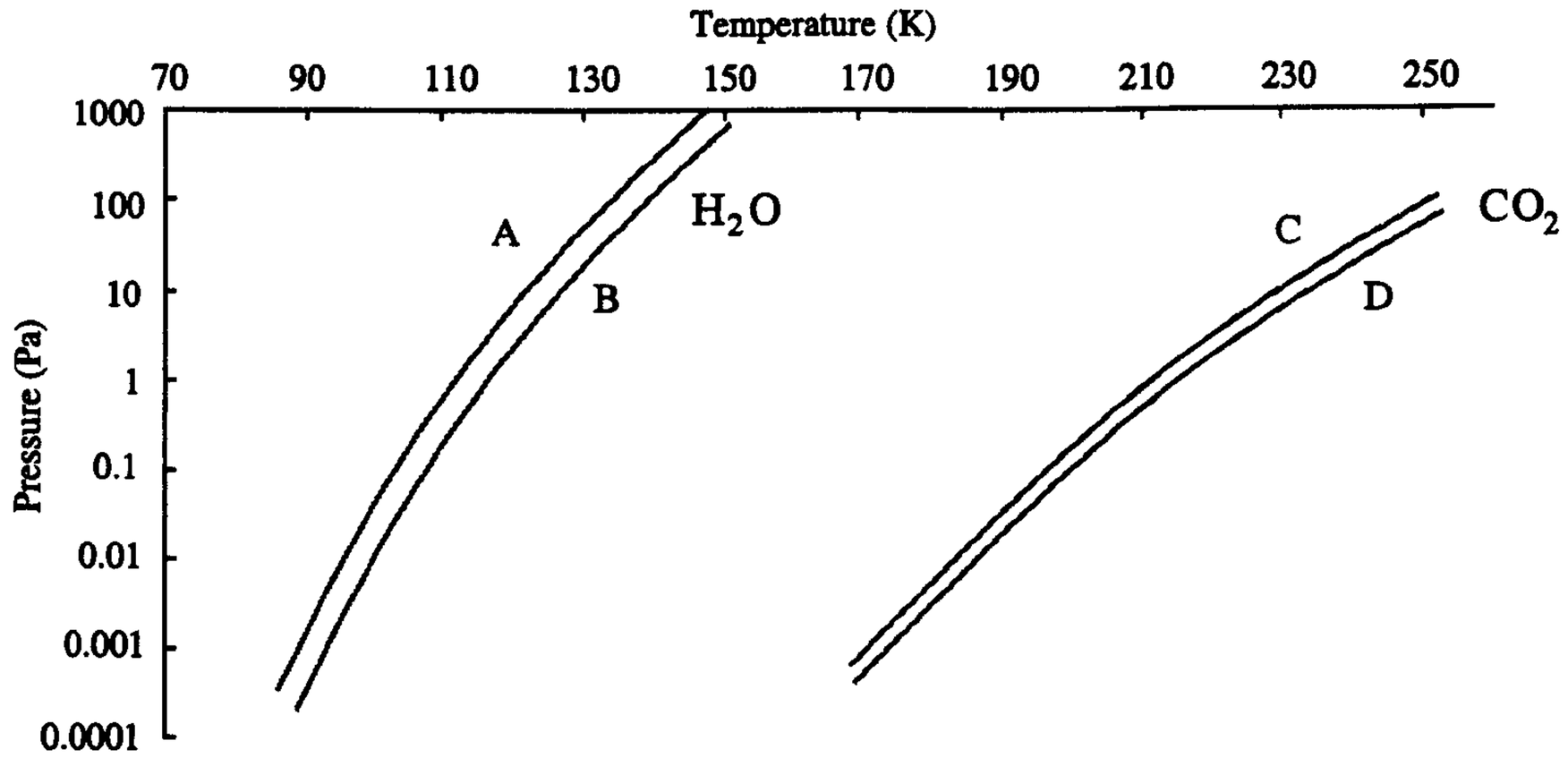

A *Kossacki et al. (1997)*

$$p(T) = a_1 \exp(-a_2 T^{-1})$$

a_1	$= 1.66 \times 10^{12}$ Pa
a_2	$= 3167.8$ K

B *Brown and Ziegler (1980)*

$$\text{Ln } p(T) = b_0 + b_1 T^{-1} + b_2 T^{-2} + \ldots$$

b_0	$= 21.380765$
b_1	$= -2570.647$
b_2	$= -77812.9489$
b_3	$= 4325062.56$
b_4	$= -120671368$
b_5	$= 1349663060$

C *Fanale and Salvail (1984)*

$$p(T) = c_1 \exp(-c_2 T^{-1})$$

c_1	$= 3.56 \times 10^{12}$ Pa
c_2	$= 6141.667$ K

D *Lebofsky (1975)*

$$\text{Ln } p(T) = d_0 T^{-1} + d_1 \log T + d_2 T + d_3 T^2 + d_4$$

d_0	$= -2445.5646$
d_1	$= 8.2312$
d_2	$= -0.0167706$
d_3	$= 1.20514E\text{-}5$
d_4	$= -6.757169$

Figure 55 - Vapour pressures of water and carbon dioxide against their solid ices.

The relatively small differences seen among the various formulations of *p(T)* suggest that the simpler Antoine models are adequate for modelling vapour pressures of sublimating solids, and their simplicity makes them the preferred model for the remainder of this work. Care should be exercised if the above pressures are used as the basis for calculations in a non-equilibrium situation in which the strict condition for no mass transfer from the condensed phase to the gas phase is violated. In such a case, which is required in the formation of ice from the gas phase, there is evidence from the experiments of Kossacki *et al.* (1999) that the kinetic efficiency with which gas molecules sublimate and condense to and from an ice is about an order of magnitude smaller than that assumed in prior studies.

5.2.1 Vapour deposition of CO_2 ice

Following the work with snows made from CO_2, a number of denser carbon-dioxide ices were formed and subsequently cored, by growing the ice from a vapour. By allowing a gas to condense slowly onto a cold substrate, a void-free material may be formed. It was hoped that producing two different structural types of condensate from a single compound would allow the upper and lower limits of the strength of carbon dioxide ices to be explored, with obvious application to the design of martian coring tools.

Carbon dioxide gas was delivered to the vacuum chamber from a cylinder of pressurized liquid carbon dioxide and regulated to a pressure of 0.5 bar above ambient atmospheric pressure. That gas flow was fed through an all-metal valve attached to a pipe-bearing flange bolted to the chamber. A stainless steel flexible hose (5 mm internal diameter) welded to the interior end of that flange's pipe allowed the gas flow to be directed to the base of the sample holder. Care was taken to ensure that the mouth of the hose was positioned in such a way that it was separated from the cooling strap and the walls of the sample holder – otherwise preferential condensation was found to occur on these nearby cold surfaces and in extreme cases the ice would eventually, over the course of some hours, form 'stalagmites' of ice that grew back towards the inlet pipe and partially obscure the gas flow.

In contrast to the many dendritic and slab-like geometries that may be displayed when water ice forms from its vapour, carbon dioxide shows a far simpler set of 'habits'. In contrast to the rich literature describing water ice's growth[1], relatively few references could be found that describe the growth of CO_2 ice from the vapour phase at temperatures similar to that used in this work. When imaged with an SEM, micron-size carbon dioxide crystals condensed from pure CO_2 gas consistently show an octahedral form, as described by Foster *et al.* (1998) and by Erbe and Wergin as reported in Becker (1998). The same geometry appears to persist at dimensions three orders of magnitude larger, as can be seen in Figure 56 which shows the vacuum system's sample stage during a deposition experiment.

---

[1]An excellent recent review is the work of Mason (1992), and photographic works such as those of Nakaya (1954) and Kobayashi and Kuroda (1987) illustrate the dozen or so structural forms visible in ice.

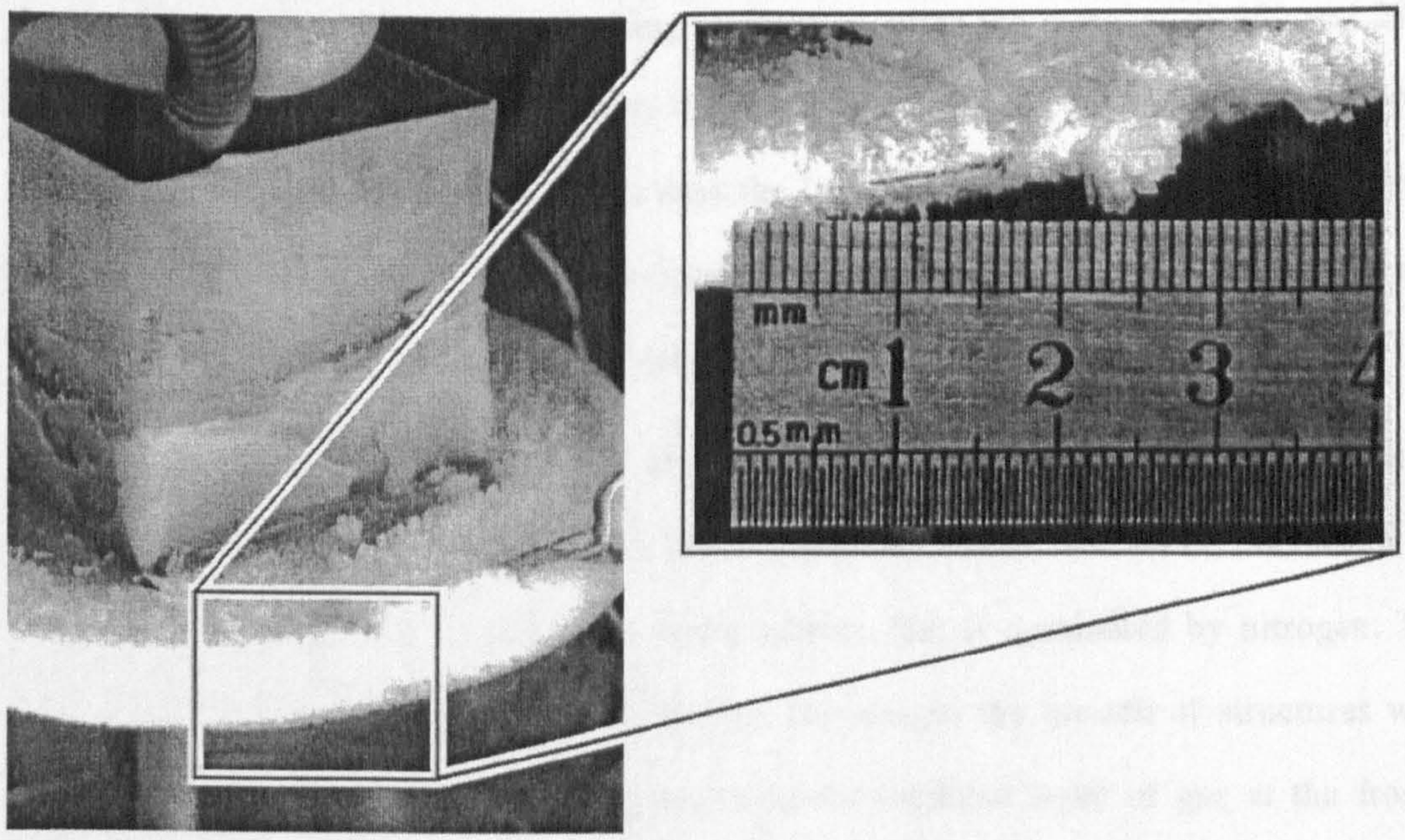

Figure 56 – Small-scale details of solid carbon dioxide grown from vapour onto a sample stage cooled by liquid nitrogen in the presence of low pressure CO_2.

The geometry of the growing grains cannot be predicted purely from the macroscopic thermal properties of carbon dioxide. However, the bulk properties of the gas can be used to evaluate the relative ease with which the CO_2 ices were grown. These indications about the formation efficiency of CO_2 were useful when, at a later time, similar condensation experiments were attempted with water ice. Values for the heat capacity and heat of sublimation for the two ices of interest are shown below.

Table 23 - Material properties relevant to ice condensation from vapour at 150K.

Property	Carbon dioxide	Water
Specific heat capacity of gas (c_p) ($J\ kg^{-1}\ K^{-1}$)	840 (at 275 K) *Eckert and Drake (1972)*	1851 (at 270 K) *Liley (1987)*
Specific heat capacity of ice ($J\ kg^{-1}\ K^{-1}$)	1087.3 *(Appendix A5)*	1228.4 *(Appendix A2)*
Latent heat of sublimation ($J\ kg^{-1}$)	0.69×10^6 *(Appendix A6)*	2.83×10^6 *(Appendix A3)*

Thermal conductivity values for the respective ices are detailed in Appendix A2 and A5.

From these figures the total cooling requirement for forming ices of the two gases can be calculated. The gases' heat capacity can be neglected as it forms a negligible part of the total cooling power needed, unlike the almost five-fold difference in the specific heats of condensation which dominates the total energy needed to condense the ice. To form one

kilogram of ice at ~150 K from vapour starting at 300K requires the removal of 750 and 2900 kJ for CO_2 and water respectively. However, the experiments within the vacuum system rely on forming given volumes of ice and in this case the low density of water ice 'improves' the efficiency with which a volume of ice can be formed; a block of water ice then takes 2.5 times the cooling energy needed to grow the same volume of carbon dioxide ice.

Although the ices' formation energies are of practical interest, the striking geometries expressed by the growing ices are worthy of some comment. Under isothermal conditions on Earth, frost forms by condensing water from a gas mixture that is dominated by nitrogen. The diffusion of water molecules through this buffer gas encourages the growth of structures with dendritic shapes that extend away from the water-vapour depleted layer of gas at the frost's surface. Such diffusion-limited growth cannot occur on Mars at present. In the near-absence of a buffer gas the carbon dioxide molecules should not condense into the spindly shapes seen in terrestrial snowflakes and hoar-frosts. Indeed, the granular forms of solid CO_2 seen in the vacuum chamber were compact and 'blocky' at scales of around 0.2 mm. However, variations were seen in the structure of the ice and these changes appeared to be influenced by the location of the growing ice. The 'randomly-glued-salt-crystal' geometry of the octahedral grains grew most readily away from the footprint of the gas delivery pipe and appeared first on the cryogen delivery pipes. These coarse polygonal grains would slowly infill to form a compact mass. Directly in the path of the feed pipe the ice instead grew as a smooth glossy material and this discrepancy in the structure of the ice is almost certainly related to the enthalpy of the vapour in the two regions. The low flow rates used, < 1 cm^3 s^{-1} as measured by observing the progress of bubbles in a narrow water-filled transparent section of pipe, and the low delivery pressures (< 1.5 bar absolute) would suggest that cooling of the gas by Joule-Thompson expansion in the body of the delivery valve was slight. Indeed, upon leaving the delivery pipe the gas had a temperature of approximately 280 K, as measured by a miniature Pt 100 thermometer element suspended in the gas-stream. The relatively hot gas would then strike the cryogenically cooled floor of the sample holder and a very large temperature gradient would be set up. This cannot accurately represent the condensation dynamics that take place at the poles of Mars and this material is at best an analogue for dense martian seasonal ice. Unlike the near-isothermal situation described earlier for diffusion limited frost growth, in this situation the tip of a growing structure protruding away from a mass of ice will

experience greater heating by being more exposed to the 'hot' gas flow. This heating and the poor conduction of heat through the stalk of a growing dendrite should prevent the growth of spiky structures. In contrast to the hot gas blowing over the sample plate, the cryogen feed pipes would be immersed in a slowly circulating gas that has already been in brief contact with the frigid sample stage. Although the ambient temperature of this gas was not accurately measured, this cooler and slower moving medium may encourage crystal-growth if the surrounding gas molecules have kinetic energies smaller than the binding energy of a growing crystal face. The successful growth of a solid dense form of CO_2 is described in the next sections and the details of ice formation will not be examined further.

5.2.2 Vapour grown CO_2 Ice properties

Ideally, some density-related property of the material might be recorded while it was held under a vacuum so that the porosity of the ice could be determined. To investigate this possibility a small air-gap capacitor was made that could be placed in the sample holder. By placing the back of the sensor flush against the sample holder floor it was expected that this capacitor could be cooled sufficiently for gas to condense between the conductive plates of the device. A comparison of the dielectric properties of the vapour-grown ice with results from earlier experiments on solid carbon dioxide should allow the relative porosity of the material grown in the vacuum chamber to be deduced.

A capacitor built from solid conductive plates was placed in the vacuum system and cooled in the presence of a stream of carbon dioxide gas. This design was then discarded for two reasons. It gave no visible indication that the air-gap volume was saturated with ice and a more serious defect was that the impinging gas could only enter the air-gap at the edges of the capacitor's plates. When cooled to 150 K in the presence of carbon dioxide, condensed ice was seen to form only around the perimeter of the capacitor. An improved version, which used a stainless steel mesh as one of the conductors, avoided both of the problems associated with the use of a solid plate. Not only could gas diffuse directly into the air gap through the mesh, but the build-up of ice in the narrow gap could be seen easily. This design is shown in Figure 57 with a ruler to indicate its size.

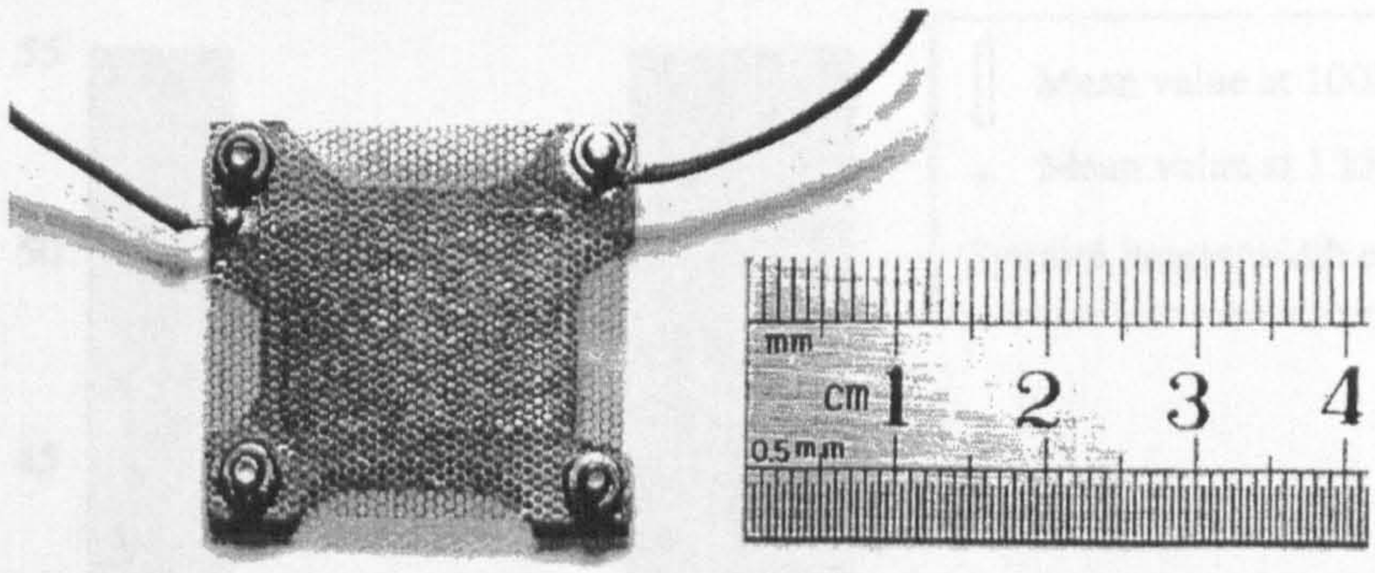

Figure 57 – The air-gap capacitor used to measure CO_2 ice's permittivity.

The capacitor was soldered to a pair of flying leads inside the chamber that could be positioned and held with wire twists. A digital LCR analyzer (model AVO B184) was connected to the two corresponding wires of the chamber's external wiring harness. The small area of the capacitor and its relatively large plate-separation of approximately 50 μm, gave it an inherent capacitance of around 25 pF, which was comparable to the stray capacitance arising from the proximity of the leads in the chamber's wiring. This stray capacitance was measured by first finding the intrinsic capacitance of the device with the analyzer connected to the capacitor by a pair of short (<15 cm) wires soldered directly to the sensor tags. The sensor was then removed from the analyzer and wired to the chamber's internal leads. When connected to the two appropriate wires on the chamber harness, the analyzer would register the sum of the sensor's intrinsic capacitance and the harness' stray capacitance. Care was taken to ensure that the internal and external wiring of the chamber was not moved during the tests and so the stray capacitance could be accounted for.

The chamber was evacuated to a low pressure (< 500 Pa) and the sample stage was cooled to around 110 K with the liquid nitrogen cryogen loop. Carbon dioxide gas was then slowly admitted to the chamber and a pressure of around 100 Pa was maintained. Over the course of one hour the sensor became suffused with a pearlescent growth of CO_2 ice. The total capacitance of the sensor, which would include the stray capacitance of the wiring and the connectors, was recorded during the growth of its icy coat. These data are shown in Figure 58 for the two working frequencies of the LCR analyzer.

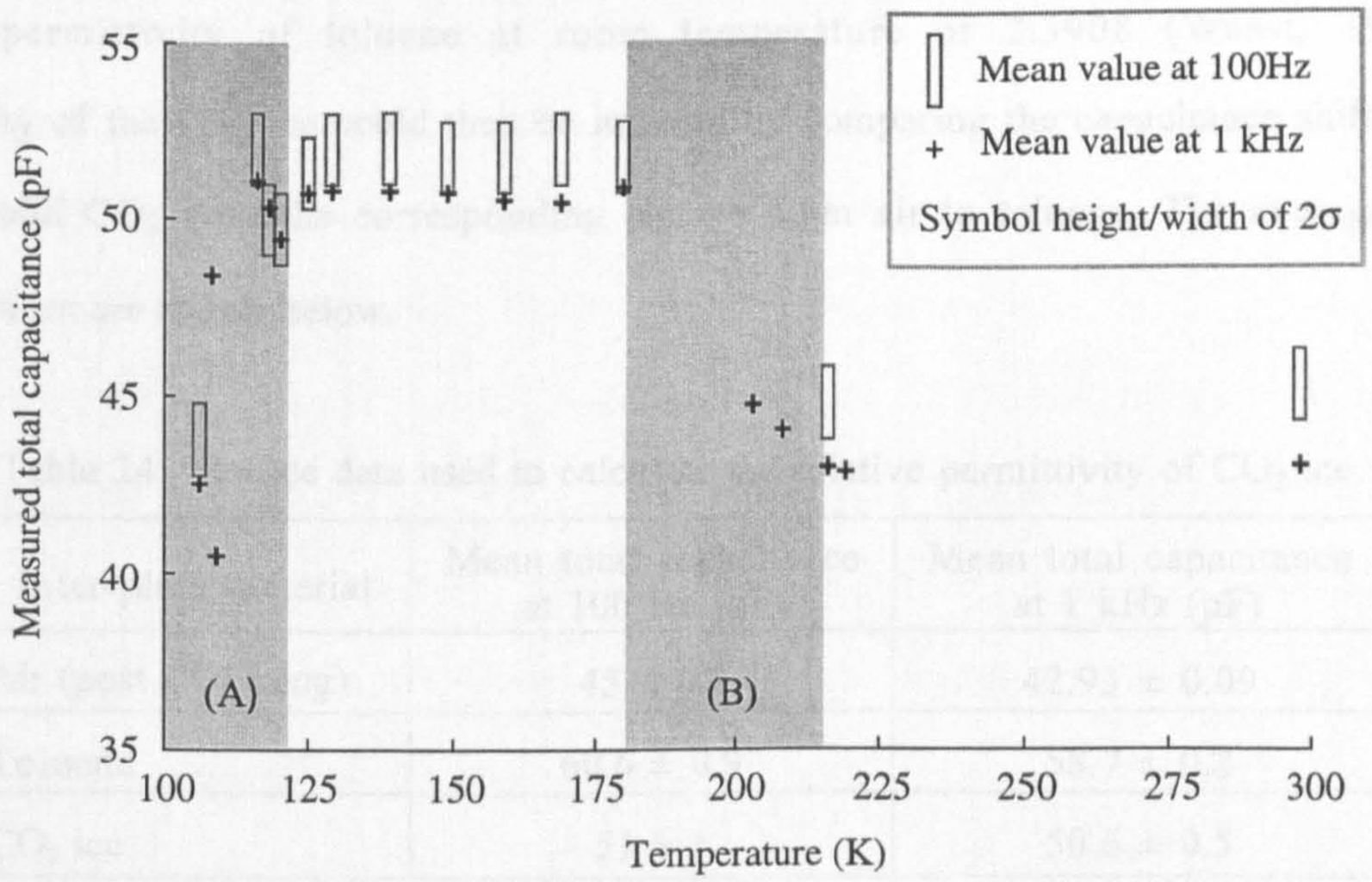

Figure 58 – The dielectric data obtained for cryogenic vapour-grown CO_2 ice.

Region (A) in Figure 58 denotes the progressive covering of the sensor face by the ice up to a depth of around 3 mm. The restrictive viewing geometry of the chamber's windows permitted only half of the sensor to be seen and so extra ice was allowed to condense once the visible half had been coated – a final thickness of around 3 to 5 mm was estimated for the ice coating the capacitor. No change was seen in the capacitance during the growth of this extra coating. After an elapsed time of around two hours the cryogen flow was then stopped, the ice was allowed to warm up and the vacuum pump to the chamber was turned off.

A second change in the measured total capacitance was noted during this warming period. The label (B) in Figure 58 indicates this shift which was accompanied by the gradual retreat of ice from the mesh plate of the capacitor. Once the carbon dioxide had left the capacitor the chamber's internal lamp was turned on at a low power setting to sublimate the remaining ice. Once the sample holder had warmed up to room temperature the chamber was opened and the two halves were parted to gain access to the capacitor. Instead of trying to measure the inter-plate spacing of the capacitor, the relative permittivity of the CO_2 ice was found by exposing the sensor to a second material with an accurately known dielectric constant. Ideally this second test material would infiltrate the sensor intimately, be well-characterized, and be readily available in the laboratory; toluene was found to match these criteria well. The liquid (Fisher chemicals, grade assayed at >99% purity with < 500 ppm water), was applied drop-by-drop to the capacitor (still in the sample holder) until it was thoroughly saturated. From the known

relative permittivity of toluene at room temperature of 2.3908 (Weast, 1985) the permittivity of the CO_2 ice could then be inferred by comparing the capacitance shift between air and solid CO_2 with the corresponding change from air to toluene. The averages of the whole data set are shown below.

Table 24 - Source data used to calculate the relative permittivity of CO_2 ice.

Inter-plate material	Mean total capacitance at 100 Hz (pF)	Mean total capacitance at 1 kHz (pF)
Air (post CO_2 icing)	45 ± 0.8	42.93 ± 0.09
Toluene	60.6 ± 0.9	58.7 ± 0.2
CO_2 ice	51 ± 1	50.6 ± 0.5

From the usual model of a parallel plate capacitor's capacitance the total measured capacitance is a function of the plate spacing, D, and area, A.

$$C_{total} = \frac{A\varepsilon_0\varepsilon_r}{D} + C_{stray} \qquad \text{Eq. 60}$$

Let the shift in total measured capacitance in going from a dielectric of air to toluene is denoted by ΔC_{at}. Similarly, if the dielectric changes from CO_2 ice to air then the measured capacitance change is labelled ΔC_{ca}. Carbon dioxide's relative permittivity, $\varepsilon_r(CO_2)$, is then;

$$\varepsilon_r(CO_2) - 1 = \left(\frac{\Delta C_{ca}}{\Delta C_{at}}\right)\left(\varepsilon_r(toluene) - 1\right) \qquad \text{Eq. 61}$$

The error in this calculated value arising from the individual errors of the mean capacitance values was then calculated in the usual manner;

$$\frac{\sigma^2\left(\varepsilon_r(CO_2)\right)}{\varepsilon_r{}^2(CO_2)} = \left(\frac{\sigma(\Delta C_{ca})}{\Delta C_{ca}}\right)^2 + \left(\frac{\sigma(\Delta C_{at})}{\Delta C_{at}}\right)^2 \qquad \text{Eq. 62}$$

For the sake of brevity the arithmetic is not shown. Carbon dioxide ice grown from the vapour phase was found[2] to have a relative permittivity of 1.68 ± 0.04 at 1 kHz, and 1.53 ± 0.13 at 100 Hz.

---

[2] An error in the preliminary calculations of Garry (2001) lead to these values being overestimated. This mistake has been reported to that conference's editor.

Only one study, by Simpson *et al.* (1980), could be found that published the dielectric values of bulk samples of carbon dioxide ice. Their work used commercially produced carbon dioxide snow[3] as its working material, relying on manual compaction to produce a denser material. With that material, figures for the relative permittivity were found by Simpson *et al.* (1980) to be 2.09 and 2.04 at 50 MHz for ices of density 1410 and 1400 kgm^{-3} respectively that had porosities[4] of around 10 %. By extrapolating their data to the point of zero-porosity Simpson *et al.* (1980) inferred a relative permittivity of 2.25 for void-free carbon dioxide ice at 50 MHz. In that work the permittivity was not seen to change with frequency in the range of 50 MHz to 4.2 GHz, although no low-frequency measurements were made with which the data in table 24 can be compared.

Although the data from the mesh-plate capacitor were gathered at only two frequencies the near-similar values can place limits on a second dielectric property of the ice. When exposed to a periodic electric field a dielectric material will dissipate some fraction of the applied electrical energy with the degree of dissipation varying with frequency and the material type. The ratio between the energy stored in each cycle and the energy that is lost is often termed the 'quality factor' and can be measured by an angular measure, the loss tangent δ, which expresses the relative magnitudes of the imaginary and real components of the electric field in the material. Large values for this parameter are associated with conductive or semi-conductive materials and the loss tangent influences the degree to which an electromagnetic signal is absorbed by the substance. If values for the loss tangent and relative permittivity of a material are known at some frequency then the relative dielectric constant $\varepsilon_r(f_1)$ at some higher frequency f_1 will be smaller than $\varepsilon_r(f_0)$ and will have a value that may modelled by;

$$\varepsilon_r(f_1) = \varepsilon_r(f_0)\left[\frac{f_1}{f_0}\right]^{\frac{-2\delta}{\pi}} \qquad \text{Eq. 63}$$

With such a relationship the similar values found for the relative permittivity of vapour-grown carbon dioxide ice at 1 kHz and 100 Hz imply that the loss tangent is near-zero at such low frequencies. No published data could be found for this property of carbon dioxide ice at radio frequencies.

---

[3] Made from a pressurized source of liquid CO_2 which is allowed to expand rapidly through a small orifice. A very fine-grained snow of micron-sized crystals is formed rapidly with this method.
[4] The density of solid CO_2 is published as being 1590 kg m^{-3} at 170 K (Thorpe and Whiteley, 1966).

These measurements of the dielectric properties of CO_2 ice are useful only if the relationship between its porosity and bulk permittivity can be found. Thus, it was necessary to measure the density, and hence the porosity of the CO_2 ice grown in the vacuum system. Successful removal of the whole sample was achieved by allowing the sample holder to warm after a thick layer of ice had been condensed. Once the ice in immediate contact with the holder had sublimated, the block could be removed with only moderate difficulty. Figures 59a-c show the progressive formation of a vapour-grown CO_2 ice sample. The recovered block is shown in Figure 59d.

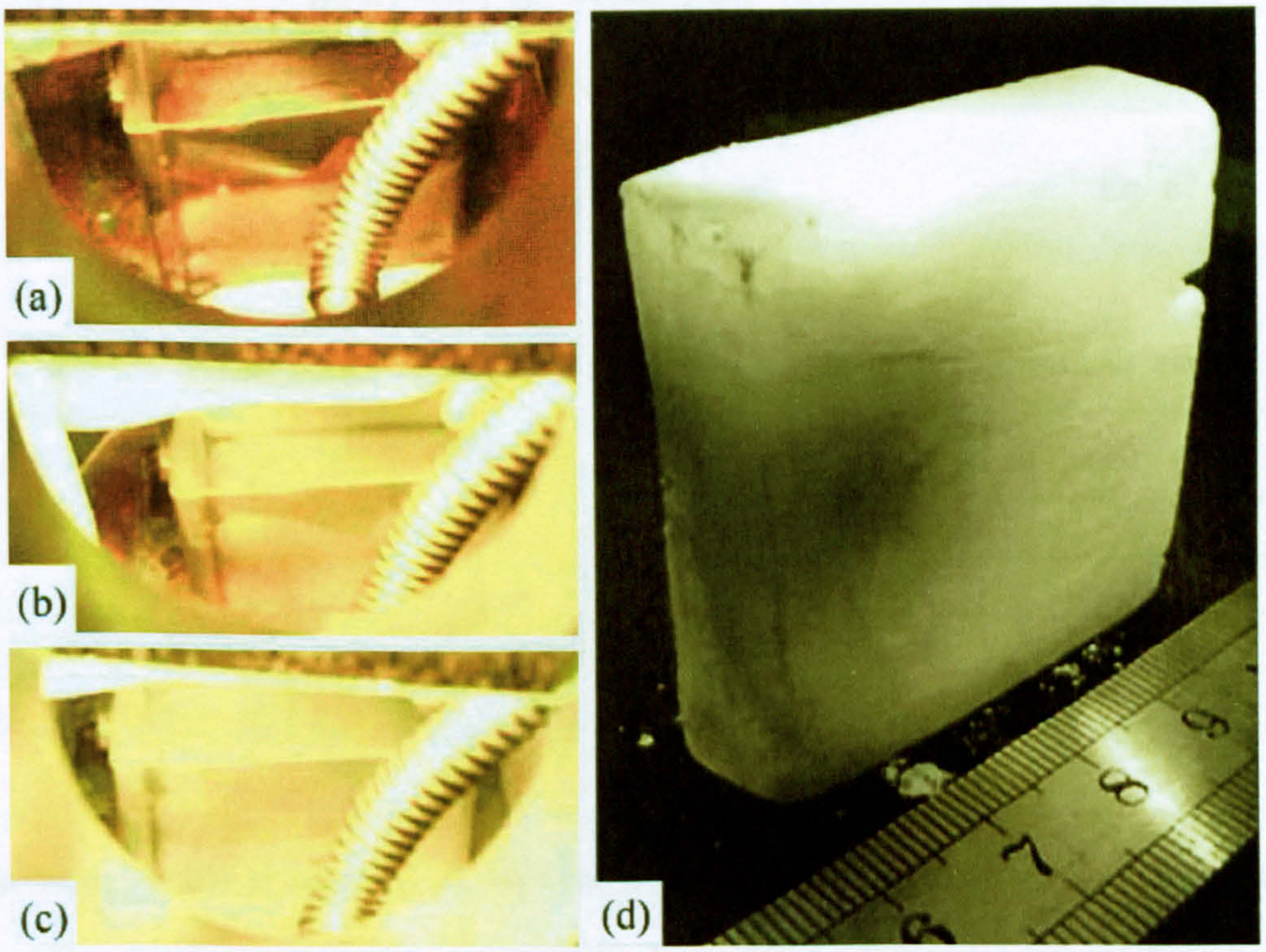

Figures 59a-d – Photographs taken of the growth (a to c) of a slab of carbon dioxide ice at a temperature of 140 K.

Four separate measurements of the mass, length, width, and height (referred to as m, a, b, and c respectively) were made of the block as it sublimated, and also of smaller cuboid sections cut from it. These data are shown in Table 25 along with the corresponding error, σ_ρ, for the density which was calculated by combining the errors arising from the measurements in the following manner.

$$\sigma_V^2 = \left(\frac{\partial V}{\partial a}\right)^2 \sigma_a^2 + \left(\frac{\partial V}{\partial b}\right)^2 \sigma_b^2 + \left(\frac{\partial V}{\partial c}\right)^2 \sigma_c^2 \qquad \text{Eq. 64}$$

Here V represents the volume of the icy mass and the derivatives with respect to the dimensions take the following form

$$\frac{\partial V}{\partial a} = bc \qquad \frac{\partial V}{\partial b} = ac \qquad \frac{\partial V}{\partial c} = ab \qquad \text{Eqs. 65 a,b,c}$$

The error associated with each density measurement can then be calculated, using the usual definition of density, and the quotient rule for the propagation of errors.

$$\sigma_\rho^2 = \left(\frac{\partial \rho}{\partial m}\right)^2 \sigma_m^2 + \left(\frac{\partial \rho}{\partial V}\right)^2 \sigma_V^2 \qquad \text{Eq. 66}$$

$$\sigma_\rho^2 = \left(\frac{1}{V}\right)^2 \sigma_m^2 + \left(-\frac{m}{2V^2}\right)^2 \sigma_V^2 \qquad \text{Eq. 67}$$

Table 25: Density measurements of one CO_2 ice sample grown from its vapour.

Record	Dimensions (mm) ± 2	Mass (g) ± 0.1	Density (kg m^{-3})	Error in density (± kg m^{-3})
1	47 x 47 x 12	41.1	1550	70
2	45 x 10 x 13	8.9	1521	103
3	44 x 10 x 11	8.2	1694	123
4	30 x 10 x 5	2.1	1400	206

The error on the average of all four density measurements is found from the root-mean-square of the individual errors from each of the four records. Thus, the average density of 1540 kg m^{-3} has an associated error of ±135 kg m^{-3} which comfortably brackets the established value of 1590 kg m^{-3} for void-free ice at 170 K (Thorpe and Whitely, 1966). The use of vapour-grown ice has avoided the use of compaction which is needed to form commercial solid carbon dioxide blocks. These are generally made from compacted CO_2 snow and produce a porous ice. For example, the ices used by Burchell *et al.* (1998) had been mechanically compressed to over 150 bar and had a bulk density of 1440 ± 50 kg m^{-3}, clearly lower than the literature value and indicative of a porosity of ~9%. The CO_2 ice grown from the vapour phase in this study displayed no visible porosity and it is difficult to see how voids could be incorporated during the slow[5] condensation of the material. Along with a lack of discernible voids the ice did not show

[5] A layer 1 mm thick could be grown at 140 K and an ambient pressure of < 1mbar in around one hour.

a preferred failure plane when it was fractured with a chisel. This suggests that the grains were closely packed, randomly oriented, and small. If the solid formed within the sample holder is indeed the most compact form of carbon dioxide ice then the role of the capacitor as a densitometer is redundant. Despite the original goal of using the capacitor to infer the porosity of the CO_2 ices used later as the target for coring experiments, it has served a second purpose instead and has extended the knowledge of this ice's electrical properties.

The unusual optical appearance of the vapour-grown ice is also of interest to studies of cold planetary ices. As mentioned earlier, the ice inside the sample holder grew as a smooth bright and slightly translucent condensate. In contrast, the cold parts of the system that did not have a direct line-of-sight to the gas supply hose were coated with coarse granular ice having an octahedral geometry. The marked difference in the visual appearance of the ice formed in the vacuum system is a clue to its internal structure. If a photon does not encounter flaws or debris in a material then its path-length is fixed only by absorption bands peculiar to the material. Thus, the opalescent nature of the ice shown in Figure 59d may arise from a scattering process. A handful of experimental studies describe the spectral absorptivity of vapour-grown CO_2 using samples several centimetres deep (e.g. Hansen, 1995; Ditteon and Kieffer, 1979). A common feature in these two works is that the ice is a weak absorber, and is much more transparent than water ice over wide bands of the IR spectrum. Ditteon and Kieffer (1979) also reported that partially optically translucent samples could be formed at unspecified higher pressures (> 6 kPa), but this is mentioned in passing and no mechanism is suggested for the formation of their cloudy solid CO_2 samples. The most likely mechanism for the scattering process that produces the partially opaque vapour-grown CO_2 samples shown in Figure 59 is that of grain boundary scattering. Larger grains would lead to a reduced volumetric density of scattering bodies in the ice and a greater degree of translucency, so it may be inferred that the ice grown in the vacuum system was made from comparatively smaller grains. Unfortunately, unlike water ice, carbon dioxide ice shows no colours under polarimetry and this hypothesis could not be tested. These concerns about the size of the CO_2 ice grains are driven by the possibility that carbon dioxide at the martian poles may condense to form competent slabs of ice which are translucent to some degree. At least two studies, Forget *et al.* (1995) and Paige *et al.* (1995) have commented on this possibility and have used its high transparency to explain the low brightness temperatures observed in parts of Mars' seasonal ice caps. Kieffer (2000)

suggests that dust settling from the atmosphere is ejected from a slab of CO_2 ice by being preferentially warmed *through* the overlying CO_2 ice and by such 'self-cleaning' the ice retains its transparency. There are obvious technical problems with constructing an experiment that controllably admits dust into a vacuum system and this aspect of martian ice analogue formation is not considered further.

These measurements are not related to the mechanical investigation of planetary materials but they do provide more experimental data for another types of exploration, namely electromagnetic sounding. By probing the martian surface with electromagnetic signals the sub-surface stratigraphy may be known along with information on the composition of the material (Plaut, 1999). At least two studies of proposed martian radar missions have presumed values for the permittivity of martian snows that differ from those measured in the short sequence of experiments outlined in this section. The theoretical radar study of Ori and Ogliani (1996), for example, uses the value of 3 for the relative permittivity of CO_2 ice, as does the study by Chappell (2000) which uses a value of exactly 3.0 for ε_r at some unspecified frequency and temperature with no mention of the expected electromagnetic losses in this medium. The discrepancy between measured and presumed figures for ε_r is as important as the loss factor to the design of a radar sounder because the penetration depth (m) of a radar signal will vary with the loss tangent as;

$$\frac{1}{2\pi\sqrt{\varepsilon_r \tan\delta}} \qquad \text{Eq. 68}$$

The electrical properties of dense carbon dioxide ice have been measured at two frequencies at low temperatures and pressures. The growth of this ice from its vapour phase has resulted in a material that is has a porosity definitely less than 4 % and, more probably, close to zero. The next section will describe the results of coring this type of ice.

5.2.3 Coring vapour deposited CO_2 ice

Strength measurements of heavily compacted CO_2 ice have been made at various speeds and strain rates, ranging from hypervelocity impacts (Burchell *et al.*, 1998) to the traditional loading methods of Durham *et al.* (1983; 1999) that used strain rates of 10^{-7} to 10^{-4} s^{-1}. The coring experiments shown in the next sections lie between these two extremes of strain rate and speed; compressive failure of brittle water ice by tools moving at a few centimetres per second yield strain rates of order 1 s^{-1} (Jones, 1997).

Samples of dense carbon dioxide ice were made in a similar manner to that described in the work with the mesh capacitor (see 5.2.2). The drill stem of the manipulator was fitted with a coring tool, as shown in Figure 29. This tool's cutting teeth had a machined zero rake angle. This choice of rake angle is broadly supported by the work of Vasilev and Talalay (1994) who showed that a small non-zero rake angle gave a more efficient cutting tool than a steeply inclined cutting face. With no data for similar drilling studies in CO_2 ice, a rake angle of zero was chosen as a compromise between cutting efficiency (which may be improved at some slightly higher rake angle) and the ease with which a tool head could be made and kept sharp.

The mechanical precision of the coring head and drive system is shown in Figure 60 where a shallow block of vapour-grown CO_2 ice has had the coring head driven into it to a depth of a few millimetres under a modest vacuum. The clarity of the cut should be compared to that shown in the photograph of a block of water ice (Figure 37) cored with the same tool. The frost visible on the tool head and tool holder is a mixture of water ice and carbon dioxide, with the water ice forming through contact with the laboratory air while the photographs were being taken.

During each coring process no discontinuities were experienced that were suggestive of layering or similar discontinuities at the scale of the tool head, and the lack of visible fissures or fracturing suggests that the CO_2 ice has a uniformly fine-grain structure. However, the CO_2 ice samples did display one unusual tendency. If the vertical motion of the tool was not immediately reversed at the end of each coring run, then once the tool had ceased to rotate it tended to bind to the ice so strongly that it could not be manually released. This phenomenon will be discussed in more detail in chapter 5.3.3. In the following coring experiments four dynamic variables were recorded: torque, rotation speed, and depth rate. Generally, two

separate coring operations were performed using one slab of vapour-grown ice. The shallowness of the vapour-grown CO_2 samples allowed at most three coring runs to be made in the same sample, yet no consistent trend was seen by 're-using' the coring site in this way[6].

Figure 60 – A sample of vapour-grown carbon dioxide ice machined by the coring tool.

From these data the work expended per unit area in cleaving the material could be calculated using equations 27 and 28. Of the two possible energy sinks it is the energy expended per unit volume, u_S, by the tool that is calculated and shown in the tables that follow; frictional effects with the cutting debris are ignored. Unlike the water ice experiments described later in 5.2.4, all of the CO_2 coring runs were made in a narrow temperature range because of limitations in the chamber's cooling system. Thus, the carbon dioxide experiments were made in materials at essentially the same temperature of 140 ± 10 K and more consideration was given instead to exploring the effects of changing the rotation rate and vertical tool speed.

Unfortunately five of the coring runs (Figures 67 to 70) did not have their ice temperatures or chamber pressures noted but the tests were identical in format to those which were logged more diligently and nominal temperatures of 140 K are presumed for these tests. The following Figures are laid out such that one coring run produces a force/torque history (top-most graph), a distance/rotation record (middle graph), and a summary table (bottom). At most two runs are shown on each page, with the charts and table for each run arranged

6 The x,y position of the coring head was kept fixed in such experiments.

vertically. The characters shown in parentheses are code-names used to identify the experiments from their laboratory records, and are not significant otherwise. Where no value can be calculated, a dash (-) is shown in place of a figure. If, for example, the trace showing the downforce does not rise rapidly to a clearly defined value, then no single figure can be assigned to the initial force encountered during the tool's penetration. Thus, no single value for the failure stress can be computed for the material at that instant.

No interpretation will be made of the data shown in the Figures until later on in this chapter, where the coring results from water ice and vapour-grown carbon dioxide ice will be compared and evaluated.

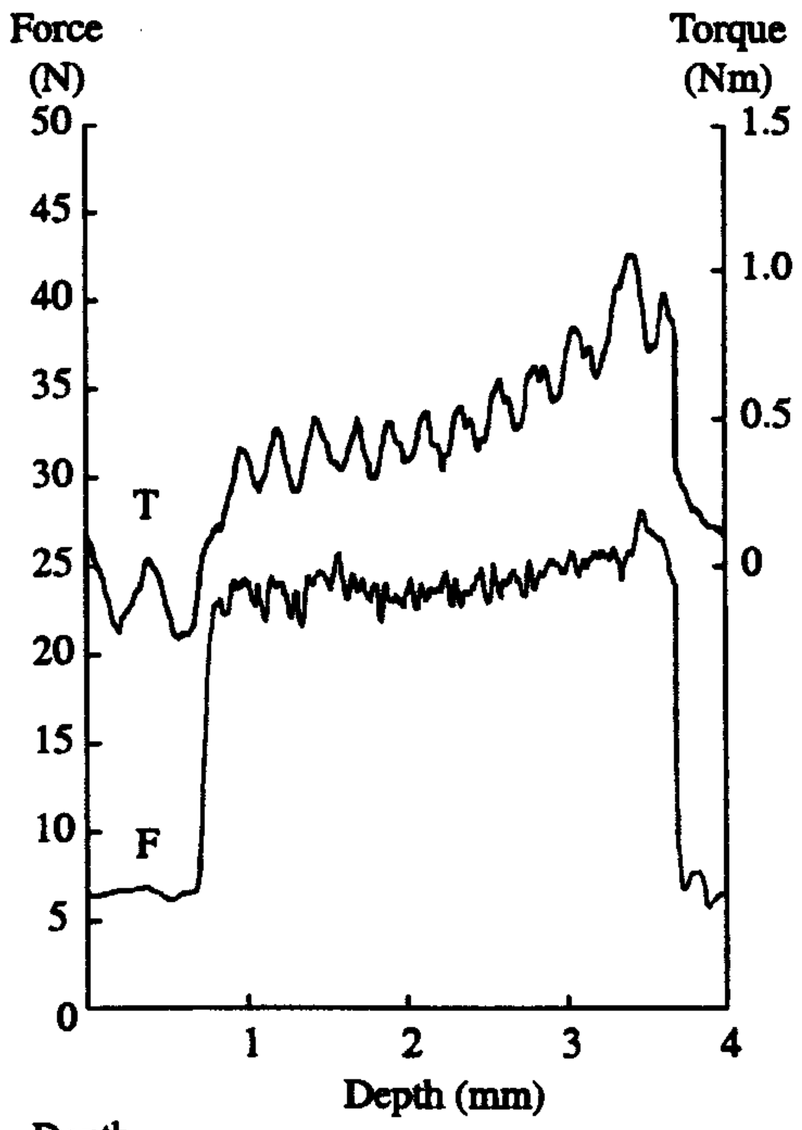

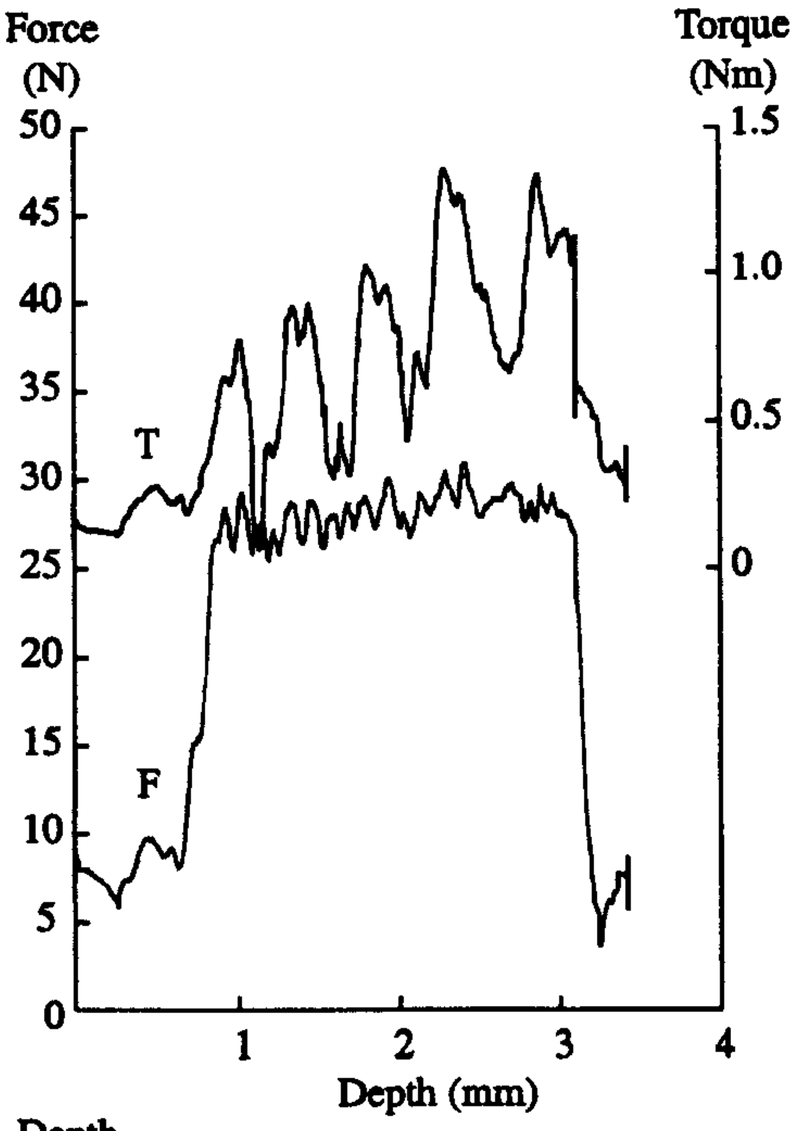

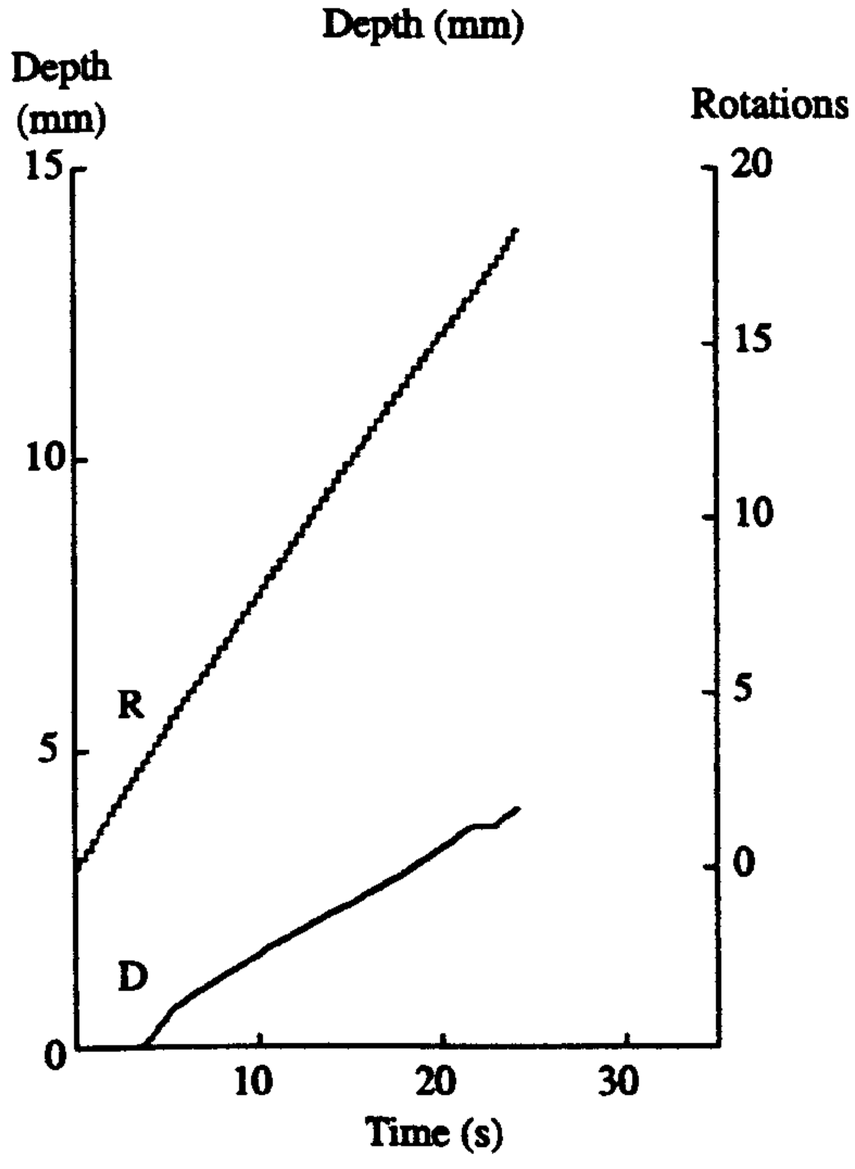

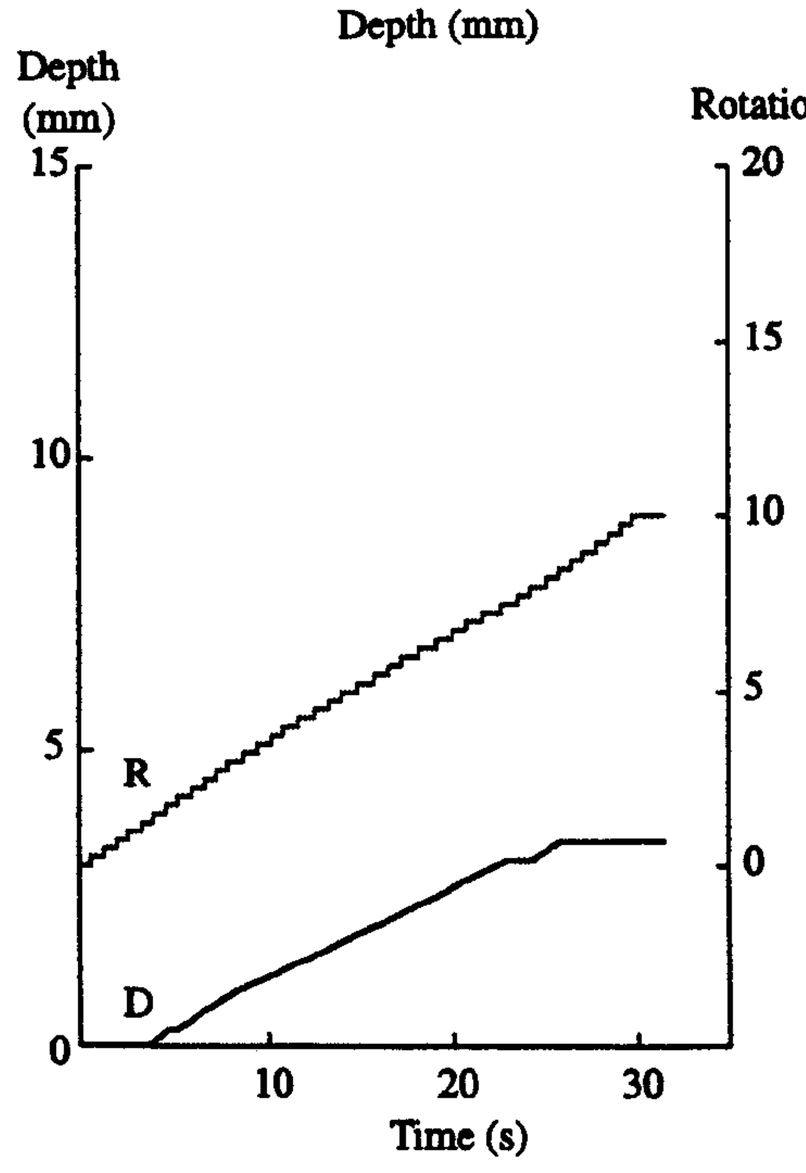

Figures 61a,b & 62a,b – Force, torque, depth and rotation data from coring CO_2 ice (1B 2C)

Tables 26a and 26b: Summary data for the above coring tests.

Sample temperature (K)	130
Chamber pressure (Pa)	50
Rotation speed (rev s^{-1})	0.751
Tool depth rate (mm s^{-1})	0.1806
Initial / final force (N)	15.9 / 18.9
Initial / final torque (Nm)	0.15 / 0.25
Cutting strength (MPa)	36 / 50
Predicted ΔT on axis (K)	4
Predicted ΔT at $r=r_{tool}$ (K)	5.8
Predicted flash ΔT (K)	110

Sample temperature (K)	125
Chamber pressure (Pa)	50
Rotation speed (rev s^{-1})	0.319
Tool depth rate (mm s^{-1})	0.155
Initial / final force (N)	18.6 / 22.5
Initial / final torque (Nm)	0.07 / 0.3
Cutting strength (MPa)	19 / 29
Predicted ΔT on axis (K)	2
Predicted ΔT at $r=r_{tool}$ (K)	3
Predicted flash ΔT (K)	21

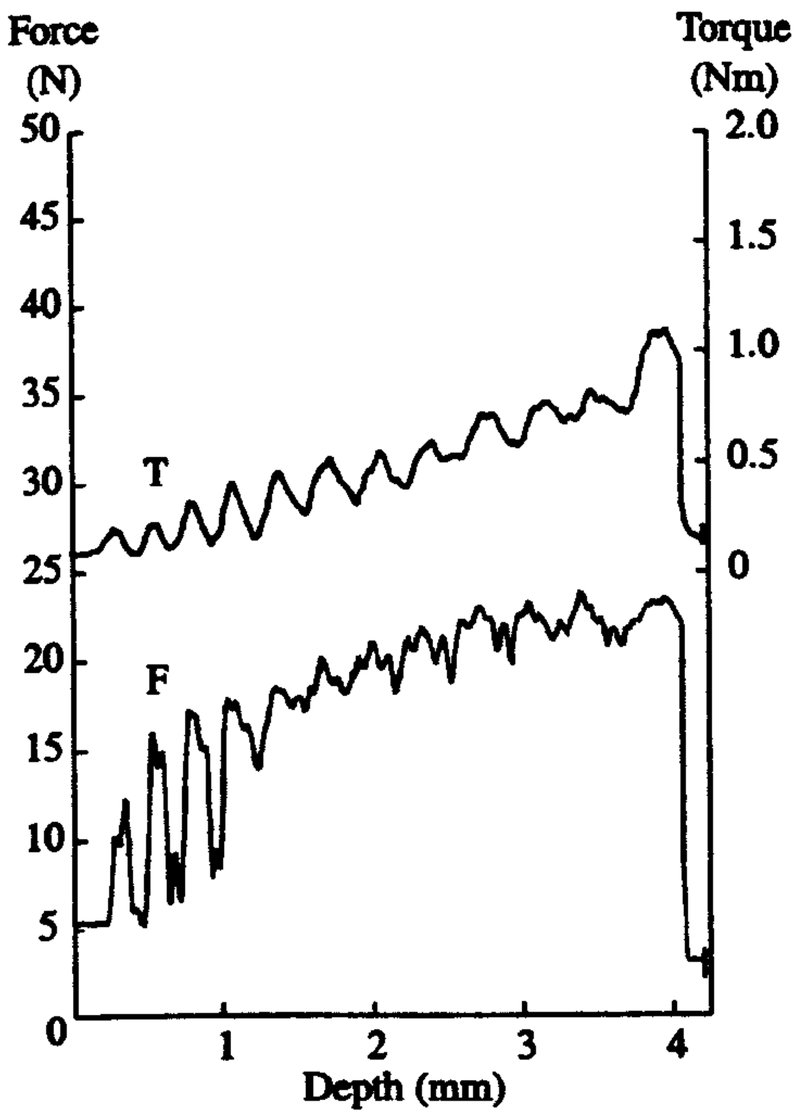

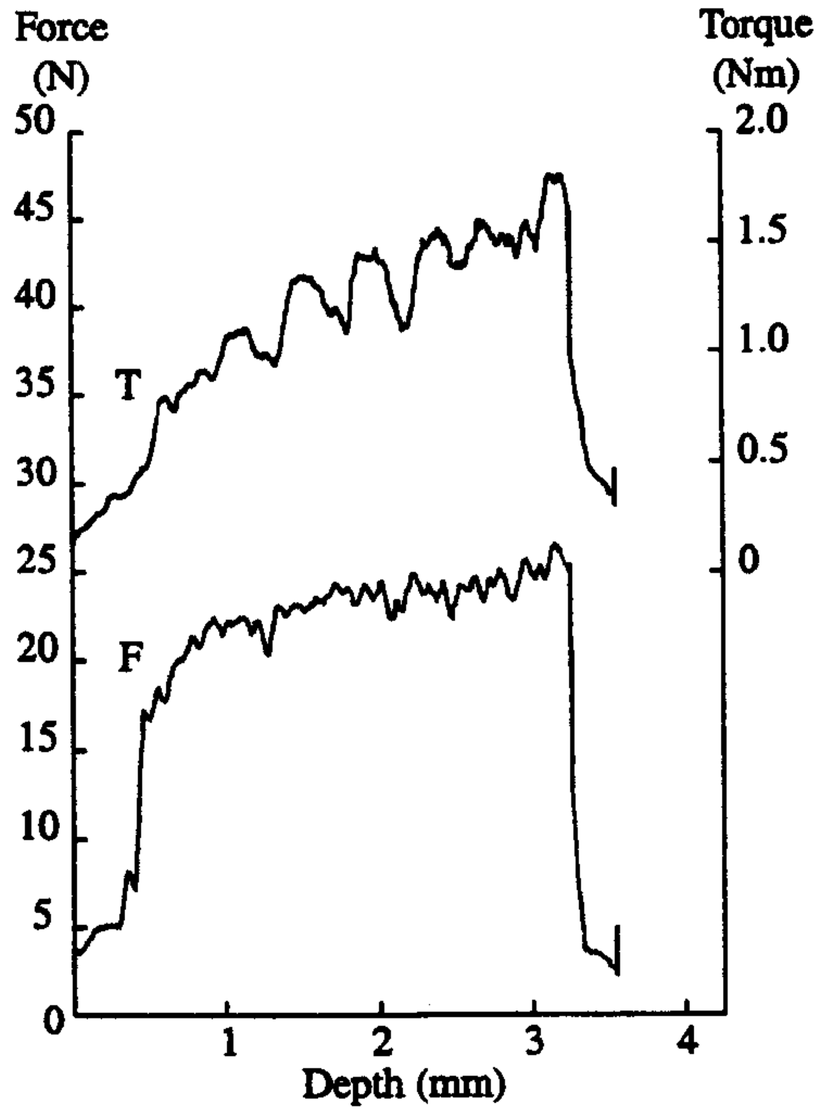

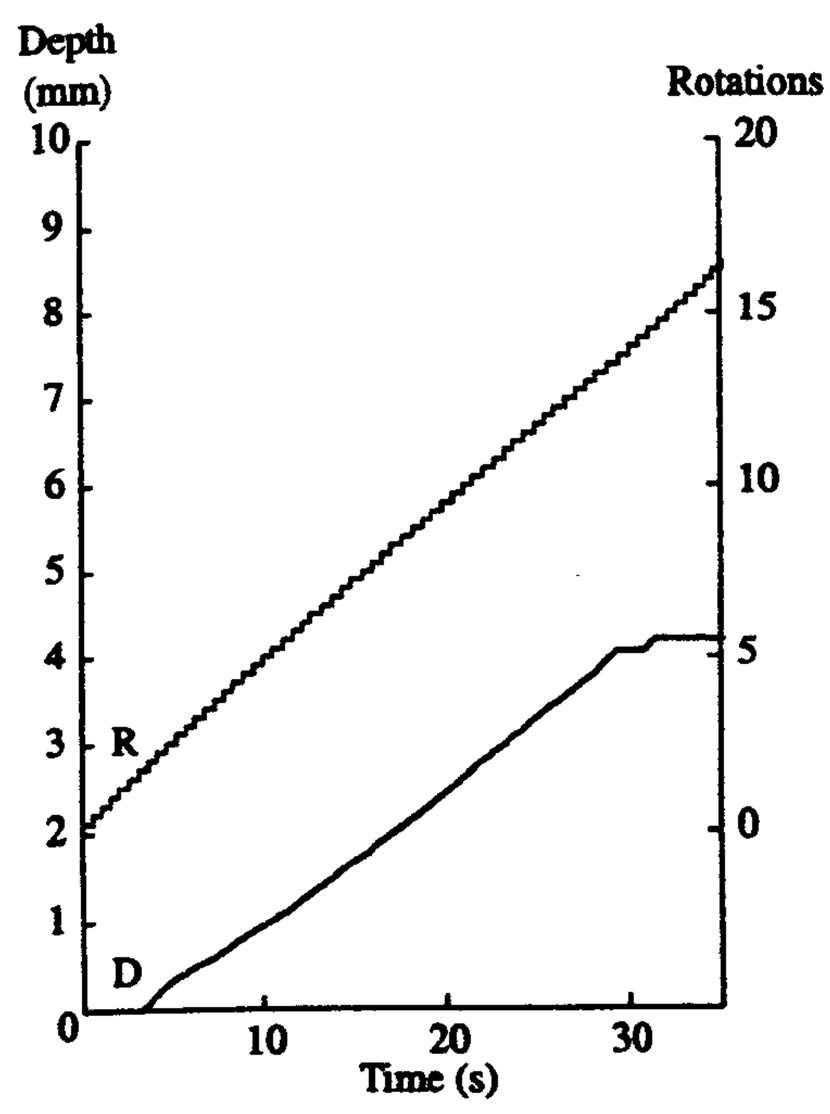

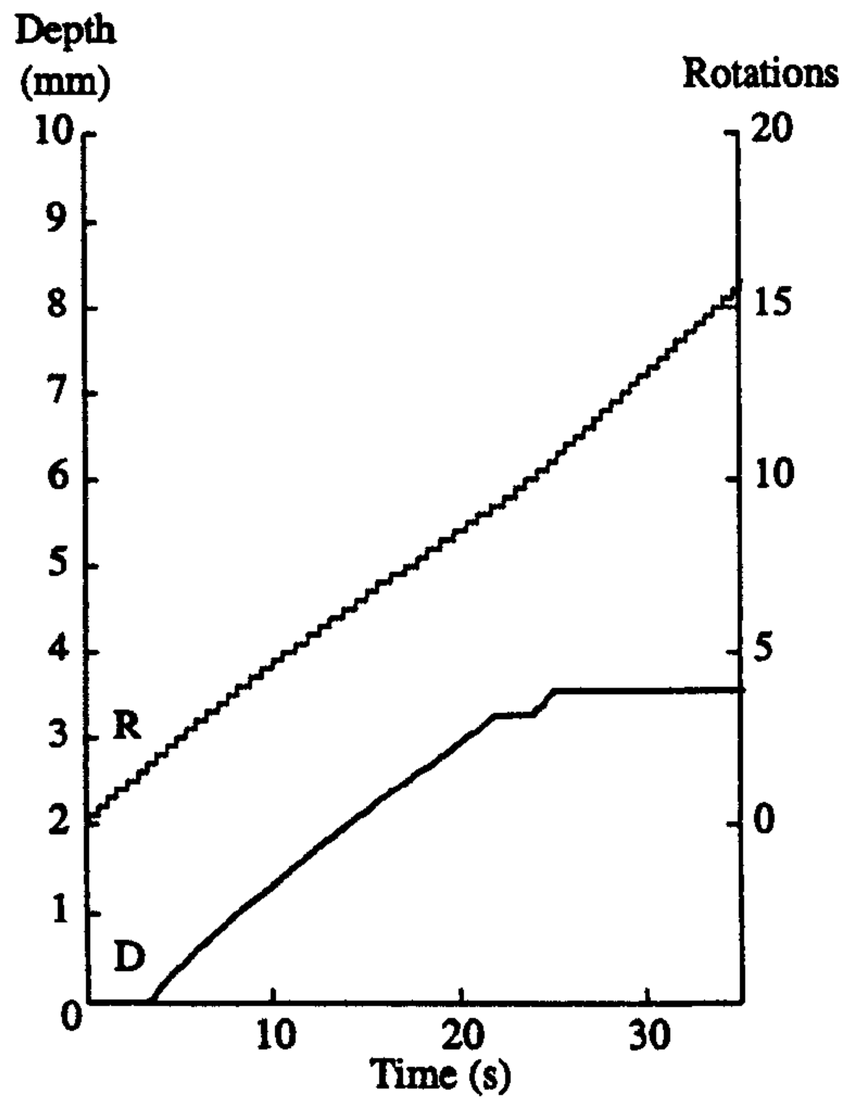

Figures 63a,b & 64a,b – Force, torque, depth and rotation data from coring CO_2 ice (9A 9B)

Tables 27a and 27b - Summary data for the above coring tests.

Sample temperature (K)	135
Chamber pressure (Pa)	10
Rotation speed (rev s^{-1})	0.389
Tool depth rate (mm s^{-1})	0.150
Initial / final force (N)	7.3 / 18.9
Initial / final torque (Nm)	0.0 / 0.89
Cutting strength (MPa)	11 / 99
Predicted ΔT on axis (K)	1.1
Predicted ΔT at $r=r_{tool}$ (K)	1.7
Predicted flash ΔT (K)	-

Sample temperature (K)	145
Chamber pressure (Pa)	45
Rotation speed (rev s^{-1})	0.345
Tool depth rate (mm s^{-1})	0.153
Initial / final force (N)	13.5 / 22
Initial / final torque (Nm)	0.73 / 1.19
Cutting strength (MPa)	71.6 / 117
Predicted ΔT on axis (K)	7.5
Predicted ΔT at $r=r_{tool}$ (K)	10.9
Predicted flash ΔT (K)	250

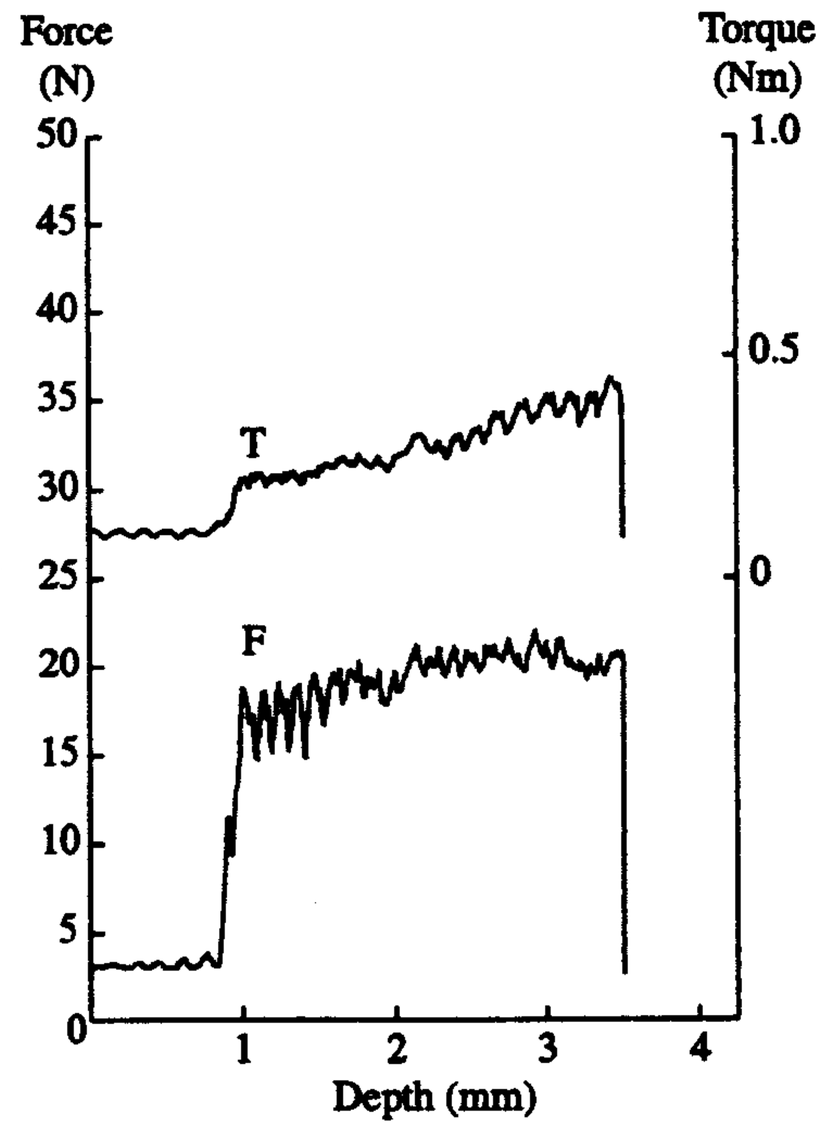

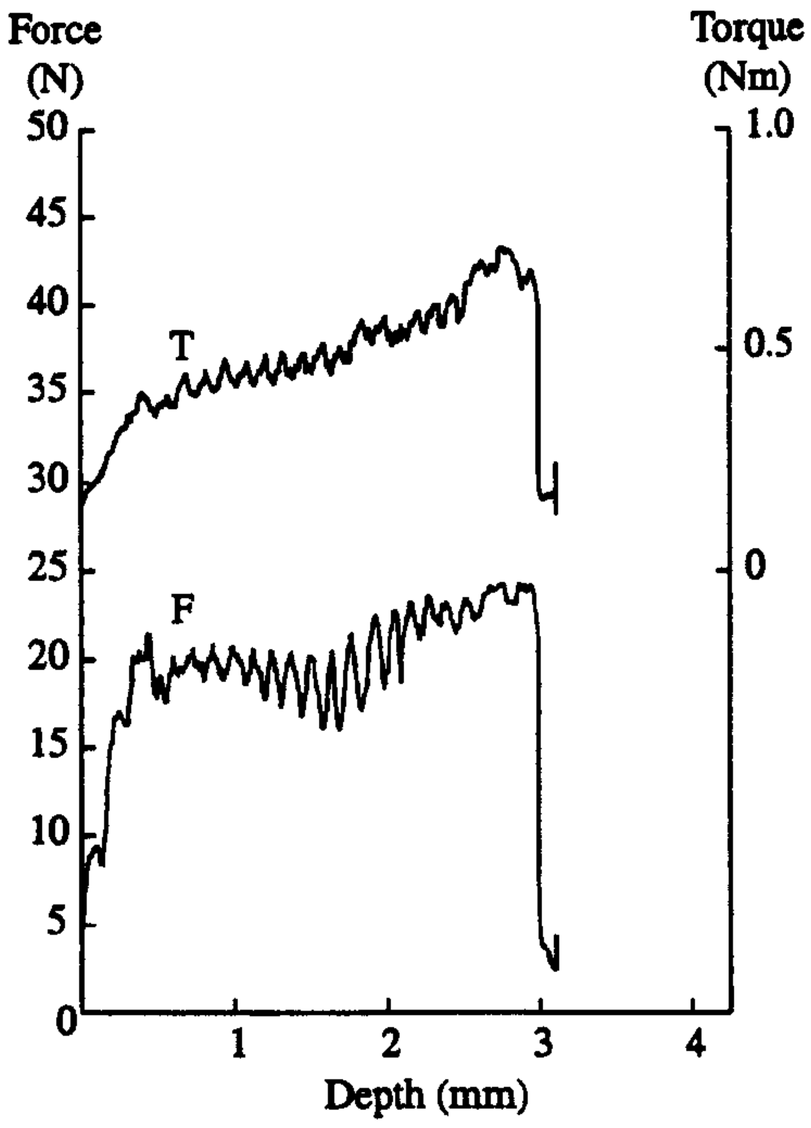

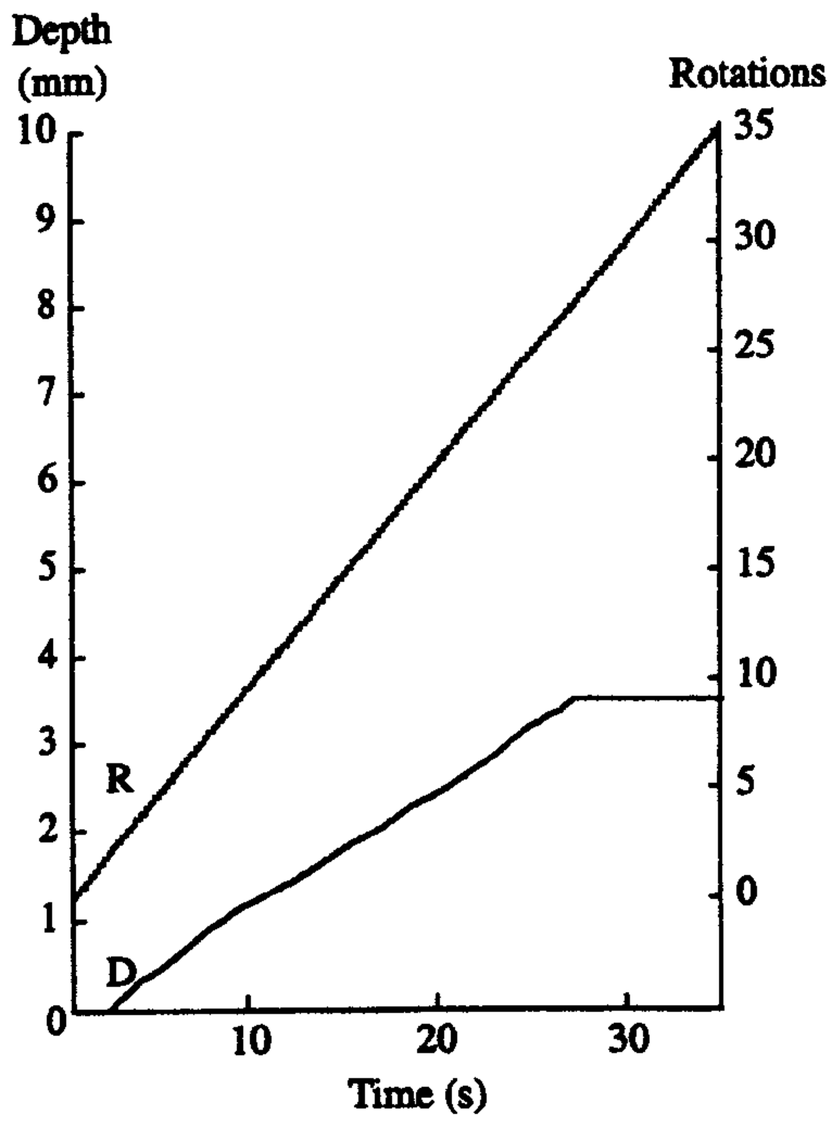

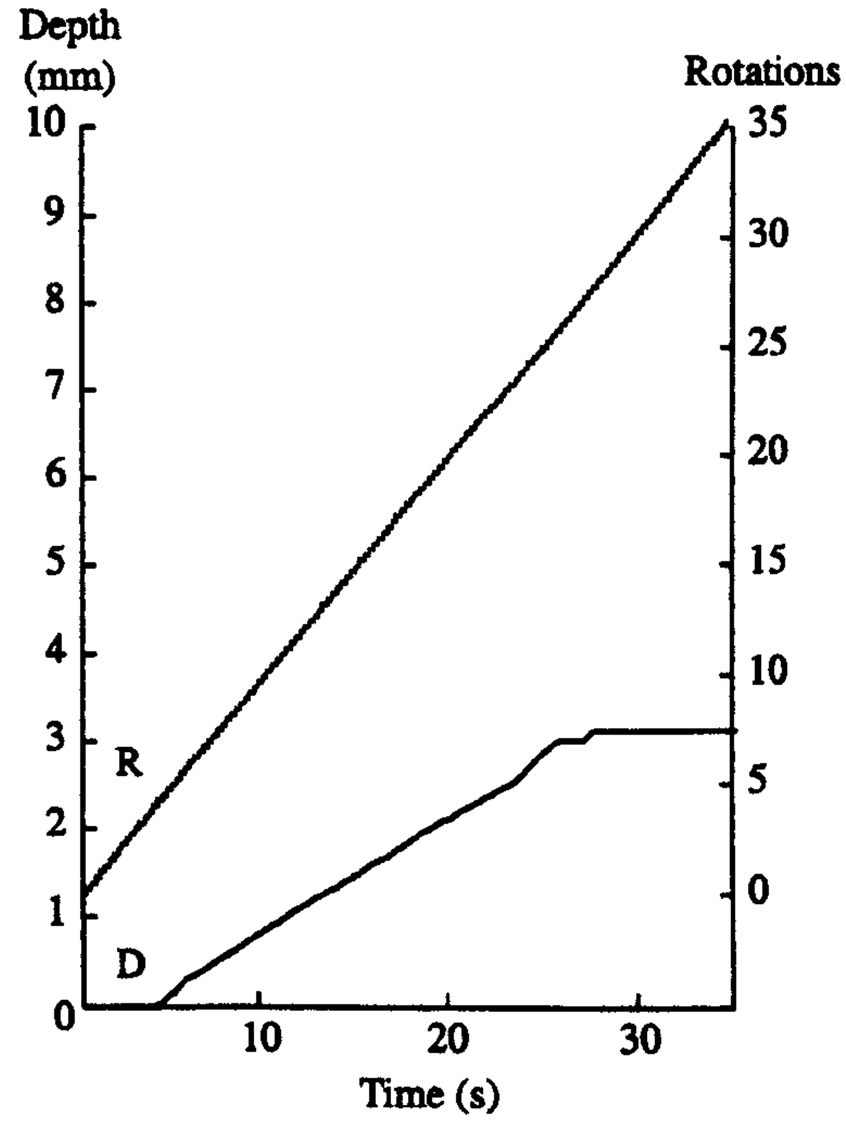

Figures 65a,b & 66a,b – Force, torque, depth and rotation data from coring CO_2 ice (12A 12B)

Tables 28a and 28b: Summary data for the above coring tests.

Sample temperature (K)	130
Chamber pressure (Pa)	20
Rotation speed (rev s^{-1})	1.013
Tool depth rate (mm s^{-1})	0.129
Initial / final force (N)	13.8 / 17.9
Initial / final torque (Nm)	0.1 / 0.33
Cutting strength (MPa)	54 / 112
Predicted ΔT on axis (K)	5.4
Predicted ΔT at $r=r_{tool}$ (K)	8.3
Predicted flash ΔT (K)	108

Sample temperature (K)	130
Chamber pressure (Pa)	20
Rotation speed (rev s^{-1})	1.032
Tool depth rate (mm s^{-1})	0.1254
Initial / final force (N)	16.5 / 20.6
Initial / final torque (Nm)	0.22 / 0.5
Cutting strength (MPa)	86 / 173
Predicted ΔT on axis (K)	8.5
Predicted ΔT at $r=r_{tool}$ (K)	13.2
Predicted flash ΔT (K)	245

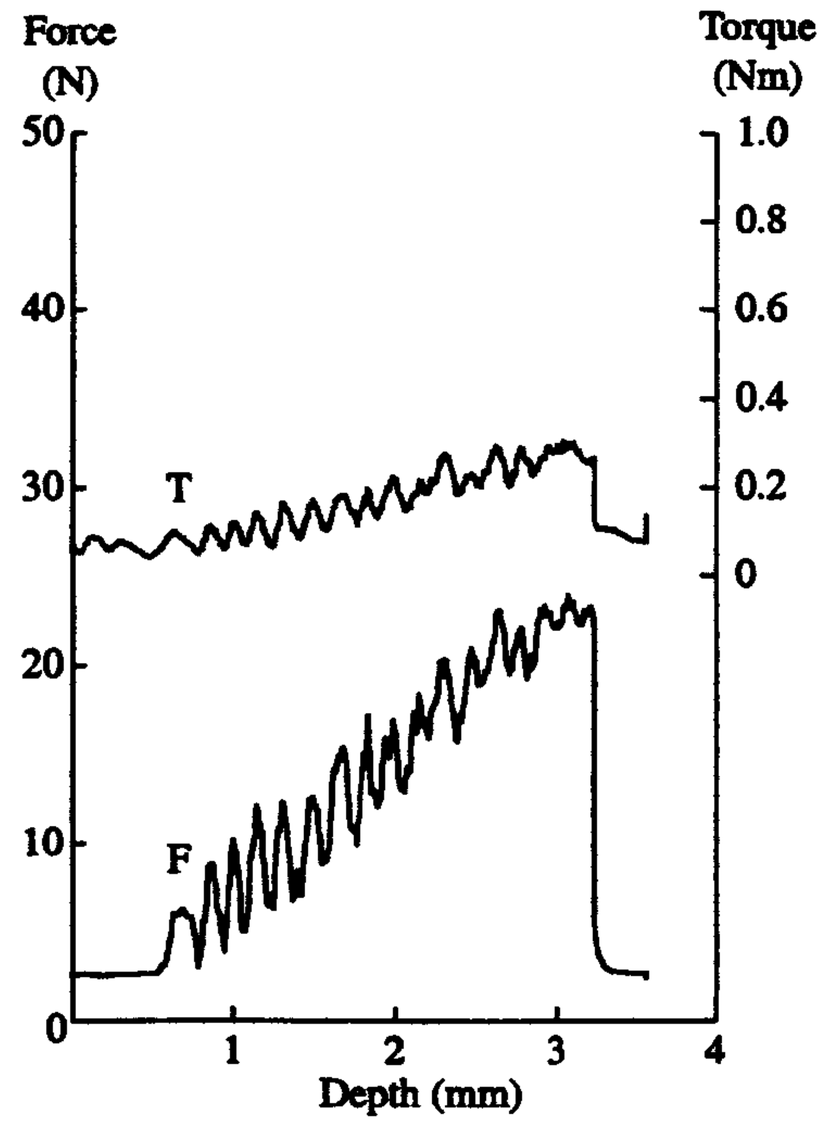

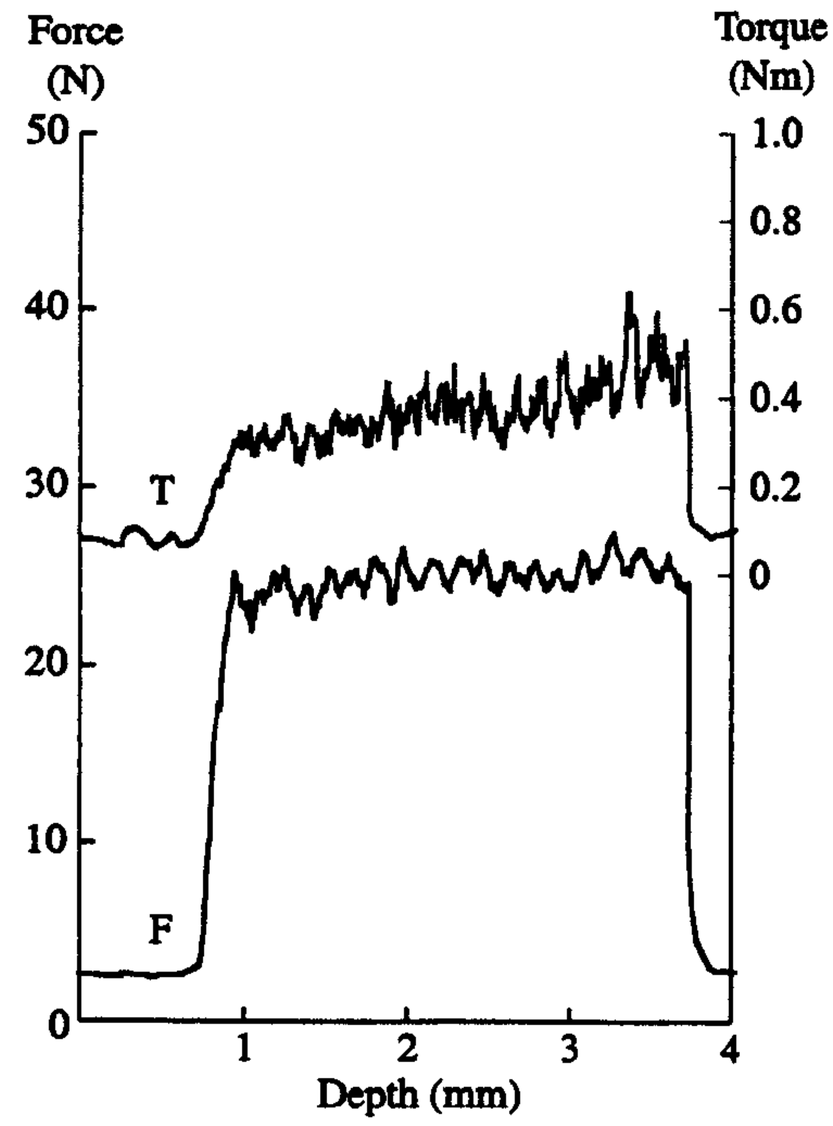

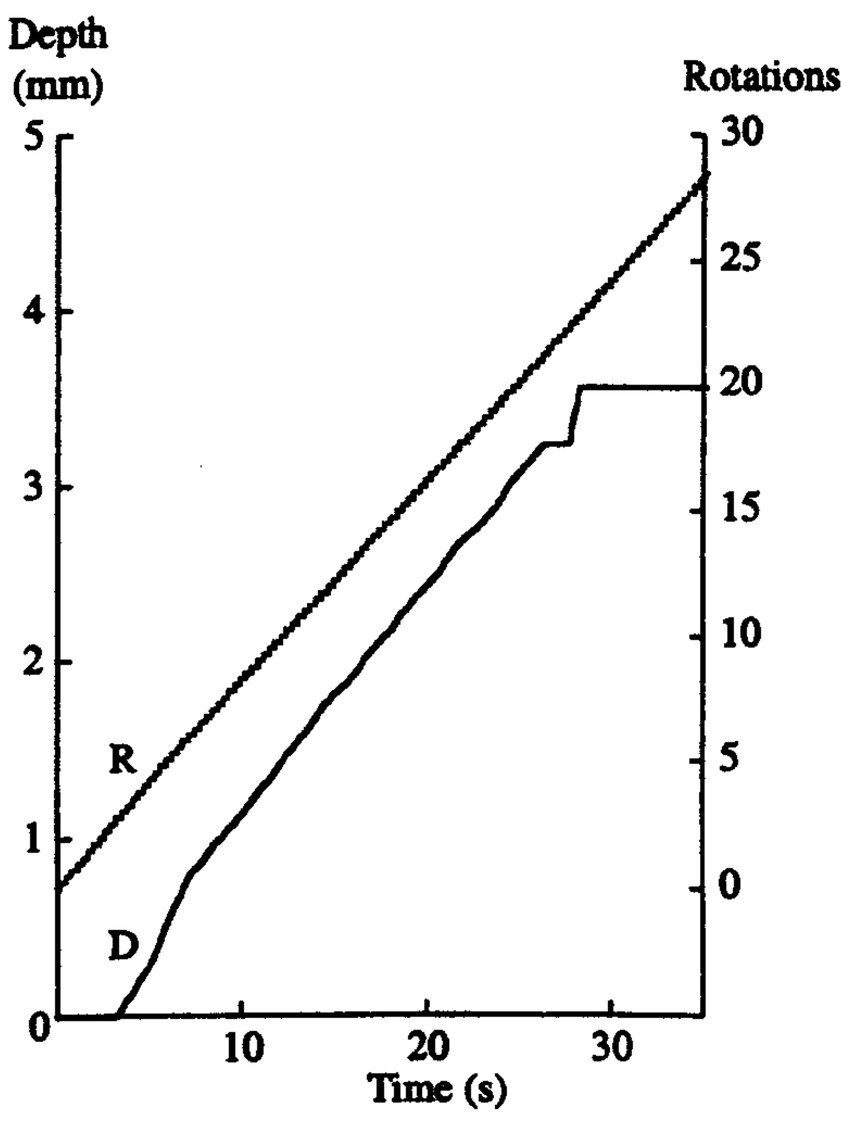

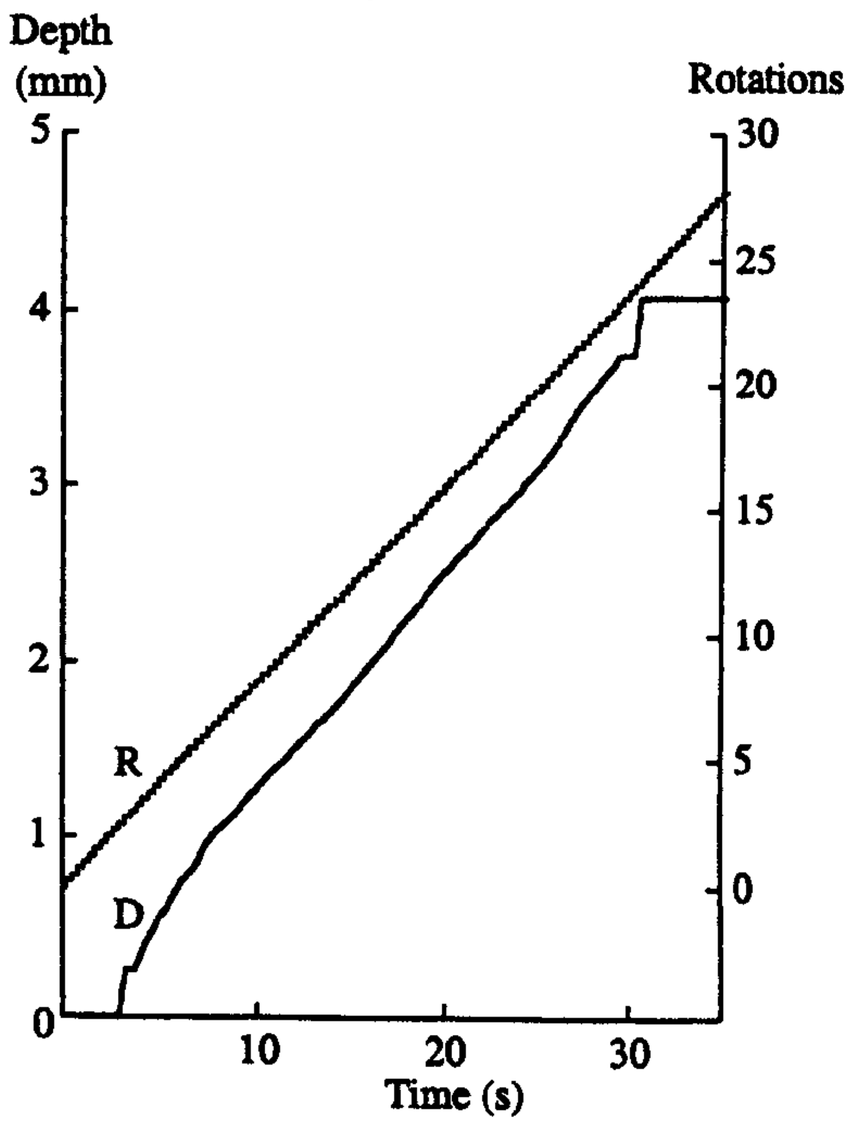

Figures 67a,b & 68a,b – Force, torque, depth and rotation data from coring CO_2 ice (A1 A2)

Tables 29a and 29b: Summary data for the above coring tests.

Sample temperature (K)	unknown
Chamber pressure (Pa)	unknown
Rotation speed (rev s^{-1})	0.815
Tool depth rate (mm s^{-1})	0.132
Initial / final force (N)	0 / 20.3
Initial / final torque (Nm)	0 / 0.15
Cutting strength (MPa)	- / 63
Predicted ΔT on axis (K)	- / 6.3
Predicted ΔT at $r=r_{tool}$ (K)	- / 9.6
Predicted flash ΔT (K)	-

Sample temperature (K)	unknown
Chamber pressure (Pa)	unknown
Rotation speed (rev s^{-1})	0.779
Tool depth rate (mm s^{-1})	0.1235
Initial / final force (N)	20.6 / 22.1
Initial / final torque (Nm)	0.21 / 0.36
Cutting strength (MPa)	72 / 101
Predicted ΔT on axis (K)	7.1
Predicted ΔT at $r=r_{tool}$ (K)	10.8
Predicted flash ΔT (K)	180

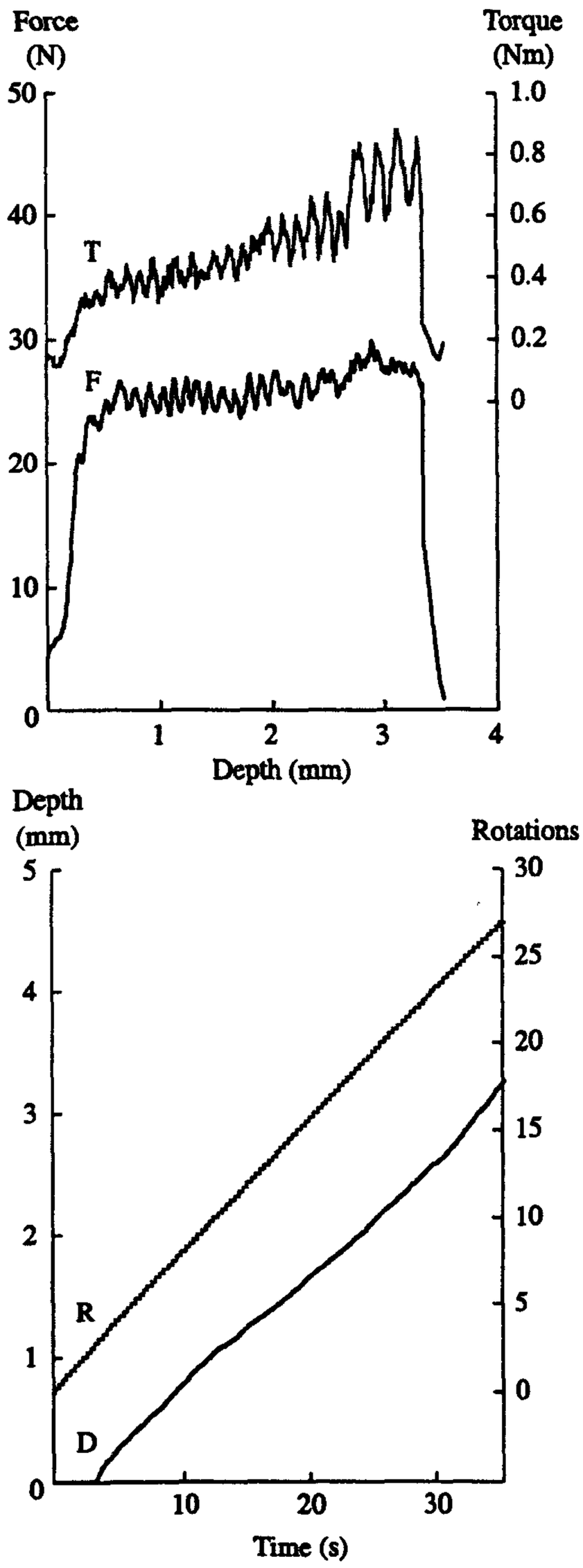

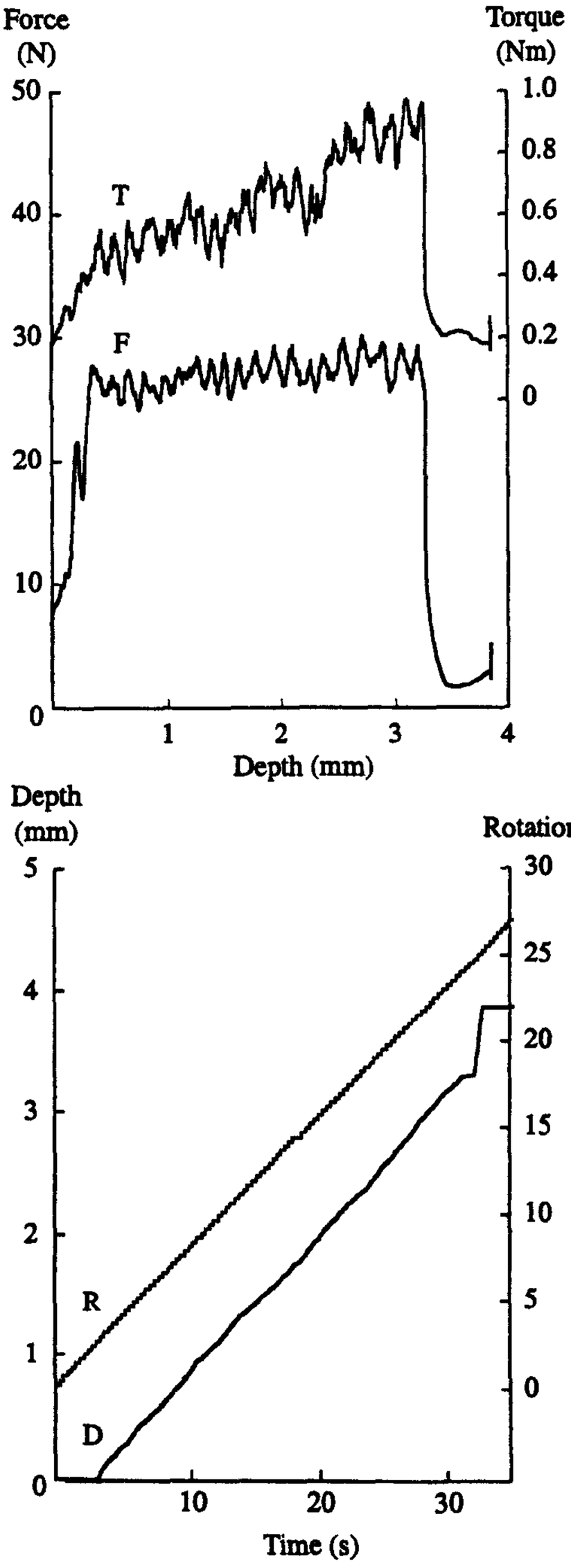

Figures 69a,b & 70a,b – Force, torque, depth and rotation data from coring CO_2 ice (A3 A4)

Tables 30a and 30b: Summary data for the above coring tests.

Sample temperature (K)	unknown
Chamber pressure (Pa)	unknown
Rotation speed (rev s^{-1})	0.758
Tool depth rate (mm s^{-1})	0.0886
Initial / final force (N)	20 / 26.2
Initial / final torque (Nm)	0.2 / 0.6
Cutting strength (MPa)	94 / 216
Predicted ΔT on axis (K)	8.2
Predicted ΔT at $r=r_{tool}$ (K)	13.3
Predicted flash ΔT (K)	200

Sample temperature (K)	unknown
Chamber pressure (Pa)	unknown
Rotation speed (rev s^{-1})	0.736
Tool depth rate (mm s^{-1})	0.1177
Initial / final force (N)	19.4 / 25.2
Initial / final torque (Nm)	0.3 / 0.71
Cutting strength (MPa)	85 / 186
Predicted ΔT on axis (K)	8.2
Predicted ΔT at $r=r_{tool}$ (K)	12.7
Predicted flash ΔT (K)	250

Figures 71-74 show the data gathered from the miniature silicon thermometer diodes described in section 4.4. One of these temperature monitoring experiments did not result in a useful temperature record because the sampling window set on the computer ended before the coring head met the diode. This 'missed' run is included for completeness, and is shown in Figure 73. Along with records of the force, torque, depth, and rotation state, two further charts are shown. In these extra graphs the voltage produced by the diode-thermometer processing circuit and the calibrated temperature are both shown as a function of the distance travelled by the coring head. The point at which the diode signal is lost is shown in the force and torque charts by a vertical arrow, but the small size of the device means that the resistance met when it is smashed cannot be seen clearly at this point.

Although this measurement method has produced valuable data it is not an ideal system. In common with any sensor that relies on small voltage variations the diodes are sensitive to electrical noise. One source of electrical noise is the cutting tool which is held at ground potential. The cylindrical form of the diodes means that before the cutting edge of the coring head breaks or dislodges the diode, it will shave through the solder-tag at the end of the diode's package - with each pass of the teeth on the coring head a layer of material only 40 μm thick is sheared away. It is hypothesized that several minute cuts may be taken from the diode's solder tags before the diode is either forced from the ice or broken. In each of these fleeting contacts one half of the diode amplifier circuit's input would be set to a voltage that causes the amplified output to swing to one of the two power rails. If the cutting head smashes the diode then the connecting wires may still be firmly held in the ice and periodically contacted by the rotating tool. This is a plausible explanation for the swift multiple full-scale deflections that are seen in the amplifier output of Figure 74 just before the diode is smashed, and afterwards at points a few millimetres deeper into the ice. Two further problems, of unknown origin may be present in the thermometry data shown. Firstly, the temperature history shown in Figure 71 does not share the smooth upward trend of Figures 72 and 74 close to the diode. No explanation can be found for this behaviour. Secondly, the large increase in the torque record of Figure 74 at a depth of 7 mm cannot be explained as no part of the tool corresponds to this length. For this reason the initial values of torque, not the average values, are used to calculate the power dissipated.

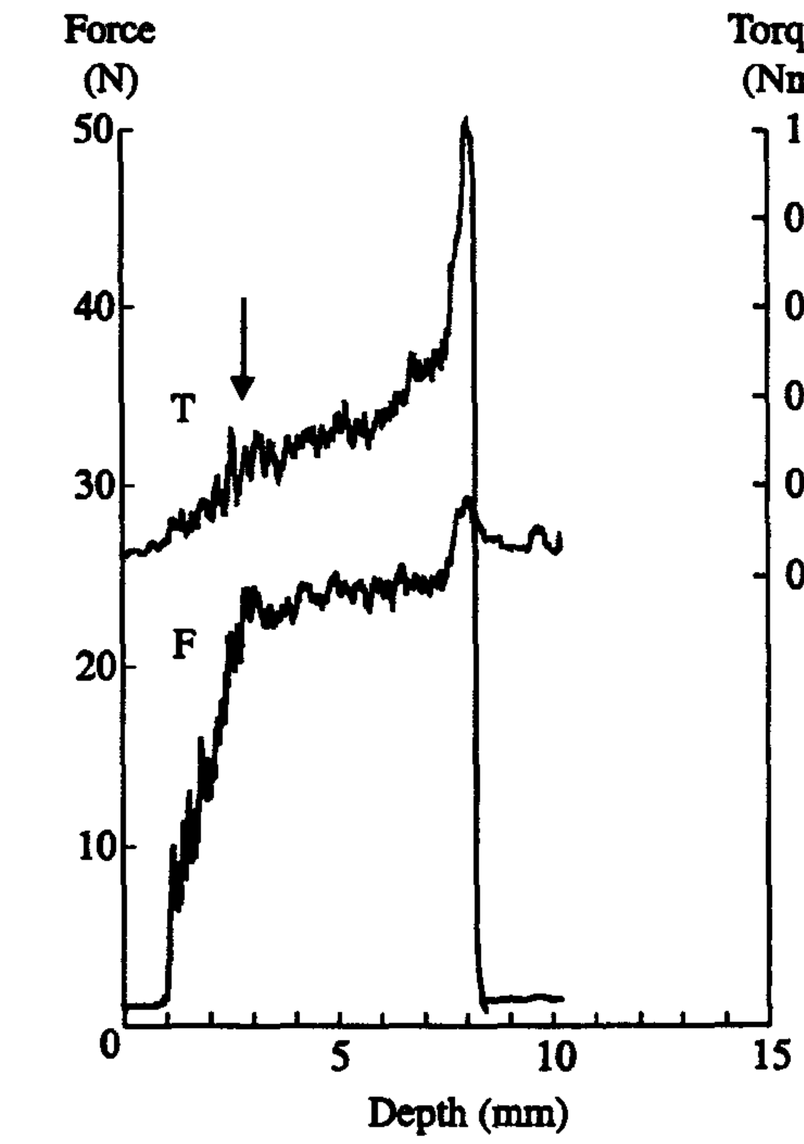

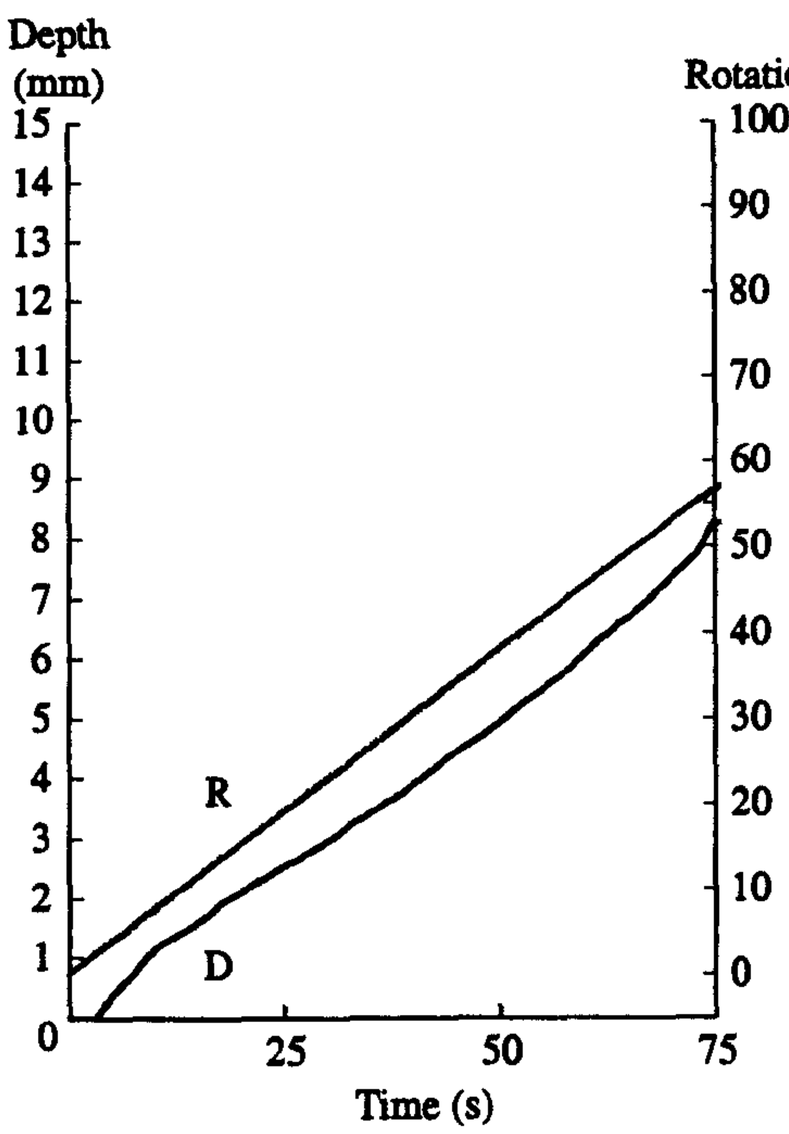

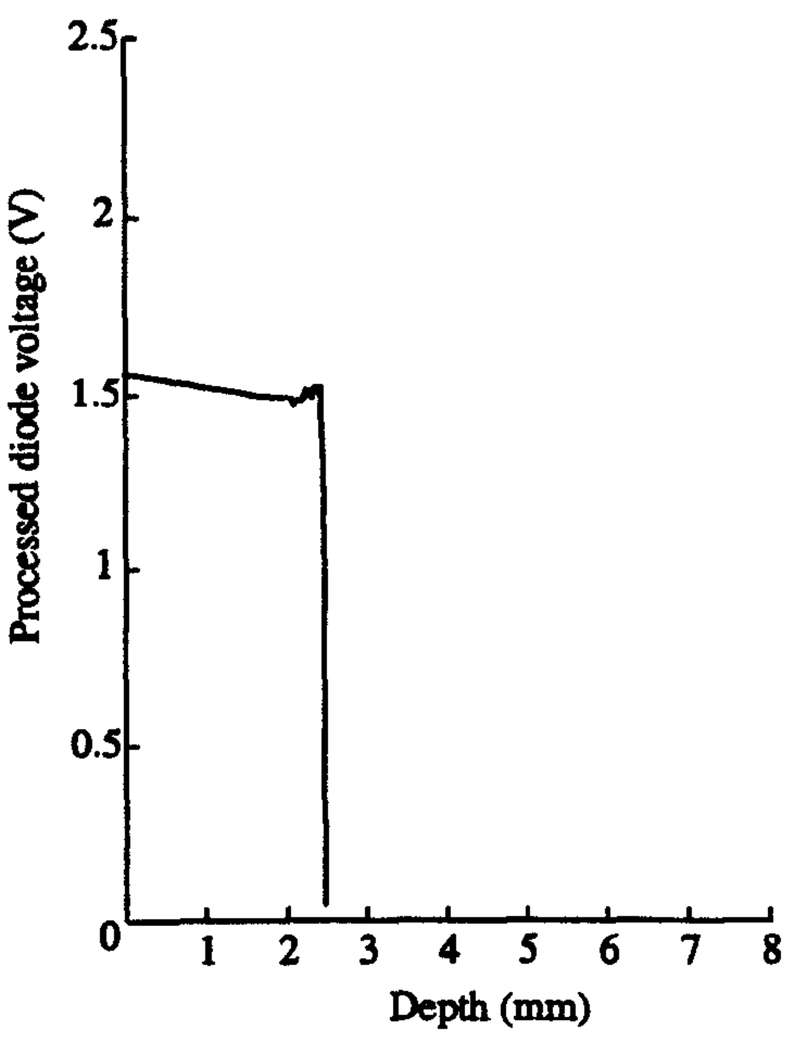

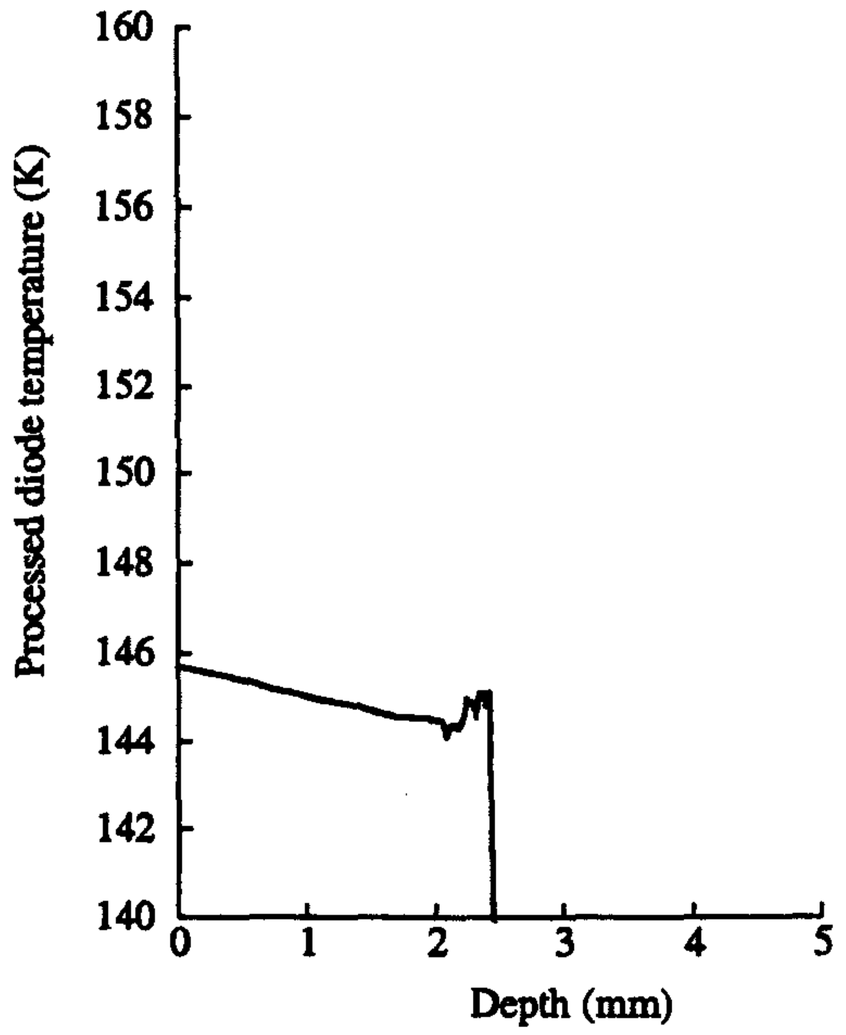

Figure 71a,b,c,d – Force, torque, depth, rotation, and measured temperature data from a CO_2 ice coring run using diode #1 (A5)

Table 31 : Summary data for the above coring test.

Sample temperature (K)	unknown
Chamber pressure (Pa)	unknown
Rotation speed (rev s^{-1})	0.7663
Tool depth rate (mm s^{-1})	0.0966
Initial / final force (N)	22.1 / 25.2
Initial / final torque (Nm)	0.2 / 0.24
Cutting strength (MPa)	93
Predicted ΔT on axis (K)	8.4
Predicted ΔT at $r=r_{tool}$ (K)	13.4
Predicted flash ΔT (K)	190

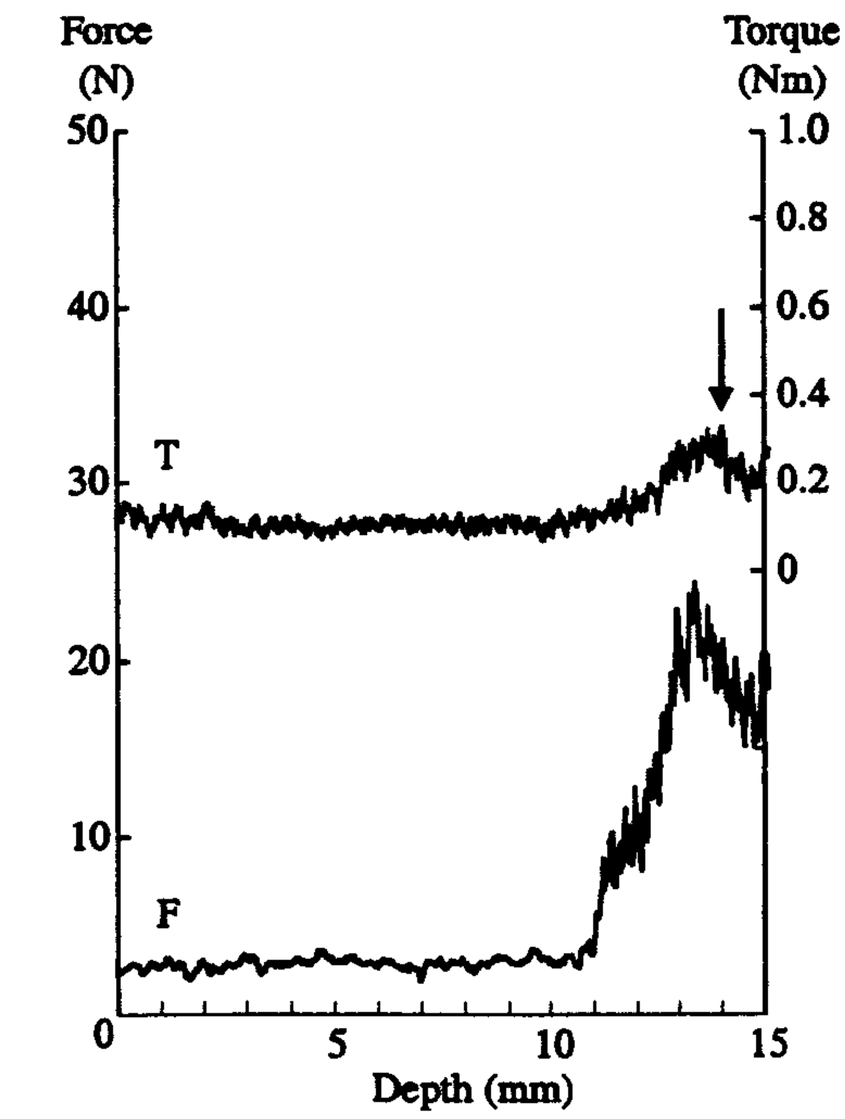

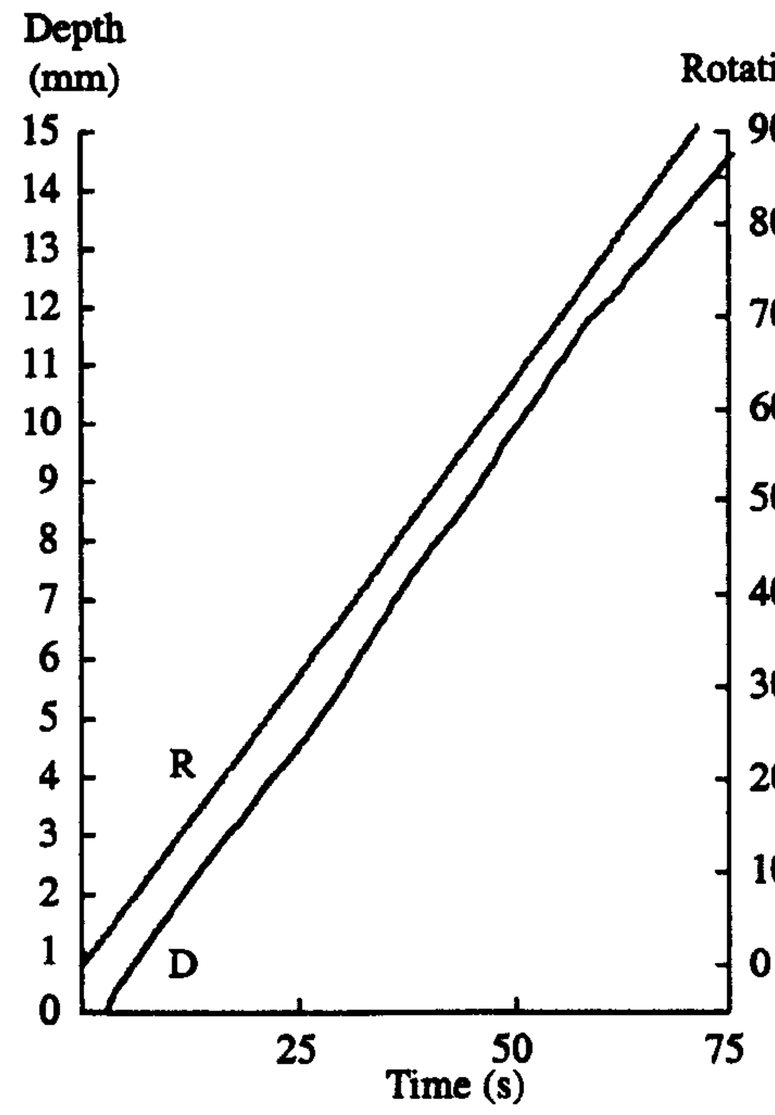

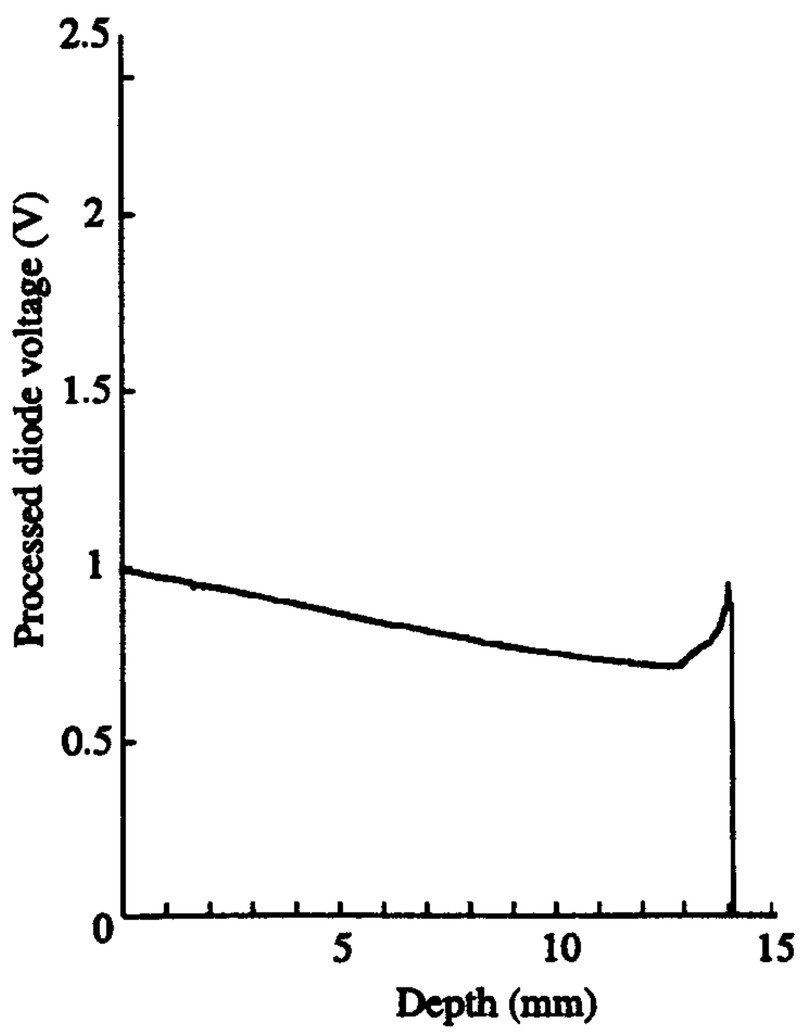

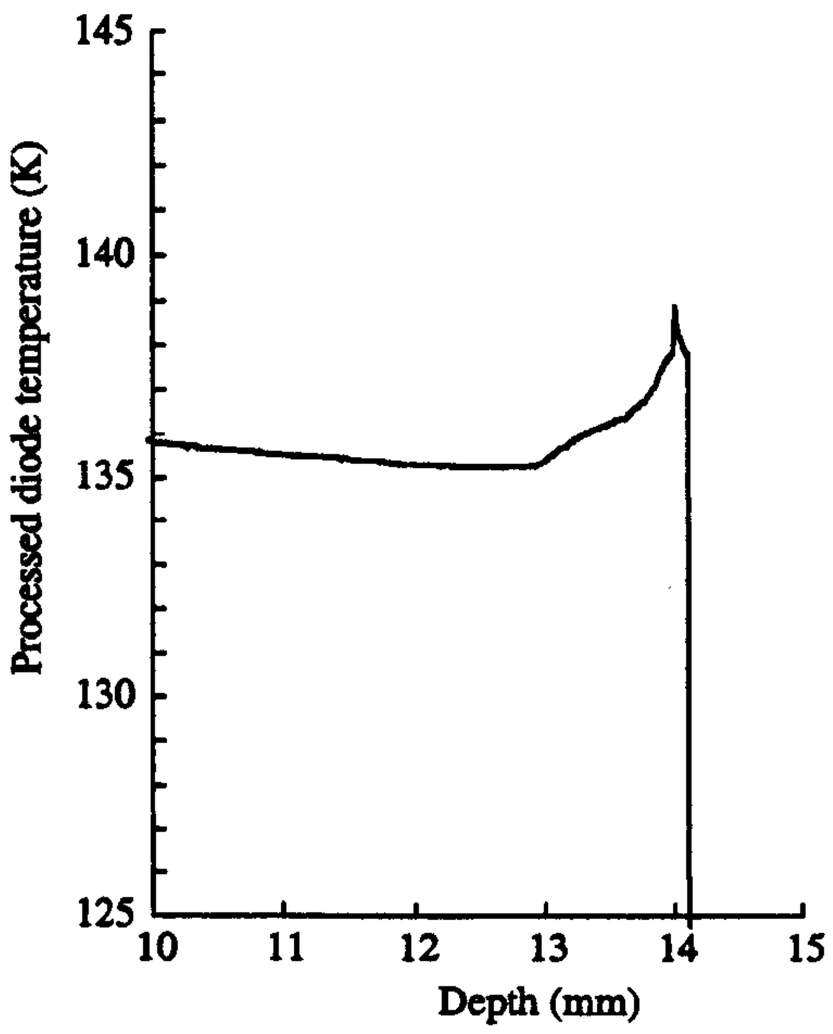

Figure 72a,b,c,d – Force, torque, depth, rotation, and measured temperature data from a CO_2 ice coring run using diode #2 (B1)

Table 32 : Summary data for the above coring test.

Sample temperature (K)	155±10
Chamber pressure (Pa)	10
Rotation speed (rev s^{-1})	1.305
Tool depth rate (mm s^{-1})	0.220
Initial / final force (N)	12.6 / 16.8
Initial / final torque (Nm)	0.11 / 0.15
Cutting strength (MPa)	39
Predicted ΔT on axis (K)	4.3
Predicted ΔT at $r=r_{tool}$ (K)	5.8
Predicted flash ΔT (K)	144

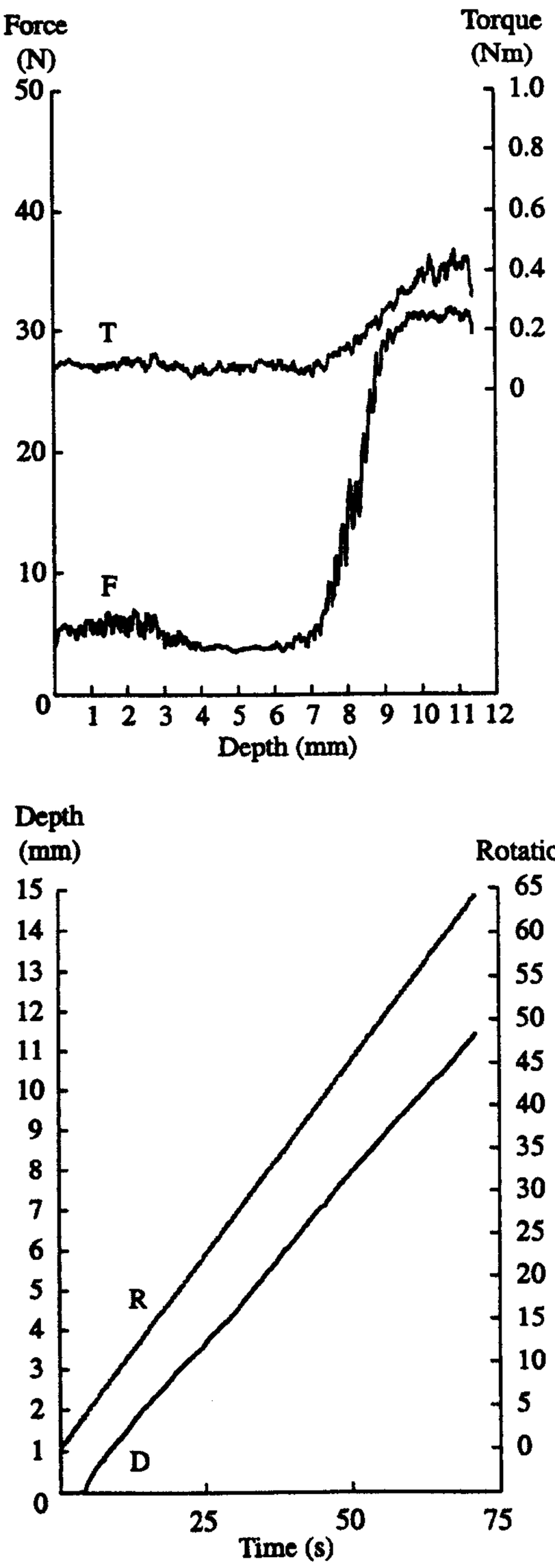

Figure 73a,b,c,d – Force, torque, depth and rotation data from a CO_2 ice coring run (C)

Table 33 : Summary data for the above coring test.

Sample temperature (K)	130±20
Chamber pressure (Pa)	30
Rotation speed (rev s^{-1})	0.9352
Tool depth rate (mm s^{-1})	0.1724
Initial / final force (N)	25.9 / -
Initial / final torque (Nm)	0.3 / -
Cutting strength (MPa)	82
Predicted ΔT on axis (K)	8.9
Predicted ΔT at $r=r_{tool}$ (K)	13.1
Predicted flash ΔT (K)	260

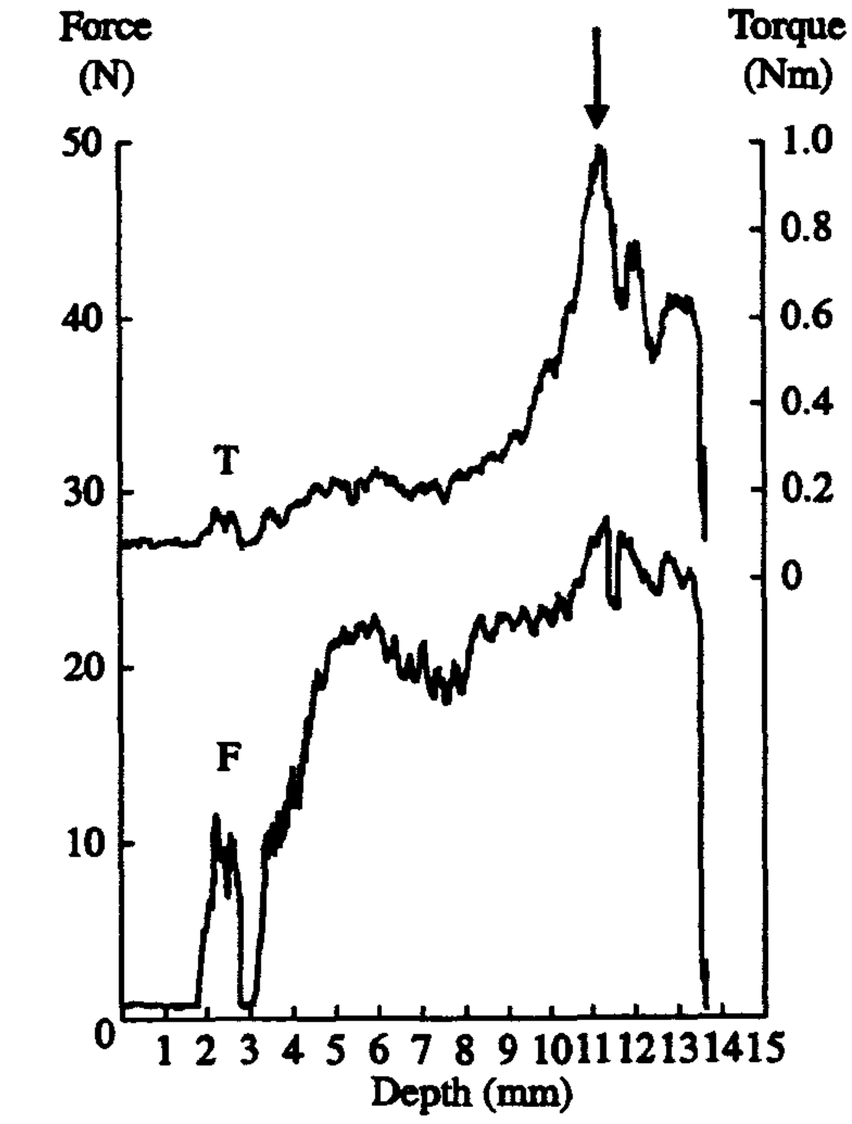

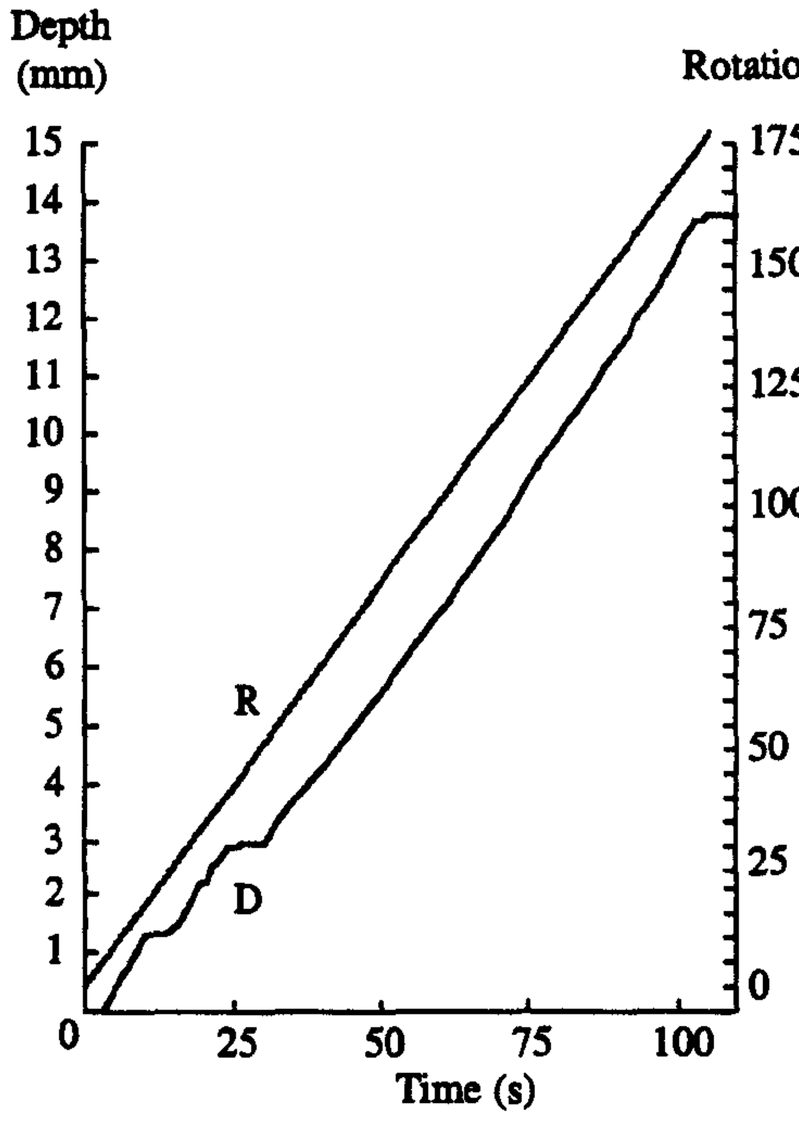

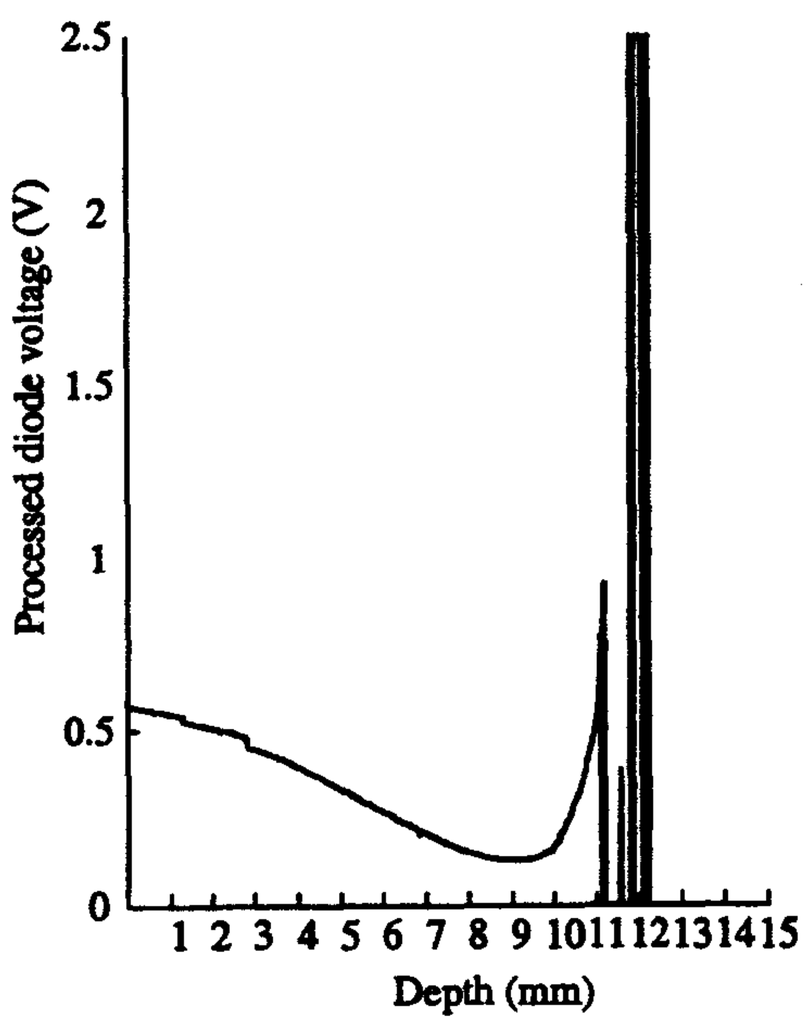

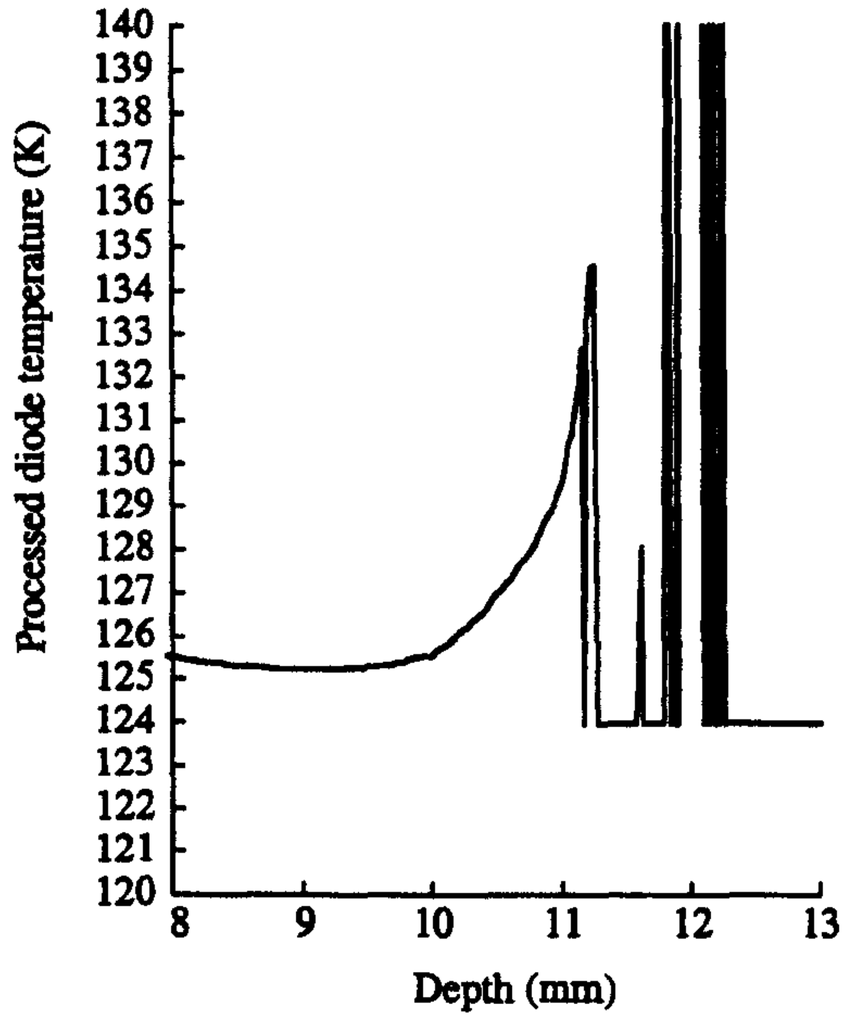

Figure 74a,b,c,d – Force, torque, depth, rotation, and measured temperature data from a CO_2 ice coring run using diode #3 (D)

Table 34: Summary data for the above coring test.

Sample temperature (K)	140±10
Chamber pressure (Pa)	15
Rotation speed (rev s^{-1})	1.704
Tool depth rate (mm s^{-1})	0.1551
Initial / final force (N)	21.7 / 27.3
Initial / final torque (Nm)	0.15 / 0.88*
Cutting strength (MPa)	119
Predicted ΔT on axis (K)	12.4
Predicted ΔT at $r=r_{tool}$ (K)	18.1
Predicted flash ΔT (K)	274

** The rise in torque many millimetres before the location of the diode cannot be explained.*

5.2.4 Forming zone-frozen water ice

Without a means of making compacted water snow samples, or any clear methods by which a snow could be produced and then compacted to make a uniform density profile, bulk water ice samples were formed in place inside the vacuum chamber. All of the ice samples were made from water that had been first boiled in a microwave oven and then siphoned into the sample holder, filling it to about four-fifths of its capacity. The chamber was then closed and the cryogen was pumped through the sample cooling pipes at a slow rate. To prevent ice from forming at the surface of the liquid, and so trapping bubbles of air exsolved from the water, the halogen lamp inside the chamber was run at half-power and the chamber's rotary vacuum pump was started. The vacuum pump was used to lower the pressure around the liquid sample and encourage dissolved air to exsolve from the water. Care was taken to prevent the internal pressure from falling too far because it was easy to reach a situation where the water would boil under the reduced pressure, which led to water droplets being thrown around the chamber. In view of the electrical risk from sprays of water inside the chamber the vacuum pump was throttled to preserve a pressure of a few tens of mbar. However, other workers (Khusnatdinov and Petrenko, 1996) describe a much more vigorous method for forming water ice samples. Instead of cooling a sample from its base their approach was to freeze a mass of water down from its surface by reducing the air pressure above the liquid, which is *not* simultaneously cooled. Such a method, although it allegedly yields single-crystal ices with a high degree of repeatability uses the boiling action to cool the water. This approach has not been tested in the vacuum drilling system nor is it suggested as a potentially safe formation method.

By slowly freezing water under reduced atmospheric pressure, a billet of bubble-free water ice could be typically formed in around three hours. A representative fragment from such a block of chamber-grown ice is shown in Figure 75 with a centimetre-scale ruler for comparison. While essentially bubble-free at the centre, a slight opacity could sometimes be seen in the ice at the base of the sample holder. This may be caused by residual air bubbles trapped in niches along the joint of the sample holder wall at the cooling plate.

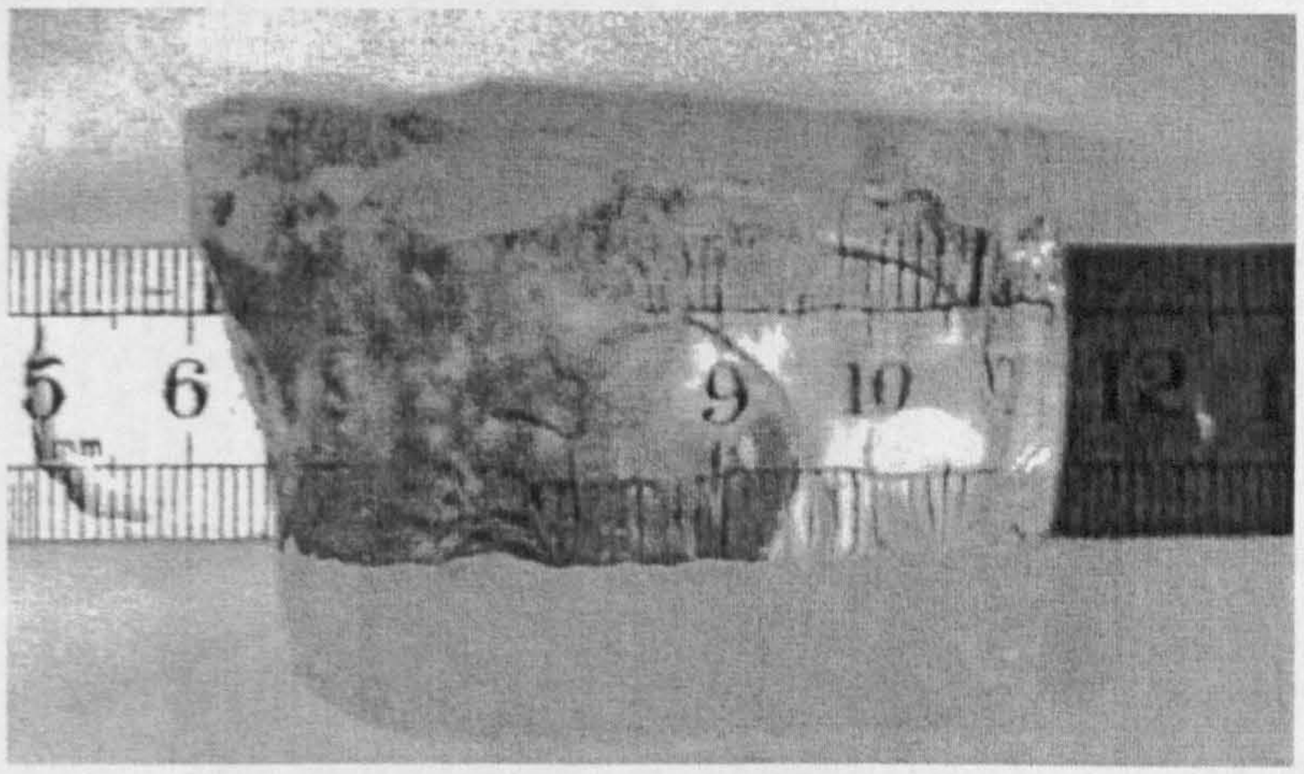

Figure 75 - A fragment of ice grown by zone-freezing in the experimental chamber.

Once the ice had fully solidified, the vacuum pump throttle was opened and the chamber was evacuated to its much lower working pressure of a few pascals. The temperature of the frozen sample would then be slowly lowered to the desired temperature using the cryogen delivery valve to control the rate of cooling. Care was exercised to prevent the ice from cracking by differential expansion and in practice the block could be cooled to 120 K without shattering. A critical factor that prevented cracking was that the temperature difference between the upper and lower surfaces of the ice had to be smaller than ~50 K, giving a maximum thermal gradient of a little over 10 K cm^{-1}. Once fully cooled the ice will contain a stress field from the overall contraction of the ice, which amounts to a volumetric shrinkage of 0.8% in cooling from 270 K to 170 K, but the effect of this internal stress on the behaviour of the ice when cored will not be assessed.

After making the coring measurements the ice was broken into small centimetre-size fragments to see if other physical properties of the ice could be measured. Of particular interest is the grain size of the ice, as the low strain rate experiments of Currier and Schulson (1982) suggest that this can play a significant role in determining the tensile strength of polycrystalline ice. No clear grain boundaries could be seen in the unsectioned and unpolished sample fragment shown in the photographs of Figure 76 and the size of the pieces shown may set a rough lower bound for the grain size in the remainder of the sample. Without a cooled microscope stage the ice could not be accurately sectioned and more chance than skill was involved when photographing a sliver of rapidly melting ice that was sandwiched between two plastic Polaroid filters. No attempts were made to try and vary the grain size of the zone-frozen ices, and the implications of varying grain size on the cutting strength of the ice have not been explored.

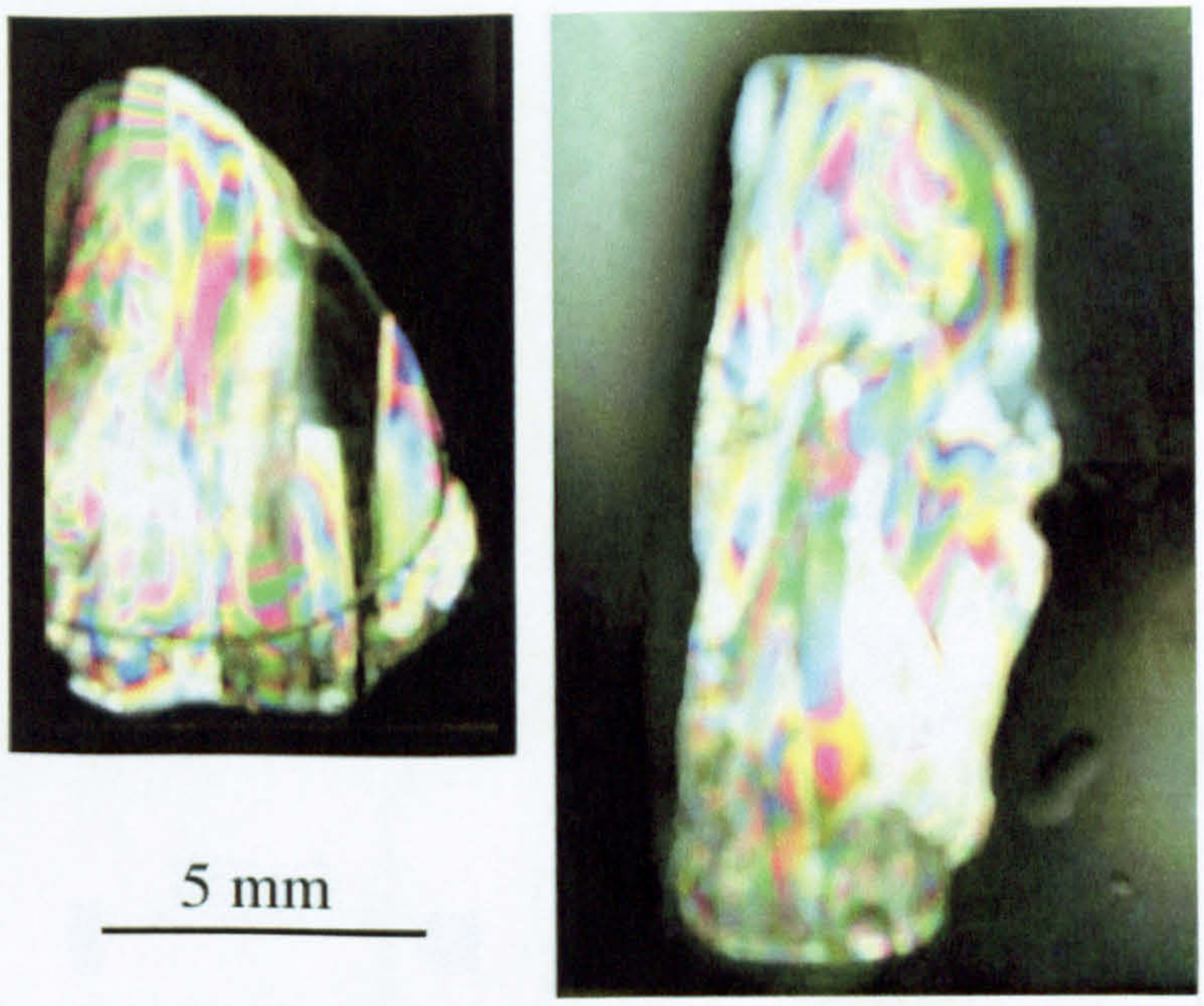

Figure 76 - Pieces of zone-frozen ice photographed with crossed polarizing filters.

5.2.5 Coring zone-frozen water ice

The coring process was very similar to that used in the vapour-grown carbon dioxide coring experiments. Once the ice had been frozen and cooled to the desired temperature the tool head was set rotating and then slowly driven into the ice sample with the downforce, torque, tool rotation speed, and depth rate being simultaneously monitored by the logging computer. Unlike the CO_2 samples, the water ices were cooled to different temperatures so that the influence of ice's temperature dependent thermal and physical properties on the coring process could be assessed. The coring data from the water ice runs are shown in the same format used by the carbon dioxide experiments and are shown in Figures 77-91 and Tables 35-42.

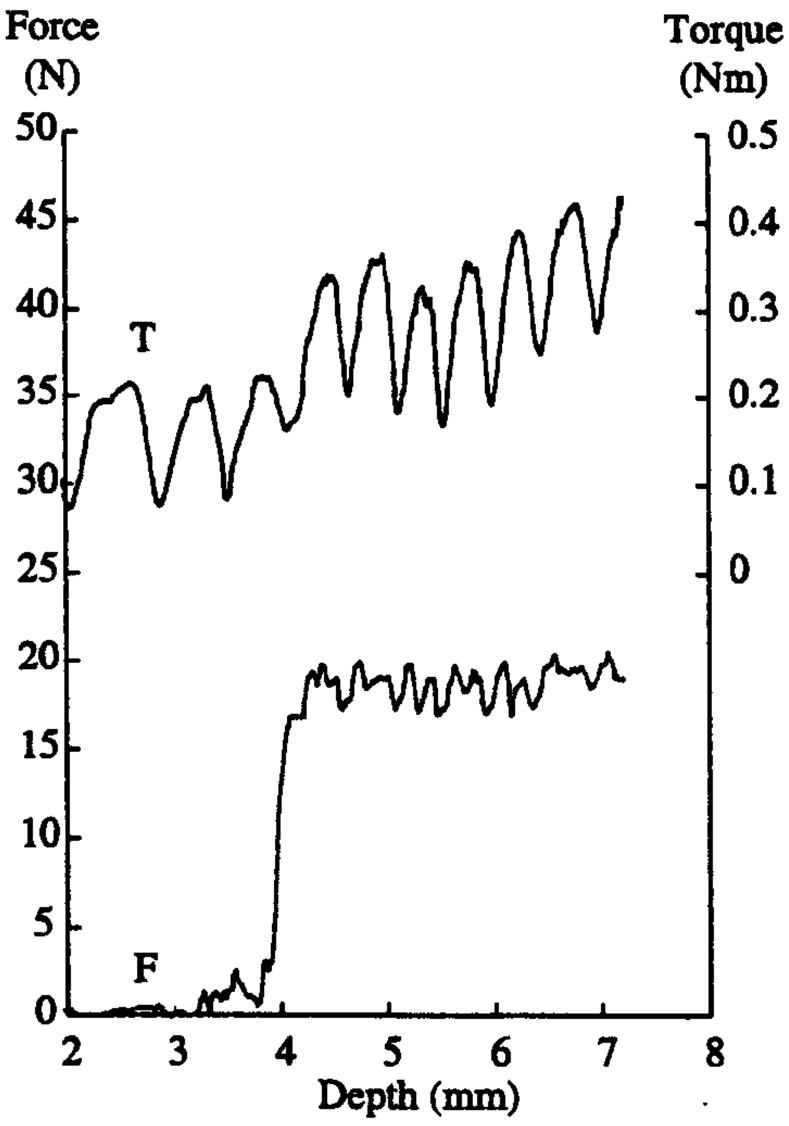

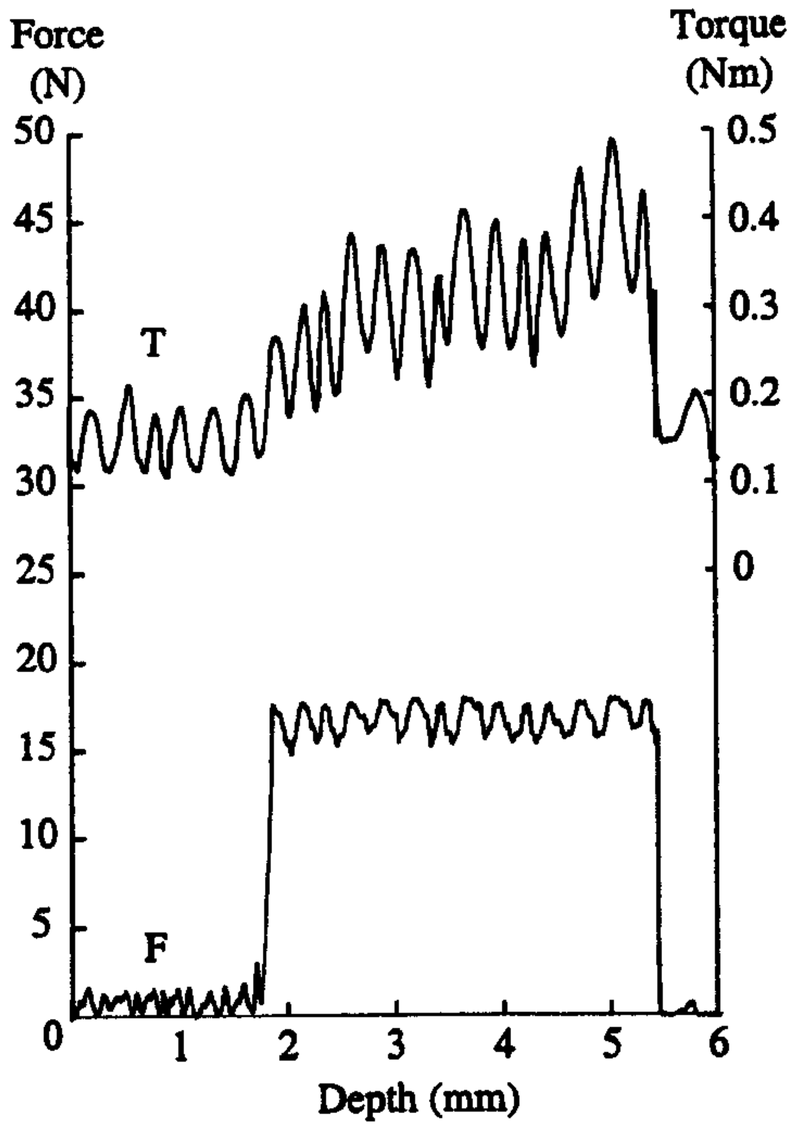

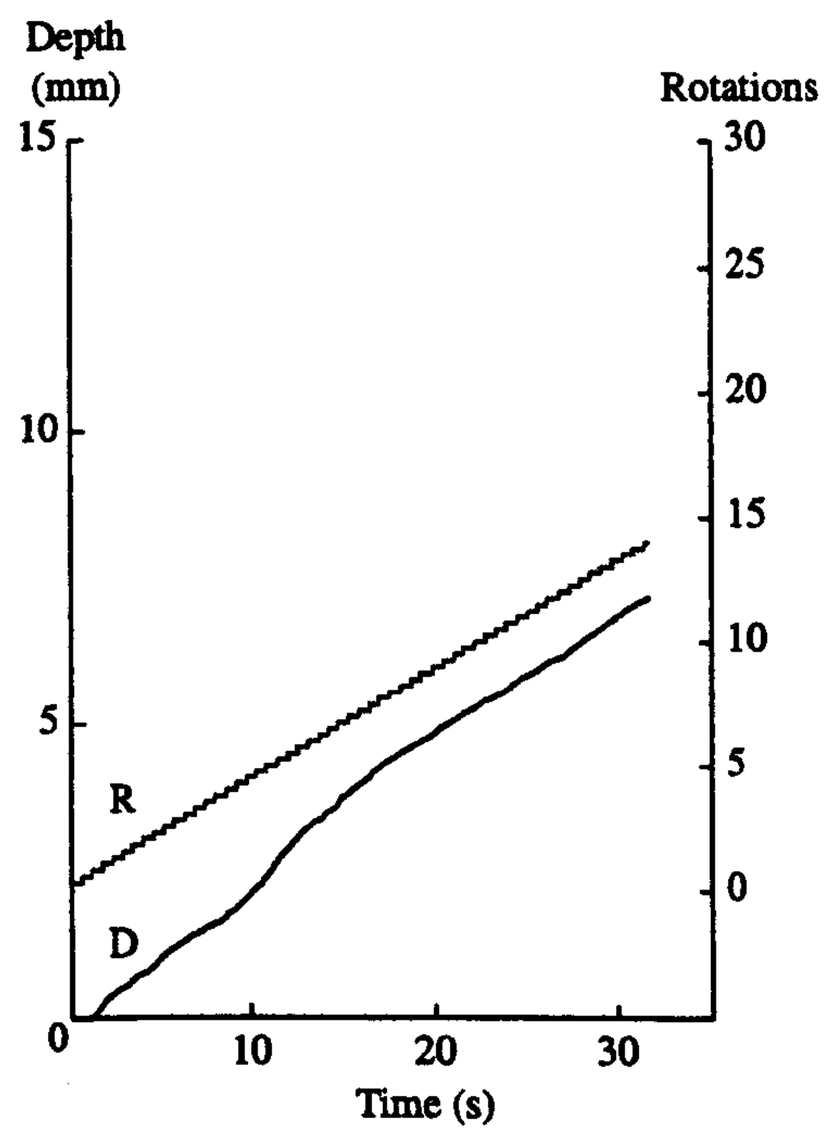

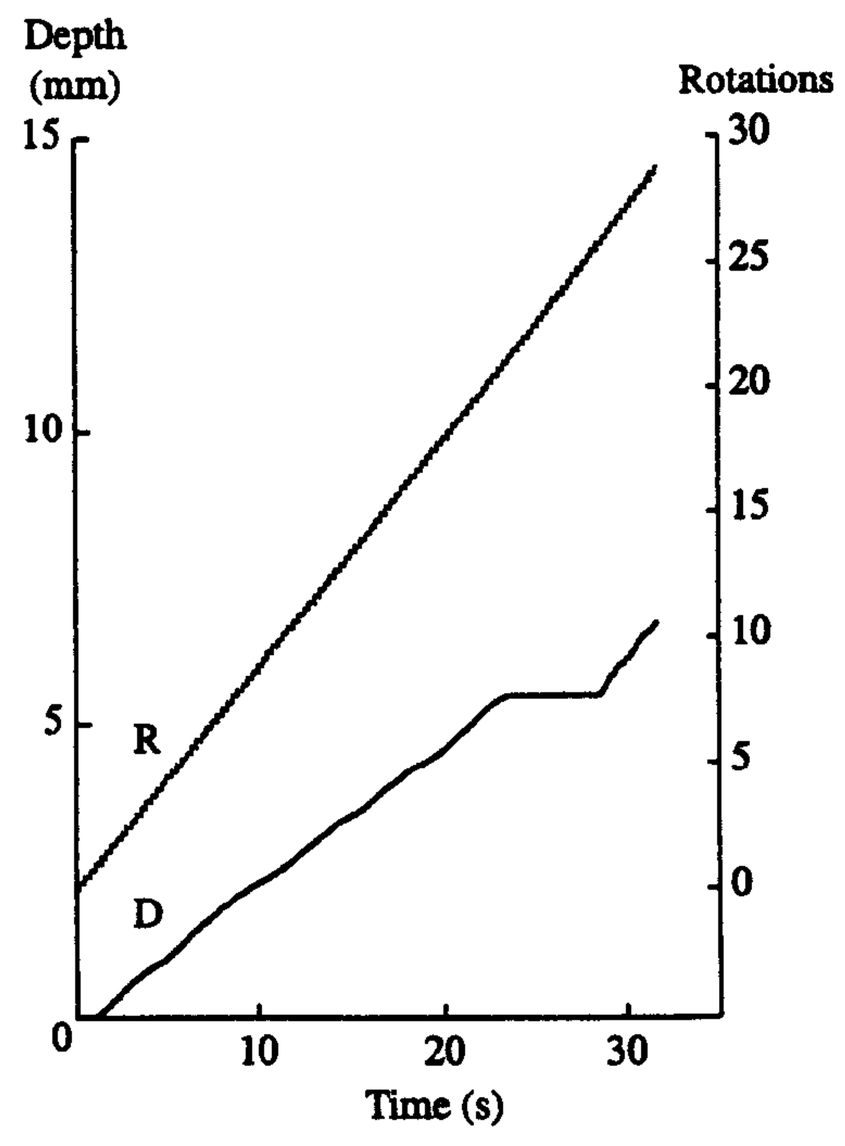

Figures 77a,b and 78a,b - Force, torque, depth, and rotation data from coring water ice (1B 1C)

Tables 35a and 35b - Summary of a coring run in zone-frozen water ice (1B 1C)

Sample temperature (K)	250
Chamber pressure (Pa)	20
Rotation speed (rev s^{-1})	0.443
Tool depth rate (mm s^{-1})	0.244
Initial / final force (N)	15.2 / 19.7
Initial / final torque (Nm)	0.27 / 0.37
Cutting strength (MPa)	21.4/ 29
Predicted ΔT on axis (K)	1.1
Predicted ΔT at $r=r_{tool}$ (K)	2
Predicted flash ΔT (K)	23

Sample temperature (K)	250
Chamber pressure (Pa)	20
Rotation speed (rev s^{-1})	0.915
Tool depth rate (mm s^{-1})	0.250
Initial / final force (N)	14.9 / 17
Initial / final torque (Nm)	0.08 / 0.22
Cutting strength (MPa)	26.6 / 38.7
Predicted ΔT on axis (K)	1.4
Predicted ΔT at $r=r_{tool}$ (K)	2.5
Predicted flash ΔT (K)	14

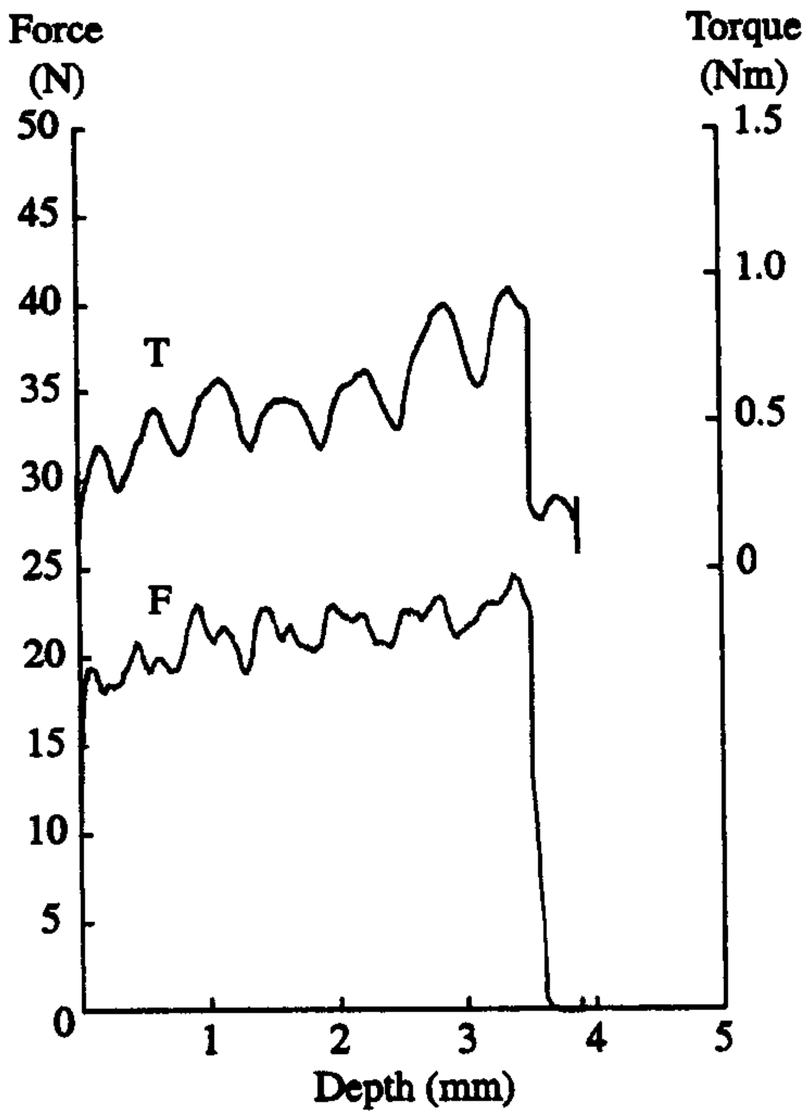

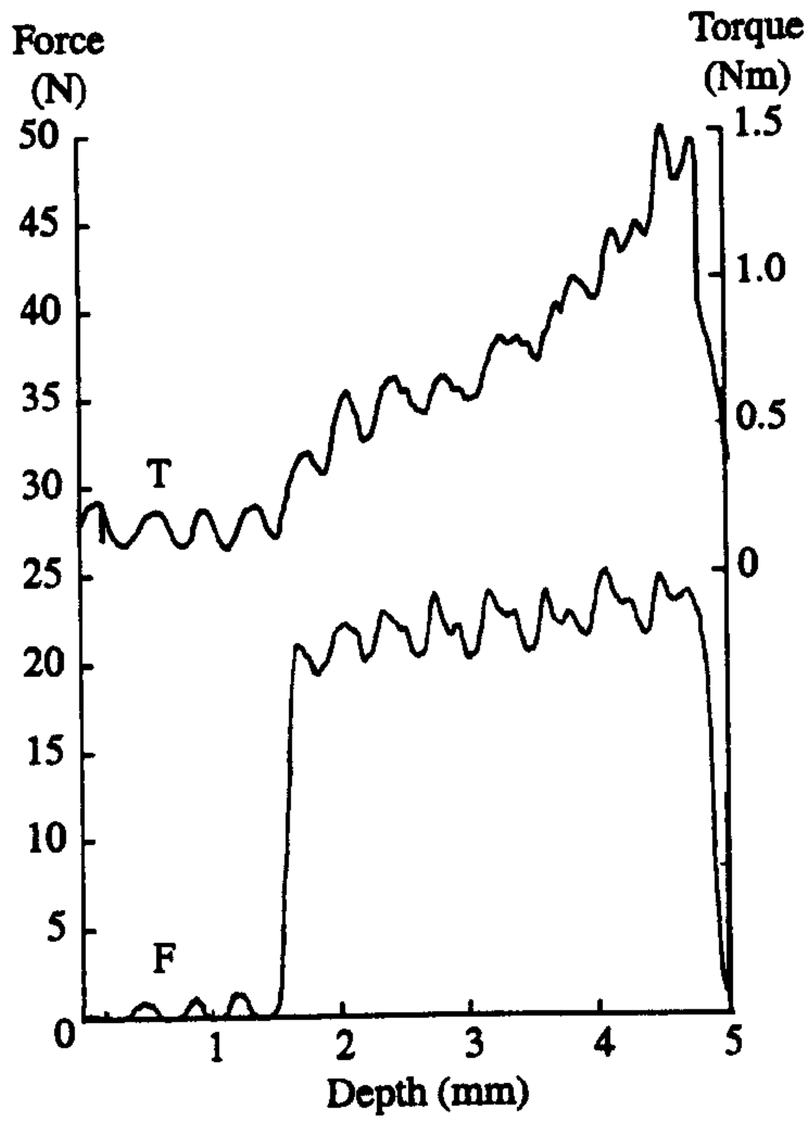

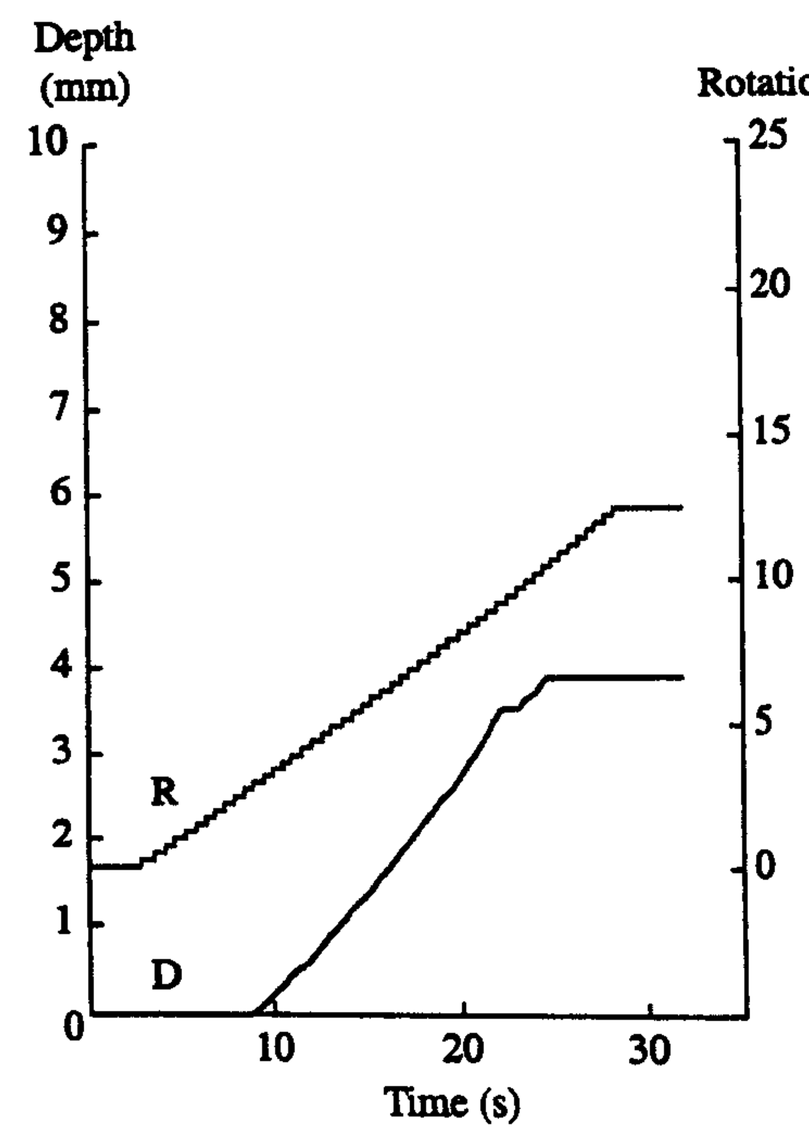

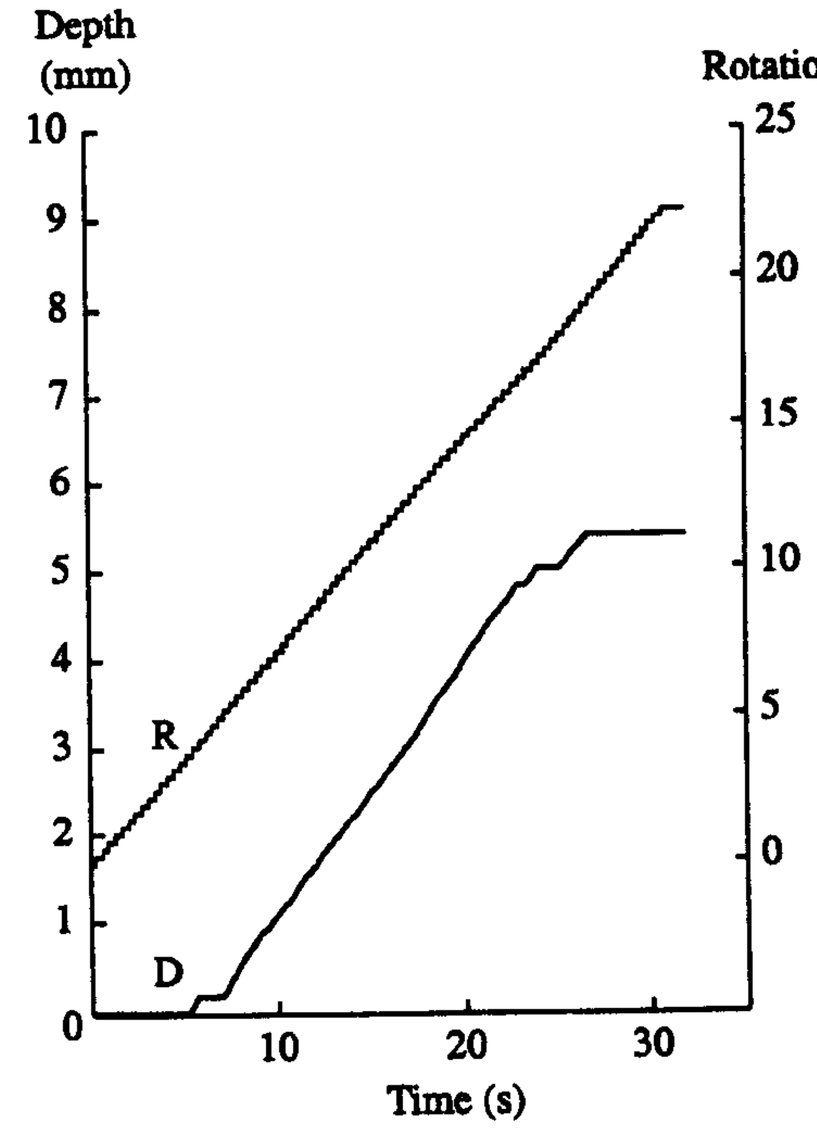

Figures 79a,b and 80a,b - Force, torque, depth, and rotation data from coring water ice (2B 2C)

Tables 36a and 36b - Summary of a coring run in zone-frozen water ice (2B 2C)

Sample temperature (K)	228
Chamber pressure (Pa)	4
Rotation speed (rev s^{-1})	0.480
Tool depth rate (mm s^{-1})	0.255
Initial / final force (N)	11.9 / 23
Initial / final torque (Nm)	0.35 / 0.66
Cutting strength (MPa)	27.6 / 51.7
Predicted ΔT on axis (K)	1.4
Predicted ΔT at $r=r_{tool}$ (K)	2.6
Predicted flash ΔT (K)	32

Sample temperature (K)	215
Chamber pressure (Pa)	3
Rotation speed (rev s^{-1})	0.720
Tool depth rate (mm s^{-1})	0.287
Initial / final force (N)	20.1 / 22.7
Initial / final torque (Nm)	0.17 / 1
Cutting strength (MPa)	26.2 / 107.2
Predicted ΔT on axis (K)	1.4
Predicted ΔT at $r=r_{tool}$ (K)	2.6
Predicted flash ΔT (K)	22

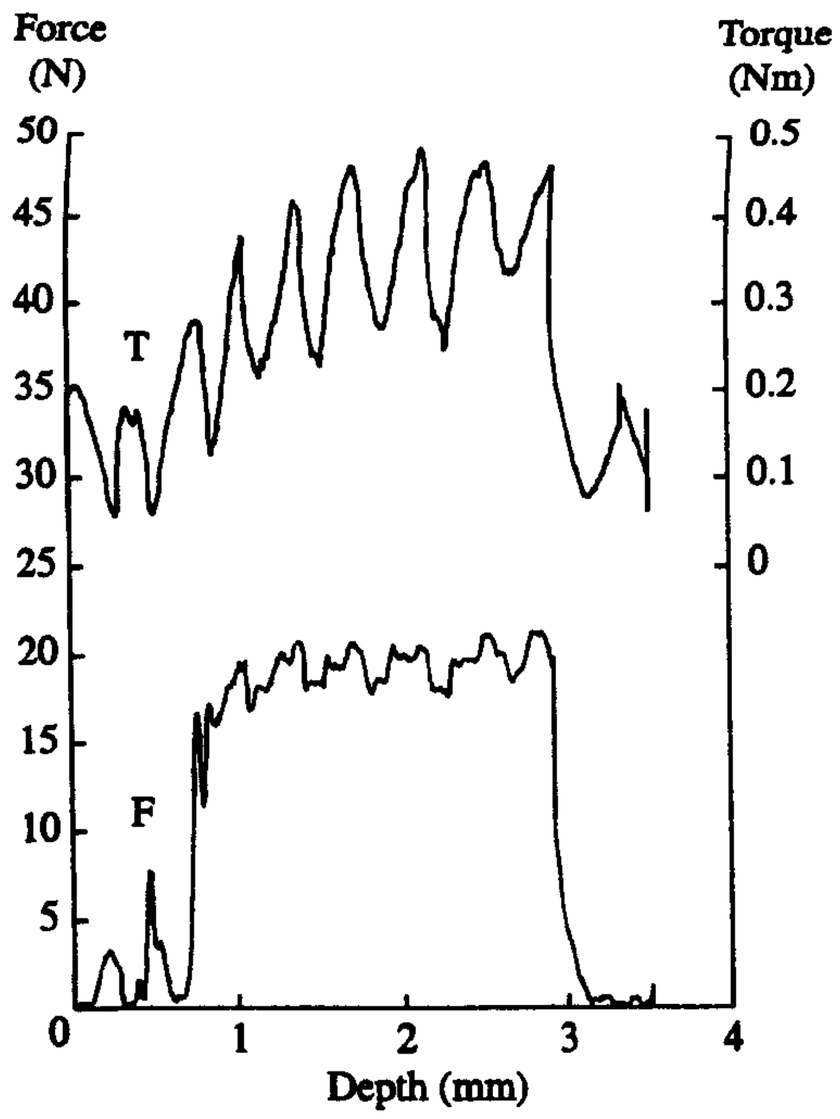

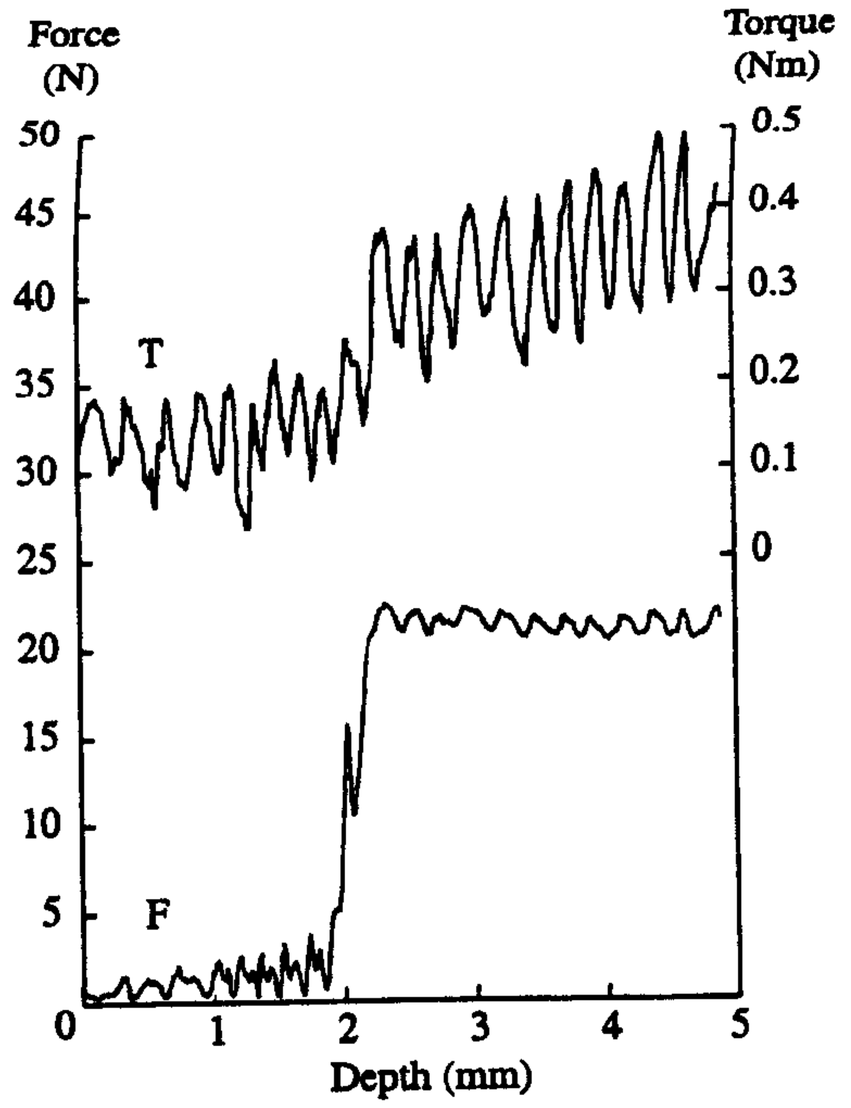

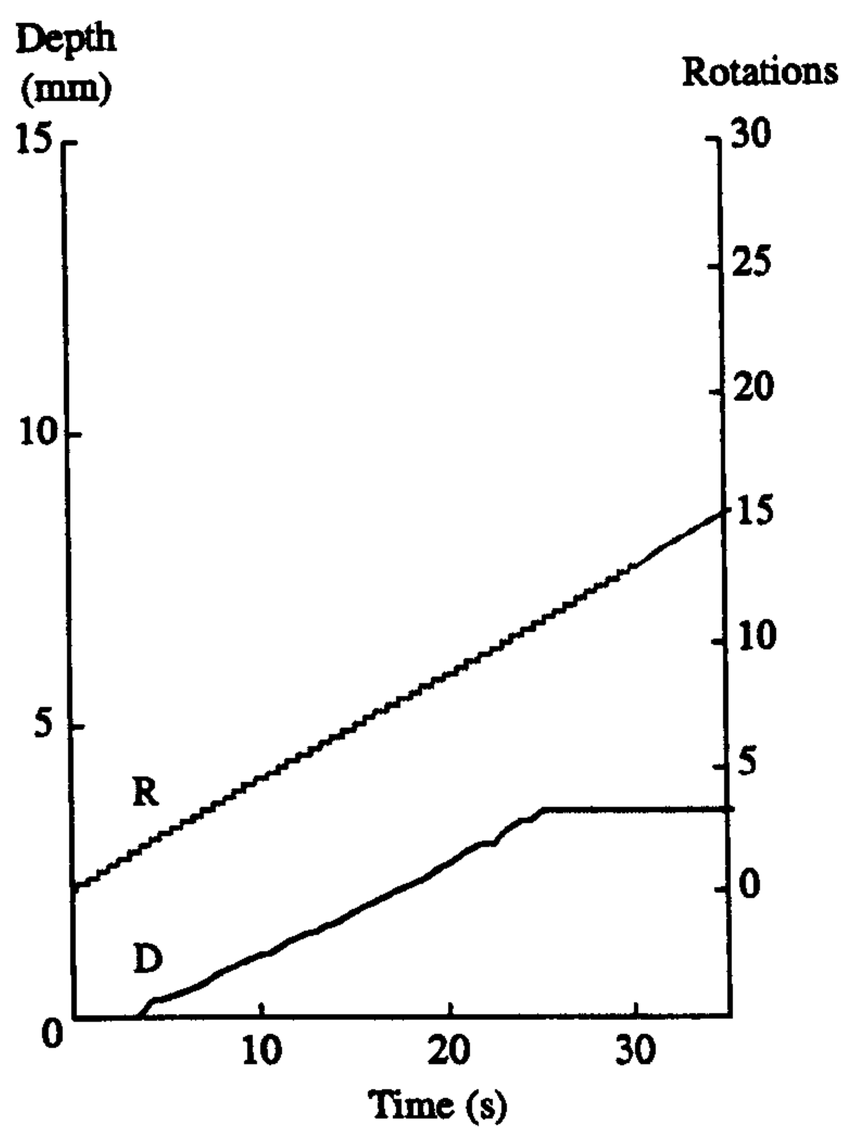

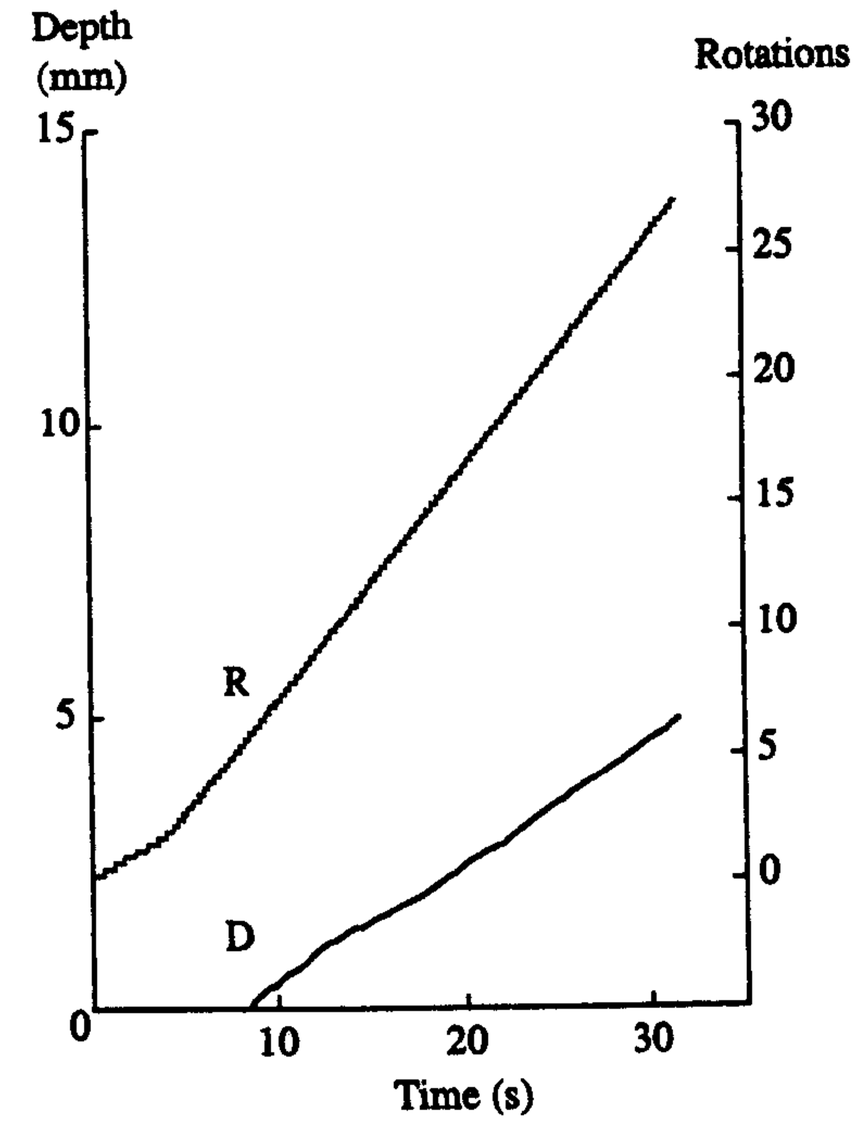

Figures 81a,b and 82a,b- Force, torque, depth, and rotation data from coring water ice (3B 3C)

Tables 37a and 37b - Summary of a coring run in zone-frozen water ice (3B 3C)

Sample temperature (K)	200
Chamber pressure (Pa)	3
Rotation speed (rev s^{-1})	0.428
Tool depth rate (mm s^{-1})	0.185
Initial / final force (N)	14.1 / 19.3
Initial / final torque (Nm)	0.15 / 0.27
Cutting strength (MPa)	18.4 / 29.1
Predicted ΔT on axis (K)	0.7
Predicted ΔT at $r=r_{tool}$ (K)	1.3
Predicted flash ΔT (K)	14

Sample temperature (K)	190
Chamber pressure (Pa)	3
Rotation speed (rev s^{-1})	0.926
Tool depth rate (mm s^{-1})	0.210
Initial / final force (N)	18.7 / 20
Initial / final torque (Nm)	0.13 / 0.23
Cutting strength (MPa)	41.2 / 51.5
Predicted ΔT on axis (K)	1.7
Predicted ΔT at $r=r_{tool}$ (K)	3.1
Predicted flash ΔT (K)	25

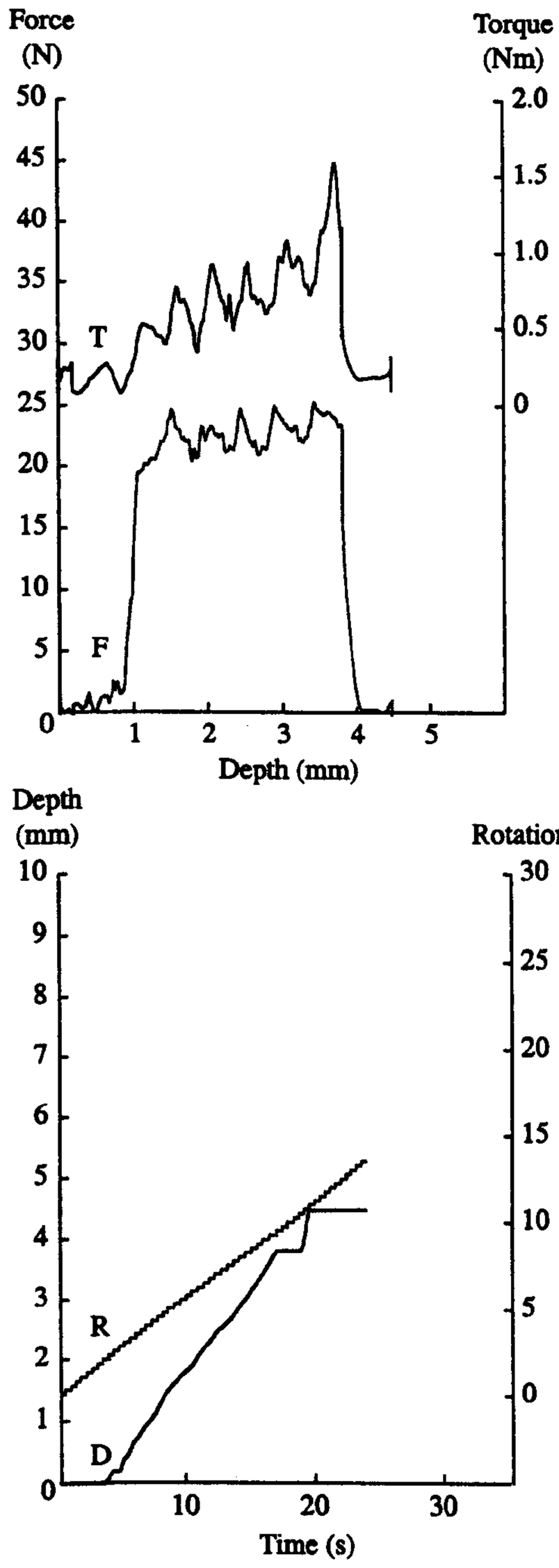

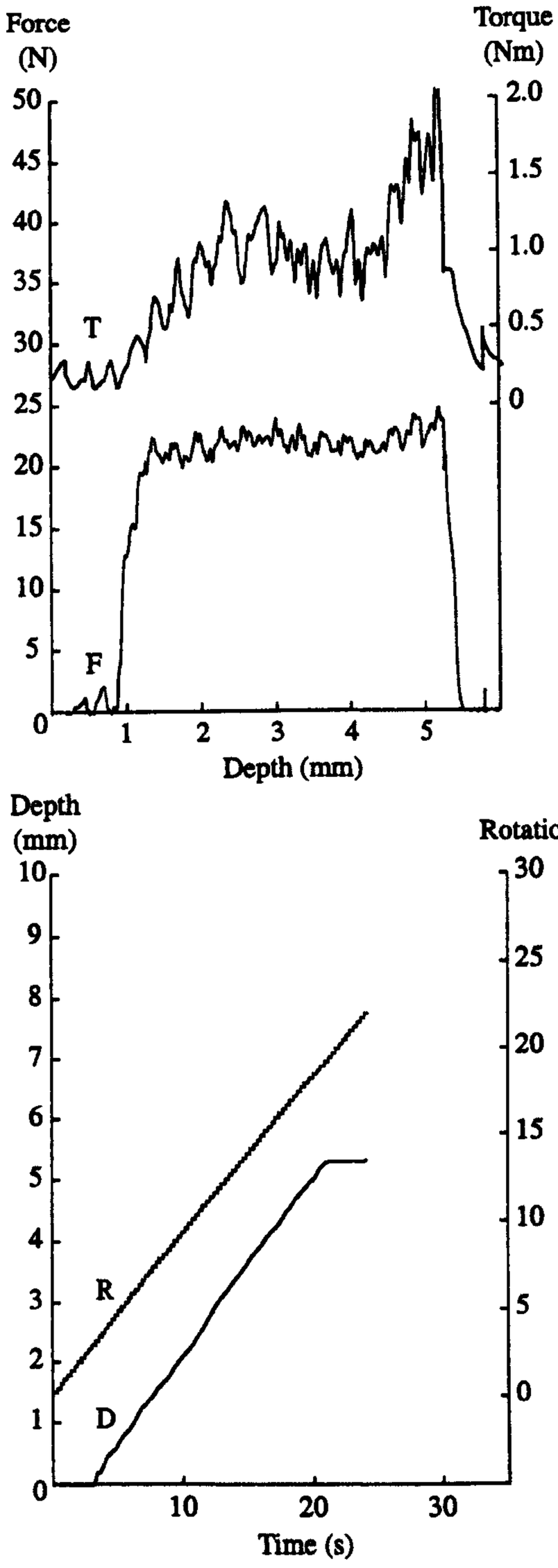

Figures 83a,b and 84a,b - Force, torque, depth, and rotation data from coring water ice (4B 4C)

Tables 38a and 38b - Summary of a coring run in zone-frozen water ice (4B 4C)

Sample temperature (K)	165
Chamber pressure (Pa)	4
Rotation speed (rev s^{-1})	0.5507
Tool depth rate (mm s^{-1})	0.267
Initial / final force (N)	20.1 / 23.3
Initial / final torque (Nm)	0.23 / 1.28
Cutting strength (MPa)	24.2 / 115
Predicted ΔT on axis (K)	1.1
Predicted ΔT at $r=r_{tool}$ (K)	2
Predicted flash ΔT (K)	23

Sample temperature (K)	165
Chamber pressure (Pa)	4
Rotation speed (rev s^{-1})	0.910
Tool depth rate (mm s^{-1})	0.295
Initial / final force (N)	19.8 / 22.7
Initial / final torque (Nm)	0.38 / 1.47
Cutting strength (MPa)	50.4 / 200
Predicted ΔT on axis (K)	2.5
Predicted ΔT at $r=r_{tool}$ (K)	4.5
Predicted flash ΔT (K)	59

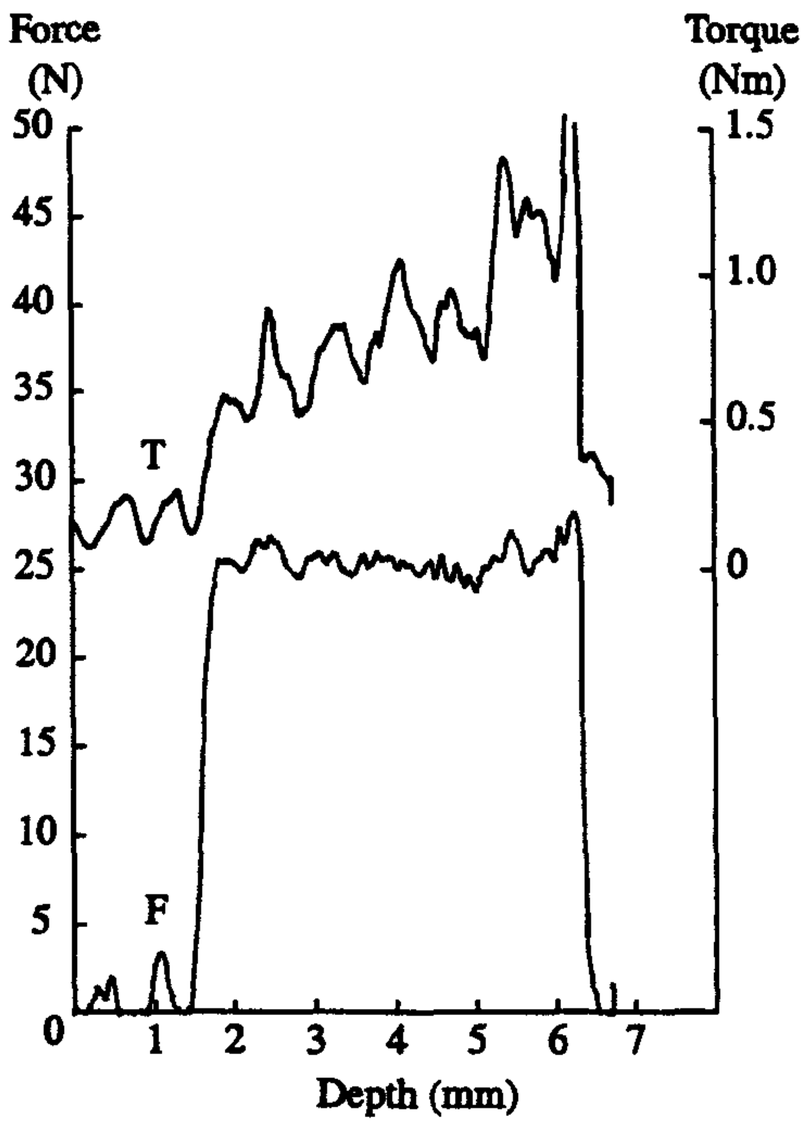

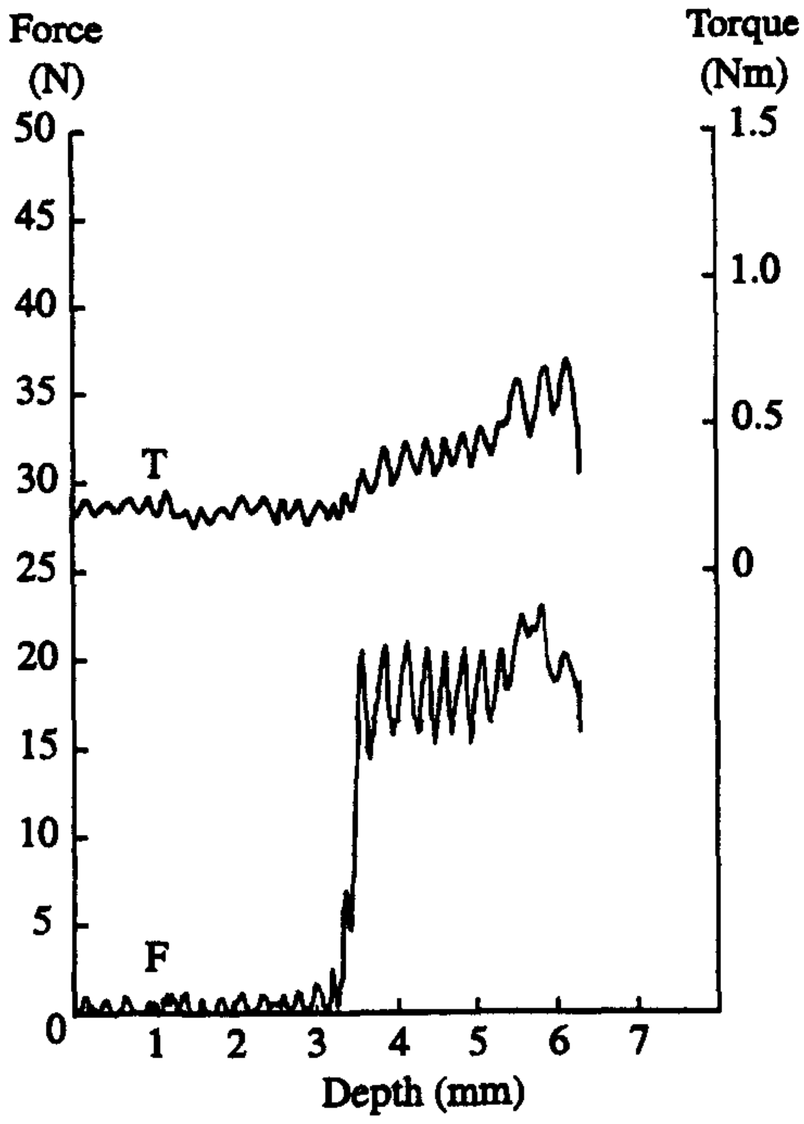

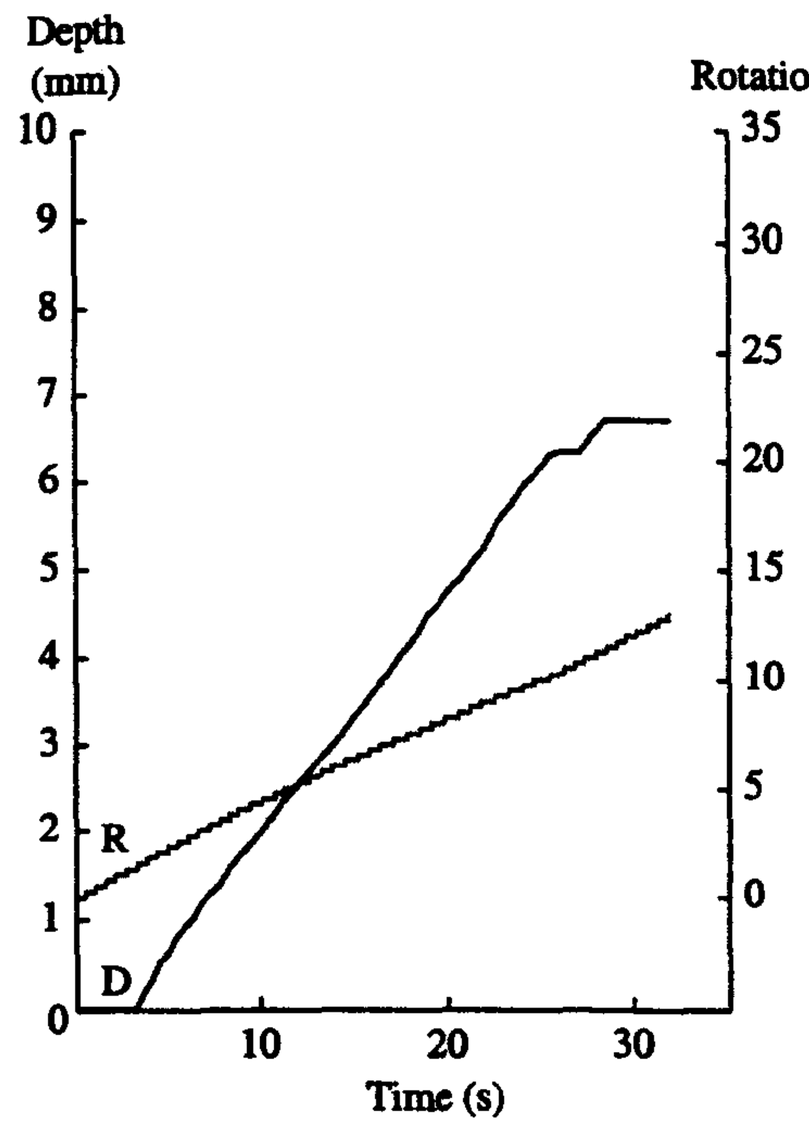

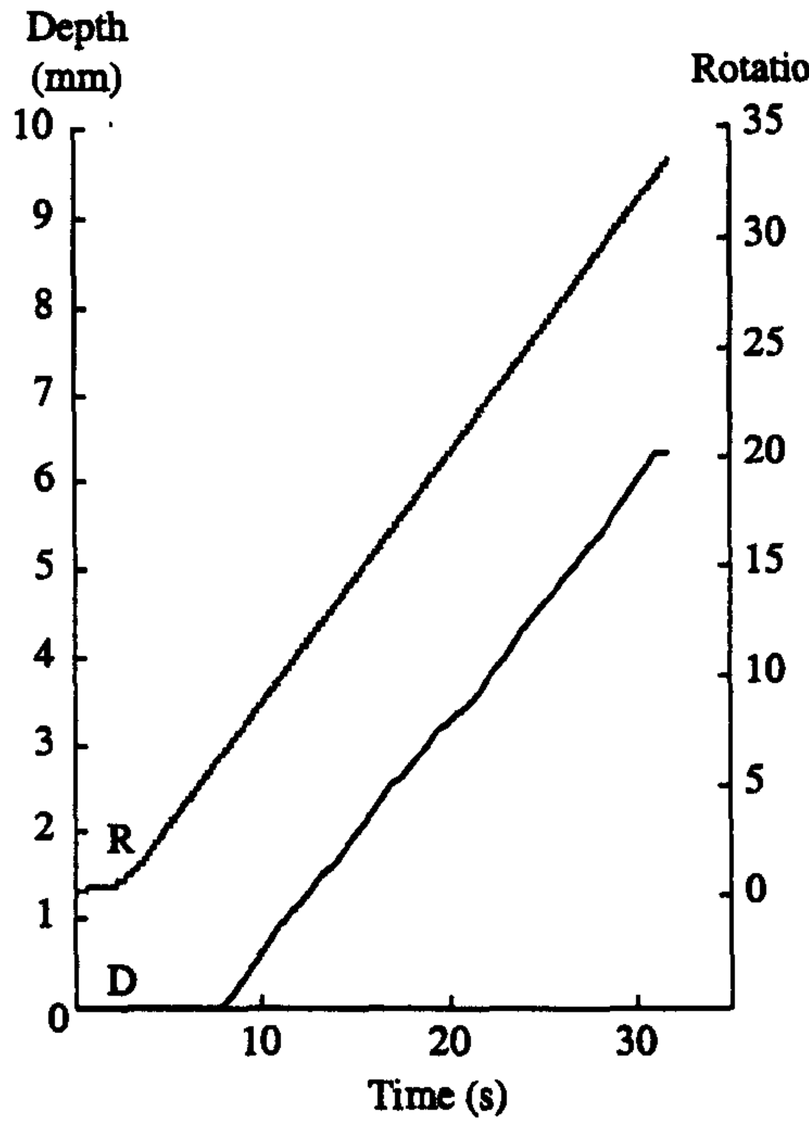

Figure 85a,b and 86a,b - Force, torque, depth, and rotation data from coring water ice (5A 5C2)

Tables 39a and 39b - Summary of a coring run in zone-frozen water ice (5A 5C2)

Sample temperature (K)	147
Chamber pressure (Pa)	3
Rotation speed (rev s^{-1})	0.371
Tool depth rate (mm s^{-1})	0.278
Initial / final force (N)	23.5 / 26.5
Initial / final torque (Nm)	0.33 / 1.32
Cutting strength (MPa)	20.5 / 76
Predicted ΔT on axis (K)	0.9
Predicted ΔT at $r=r_{tool}$ (K)	1.6
Predicted flash ΔT (K)	21

Sample temperature (K)	147
Chamber pressure (Pa)	3
Rotation speed (rev s^{-1})	1.173
Tool depth rate (mm s^{-1})	0.271
Initial / final force (N)	17 / 17.5
Initial / final torque (Nm)	0.13 / 0.31
Cutting strength (MPa)	37.4 / 58.5
Predicted ΔT on axis (K)	1.6
Predicted ΔT at $r=r_{tool}$ (K)	3
Predicted flash ΔT (K)	27

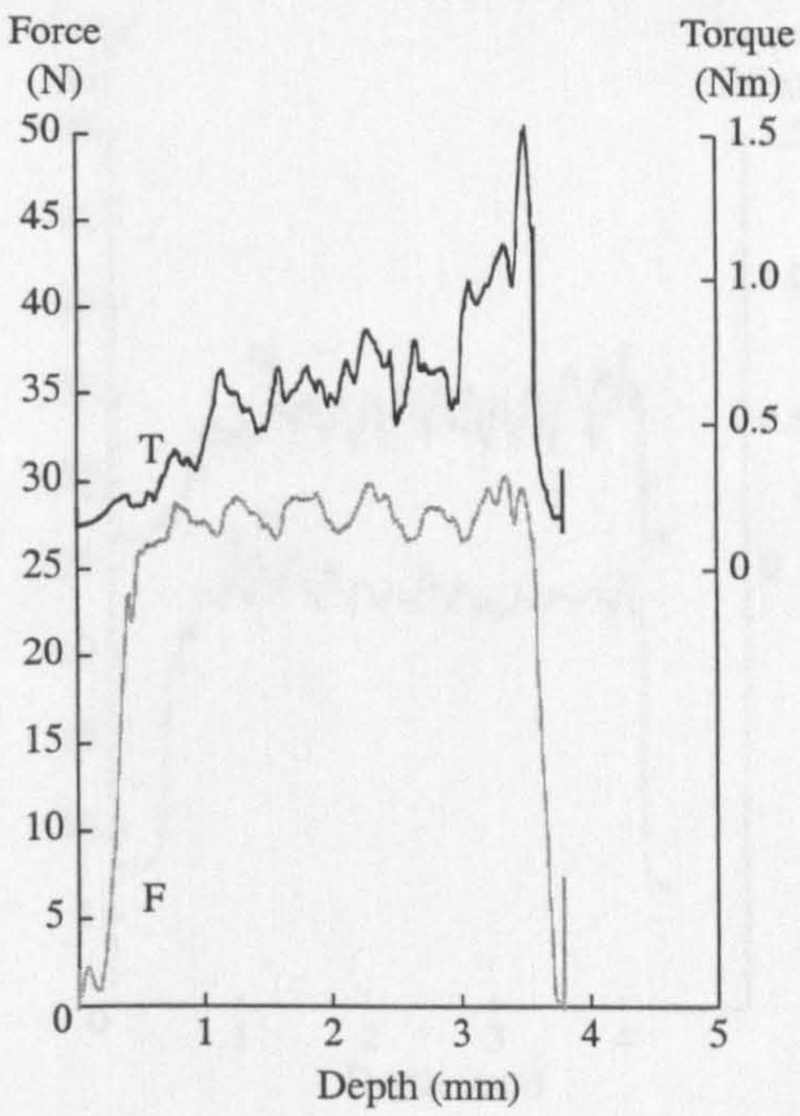

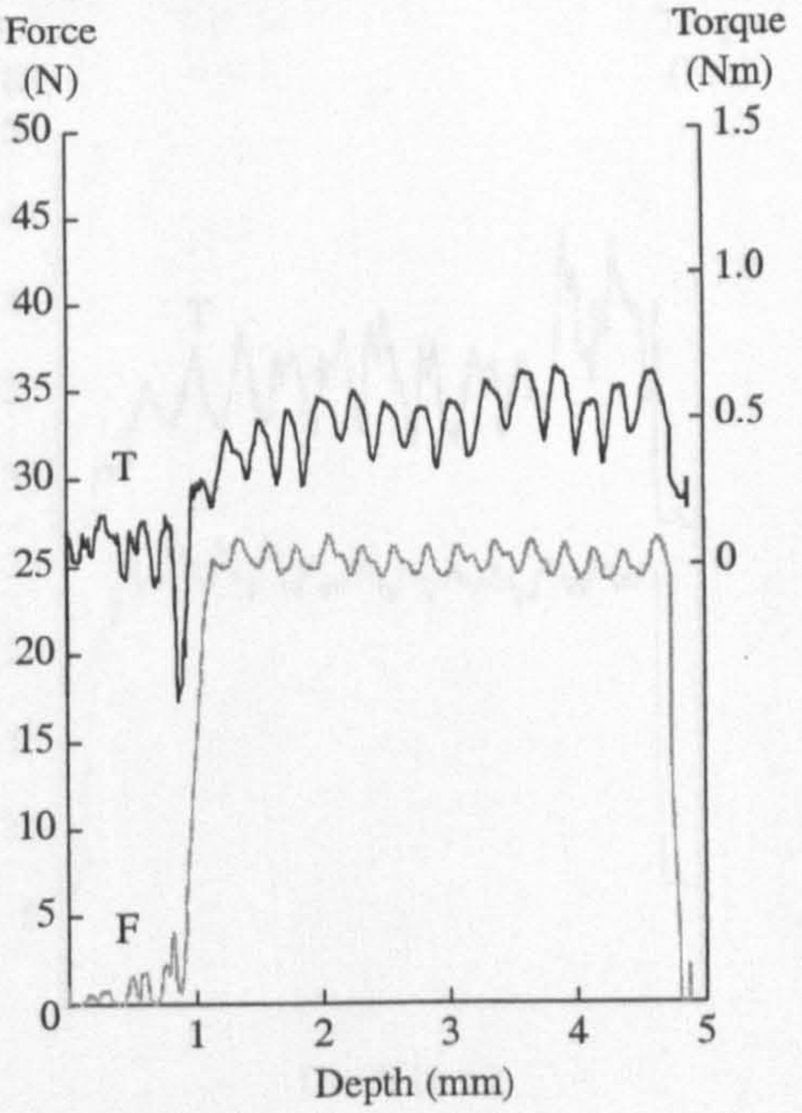

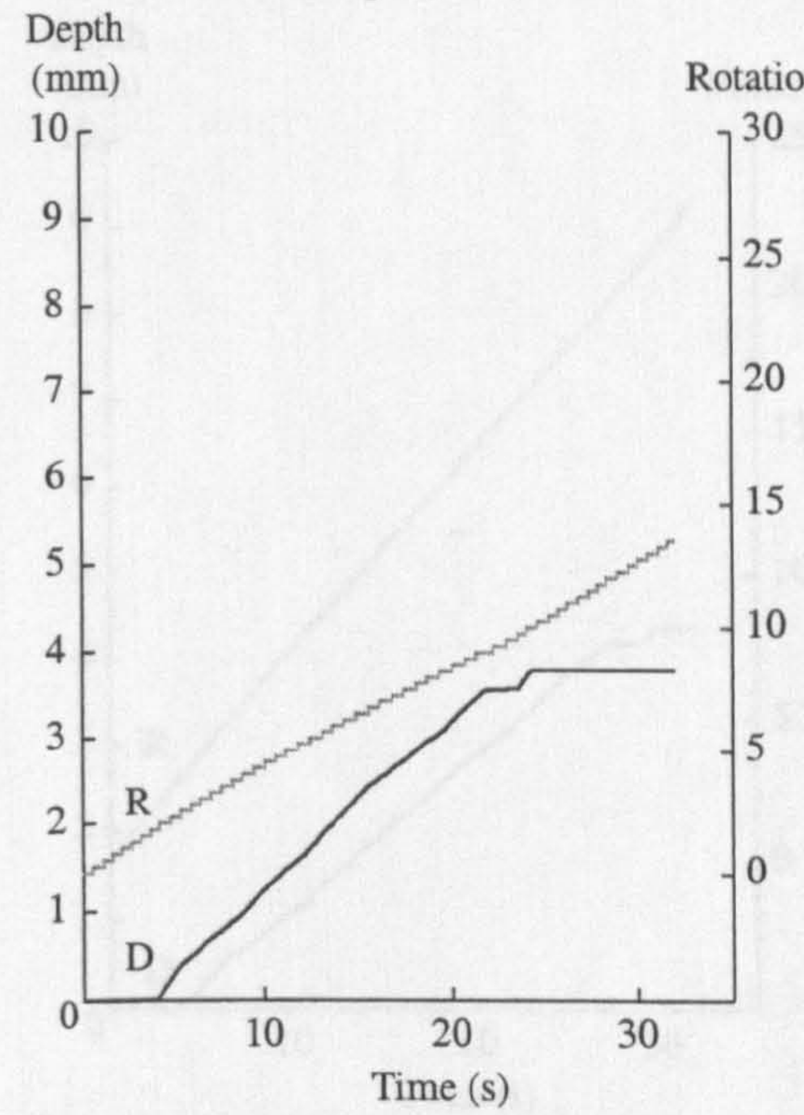

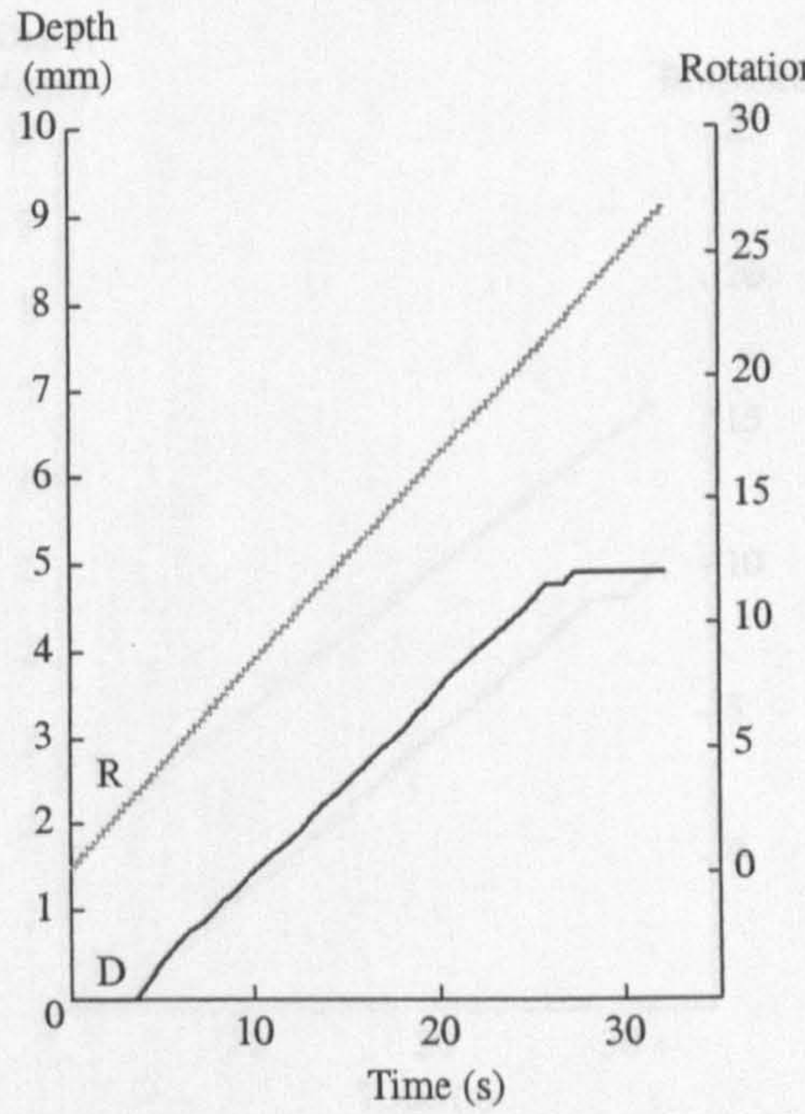

Figures 87a,b and 88a,b- Force, torque, depth, and rotation data from coring water ice (8A 8B)

Tables 40a and 40b - Summary of a coring run in zone-frozen water ice (8A 8B)

Sample temperature (K)	145
Chamber pressure (Pa)	3
Rotation speed (rev s^{-1})	0.399
Tool depth rate (mm s^{-1})	0.178
Initial / final force (N)	24.3 / 28.4
Initial / final torque (Nm)	0.12 / 1.16
Cutting strength (MPa)	26.5 / 110
Predicted ΔT on axis (K)	0.8
Predicted ΔT at $r=r_{tool}$ (K)	1.5
Predicted flash ΔT (K)	10

Sample temperature (K)	160[1]
Chamber pressure (Pa)	unknown
Rotation speed (rev s^{-1})	0.825
Tool depth rate (mm s^{-1})	0.201
Initial / final force (N)	23 / 24.6
Initial / final torque (Nm)	0.28 / 0.34
Cutting strength (MPa)	56.8 / 65.4
Predicted ΔT on axis (K)	2
Predicted ΔT at $r=r_{tool}$ (K)	3.7
Predicted flash ΔT (K)	48

[1] Extrapolated from the slow warming trend. In this second run the temperature and pressure were regrettably not written down - both would be similar to the earlier run.

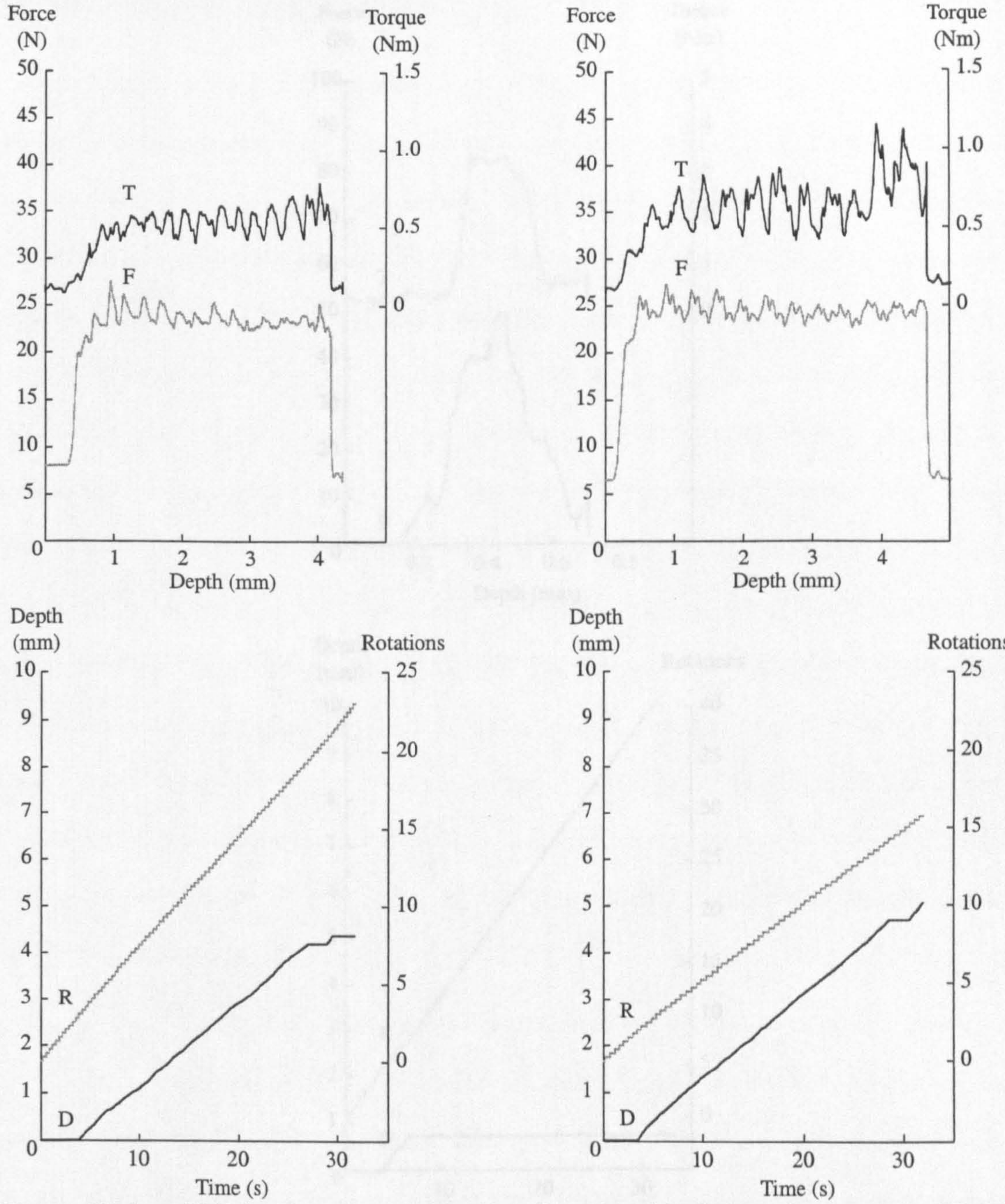

Figures 89a,b and 90a,b - Force, torque, depth, and rotation data from coring water ice (9B 9D)

Tables 41a and 41b - Summary of a coring run in zone-frozen water ice (9B 9D)

Sample temperature (K)	145
Chamber pressure (Pa)	3
Rotation speed (rev s^{-1})	0.712
Tool depth rate (mm s^{-1})	0.181
Initial / final force (N)	16.1 / 15.6
Initial / final torque (Nm)	0.36 / 0.49
Cutting strength (MPa)	59.8 / 80.6
Predicted ΔT on axis (K)	1.8
Predicted ΔT at $r=r_{tool}$ (K)	3.3
Predicted flash ΔT (K)	55

Sample temperature (K)	145
Chamber pressure (Pa)	4
Rotation speed (rev s^{-1})	0.480
Tool depth rate (mm s^{-1})	0.187
Initial / final force (N)	18.1 / 17.7
Initial / final torque (Nm)	0.44 / 0.68
Cutting strength (MPa)	47.4 / 73.8
Predicted ΔT on axis (K)	1.6
Predicted ΔT at $r=r_{tool}$ (K)	2.9
Predicted flash ΔT (K)	45

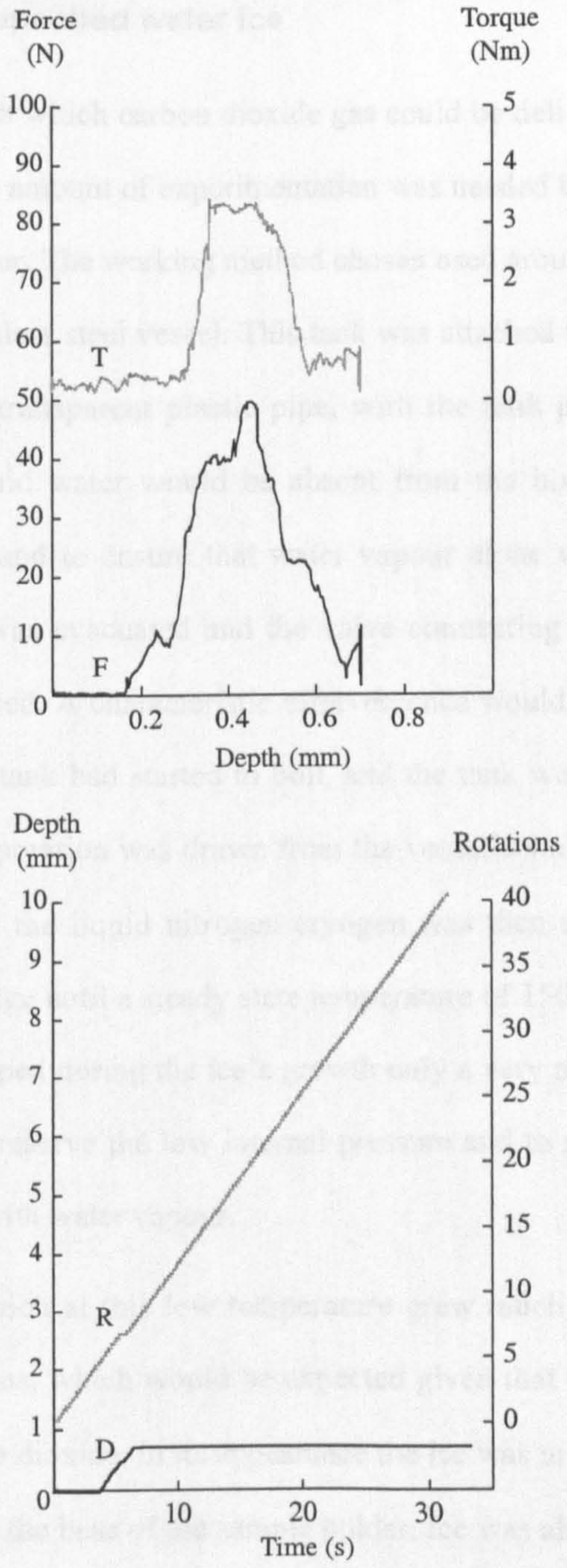

Figures 91a,b - Force, torque, depth, and rotation data from a stalled coring run in water ice (8stall)

Table 42: Summary of a stalled coring run in zone-frozen water ice (8stall)

Sample temperature (K)	140
Chamber pressure (Pa)	3
Rotation speed (rev s^{-1})	1.948
Tool depth rate (mm s^{-1})	0.2755
Initial / final force (N)	47.9
Initial / final torque (Nm)	2.9
Cutting strength (MPa)	N/A
Predicted ΔT on axis (K)	N/A
Predicted ΔT at $r=r_{tool}$ (K)	N/A
Predicted flash ΔT (K)	N/A

5.2.6 Forming vapour deposited water ice

In contrast to the ease with which carbon dioxide gas could be delivered to the sample holder of the chamber, a considerable amount of experimentation was needed to find a way of generating a reliable source of water vapour. The working method chosen used around 100 cm^3 of liquid water that was held in a capped stainless steel vessel. This tank was attached to the gas delivery hose of the chamber via a 1 m long transparent plastic pipe, with the tank placed on the floor of the laboratory to ensure that liquid water would be absent from the hose's opening. To remove dissolved air from the water and to ensure that water vapour alone was being admitted to the chamber, the main chamber was evacuated and the valve connecting the water tank to the gas delivery hose was slowly opened. A characteristic effervescence would be seen in the transparent piping when the liquid in the tank had started to boil, and the tank would become chilled to the touch as the latent heat of evaporation was drawn from the vessel's walls. With the water boiling vigorously in its storage tank the liquid nitrogen cryogen was then made to flow through the cooling pipes of the sample stage until a steady state temperature of 150 K was reached. Although the chamber was actively pumped during the ice's growth only a very modest flow of vapour was allowed into the chamber to preserve the low internal pressure and to prevent the rotary vacuum pump from being overloaded with water vapour.

The ice made in this fashion at this low temperature grew much more slowly than carbon dioxide under similar conditions, which would be expected given that water has a heat of fusion much larger than that of carbon dioxide. In its appearance the ice was unexceptional and it grew as a smooth bright glossy solid at the base of the sample holder. Ice was also seen to form around the cryogen delivery pipes and over the plate that carried the sample holder. The structural nature of this ice could not be measured in-situ but it is possible that Ih ice was not formed in the sample holder. Many studies (such as that of Whalley, 1983) describe the formation of cubic water ice at temperatures used in this coring experiment but without suitable data the ice's phase must remain uncertain.

5.2.7 Coring vapour deposited water ice

The very slow deposition rate resulted in a sample thickness of no more than a few millimetres after 7 hours of continuous operation of the chamber and water vapour source although this thickness is an estimate given the restricted view of the chamber's viewing ports. Nevertheless, two short coring runs were made into the material and a total vertical distance of 2.5 mm was covered. Unfortunately a connection to the torque sensor failed at some point before the data were taken and despite attempts to reconstruct the torque record from only half of the bridge output, noise on the free-floating line has prevented a reliable history from being reconstructed. For completeness, the charts of force with respect to depth for the two coring runs and the depth and rotation histories are shown in Figures 92 and 93.

Unfortunately, the loss of the torque data prevents a specific cutting energy, u, from being calculated for the material. Recall that the definition of u is dependent on the applied torque in that the term F_S appears in equation 27, and this horizontal force is determined purely by the torque applied to the tool head. At best a lower bound can be place on the specific cutting energy of this vapour-grown ice by assuming a vanishingly small torque. The work expended in removing a unit volume of ice is then determined only by the downforce applied, the vertical distance travelled, and the geometry of the coring head. These lower estimates for the specific cutting energy are shown in the summary tables of the following Figures. Furthermore, the heating model of SB89 cannot be used for these experiments. Firstly, because the model requires a well defined value for the specific cutting energy, and secondly, because the thermal properties of this material could not be known with confidence in the absence of definite information about the ice's phase.

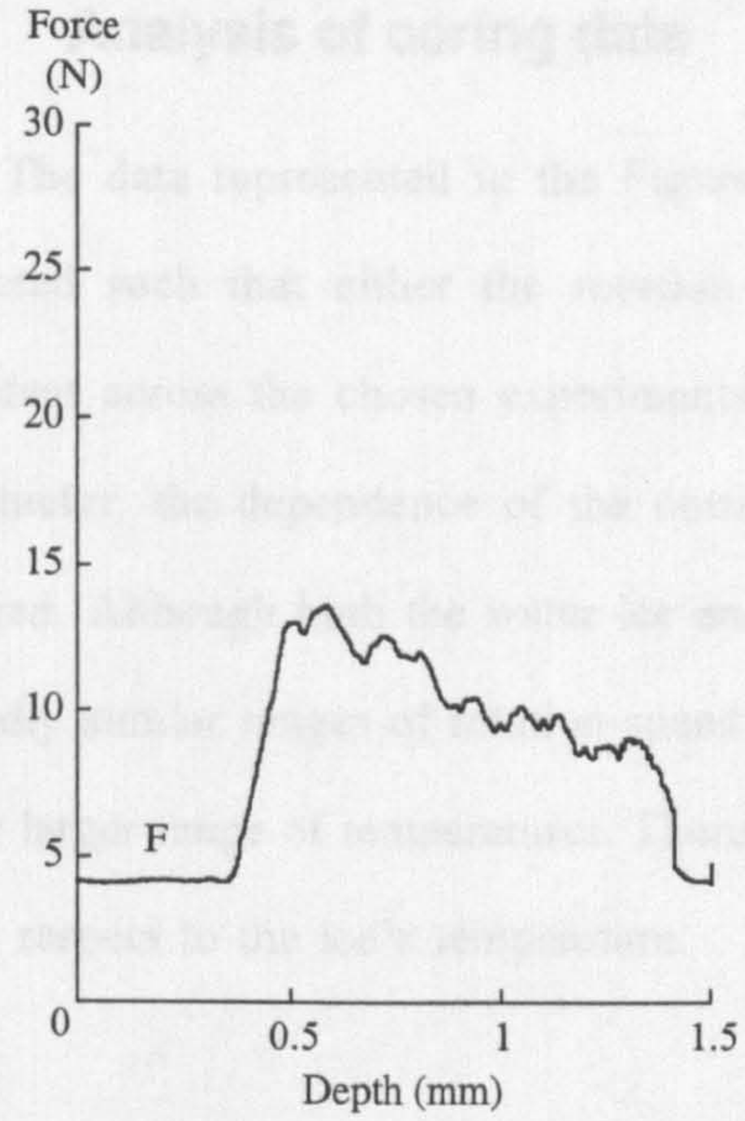

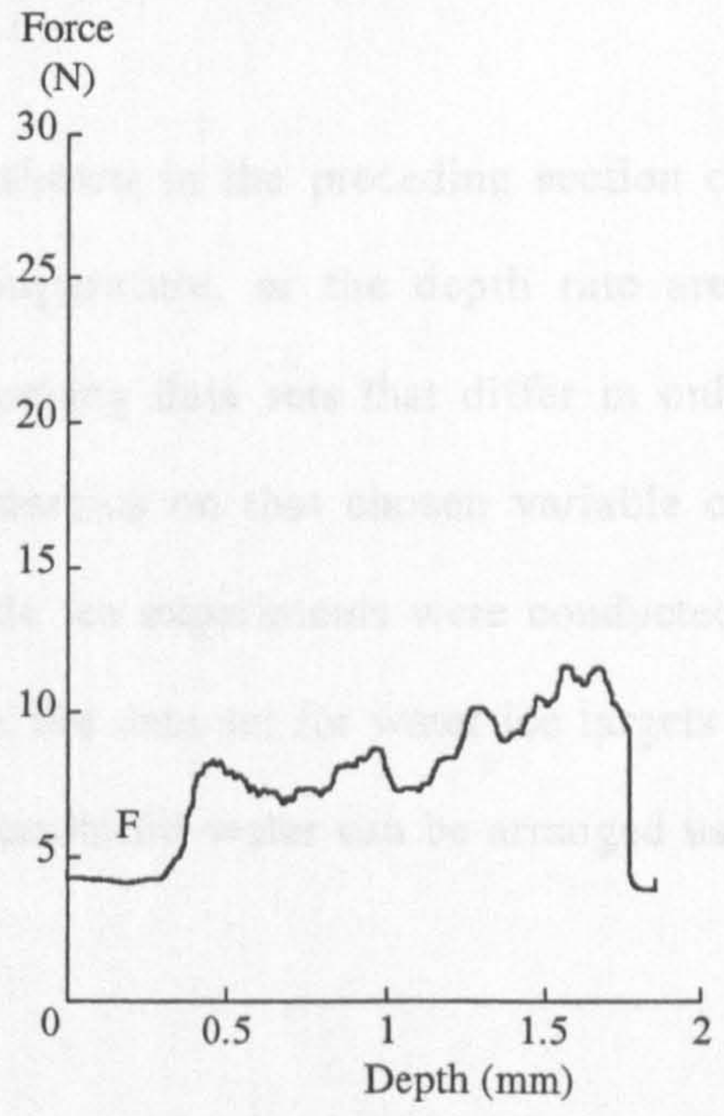

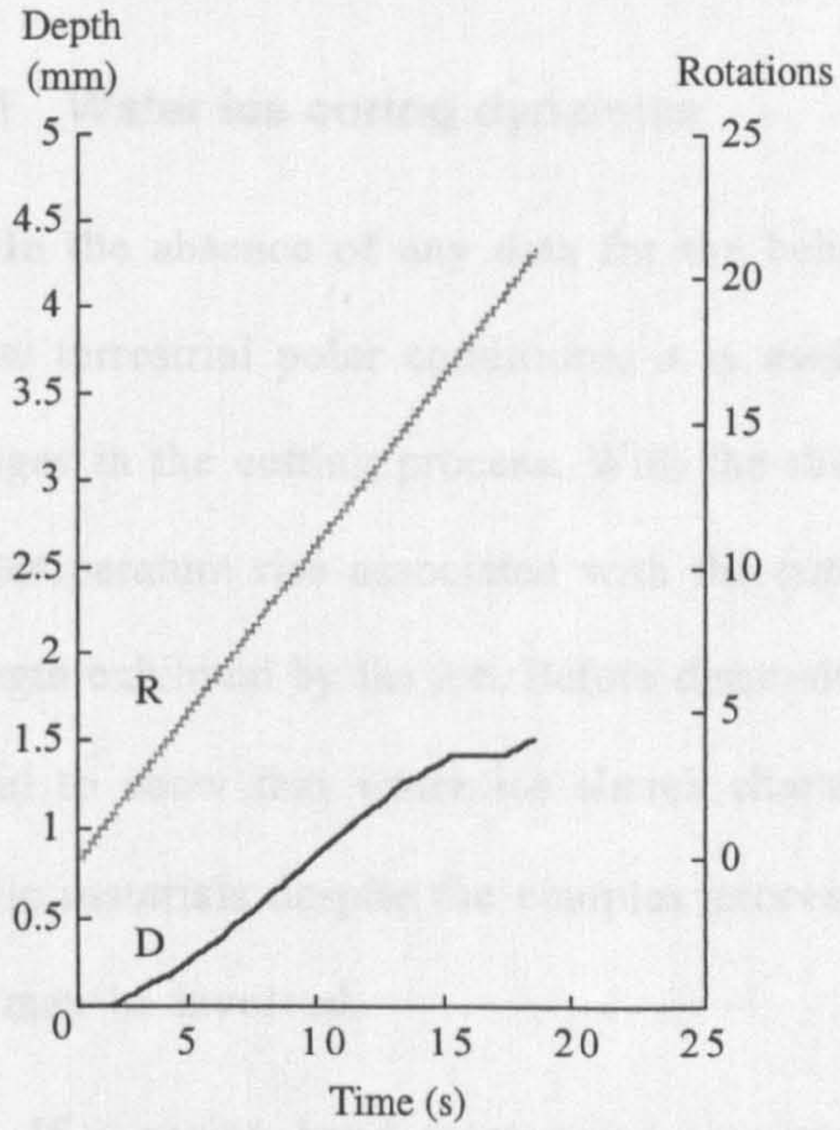

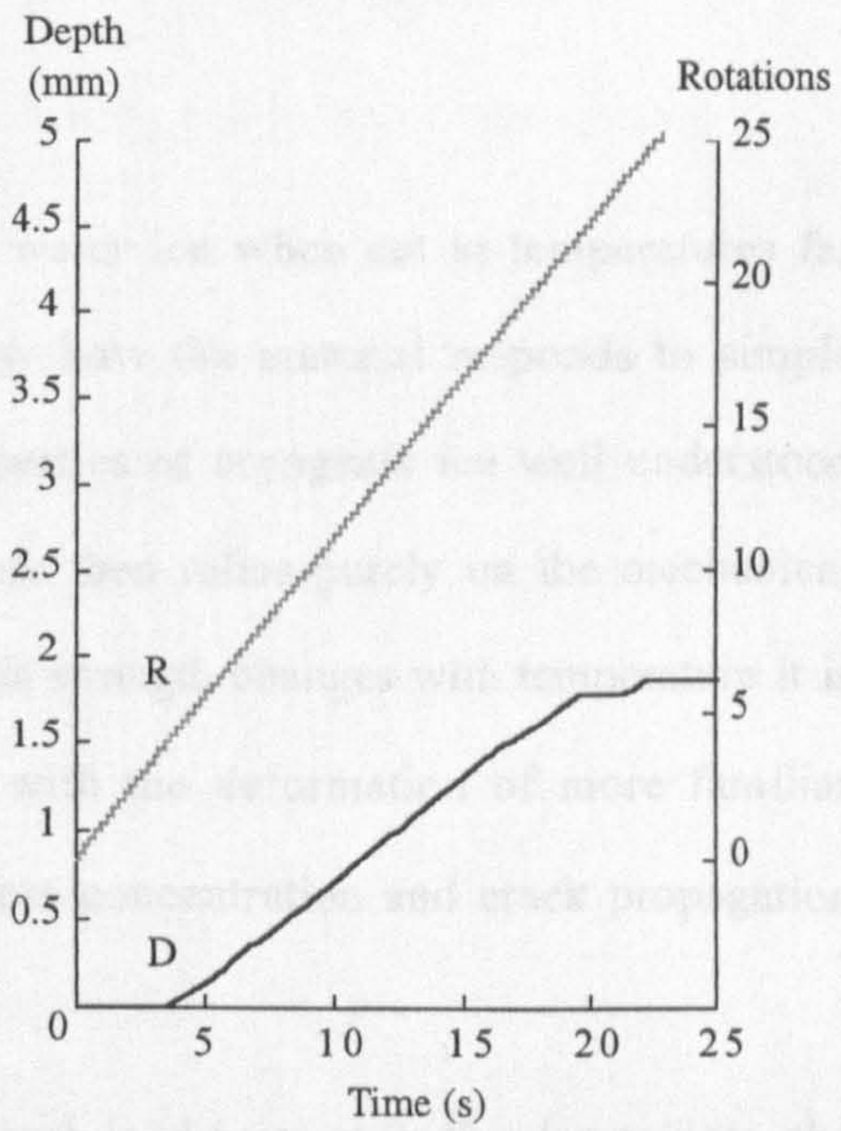

Figures 92a,b and 93a,b- Force, torque, depth and rotation data from coring water ice (vap)

Tables 43a and 43b - Summary of a coring run in vapour-grown water ice (vap)

Sample temperature (K)	138
Chamber pressure (Pa)	100
Rotation speed (rev s^{-1})	1.194
Tool depth rate (mm s^{-1})	0.122
Initial / final force (N)	9.1 / 4.7
Initial / final torque (Nm)	- / -
Cutting strength (MPa)	53 / 27
Predicted ΔT on axis (K)	/
Predicted ΔT at $r=r_{tool}$ (K)	/
Predicted flash ΔT (K)	-

Sample temperature (K)	not recorded
Chamber pressure (Pa)	not recorded
Rotation speed (rev s^{-1})	1.112
Tool depth rate (mm s^{-1})	0.117
Initial / final force (N)	3.9 / 7.1
Initial / final torque (Nm)	- / -
Cutting strength (MPa)	22 / 40
Predicted ΔT on axis (K)	/
Predicted ΔT at $r=r_{tool}$ (K)	/
Predicted flash ΔT (K)	-

5.3 Analysis of coring data

The data represented in the Figures and Tables shown in the preceding section can be selected such that either the rotation speed, ice temperature, or the depth rate are held constant across the chosen experiments. Then, by choosing data sets that differ in only one parameter, the dependence of the cutting process dynamics on that chosen variable can be gauged. Although both the water ice and carbon dioxide ice experiments were conducted over broadly similar ranges of rotation speed and depth rate, the data set for water ice targets spans a far larger range of temperatures. Therefore only the results for water can be arranged usefully with respect to the ice's temperature.

5.3.1 Water ice coring dynamics

In the absence of any data for the behaviour of water ice when cut at temperatures far below terrestrial polar conditions, it is useful to show how the material responds to simple changes in the cutting process. With the thermal properties of cryogenic ice well understood the temperature rise associated with the cutting process then relies purely on the mechanical strength exhibited by the ice. Before discussing how this strength changes with temperature it is useful to show that water ice shares characteristics with the deformation of more familiar plastic materials despite the complex processes of stress concentration and crack propagation that may be involved.

If a coring head rotates at a constant speed and is driven at a fixed rate into the workpiece then the torque applied by the coring motor has to scale with the specific cutting energy (J m^{-3}) to the first power, or equivalently, as the failure strength (Pa) at the particular strain rate. Furthermore, the torque experienced should scale directly with the thickness of unworked material ahead of a cutting edge. However, this thickness t_1 varies inversely as the rotation speed if the entire coring head is being driven at a fixed rate into the material vertically. So it can be said that the torque, for a fixed depth rate, should vary inversely with the tool rotation speed and this is apparent in Figures 94a and 94b which show the initial and average torque values experienced when cutting water ice.

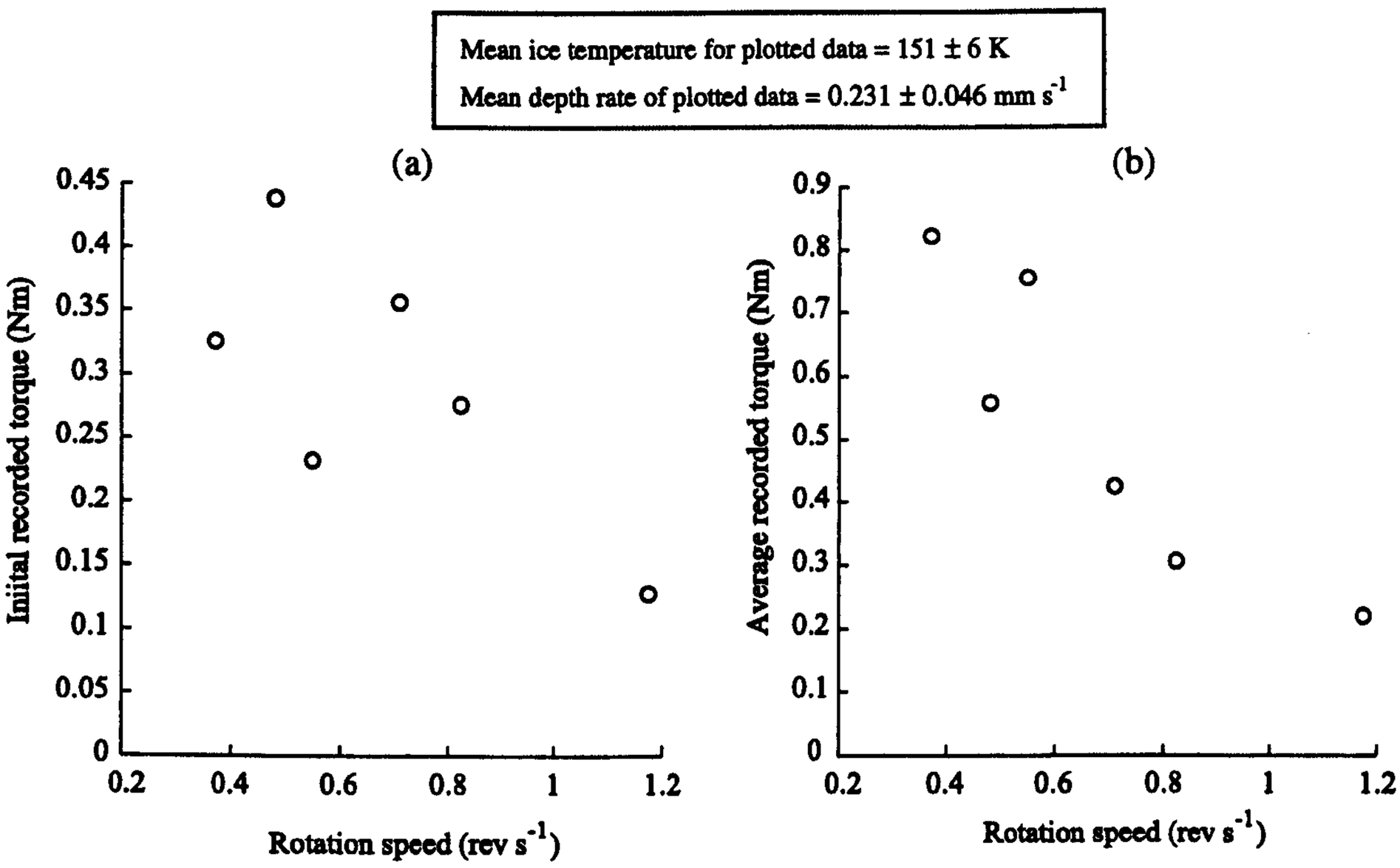

Figure 94a,b - Initial and average torques recorded while coring water ice at similar temperatures and vertical coring speeds.

Figure 94b shows that once the tool has become embedded in the material an extra drag is applied to the corer, which would explain why the average torque over the whole run is higher than the initial cutting torque. This extra resistance to rotation is thought to arise from the sliding friction and additional cutting action of vertical faces on the coring tool's teeth. Figure 94a can be re-plotted to show $\tau + t_1$ as a function of rotation speed so that the effect of rotation speed on the thickness of the uncut material is removed. Despite the slight scatter in the data shown in the above charts the trends are not in conflict with the scaling that might be expected if the ice fractured finely enough for the material to be treated as a continuum. An important conclusion at this point is:

1 *Void-free water ice at temperatures around 150 K can be machined with applied loads of tens of Newtons applied over a total cutting edge length of a few millimetres without catastrophic fracturing. The material is well behaved in this sense and is a suitable material for repeatable machining experiments.*

Having shown that there are no peculiarities uncovered by cutting water ice it is now appropriate to discuss the variation of strength-related properties such as the specific cutting energy u with respect to the ice's temperature. As has been mentioned, the torque requirement

should scale with the specific cutting energy of the worked material. Thus, if experiments with comparable rotation speed and depth rates are performed at various temperatures the changes seen in the recorded torque should vary directly with the specific cutting energy. The water ice experiments were examined to find those tests which had broadly similar rotation speeds and depth rates and these points are plotted below.

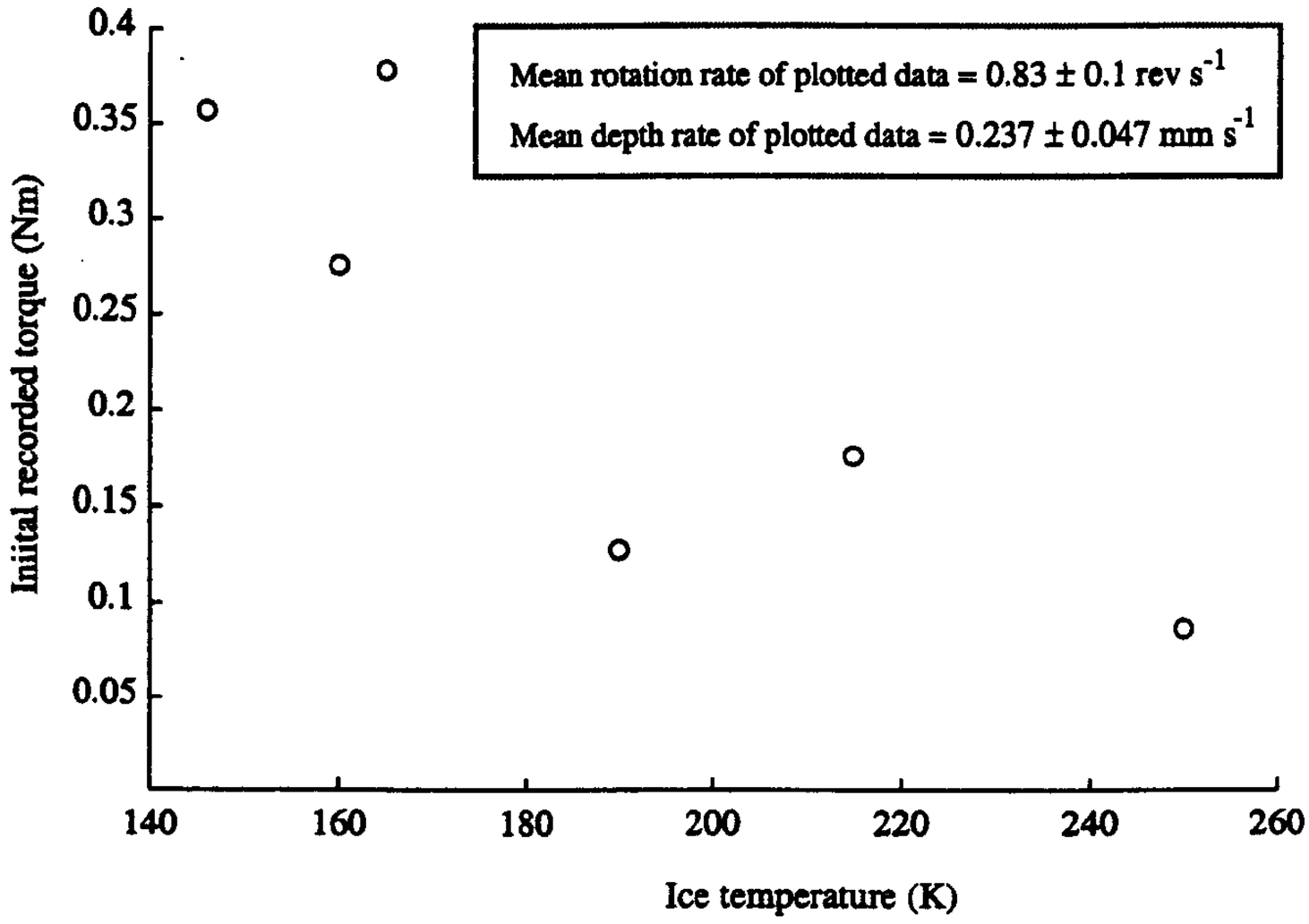

Figure 95 - Recorded initial torque as a function of ice temperature when coring water ice at a near constant rotation speed and depth rate.

The chart suggests that the resistance to failure of the ice trebles as the temperature of the ice samples changes from 240 to 140 K. More usefully, the specific cutting energy can be estimated from these torque data for a given pair of rotation speed and depth rate values with equation 29, which, it should be recalled, uses none of the assumptions of section 2.2 that were used to calculate u in the summary tables of each coring experiment.

Table 44 : Predictions for u using three representative torque values from Figure 95.

Temperature (K)	Initial torque (Nm)	Predicted value of u (MPa)
250	0.086	19
215	0.175	35
145	0.357	73

The temperature dependence of this estimate of the specific cutting energy is in broad agreement with the well-established changes in the compressive and tensile strengths of water ice that were discussed in section 2.3.1. This is of some note, as coring occurs through the two-dimensional failure of thin (<50 μm) layers in contrast to the uniaxial loads that are applied to samples four orders of magnitude larger in material testing rigs.

Along with the specific cutting energy u a second useful metric can be found; the power consumed by the tool. In the experiments of the preceding chapter it can be shown that the majority of the power applied was expended by the forced horizontal motion of each tooth as it revolved around the axis of the tool[1]. This power dissipation, P (W), can be found from the torque τ (Nm) needed to rotate a tool at a rate of ω revolutions s^{-1} as

$$P = 2\pi\omega\tau \qquad \text{Eq. 69}$$

Figure 96b shows the variation of the calculated initial specific cutting energy, u, as a function of temperature for those experiments that used similar rotation rates and vertical speeds. For those same points the power expended in forcing the cutting teeth through the unworked material is calculated and plotted in Figure 96a.

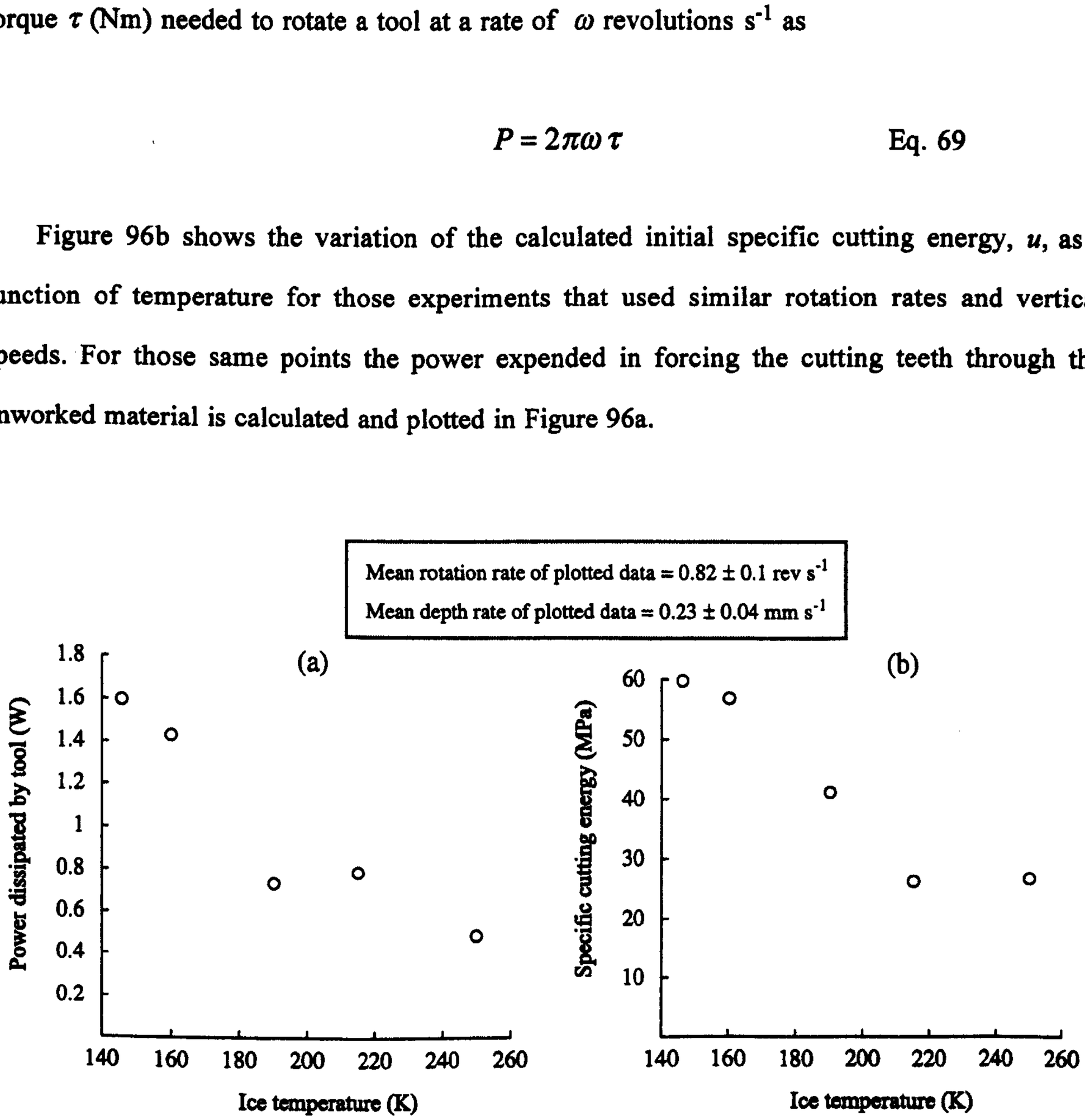

Figure 96a,b - The power dissipated by the coring tool and the specific cutting energy of cryogenic water ice as calculated from 'initial' conditions in the coring processes.

[1] The power dissipated in vertical motion is the downthrust multiplied by the depth rate. For the experiments of the last chapter this power is equivalent to a few milliwatts.

With the current data set it is not possible to make predictions about the behaviour of this tool at significantly higher rotation speeds or at substantially different penetration rates. However, for the conditions given in the above charts it can be stated that

2 *Water ice at a temperature of 240 K has a specific cutting energy of less than 30 MPa. To core the same amount of ice at a temperature of 140 K requires twice as much energy.*

5.3.2 Carbon dioxide ice coring dynamics

The coring experiments made with carbon dioxide were made in a narrow temperature range and so the properties of this ice as a function of temperature will not be studied. However, the analyses that were applied to water ice regarding the variation of torque and rotation speed can be reapplied for CO_2 ice.

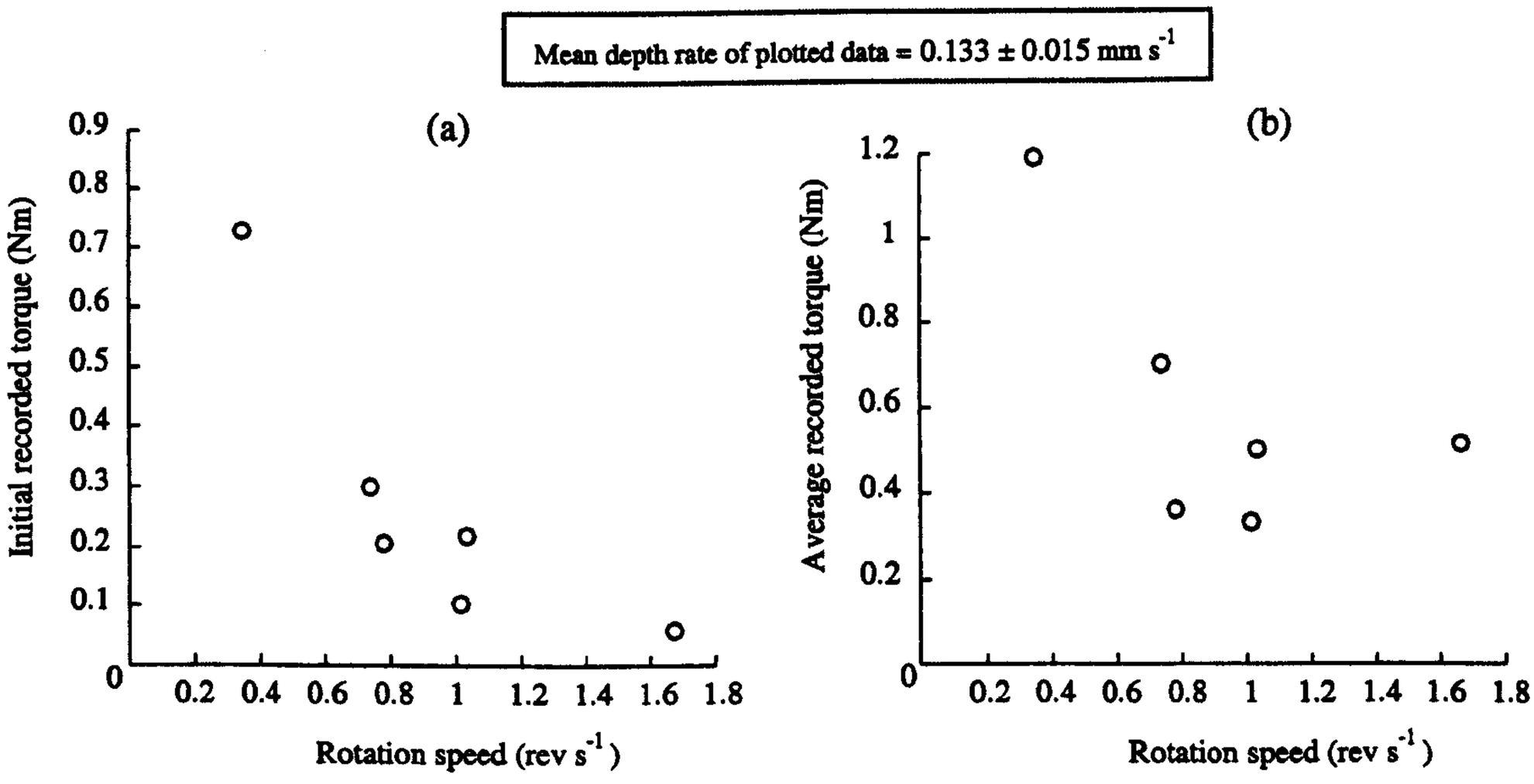

Figure 97a,b - Initial and average torque data recorded while coring CO_2 ice samples at broadly similar vertical coring speeds.

In a similar manner to that seen in the records for water ice, the torque requirement for coring CO_2 ice scales with the reciprocal of the rotation speed for a fixed depth rate. This, as was suggested earlier for water ice, is fully understood by the need for an ever-thinner slice of material to be removed by the cutting teeth at higher rotation speeds (for a constant depth rate). Another visible trend in the two ice's torque traces is that the average torque demand

upon the coring motor is almost uniformly higher than the initial figures. The small variation in the temperature of the CO_2 samples makes it impossible to compare the specific cutting energy of carbon dioxide and water ices as a function of temperature. Instead, the two data sets were filtered so that the sample temperatures were similar among the chosen data points and a sufficient number of data from the water ice tests could be found at temperatures of around 150 K. Before introducing the carbon dioxide strength relationships it is worth summarising the corresponding figures for water ice in the temperature region (~150 K) where the two ice's data sets do overlap. In Figures 96a and 96b the values of the dissipated power and the specific cutting energy at 150 K were ~1.5 W (±0.2 Watt) and ~60 MPa (±5 MPa) respectively for water ice. These values are applicable for a coring head moving with a mean rotation speed of 0.8 rev s^{-1} and a depth rate of 0.23 mm s^{-1}. Although no samples of carbon dioxide ice were cored under those exact same conditions a close match can be found in the data shown below, which were acquired at a similar temperature and rotation rate.

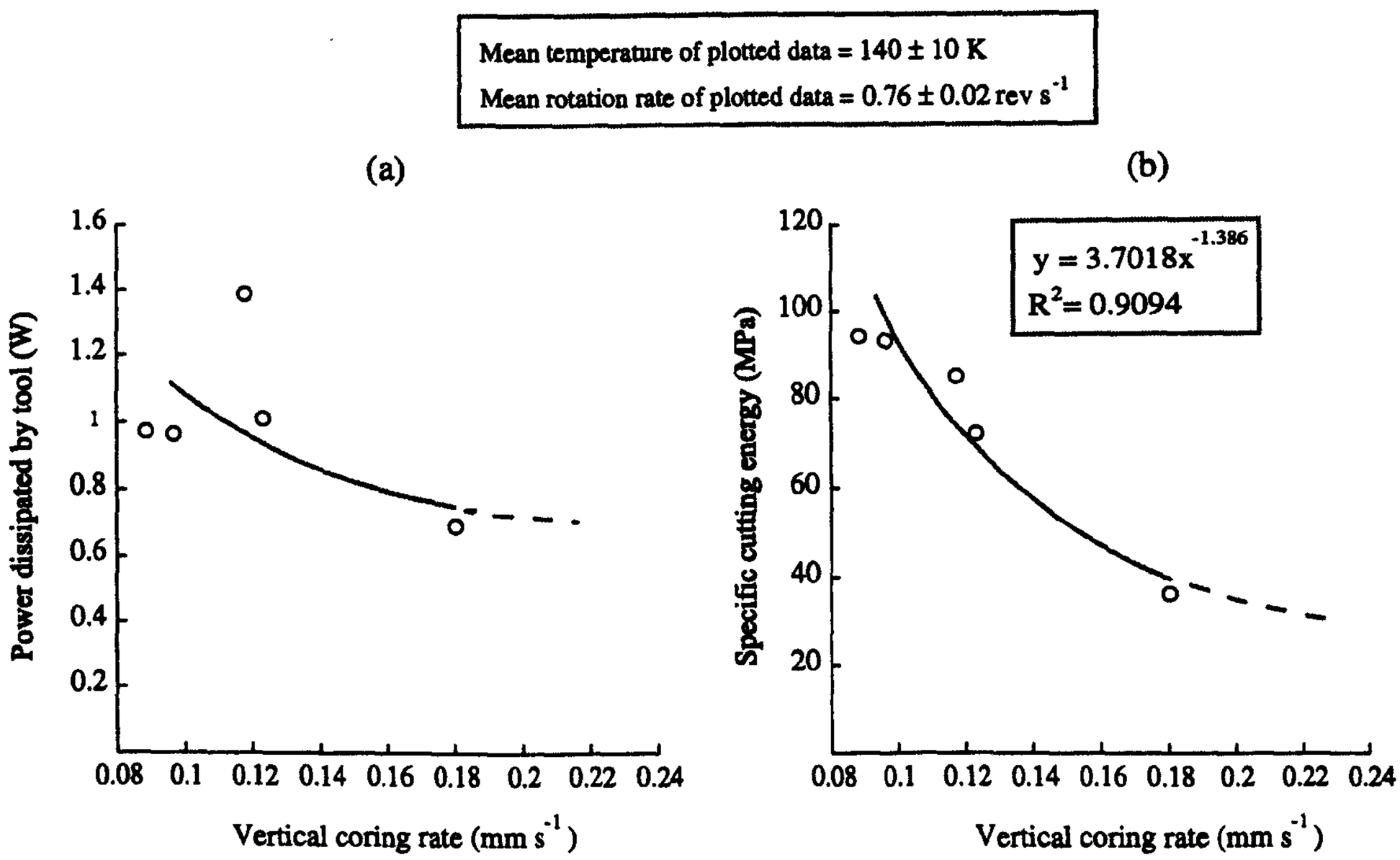

Figure 98a,b - Power dissipated by the coring tool and the specific cutting energy for carbon dioxide ice at 140 K as calculated from conditions early in the coring process.

Figures 98a and 98b are drawn so that they encompass the vertical depth rate of 0.23 mm s^{-1} that was used in the water ice charts and power-law curves (solid grey lines) are shown along with suggestive extrapolations (dashed lines). However, the data in Figure 98a cannot credibly be fitted with any particular model as the points are few in number and too wildly scattered: the

curve shown is purely a guide. To facilitate comparison between the ices used, Table 45 lists the specific cutting energy and dissipated power at these near-identical drilling conditions and temperatures.

Table 45 : Measured and extrapolated coring behaviour of ices at 140 to 150 K at an average rotation speed of 0.76 rev s^{-1} and a depth rate of 0.24 mm s^{-1}.

Ice	Power dissipated	Specific cutting energy
CO_2 (vapour grown)	~0.4 W (weakly known from fig 98a)	~30 MPa (firmly known from fig 98b)
H_2O (zone frozen)	>1.5 W (taken from fig 96a)	>55 MPa (taken from fig 96b)

Despite the difficulties of drawing conclusions from two different data sets that do not completely overlap it is suggested that;

3 *Water ice at temperatures of between 140 and 150 K has twice the specific cutting energy of dense carbon dioxide when cored under the same conditions of rotation rate and vertical speed. For a specific pair of these drilling parameters the act of coring a given volume of water ice at these low temperatures is seen to draw roughly four times the power needed to core the same volume of CO_2 ice in the same period of time.*

It is probable that this trend will continue to hold for marginally warmer and cooler temperature regimes although without a substantially larger data set this hypothesis cannot be tested. Similarly, carbon dioxide ice is likely to be more readily drilled and cored than water ice at vertical rates and rotation speeds that differ from those that have been used in the experiments. The experiments made to date have examined only single-component ices. It is likely, but not yet demonstrated, that mixtures of both water and carbon dioxide ices may, when cored, display strengths that lie between those corresponding to the pure water ice and carbon dioxide ice samples.

5.3.3 Temperature rises

The two ices examined in this work have thermal properties that lead to a significant variation in their response to the heating power delivered by a coring tool. The value of λc affects the temperature gradient that a given dissipated power will develop in the ice and at cryogenic temperatures (~150 K) the value of this product for carbon dioxide ice is one order of magnitude larger than for water ice (Figures 14 and 15). For a given amount of power expended in cutting a fixed volume of ice, a slab of dense carbon dioxide should display a temperature gradient around the tool that is three times (see equation 33) greater than that produced in cutting a similar sample of water ice at the same temperature.

In three of the carbon dioxide ice coring experiments small thermometers recorded the temperature in the path of the advancing coring tool. In the following table the temperature rises predicted by the model of SB89 and the 'flash' heating temperatures are listed along with the measured shifts. These measurements show a weak agreement between the measured values and those predicted by the model of SB89 for the tool bit temperature rise..

Table 46: Predicted and measured bit temperatures for CO_2 ices.

Experiment	Axial ΔT (K)	Tool bit ΔT (K)	Flash ΔT (K)	Recorded ΔT (K)
Fig. 71 (A5)	8.4	13.4	190	1*
Fig. 72 (B1)	4.3	5.8	144	4
Fig. 74 (D)	12.4	18.1	274	9.2

** The unusual shape of the temperature record in Figure 71 suggests that this may not be an accurate record of the ice temperature, but no clear reasons have been found for dismissing it entirely.*

The very large 'flash' temperatures suggested by the model of Tian and Kennedy (1995) are not seen in the recorded data from the diode thermometers. Nor is any periodic behaviour shown in the diode's reported temperature that might correlate with the motion of the individual cutting teeth. There are at least two explanations for these discrepancies. Firstly, the region in which the localized heating from the individual cutting teeth is significant may be too small for the millimetre-scale thermometers to sense. The figures shown in Table 10 for the flash-heating depths, suggest that the scaling distance for the temperature rises are smaller than, or at most, comparable to the physical size of the thermometer diodes. Secondly, it is also possible that the model used for the flash heating temperature rises is inappropriate in this

application. The original work of Tian and Kennedy (1995) employed a sliding contact that developed heat by frictional dissipation of mechanical work. This may be a poor model for the generation of heat by the expenditure of work by a cutting and excavation process. Strictly, the model of the cutting process used in the ice coring tests involves no frictional sliding, and assumes that material deformation is the sink of mechanical work and thus the source of heat. The presumption that work is efficiently converted into heat may therefore not be valid, but for this to be tested would require an independent method of measuring the total amount of heat delivered to the sample, and not simply the temperature at a given point in a changing temperature field. Without a method for testing the veracity of the 'flash' heating model, its predictions should be regarded as being at best suggestive of the peak temperatures that might be produced in vanishingly small regions around the tool head.

However, it is suggested that temperature rises larger than those reported by the diodes are being produced in at least some of the coring tests. For both water and carbon dioxide ices the specific heat of sublimation dominates the total heat needed to warm and vaporize a given mass of ice. However, the specific heat of sublimation of carbon dioxide is one quarter that of H_2O. Thus, for a fixed heating power, one might expect that carbon dioxide-rich ices may be more readily altered through sublimation than water ices. If the source of the heating power is removed, as will occur at the end of a coring experiment with the cessation of the tool's rotation, it is possible that gas evolved from the ice can then recondense. A bond may then be made between the ice and the tool head, with the machining grooves on the tool giving purchase for the newly formed ice. This is the inferred process that, during the coring of CO_2 ices, led to the drill head becoming stuck inside the ice on the few occasions in which the drill was not removed from the ice after its rotation had been stopped. In these instances the tool was stuck so firmly that it could not be removed from the ice for fear of damaging the motor drive and the sample holder.

5.4 Possible future experiments

The following sub-sections describe experiments that can be performed without the need for physical changes to the vacuum system from its state as described in chapter 4.

5.4.1 Data set expansion

Although only single component ices have been examined in this work it would be useful to fill the gaps that exist in the three dimensional parameter space that is formed from ice temperature, rotation speed, and depth rate. For example, the depth rate has been varied least of all in the coring tests and although the rotation rate was varied by as much as a factor of five, that variation was not been applied across all temperatures. Such a data gathering schedule would be simple but lengthy. With only four subdivisions per parameter, 4^3 separate experiments would be needed. At most three coring runs can be made from one ice sample and one experiment from preparation of the chamber to plotting of the data takes around two days of work. Half a year might therefore be spent in this exercise, but it is difficult to see how else the trends seen in this work could be studied in finer detail.

Aside from carbon dioxide and water the system can condense other ices such as solid ethane and methane from the vapour phase if the gas can be disposed of safely. The system might also be able to make multi-component ices. Hydrates of ammonia are believed to be present on satellite surfaces throughout the Solar System (Brown and Calvin, 2000) and careful cooling of aqueous ammonia solutions might allow hydrate ices to be made.

Other more complex ices may also be manufactured with the current vacuum system. It should be possible to form ices that contain significant concentrations of powdered or granular materials. The most obvious means by which particle-loaded water ices might be made would be to introduce a quantity of the chosen substance, such as sand or some other finely divided mineral, into the sample holder and to then pour in an amount of water. If this powder is then barely saturated, a relatively uniform block of frozen particle-loaded ice might be produced after the usual freezing procedure has been applied. Dust-loaded ices of carbon dioxide might also be manufactured, although in a different manner. A bed of relatively coarse grains of the chosen mineral might be laid down in the vacuum system's sample holder. This granular medium could then be exposed to a vacuum and the base plate of the sample holder might then

be cooled with the current cryogen loop arrangement. If the surface of this sample is then gently warmed with the vacuum chamber's internal lamp then a temperature gradient might be established through the material. A partial atmosphere of carbon dioxide may then result in the condensation of ice within the granular medium at the base of the sample holder, and with time the ice layer may thicken until the whole of the sample is suffused with ice.

Neither of these methods are suitable for generating ices with low mixing fractions of the added dense granular material.

5.4.2 Thermometry re-examined

Measurement of the temperature field during the coring process has been demonstrated successfully. If sufficient data could be obtained in a number of locations around a coring head it might be possible to model the temperature field in more than one dimension. In this work the temperature of the material within the hollow of a coring tool has not been measured and it has been assumed that the most significant heating occurs directly in the path of the cutting teeth. For shallow cuts in a material this is a fair assumption but when deeper holes are bored a hollow tool will be in prolonged contact with the walls of the hole at the outer surface of the drill and at both the inner and outer faces of the head. No information can be recovered from this fixed location about the temperature gradient within the material around the coring head. The addition of a second miniature thermometer to the sample holder would allow a temperature gradient to be measured in, say, the undisturbed central plug of material in a core. This would test the assumptions used in the thermal model (section 2.4) of Sgubini and Buratti (1989) and also determine the spatial extent of the local heating produced by the motion of the cutting teeth of a hypothetical sampling tool.

The above approach differs from the experiments that have been performed only in the quantity of thermometers used. A more radical approach would be to embed a single temperature sensing element in the tool at a point close to the cutting face, as was described in chapter 2. Motion may then be set up between the tool and the sample in one of two ways: the tool may be rotated with respect to the static sample, or the sample itself may be made to revolve while the tool is held fast. The approach described in this thesis is, on balance, the simpler of the two methods for studying cryogenic ices, in that only a pair of slip-rings need to

be added to the tool stem for an electrical sensor embedded in the cutting tool to be sensed. Rotating the sample stage would necessitate a much more elaborate method of cooling the worked material if low temperatures were to be maintained. That last condition is important; if a separate study was to be conducted on the temperature rise experienced when machining relatively warm ice, then the need for a cryogen cooling loop would be avoided and a better arrangement would involve the ice sample being spun by a lathe-like device, while the cutting tool and its internal thermometer element would be introduced progressively to the moving face of the ice.

5.4.3 Volatile migration in regoliths

Although there is no practicable method for forming intimate mixtures of dust grains and ice within the chamber it would be possible to fill the sample holder with a granular medium and then expose the regolith analogue to a vapour. If the sample holder is cooled to a fixed temperature then a thermal gradient can be set up that induces ice to form at depth in the sample; the upper surface could also have its temperature held constant with the radiant heating lamp. The goal of such a study would be to test the percolation models that are used to model the evolution of porous refractory materials representative of desiccated planetary or cometary surfaces. Instruments such as transient-hot-wire thermal sensors could be embedded within the material to monitor the growth and advance of ice condensation fronts.

5.5 Work requiring system modifications

The use of spare parts and *ad-hoc* mechanisms has lead to a system that is, in many ways, not ideal. Some areas of research may require that the chamber, its logging system, and ancillary equipment be changed, and suggested modifications are listed below.

5.5.1 Gas capture studies

The *in-situ* thermometry described in chapter 5 can be improved upon by changing the temperature sensing method used. The glass-envelope diodes employed do not represent the smallest discrete devices produced by the electronics industry. A limiting scale is that at which it is no longer possible to handle the devices manually, and the additional difficulty of soldering wires to such small components will probably prevent devices shorter than 0.5 mm in length from being used. By using diodes with a glass envelope around the sensitive junction a small thermal barrier is introduced, unfortunately. Thus, the changes detected by the diodes are likely to underestimate the peak temperatures seen in the region around a cutting tool and more intimate methods might be used to determine more accurately the peak temperatures produced in the material by a machine tool. To avoid this problem a source of miniature thermistors has been found (Thermometrics, New Jersey, US). These small (0.1mm x 0.6 mm) devices do not have an evacuated glass envelope around their junctions and their use as thermometers is being investigated.

Another approach to the goal of *in-situ* thermometry may involve the use of the peculiar gas-trapping properties of amorphous water ice, and perhaps other phases of other ices. The rate at which amorphous water ice releases a guest vapour is known to be strongly dependent upon the ice's temperature and the detection of the released gas with a mass-spectrometer may then be used to infer temperature of the region around a cutting head. A broad range of gases may be used to dope the ice, with hydrogen, helium, carbon monoxide, methane, argon, neon, all having been used at some time as guest compounds in amorphous water ice. It is worth mentioning that ice Ih may also be used as a host ice. The crystalline form of water ice is not only simpler to make than amorphous ice, but it is perhaps a more representative material for the shallower layers of an active comet. A suitable dopant would need to be soluble in water if the ice is formed by zone-freezing, and should be readily handled without adding unusual dangers

or difficulties. Ammonia and its aqueous solutions have many properties that fit the criteria, but it readily forms a hydrate structure with water and is largely retained by water ice at temperatures as high as 170 K (Klinger, 1989), which makes it a poor candidate as a tracer-component for elevated temperatures in Ih ice.

If the gas evolved through coring can indeed be distinguished in some way from the background sublimation of a cold sample then such a result may justify the inclusion of a mass-spectrometer inside the chamber to monitor the chemical and isotopic evolution of ice-rich materials prior to, during, and after sampling methods have been applied.

5.5.2 Chamber alterations

The vacuum chamber described in this thesis was built without an initial blueprint. Some of its components are not well-suited to the purpose for which they are used and this section describes some changes that may be considered if this work is expanded upon.

1) The manipulator used to drive the coring heads is poorly suited to the high speeds at which it is operated. The manufacturer's notes do not describe the manipulator as being suitable for anything other than hand-driven rotation, and as a result of the speeds used in this work, the bearings of the rotating stem are showing some signs of wear after several hours of accumulated use. No suitable drive train could be found from the usual vacuum system suppliers when the manipulator was being considered as an extension to the chamber and a dedicated manipulator may need to be built. An alternative scheme with some merit involves placing the shaft's rotary motor inside the chamber. This removes the need to have a series of rotary seals along the length of the manipulator stem[2]. Changes to the drive shaft could be combined with re-engineering the tool holder and tool cooling method, which were also built in an incremental manner.

2) Thought may also be given to a means of electrically driving the vertical axis of the manipulator stem with a geared-down stepper motor. This would allow the head to be driven vertically at a more uniform rate than can be achieved with the manual gear handle on the

---

[2] Although devising a motor and gear box capable of operating at high speed and torque in a modest vacuum brings its own problems.

vertical axis of the manipulator. The load on this highly geared control is slight and a batch of combined stepper motors and gearboxes have been identified for this option.

3) Most of the current vacuum chamber's volume plays no part in the formation and processing of the ices that are made inside it. This 'wasted' volume slows the rate at which the chamber can be evacuated to a useful vacuum. If the analysis of evolved gas from drilling operations becomes an important topic of work then it may be advantageous to use a smaller chamber which could be baked-out and cleaned more easily.

4) A cuboid sample holder is used in the current system. This container is connected to the cryogen supply by *Swagelok*® connectors which show some tendency to loosen over time, presumably from the rapid thermal cycling that the pipework experiences. An improved sample holder could be made in such a way that removes the need for manually tightened fasteners and an example of such a stage is shown in Figure 99 in which hard soldering or brazing may be used to join the cryogen pipes to the sample holder.

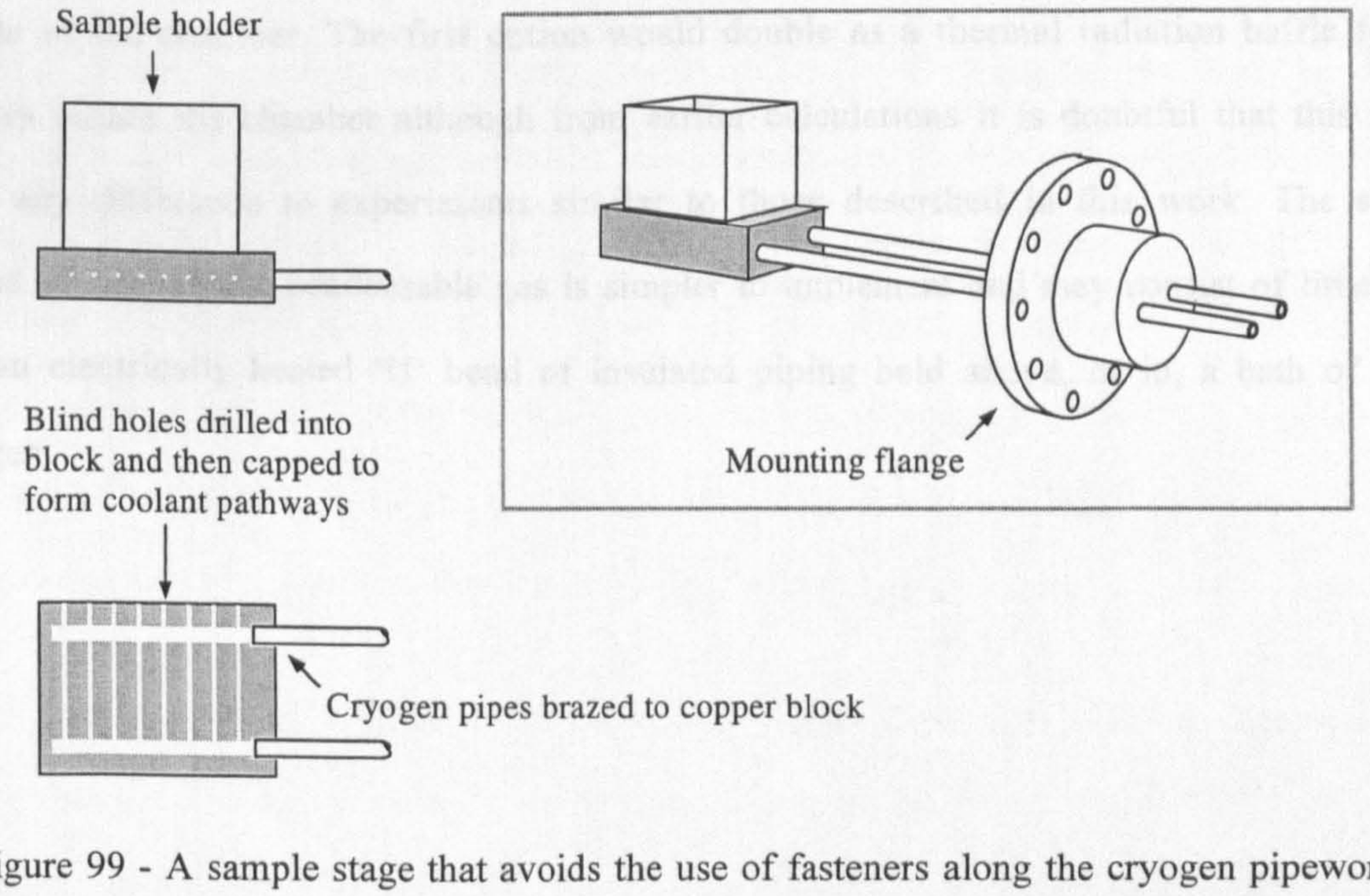

Figure 99 - A sample stage that avoids the use of fasteners along the cryogen pipework.

By using a more massive sample holder than the present plate-like design, a less demanding control system would be needed to ensure that the sample holder's temperature does not change rapidly. At present the flow rate of liquid nitrogen is governed by a manual admittance valve in-line with the cryogen pump, and fine control of the flow rate is not

possible. This rather coarse degree control means that the sample holder's temperature cannot be easily constrained without manual intervention over time spans of tens of seconds. Part of this problem arises from the use of a liquid cryogen which boils within the cooling pipes at poorly constrained locations.

5) The current arrangement used to deliver gas to the sample holder for condensation experiments is unsatisfactory for two reasons. Firstly, the gas flow rate is managed by manually adjusting a coarse flow valve with no indication of the flow rate. Secondly, the gas leaves the delivery pipe in the chamber at room temperature and a means of lowering the gas' temperature would be useful if condensation processes at work on planetary or cometary bodies are to be modelled. By pre-cooling the gas flow, frost/snow formation and sintering could be simulated more closely, and experiments on these ices would be looked upon as having a greater degree of applicability to spacecraft sampling tools.

Equipment for providing a cooled ambient atmosphere may take the form of a hollow thermal shroud inside the chamber or a cooling loop attached to the gas delivery line on the outside of the chamber. The first option would double as a thermal radiation baffle for the samples within the chamber although from earlier calculations it is doubtful that this would make any difference to experiments similar to those described in this work. The second method of cooling the condensable gas is simpler to implement and may consist of little more than an electrically heated 'U' bend of insulated piping held above, or in, a bath of liquid nitrogen.

6 Conclusions and implications

"One never notices what has been done,
one can only see what remains to be done."

Marie Curie

From the preceding discussions a number of conclusions can be drawn about the thermodynamics of coring ices of water and carbon dioxide. These points are listed below in the order that they were introduced in earlier chapters.

1) Excavation is most efficiently achieved, in terms of the total energy expended, by a tool that removes as much material as possible with each pass of its cutting teeth. Note, this approach has high power needs and develops large resistance forces. A compromise should be sought between a) the (inefficient) use of small downforce or many cutting teeth, and b) the more efficient deployment of tools with fewer teeth or the use of higher downforces.

2) Water ice, along with most other materials, has a specific heat capacity that is proportional to temperature, and a thermal conductivity that is broadly *inversely* proportional to temperature. The product of these two properties changes by a little less than 15 % in the temperature range of 100 to 270 K (Figure 14) but differs among ices. The value of λc determines the temperature gradient that a given dissipated power will develop in the ice. If a given amount of power is dissipated in water ice, a temperature gradient will be set up that is one third the size of that which would be made in CO_2 ice with the same power applied.

3) The strength of solid water ice at high strain rates under uniaxial compression or tension rises by a factor of around three as its temperature falls from 270 to 100 K. A similar rise is seen in the specific cutting energy of water ice in the more complicated failure process that accompanies drilling or coring (Figure 96a/b).

4) Temperature rises around a tool vary with the product $(\lambda \rho c)^{-0.5}$, and also vary directly with the specific cutting energy of the worked material. The temperature dependence of the density of carbon dioxide and water ice is small and will be ignored. The term λc varies little with temperature for both water and CO_2 ice and so the variation of the temperature rise

caused by a tool as a function of the ice's overall temperature is determined mostly by the temperature dependence of the ice's specific cutting energy, u.

5) The rise seen in water ice's specific cutting energy with falling temperature leads to increased power consumption for the removal of a fixed volume of material in a given period. When coring water ice at 140 K, this power expenditure should lead to rises in bit temperatures that are more than twice as large as those expected to occur at 250 K.

6) While carbon dioxide ice's strength variation with temperature has not been measured, at ~140 K this dense material has approximately 50 % of the strength of water ice at the same temperature. Coring a given volume of carbon dioxide ice therefore needs only one half of the energy used in cutting water ice at 140 K to remove a specified volume. If the densities[1] of the ices are accounted for, coring a given mass of CO_2 ice at 140 K requires a little over 80 % of the energy needed to core the same volume of cryogenic water ice.

7) Carbon dioxide ice at 140 K has, however, a product $\lambda\rho c$ that is much smaller than that of water ice. The removal of a given volume in a period of time should lead to a temperature rise around a cutting tool in CO_2 ice that is larger by about 2.7 times than that which should occur in water ice. Temperature rises measured when cutting carbon dioxide can be used to predict that under similar conditions, the action of coring water ice at a temperature of 140 K would result in peak temperatures no larger than ~37 % of those seen in carbon dioxide ice.

8) The speed at which an ice is cut influences both the peak temperature at the cutting bit and the total temperatures reached by the bulk of the cored material. The variation of the peak ('flash') temperature and the background temperature change should vary as approximately the one-half power of the tool cutting speed. Experimental data from *in-situ* measurements of temperature have not shown that the localized temperature field around each cutting tooth can be measured with thermometers that are comparable to the millimetre-scale depth of this heated region. The broader temperature rise associated with the whole tool does appear to have been measured in at least two separate experiments. With the tool geometry used and applied power loads of up to 1.5 W the material made to fail in the path of the tool

---

[1] The ratio of $\rho(CO_2) : \rho(H_2O)$ is roughly 0.6

has been shown to result in peak temperatures of at least 10 K in dense carbon dioxide ice. The same tool, and the same applied power should cause water ice at 140 K to experience a temperature shift in the path of the tool of 3 to 4 K.

These are the conclusions about the thermomechanical response of low-porosity water ice and carbon dioxide ice that can be safely drawn from the existing data set. It is likely that they will be applicable to situations which are not too dissimilar in terms of the material properties of the sample, the dynamics of the coring tool, and the power and load levels applied. Changes in these parameter values can be incorporated into the models that have been described and it is expected that similarly fair agreement will be seen between expected and measured temperature changes in cored samples taken from cryogenic ices.

6.1 Sample alteration

For the coring process to pose a hazard to the integrity of a sample the temperature rise applied to the sample should lie outside the normal temperature span that the material experiences in its unaltered setting. For objects in the Solar System these natural temperature changes are often driven by changes in the levels of solar insolation, alterations in the rotation state of the body, or weathering and gardening processes that change the depth at which a material is buried. If these normally occurring temperature changes are much larger than the warming brought on by a sampling tool then the question of sample alteration is moot. Where the temperature rise is significant, the alteration phenomena listed in Figure 11 may be active.

The temperature field associated with a coring tool (as modelled by SB89) travels vertically through the bored medium at a speed no faster than the coring head itself. This temperature field has been sensed and found to be modest for the power levels used in the coring experiments. It is possible that comparable power levels applied by a tool such as the SD2 sampler will yield similar temperature shifts in the vicinity of the coring head. However, this device will operate at a relatively shallow depth (<0.3 m) in the surface of comet 46P/Wirtanen. Models for cometary temperature gradients have been constructed for this comet by Klinger *et al.* (1996) and equatorial peak temperatures may be as high as 370 K at the comet's perihelion, and always higher than 170 K at that point in the absence of an insulating dust layer. In all of their scenarios the diurnal temperature changes propagate several

10s of cm into the surface and if the coring tool used in chapter 5 is a fair analogue for the SD2 coring head then it is unlikely that the additional warming generated by the SD2 will pose an unusual thermal hazard to the cored material at its operating depth.

Although many other ill-defined parameters[2] may play a role it does not seem likely that the sampling tool of the *Rosetta* lander will cause a temperature disturbance that will alter its retrieved samples in excess of the changes that natural orbital motion will have caused. Therefore it is not likely that a sensible change will be caused in the composition of material extracted from the near-surface of cometary nuclei with the tool considered in this work using the power levels discussed. At higher power levels, or when coring target materials that do not regularly experience solar heating, it is possible that the temperature rise associated with the cutting process may exceed other natural changes in the sample's temperature. The changes that may occur (see Figure 11) in this situation will depend on the ambient temperature of the ice and the temperature shift caused by the tool. Where the substance being cored has a solid component that is distinctly more volatile than the dominant constituent of the material, such as may occur in a water ice and carbon monoxide mixture, then preferential loss of the more fugitive compound can be expected.

At present the vacuum system has no means of measuring the degree of alteration caused by coring ice samples, and accurate predictions for the amount of material that sublimates from ahead of the cutting teeth cannot be made. Some evidence for ice-loss by sublimation was found indirectly from the strong adhesive forces that appeared rapidly at the end of certain CO_2 coring experiments. It is expected that more volatile ices such as carbon monoxide would display similar behaviour when cored, and that water ice with its higher heat of sublimation would be relatively immune to mass-loss through sublimation during a coring process. That water ice has been the subject of much of preceding discussions is a result of its relatively high abundance on Solar System bodies of interest to present spacecraft sampling missions. It is also, in comparison to the gas-phase isotope chemistry of other solid ices, more widely studied. However, the thermal and mechanical properties of water ice result in lower cutting temperature rises, and proportionately smaller degrees of sublimation than might be seen in other ices.

---

2 Such as the extent to which the borehole is blocked by the drill stem.

6.2 Water ice rich solids

This work has concentrated on pure ices with well-described thermal and material properties so as to simplify the experimental schedule. On planetary and satellite surfaces it is unlikely that the processes (such as sintering) that seek to remove structural and chemical inhomogeneities will be un-opposed by other phenomena. Ices in a planetary surface setting are likely to be combined with foreign chemicals and materials over a wide range of possible mixing fractions. In particular, water, and its high solvation ability, allows salt solutions to form complex hydrated minerals upon exposure to near-vacuum atmospheric pressures and this chapter will close with a brief discussion about the implications of adding other materials to water ices. Figure 100a, taken from Prieto and Kargel (2001), shows the specific heat capacities for two hydrated minerals that are thought to be good candidates for the non-ice component seen on the surfaces of Ganymede and Europa.

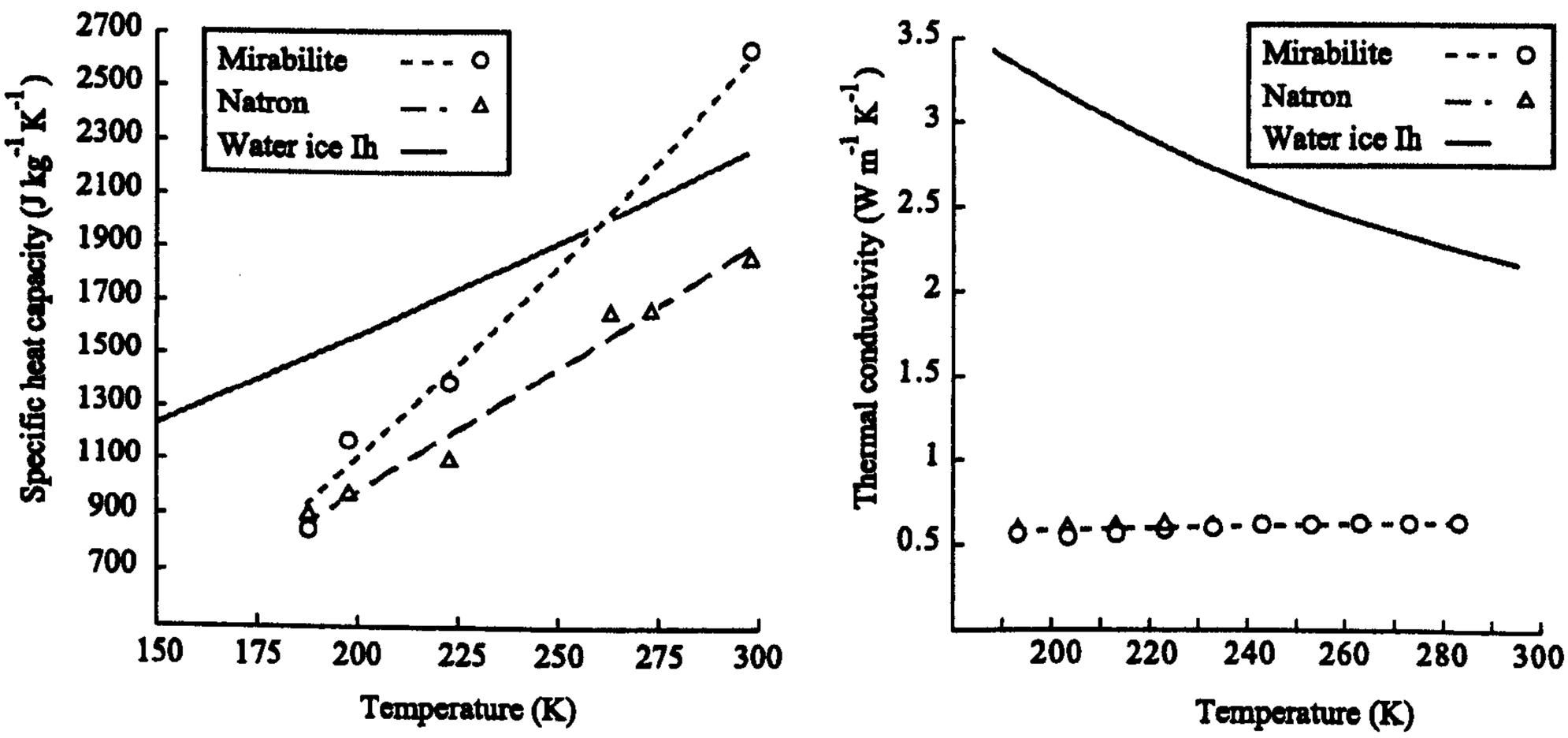

Figures 100a/b - Specific heat capacities and thermal conductivities of some candidate Europan surface minerals - adapted from Prieto and Kargel (2001, 2002).

Mirabilite ($Na_2SO_4.10H_2O$) has a non-water 'mass fraction' of 142:180 (44%) and yet has a heat capacity that differs by only 20% or so from water ice in the data range shown above. Figure 100b, by contrast, shows that the thermal conductivity values of these two minerals are smaller than that of water ice by a factor of at least 7 at temperature lower than 200 K. Minerals that are more heavily desiccated may have properties that deviate more strongly from those of water ice, but it is likely that a similar variation with temperature will be seen.

As well as variations in the thermal properties of a complex ice, the addition of some other non-ice fraction can alter the strength of such a composite ice. It might be expected that intimate mixtures of water ice and some other material may have properties that vary with the mixing fraction of the second material. Although no data could be found for the cutting behaviour of cryogenic ice and rock mixtures, related data sets do exist. Ductile compression tests at low strain-rates[3] on water ice-sand mixtures at temperatures between 77 and 223 K (Durham *et al.*, 1992) show that samples with sand volume mixing fractions up to 56% roughly double their compressive strength when compared to ice samples at the same temperature. Unfortunately, the viscous-drag mechanism invoked by Durham *et al.* (1992) to explain the strengthening effect caused by the addition of powdered minerals to ice samples cannot be applied to conditions of brittle failure which arise in the high strain-rate deformation of a cutting process. One study (Lange and Ahrens, 1983) *has* examined the strength of water ice and silicate mixtures at rapid strain rates, but only at the relatively high temperatures of ~230 to 250 K. By fitting a failure model to their data, Lange and Ahrens (1983) generated a series of trends for the tensile strength of sand and water ices at these temperatures; their results are shown in Figure 101.

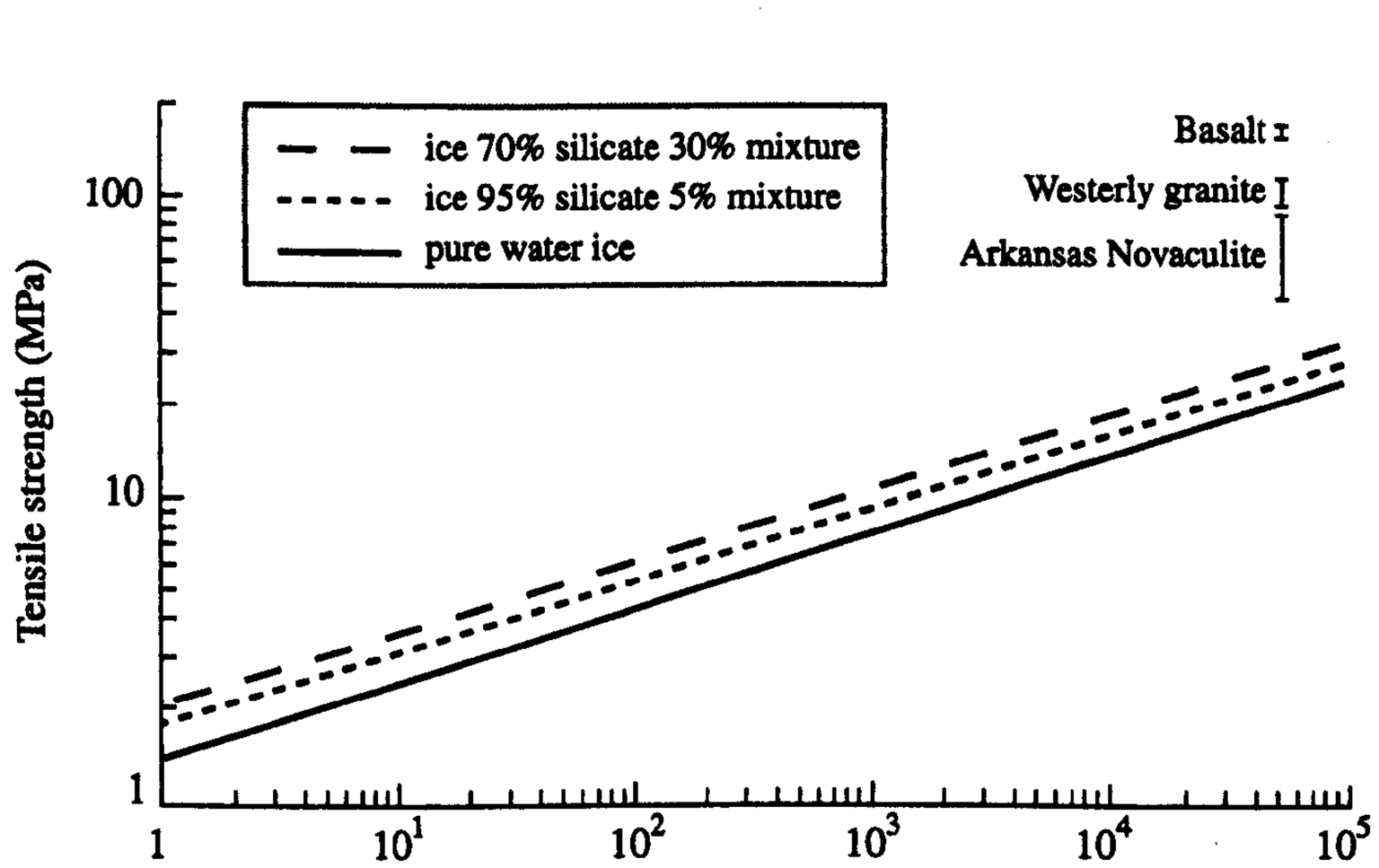

Figure 101 - The variation of tensile strength in silica-sand loaded water ices as a function of strain rate for three sand loads (weight % shown) adapted from Lange and Ahrens (1983).

Data points from one other study (Cohn and Ahrens, 1981) regarding the high-strain rate tensile strength of solid rocks are also shown in that Figure for comparison - the tensile

[3] Strain rate < 10^{-4} s^{-1}

strengths of those rock being approximately one order of magnitude higher than that of water ice. It appears that the addition of sand to a water ice at fractions of up to 30 % by weight can raise the failure strength of that material under rapid strain conditions by no more than 50%. Therefore it would seem that the addition of sand, and perhaps other comparably hard minerals, to an ice sample will probably not double the bulk material's specific cutting energy. To achieve the same vertical cutting rate in such a sand-loaded ice a tool may thus require 280% (1.5 x 1.85) of the mechanical effort needed to core water ice[4], if the temperature dependence of the ice's strength is unchanged by the addition of mineral grains. Experiments to examine the effect of particulate loading in cryogenic ices are practical with the current vacuum drilling system as was briefly discussed in chapter 5.

Whether the non-ice materials are mineral fragments or frozen grains of some water-soluble material, the temperature rise seen in coring more complicated multi-component ices may be analysed with the models in this thesis provided that the mechanical and thermal properties of the bulk material are known. However, it is possible that the bulk properties of a complex ice-rich solid are not predictable simply from their constituent substances. Preliminary studies of ammonia doped water ice by Shandera and Lorenz (2000) suggest that there may not be a trivial relationship between the ammonia fraction in a water ice sample and the resulting solid's bulk thermal conductivity, λ. Their work with small cryogenic samples indicates a rise in λ of 20% from 4 to 5 $Wm^{-1}K^{-1}$ for an ammonia-concentration varying from 0 to 20%. This is not expected from the value of 2 $Wm^{-1}K^{-1}$ for *pure* ammonia offered by Croft (1987) for that temperature. Having warned of the uncertainties in evaluating the thermomechanical properties of arbitrary ice-based compounds, it is possible to summarize broadly the relationships between an icy sample's composition and the temperature rise produced around a cutting head in that material at cryogenic temperatures.

a) Mixtures of water ice and silicate grains may display specific cutting energies of 280% those of water ice at a given temperature. From Equation 33, the temperature rise seen ahead of a coring tool will therefore be around three times that developed around the same head in a water ice sample. No comprehensive data could be found for the thermal properties of minerals at cryogenic temperatures and extrapolations from data taken above 270 K (Clauser and

---

[4] Recall that the specific cutting energy is per unit volume and a 50:50 sand:ice volumetric mixture can have a density of around 1850 kg m^{-3}.

Huegnes, 1995) should be treated with caution; the thermal conductivity of cryogenic Ih water ice may be unexceptional among the values predicted for low temperature properties of minerals such as the olivine group and non-silicate oxides.

(b) At low temperatures (~170 K) natron and mirabilite probably have values of λc that are around 13 times smaller than the value of the same product of properties for water ice (Figure 100), with the difference rising at lower temperatures. Without data for the strength of these minerals at high strain rates and low temperatures, once again a tentative assumption is made that these minerals are comparable in strength to water ice at cryogenic temperatures. From their thermal properties alone it is then possible to predict that a 50:50 volumetric mixture[5] of water ice and either of these two hydrated minerals will give rise to a peak temperature at the head of a coring tool that is 2.9 ($=13^{0.5} \div 1.2$) times larger than the temperature rise associated with coring water ice in the same conditions.

The addition of either silicate grains, or hydrated minerals, to a water ice appears to lead to cutting head temperatures that, for the same vertical depth rate, material temperature, and tool geometry, are approximately three times higher than those expected for a pure water ice sample, and comparable to those seen when coring pure carbon dioxide ice. Surface environments in the Solar System with either complex water-based ices, or ices dominated by carbon dioxide, will need to be approached with more care from the standpoint of sample extraction than coring studies with pure water ice would suggest.

---

[5] For both natron and mirabilite the bulk density of this composite ice is ~1.2 kg m^{-3}.

6.3 RoLand's SD2 at Wirtanen

The goal of assessing the effect of sample acquisition on the state of an ice-rich sample has been examined by theoretical and experimental work. Measurable temperature rises have been caused by the action of a coring tool that has been operated under conditions that are broadly similar to those of current planetary sampling tools. Of particular interest is the sample acquisition sub-system of the *RoLand* spacecraft which is expected to develop roughly four times[6] the peak power consumed during the coring experiments described in chapter 5. However, the SD2 cutting head dissipates this higher power through at least six cutting edges, unlike the tool described in this work which used only four teeth. Each cutting edge of the SD2 will, if all other aspects of the operation are equal, expend through each cutting edge $2^2/_3$ times the power dissipated by each tooth in the coring experiments of chapter 5. Unfortunately, without knowledge of either the nominal speed of rotation or the mean vertical speed of the SD2 head it is impossible to predict the peak temperatures developed. However, the size, power drain, and operating speeds of the tool used in the coring experiments described in this work probably do not differ greatly from those parameters of the SD2. In which case, the temperature rises predicted, and measured, for dense water ice and carbon dioxide ices will be similar to those that might be produced by the SD2.

The main differences between the coring experiments of chapter 5 and the operation of the SD2 on 46P/Wirtanen will be in the type of material cut by the tool. Given the relatively modest reach of the tool, it is likely that the SD2 will not be able to drill down to a point at which completely solid ices are found. Thermal models of 46P/Wirtanen indicate that at best, significantly *porous* crystalline water ice with some admixture of silicate grains, will be sampled at sub-metre depths (Capria *et al.*, 1996). As has been stated, the addition of mineral grains can lead to raised cutting temperatures when compared to pure water ice. However, the likely weakness of porous sub-surface cometary materials suggests that the SD2 tool may not produce significant temperatures around its head as little power will be needed to form the bore-hole. Thermal processing during sampling is therefore unlikely if solid ices are not encountered. However, uncertainties are legion, and this form of material alteration cannot be excluded in a detailed study of a cometary sample's progress through a lander's acquisition and analysis suite.

---

[6] A nominal electrical power drain of 6 W is stated for the SD2 (Camaschella, 1998). The mechanical power produced at its tip will necessarily be smaller, but this information is not known to the author at present.

Appendix A - Ice property data sets

Predictions made for the temperature shifts produced by mechanically coring ice-rich materials are dependent on an accurate knowledge of the ice's thermal properties. The thermal conductivity, specific heat capacity, and latent heat of sublimation for water ice and carbon dioxide ice are examined here to find appropriate models over the temperature range considered in this thesis, namely 130 to 250 K. Each of the properties reviewed is described in the following sections. Each section is accompanied by part of a spreadsheet - the values within which have not been truncated or rounded-up so as to preserve the data set's accuracy.

A1 - Heat capacity of water ice

The data of Giauque and Stout (1936) are plotted and tabulated for the temperature range described above.

A2 - Thermal conductivity of water ice

The model described by Klinger (1981) for the thermal conductivity of water ice Ih is compared to the data sets collated by Slack (1980). A maximum discrepancy of 13 % appears between the data set and the model presented by Klinger.

A3 - Latent heat of sublimation for water ice

Data for the specific latent heat of sublimation are shown. This property may be treated as being invariant with temperature; in the temperature span considered, the experimentally determined values change by only 6 %.

A4 - Heat capacity of carbon dioxide ice

The original experimental data of Giauque and Egan (1937) are plotted and fitted with an appropriate linear model.

A5 - Thermal conductivity of carbon dioxide ice

In lieu of a tabulated data set, the compilation charts produced by Croft (1987) on the thermophysical properties of cryogenic planetary ices were scanned digitally and the data captured using the software program 'Datathief' written by K. Huyser and J. van der Laan.

A6 - Latent heat of sublimation for carbon dioxide ice

Data for the specific latent heat of sublimation are taken from the work of Brown and Ziegler (1980).

A1 - Heat capacity of water ice

A	B	C
T (K)	c (cal mol^{-1} K^{-1})	c (J $kg^{-1}K^{-1}$)
16.43	0.303	70.36
18.37	0.41	95.20
20.78	0.528	122.6
24.2	0.7	162.5
28.05	0.883	205.0
31.64	1.065	247.3
35.46	1.251	290.5
39.62	1.449	336.5
43.96	1.641	381.0
48.52	1.837	426.5
52.98	2.014	467.6
57.66	2.203	511.5
62.63	2.418	561.5
67.83	2.612	606.5
70.61	2.723	632.3
73.01	2.821	655.0
75.6	2.922	678.5
78.51	3.016	700.3
79.98	3.07	712.9
81.44	3.115	723.3
82.42	3.163	734.4
83.72	3.191	740.9
83.94	3.199	742.8
86.66	3.286	763.0
87.25	3.336	774.6
89.2	3.389	786.9
91.32	3.488	809.9
91.93	3.532	820.1
94.93	3.649	847.3
95.85	3.66	849.8
97.37	3.724	864.7
99.57	3.814	885.6
100.69	3.832	889.7
104.69	3.985	925.3
110.13	4.136	960.3
115.84	4.315	1002
121.74	4.489	1042
127.54	4.655	1081
133.5	4.808	1116
139.48	4.978	1156
145.43	5.135	1192
151.43	5.306	1232
157.48	5.466	1269
163.52	5.663	1315
169.42	5.842	1357
175.36	6.007	1395
181.25	6.185	1436
187.2	6.359	1477
192.96	6.53	1516
199.11	6.71	1558
205.32	6.935	1610
211.56	7.119	1653
217.97	7.326	1701
224.36	7.519	1746
230.08	7.711	1790
236.19	7.887	1831
242.4	8.048	1869
249.31	8.295	1926
256.17	8.526	1980
262.81	8.732	2028
267.77	8.909	2069

Data source
Giauque W. F. and Stout J. W., 1936.
J. Am. Chem. Soc. **58**, 1144-1150

Column A lists the ice's temperature (K).

Column B holds the value of c (strictly, c_p) in cal mol^{-1}.

Column C holds the value of c in J $kg^{-1}K^{-1}$.

Giauque and Stout refer to a value of 4.1832 'international' joules as being equivalent to 1 calorie of heat and use a value of 18.0156 g per mole.

Summary
$c = 6.962T + 185$ is an acceptable fit to the data in the range of 100 K to 270 K
This model is shown in the chart overleaf as a solid line, the dotted line represents the commonly seen model of $c = 7.49T + 90$

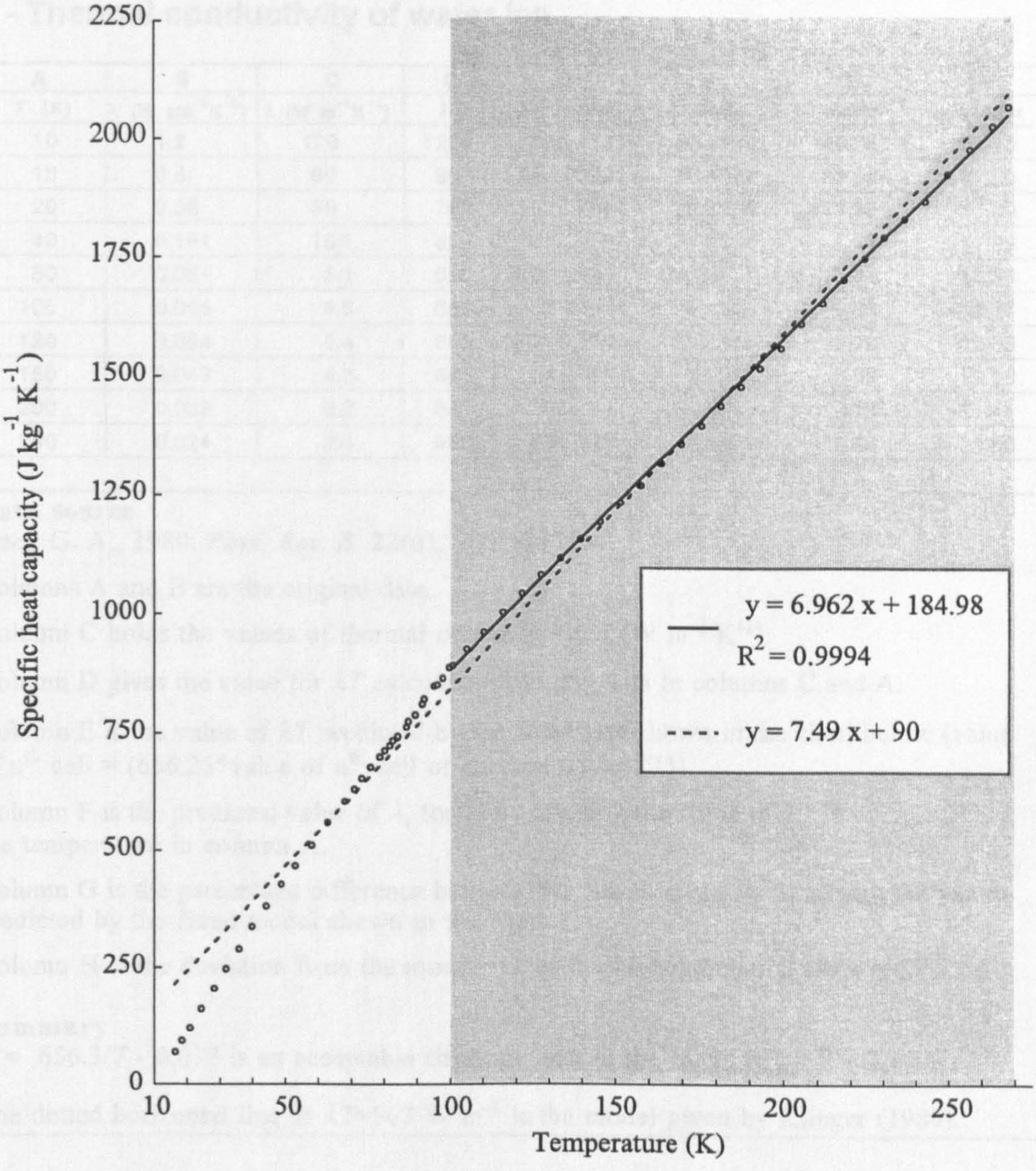
Specific heat capacity (J kg-1 K-1)
2250
2000
1750
1500
1250
1000
750
500
250
0
10
50
100
150
200
250
Temperature (K)
y = 6.962 x + 184.98
R2 = 0.9994
y = 7.49 x + 90

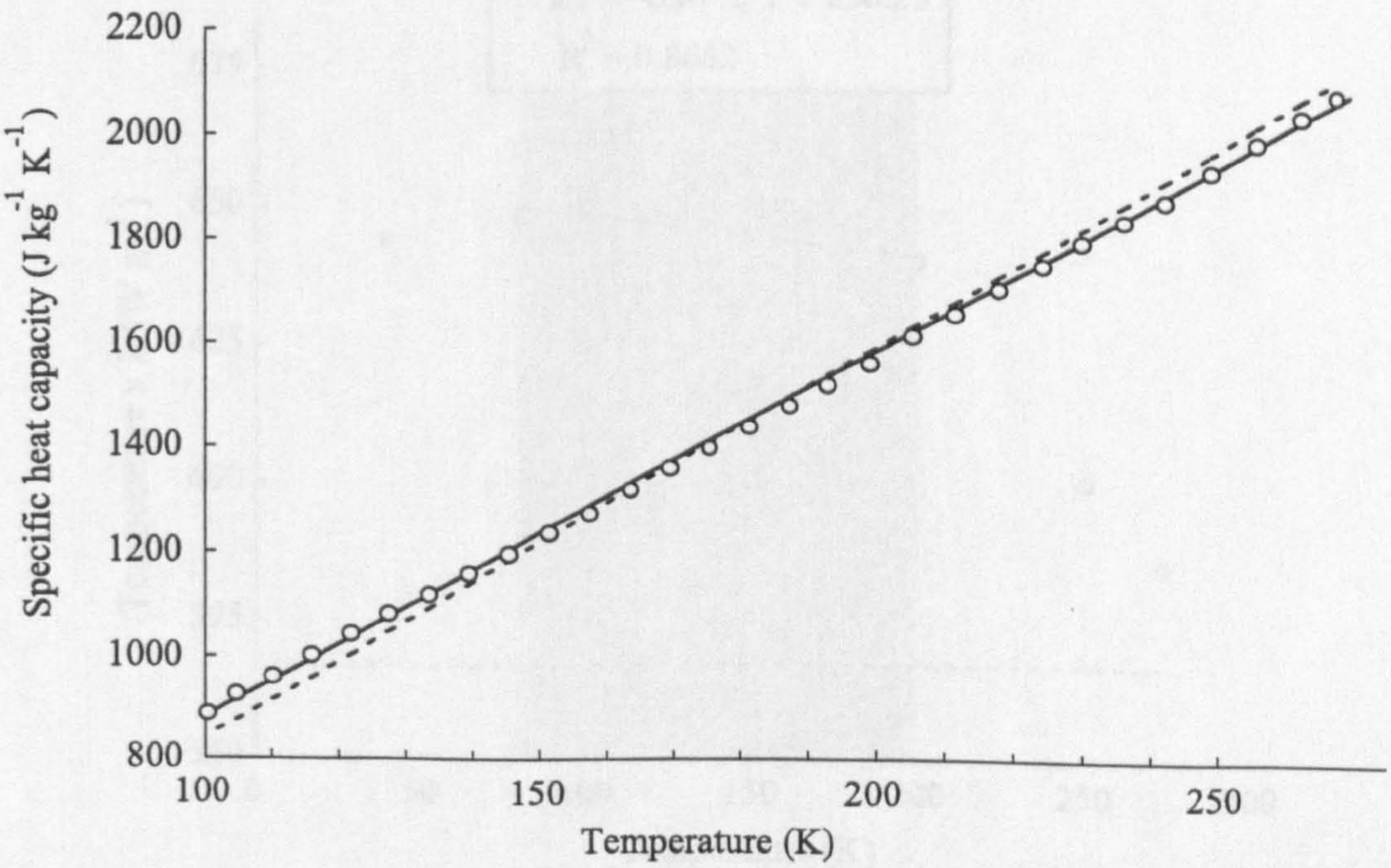
Specific heat capacity (J kg-1 K-1)
2200
2000
1800
1600
1400
1200
1000
800
100
150
200
250
Temperature (K)

A2 - Thermal conductivity of water ice

A	B	C	D	E	F	G	H
T (K)	λ (W $cm^{-1}K^{-1}$)	λ (W $m^{-1}K^{-1}$)	λT	λT model	λ model	% model	% Klinger
10	1.2	120	1200	655.477	65.5477	-45.38	-52.75
15	0.6	60	900	655.0905	43.6727	-27.21	-37.00
20	0.38	38	760	654.704	32.7352	-13.85	-25.39
40	0.161	16.1	644	653.158	16.32895	1.42	-11.96
80	0.081	8.1	648	650.066	8.125825	0.32	-12.50
100	0.065	6.5	650	648.52	6.4852	-0.23	-12.77
120	0.054	5.4	648	646.974	5.39145	-0.16	-12.50
150	0.043	4.3	645	644.655	4.2977	-0.05	-12.09
200	0.032	3.2	640	640.79	3.20395	0.12	-11.41
250	0.024	2.4	600	636.925	2.5477	6.15	-5.50

Data source
Slack G. A., 1980. *Phys. Rev. B.* **22**(6), 3065-3071.

Columns A and B are the original data.

Column C holds the values of thermal conductivity, λ (W m^{-1} K^{-1}).

Column D gives the value for λT calculated from the data in columns C and A.

Column E is the value of λT predicted by the fitted line shown in the chart below (value of n^{th} cell = (656.25*value of n^{th} cell of column A)-0.0773).

Column F is the predicted value of λ, found by dividing the value of λT in column E and the temperature in column A.

Column G is the percentage difference between the values given by Slack and the values predicted by the fitted model shown in the chart.

Column H is the deviation from the model values in column E and another model.

Summary
$\lambda = 656.3/T - 0.077$ is an acceptable fit to the data in the range of 80 K to 200 K.

The dotted horizontal line at λT=567 W m^{-1} is the model given by Klinger (1980).

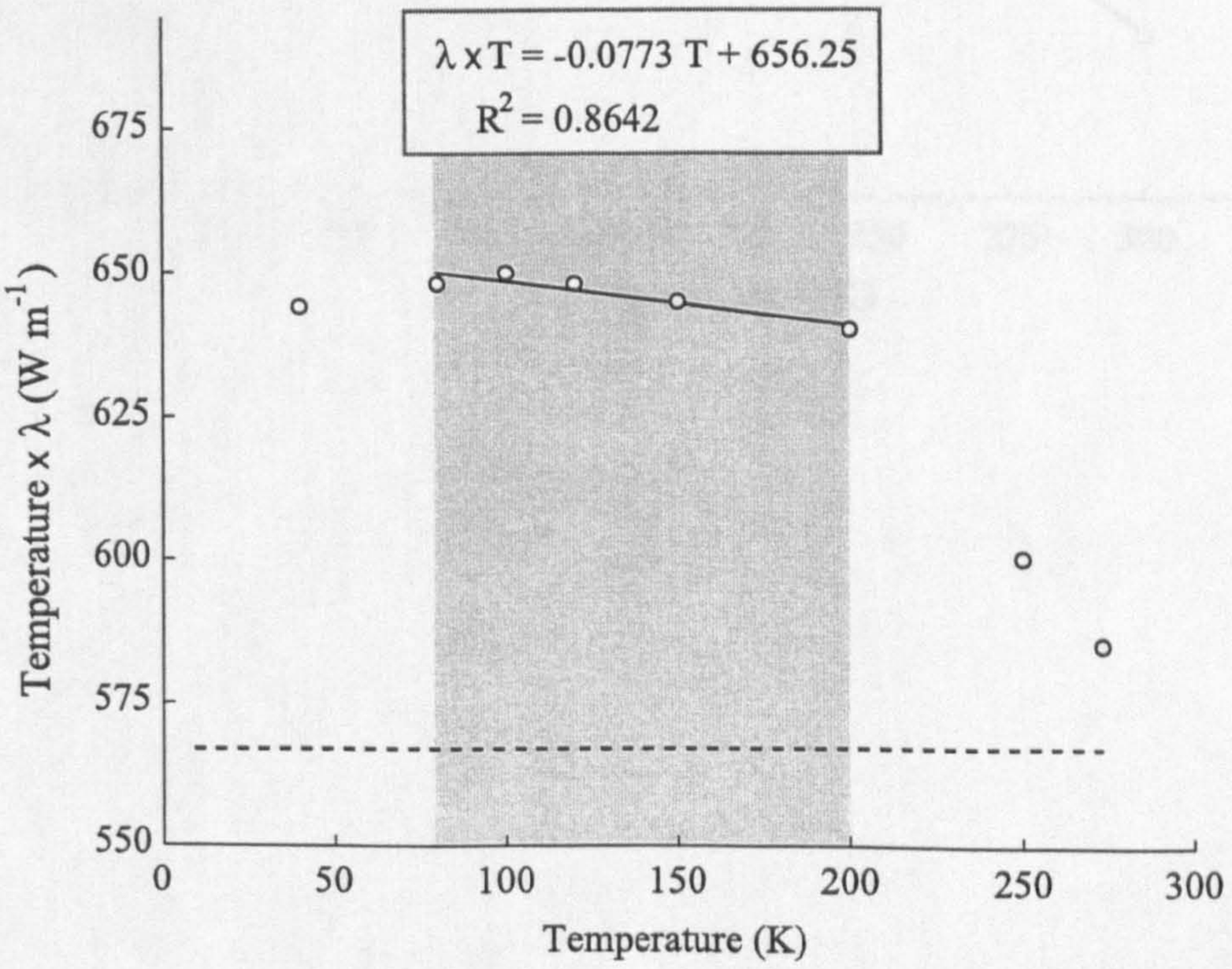

A3 - Latent heat of sublimation for water ice

A	B	C
T (K)	c_{sub} (cal mol.$^{-1}$)	c_{sub} (J kg^{-1})
150	11700	2717290.30
200	11480	2666195.96
250	11220	2605811.73
300	10980	2550072.44

Data source
Delsemme A. H. and D. C. Miller, 1971. *Planet. Space Sci.* **19**, 1229-1257.

The above commonly used reference takes its data from the following work

Washburn E. W. (1928), International Critical tables, 3, 210, McGraw Hill, New York.

Columns A and B are the original data.

Column C holds the value of latent heat of sublimation (J kg^{-1}).

Summary
$c_{sub} = 3 \times 10^6 - 1124T$ is an acceptable fit to the data in the range of 150 to 300 K.

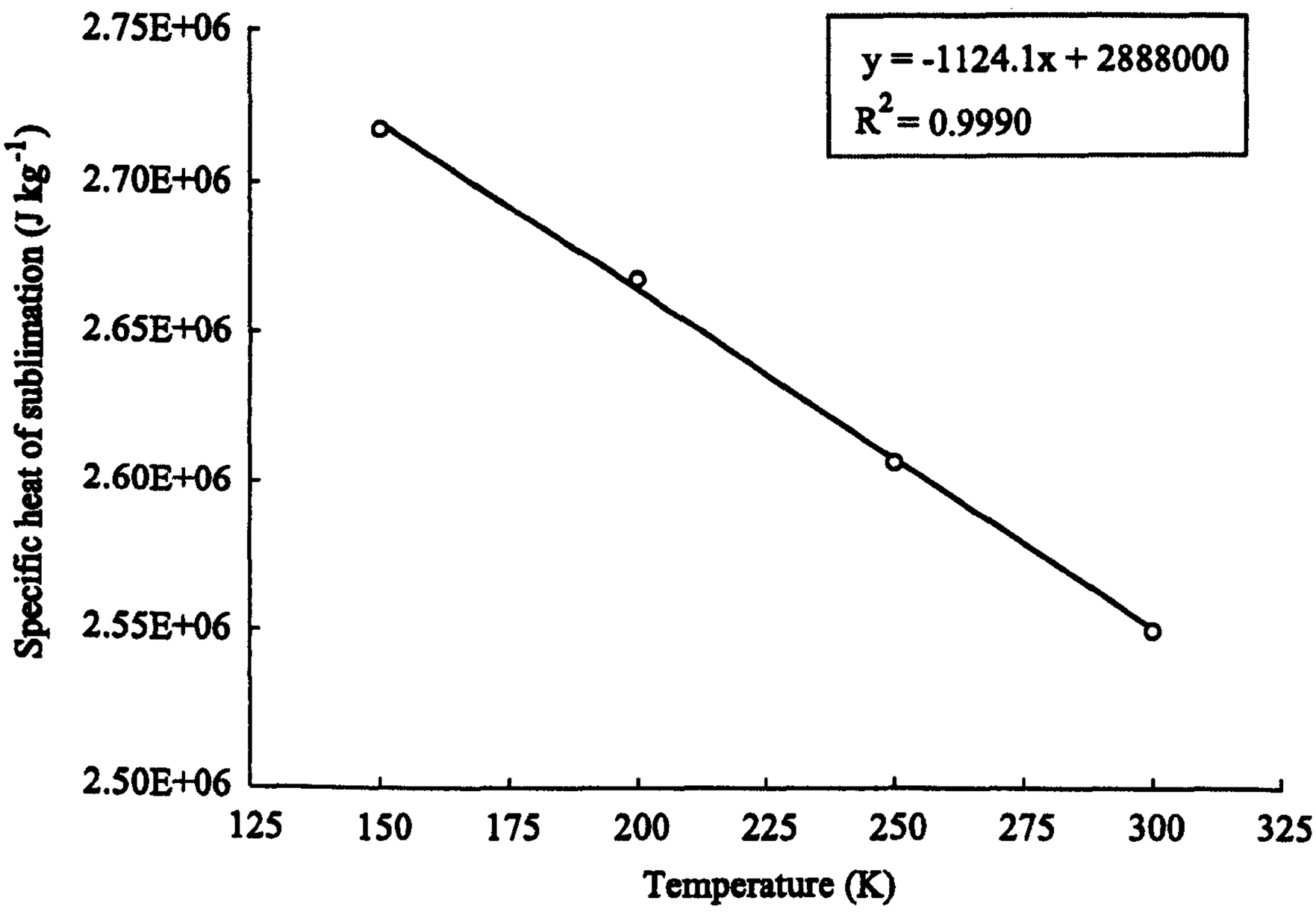

A4 - Thermal conductivity of carbon dioxide ice

A	B	C
T (K)	λ (W $cm^{-1}K^{-1}$)	λ (W $m^{-1}K^{-1}$)
111.0	4.80E-03	0.480
114.0	4.67E-03	0.467
117.0	4.54E-03	0.454
120.0	4.44E-03	0.444
124.0	4.32E-03	0.432
127.0	4.20E-03	0.420
131.0	4.06E-03	0.406
135.0	3.97E-03	0.397
138.0	3.86E-03	0.386
142.0	3.76E-03	0.376
146.0	3.68E-03	0.368
150.0	3.56E-03	0.356
155.0	3.50E-03	0.350
159.0	3.34E-03	0.334
164.0	3.29E-03	0.329
168.0	3.22E-03	0.322
173.0	3.09E-03	0.309
178.0	3.03E-03	0.303
183.0	2.94E-03	0.294
188.0	2.86E-03	0.286
193.0	2.77E-03	0.277
199.0	2.68E-03	0.268
204.0	2.61E-03	0.261
210.0	2.52E-03	0.252
216.0	2.46E-03	0.246

Data source
Croft S. K., 1987, NASA TM 89810

Column A is the temperature (K).

Column B is the thermal conductivity (W cm^{-1} K^{-1}).

Column C is the thermal conductivity (W m^{-1} K^{-1}).

Summary
$\lambda = 52.48T^{(-0.9963)}$ is an acceptable fit to the data in the range of 110 to 220 K.

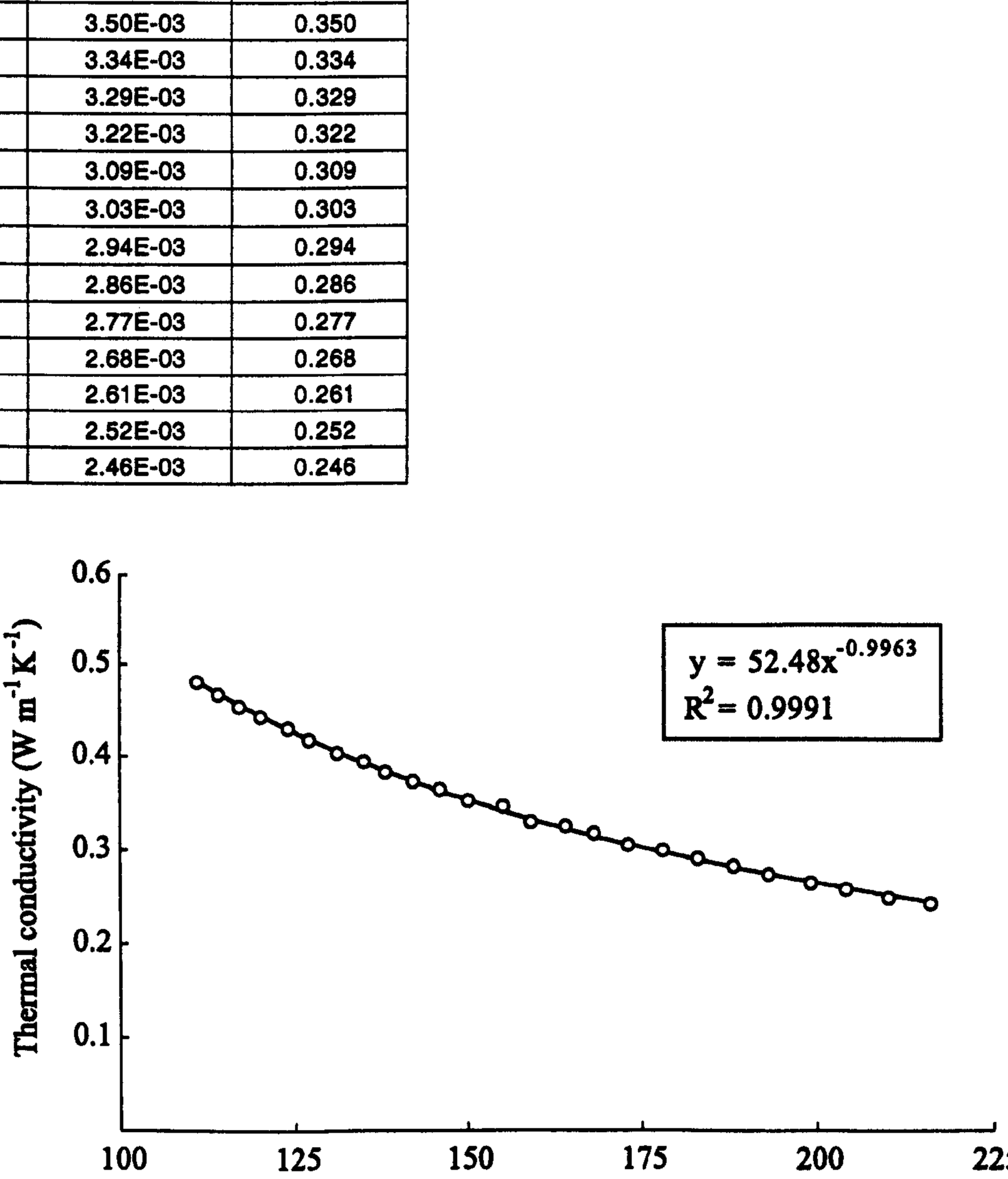

A5 - Specific heat capacity of carbon dioxide ice

A	B	C
T (K)	c_p (cal $mol^{-1}K^{-1}$)	c_p (J $kg^{-1}K^{-1}$)
103.26	9.671	919.47
108.56	9.893	940.58
113.91	10.07	957.41
119.24	10.27	976.42
124.58	10.44	992.58
130.18	10.69	1016.35
135.74	10.88	1034.42
141.14	11.08	1053.43
146.48	11.27	1071.50
151.67	11.45	1088.61
156.72	11.64	1106.67
162	11.84	1125.69
167.62	12.07	1147.56
173.36	12.32	1171.32
179.12	12.57	1195.09
184.58	12.82	1218.86
189.78	13.05	1240.73

Data source
Giauque W. F. and C. J. Egan, 1937.
J. Chem. Phys. **5**, 45-54

Column A holds the temperature (K).

Column B is the heat capacity in calories per mole per degree K.

Column C is the heat capacity (J kg^{-1} K^{-1}).

Summary
An acceptable fit to the data in the temperature range of 105 K to 190 K is given by the equation.

$c_p = 3.65T + 540.$

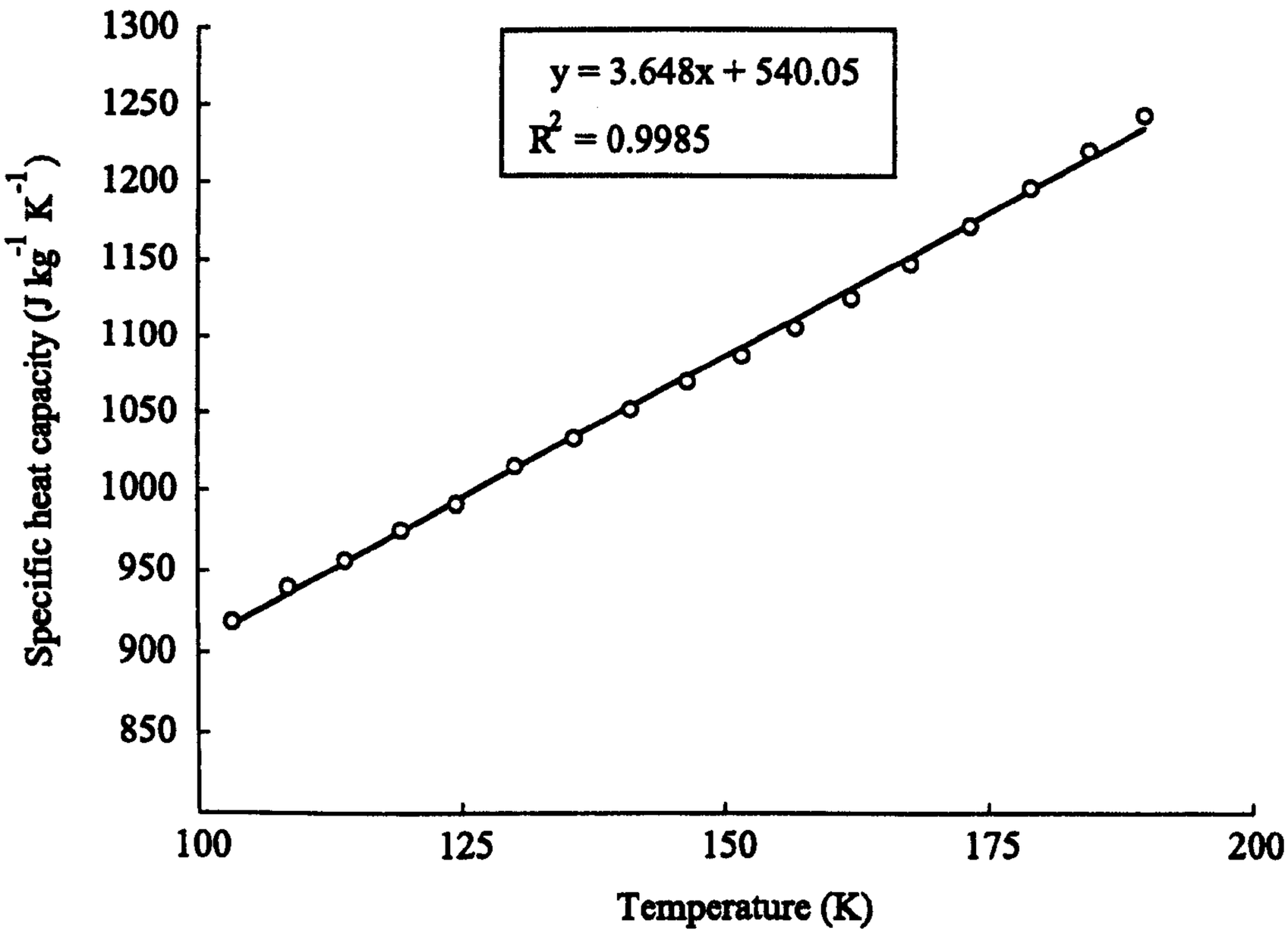

A6 - Latent heat of sublimation for carbon dioxide ice

A	B	C
T (K)	c_{sub} (J mol^{-1})	c_{sub} (J kg^{-1})
110	26858.7	610424.9
120	26729.5	607489.6
130	26587.8	604269.0
140	26433.4	600758.8
150	26264.7	596925.8
160	26079.1	592707.5
170	25872.6	588012.7
180	25639.7	582721.1
190	25374.1	576683.6
200	25067.8	569721.8
210	24711.7	561628.5

Data source
Brown G. N. and W. T. Ziegler, 1980. *Advances in Cryogenic Engineering*, **25**, 662-670.

Column A is the temperature of the ice (K).

Column B is the specific heat of sublimation (J mol^{-1}).

Column C is the specific heat of sublimation (J kg^{-1}).

Summary
The marginal variation of c_{sub} (in J kg^{-1}) with temperature is modelled tolerably with the linear equation for temperature (K).

$c_{sub} = 666200\text{-}475.3T$

Better, but more complicated models are not necessary given the very slight change in this property with temperature.

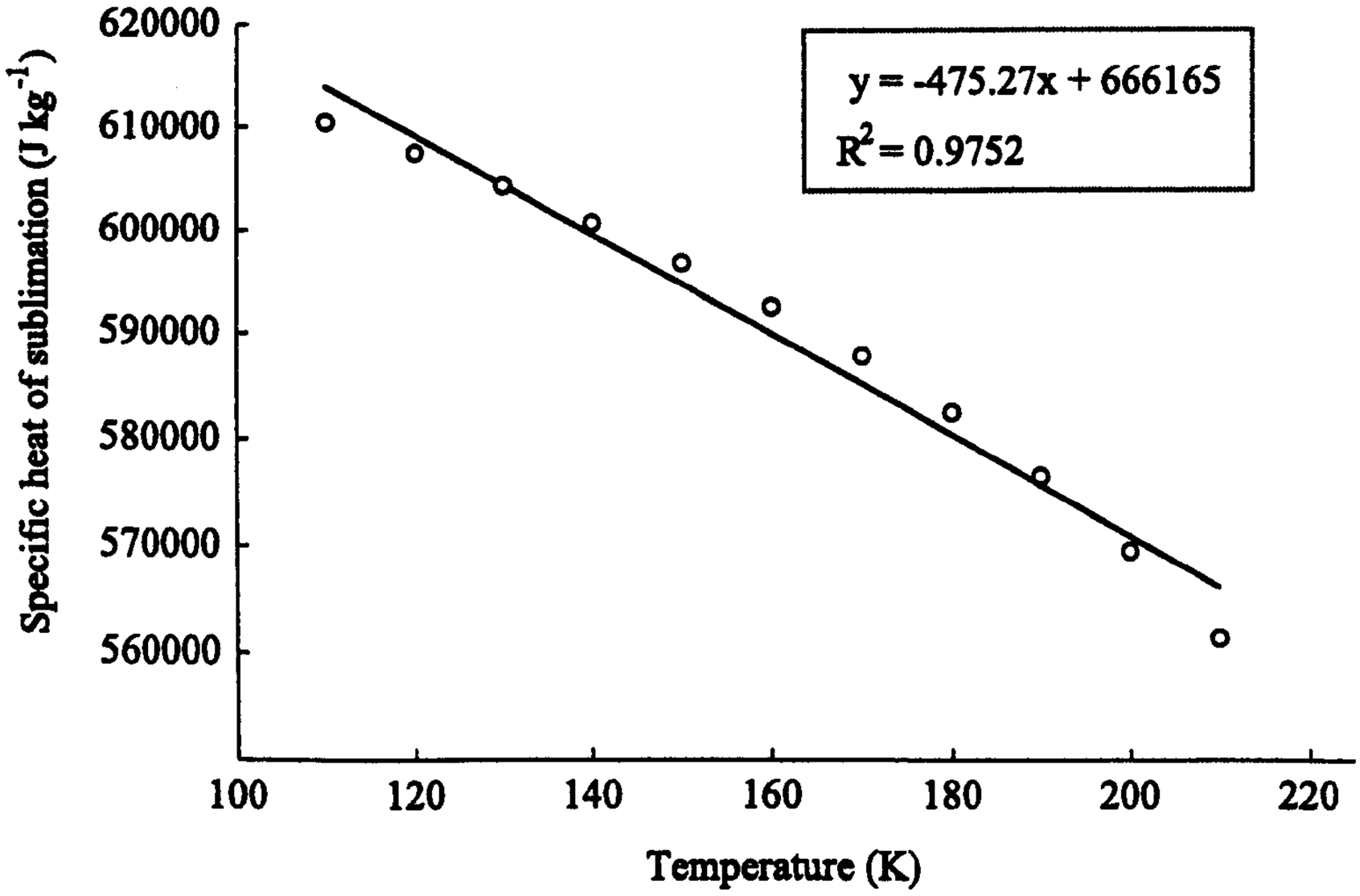

Appendix B - Thermomechanical computer codes

The BASIC language was chosen over other more advanced languages as the tool for implementing algorithms used in this work because of its simplicity and comprehensible syntax. The specific BASIC dialect employed was 'Chipmunk BASIC' (v. 3.5.7b1) written by Ronald Nicholson for the Macintosh operating system.

B1 - Specific cutting energy

From the forces and speeds encountered in driving a cutting edge across the face of a plastic material, the energy consumed in removing a unit volume of material can be found. The following program uses the general nomenclature described in Shaw (1984) with a simple slip-line failure model to evaluate the shear-plane angle.

```
10 rem A cutting model taken from Milton C. Shaw's text
20 rem 'Metal Cutting Principles", Oxford Univ. press, 1984
30 rem
40 rem fp is the cutting force in the direction of travel (N)
50 rem fq is the force normal to the work surface (N)
60 rem fs is the force along the shear plane (N)
70 rem fc is the force into the work along the tool face (N)
80 rem v is the speed at which the work meets the tool (m/s)
90 rem vs is the speed of deformation along the shear plane (m/s)
100 rem vc is the speed, relative to the tool face, of the chip (m/s)
110 rem rev is the rotation speed of the drill stem (rev per sec)
120 rem t is the undeformed chip depth (the feed) (m)
130 rem alpha is the rake angle = zero for tool heads used (rad)
140 rem phid is the shear angle (deg)
150 rem phi is the shear plane inclination angle (rad)
160 rem beta is the friction angle (rad)
170 rem torquearm is the radial dist. from torque sensor to work axis (m)
180 rem torqueforce is measured on the torque load meter (N)
190 rem nload is the normal load (N)
200 rem toolr is the tool outer radius (m)
210 rem toolwid is the width of each tooth (m)
220 rem depthrate is the vertical depth rate (m/s)
230 rem n is the number of cutting teeth (int)
240 rem a$ is a formatting string
250 rem
260 a$ = "              "
270 input "Rotation rate (rps) = ";rev
280 input "Depth speed (m/s) = ";depthrate
290 input "Downforce (N) = ";dforce
300 input "Torque (Nm) = ";torque
310 n = 18
320 torquearm = 0.285
330 alpha = 0
340 toolr = 0.0125
350 toolwid = 1.500000E-03
360 rem
370 rem Having established values for variables, calculate
380 rem a number of characteristic forces in the geometry.
390 rem
```

```
400 fq = dforce/n
410 fp = torque/toolr/n
420 fc = fp*sin(alpha)+fq*cos(alpha)
430 nc = fp*cos(alpha)-fq*sin(alpha)
440 beta = arctan(fc/nc)
450 rem
460 rem Phi should ideally be *measured* but an approximation
470 rem is available that evaluates it from alpha and forces.
480 rem
490 phi = (pi/4)-beta+(alpha/2)
500 fs = fp*cos(phi)-fq*sin(phi)
510 ns = fq*cos(phi)+fp*sin(phi)
520 rem
530 rem Calculate the speed of the chip's motion, vc, and the speed
540 rem of material deformation along the shear plane, vs.
550 rem
560 v = 2*pi*toolr*rev
570 vs = v*cos(alpha)/cos(phi-alpha)
580 vc = v*sin(phi)/cos(phi-alpha)
590 t = depthrate/rev/n
600 us = fs*vs/(v*toolwid*t)
610 uf = fc*vc/(v*toolwid*t)
620 u = us+uf
630 print "Fs (N)";a$;"Fc (N)";a$;"nc (N)";a$;"t (m)"
640 print fs,fc,nc,t
650 print "Resistance to deformation = ";u;"Pa  =  ";u/1000000;"MPa"
660 print "Friction 'strength' ";uf;"Pa"
670 print "Shear 'strength' ";us;"Pa"
```

B2 - The model of Sgubini and Buratti

Before introducing the model developed by SB89 (Sgubini and Buratti, 1989), it is worth recapping the underlying physics of heat conduction. In a stationary medium the temperature distribution around some point is related to the rate at which the temperature of a point changes by

$$\nabla^2 T(r,t) = \frac{\rho c}{\lambda} \frac{\partial T(r,t)}{\partial t} \qquad \text{Eq. B1}$$

For physically useful problems the boundary conditions in integrating the above equation are that the heat fluxes at infinity are zero. Particular solutions of such diffusion equations are commonplace in many introductory physics texts and the following equations are given to show the general form of the analytical solutions and to note that an important modification can be made that considers the heat source as moving at a velocity v. In one dimension

$$\frac{\partial T(r,t)}{\partial t} = \frac{\partial T(r,t)}{\partial x} \frac{\partial x}{\partial t} \qquad \text{Eq. B2}$$

and

$$\frac{\partial T(r,t)}{\partial t} = v \frac{\partial T(r,t)}{\partial x} \qquad \text{Eq. B3}$$

For the general solution to the case of the static heat source, a plausible solution with ϕ as an unknown function of (x,y,z), is usually employed

$$T(r,t) = T_0 + \exp\left[\frac{-vz\lambda}{\rho c}\right]\phi(x,y,z) \qquad \text{Eq. B4}$$

In three dimensions, substitution of such a solution into equation B1 gives an equation for the spatial distribution, which for cylindrical polar geometry, gives a solution of the form

$$\nabla^2\phi(r) = \left(\frac{v\lambda}{2\rho c}\right)\phi(r) \qquad \text{Eq. B5}$$

and this has solutions, when integrated, that appear like

$$T - T_0 = \frac{1}{R}\left(\frac{Q}{4}\exp\left[\frac{-v\lambda}{2\rho c}\right]\right)\exp\left[\frac{-vR\lambda}{2\rho c}\right] \qquad \text{Eq. B6}$$

Instead of directly solving the above functions, SB89 opted instead to approximate the more complicated problem of an extended moving source. With plenty of computing power to hand this may not be an appropriate route for a modern reassessment, but for completeness their model has been implemented as presented for their comet drilling scenarios. The following code implements the analytical model of SB89 and calculates the temperature rises expected along the axis of a generic coring tool, and at the position of the teeth on such an annular tool. The tool is represented by a static heat source and no localised heating of the material caused by the shearing action of the cutting edges is accounted.

```
10 rem This code evaluates the heating model derived, and
20 rem published by S. Sgubini and A. Buratti in:
30 rem ESA SP-302, 1989, p153-158.
40 rem
50 rem toolr is the tool outer radius (m)
60 rem xsecarea is the cross-sectional (annular) area of the tool (m^2)
70 rem toolwid is the width of each tooth (m)
80 rem depthrate is the vertical depth rate (m/s)
90 rem k is the workpiece thermal conductivity (W/m/K)
100 rem rho is the workpiece density (kg/m^3)
110 rem c is the specific heat capacity by mass (J/K/kg)
120 rem cv is the specific heat capacity (by unit volume) (J/K/m^3)
130 rem sigmar is the failure strength of the material (Pa)
140 rem a is a convenient variable = cv*toolr*depthrate/4k
150 rem amod is 'a' scaled for the disc heat-source
160 rem term1, term2 are temporary terms in equations
170 input "Depth speed (m/s) = ";depthrate
```

```
180 rem
190 rho = 930
200 c = 1232
210 k = 4.3
220 cv = c*rho
230 sigmar = 45000000
240 toolr = 0.0125
250 toolwid = 1.500000E-03
260 rem
270 xsecarea = pi*((toolr+toolwid/2)^2-(toolr-toolwid/2)^2)
275 r = sqr(xsecarea/pi)
280 q = sigmar*depthrate*xsecarea
290 a = cv*r*depthrate/(4*k)
300 rem
310 rem Now work out the maximum temperature on the axis of the
320 rem tool, at the workface.
330 rem
340 a2 = a*a
350 term1 = q/(4*pi*k*toolr)
360 term2 = exp(-2*a*(sqr(a2+1)-a))
370 term3 = sqr(a2+1)
380 tmaxax = term1*term2/term3
390 print "Tmax rise on axis = ",tmaxax,"  K"
400 rem
410 rem Now calculate the temperature rise at the tool bit
420 rem by modelling the annular heating source as a disc
430 rem having the same area as the annulus. Eq 18 in S+B.
440 rem
450 discrad = sqr(xsecarea/pi)
460 amod = cv*discrad*depthrate/(4*k)
470 term1 = q/(16*pi*k*amod*discrad)
480 term2 = 1-exp(-4*amod)
490 tmaxbit = term1*term2
500 print "Tmax rise at bit = ",tmaxbit," K"
```

In the model described one of the more important quantities that must be calculated is the amount of heat produced per unit time by the cutting process. This heating power, Q, is defined by SB89 as

$$\frac{Q}{u} = \sigma_R A \qquad \text{Eq. B7}$$

Where u is the rate of vertical progress through the material, and σ_R is the failure strength of the material. The quantity A must be related to the cross-sectional area of the cutting tool and for a hollow tool head it would be expected that this parameter is identical to the annular area of the tool face in contact with the material. Six of the graphs presented in SB89 list the parameter values used in generating the plotted data. The same tool geometry is used in all of these modelled cutting processes, having an outer radius of 8 cm and an inner radius of 6 cm. From the failure strength and value of Q/u listed in SB89 it is possible to calculate the value for A that this head corresponds to. For example, an ice coring run is described in which Q/u is

listed as 300 kJ m^{-1} for a material failure strength of 20 MPa. From equation B7 the value of A is then 0.015 m^2 which is the area of a solid disc having a radius of 7 cm. This suggests, erroneously, that the effort and heating experienced in driving an annular tool with a vanishing wall thickness through a material is identical to the work required to drill a cylindrical hole of the same radius. It is more reasonable to believe that the material directly beneath the annular area of the tool is the only part of the sample which is made to deform, so

$$\frac{Q}{u} = \sigma_R \pi \left[\left(R + \frac{w}{2} \right)^2 - \left(R - \frac{w}{2} \right)^2 \right] \qquad \text{Eq. B8}$$

This error may have arisen from confusion between the tool radius and the radius of the hypothesised disc having the same area as the cross-section of the tool. However, inspection of a further chart in SB89 shows that for a tool having "R = 0.07 m", that the peak temperature occurs at a distance of 7 cm from the axis. Clearly the simplest explanation is that the authors of SB89 used the actual tool radius instead of the effective radius[1] of the tool. This is borne out by calculation and the program listed on the preceding page uses the correct definition of the tool geometry.

A second code based on the program listed earlier was also developed. This second code calculated the flash-heating relationship of equation 44 and will not be listed because it differed by only a few lines from its parent code.

---

[1] Being the radius of a disc of equivalent area to the annulus of the tool head.

Appendix C - Snow compaction by overburden

In spherical polar co-ordinates, the internal pressure with a uniform body can be found by considering an elemental shell of density ρ and mass dm at a distance r from the body's centre.

$$dm = 4\pi r^2 \rho \, dr \qquad \text{Eq. C1}$$

The differential pressure, dP, experienced by this shell is determined by its weight in the local gravitational field, $g(r)$ which, in general is given by

$$g(r) = \frac{G}{r^2} \int_{r'=0}^{r'=r} 4\pi r^2 \rho(r') \, dr' \qquad \text{Eq. C2}$$

If the material has a constant density at all depths then $g(r)$ becomes

$$g(r) = \frac{4\pi}{3} G\rho r \qquad \text{Eq. C3}$$

In the above, G, is the constant of universal gravitation. Since the shell's weight is simply

$$dF = g(r) \, dm \qquad \text{Eq. C4}$$

this weight, exerted over the shell's area, can be written as a pressure and so

$$dP = \frac{dF}{4\pi r^2} \qquad \text{Eq. C5}$$

Substituting C1 and C3 into C4 gives

$$dP = \frac{4\pi r^2}{4\pi r^2} \rho \left(\frac{4\pi G \rho r}{3} \right) dr \qquad \text{Eq. C6}$$

$$P_{\text{int}} = \frac{4\pi G}{3} \rho^2 \int_{r'=0}^{r'=R} r \, dr' \qquad \text{Eq. C7}$$

which yields

$$P_{\text{int}} = \frac{2\pi G}{3} \rho^2 R^2 \qquad \text{Eq. C8}$$

If the material is allowed to deform and become denser under pressure then the problem is becomes much harder to solve. The extra complication arises because the density of a compressible material at some radius will be affected by the local compressive pressure, or overburden, which in turn depends on the amount of mass (and thus the density distribution) within the body. A common approach, as discussed by Cole (1984), is to differentiate the model for $g(r)$ with respect to r in order to remove the integral in equation C2 and so produce a second order differential equation. Instead, as a short exercise, a program was written to calculate numerically the density distribution in a self-gravitating and non-rotating sphere built from non-cohesive concentric shells. The only modelled mechanism for compaction is that of overburden, and other processes such as creep and pore migration by vapour transport are ignored. These last two processes are strongly driven by the temperature of the body through the dependence of ice's vapour pressure with temperature and the empirically measured faster flow of water ice under stress at raised temperatures. By modelling the change in porosity from these two processes, Smoluchowski and McWilliam (1984) show that for cold ice bodies (~ 100 K) these processes are too slow to be of importance even over cosmic time scales.

Before the code's results are introduced it is necessary to know how the density of a material will react to various compressive stresses. A naïve model of a spherical body is shown below, in which an elemental cube of the porous material is examined. If the compressive failure stress of the material varies with the cross-sectional area of the material in the unit cube, then the limiting compressive strength will vary with the relative density ρ_{rel} (compared to the fully compacted density ρ) to the two-thirds power.

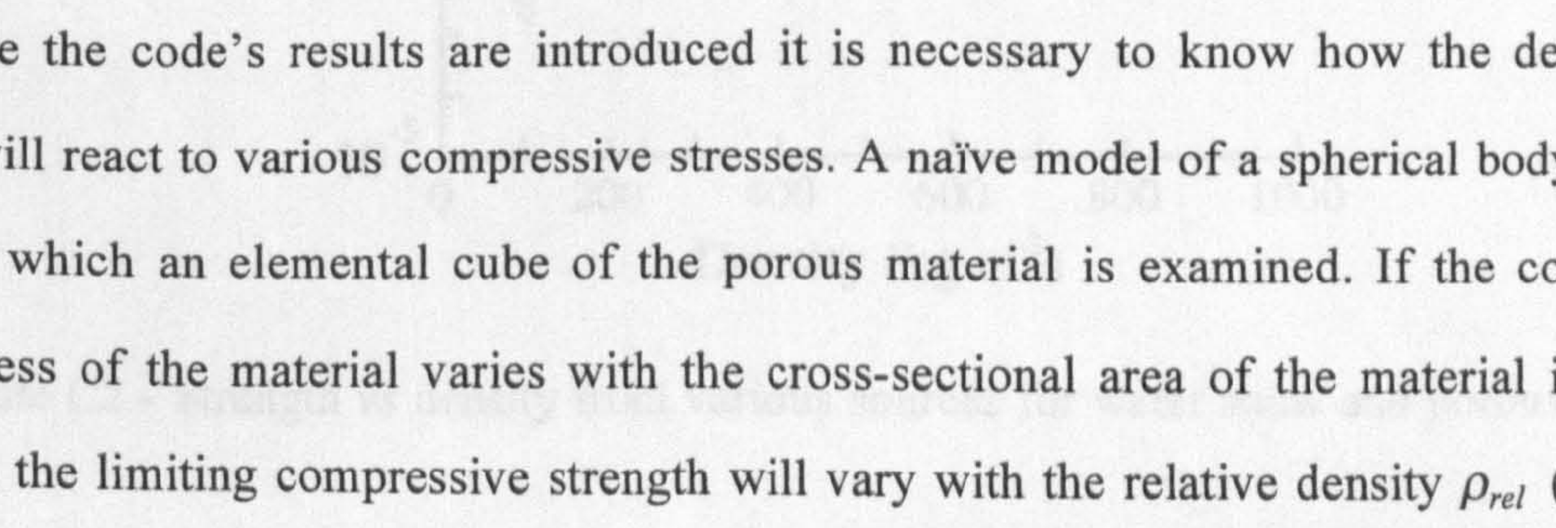

Figure C1 - Arrangement and micro-structure assumed for the compressive model.

This simple model of how a porous material's strength changes with density is not borne out from experimental data and other works, such as the comet material analogue experiments of Seiferlin *et al.* (1995), suggest a non-linear relationship between compressive strength and density. In the following chart, taken from the review paper of Shapiro *et al.* (1997), a number of data sources are plotted which show that the compressive strength of porous ice and snow varies more rapidly with density than the 2/3 power relationship postulated above.

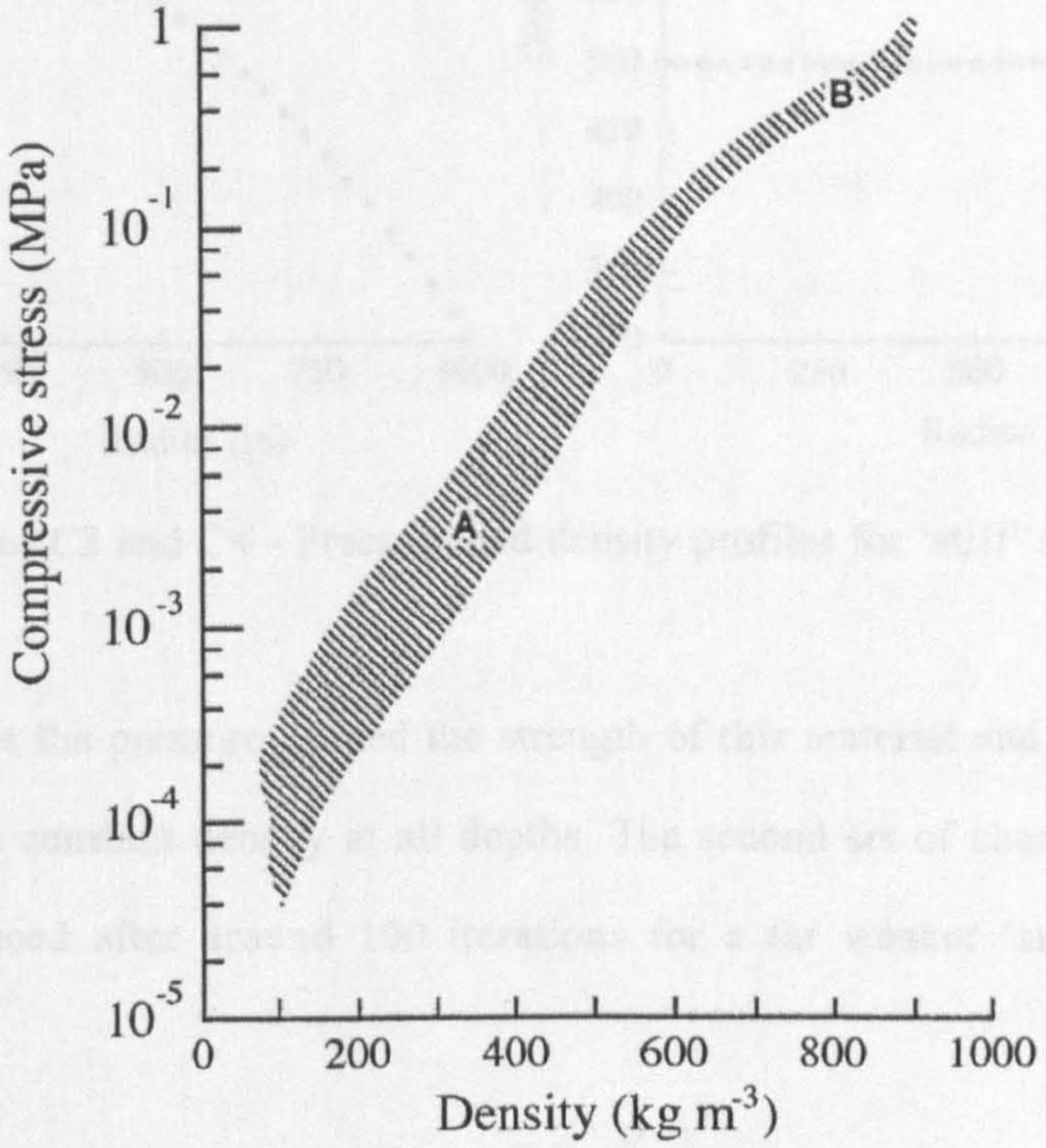

Figure C2 - Strength *vs* density from various sources for water snow and porous ice.

The region marked 'A' represents data taken from the natural densification of snow, and 'B' represents data for porous ice and dense firn taken from terrestrial polar studies. A crude fit through both of these regions suggests that the limiting compressive strength for water snow of density ρ has the form;

$$\sigma_{comp} = 65\left(\frac{\rho}{100}\right)^3 \qquad \text{Eq. C9}$$

For the sake of this exercise it is assumed that snow is a fair mechanical analogue for the material of a cometary nucleus. By implementing failure laws similar to the above equation into the numerical model it is possible to show the degree of compaction that might occur in a self-gravitating spherical body.

The following Figures show the pressure and density distribution within a 1 km radius body formed from a material that has an initial density of 500 kg m^{-3}.

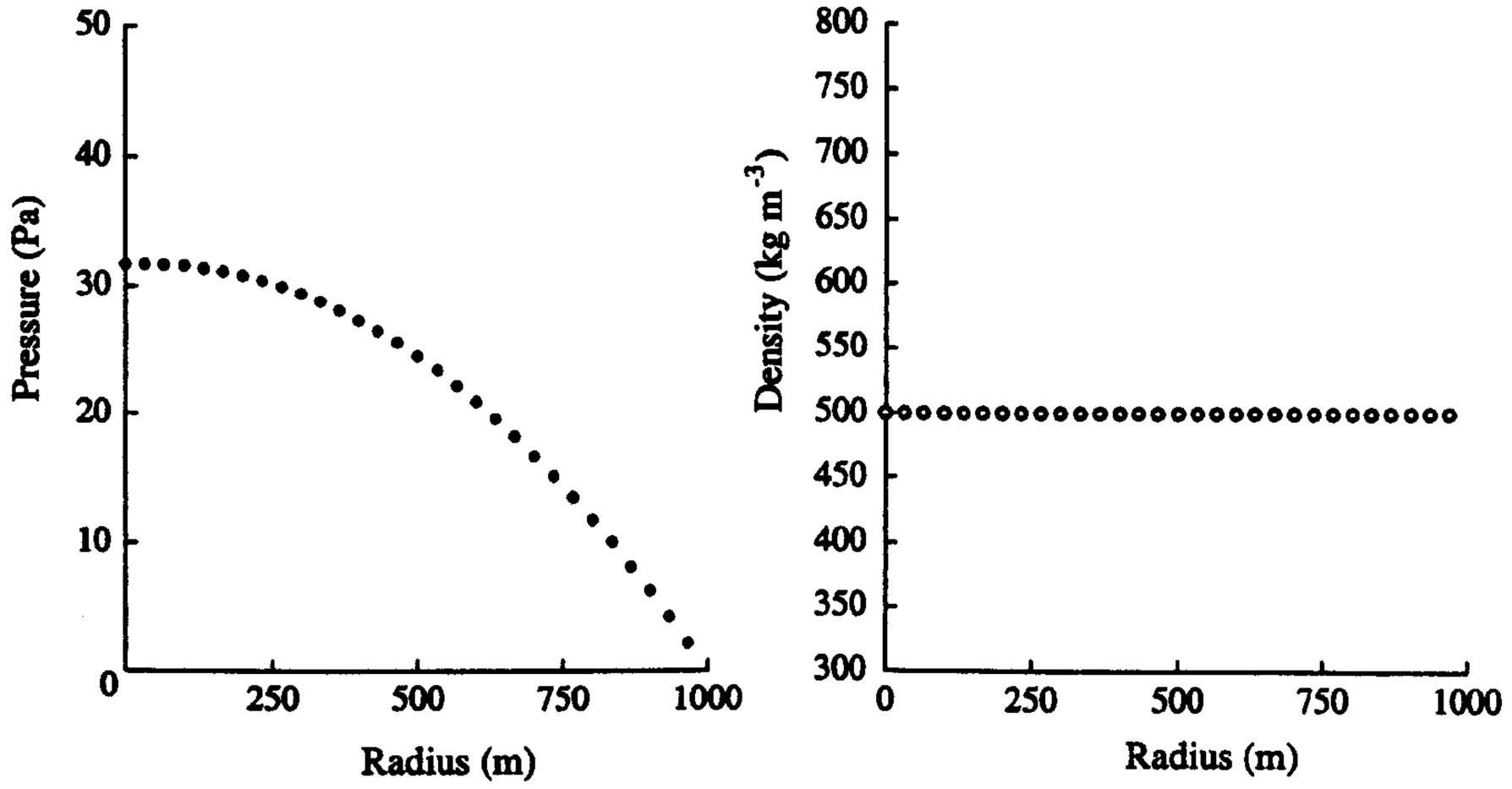

Figures C3 and C4 - Pressure and density profiles for 'stiff' snow.

At no point does the pressure exceed the strength of this material and so the code delivers a solution that has a constant density at all depths. The second set of charts show the solution that the code produced after around 100 iterations for a far weaker 'snow' which had the failure law

$$\sigma_{comp} = 0.1\left(\frac{\rho}{100}\right)^3 \qquad \text{Eq. C10}$$

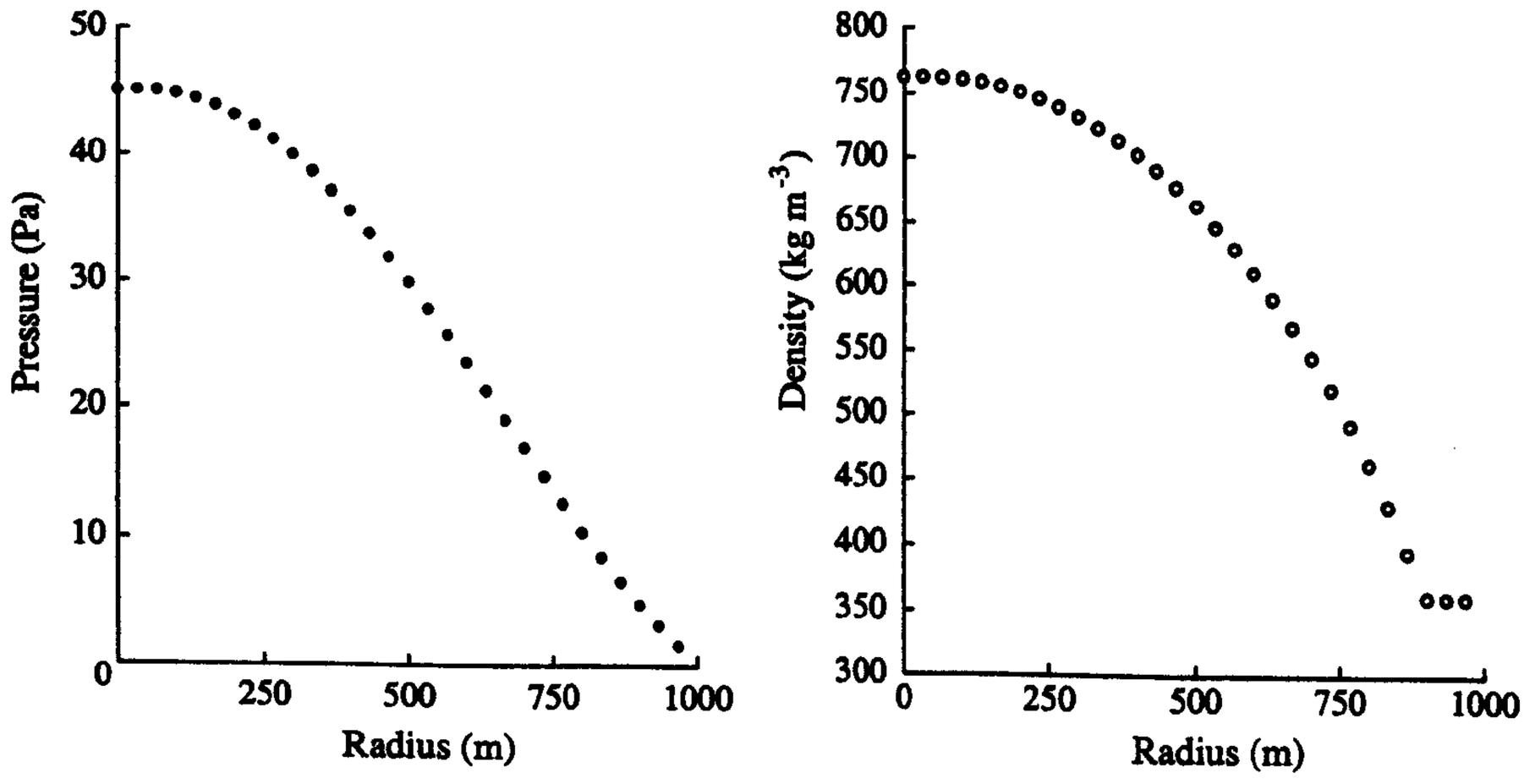

Figures C5 and C6 - Pressure and density profiles for 'soft' snow.

The second material fails through compression when the local differential stress exceeds its strength and the code responds to this by increasing the density of the failed spherical shell until it can support the pressure difference across it. Mass is conserved by lowering the density of those shells which have not yet failed through compression. It should be noted that the failure criteria for this material is problematically weak, as it is difficult to imagine a material with a density of 500 kg m^{-3} which nevertheless fails under a compressive stress of 13 Pa. Despite the difficulty of imagining such a fluffy material, this failure strength does barely lie within the limit of those ascribed to cometary nuclei. The 50 % higher internal density seen for this unreasonably weak snow probably represents the maximum degree by which a body of this size can be compacted. Stronger materials will display a smaller degree of internal compaction and the uniform density model shown in equation C8 will then be applicable. In conclusion, a body two kilometres in diameter made from porous ice or snow has an internal pressure at least four orders of magnitudes too small for the compressive failure strength of water ice to be altered, even if self-compaction through gravity is allowed for. The data from the tests by Durham *et al.* (1983) on unconfined water ice are therefore appropriate for this work.

The listing for the code to calculate the self-compaction of a spherical mass is shown on the following two pages.

```
10 rem This code calculates the pressure distribution inside a sphere
20 rem made from a material that is allowed to compact under stress.
30 rem array m holds the shell masses, m(0) is innermost shell/sphere (kg)
40 rem array r holds the shell radii, r(0) is the centre (m)
50 rem array pl holds the local total pressure exerted on each shell (Pa)
60 rem array plim holds the max. stress sustainable by each shell (Pa)
70 rem array rho holds the shell densities (kg m^-3)
80 rem array drho holds the next iteration change in shell density (kg m^-3)
90 rem array massinside holds the mass enclosed in the ith shell (kg)
100 rem dp is the differential pressure on one shell (Pa)
110 rem rmax is the outer radius of the body (m)
120 rem g is the universal constant of gravitation (N kg^-2 m^2)
130 rem frac is a scalar that determines how quickly a solution is found
140 rem rholim is the density of the fully compacted material (kg m^-3)
150 rem num is the number of shells present (int)
160 rem Reference used for ice strength is:
170 rem Shapiro LH, JB Johnson, M Sturm, CRREL report 97-3, 1997.
180 mass = 2.094000E+12 : g = 6.670000E-11
190 frac = 1 : rholim = 1000
200 rmax = 1000
210 dim pl(100) : dim plim(100)
220 dim m(100) : dim w(100)
230 dim r(100) : dim massinside(100)
240 dim rho(100) : dim drho(100)
250 num = 30
260 r(0) = 0
270 rem
280 rem The radius array starts at the centre and marks shell boundaries.
290 rem
300 for i = 0 to num
310   r(i) = i*rmax/num
320   rho(i) = 500
330 next i
340 rho(num) = 0
350 dr = rmax/num
360 rem
370 rem Work out the mass of each shell and keep a running
380 rem total of the mass at smaller radii than the ith shell.
390 rem
400 for i = 0 to num-1
410   r2 = ((r(i+1)+r(i))/2)^2
420   m(i) = 4*pi*r2*dr*rho(i)
430   for j = 1 to i
440     massinside(i) = massinside(i)+m(j-1)
450   next j
460 next i
470 rem
480 rem Now find the mass outside this shell and calculate the
490 rem pressure load from these outer shells on the ith shell.
500 rem
510 for i = num-1 to 0 step -1
520   pl(i) = 0
530   r2 = ((r(i+1)+r(i))/2)^2
540   dp = rho(i)*g*massinside(i)*dr/r2
550   pl(i) = pl(i+1)+dp
560 next i
570 rem
580 rem With the weights known for each concentric shell, decide
590 rem whether the pressure on the ith shell exceeds its strength
600 rem at this porosity. A strength law like 65(rho(in kg/m3)/100)^3
610 rem is appropriate for porous ice and snow (Shapiro, 1997)
620 rem
630 for l = 0 to num-1
640   plim(l) = 65*(rho(l)/100)^3
650   drho(l) = 0
660   if pl(l) > plim(l) then drho(l) = frac*abs((pl(l)-plim(l)))
670   rho(l) = rho(l)+drho(l)
```

```
680   if rho(1) > rholim then rho(1) = rholim
690 next 1
700 rho(0) = rho(1)
710 rem
720 rem Having scaled the excess  shell densities, renormalize
730 rem the whole sphere. First find the new mass of the sphere.
740 rem
750 newmass = 0
760 for i = 0 to num-1
770   r2 = ((r(i+1)+r(i))/2)^2
780   newmass = newmass+(4*pi*r2*dr*rho(i))
790 next i
800 input "Print (1), stop(2), or file(3)";ask
810 if ask = 1 then
820   print "r(i)   pl(i)    rho(i)    drho(i)    lim"
830   for i = 0 to num-1
840     print r(i),pl(i),rho(i),drho(i);plim(i)
850   next i
860 endif
870 if ask = 3 then
880   print #1,"Radius Pressure  Density  Delta_density  Strength"
890   open "compact.dat" for output as #1
900   for i = 0 to num-1
910     print #1,r(i),pl(i),rho(i),drho(i);plim(i)
920   next i : close #1
930 endif
940 if ask = 2 then stop
950 endif
960 rem
970 rem With the new mass for the sphere, rescale all the densities
980 rem to fit the originally specified mass.
990 rem
1000 for i = 0 to num-1
1010   rho(i) = rho(i)*mass/newmass
1020   massinside(i) = 0
1030 next i
1040 goto 400
```

Appendix D - Heat conduction in a periodically heated mass

Fourier's heat conduction equation relates the rate at which heat flows through an area to the temperature differential across the medium. If an infinite half-space is considered, with a plane boundary that has a temperature T(z=0,t) a thermal conductivity λ, specific heat capacity c, and density ρ, then across some patch of unit area the rate at which heat flows out of that area can be related to the vertical thermal gradient.

$$\nabla^2 T(z,t) = \frac{\rho c}{\lambda} \frac{\partial T(z,t)}{\partial t} \qquad \text{Eq. D1}$$

Now let the temperature at the surface of this infinite plane vary with time in a periodic manner.

$$T(z=0,t) = T_0 + A\sin(\omega t) \qquad \text{Eq. D2}$$

With this boundary condition solutions of equation D1 can now be written as a compound function of an exponential decay with depth and a second function that is also periodic in t, but which differs from $T(z=0,t)$ by some phase angle which in turn varies with depth.

$$T(z=L,t) = T_0 + A\exp\left[-\frac{z}{d}\right]\sin\left(\omega t - \frac{z}{d}\right) \qquad \text{Eq. D3}$$

The scaling depth d is found to be

$$d = \sqrt{\frac{\kappa t}{\pi}} \qquad \text{Eq. D4}$$

Below this depth the temperature is never greater than T_0+eA nor lower than T_0-eA, and d is therefore sometimes referred to as the thermal 'skin', or penetration, depth. The above steps are not intended to be a rigorous derivation and many undergraduate physics texts discuss these scenarios in detail.

Appendix E - Heating of a rotating body

If the Sun is considered to have a radius r_{sun} and a black-body temperature T_{sun} then a body at some distance R from it receives a radiation flux E (W m^{-2}) of

$$E = \frac{4\pi r_{sun}^2 \sigma_{SB} T_{sun}^4}{4\pi R^2} \qquad \text{Eq. E1}$$

This heat, if intercepted by a rapidly spinning object, is re-radiated over the object's surface which reaches an equilibrium temperature of T_{body}. If the body has an albedo of a then for the heat radiated by the body to balance the heat absorbed over its sunlit half, the body's temperature must be

$$(1-a)\pi r^2 E = 4\pi r^2 \sigma_{SB} T_{eq}^4 \qquad \text{Eq. E2}$$

and so

$$T_{eq} = (1-a)^{\frac{1}{4}} \left(\frac{r_{sun}}{2E} \right)^{\frac{1}{2}} T_{sun} \qquad \text{Eq. E3}$$

The assumption that the object's surface temperature is uniform can be examined in a similar manner to that of Appendix D. The radiant heating of a flat plate by a periodically varying heat flux is physically similar to heating a flat patch on a rotating sphere by a distant radiant source. Thus, for a body spinning with a period t, having a thermal diffusivity κ, the depth, d, at which the temperature differs by a factor of the natural Euler number e from the surface temperature is

$$d = \sqrt{\frac{\kappa t}{\pi}} \qquad \text{Eq. E4}$$

Some experimental comet analogues made in the laboratory have thermal diffusivity values of ~10^{-8} m^2 s^{-1}, (Benkhoff and Spohn, 1991). Adding organic materials such as paraffin (at up to 1:1 mixing ratios of the dust content) raises the thermal diffusivity of the desiccated residua to around 2 x 10^{-7} m^2 s^{-1} (Kömle *et al.* 1996). With a rotation period of 50 hours for a notional comet nucleus, the diurnal heat wave may therefore not penetrate beyond half a metre of such material. In reality a minor body such as a comet nucleus may rotate in such a way that topographic undulations as seen on comet 19P/Borrelly (Soderblum *et al.*, 2001) could produce striking temperature variations and the constant-temperature assumption would not hold.

Appendix F - Photographs of the vacuum coring system

(a)

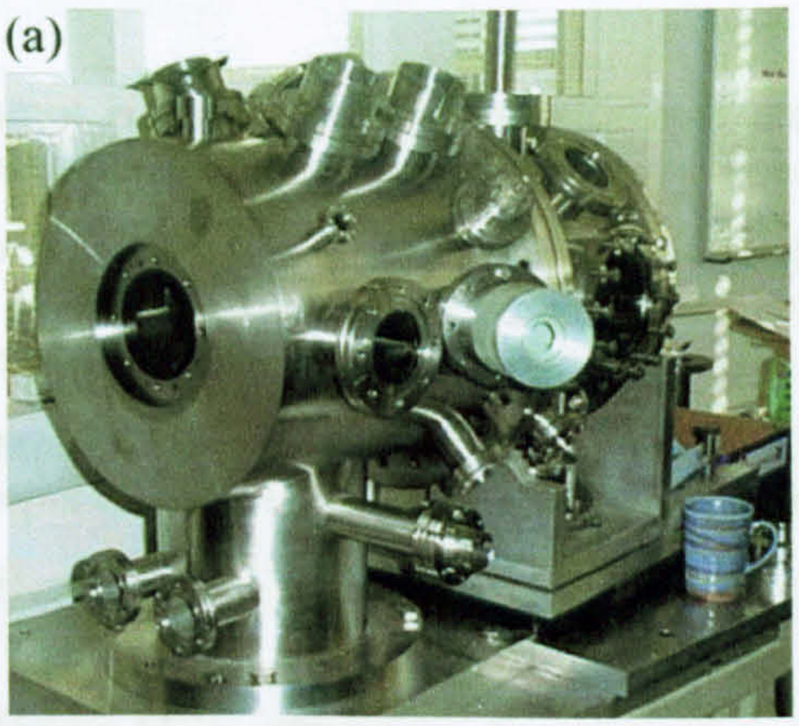

(b)

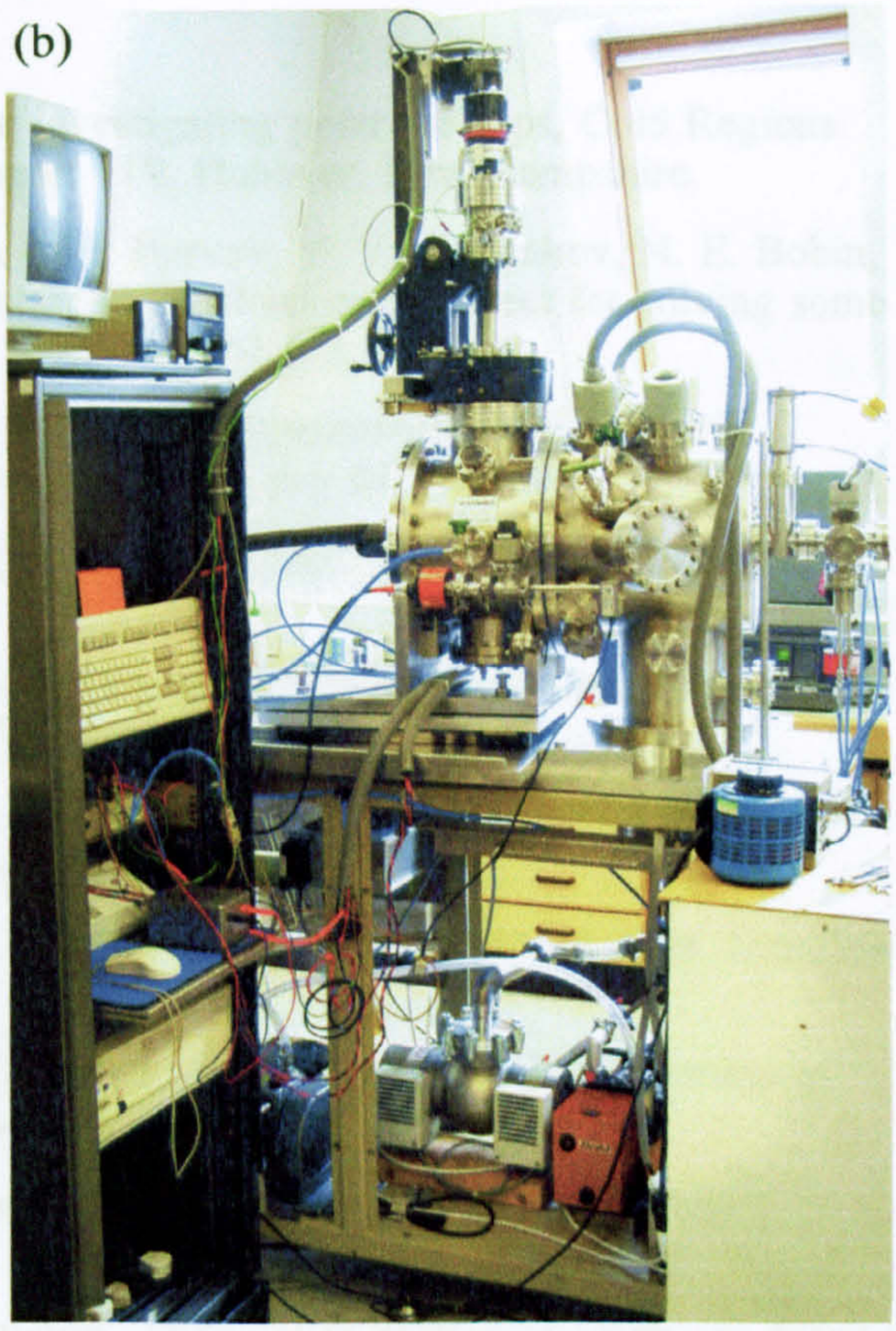

Figure F1a - (top)
This picture, taken in October 1998, shows all of the initial parts of the vacuum system.

Figure F1b - (right)
In this photograph the chamber and most of its support equipment are shown in their final working arrangement.

Figure F2 - (below)

These images of the chamber interior show the relationship between the tool, sample holder, and associated components such as the wiring and cryogen pipework.

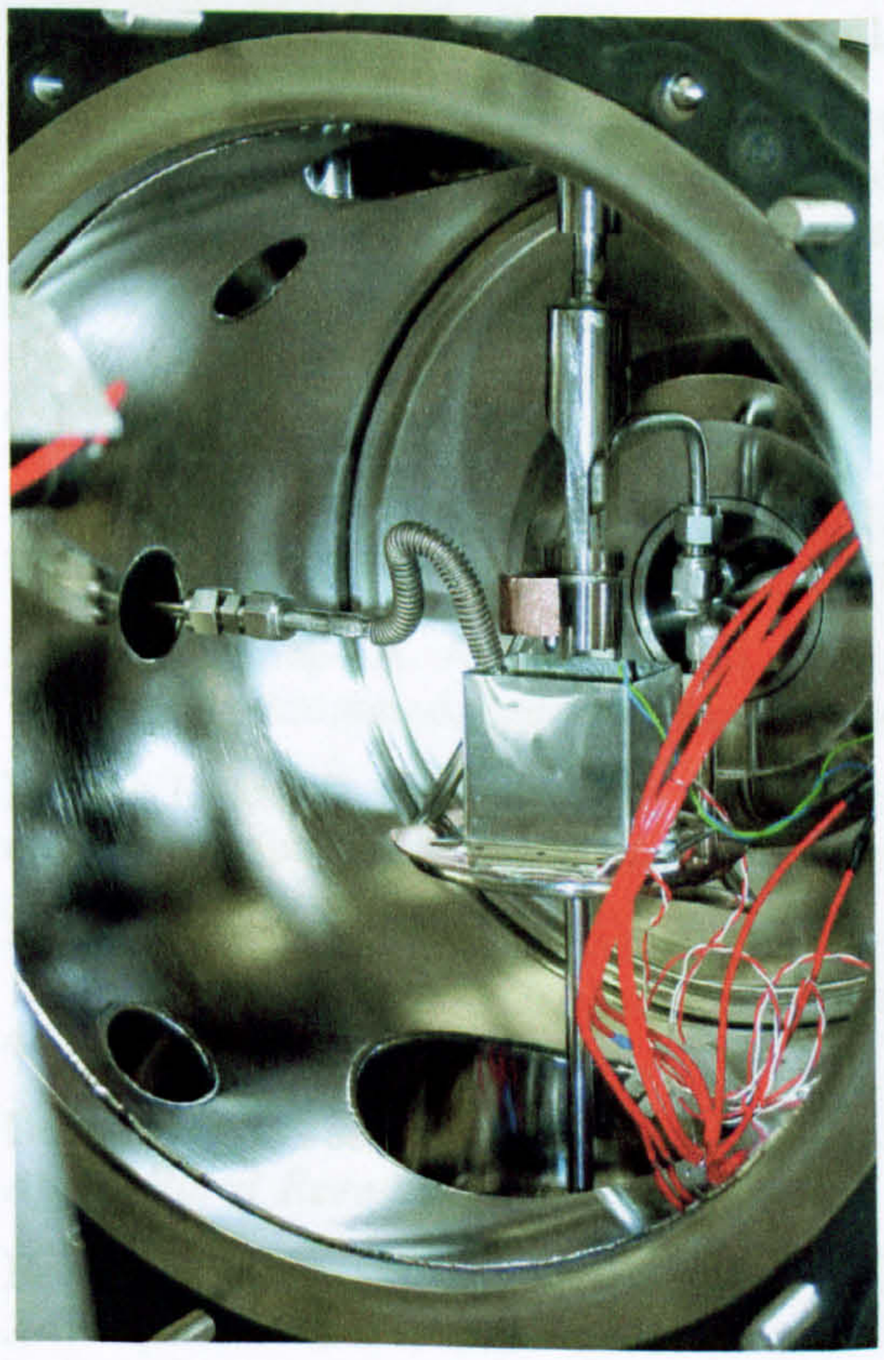

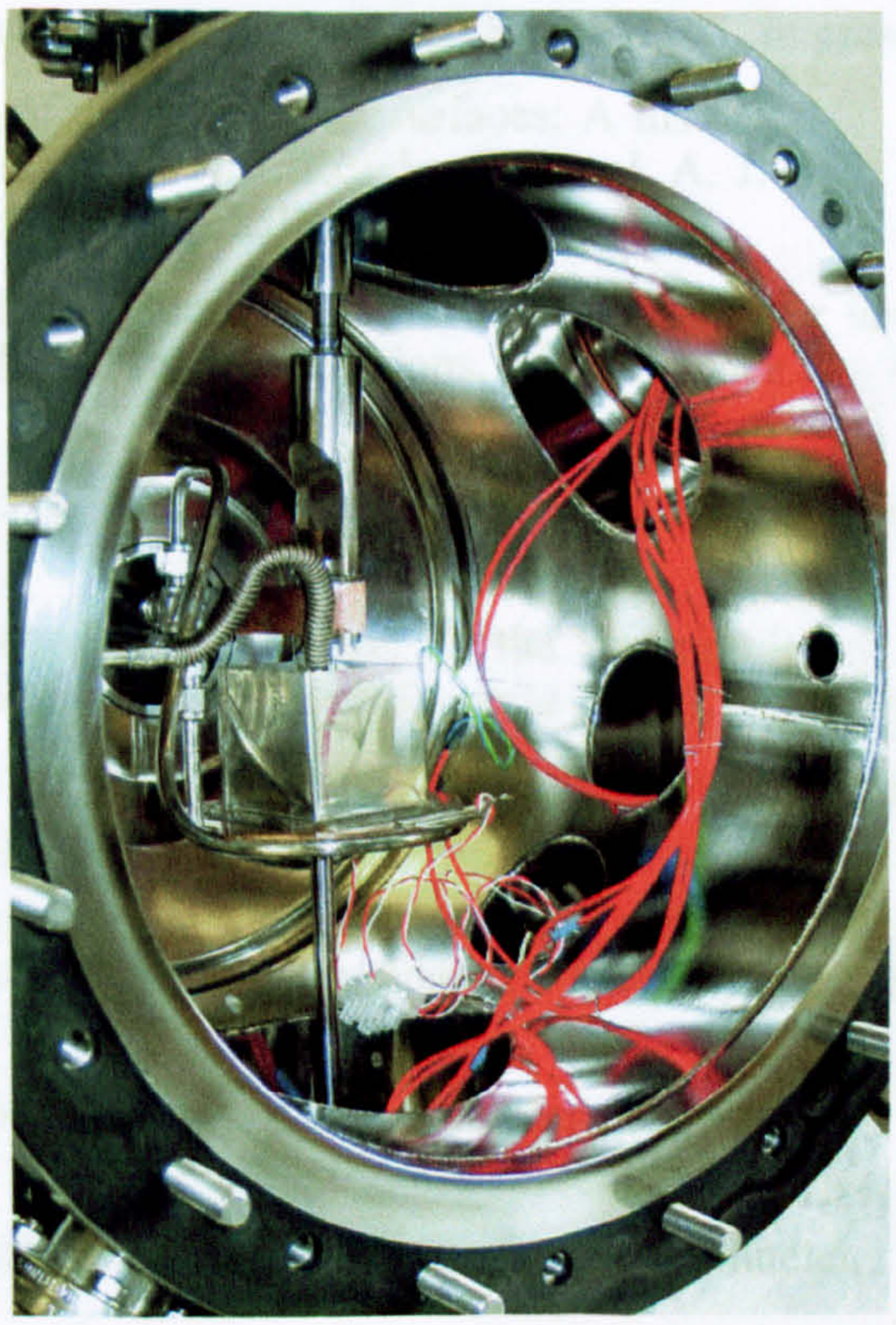

References

Aamot H. W. C., 1967. The Philberth probe for investigating polar ice caps, Cold Regions Research & Engineering Laboratory, special report 119, Hanover, New Hampshire.

Abyzov S., I. N. Mitskevitch, M. N. Poglazova, N. I. Barkov, V. Ya. Lipenkov, N. E. Bobin, B. B. Kudryashov, V. M. Pashkevich, 1999. Antarctic ice sheet as an object for solving some methodological problems of exobiology, *Adv. Space Res.* **23** (2), 371-376.

Agapiou J. S. and D. A. Stephenson, 1994. Analytical and experimental studies of drill temperatures, Trans. ASME Journal of Engineering for Industry **116**, 54-60

A'Hearn M. F., 1988. Observations of cometary nuclei, *Ann. Rev. Earth Planet Sci.* **16**, 273-293.

A'Hearn M. F. and M. C. Festou. 1990. The neutral coma, in "Physics and Chemistry of Comets", ed. W. F. Huebner, Springer-Verlag [Berlin], pp69-112.

Altwegg K., H. Balsiger, and J. Geiss, 1999. Composition of the volatile material in Halley's coma from in-situ measurements, *Space Sci. Rev.* **99**, 3-18.

Anders E. and N. Grevesse, 1989. Abundances of the elements: meteoritic and solar, *Geochim. Cosmochim. Acta* **53**, 197-214.

Anderson W. W., T. J. Ahrens, A. Gibson, R. Scott, and K. Suzuki, 1996. Emplacement of penetrators into planetary surfaces, *J. Geophys. Res.* **101** (E9), 21137-21149.

Angrist S. W. and L. G. Hepler, 1973. "Order and Chaos - laws of energy and entropy", Penguin Books Ltd, [Harmondsworth], pp53.

Arthern R. J., D. P. Winebrenner, E. D. Waddington, 2000. Densification of water ice deposits on the residual north polar cap of Mars, *Icarus* **144**, 367-381.

Asphaug E. and W. Benz, 1994. Density of comet Shoemaker-Levy 9 deduced by modelling breakup of the parent 'rubble pile', *Nature* **370**, 120-124.

Badash L., 1968. Rutherford, Boltwood, and the age of the Earth: the origin of radioactive dating techniques, *Proc. of the Am. Phil. Soc.* **112**, 157-69.

Ball A. J. and N. I. Kömle. Forces on the lander at the nucleus surface, ESA-SP 1165, in press.

Ball A. J. and R. D. Lorenz, 2001. Penetrometry of extraterrestrial surfaces: A historical overview, in Proc. of Penetrometry Workshop (Graz), ed. N. I. Kömle, G. Kargl, A. J. Ball, and R. D. Lorenz, Österreichischen Akademie der Wissenschaften [Vienna], pp3-23.

Ball A. J., C. J. Solomon, and J. C. Zarnecki, 1996. A Compton backscatter densitometer for the RoLand comet lander - design concept and Monte Carlo simulations, *Planet. Space Sci.* **44** (3), 283-293.

Bar-Nun A., J. Dror, E. Kochavi, and D. Laufer, 1987. Amorphous water ice and its ability to trap gases, *Phys. Rev. B* **35** (5), 2427-2435.

Barmin I. V. and A. A. Shevchenko, 1983. Soil-scooping mechanism for the Venera 13 and Venera 14 unmanned interplanetary spacecraft, *Kosmicheskie Issledovaniia* **21** (2), 171-175.

Barone L. and S. Faugno, 1996. Penetration tests for measurement of soil strength: assessment of the contribution of shaft friction, *J. agric. Engng Res.* **64**, 103-108.

Barucci M. A., A. Doressoundiram, M. Fulchignoni, M. Florczak, M. Lazzarin, and Angeli C., 1998. Compositional type characterization of Rosetta asteroid candidates, *Planet. Space Sci.* **46**, 75-82.

Becker H., 1998. From Earth to Mars - carbon dioxide crystals help interplanetary studies, *Agricultural Research*, October, 32-33.

Belton M. J. S. and M. F. A'Hearn, 1999. Deep sub-surface exploration of cometary nuclei, *Adv. Space Res.* **24**, 1167-1173.

Benkhoff J. and T. Spohn, 1991. Thermal histories of the KOSI samples, *Geophys. Res. Lett.* **18**, 261-264.

Black G. J., D. B. Campbell, P. D. Nicholson, 2001. Icy Galilean satellites: modelling radar reflectivities as a coherent backscatter effect, *Icarus* **151**, 167-180.

Blake G. A., C. Qi, M. R. Hugerheijde, M. A. Gurwell, and D. O. Muhleman, 1999. Sublimation from icy jets as a probe of the interstellar volatile content of comets, *Nature* **398**, 213-216.

Boss A. P., 1994. Comet Shoemaker-Levy 9: An upper bound on its mean density, Lunar and Planetary Science Conference XXV, 147-148.

Boucher D. S. and E. Dupuis, 2000. Core drilling for extra-terrestrial mining, Space Resources Roundtable II conference held at the Colorado School of Mines, abstract #7008.

Boynton W. V. and R. P. Reinert, 1995. The cryo-penetrator: an approach to exploration of icy bodies in the solar system, *Acta Astronautica* **35**, 59-68.

Brin G. D. and D. A. Mendis, 1979. Dust release and mantle development in comets, *Ap. J.* **229**, 402-408.

Brown G. I., 1998. "The Big Bang – a history of explosives", Sutton publishing [Stroud], pp240.

Brown G. N. Jr. and W. T. Ziegler, 1980. Vapor pressure and heats of vaporization and sublimation of liquids and solids of interest in cryogenics below 1-atm pressure, *Advances in Cryogenic Engineering* **25**, 662-670.

Brown M. E. and W. M. Calvin, 2000. Evidence for crystalline water and ammonia ices on Pluto's satellite Charon, *Science* **287**, 107-109.

Buratti B. J., L. A. Soderblom , D. T. Britt, M. D. Hicks, N. Thomas, J. Oberst, R. H. Brown, R. M. Nelson, J. A. Mosher, J. K. Hillier, 2001. Photometry and Surface Physical Properties of Comet 19P/Borrelly, 33rd DPS meeting abstract #28.04.

Burchell M. J., W. Brooke-Thomas, J. Leliwa-Kopystynski, and J. C. Zarnecki, 1998. Hypervelocity impact experiments on solid CO_2 targets, *Icarus* **131**, 210-222.

Calvin W. M., R. N. Clark, R. H. Brown, and J. R. Spencer, 1995. Spectra of the icy Galilean satellites from 0.2 to 5 μm: a compilation, new observations, and a recent summary. *J. Geophys. Res.* **100**, 19041-19048.

Camaschella G. L., 1998. Rosetta project SD2 sub-system specification, Tecnospazio S.p.A., Doc no. SHARK-AB-TS-003 rev. A.

Campbell D. B., J. F. Chandler, S. J. Ostro, G. H. Pettengill, and I. I. Shapiro, 1978. Galilean satellites: 1976 radar results, *Icarus* **34**, 254-267.

Capria M. T., F. Capaccioni, A. Coradini, M. C. De Sanctis, S. Espinasse, C. Federico, R. Orosei, and M. Salomone, A P/Wirtanen evolution model, *Planet. Space Sci.* **44** (9), 987-1000.

Carr M. H., M. J. S. Belton, C. R. Chapman, M. E. Davies, P. Geissler, R. Greenberg, A. S. McEwen, B. R. Tufts, R. Greeley, R. Sullivan, J. W. Head, R. T. Pappalardo, K. P. Klaasen, T. V. Johnson, J. Kaufman, D. Senske, J. Moore, G. Neukum, G. Schubert, J. A. Burns, P. Thomas, J. Veverka, 1998. Evidence for a subsurface ocean on Europa, *Nature* **391**, 363-365.

Carrier D. W. III, G. R. Olhoeft, and W. Mendell, 1995. in "Lunar Sourcebook: A user's guide to the Moon", ed. G. H. Heiken, D. T. Vaniman, and B. M. French, Cambridge University Press [New York], pp475-594.

Cartwright I. M., A. Fitzsimmons, I. P. Williams, S. N. Kemp, 1997. CCD photometry of comet 46P/Wirtanen, *Planet. Space Sci.* **45** (7), 821-826.

Chao B. T., H. L. Li, and K. J. Trigger, 1961. An experimental investigation of temperature distribution at tool-flank surface, Trans. ASME Journal of Engineering for Industry, November issue, 496-504.

Chapman C. R. and D. Morrison, 1994. Impacts on the Earth by asteroids and comets: assessing the hazard, *Nature* **367**, 33-40.

Chappell D. T., 2000. High-power Mars subsurface radar, in "Case for Mars VI", vol. 98 the AAS Science and Technology Series. ed. K. R. McMillen. Univelt [San Diego], pp279-301.

Cherkasov I. I., A. L. Kemurdzhian, L. N. Mikhaylov, V. V. Mikheyev, A. A. Morozov, A. A. Musatov, I. A. Savenko, M. I., Smorodinov, and V.V. Shvarov, 1967. Determination of density and mechanical strength of lunar surface layer at the landing site of the automatic station *Luna 13*. NASA ST-LPS-LSL-10640, pp3.

Chodas P. W. and D. K. Yeomans, 1996. The orbital motion and impact circumstances of comet Shoemaker-Levy 9, in "The collision of comet Shoemaker-Levy 9 and Jupiter", ed. K. S. Noll, H. A. Weaver, P. D. Feldman, Cambridge University Press, pp31-54.

Chyba C. F. and C. B. Phillips, 2001. Possible ecosystems and the search for life on Europa, *Proc. Natl. Acad. Sci. USA* **98** (3), 801-804.

Chyba C. F., P. J. Thomas, L. Brookshaw, and C. Sagan, 1990. Cometary delivery of organic molecules to the early Earth, *Science* **249**, 366-373.

Clark B. C., R. J. Amundsen, and D. P. Blanchard, 1986. Sampling the cometary nucleus, proc. "The Comet Nucleus Sample Return Mission". held Canterbury, 15-17 July 1986; printed as ESA SP-249 [Noordwijk], 211-216.

Clauser C. and E. Huenges, 1995. Thermal conductivity of rocks and minerals, in "Rock physics and phase relations: a handbook of physical constants", ed. T.J. Ahrens, American Geophysical Union [Washington], pp118-122.

Clifford S. M., D. Crisp, D. A. Fisher, K. E. Herkenhoff, S. E. Smrekar, P. C. Thomas, D. D. Wynn-Williams, R. W. Zurek, J. R. Barnes, B. G. Bills, E. W. Blake, W. M. Calvin, J. M. Cameron, M. H. Carr , P. R. Christensen , B. C. Clark , G. D. Clow, J. A. Cutts, D. Dahl-Jensen, W. B. Durham, F. P. Fanale, J. D., Farmer, F. Forget, K. Gotto-Azuma, R. Grard, R. M. Haberle, W. Harrison, R. Harvey, A.D. Howard, A. P. Ingersoll, P.B. James, J.S. Kargel, H. H. Kieffer, J. Larson, K. Lepper, M.C. Malin, D. J. McCleese, B. Murray, J. F. Nye, D. A. Paige, S. R. Platt, J. J. Plaut, N. Reeh, J. W. Rice, Jr., D. E. Smith, C. R. Stoker, K. L. Tanaka, E. Mosley-Thompson, T. Thorsteinsson, S. E. Wood, A. Zent, M. T. Zuber, and H. Jay Zwally, 2000. The state and future of Mars polar science & exploration, *Icarus* **144**, 210-242.

Clube S. V. M. and W. M. Napier, 1984. The microstructure of terrestrial catastrophism, *Mon. Not. R. astr. Soc* **211**, 953-968.

Clube S. V. M. and W. M. Napier, 1987. The cometary breakup hypothesis re-examined: a reply, *Mon. Not. R. astr. Soc.* **225**, 55-58.

Cohn S. N. and T. J. Ahrens, 1981. Dynamic tensile strength of lunar rock types, *J. Geophys. Res.* **86**, 1794-1802.

Cole G. H. A., 1984. "Physics of planetary interiors", Adam Hilger Ltd. [Bristol], pp58,

Colom P., E. Gérard, J. Crovisier, D. Bockelée-Morvan, N. Biver, H. Rauer, 1997. Observations of the OH radical in comet C/1995 O1 (Hale-Bopp) with the Nançay radio telescope, *Earth, Moon and Planets* **78**, 37-43.

Costes N. C., G. T. Cohron, and D. C. Moss, 1971. Cone penetration resistance test - an approach to evaluating in-place strength and packing characteristics of lunar soils, Proc. 2nd Lunar Science Conf., 1973-1987.

Croft S. K., 1987. Mechanical and thermal properties of planetologically important ices, NASA TM-89810, 15-17.

Crovisier J. and D. Bockelé-Morvan, 1999. Remote observations of the compositions of cometary volatiles, *Space Science Reviews* **90**, 19-32.

Currier J. H. and E. M. Schulson, 1982. The tensile strength of ice as a function of grain size, *Acta mettal.* **30**, 1511-1514.

Cutts J. A. and B. H. Lewis, 1982. Models of climatic cycles record in Martian polar layered deposits, *Icarus* **50**, 216-244.

Delchar T. A., 1993. "Vacuum physics and techniques", Chapman and Hall [London], pp33.

Delsemme A. H. and D. C. Miller, 1971. Physico-chemical phenomena in comets - III The continuum of comet Burnham (1960 II), *Planet. Space Sci.* **19**, 1229-1257.

Delsemme A. H., 1995. Cometary origin of the biosphere: a progress report, *Adv. Space Res.* **15** (3), (3)49-(3)57.

Divine N., 1993. Five populations of interplanetary meteoroids, *J. Geophys. Res.* **98** (E9), 17029-17048.

Di Pippo S., R. Mugnuolo, P. Vielmo, and W. Prendin, 1999. The exploitation of Europa ice and water basins: an assessment on required technological developments, on system design approaches and on relevant expected benefits to space and Earth based activities, *Planet. Space Sci.* **47**, 921-933.

Ditteon R. and H. H. Kieffer, 1979. Optical properties of solid CO_2: application to Mars, *J. Geophys. Res.* **84**, B14, 8294-8300.

Doressoundiram A., P. R. Weissman , M. Fulchignoni , M. A. Barucci , A. Le Bras , F. Colas , J. Lecacheux , M. Birlan , M. Lazzarin , S. Fornasier , E. Dotto , C. Barbieri , M.V. Sykes , S. Larson, and C. Hergenrother, 1999. 4979 Otawara: flyby target of the Rosetta mission, *Astron. Astrophys.* **352** (2), 697-702.

Duncan M., T. Quinn, and S. Tremaine, 1988. The origin of short-period comets, *Ap. J.* **328**, L69-L73.

Dunn B. D., 1997. "Metallurgical assessment of spacecraft parts, materials and processes", John Wiley and Sons in association with Praxis Publishing [Chichester], pp348-356.

Durham W. B., H. C. Heard, and S. H. Kirby, 1983. Experimental deformation of polycrystalline H_2O ice at high pressure and low temperature: preliminary results, *J. Geophys. Res.* **88**, B377-B392.

Durham W. B., S. H. Kirby, and L. A. Stern, 1992. Effects of dispersed particulates on the rheology of water ice at planetary conditions, *J. Geophys. Res.* **97**, (E12), 20883-20897.

Durham W. B., S. H. Kirby, and L. A. Stern, 1999. The rheology of solid carbon dioxide: new measurements, LPSC XXX, abstract #2017.

Eberhardt P., M. Reber, D. Krankowsky, and R. R. Hodges, 1995. The D/H and $^{18}O/^{16}O$ ratios in water from comet P/Halley, *Astron. Astrophys.* **302**, 301-316.

Ebert S., M. Thiel, C. Rohé, and A. Steinhof, 2000. Rosetta lander subsystem landing gear tests of the ice screws, Rosetta project document RO-LLG-TR-350001-ASt rev. 0.

Eckert E. R. G. and R. M. Drake Jr, 1972, "Analysis of heat and mass transfer", McGraw-Hill Book Company [New York], pp 782.

Edgett K. S. and M. C. Malin, 1999. MGS MOC the first year: sedimentary materials and relationships, LPSC XXX, abstract #1029.

Edgeworth K. E., 1949. The origin and evolution of the Solar System, *Mon. Not. R. astron. Soc.* **109**, 600-609.

Eiden M. J. and P. Coste, 1991, The challenge of sample acquisition in a cometary environment, *ESA Journal* **15**, 199-211. This article also appears as:

> Eiden M. J. and P. Coste, 1992, The challenge of sample acquisition in a cometary environment, *Ann. Geophysicæ* **10**, 131-140.

Ellis H., R. D. Harrizon, and H. D. B. Jenkins, 1984. Editors of revised Nuffield advanced data book, Longman Group ltd [Harlow], pp133.

Eluszkiewicz J., 1993. On the microphysical state of the Martian seasonal caps, *Icarus* **103**, 43-48.

Emerich C., J. M. Lamarre, V. I. Moroz, M. Combes, N. F. Sanko, Y. V. Nikolsky, F. Rocard, R. Gispert, N. Coron, J. -P. Bibring, T. Encrenaz, and J. Crovisier, 1987. Temperature and size of the nucleus of comet P/Halley deduced from IKS infrared Vega 1 measurements, *Astron. Astrophys.* **187**, 839-842.

Fanale F. P. and Salvail J. R. 1984. An idealized short-period comet model: surface insolation, H_2O flux, dust flux, and mantle evolution, *Icarus* **60**, 476-511.

Farmer C. B., D. W. Davies, and D. D. LaPorte, 1976. Mars: northern summer ice cap - water vapour observations from Viking 2, *Science* **194**, 1339-1341.

Feldman W. C., S. Maurice, A. B. Binder, B. L. Barraclough, R. C. Elphic, and D. J. Lawrence, 1998. Fluxes of fast and epithermal neutrons from lunar prospector: Evidence for water ice at the lunar poles, *Science* **281** (5382), 1496-1500

Feltham P., 1966. "Deformation and strength of materials", Butterworths [London]

Fenzi M., E. Pozzi, and P. A. Coste, 1992. A system for the challenging task of collecting samples from a comet surface, Proc. of 5th European Space Mechanisms and Tribology Symposium, printed as ESA SP-334. pp137-142.

Fernández J. A., 1980. On the existence of a comet belt beyond Neptune. *Mon. Not. R. astro. Soc.* **192**, 481-491.

Fernández J. A., W.-H. Ip, 1983. On the time evolution of the cometary influx in the region of the terrestrial planets, *Icarus* **54**, 377-387.

Festou M. C., 1999. On the existence of distributed sources in comet comæ, *Space Sci. Rev.* **90**, 53-67.

Forget F., 1995. Mars CO_2 ice polar caps, in "Solar System Ices", ed. B. Schmitt, C. de Bergh, M. Festou, Kluwer Academic Publishing [Dordrecht], pp477-507.

Forget F., J. B. Pollack, and G. B. Hansen, 1995. Low brightness temperatures of martian polar caps: CO_2 clouds or low spectral emissivity?, *J. Geophys. Res.* **100**, 21 119, 21 234.

Foster J. L., A. T. C. Chang, D. K. Hall, W. P. Wergin, E. F. Erbe, and J. Barton, 1998. Carbon dioxide crystals: An examination of their size, shape, and scattering properties at 37 GHz and comparisons with water ice (snow) measurements, *J. Geophys. Res.* **103** (E11): 25839-25850.

Foster M. J., S. F. Green, N. McBride, and J. K. Davis, 1999. Detection of water ice on 2060 Chiron, *Icarus* **141**, 408-410.

Franks F., 1972. In "Water. A comprehensive treatise", ed. F. Franks, Plenum Press [New York, London], pp142.

Fulle M., L. Colangelli, V. Mennella, A. Rotundi, E. Bussoletti, 1997. Simulation of the dust flux on the *Rosetta* probe during the orbiting phase around comet 46P/Wirtanen, *Astron. Astrophys.* supp. series **126**, 183-195.

Garry J. R. C., 2001. Experiments on drilling cold water ices for planetary sampling, proc. of Penetrometry Workshop (Graz), ed. N. I. Kömle, G. Kargl, A. J. Ball, R. D. Lorenz, Österreichischen Akademie der Wissenschaften [Vienna], pp41-47.

Garry J. R. C., M. C. Towner, A. J. Ball, J. C. Zarnecki, and G. Marçou, 1999. The effect of ambient pressure and impactor geometry on low speed penetration of unconsolidated materials, *Adv. Space Res.* **23** (7), 1229-1234.

Geiss J., 1987. Composition measurements and the history of cometary matter, *Astron. Astrophys.* **187**, 859-866.

Geiss J., K. Altwegg, E. Anders, H. Balsiger, W. -H Ip, A. Meier, M. Neugebauer, and E. G. Shelley, 1991. Interpretation of ion mass spectra in the mass per charge range 25-35 amu/e obtained in the inner coma of Halley's comet by the HIS-sensor of the Giotto IMS experiment, *Astron. Astrophys.* **247**, 226-234.

Gensheimer P. D., R. Mauersberger, and T. L. Wilson, 1996. Water in galactic hot cores. *Astron. Astrophys.* **314**, 281-294.

Giauque W. F. and C. J. Egan, 1937. Carbon dioxide. The heat capacity and vapor pressure of the solid. The heat of sublimation. Thermodynamic and spectroscopic values of the entropy. *J. Chem. Phys.* **5**, 45-54.

Giauque W. F. and J. W. Stout, 1936. The entropy of water and the third law of thermo-dynamics. The heat capacity of ice from 15 to 273°K, *J. Am. Chem. Soc.* **58**, 1144-1150.

Gombosi T. I., T. E. Cravens, and A. F. Nagy, 1985. Time-dependent dusty gasdynamical flow near cometary nuclei, *Ap. J.* **293**, 328-341.

Gooding J. L. (editor) 1990. "Scientific guidelines for preservation of samples collected from Mars", NASA TM 4184, NASA [Houston, Texas], pp15-16.

Gray D. E., 1972. "American Institute of Physics Handbook", McGraw-Hill Book Co. [New York], pp4-106.

Green J. R., 1998. The Deep Space 4 / Champollion comet simulation laboratory, IAU Colloquium 168 "Cometary nuclei in time and space", May 18-22, Nanjing, China. abstract #59.30.

Greenberg R., P. Geissler, D. O'Brien, G. V. Hoppa, and B. R. Tufts, 2001. Ocean-to-surface linkages resurface Europa: an invited review, Lunar and Planetary Science Conference XXXII, abstract #1428.

Griffin R. H., 1995. Seismic design provisions for roller compacted concrete dams, US Army Corps of Engineers, document EP 1110-2-12. Appendix E.

Gromov V. V., A. V. Misckevich, E. N. Yudkin, H. Kochan, P. Coste, and E. Re, 1997. The mobile penetrometer, a "mole" for sub-surface soil investigation, ESA-SP 410, 151-156.

Grün E., H. Kochan, and K. J. Seidensticker, 1991. Laboratory simulation, a tool for comet research, *Geophys. Res. Lett.* **18** (2), 245-248.

Haas J. W. and J. D. Shinn, 2000. Miniature cone penetrometer for *in situ* characterization and sampling of the Martian subsurface, proceedings of Concepts and approaches for Mars Exploration, hosted by the Lunar and Planetary Institute, abstract #6115.

Hansen G. B., 1995. The spectral absorption of CO_2 ice from the UV to the far-infrared, 27th meeting of the Division for Planetary Sciences of the American Astronomical Society, Hawaii, abstract #12.08

Hapke B., 1990. Coherent backscatter and the radar characteristics of outer planet satellites, *Icarus* **88**, 407-417.

Harmon J. K., D. B. Campbell, A. A. Hine, I. I. Shapiro, and B. G. Marsden, 1989. Radar observations of comet IRAS-Araki-Alcock 1983d, *Ap. J.* **338**, 1071-1093.

Harmon J. K., P. J. Perillat, and M. A. Slade, 2001. High-resolution radar imaging of Mercury's north pole, *Icarus* **149**, 1-15.

Harmon J. K., M. A. Slade, R. A. Vélez, A. Crespo, M. J. Dryer, and J. M. Johnson, 1994. Radar mapping of Mercury's polar anomalies, *Nature* **369**, 213-215.

Harris W. M., M. R. Combi, R. K. Honeycutt, B. E. A. Mueller, F. Scherb, 1997. Evidence for interacting gas flows and an extended volatile source distribution in the coma of comet C/1996 B2 (Hyakutake), *Science* **277**, 676-681.

Hart H. M. and B. M. Jakosky, 1986. Composition of the condensate observed at the Viking Lander 2 site on Mars, *Icarus* **66**, 134-142.

Haubold H. J., 1997. Entry for 'Tycho Brahe' in "Encyclopedia of Planetary Sciences", ed. J. H. Shirley and R. W. Fairbridge, Chapman and Hall [London], pp70.

Hesselbarth P., D. Krankowsky, P. Lämmerzahl, K. Mauersberger, A. Winkler, P. Hsiung, and K. Rössler, 1991. Gas release from ice/dust mixtures, *Geophys. Res. Lett.* **18** (2), 269-272.

Heucke E., 1999. A light portable steam-driven ice drill suitable for drilling holes in ice and firn, *Geografisika Annaler* Series A – Physical Geography, **81** (4), 603-609.

Herr K. C. and Pimentel G. C., 1969. Infrared absorptions near three microns recorded over the polar cap of Mars, *Science* **166** (3904), 496-499.

Horvath J., F. Carsey, J. Cutts, J. Jones, E. Johnson, B. Landry, L. Lane, G. Lynch, K. Jezek, J. Chela-Flores, T-W Jeng, and A. Bradley, 1997. Searching for ice and ocean biogenic activity on Europa and Earth, proc. SPIE 3111, 490-500.

Houlsby G. T. and R. Hitchman, 1988. Calibration chamber tests of a cone penetrometer in sand, *Géotechnique* **38** (1), 39-44.

Hsiung P. and K. Roessler, 1990. Diffusion of volatiles in cometary analogs, Lunar and Planetary Science Conference XXI, pp538-539.

Hudson R. L. and B. Donn, 1991. An experimental study of the sublimation of water ice and the release of trapped gases. *Icarus* **94**, 326-332.

Huebner W. F., (editor) 1990. "Physics and chemistry of comets", in the Astronomy and Astrophysics library series of Springer-Verlag [Berlin].

Huebner W. F., D. C. Boice, H. U. Schmitt, and R. Wegmannm 1991. Structure of the coma: chemistry and solar wind interaction, in "Comets in the Post-Halley Era" Vol 2. ed. R. L. Newburn Jr, M. Neugebauer, and J. Rahe, Kluwer Academic Publishers [Dordrecht], pp907-936.

Huebner W. F. and J. M. Greenberg, 2000. Needs for determining strength and bulk properties of NEOs, *Planet. Space Sci.* **48**, 797-799.

Hughes D. W., 1991. Possible mechanisms for cometary outbursts, in "Comets in the post-Halley era", Vol 2. ed. R. L. Newburn Jr, M. Neugebauer, and J. Rahe, Kluwer Academic Publishers [Dordrecht], pp825-851.

Hughes D. W., 1996. The interior of a cometary nucleus, *Planet. and Space Sci.* **44** (7), 705-710.

Huntress Jr. W. T., 1999. Missions to comets and asteroids, *Space Sci. Rev.* **90**, 329-340.

Hut P., W. Alvarez, W. P. Elder, T. Hansen, E. G. Kauffman, G. Keller, E. M. Shoemaker, and P. R. Weissman, 1987. Comet showers as a cause of mass extinctions, *Nature* **329**, 118-126.

Ibadinov Kh. I., 1989. Laboratory investigation of the sublimation of comet nucelus models, *Adv. Space Res.* **9** (3), (3)97-(3)112.

Ibadinov Kh. and E. A. Kaimakov, 1970. Formation and destruction of dust matrices during sublimation of dusty ice, *Komety i Meteory* **19**, 20-24.

Jakosky B. M., 1985. The seasonal cycle of water on Mars, *Space Sci. Rev.* **41**, 131-200.

Jakosky B. M. and E. S. Barker, 1984. Comparison of ground-based and Viking orbiter measurements of martian water vapour: variability of the seasonal cycle, *Icarus* **57**, 322-334.

Jenniskens P. and D. F. Blake, 1994. The structural changes of water ice I during warmup, Lunar and Planetary Science Conference XXV, pp621-622.

Jessberger E. K., A. Christoforidis, and J. Kissel, 1988. Aspects of the major element composition of Halley's dust, *Nature* **332**, 691-695.

Jessberger H. L. and M. Kotthaus, 1989. Compressive strength of synthetic comet nucleus samples, proc. "International Workshop on Physics and Chemistry of Cometary Materials", held Münster, October 9-11, printed as ESA SP-302 [Noordwijk], 141-146.

Jewitt D., 1999. Kuiper belt objects, *Annu. Rev. Earth. Planet. Sci.* **27**, 287-312.

Jewitt D. and J. Luu, 1992. International Astronomical Union Circular 5611.

Johnson N. L., 1979. "Handbook of Soviet lunar and planetary exploration", volume 47 in the AIAA Science and Technology series, published by Univelt Inc. [San Diego]

Jones S. J., 1997. High strain-rate compression tests on ice, *J. Phys. Chem. B.* **101**, 6099-6101.

Joss P. C., 1973. On the origin of short-period comets, *Astron. Astrophys.* **25**, 271-273.

Kapitsa A. P., J. K. Ridley, G. de Q. Robin, M. J. Siegert, and I. A. Zotikov, 1996. A large deep freshwater lake beneath the ice of central east Antarctica, *Nature* **381**, 684-686.

Kargl G., 1998. Physical processes on the surface of a cometary nucleus: experimental investigation of the influence of organic constituents on the thermal properties, Doctoral thesis for the Institute of Geophysics and Meteorology, Karl-Franzens University, Graz, Austria.

Kargel J. S., J. Z. Kaye, J. W. Head III, G. M. Marion, R. Sassen, J. K. Crowleym O. P. Ballesteros, S. A. Grant, D. L. Hogenboom, 2000. Europa's crust and ocean: origin, composition, and the prospects for life, *Icarus* **148**, 226-265.

Kato M., Y. Iijima, Y. Okimura, M. Arakawa, N. Maeno, A. Fujimura, and H. Mizutani, 1992. Impact experiments on low temperature H_2O, in "Physics and Chemistry of Ice". ed. N. Maeno and T. Hondoh, Hokkaido University Press [Sapporo], pp237-244.

Kaye J. A., 1987. Mechanisms and observations for isotope fractionation of molecular species in planetary atmospheres, *J. Geophys. Res.* **25** (8), 1609-1658.

Kerr R. A., 1988. Another asteroid has turned comet, *Science* **241**, 1161.

Keller H. U., 1990. The Nucleus, in "Physics and Chemistry of Comets". ed. W. F. Huebner, Springer-Verlag [Berlin], pp13-68.

Keller, H. U., C. Arpigny, C. Barbieri,R. M. Bonnet, S. Cazes, M. Coradini, C. B. Cosmovici, W. A. Delamere. W. F. Huebner, D. W. Hughes, C. Jamar, D. Malaise, H. J. Reitsema, H. U. Schmidt, W. K. H. Schmidt, P. Seige, F. L. Whipple, and K. Wilhelm, 1986. First Halley multicolour camera imaging results from Giotto, *Nature* **321**, 320-326.

Khurana K. K., M. G. Kivelson, D. J. Stevenson, G. Schubert, C. T. Russell, R. J. Walker, and C. Polanskey, 1998. Induced magnetic fields as evidence for subsurface oceans in Europa and Callisto, *Nature* **395**, 777-780.

Khusnatdinov N. N. and V. F. Petrenko, 1996. Fast-growth technique for ice single crystals, *J. Crystal Growth* **163**, 420-425.

Kieffer H. H., 1979. Mars south polar spring and summer temperatures: a residual CO_2 frost, *J. Geophys. Res.* **84** B14, 8263-8288.

Kieffer H. H., 2000. Annual punctuated CO_2 slab-ice and jets on Mars, 2nd international conference on Mars polar science and exploration [Reykjavik], abstract #4095.

Kieffer H. H., S. C. Chase, T. Z. Martin, E. D. Miner, and F. D. Palluconi, 1976. Martian north pole summer temperatures: dirty water ice, *Science* **194**, 1341-1343.

Klinger J., 1981. Some consequences of a phase transition of water ice on the heat balance of comet nuclei, *Icarus* **47**, 320.

Klinger J., 1989. Physical processes in cometary ices inferred from laboratory studies, proc. "International Workshop on Physics and Chemistry of Cometary Materials", held Münster, October 9-11, printed as ESA SP-302 [Noordwijk], 55-63.

Klinger J., A. C. Chantal Levasseur-Regourd, N. Bouziani, and A. Enzian, 1996. Towards a model of cometary nuclei for engineering studies for future space missions to comets, *Planet. Space Sci.* **44** (7), 637-653.

Kobayashi T. and T. Kuroda, (1987), in "Morphology of Crystals, Part B". ed. I. Sunagawa, Terra Scientific Publishing [Tokyo], pp654-656.

Kochan H., K. Roessler, L. Ratke, M. Heyl, H. Hellman, and G. Schwehm, 1989. Crustal strength of different model comet materials, proc. "International Workshop on Physics and Chemistry of Cometary Materials", held Münster, October 9-11, printed as ESA SP-302 [Noordwijk], 115-119.

Kömle N. I., A. J. Ball, G. Kargl, J. Stöcker, M. Thiel, H. S. Jolly, M. Dziruni, and J. C. Zarnecki, 1997. Using the anchoring device of a comet lander to determine surface mechanical properties, *Planet. Space Sci.* **45** (12), 1515-1538.

Kömle N. I., G. Kargl, K. Thiel, and K. Seiferlin, 1996. Thermal properties of cometary ices and sublimation residua including organics, *Planet. Space Sci.* **44** (7), 675-689.

Kossacki K. J., N. I. Kömle, G. Kargl, and G. Steiner, 1994. The influence of grain sintering on the thermoconductivity of porous ice, *Planet. Space Sci.* **42**, 383-389.

Kossacki K. J., N. I. Kömle, J. Leliwa-Kopystynski, and G. Kargl, 1997. Laboratory investigation of the evolution of cometary analogs: results and interpretation, *Icarus* **128**, 127-144.

Kossacki K. J., W. J. Markiewicz, Yu. Skorov, and N. I. Kömle, 1999. Sublimation coefficient of water ice under simulated cometary-like conditions, *Planet. Space Science* **47**, 1521-1530.

Kragelsky I. V., 1981. "Friction, wear, lubrication - tribilogy handbook", Pergamon Press, [Oxford].

Krankowsky D., P. Lämmerzahl, I. Herrwerth, J. Woweries, P. Eberhardt, U. Dolder, U. Herrmann, W. Schulte, J. J. Berthelier, J. M. Illiano, R. R. Hodges, and J. H. Hoffman, 1986. In situ gas and ion measurements at comet Halley, *Nature* **321**, 326-329.

Kronenberg M., 1949. Math cuts cost of machining studies, *Am. Mech.* September 22 issue, 104-106.

Kronk G. W., 1999. "Cometography: A catalog of comets", volume 1: Ancient-1799, Cambridge University Press [Cambridge], pp1.

Kuiper G. P., 1955. On the martian surface features, *Pub. A.S.P.* **67** (398), 271-282.

Kührt E. and H. U. Keller, 1994. The formation of cometary surface crusts, *Icarus* **109**, 121-132.

Lämmerzahl P., 1995. Ice/dust mixtures in simulated space environment: a study of sublimation and related phenomena, *Adv. Space Res.* **15** (10), 19-28.

Lange M. A. and T. J. Ahrens, 1981. Fragmentation of ice by low velocity impact, *Proc. Lunar Planet. Sci.* **12B**, 1667-1687.

Lange M. A. and T. J. Ahrens, 1983. The dynamic tensile strength of ice and ice-silicate mixtures, *J. Geophys. Res.* **88**, B2, 1197-1208.

Larson H. P. and U. Fink, 1972, Identification of carbon dioxide frost on the martian polar caps, *Ap. J.*, **171**, L91-L95.

Laufer D., G. Notesco, and A. Bar-Nun, 1999. From the interstellar medium to Earth's oceans via comets - an isotopic study of HDO/H_2O, *Icarus* **140**, 446-450.

LaViolette P. A., 1987. The cometary breakup hypothesis re-examined, *Mon. Not. R. astr. Soc.* **224**, 945-951.

Le Mouélic S., O. Forni, and E. Quirico, 2001. Near infrared spectral observations of the asteroid 140 Siwa, second flyby target of the Rosetta mission, Lunar and Planetary Science Conference XXXII, abstract #1094.

Lebofsky L. A., 1975. Stability of frosts in the Solar System, *Icarus* **25**, 205-217.

Lide D. R., 2000, CRC Handbook of Chemistry and Physics, CRC Press [Boca Raton], pp12-201.

Liley P. E., 1987, Thermophysical properties, in "Handbook of single-phase convective heat transfer", ed. S. Kakaç, R. K. Shas, and W. Aung, John Wiley and Sons Inc. [New York], pp22-32.

Lisse C. M., Y. R. Fernández, A. Kundu, M. F. A'Hearn, A. Dayal, L. K. Deutsch, G. G. Fazio, J. L. Hora, and W. F. Hoffmann, 1999. The nucleus of comet Hyakutake (C/1996 B2), *Icarus* **140**, 189-204.

Lobban C., J. L. Finney, and W. F. Kuhs, 1998. The structure of a new phase of ice, *Nature* **391**, 268-270.

Lodders K. and B. Fegley Jr., 1998. "The Planetary Scientist's Companion", Oxford University Press, [New York], pp207.

Lœwy M. and P. Puiseux, 1897. Article on 'The photographs of the Moon taken at the Paris observatory', *Nature* **56**, 280-281.

Lowell P., 1908. "Mars as the abode of life", Macmillan [New York], pp81-82.

Lunne T., P. K. Robertson, and J. J. M. Powell, 1997. "Cone penetration testing in geotechnical practice", Chapman and Hall [London], pp1-7.

Marchesi M., R. Campaci, P. Magnani, R. Mugnuolo, A. Nista, A. Olivieri, and E. Re, 2001. Comet sample acquisition for Rosetta lander mission, proc. of 9th European Space Mechanisms and Tribology Symposium, ESA SP-480, pp91-96.

Mason B. J., 1992. Snow crystals, natural and man made, *Contemporary Physics* **33** (4), 227-243.

Matese J. and D. Whitmire, 1996. Tidal imprint of distant galactic matter on the Oort comet cloud, *Ap. J.* **472**, L41-L43.

Maurer W. C., 1968. "Novel Drilling Techniques", Pergamon Press Ltd [London], pp96

Mayer E. and A. Hallbrucker, 1987. Cubic ice from liquid water, *Nature* **325**, 601-602.

McCord T. B., G. B. Hansen, F. P. Fanale, R. W. Carlson, D. L. Matson, T. V. Johnson, W. D. Smythe, J. K. Crowley, P. D. Martin, A. Ocampo, C. A. Hibbitts, J. C. Granahan, and the NIMS team, 1998. Salts on Europa's surface detected by Galileo's Near Infrared Mapping Spectrometer, *Science* **280**, 1242-1245.

McCord T. B., G. B. Hansen, and C. A. Hibbitts, 2001. Hydrated salt minerals on Ganymede's surface: Evidence of an ocean below, *Science* **292**, 1523-1525.

McCord T. B., G. B. Hansen, D. L. Matson, T. V. Johnson, J. K. Crowley, F. P. Fanale, R. W. Carlson, W. D. Smythe, P. D. Martin, C. A. Hibbitts, J. C. Granahan, A. Ocampo, 1999. Hydrated salt minerals on Europa's surface from the Galileo near-infrared mapping spectrometer (NIMS) investigation, *J. Geophys. Res.* **104**, E5, 11827-11851.

Meier R., T. C. Owen, H. E. Mattews, D. C. Jewitt, D. Bockelée-Morvan, N. Biver, J. Crovisier, and D. Gautier, 1998. A determination of the HDO/H_2O ratio in comet C/1995 O1 (Hale-Bopp), *Science* **279**, 842-844.

Mekler Yu., D. Prialnik, and M. Podolak, 1990. Evaporation from a porous cometary nucleus, *Ap. J.* **356**, 682-686.

Mellor M., 1989. First impressions of the comet drilling problem, proc. "International Workshop on Physics and Chemistry of Cometary Materials", held Münster, October 9-11, printed as ESA SP-302 [Noordwijk], 229-232.

Moore, M. H. Carr, J. M. Moore, M. J. S. Belton, and D. L. Goldsby, 1998. Geological evidence for solid-state convection in Europa's ice shell, *Nature* **391**, 365-368.

Morrison D. (editor), 1982. "Satellites of Jupiter", University of Arizona Press [Tucson].

Muirhead B. and S. Kerridge, 1999. The Deep Space 4 / Champollion mission, *Acta Astronautica* **45** (4-9), 407-414.

Nakaya U., 1954. "Snow Crystals: Natural and Artificial", Harvard University Press [Cambridge], pp23.

Narita H., K. Shinbori, and Y. Kodama, 1994. An experiment on ice cutting under high liquid pressure and low temperature, *Mem. Natl. Inst. Polar Res.* Special Issue **49**, 124-131.

Narten A. H., C. G. Venkatesh, and S. A. Rice, 1976. Diffraction pattern and structure of amorphous solid water at 10 and 77°K, *J. Chem. Phys.* **64**, 1106-1121.

Neal C. R., 2000. Issues involved in a Martian sample return: Integrity preservation and the Curation and Analysis Planning Team for Extraterrestrial Materials (CAPTEM) position, *J. Geophys. Res.* **105** (E9), 22487-22506.

Needham A. E., 1965. "The uniqueness of biological materials", Pergamon Press, [Oxford], pp13-14.

Nelson R. N., B. P. Michael, and J. E. Allen Jr. 1999. Experimentally determined vapor pressures of carbon dioxide from 167 to 87 K, 31st Meeting of the Division for Planetary Sciences of the American Astronomical Society.

Neugebauer M. and J.-P. Bibring, 1998. Champollion, *Adv. Space Res.* **21** (11), 1567-1575.

Newburn Jr. R. L., M. Neugebauer, and J. Rahe, 1991. "Comets in the post-Halley era", Vol I and II, Kluwer Academic Publishers, [Dordrecht].

Nozette S., C. L. Lictenberg, P. Spudis, R. Bnner, W. Ort, E. Malaret, M. Robinson, and E. M. Shoemaker, 1996. The Clementine bistatic radar experiment, Science **274** (5292), 1495-1498.

Ocampo J., B. Schmitt, and J. Klinger, 1986. Risk of physical and chemical alteration of comet nucleus samples during transfer to Earth, proc. 'The Comet Nucleus Sample Return Mission'. held Canterbury, 15-17 July 1986; printed as ESA SP-249 [Noordwijk], 169-171.

Oort J. H., 1950. The structure of the cloud of comets surrounding the Solar System and a hypothesis concerning its origin. *Bull. Astron. Inst. Neth.* **11**, 91-110.

Ori G. G. and F. Ogliani, 1996. Potentiality of the ground penetrating radar for the analysis of the stratigraphy and sedimentology of Mars, *Planet. Space Sci.* **44** (11), 1303-1315.

Ostro S. J. and E. M. Shoemaker, 1990. The extraordinary radar echoes from Europa, Ganymede, and Callisto: a geological perspective, *Icarus* **85**, 335-345.

Paige D. A., D. S. Bass, and S. E. Wood, 1995. Mars polar caps: Viking evidence for clear solid CO_2 ice, 27th meeting of the Division for Planetary Sciences of the American Astronomical Society, Hawaii, abstract #15.05

Paige D. A., K. E. Herkenhoff, and B. C. Murray, 1990. Mariner 9 observations of the south polar cap of Mars: evidence for residual CO_2 frost, *J. Geophys. Res.* **95** (B2), 1319-1335.

Pappalardo R. T., J. W. Head, R. Greeley, R. J. Sullivan, C. Pilcher, G. Schubert, W. B. Moore, M. H. Carr, J. M. Moore, M. J. S. Belton, D. L. Goldsby, 1998. Geological evidence for solid-state convection in Europa's ice shell, *Nature* **391**, 365-368.

Peale, S. J., 1989. On the density of Halley's comet. *Icarus* **82** (1), 36-49.

Pilcher C. B., S. T. Ridgway, and T. B. McCord, 1972. Galilean satellites: identification of water frost, *Science* **178**, 1087-1089.

Pinkus R. L. B., L. J. Shuman, N. P. Hummon, and H. Wolfe, 1997. 'Engineering ethics : balancing cost, schedule, and risk - Lessons learned from the space shuttle', Cambridge University Press [Cambridge], pp149-170.

Plaut J. J., 1999. Probing the crust of Mars with orbital sounding radar: The MARSIS experiment on Mars Express, Lunar and Planetary Science Conference XXX, abstract #1136.

Podolak M. and D. Prialnik, 1996. Models of the structure and evolution of comet P/Wirtanen, *Planet Space Sci.* **44** (7), 655-664.

Prialnik D. and A. Bar-Nun, 1988. The formation of a permenent dust mantle and its effect on cometary activity, *Icarus* **74**, 272-283.

Prieto O. and J. S. Kargel, 2001, Specific heat capacity data of some hydrated salts at low temperature. Applications to Europa satellite, Lunar and Planetary Science Conference XXXII, abstract #1625.

Prieto O. and J. S. Kargel, 2002, Thermal conductivity and thermal diffusivity of some hydrated salts at low temperatures: implications for Jupiter's satellite, Europa, Lunar and Planetary Science Conference XXXIII, abstract #1726.

Raphael, J. M., 1984. The tensile strength of concrete, *J. of the American Concrete Institute* **81** (2), 158-165.

Reinhard R., 1986. The Giotto project, ESA-SP **1066**, 25-48.

Rickman H., 1986. Masses and densities of comets Halley and Kopff, proc. 'The Comet Nucleus Sample Return Mission'. held Canterbury, 15-17 July 1986; printed as ESA SP-249 [Noordwijk], 195-205.

Rickman H. 1994. Cometary nuclei, proc. Asteroids Comets and Meteors 1993, ed. A. Milani, M. Di Martino, A. Cellino, Kluwer [Dordrecht], 297-312.

Rickman H., J. A. Fernández, and B. Å. S. Gustafson, 1990. Formation of stable dust mantles on short-period comet nuclei, *Astron. Astrophys.* **237**(2), 524-535.

Robert F., 2001. The origin of water on Earth, *Science* **293**, 1056-1058.

Roessler K., P. Hsiung, H. Kochan, H. Hellmann, H. Düren, K. Thiel, and G. Kölzer, 1989. A model comet made from mineral dust and H_2O-CO_2 ice: sample preparation development, Lunar and Planetary Science Conference XX, abstract #920.

Roessler K. and B. Nebeling, 1986. Temperature recommendation to preserve a chemical staus quo of cometary samples, proc. 'The Comet Nucleus Sample Return Mission'. held Canterbury, 15-17 July 1986; printed as ESA SP-249 [Noordwijk], 165-167.

Rosenberg H. M., 1965. 'Low temperature solid state physics, some selected topics', Clarendon Press [Oxford], pp126.

Roush T. L., J. B. Pollack, F. C. Witteborn, and J. D. Bregman, 1990. Ice and minerals on Callisto: a reassessment of the reflectance spectra, *Icarus* **86**, 355-382.

Ruzmaikina T. V., 1997. Solar system: origin, in 'Encyclopedia of Planetary Sciences', ed. J. H. Shirley and R. W. Fairbridge, Chapman and Hall [London], pp756-762.

Ruzmaikina T. V., 1999. Role of volatiles in a tidal disruption of ice rich bodies, Lunar and Planetary Science Conference XXVIII, abstract #1719.

Sack N. J. and R. A. Baragiola, 1993. Sublimation of vapor-deposited water ice below 170 K, and its dependence on growth conditions, *Phys. Rev. B* **48** (14), 9973-9978.

Sagdeev R. Z., G. A. Avanesov, Y. L. Ziman, V. I. Moroz, V. I. Tarnopolsky, B. S. Zhukov, V. A. Shamis, B. Smith, I. Tóth, 1986. TV experiment of the Vega mission: image processing technique and some results, in 20th ESLAB Symposium on the Exploration of Halley's comet, ed. B. Battrick, E. J. Rolfe, and R. Reinhard, printed as ESA SP-250 II [Noordwijk], 317-326.

Saunders R. S., F. P. Fanale, T. J. Parker, J. B. Stephens, and S. Sutton, 1986. Properties of filamentary sublimation residues, *Icarus* **66**, 94-104.

Scheeres D. J., F. Marzari, L. Tomasella, and V. Vanzani, 1998. Rosetta mission: satellite orbits around a cometary nucleus, *Planet. Space Sci.* **46** (6/7), 649-671.

Schenk P. M. and W. B. McKinnon, 1997. 'Callisto' in 'Encyclopedia of Planetary Sciences', ed. J. H. Shirley and R. W. Fairbridge, Chapman and Hall [London], pp73-75.

Schubert G., T. Spohn, and R. T. Reynolds, 1986. Thermal histories, compositions and internal structures of the moons of the Solar System, in "Satellites", ed. J. A. Burns and M. S. Matthews, University of Arizona Press [Tucson], pp228.

Schulson E. M., 1999. The structure and mechanical behaviour of ice, *J. of Metals* **51** (2), 21-27.

Schwehm G. and R. Schulz, 1999. Rosetta goes to comet Wirtanen, *Space Sci. Rev.* **90**, 313-319.

Sears D. W. G. and B. C. Clark, 2000. Sample collection devices for near-Earth asteroid sample return, 1st Near-Earth Asteroid Sample Return, abstract #8036.

Sears D. W. G., H. W. Kochan, and W. F. Huebner, 1999. Laboratory simulation of the physical processes occurring on and near the surfaces of comet nuclei, *Meteorit. Planet. Sci.* **34**, 497-525.

Seidensticker K. J., H. Kochan, and D. Möhlmann, 1995. The DLR small simulation chamber: a tool for cometary research in the lab, *Adv. Space Res.* **15** (10), 29-34.

Seiferlin K., N. I. Kömle, G. Kargl, T. Spohn, 1996. Line heat-source measurements of the thermal conductivity of porous H_2O ice, CO_2 ice and mineral powders under space conditions, *Planet. Space Sci.* **44** (7), 691-704.

Seiferlin K., T. Spohn, and J. Benkhoff, 1995. Cometary ice texture and the thermal evolution of comets, *Adv. Space Res.* **15** (10), 35-38.

Sekanina Z., 1982. The problem of split comets in review, in "Comets", ed. L. L. Wilkening, University of Arizona Press [Tucson], pp251-287.

Sekanina Z., 1991. Cometary activity, discrete outgassing areas, and dust-jet formation, in "Comets in the Post-Halley Era" vol 2, ed. R. Newburn and J. Rahe, Kluwer Academic [Dordrecht], pp769-823.

Sekanina Z. and D. K. Yeomans, 1985. Orbital motion, nucleus precession, and splitting of comet Brooks 2, *Astron. J.* **90**, 2335-2352.

Sgubini S. and A. Buratti, 1989. Thermal perturbation of comet samples during their acquisition, proc. "International Workshop on Physics and Chemistry of Cometary Materials", held Münster, October 9-11, printed as ESA SP-302 [Noordwijk], 153-158.

Shandera S. E. and R. D. Lorenz, 2000. Thermal conductivity and microwave absorptivity of ammonia hydrate ice, Lunar and Planetary Science Conference XXX, abstract #1485.

Shapiro L. H., J. B. Johnson, M. Sturm, and G. L. Blaisdell, 1997. Snow mechanics. Review of the state of knowledge and applications, Cold Regions Research and Engineering Laboratory report 97-3.

Shaw M. C., 1984. "Metal Cutting Principles", Clarendon Press [Oxford].

Sheenan W., 1996. "The Planet Mars: A History of Observation and Discovery", University of Arizona Press, [Tucson].

Siegel R. and J. R. Howell, 1981. "Thermal Radiation Heat Transfer", 2nd edition, Hemisphere Publishing Corporation [London], pp135.

Siegert, M J., J. A. Dowdeswell, M. R. Gorman, and N. F. McIntyre, 1996. An inventory of Antarctic subglacial lakes, *Antarctic Science* **8**, 281-286.

Simpson R. A., B. C. Fair, and H. T. Howard, 1980. Microwave properties of solid CO_2, *J. Geophys. Res.* **85**(B10), 5481-5484.

Slack G. A., 1980. Thermal conductivity of ice, *Phys. Rev. B* **22**(6), 3065-3071.

Slade M. A., Butler B. J., and Muhleman D. O., 1992. Mercury radar imaging: evidence for polar ice, *Science* **258**, 635-640.

Slipher E. C., 1962. "The Photographic Story of Mars", Sky Publishing Corporation [Cambridge, Mass.], pp15.

Smith D. E., M. T. Zuber, and G. A. Neumann, 2001. Seasonal variation of snow depth on Mars, *Science* **294**, 2141-2146.

Smoluchowski R. and M. A. Marie, 1983. Mobility of pores in ices in the solar system, Lunar and Planetary Science Conference 14, 719-720.

Smoluchowski R. and A. McWilliam, 1984. Structure of ices on satellites, *Icarus* **58**, 282-287.

Soderblom L. A., D. C. Boice, D. T. Britt, R. H. Brown, B. J. Buratti, M. D. Hicks, R. M. Nelson, J. Oberst, B. R. Sandel, S. A. Stern, N. Thomas, R. V. Yelle, 2001. Observations of Comet 19P/Borrelly from the Miniature Integrated Camera and Spectrometer (MICAS) aboard Deep Space 1 (DS1), 33rd DPS meeting, abstract #26.02.

Solem J. C., 1993. Interception of comets and asteroids on collision course with Earth, *J. Spacecraft and Rockets* **30** (2), 222-228.

Space Studies Board, 1999. "A science strategy for the exploration of Europa", *Natl. Acad. Press*, [Washington].

Spencer-Jones H., 1947. "A picture of the Universe", Raven Books Limited [London], pp63.

Squyres S. W., C. P. McKay, and R. T. Reynolds, 1985. Temperatures within comet nuclei, *J. Geophys. Res.* **90**, B14 12381-12392.

Stabler G. V., 1951, The fundamental geometry of cutting tools, *Proc. Inst. Mech. Engng.*, **165**, 14-21.

Stacy N. J. S. D. B. Campbell, and P. G. Ford, 1997. Arecibo radar mapping of the lunar poles: a search for ice deposits, *Science* **276**, 1527-1530,

Starukhina L. V. and Yu. G. Shkuratov, 2000. The lunar poles: water ice or chemically trapped hydrogen?, *Icarus* **147**, 585-587.

Steel D. I., 1997. The ABC of ACM: asteroids, Buffon and comets, *Planet. Space Sci.* **45** (12), 1501-1503.

Steel D., 1998. Distributions and moments of asteroid and comet impact speeds upon the Earth and Mars, *Planet. Space Sci.* **46** (5), 473-478.

Steiner G. and N. I. Kömle, 1991. A model of the thermal conductivity of porous water ice at low gas pressures, *Planet. Space Sci.* **39** (3), 507-513.

Stevenson D. J., A. W. Harris, and J. I. Lunine, 1986. Origins of satellites, in "Satellites", ed. J. A. Burns and M. S. Matthews, University of Arizona Press, [Tucson], pp39-88, especially 47.

Stöffler D. and H. Düren, 1992. Cometary analogue material: types, tests, and results, *Ann. Geophysicæ* **10**, 206-216.

Stöffler D., H. Düren, J. Knölker, R. Hische, and A. Bischoff, 1991. Cometary analogue material: preparation, composition, and thin section petrography, *Geophys. Res. Lett.* **18** (2), 285-288.

Suzuki Y. and K. Shiraishi, 1982. The drill system used by the 21st Japanese Antarctic research expedition and its later improvement, *Mem. Natl. Polar Res.* Special Issue **24**, 259-273.

Taylor S. R., 1992. "Solar System Evolution: A New Perspective", Cambridge University Press.

Thompson T. D. (ed.), 1997. "Space Log 1996", TRW Space & Electronics Group [Redondo Beach].

Thomson W., 1863. On the secular cooling of the Earth, *Phil. Mag. and J. of Sci.*(ser. 4) **25**, no. 165, I, 1-14.

Thorpe J. F. and M. A. Whitely, 1966. "Thorpe's dictionary of applied chemistry", Longmans [London], pp325.

Tian X. and F. E. Kennedy, 1995. Prediction and measurement of surface temperature rise at the contact interface for oscillatory sliding, *Proc. Inst. Mech. Eng.* **209**, 41-51.

Tillman J. E., N. C. Johnson, P. Guttorp, and D. B. Percival. The martian annual atmospheric pressure cycle: years without great dust storms; special edition, *J. Geophys. Res.* **84**, 10,963-10.971, 1993. XXX

Torbett M. V., 1986. Injection of Oort cloud comets to the inner Solar System by galactic tidal fields, *Mon. Not. R. ast. Soc.* **223**, 885-895.

Trent E. M., 1977. "Metal Cutting", Butterworth & Co. ltd. [London].

Ulamec S., B. Feuerbacher, K. Wittmann, H. Rosenbauer, J.-P. Bibring, D. Moura, R. Mugnuolo, and G. Haerendel, 1997. Rosetta lander - in situ investigation of a comet's nucleus, Lunar and Planetary Science Conference XXVIII, abstract #1612.

Vasavada A. R., D. A. Paige, and S. E. Wood, 1999. Near-surface temperatures on Mercury and the Moon and the stability of polar ice deposits, *Icarus* **141**, 179-193.

Vasiliev N. I. and P. G. Talalay, 1994. Investigation of the ice cutting process by the rotary drill, *Mem. Natl. inst. Polar Res.* Special Issue **49**, 132-137.

Walker M. F., 1959. Observations of comet Schwassmann-Wachmann 1 during an outburst, *Publ. Astron. Soc. Pacific* **71**, 169-170.

Walsh M. R., 1999. The CRREL South Pole Tunneling System, Cold Regions Research & Engineering Laboratory report 99-1, pp7.

Warren S. G., W. J. Wiscombe, J. F. Firestone, 1990. Spectral albedo and emissivity of CO_2 in martian polar caps: model results, *J. Geophys. Res.* **95**, 14717-14741.

Weast R. C. (ed.), 1985. 66th CRC Handbook of Chemistry and Physics, CRC Press [Boca Raton].

Weaver H. A., P. D. Feldman, M. F. A'Hearn, C. Arpigny, J. C. Brandt, M. C. Festou, M. Haken, J. B. McPhate, S. A. Stern, G. P. Tozzi, 1997. The activity and size of the nucleus of comet Hale-Bopp (C/1995 O1), *Science* **275**, 1900-1904.

Weaver H. A. and D. Jewitt, 1995. "The great comet crash: the impact of comet Shoemaker-Levy 9 on Jupiter", ed. J. R. Spencer and J. Mitton, Cambridge University Press [Cambridge], pp49.

Weidenschilling S. J., 1997. The origin of comets in the solar nebula: a unified model, *Icarus* **127**, 290-306.

Weiss B. P. and A. P. Ingersoll, 2000. Cold spots in the martian polar regions: evidence of carbon dioxide depletion?, *Icarus* **144**, 432-435.

Weissman P. R., 1995. The Kuiper belt, *Annu. Rev. Astron. Astrophys.* **33**, 327-357.

Weissman P. R., 1997. Champollion: a comet lander and sample return demonstration mission, Lunar and Planetary Science Conference XXVIII, abstract #1785.

Weissman P. R., 1998. The Oort cloud., *Science* **279** (3), 84-89.

Whalley. E., 1983. Cubic ice in nature, *J. Phys. Chem.* **87**, 4174-4179.

Whipple F. L., 1987. The cometary nucleus: current concepts, *Astron. Astrophys.* **187**, 852-868.

Whitney C., 1955. Comet outbursts, *Ap. J.* **122**, 190-195.

Wynn-Williams D. D. and H. G. M. Edwards, 2000. Antarctic ecosystems as models for extraterrestrial surface habitats, *Planet. and Space Sci.* **48**, 1065-1075.

Yang G., A. D. Migone, and K. W. Johnson, 1992. Heat capacity and thermal diffusivity of a glass sample, *Phys. Rev. B* **45**, 157-160.

Zagorodnov V., L. G. Thompson, J. J. Kelley, B. Koci, and V. Mikhalenko, 1998. Antifreeze thermal ice core drilling: an effective approach to the acquisition of ice cores, *Cold Regions Science and Technology* **28**, 189-202.

Zahnle K., 2001. Cratering rates on Europa, Lunar and Planetary Science Conference XXXII, abstract #1699.

Zahnle K., L. Dones, and H. F. Levison, 1998. Cratering rates on the Galilean satellites, *Icarus* **136**, 202-222.

Zolotov M. Yu. and E. L. Shock, 2000. Freezing of oceanic water on Europa: Theoretical modelling, Lunar and Planetary Science Conference XXXI, abstract #1726.